Study of stabilisation and development of a downward inverse diffusion flame for an industrial optimisation

Khriscia Utria Salas

▶ **To cite this version:**

Khriscia Utria Salas. Study of stabilisation and development of a downward inverse diffusion flame for an industrial optimisation. Thermics [physics.class-ph]. Université de Lyon, 2022. English. NNT : 2022LYSEI044 . tel-04213377

HAL Id: tel-04213377

https://theses.hal.science/tel-04213377v1

Submitted on 21 Sep 2023

HAL is a multi-disciplinary open access archive for the deposit and dissemination of scientific research documents, whether they are published or not. The documents may come from teaching and research institutions in France or abroad, or from public or private research centers.

L'archive ouverte pluridisciplinaire **HAL**, est destinée au dépôt et à la diffusion de documents scientifiques de niveau recherche, publiés ou non, émanant des établissements d'enseignement et de recherche français ou étrangers, des laboratoires publics ou privés.

N°d'ordre NNT : 2022LYSEI044

THESE de DOCTORAT DE L'UNIVERSITE DE LYON
opérée au sein de
L'Institut National des Sciences Appliquées de Lyon

Ecole Doctorale MEGA N° ED 162
Mécanique, Energétique, Génie Civil, Acoustique

Spécialité/ discipline de doctorat :
Thermique et Energétique

Soutenue publiquement le 29/04/2022, par :
Khriscia UTRIA SALAS

Study of stabilisation and development of a downward inverse diffusion flame for an industrial optimisation

---

Devant le jury composé de :

HONORE, David	Professeur des Universités	Université de Rouen	Rapporteur
SCHULLER, Thierry	Professeur des Universités	Université Paul Sabatier	Rapporteur
MORIN, Céline	Professeure des Universités	Université Polytechnique Hauts-De-France	Examinatrice
KÜHNI, Manuel	Maître de Conférences	INSA-Lyon	Examinateur
LABOR, Serge	Docteur	RSA Le Rubis	Examinateur
GALIZZI, Cédric	Maître Conférences HDR	INSA-Lyon	Directeur de thèse

Cette thèse est accessible à l'adresse : http://theses.insa-lyon.fr/publication/2022LYSEI044/these.pdf
© [K. Utria Salas], [2022], INSA Lyon, tous droits réservés

Cette thèse est accessible à l'adresse : http://theses.insa-lyon.fr/publication/2022LYSEI044/these.pdf
© [K. Utria Salas], [2022], INSA Lyon, tous droits réservés

Département FEDORA – INSA Lyon - Ecoles Doctorales

SIGLE	ECOLE DOCTORALE	NOM ET COORDONNEES DU RESPONSABLE
CHIMIE	**CHIMIE DE LYON** **https://www.edchimie-lyon.fr** Sec. : Renée EL MELHEM Bât. Blaise PASCAL, 3e étage secretariat@edchimie-lyon.fr	**M. Stéphane DANIELE** C2P2-CPE LYON-UMR 5265 Bâtiment F308, BP 2077 43 Boulevard du 11 novembre 1918 69616 Villeurbanne **directeur@edchimie-lyon.fr**
E.E.A.	**ÉLECTRONIQUE, ÉLECTROTECHNIQUE, AUTOMATIQUE** **https://edeea.universite-lyon.fr** Sec. : Stéphanie CAUVIN Bâtiment Direction INSA Lyon Tél : 04.72.43.71.70 secretariat.edeea@insa-lyon.fr	**M. Philippe DELACHARTRE** INSA LYON Laboratoire CREATIS Bâtiment Blaise Pascal, 7 avenue Jean Capelle 69621 Villeurbanne CEDEX Tél : 04.72.43.88.63 **philippe.delachartre@insa-lyon.fr**
E2M2	**ÉVOLUTION, ÉCOSYSTÈME, MICROBIOLOGIE, MODÉLISATION** **http://e2m2.universite-lyon.fr** Sec. : Sylvie ROBERJOT Bât. Atrium, UCB Lyon 1 Tél : 04.72.44.83.62 secretariat.e2m2@univ-lyon1.fr	**M. Philippe NORMAND** Université Claude Bernard Lyon 1 UMR 5557 Lab. d'Ecologie Microbienne Bâtiment Mendel 43, boulevard du 11 Novembre 1918 69 622 Villeurbanne CEDEX **philippe.normand@univ-lyon1.fr**
EDISS	**INTERDISCIPLINAIRE SCIENCES-SANTÉ** **http://ediss.universite-lyon.fr** Sec. : Sylvie ROBERJOT Bât. Atrium, UCB Lyon 1 Tél : 04.72.44.83.62 secretariat.ediss@univ-lyon1.fr	**Mme Sylvie RICARD-BLUM** Institut de Chimie et Biochimie Moléculaires et Supramoléculaires (ICBMS) - UMR 5246 CNRS - Université Lyon 1 Bâtiment Raulin - 2ème étage Nord 43 Boulevard du 11 novembre 1918 69622 Villeurbanne Cedex Tél : +33(0)4 72 44 82 32 **sylvie.ricard-blum@univ-lyon1.fr**
INFOMATHS	**INFORMATIQUE ET MATHÉMATIQUES** **http://edinfomaths.universite-lyon.fr** Sec. : Renée EL MELHEM Bât. Blaise PASCAL, 3e étage Tél : 04.72.43.80.46 infomaths@univ-lyon1.fr	**M. Hamamache KHEDDOUCI** Université Claude Bernard Lyon 1 Bât. Nautibus 43, Boulevard du 11 novembre 1918 69 622 Villeurbanne Cedex France Tél : 04.72.44.83.69 **hamamache.kheddouci@univ-lyon1.fr**
Matériaux	**MATÉRIAUX DE LYON** **http://ed34.universite-lyon.fr** Sec. : Yann DE ORDENANA Tél : 04.72.18.62.44 yann.de-ordenana@ec-lyon.fr	**M. Stéphane BENAYOUN** Ecole Centrale de Lyon Laboratoire LTDS 36 avenue Guy de Collongue 69134 Ecully CEDEX Tél : 04.72.18.64.37 **stephane.benayoun@ec-lyon.fr**
MEGA	**MÉCANIQUE, ÉNERGÉTIQUE, GÉNIE CIVIL, ACOUSTIQUE** **http://edmega.universite-lyon.fr** Sec. : Stéphanie CAUVIN Tél : 04.72.43.71.70 Bâtiment Direction INSA Lyon mega@insa-lyon.fr	**M. Jocelyn BONJOUR** INSA Lyon Laboratoire CETHIL Bâtiment Sadi-Carnot 9, rue de la Physique 69621 Villeurbanne CEDEX **jocelyn.bonjour@insa-lyon.fr**
ScSo	**ScSo*** **https://edsciencessociales.universite-lyon.fr** Sec. : Mélina FAVETON INSA : J.Y. TOUSSAINT Tél : 04.78.69.77.79 melina.faveton@univ-lyon2.fr	**M. Christian MONTES** Université Lumière Lyon 2 86 Rue Pasteur 69365 Lyon CEDEX 07 **christian.montes@univ-lyon2.fr**

*ScSo : Histoire, Géographie, Aménagement, Urbanisme, Archéologie, Science politique, Sociologie, Anthropologie

Cette thèse est accessible à l'adresse : http://theses.insa-lyon.fr/publication/2022LYSEI044/these.pdf
© [K. Utria Salas], [2022], INSA Lyon, tous droits réservés

Abstract

English

Combustion has been the cornerstone of industrial development for nearly two centuries, providing heat for many industrial processes and accounting for over 80% of the power used by turbines to generate electricity. Over the years, much progress has been made in understanding the fundamental science of combustion. Nevertheless, regulatory and competitive forces are driving the need for combustion equipment with better performance, lower environmental impact, and greater flexibility, all at a reasonable cost (e.g. Paris agreement 2015, UN Climate Change Conference (COP26) 2021). Keep in mind that the existing energy system is primarily non-renewable, using carbon-based energy sources. The new energy transition challenges require installing and integrating a new renewable energy system while securing the supply and resilience of the actual demand. Hydrogen, considered by many the clean alternative fuel, seems to be one of the answers. Despite the associated security issues, developing this technology contributes to countries meeting their climate goals, boosting green growth and creating sustainable jobs.

This thesis is part of the actions carried out at the collaborative laboratory RAInBOV that associates the Cethil and the company RSA. They specialise in the manufacture of sapphire crystals, mainly used in the field of watchmaking and glass. Their production requires fusing the raw material and crystallising it. To this effect, they use the Verneuil method, which consists of a downward vertical burner that generates an H_2/O_2 inverse diffusion flame located in a confined enclosure and loaded with alumina particles deposited on a crystalline seed. Within this framework, this thesis's main objective is to comprehend the aerothermochemical mechanisms present in this configuration. Concretely, the stabilisation, the structure and the development of the flames produced by this particular burner are analysed along the thermal behaviour of the crystal growth environment.

Français

La combustion est la pierre angulaire du développement industriel depuis près de deux siècles, fournissant de la chaleur pour de nombreux procédés industriels et représentant plus de 80% de la puissance utilisée par les turbines pour produire de l'électricité. Au fil des ans, de nombreux progrès ont été réalisés dans la compréhension de la science fondamentale de la combustion. Néanmoins, les forces réglementaires et concurrentielles engendrent le besoin d'équipements de combustion plus performants, avec un impact environnemental moindre et une plus grande flexibilité, le tout à un coût raisonnable (par

Cette thèse est accessible à l'adresse : http://theses.insa-lyon.fr/publication/2022LYSEI044/these.pdf
© [K. Utria Salas], [2022], INSA Lyon, tous droits réservés

exemple, accord de Paris 2015, Conférence des Nations Unies sur le changement climatique (COP26) 2021). Dans l'esprit que le système énergétique existant est principalement non renouvelable, utilisant des sources d'énergie à base de carbone. Les nouveaux enjeux de la transition énergétique nécessitent d'installer et d'intégrer un nouveau système d'énergie renouvelable tout en sécurisant l'approvisionnement et la résilience de la demande réelle. L'hydrogène, considéré par beaucoup comme le carburant alternatif propre, semble être l'une des réponses. Malgré les problèmes de sécurité associés, le développement de cette technologie contribue à ce que les pays atteignent leurs objectifs climatiques, stimulent la croissance verte et créent des emplois durables.

Cette thèse s'inscrit dans le cadre des actions menées au sein du laboratoire collaboratif RAInBOV qui associe le Cethil et la société RSA. Ils sont spécialisés dans la fabrication de verres saphir, principalement utilisés dans le domaine de l'horlogerie et du verre. Leur production nécessite de fondre la matière première et de la cristalliser. Pour cela, ils utilisent la méthode Verneuil qui consiste en un brûleur vertical descendant qui génère une flamme à diffusion inverse H_2/O_2 située dans une enceinte confinée et chargée de particules d'alumine déposées sur une germe cristalline. Dans ce cadre, l'objectif principal de cette thèse est de comprendre les mécanismes aérothermochimiques présents dans cette configuration. Concrètement, la stabilisation, la structure et le développement des flammes produites par cette configuration particulière sont analysés, ainsi que le comportement thermique du milieu de croissance cristalline.

Cette thèse est accessible à l'adresse : http://theses.insa-lyon.fr/publication/2022LYSEI044/these.pdf
© [K. Utria Salas], [2022], INSA Lyon, tous droits réservés

Acknowledgements

Il y a tant de personnes que je voudrais remercier pour m'avoir aidée jusqu'à la fin de ce projet qui a commencé il y a de nombreuses années. D'abord je tiens à remercier les membres du jury, professeur.e.s David Honoré, Thierry Schuller et Céline Morin d'avoir accepté de participer à cette soutenance de thèse de doctorat.

Je tiens à remercier Dany Escudié qui pendant 2 ans de projet était la directrice de thèse, avec qui j'ai beaucoup échangé, pour toute sa sagesse, son expérience, et les très bonnes idées qu'elle seule a réussi à visualiser malgré leur difficulté. J'ai beaucoup appris d'elle de manière professionnelle et personnelle. Je veux remercier Manuel Kühni de m'avoir appris à utiliser tout l'équipement et toute son aide sans laquelle je n'aurais pas pu arriver à finir mes manipulations, pour ses discussions en salle manip et autour d'un café, et surtout pour toutes ses bonnes idées. De la même manière, je veux remercier Serge Labor, qui est une personne que j'admire beaucoup d'un point de vue professionnel et personnel. J'aimerais bien avoir sa passion pour fabriquer des saphirs. Je voudrais surtout le remercier pour tout le temps qu'il a consacré à tout m'expliquer dans le moindre détail. Pour sa gentillesse et pour toutes les discussions autour de déjeuners. J'aimerais adresser un remerciement spécial à mon Directeur de thèse Cédric Galizzi sans qui je ne serais pas ici en France, depuis le début il m'a confié cette mission que j'ai eu souvent l'impression de ne jamais pouvoir finir, je te remercie Cédric pour toutes les discussions professionnelles et personnelles, pour ton soutien et surtout ton dévouement.

Au sein RSA, je tiens à remercier aussi tout le personnel de production spécialement les chefs de quart et Raphaël de m'avoir appris à allumer une rampe de chalumeaux. Je remercie les gens du laboratoire pour tous les cafés et petites discussions que j'ai eus avec eux, Delphine, Jose, Lionel, Alexandre et Thomas. Les filles de qualité qui étaient très gentilles avec moi. Le personnel de la DRH de RSA. Je veux remercier aussi Alexandre Ducmauge et Denis Guignier pour le soutien. Guillaume Alombert, Raphaël Pierrel et Philippe Tonnelet. L'équipe de maintenance Philippe Vasquez, Juani et Jérémy. Et tout spécialement, dans l'équipe R&D, Jérémy, de m'avoir aidée pendant les derniers essais chez RSA. Jessica pour toutes les discussions et surtout pour tous les repas qu'elle a préparés pendant je ne sais pas combien confinements.

Au CETHIL, je vais commencer par remercier le secrétariat, Edwige, Marilyn, Lisa, Meriem et Nazaré qui n'est plus là mais qui m'a beaucoup aidée, l'instrumentation, Serge, Anthony et Pierrick. J'aimerais adresser un remerciement à l'équipe de l'atelier, Nicolas, Xavier et Christophe, qui m'ont accompagnée pendant ces trois ans de thèse et qui m'ont tenu compagnie pendant les confinements. Je vous remercie pour toutes les idées et le

Cette thèse est accessible à l'adresse : http://theses.insa-lyon.fr/publication/2022LYSEI044/these.pdf
© [K. Utria Salas], [2022], INSA Lyon, tous droits réservés

soutien sur mes manipulations, je veux spécialement remercier Nico pour toutes les fois où a branché les bouteilles d'oxygène.

Je veux également remercier tou.te.s les ingénieur.e.s d'études, les doctorant.e.s et post-doctorant.e.s du CETHIL avec qui j'ai beaucoup partagé, toutes les bonnes pauses café et les déjeuners à la cantine de l'INSA et aussi pour toutes les conversations et leur soutien. Je remercie en particulier les anciens qui étaient là et qui m'ont intégrée à mon arrivée au laboratoire Eloïse, Thomas, David, Julie, Nicolas C, Kevin T, Quentin, Christophe, Ghadi. Les doctorants qui ont commencé avec moi Paul D, Jean, Mathilde, Janett, à ma copine de Combustion Sophie pour toutes tes bonnes idées et ta bienveillance, toujours. Damien grâce à qui j'ai fait partie des Kfêteriens et Sébastien pour tout le bonheur et "la bonne énergie". Aux petits jeunes, Celia, Paul G, Ana et tout spécialement Florent pour tout son soutien et son aide dans cette dernière ligne droite.

Tous mes amis à Lyon, spécialement à Arnaud pour son soutien durant ces dernières années. Estos son los agradecimientos en español a todos mis parceritos cachacos en Lyon, Liliana R, Ian Carlo, Isabella, Alejandra y Margaud (même si elle est française), gracias a ustedes cada día era un mejor día sobretodo en este último invierno. A Mabel por siempre estar allí desde el principio conmigo apoyándome. A mis amigos en Francia, Colombia y el resto del mundo que siempre me han apoyado desde lejos Liane, Dave, José Luis, Nancy, Melissa, Sandra, Serlys, Esteyci Malibu, Pamela, Katty, Cristina, Fred, Gabriel S, La Jani, Liliana S, Hélène, Robinson, Camille, Sulivan, Serena, Natasha, Argemiro. A mis compañeros de la UAC Mauricio, Armando, Beatriz, Débora, Kelvin, Carlos D, Francisco, Omaira y Elda.

Finalmente, a mi familia, mis tías Raquel y Cecilia, mis primos Roberto y Yolima. A mi tío Paye y mi tío Noel, a mi cuñada Giselle, de la que he aprendido muchísimo, a Petra por su cariño y dedicación.

Sobretodo, quiero agradecerle el apoyo a mi Papá y mi hermano Rommell por siempre haber creído en mí y en todos mis proyectos. A mi Mamá que, aunque no está con nosotros en estos momentos sé que estaría orgullosa porque gracias a ella y todas sus enseñanzas soy la persona en la que me he convertido.

Cette thèse est accessible à l'adresse : http://theses.insa-lyon.fr/publication/2022LYSEI044/these.pdf
© [K. Utria Salas], [2022], INSA Lyon, tous droits réservés

Contents

Cette thèse est accessible à l'adresse : http://theses.insa-lyon.fr/publication/2022LYSEI044/these.pdf
© [K. Utria Salas], [2022], INSA Lyon, tous droits réservés

Cette thèse est accessible à l'adresse : http://theses.insa-lyon.fr/publication/2022LYSEI044/these.pdf
© [K. Utria Salas], [2022], INSA Lyon, tous droits réservés

Cette thèse est accessible à l'adresse : http://theses.insa-lyon.fr/publication/2022LYSEI044/these.pdf
© [K. Utria Salas], [2022], INSA Lyon, tous droits réservés

Cette thèse est accessible à l'adresse : http://theses.insa-lyon.fr/publication/2022LYSEI044/these.pdf
© [K. Utria Salas], [2022], INSA Lyon, tous droits réservés

List of Tables

Cette thèse est accessible à l'adresse : http://theses.insa-lyon.fr/publication/2022LYSEI044/these.pdf
© [K. Utria Salas], [2022], INSA Lyon, tous droits réservés

Cette thèse est accessible à l'adresse : http://theses.insa-lyon.fr/publication/2022LYSEI044/these.pdf
© [K. Utria Salas], [2022], INSA Lyon, tous droits réservés

Cette thèse est accessible à l'adresse : http://theses.insa-lyon.fr/publication/2022LYSEI044/these.pdf
© [K. Utria Salas], [2022], INSA Lyon, tous droits réservés

Cette thèse est accessible à l'adresse : http://theses.insa-lyon.fr/publication/2022LYSEI044/these.pdf
© [K. Utria Salas], [2022], INSA Lyon, tous droits réservés

List of Figures

Cette thèse est accessible à l'adresse : http://theses.insa-lyon.fr/publication/2022LYSEI044/these.pdf
© [K. Utria Salas], [2022], INSA Lyon, tous droits réservés

Cette thèse est accessible à l'adresse : http://theses.insa-lyon.fr/publication/2022LYSEI044/these.pdf
© [K. Utria Salas], [2022], INSA Lyon, tous droits réservés

Cette thèse est accessible à l'adresse : http://theses.insa-lyon.fr/publication/2022LYSEI044/these.pdf
© [K. Utria Salas], [2022], INSA Lyon, tous droits réservés

Cette thèse est accessible à l'adresse : http://theses.insa-lyon.fr/publication/2022LYSEI044/these.pdf
© [K. Utria Salas], [2022], INSA Lyon, tous droits réservés

Cette thèse est accessible à l'adresse : http://theses.insa-lyon.fr/publication/2022LYSEI044/these.pdf
© [K. Utria Salas], [2022], INSA Lyon, tous droits réservés

Cette thèse est accessible à l'adresse : http://theses.insa-lyon.fr/publication/2022LYSEI044/these.pdf
© [K. Utria Salas], [2022], INSA Lyon, tous droits réservés

Cette thèse est accessible à l'adresse : http://theses.insa-lyon.fr/publication/2022LYSEI044/these.pdf
© [K. Utria Salas], [2022], INSA Lyon, tous droits réservés

Cette thèse est accessible à l'adresse : http://theses.insa-lyon.fr/publication/2022LYSEI044/these.pdf
© [K. Utria Salas], [2022], INSA Lyon, tous droits réservés

Abbreviations

Al_2O_3 Aluminium oxide.
BC Boundary conditions.
CETHIL Center of Energy and Thermal of Lyon.
CFD Computational Fluid Dynamics.
CG Classic Geometry.
CL Chemiluminescence.
CT Crystallisation cycle.
df Degree of freedom.
DV Direct Visualisation.
F_f Crystal Final Formation Cycle.
F_i Crystal Initial Formation Cycle.
FS Full Scale.
FWHM Full Width at Half Maximum.
G_f Crystal Final Growth Cycle.
G_i Crystal Initial Growth Cycle.
IDF Inverse Diffusion Flames.
LOS Light-of-Sight.
MIDF Multi-jet Inverse Diffusion Flames.
MS Mean Squared.
MSE Mean Squared Error.
MSF Factorial Mean Squared.
NDF Normal Diffusion Flames.
NG New Geometry.
NR Non-Reactive.
R Reactive.
RAInBOV Research, Analysis and Innovation for Verneuil Growth Burners.
RSA RSA Le Rubis SA.
SS Sum of Squares.
SSE Error sum of Squares.
SSF Factorial sum of Squares.
SST Total sum of Squares.

Cette thèse est accessible à l'adresse : http://theses.insa-lyon.fr/publication/2022LYSEI044/these.pdf
© [K. Utria Salas], [2022], INSA Lyon, tous droits réservés

Cette thèse est accessible à l'adresse : http://theses.insa-lyon.fr/publication/2022LYSEI044/these.pdf
© [K. Utria Salas], [2022], INSA Lyon, tous droits réservés

Nomenclature

Alphanumeric

A	Einstein Constant [m^{-1}].
C	Covariance.
C_p	specific heat capacity [$J/kg\cdot$]].
D	Outlet Diameter [mm].
$\oslash_{boule}$	Diameter of the crystal boule [mm].
D_i	Inner jet diameter [mm].
D_o	Outer jet diameter [mm].
G	Momentum [$kg \cdot m/s$].
I_{N,OH^*}	Normalised intensity of OH^* emission.
I	Local intensity of OH^* emission.
I_{turb}	Overall Turbulence Intensity [%].
k	Thermal conductivity [$W/m \cdot K$].
L_{boule}	Length of the crystal boule [mm].
l_f	Flame length [cm].
O_{in}	Ovalisation index [%].
h_c	Planck constant [m^2 kg/s].
P	Probability an event to occur [%].
Q_a	Air flow rate [Nm^3/min].
Re	Reynolds number.
R_{therm}	Thermal resistance [$°C/W$].
R_u	Universal gas constant [$J/mol \cdot K$].
t_{cycle}	Time passed during a crystallisation cycle after the flame lighting [h].
T	Temperature [°C].
T_m	Mean experimental temperature of the flame.
T_{OH^*}	Calculated temperature based on OH^* emission intensities.
$\overline{U}$	Mean axial velocity [m/s].
U_0	Centreline injection velocity [m/s].
$\overline{v'}$	Turbulence fluctuation of the mean transversal velocity.
U_C	Axial centreline velocity [m/s].
$\overline{U}_{C,0}$	Centreline value of $\overline{U}$ at the nozzle exit [m/s].
U_i	Inlet velocity of the inner jet [m/s].
U_o	Inlet velocity of the outer jet [m/s].
U_{rms}	Turbulence intensity of the axial velocity [m/s].
$\overline{u'}$	Turbulence fluctuation of the mean axial velocity.
U	Inlet Velocity [m/s].
v	Kinematic viscosity [m^2/s].

Cette thèse est accessible à l'adresse : http://theses.insa-lyon.fr/publication/2022LYSEI044/these.pdf
© [K. Utria Salas], [2022], INSA Lyon, tous droits réservés

$W_{OH^*,max}$	Total flame thickness (80% OH^* maximum emission intensity) [mm].
y_d	Diffusion flame height [mm].
y_f	Flame height [m].
y_j	Position of flame closure in Y-axis [mm].
y_T	Total flame height [mm].

Greek letters

Λ	Area [m^2].
δ_{OH^*}	Flame thickness [mm].
δ	Thickness [mm].
ε	Emissivity.
μ	Dynamic viscosity [Pa·s].
μ_m	group mean.
ϕ	Equivalence ratio.
ρ	Density [kg/m^3].
R_ρ	Density ratio.
σ	Stefan-Boltzmann constant [kg s^{-3} K^{-4}].
σ_s	Standard deviation.
$\overline{\nu}$	Normalised flow rate.
$\dot{\nu}_{av}$	Mean flow rate [m^3/s].
$\dot{\nu}$	Flow rate [m^3/s].

Subscripts

ad	adiabatic.
cer	ceramic insulation.
$conv$	convection.
f	fuel.
H_2	Hydrogen.
max	maximum.
O_2	Oxygen.
O	Oxidiser.
rad	radiation.
rms	root mean squared.
$stoic$	stoichiometry.
$therm$	thermal.

Cette thèse est accessible à l'adresse : http://theses.insa-lyon.fr/publication/2022LYSEI044/these.pdf
© [K. Utria Salas], [2022], INSA Lyon, tous droits réservés

Introduction

Combustion has been the cornerstone of industrial development for nearly two centuries. The burning of fossil fuels provides heat for many industrial processes and accounts for over 80% of the power used by turbines to generate electricity (U.S. Energy Departement, 1999). Over the years a lot of progress has been made in understanding the fundamental science of combustion. Nevertheless, regulatory and competitive forces are driving the need for combustion equipment with better performance, lower environmental impact, and greater flexibility, all at reasonable cost (U.S. Energy Departement, 1999). In December 2015 in Paris, 195 countries signed an agreement to limit global warming to well below 2, preferably to 1.5 degrees Celsius, compared to pre-industrial levels. In November 2021 the UN Climate Change Conference (COP26) convened in Glasgow. Countries reaffirmed this objective and also concluded that the Paris Agreement temperature goal is now small and rapidly depleted.

Achieving these objectives generates new energy transition challenges because the existing energy system is primarily non-renewable with carbon-based energy sources. Therefore, it is required to install and integrate a new renewable energy system while securing the supply and resilience of the actual demand (Council, 2017). Hydrogen, considered by many the clean alternative fuel (Ogden, 1999; Barreto et al., 2003; Barbir, 2009), seems to be one of the answers, despite the associated security issues. The development of this technology allow countries to meet their climate goals, boost green growth and create sustainable jobs.

Actually, hydrogen is very versatile and offers several production, distribution, and use options, which explains its widespread use in different technologies for a long time. Its unique properties such as high energy density, high flammability range, low density, high diffusivity, high adiabatic temperature and high laminar burning velocity, make it to be considered as a near-perfect energy carrier. Besides, hydrogen can be produced from various widely available feed-stocks like natural gas, coal, biomass, wastes, nuclear resources, wind, and solar resources (Barbir, 2009; Nowotny et al., 2005; Zhang et al., 2010).

Hydrogen has a central role in helping the world reach net-zero emissions by 2050 and limit global warming. Therefore, the Hydrogen Council CEO coalition in Brussels is asking the world leaders – public and private – to show concerted effort to materialise announced hydrogen plans around the globe to get the world on track with climate targets. They demand to synchronise the development of the hydrogen economy with electrification, to enable deep decarbonisation worldwide cost-effectively and efficiently. Complementing

Cette thèse est accessible à l'adresse : http://theses.insa-lyon.fr/publication/2022LYSEI044/these.pdf
© [K. Utria Salas], [2022], INSA Lyon, tous droits réservés

other decarbonisation technologies like renewable power, biofuels, or energy efficiency improvements, clean hydrogen (both renewable and low carbon) offers the only long-term, scalable, and cost-effective option for deep decarbonisation in sectors such as steel, maritime, aviation, and ammonia. Furthermore, hydrogen can prevent 80 gigatons (GT) of cumulative CO_2 emissions, contributing to 20% of the total reduction needed in 2050 (diminishing potentially 7 GT per year). To this effect, six hundred sixty million metric tons (MT) of renewable and low-carbon hydrogen is required in 2050, equivalent to 22 % of the world's final energy demand (Council, 2021).

Regarding the combustion context, different practical systems use diffusion flames widely due to their safety and wide operating range compared to premixed combustion (Mahesh and Mishra, 2010). Diffusion flames can be classified as Normal Diffusion Flames (NDF), and Inverse Diffusion Flames (IDF). IDF configuration appears to accommodate the current environmental demands. Nevertheless, the available information in IDF mainly concerns hydrocarbons and air. Some researchers have lately focused on adding H_2 in classical hydrocarbons applications (Miao et al., 2016, 2013; Zhen et al., 2011). They found that the addition of H_2 in the fuel side can effectively widen the range of flame stability and increase the heat flux, while limiting the pollutant emissions. Another mechanism to improve the combustion is the enhancement of O_2 on the oxidiser side without changing the overall equivalence ratio (Miao et al., 2016). The research in H_2/O_2 inverse diffusion flames has focused on propulsion rocket applications (Benduneau, 2001; Raghib Shakeel et al., 2017; Kim et al., 2018, 2019), which are supercritical conditions. Nonetheless, the IDF H_2/O_2 burners are of great interest, particularly for several industrial applications such as synthetic crystal production and metal and chemical processes. It is necessary to control the flame shape, structure characteristics and temperature distribution. These features are related to the aerodynamics and chemistry correlations during combustion (Wu and Essenhigh, 1984; Sze et al., 2004, 2006; Bindar and Irawan, 2012). Within this framework, this thesis's main objective is to comprehend the aerothermochemical mechanisms present in a downward vertical burner that generates an H_2/O_2 inverse diffusion flame located in a confined enclosure (furnace) and loaded with alumina particles. Those will be deposited on a crystalline seed constituting a stagnation point at the furnace. This specific configuration constitutes an industrial application in the watch market industry, called *Verneuil Method*. Concretely, this study analyses the stabilisation, structure and development of the flames produced by this particular configuration under different injection conditions.

Following, this chapter presents the *Verneuil Method*, that created the study interest of this work. This section allows understanding the process to fabricate artificial sapphire crystals. Secondly, the problem that confronts this method is described. Finally, the outline of the thesis is exposed.

Cette thèse est accessible à l'adresse : http://theses.insa-lyon.fr/publication/2022LYSEI044/these.pdf
© [K. Utria Salas], [2022], INSA Lyon, tous droits réservés

Context of this study

Verneuil Method

This thesis is part of the actions carried out at the collaborative laboratory Research, Analysis and Innovation for Verneuil Growth Burners (RAInBOV) that associates the Center of Energy and Thermal of Lyon (CETHIL) and the company RSA Le Rubis SA (RSA). The company specialises in the manufacture of sapphire crystals, mainly used in the field of watchmaking and glass. In order to produce sapphire crystals, it is necessary to fuse the raw material (alumina powder) and crystallise the material. To this effect, various crystal growth processes are utilised, including the Verneuil method, which has a flame as a source of heat energy. Over the past five years, global competition from sapphire producers has intensified considerably. The growth technologies dedicated to the design of sapphire substrates for micro and optoelectronics have been directed towards the markets historically held by the Verneuil process, forcing RSA to reflect on an evolution of this technology that would preserve its competitiveness. In this regard, RSA has chosen to improve several areas of development: improvement and understanding of the mechanical resistance of sapphire, reduction of gaseous inclusions in the material, diversification and optimisation of growth methods. The collaboration between CETHIL and RSA aims to optimise the method Verneuil regarding production costs and crystal quality. This entails the need to acquire a detailed understanding of the crystal growth environment.

The Verneuil method, also called flame fusion, is a technique of crystal growth whose main objective is the production of synthetic sapphire crystals using as starting material the powder of alumina (Al_2O_3). A Verneuil furnace is composed of three vertically oriented parts: the seeder, the burner and the confinement (Figure 1). This method requires achieving the fusion temperature of the alumina, that is 2050°C. Therefore, an inverse diffusion flame is used as energy source. The flame reactants are hydrogen and oxygen due to their high combustion temperatures. One of the characteristics of this technique is its inverted configuration because of the following reasons:

1. To avoid diffusion of the hydrogen in the alumina.
2. To recuperate the microbeads or sapphire crystal produce.

In a *Verneuil furnace*, the upper part is called the seeder, which is a closed box. The oxygen and the alumina powder are injected at this section, and a sieve contains the alumina. A hammer located above the seeder strikes it and enables the alumina to go down through the sieve and mix with oxygen gas flow. The seeding frequency is set depending on the amount of alumina required by the crystallisation process. The seeded gas goes down into the burner, consisting of two coaxial tubes. The O_2 seeded with

Cette thèse est accessible à l'adresse : http://theses.insa-lyon.fr/publication/2022LYSEI044/these.pdf
© [K. Utria Salas], [2022], INSA Lyon, tous droits réservés

alumina particles arrive in the narrow central tube and goes out at the O_2 nozzle. The hydrogen injection is performed independently into the outer tube at the burner level. The hydrogen nozzle is a perforated annular ring. The contact between the hydrogen and the oxygen occurs at the oxygen nozzle, which is surrounded by a ceramic tube, called burner nozzle. At this point, the inversion diffusion flame is formed and it is surrounded by an insulation confinement composed of different layers.

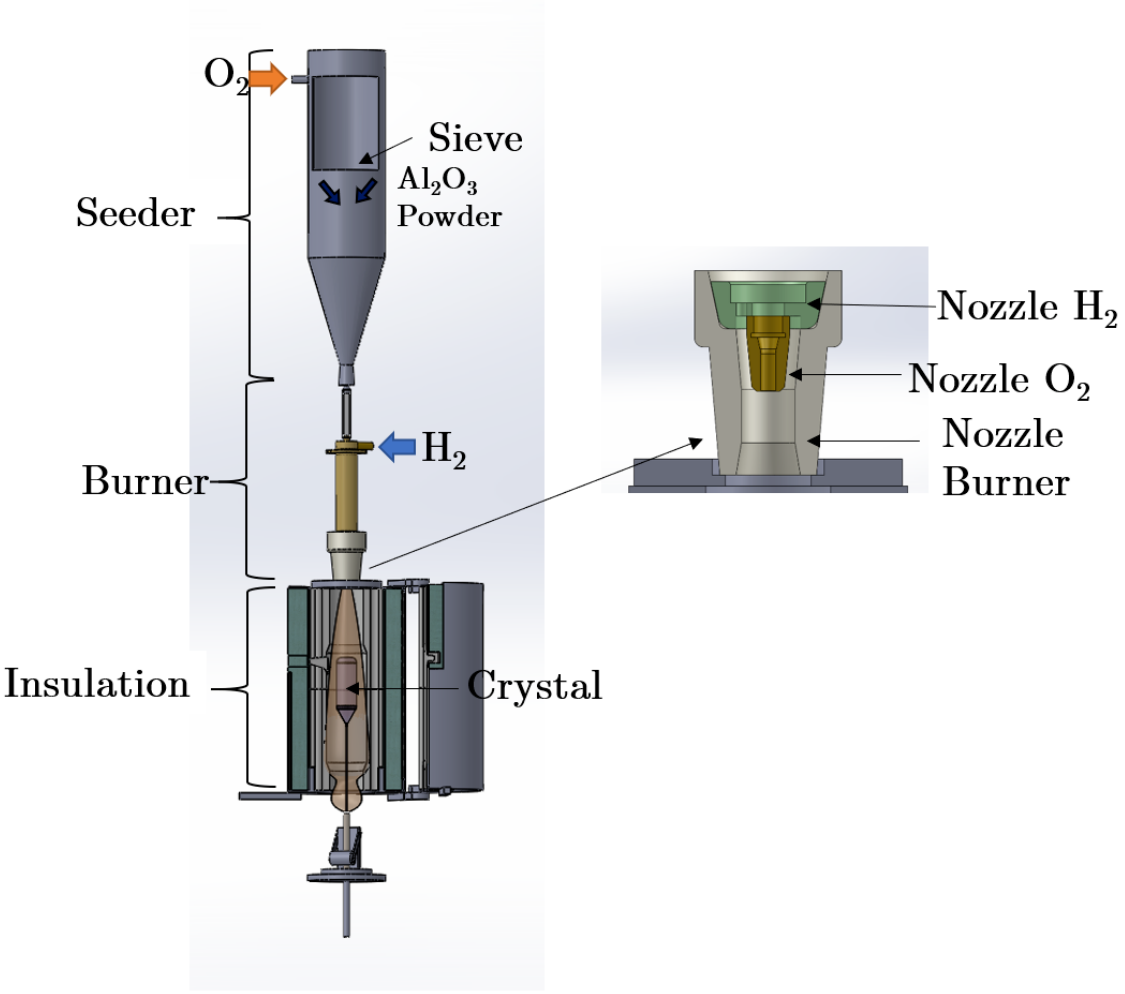

Figure 1: Schematic view of a *Verneuil furnace*

The particles of alumina pass through the flame and melt into small droplets when they reach alumina's fusion temperature. The droplets are deposited on a crystalline seed that functions as a seed on a vertically turning and descending surface. At this moment they form a shallow pool of melt. As more droplets fall down the seed is slowly moved downward, allowing the lower part of the liquid to crystallise and grow. As a result, a synthetic columnar sapphire crystal, called "boule" (French word), is formed. This growth process lasts about 3-4 hours, depending on the desired crystal length. Once it is achieved, the powder injection is stopped. Then, the boule is left inside the confinement until the system is cooled (Bhat, 2014).

Cette thèse est accessible à l'adresse : http://theses.insa-lyon.fr/publication/2022LYSEI044/these.pdf
© [K. Utria Salas], [2022], INSA Lyon, tous droits réservés

The following section explains the industrial problematic when using this technique to fabricate sapphire crystals and the objectives of this study.

Industrial and scientific challenges

In the context of watchmaking applications, improving the quality of crystals obtained by the Verneuil method is necessary to ensure the sustainability of this process at RSA. The experience acquired with RAInBOV laboratory has shown that this is an ambitious work, both from a technological and scientific point of view. In order to conserve RSA competitive advantage through the Verneuil method, it is essential to find solutions allowing to drastically reduce the number of defects in the crystals, thus increasing the method efficiency. In particular, the problems encountered in the material are isolated defects of gaseous inclusions type but above all micro-inclusions grouping together in grain sub-boundaries present in the crystal structure. Previous studies showed that these structural anomalies are generated during growth, under the effect of the strong temperature gradients to which the crystals are submitted. The reduction of these temperature gradients and their compatibility with the growing conditions are, therefore, the key points to reduce the occurrence of defects in sapphire.

The scientific barriers to be removed in this area are essential because the complex process of crystal growth is intimately coupled to the flame aerothermochemistry, to the boundary conditions imposed by the confinement of the burners and the crystal itself. The particular burner configuration (directed downwards, oxycombustion and fuel-oxidant inversion) raises many questions regarding the nature of the flames produced by this device (e.g flame stabilisation mechanism, flame structure and development).

As part of the dynamics of the actions undertaken within the framework of the RAInBOV laboratory, the current study aims to optimise the industrial burner based on fine and detailed analyses of the parameters that control the final crystallisation process and an assessment of their relative importance. Industrial burners and non-premixed flames have been the subject of many studies. However, the particularities described above make them an unprecedented configuration which, to our knowledge, has never been the subject of a detailed study. Beyond the purely reactive aspects, this configuration is particularly complex from a thermal point of view due to:

- very high temperatures of the oxygen-hydrogen flame,
- thermal confinement around the reactive zone,
- the presence of a growing crystal in this area (strong radiation).

The academic configuration closest to this industrial burner is a “jet flame”. This type of

Cette thèse est accessible à l'adresse : http://theses.insa-lyon.fr/publication/2022LYSEI044/these.pdf
© [K. Utria Salas], [2022], INSA Lyon, tous droits réservés

flame has already been the subject of a large number of publications which have shown the importance of aerodynamic mechanisms, in particular the flame stabilisation (Barr, 1953; Vranos et al., 1968; Leung and Wierzba, 2009). More recent studies have clarified the role of heat transfer between the flame and the burner on this issue (Lamige et al., 2013, 2014, 2015). However, the specificities of the configuration used by RSA imply the consideration of other mechanisms whose influence cannot be neglected. Thus, it is relevant to emphasise the importance of buoyancy effects related to the orientation of the burner and the use of hydrogen whose characteristics (diffusivity, flammability, Lewis number lower than 1, etc.) lead to particularly complex situations. At the same time, the influence of thermal effects is reinforced by the confinement, the presence of the growing crystal and the very high temperature levels associated with oxycombustion.

In this specific configuration where the aerothermochemical couplings are particularly complex, the preliminary studies have underlined the need to analyse the temperature field and the associated thermal gradients in detail.

In addition, knowledge of the importance and role of the different types of heat transfer (convection, conduction and radiation) between the flame, the burner, the containment furnace, and the crystal is essential to understand the inherent interactions to the process. In this context, this research meets mainly two objectives:

- **The first objective** is to understand the overall thermal behaviour of the device and to specify the role of heat transfers between the different elements constituting the growth environment (burner, flame, refractory confinement, crystal). An originality of the project will be the consideration of the retroactive effect of the stagnation point that constitutes the sapphire downstream of the device. This naturally generates strong aerodynamic constraints that influence the flame structure and development. In concrete, the first objective is to ***understand the overall thermal operation of the Verneuil Furnace and to identify the parameters that can modify the thermal behaviour of the growth environment, more specifically the temperature level and the thermal gradients.***
- **The second objective** concerns understanding the influence of the thermal field in the crystal growth environment. More precisely, ***to specify the role of temperature levels and gradients on crystal growth by taking as validation criteria the quality of the crystal.***

Cette thèse est accessible à l'adresse : http://theses.insa-lyon.fr/publication/2022LYSEI044/these.pdf
© [K. Utria Salas], [2022], INSA Lyon, tous droits réservés

Outline

This document is organised in three parts regarding the objectives of the study:

- **Part I** aims to understand the influence of the thermal field in the area of crystal growth. For this purpose, the growth conditions were analysed under real production conditions for a specific crystal geometry. Its internal and external quality was characterised through crystal optics properties. The parameters that control the final process of sapphire crystallisation were identified, and their relative importance was assessed.
- **Part II** looks for the understanding of the thermal behaviour of the overall system, specifically the role of heat transfer and the stabilisation mechanisms and development of the flame. This part contains the study at laboratory-controlled conditions due to the industrial environment's complexity. Thus, this chapter describes the aerothermodynamics behaviour of H_2/O_2 inverse diffusion flames in a transparent confinement under different conditions of injection flow rates.
- **Part III** analyses the effects of the stagnation point (crystal in growing) in a laboratory environment and uses a computational fluid dynamics (CFD) software to understand its influence on the crystal growth environment. This part reports recommendations for improving the process and the preliminary tests of these solutions carried out at real production conditions. Furthermore, the influences of these changes on the crystal growth environment are analysed by CFD.

At the end of the document, the conclusions of the study are exposed and the perspectives to solve the questions arise during the development of the current research.

Cette thèse est accessible à l'adresse : http://theses.insa-lyon.fr/publication/2022LYSEI044/these.pdf
© [K. Utria Salas], [2022], INSA Lyon, tous droits réservés

Cette thèse est accessible à l'adresse : http://theses.insa-lyon.fr/publication/2022LYSEI044/these.pdf
© [K. Utria Salas], [2022], INSA Lyon, tous droits réservés

Part I

Analysis of crystalline growth environment and influence on crystal quality

The following part presents a sapphire production study carried out in actual industrial conditions. The principal objective is to comprehend the thermal conditions of the crystalline growth environment and their effects on crystal quality. For this purpose, two chapters are exposed. At first, chapter 1 presents the evolution of parameters that determine the crystalline growth environment. Subsequently, chapter 2 describes a statistical study performed to understand the correlations between all these parameters.

Cette thèse est accessible à l'adresse : http://theses.insa-lyon.fr/publication/2022LYSEI044/these.pdf
© [K. Utria Salas], [2022], INSA Lyon, tous droits réservés

Cette thèse est accessible à l'adresse : http://theses.insa-lyon.fr/publication/2022LYSEI044/these.pdf
© [K. Utria Salas], [2022], INSA Lyon, tous droits réservés

Contents

Cette thèse est accessible à l'adresse : http://theses.insa-lyon.fr/publication/2022LYSEI044/these.pdf
© [K. Utria Salas], [2022], INSA Lyon, tous droits réservés

Cette thèse est accessible à l'adresse : http://theses.insa-lyon.fr/publication/2022LYSEI044/these.pdf
© [K. Utria Salas], [2022], INSA Lyon, tous droits réservés

Chapter 1 | Crystal growth environment in industrial context

One artificial sapphire crystal is fabricated during one crystallisation cycle and is called *"Verneuil boule"*, for its name in french, that means Verneuil ball (see figure 1.1). The growing crystal is confined inside a ceramic insulation with a life cycle of around twenty-nine crystallisations. During one crystallisation, some crystallised alumina powder deposits on the internal ceramic insulation surface, its accumulation affects the geometry of the crystal and could lead to undesirable shape of the *"Verneuil boule"*. In order to avoid this kind of problem, at the end of each crystallisation, the production operators remove the crystallised alumina from the ceramic insulation internal surface. This procedure causes a degradation of the ceramic, that loses a considerable material thickness in each crystallisation changing at the same time the insulation conditions.

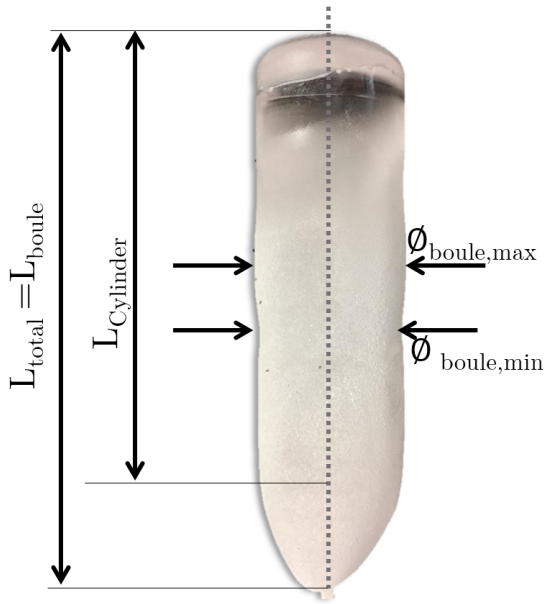

Figure 1.1: Verneuil Boule, typical dimensions: Boule Diameter ($\oslash_{boule}$) = [32 mm 35mm] [max min] and boule length (L_{boule}) = [150 180mm] [total cylinder]

The present study has analysed three complete life cycles of the insulation, based on different parameters. They were classified as thermal and flame combustion parameters and crystal quality parameters which in turn are divided into different parameters shown in figure 1.2. Ensuing the experimental bench is described, and the evolution of these parameters during an insulation life cycle. The different aspects that have an important role in RSA production are described in table 1.1.

Cette thèse est accessible à l'adresse : http://theses.insa-lyon.fr/publication/2022LYSEI044/these.pdf
© [K. Utria Salas], [2022], INSA Lyon, tous droits réservés

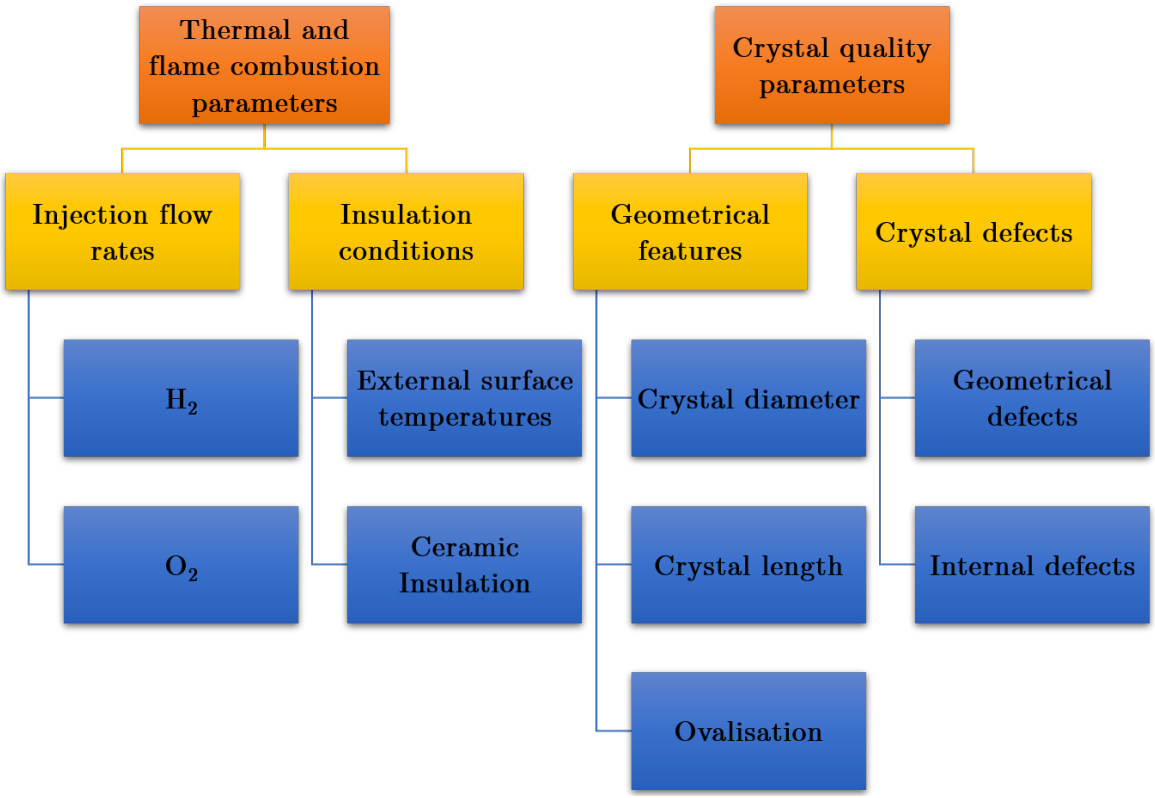

Figure 1.2: Parameters analysed during one crystallisation cycle

Aspects	
Number of Verneuil Furnace per production line	45
Number the crystallisation cycles per ceramic insulation life cycle	29
Time of one crystallisation [hours]	16

Table 1.1: RSA Production Aspects

Cette thèse est accessible à l'adresse : http://theses.insa-lyon.fr/publication/2022LYSEI044/these.pdf
© [K. Utria Salas], [2022], INSA Lyon, tous droits réservés

1.1 Experimental test bench

1.1.1 Experimental setup

In industrial conditions, the production area is composed of production lines, each containing forty-five Verneuil furnaces (see figure 1.3). One furnace is composed of the parts explained in **Verneuil Method** and produces one synthetic crystal per crystallisation. This process lasts between sixteen and nineteen hours in total, with a cooling period of three hours. In total, a *"Verneuil boule"* is fabricated in approximately twenty-four hours.

Figure 1.3: Verneuil production line

Different burner configurations are used to fabricate white synthetic sapphire crystal. These configurations are usually dependent of the production requirements which are related to production times and crystal geometrical characteristics demanded by the clients. The upper part of the Verneuil furnace always reminds the same; the burner, however, can change. The study focuses on the classic configuration shown in figure 1.4. This burner has nine annular peripheral jets of hydrogen equally spaced around a circumference of five times one hydrogen outlet diameter (D_{H_2}), and one central jet of oxygen (with a diameter of 1.4 D_{H_2}). The distance between the outlet nozzles is also five times D_{H_2}.

Cette thèse est accessible à l'adresse : http://theses.insa-lyon.fr/publication/2022LYSEI044/these.pdf
© [K. Utria Salas], [2022], INSA Lyon, tous droits réservés

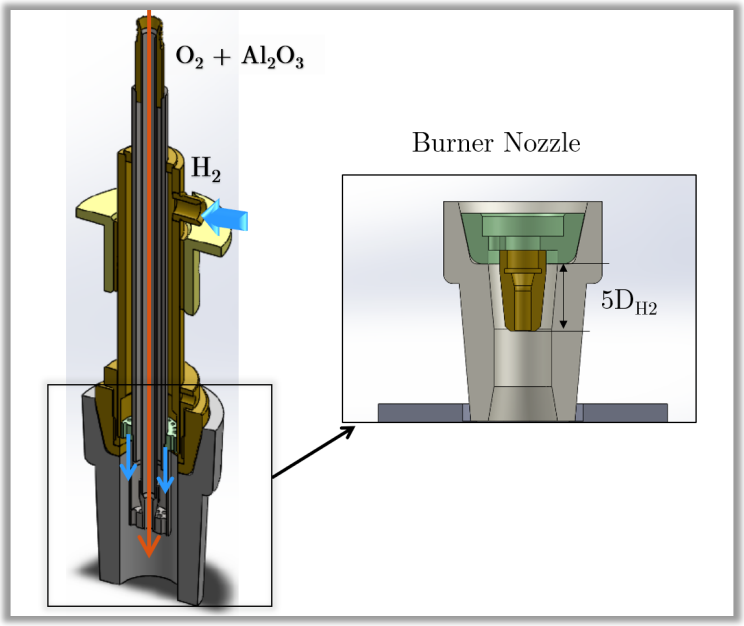

(a) Crossed section of a classic Verneuil burner

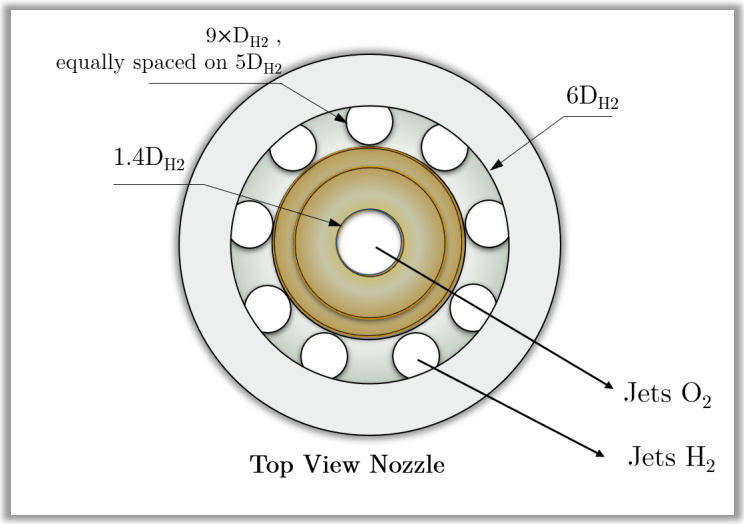

(b) Top View

Figure 1.4: Geometry of a classic Verneuil burner

The industrial part of this study chose to focus on two Verneuil furnaces of one production line. They were located at one extreme, that is called "*Furnace 1*" and in the middle of the line,"*Furnace 2*" (see figure 1.3). An important part of the study is linked to the insulation confinement, that degrades in each crystallisation cycle due to the material removing process on the ceramic internal surface. Figure 1.5 represents the different layers: an external stainless steel layer, followed by a silica (SiO_2) insulation fibre, a polycrystalline alumina fibre and a ceramic confinement.

Cette thèse est accessible à l'adresse : http://theses.insa-lyon.fr/publication/2022LYSEI044/these.pdf
© [K. Utria Salas], [2022], INSA Lyon, tous droits réservés

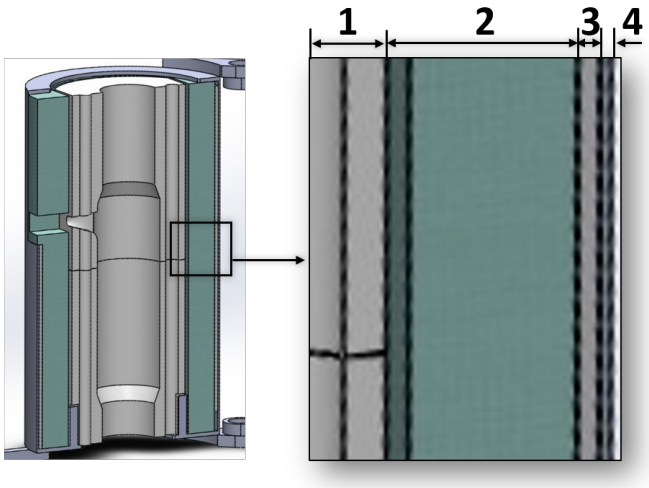

Figure 1.5: Insulation Confinement Configuration: (1) Ceramic confinement, (2) Polycrystalline Alumina Fibre, (3) Silica insulation fibre (4) Stainless steel layer.

Cette thèse est accessible à l'adresse : http://theses.insa-lyon.fr/publication/2022LYSEI044/these.pdf
© [K. Utria Salas], [2022], INSA Lyon, tous droits réservés

1.2 Evolution of thermal and flame combustion parameters

The crystallisation process has many parameters, within which some are controlled, and others are dependent parameters. Among those controlled are H_2 and O_2 flow rates, which define the combustion conditions. This section focuses on them and the heat transfer environment, which is analysed through the ceramic insulation evolution and the ceramic insulation temperatures.

1.2.1 Evolution of H_2 and O_2 flow rates

Owing the empirical knowledge acquired by RSA after the eighty years of activity in crystal fabrication, conditions and procedures have been established to obtain the desired crystal features. The aimed geometrical characteristics with the best geometrical and internal quality are settled under particular conditions for each crystallisation.

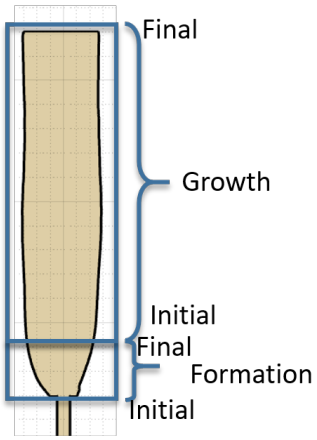

Figure 1.6: Cycle of a crystallisation

The controlled parameters as H_2 and O_2 flow rates are selected according to the desired crystal diameter. The flow rates used during the study were normalized with respect to Z-Score method:

$$\overline{\nu} = \frac{\dot{\nu}_i - \dot{\nu}_{av}}{\sigma_s} \tag{1.1}$$

Where $\overline{\nu}$ is the normalised flow rate, $\dot{\nu}_i$ is the flow rate, $\dot{\nu}_{av}$ is the mean flow rate (calculated from all the values) and σ_s, the standard deviation. Z-scores measure the distance of a data point from the mean in terms of the standard deviation. The standardised data set has mean 0 and standard deviation 1, and retains the shape properties of the original data set.

A crystallisation cycle comprehends two main phase: the formation of the crystal and the growth of the crystal (see figure 1.6). The crystallisation cycle begins with the flame

Cette thèse est accessible à l'adresse : http://theses.insa-lyon.fr/publication/2022LYSEI044/these.pdf
© [K. Utria Salas], [2022], INSA Lyon, tous droits réservés

ignition in the confinement, which contains an initial germ that starts to grow into the desired sapphire boule. In figure 1.7, a classic evolution of the flow rates are shown for an insulation life cycle.

The initial phase is called crystal initial formation, F_i, and all the crystallisation cycles have the same flow rates for this phase. In order to achieve the boule cylindrical shape, the flow rates are the lowest of the crystallisation cycle during this phase, as can be observed in figure 1.8. Furthermore, it is important to mention that these flow rates are also adjusted to avoid the spilling of the liquid sapphire, if the power is too high. In other words, the flow rates are controlled to maintain in liquid state a small surface of the germ to form the cylindrical shape without spilling the liquid sapphire.

The second curve in figure 1.7 is the final formation phase, F_f, which corresponds to the flow rates at the end of the formation phase. This moment is very important and defines the crystal diameter. The growth phase follows with higher flow rates to finish the cylindrical ball. The small liquid surface is always maintained until reaching the desired boule length.

Regarding the evolution of the flow rates between each crystallisation cycle, it can be observed that the first six cycles comprehend an adjusting stage. At this point, the insulation is new and therefore their efficiency is higher. The objective diameters of the crystal for these crystallisations are small, around 32 mm, with the purpose to have enough space between the insulation and the crystal to form a cylindrical shape. As mentioned, these dimensions have been defined after years of experience, and they are examined in section 1.3.

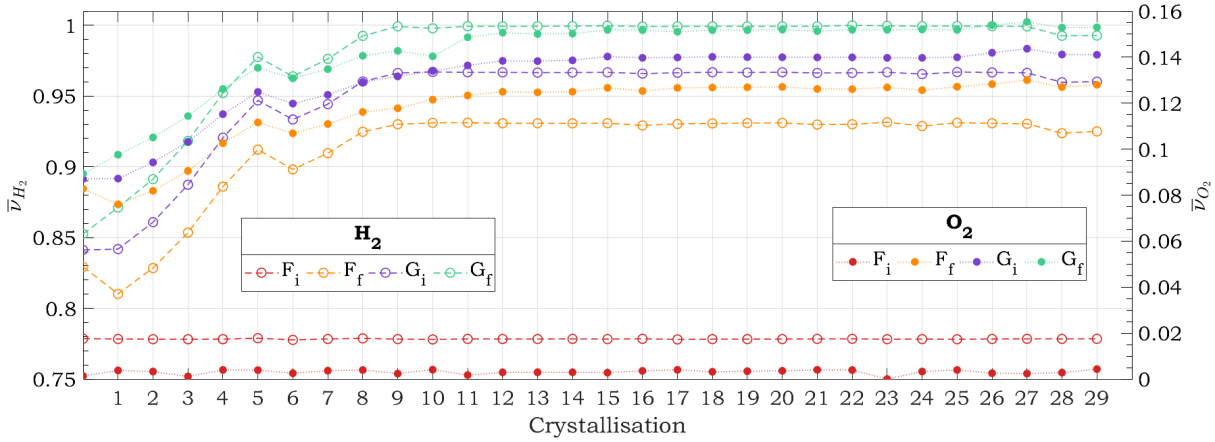

Figure 1.7: Evolution of Normalised flow rates during the first cycle studied. F: Crystal Formation, G: Crystal Growth, i: initial, f: final

On the other hand, a parameter to calculate the dispersion between the flow rates between

Cette thèse est accessible à l'adresse : http://theses.insa-lyon.fr/publication/2022LYSEI044/these.pdf
© [K. Utria Salas], [2022], INSA Lyon, tous droits réservés

the crystallisations is defined as:

$$\%Dispersion = \frac{\dot{\nu}_i - \dot{\nu}_{i-1}}{\dot{\nu}_{i-1}} \tag{1.2}$$

$\dot{\nu}$: Flow rates (H_2 or O_2) [m^3/s]

i: Number of the crystallisation (2-29)

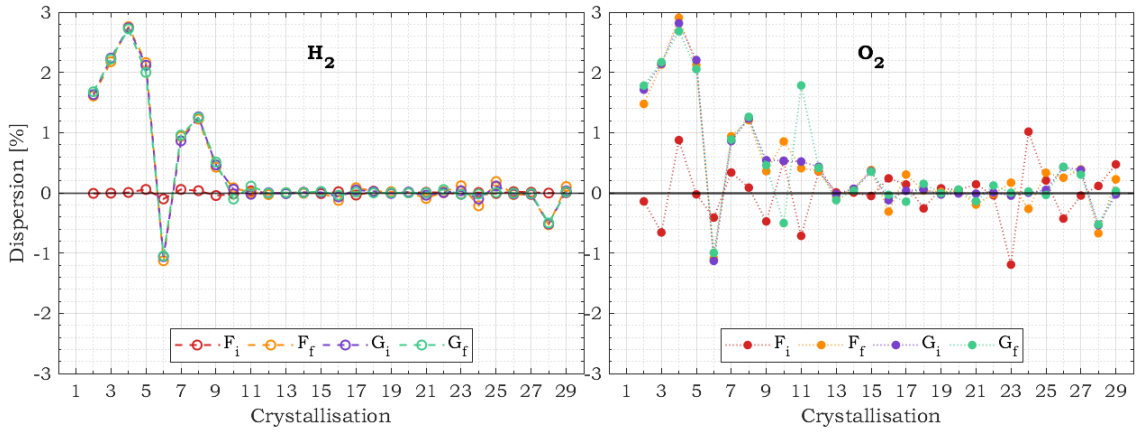

Figure 1.8: Dispersion of flow rates during a insulation life cycle. F: Crystal Formation, G: Crystal Growth, i: initial, f: final

Figure 1.8 highlights the adjusting period between crystallisations No.1 and No.6, where the main changes of flow rates are performed. This period also corresponds to the beginning of the ceramic insulation life cycle. Furthermore, the flow rates are drastically lower at crystallisation No.6. Operators often perform this action when the crystal diameter is too large for confined conditions and has many defects. Between crystallisations No.6 and No.10 small changes are effectuated. Posteriorly, they remain the same until the end of the insulation cycle. These settings are adjusted throughout the life cycle of the ceramic insulation, and their impact in the other parameters is analysed in chapter 2.

From these results, it can be concluded that the crystallisation process implies an adaptation of the two reactive flow rates whether to initiate the formation of the crystal (from the formation phase until the growth phase) or to adjust the boule diameter. For the two cases, these modifications influences the combustion and the thermal conditions of the crystal growth environment.

1.2.2 Insulation conditions

This section is divided into two parts: the first one is about the temperature evolution on the external surface of the ceramic insulation and in the second part the evolution of the

Cette thèse est accessible à l'adresse : http://theses.insa-lyon.fr/publication/2022LYSEI044/these.pdf
© [K. Utria Salas], [2022], INSA Lyon, tous droits réservés

ceramic insulation geometry is evaluated.

1.2.2.1 Temperature evolution on the ceramic insulation

Temperature were measured on the external surface of the ceramic insulation as show in figure 1.9 using thermocouples type R. Thermocouples type R have a composition of Platinum Rhodium-13% and Platinum. Their temperature range is:

- Thermocouple grade wire, -58 to 2700°F (-50 to 1480°C)
- Extension wire, 32 to 392°F (0 to 200°C)

and accuracy:

- Standard: ±1.5°C or ±.25%
- Special Limits of Error: ±0.6°C or 0.1%

The Y-positions were chosen regarding the furnace configuration. As mentioned, in order to produce a crystal with Verneuil method, a small area of the germ must achieve the fusion. Owing RSA experience, Y=130mm has shown to be the adequate height to locate the crystal at the crystallisation cycle beginning, making this zone the hottest in the furnace. Although this position would be the most accurate to measure temperature, it is impossible to set a thermocouple at this height due to technical conditions on the furnace front face. A window is located here to have visual access to correctly situate the germ. Therefore, Y=160mm was a more technical suitable height to place the thermocouple. The other thermocouples were distributed according to this Y-Position reference.

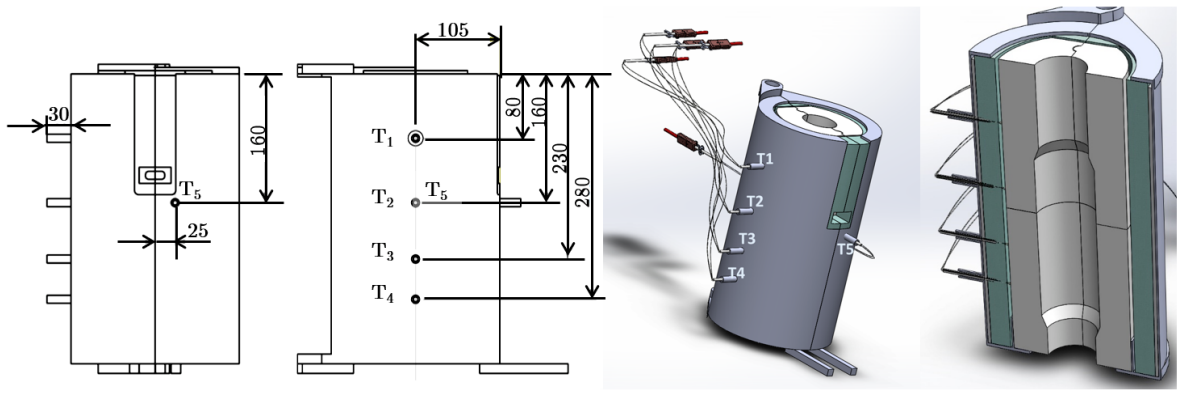

Figure 1.9: Thermocouples set up dimensions in [mm]

As mentioned, the first crystallisation cycles of the insulation "life" correspond to an adjusting period where the flow rates and the objective boule dimensions change. Figure

Cette thèse est accessible à l'adresse : http://theses.insa-lyon.fr/publication/2022LYSEI044/these.pdf
© [K. Utria Salas], [2022], INSA Lyon, tous droits réservés

1.10 shows the evolution in time of the temperature for four of these crystallisation cycles (CT): crystallisation cycles No.1, 2, 4 and 6. It can be observed that the external ceramic surface achieves more than 800 °C after two hours of operation for *Furnace 1* and more than 1000 °C for *Furnace 2*. The latter is surrounded by two other furnaces, which causes an increase in temperature of 160 °C.

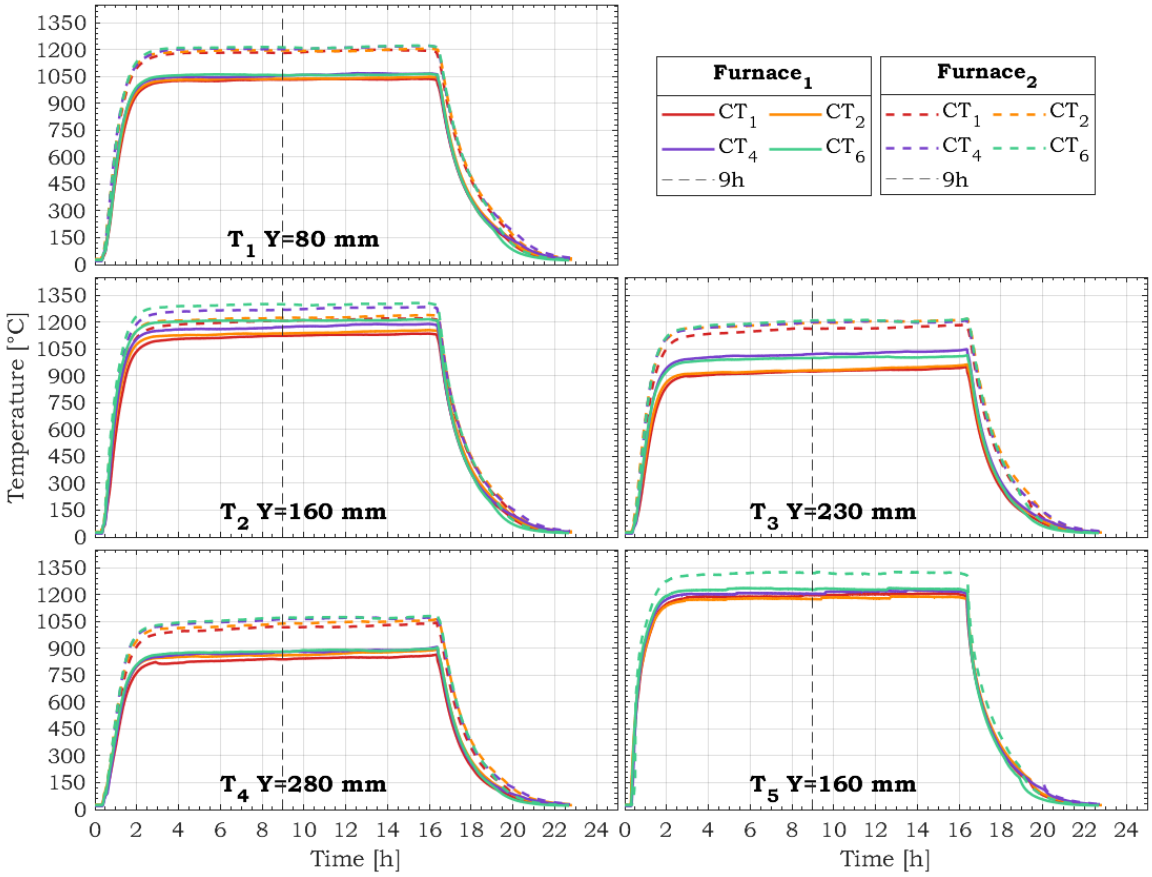

Figure 1.10: Temperature evolution for crystallisation cycles (CT): 1, 2, 4, 6

Figure 1.11 shows the temperatures at nine hours after flame ignition are highlighted (t_{cycle}). This time corresponds to half of the crystallisation cycle and represents the highest temperature of the crystallisation cycle. The Y-position of the crystal upper surface (Y=130 mm) is indicated with discontinuous lines. The results indicate that the temperature distribution in *Furnace 2* is more homogeneous, as observed, the difference between temperatures T_1, T_2 and T_3 is less considerable than in *Furnace 1*, specially for crystallisation cycles No.1 and No.2.

Cette thèse est accessible à l'adresse : http://theses.insa-lyon.fr/publication/2022LYSEI044/these.pdf
© [K. Utria Salas], [2022], INSA Lyon, tous droits réservés

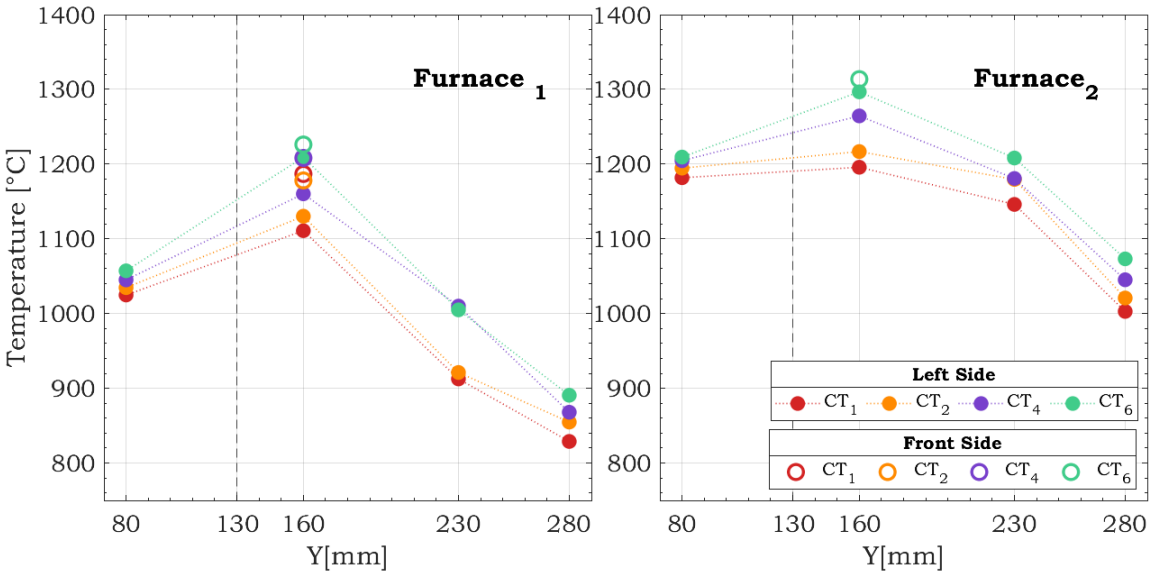

Figure 1.11: Temperatures for crystallisation cycles (CT): 1, 2, 4, 6 at $t_{cycle} = 9h$

From these two figures, it can be seen that the highest temperatures are found at the front of the furnace (T_5). An explanation for this is that thermocouple No.5 is located closer to the crystal growth environment because the thickness of the ceramic is lower in the front side. Besides, some flame flows out through the window. Regarding the left side, the highest temperatures are found at the crystal location, Y=160mm, as expected.

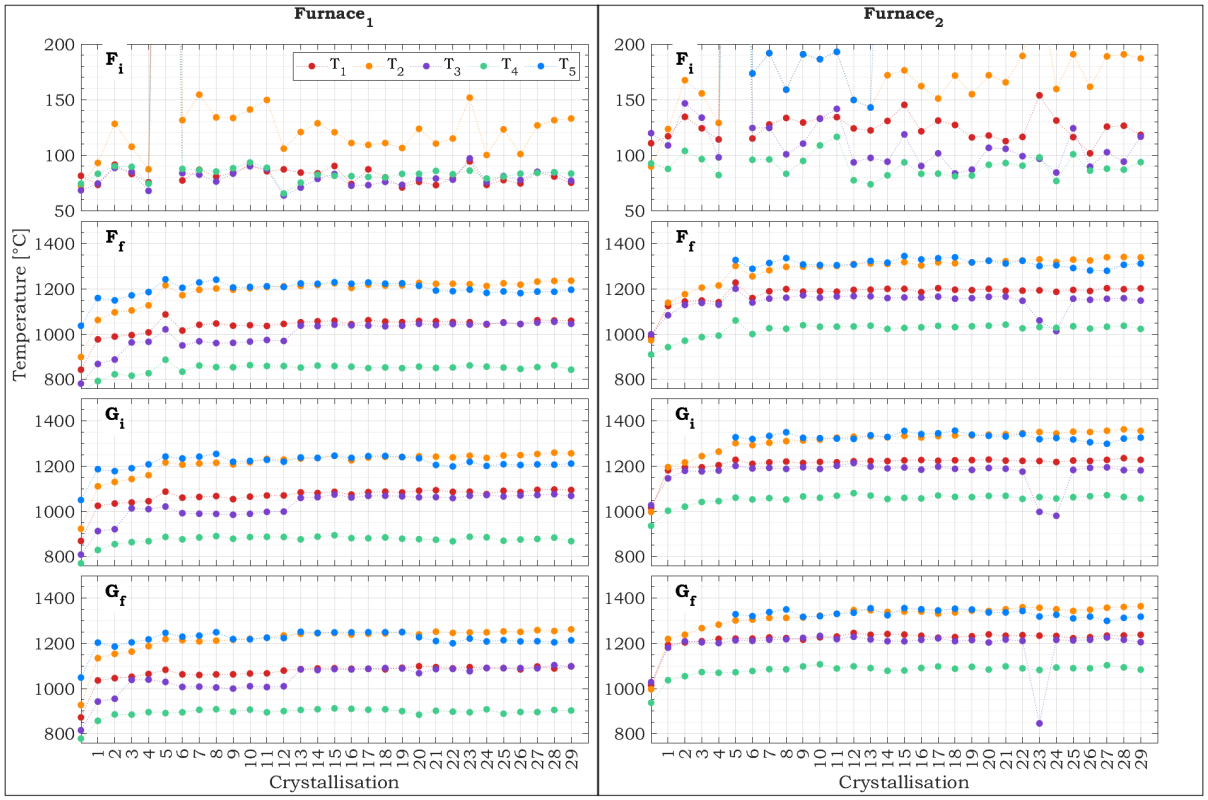

Figure 1.12: Temperature evolution at the beginning of each cycle during a crystallisation

Cette thèse est accessible à l'adresse : http://theses.insa-lyon.fr/publication/2022LYSEI044/these.pdf
© [K. Utria Salas], [2022], INSA Lyon, tous droits réservés

In addition, the temperature evolution throughout the entire insulation cycle for the four crystallisation phases are presented in figure 1.12. As observed, the increase in the temperature with the crystal presence is $\sim$ 150°C at all positions.

The most significant changes in temperatures are found between crystallisation No.1 and No.7. An increment is observed between 30 and 45°C at Y =160mm from one crystallisation to another. At Y=230mm (T_3) temperature increased $\sim$ 70°C between crystallisation No.2 and No.4 for *Furnace 1*, this increase was not seen in *Furnace 2*. At the other positions and crystallisations after cycle No.7, the increase is lower than 20 °C for both furnaces.

This subsection exposes the changes on the thermal and flame combustion conditions for the different crystallisation phases and crystallisation cycles. It is important to point out that the temperature depends not only on injection flow rates but also on different geometrical parameters of the ceramic confinement and the crystal itself. These parameters, their interactions and their influence on the temperatures are analysed in later sections (see sections 1.2.2.2 and 2.2).

1.2.2.2 Ceramic insulation evolution

This subsection is divided into two parts: the first part is about the evolution of the ceramic insulation geometry, in the second part the evolution of the thermal thickness of the crystal growth environment is analysed.

Ceramic insulation thickness evolution

In figure 1.13 the ceramic insulation thickness, δ_{cer}, represents the ceramic insulation available and the thermal thickness, δ_{therm} is the free space between the crystal and the internal ceramic surface. The crystal is always located at Y=130 mm from the top of the confinement.

The ceramic thickness is a parameter that defines the δ_{therm} and impacts the ceramic external surface temperature, hence the overall heat transfer. The adequate distribution of the temperature in the ceramic insulation contributes to improve the quality of the crystal. Therefore, the conduction heat transfer mechanism is analysed under three different δ_{cer} to determine the influence of this parameter on the temperature distribution of the crystal growth environment.

The general form of the heat flux vector according to Fourier's law in cylindrical coordi-

Cette thèse est accessible à l'adresse : http://theses.insa-lyon.fr/publication/2022LYSEI044/these.pdf
© [K. Utria Salas], [2022], INSA Lyon, tous droits réservés

nates is:

$$q'' = -k\nabla T = -k\left(i\frac{\partial T}{\partial r} + j\frac{\partial T}{\partial \psi} + k\frac{\partial T}{\partial z}\right) \tag{1.3}$$

where
$q''_r = -k\frac{\partial T}{\partial r}$ $q''_\psi = \frac{-k}{r}\frac{\partial T}{\partial \psi}$ $q''_z = -k\frac{\partial T}{\partial z}$
are heat flux components in the radial, circumferential, and axial directions, respectively.

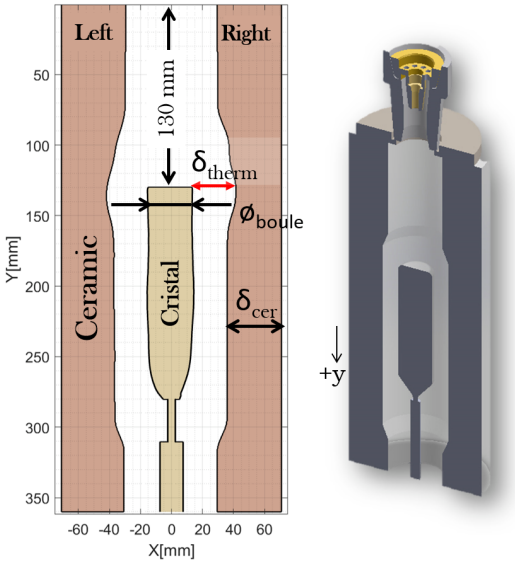

Figure 1.13: Front profile of the insulation ceramic in crystallisation (CT) No.2

Applying an energy balance to the differential control volume of figure 1.14, the following general form of the heat equation is obtained:

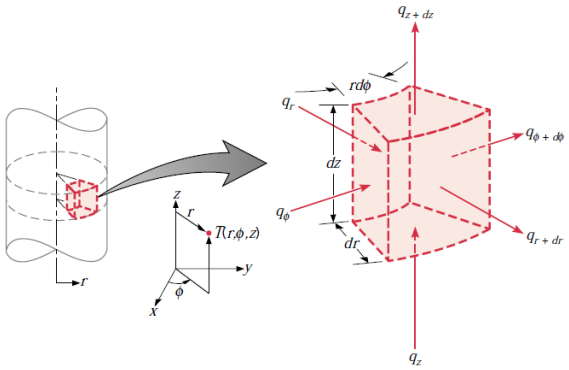

Figure 1.14: Differential control volume, dr·r dψ·dz, for conduction analysis in cylindrical coordinates (r,ψ, z) (Incropera et al., 2015)

$$\frac{1}{r}\frac{\partial}{\partial r}\left(kr\frac{\partial T}{\partial r}\right) + \frac{1}{r^2}\frac{\partial}{\partial \varphi}\left(k\frac{\partial T}{\partial \varphi}\right) + \frac{\partial}{\partial z}\left(k\frac{\partial T}{\partial z}\right) + \dot{q} = \rho C_p\frac{\partial T}{\partial t} \tag{1.4}$$

Cette thèse est accessible à l'adresse : http://theses.insa-lyon.fr/publication/2022LYSEI044/these.pdf
© [K. Utria Salas], [2022], INSA Lyon, tous droits réservés

where k is the thermal conductivity of the ceramic insulation $[W/m \cdot K]$
$\dot{q}$ is the rate at which energy is generated per unit volume of the medium $[W/m^3]$. This depends on the convection and radiative heat transfer coefficients which likewise depend on combustion conditions and crystal growth environment.
ρ is the density $[kg/m^3]$
C_p is the specific heat capacity $[J/kg.K]$

The general conduction heat transfer equation in cylindrical coordinates for our study is according to figure 1.15 and can be express as:

$$\frac{1}{r}\frac{\partial}{\partial r}\left(kr\frac{\partial T}{\partial r}\right) + \frac{1}{r^2}\frac{\partial}{\partial \varphi}\left(k\frac{\partial T}{\partial \varphi}\right) + \frac{\partial}{\partial y}\left(k\frac{\partial T}{\partial y}\right) + \dot{q} = \rho C_p \frac{\partial T}{\partial t} \tag{1.5}$$

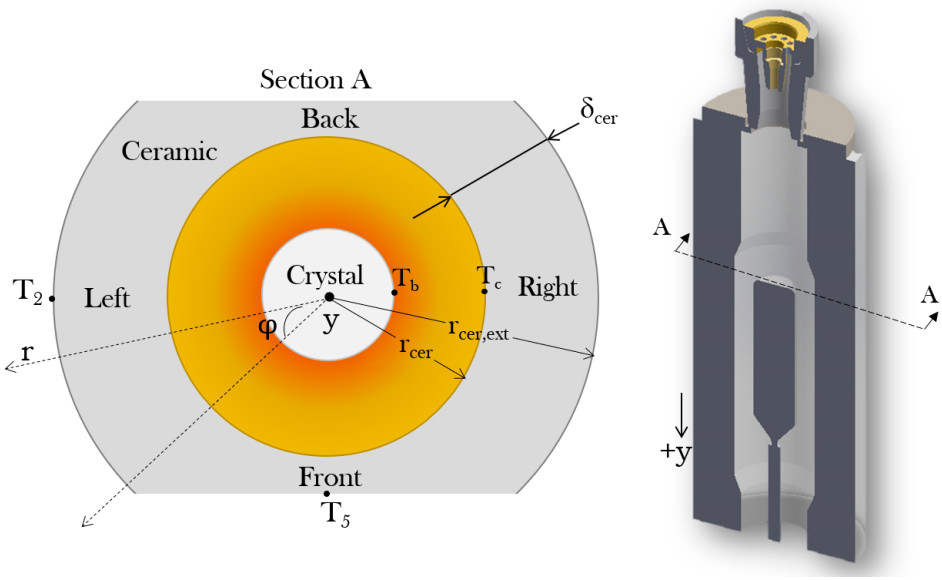

Figure 1.15: Ceramic Thickness,δ_{cer}

Considering the furnace as axisymmetric along Y-axis the equation 1.5 is:

$$\frac{1}{r}\frac{\partial}{\partial r}\left(kr\frac{\partial T}{\partial r}\right) + \frac{\partial}{\partial y}\left(k\frac{\partial T}{\partial y}\right) + \dot{q} = \rho C_p \frac{\partial T}{\partial t} \tag{1.6}$$

Considering that after three hours of operation the changes in the temperatures are almost negligent, the heat transfer can be consider as constant, and the thermal conductivity of the insulation material as constant. The equation for the conduction heat transfer along r and y is:

$$\frac{1}{r}\frac{\partial}{\partial r}\left(kr\frac{\partial T}{\partial r}\right) + \frac{\partial}{\partial y}\left(k\frac{\partial T}{\partial y}\right) + \dot{q} = 0 \tag{1.7}$$

Cette thèse est accessible à l'adresse : http://theses.insa-lyon.fr/publication/2022LYSEI044/these.pdf
© [K. Utria Salas], [2022], INSA Lyon, tous droits réservés

$r_i \leq r \leq r_0;\ 0 \leq y \leq L_{cer}$
where
r_i is the internal radius of the ceramic insulation
r_0 is the external radius of the ceramic insulation
L_{cer} is the total length of the ceramic insulation

Simplifying:

$$\frac{\partial^2 T}{\partial r^2} + \frac{1}{r}\frac{\partial T}{\partial r} + \frac{\partial^2 T}{\partial y^2} + \frac{\dot{q}}{k} = 0 \tag{1.8}$$

Resolving with Finite-Difference equations, explained in appendix A.1, the temperature distribution and the thermal gradients with different δ_{cer} are depicted in figure 1.16:

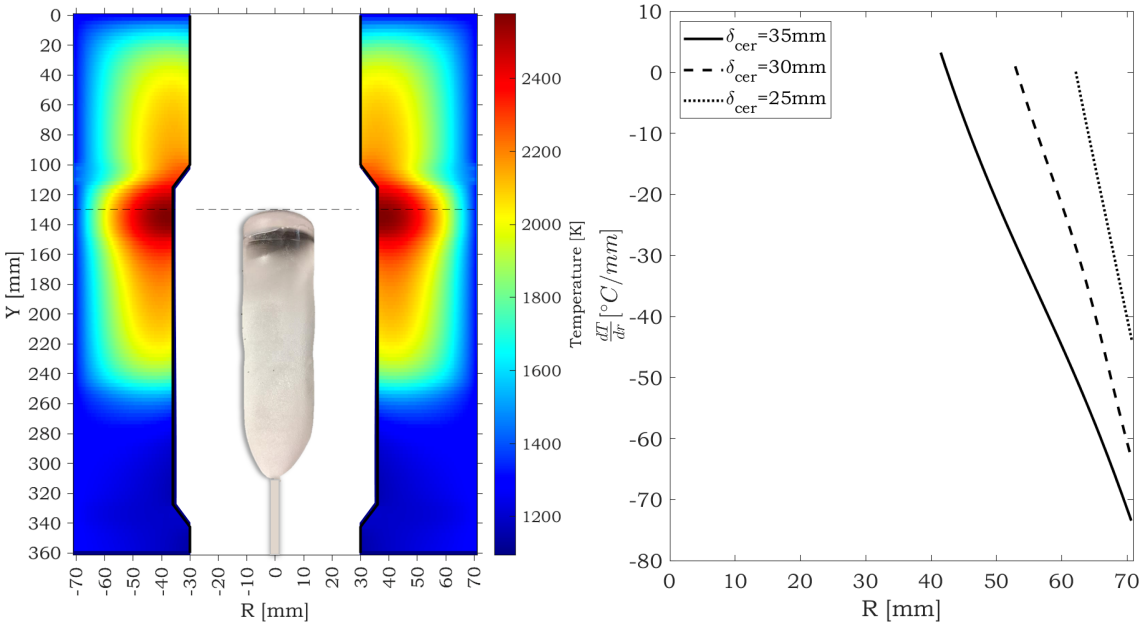

(a) Temperature Distribution [K] $\delta_{cer} = 35$mm (b) Thermal gradients Y=130mm

Figure 1.16: Temperature distribution and thermal gradient

Although, equation 1.8 is an approximation to describe the real thermal conditions of the crystal growth environment, it is helpful to asses the influence of the ceramic insulation geometry. It can be observed that at lower δ_{cer} the temperature gradient decreases between the external an internal surface of the ceramic insulation. These results indicate that a modification on the ceramic insulation geometry affects the thermal conditions in the crystal growth environment. Therefore, the δ_{cer} evolution during an insulation life cycle at the thermocouple positions are analysed in figure 1.17 for both furnaces. The most important changes were found between the first seven crystallisation cycles (to observe the complete profile of the ceramic see appendix A.2 figure A.4). These findings show that during this period the thermal conditions of the crystal environment are changing. In

Cette thèse est accessible à l'adresse : http://theses.insa-lyon.fr/publication/2022LYSEI044/these.pdf
© [K. Utria Salas], [2022], INSA Lyon, tous droits réservés

addition, farther in the insulation life cycle for crystallisation No.21 the ceramic thickness diminishes which also impacts the thermal conditions. The effect of the ceramic insulation geometrical characteristics on the crystal quality is analysed in section 2.4.

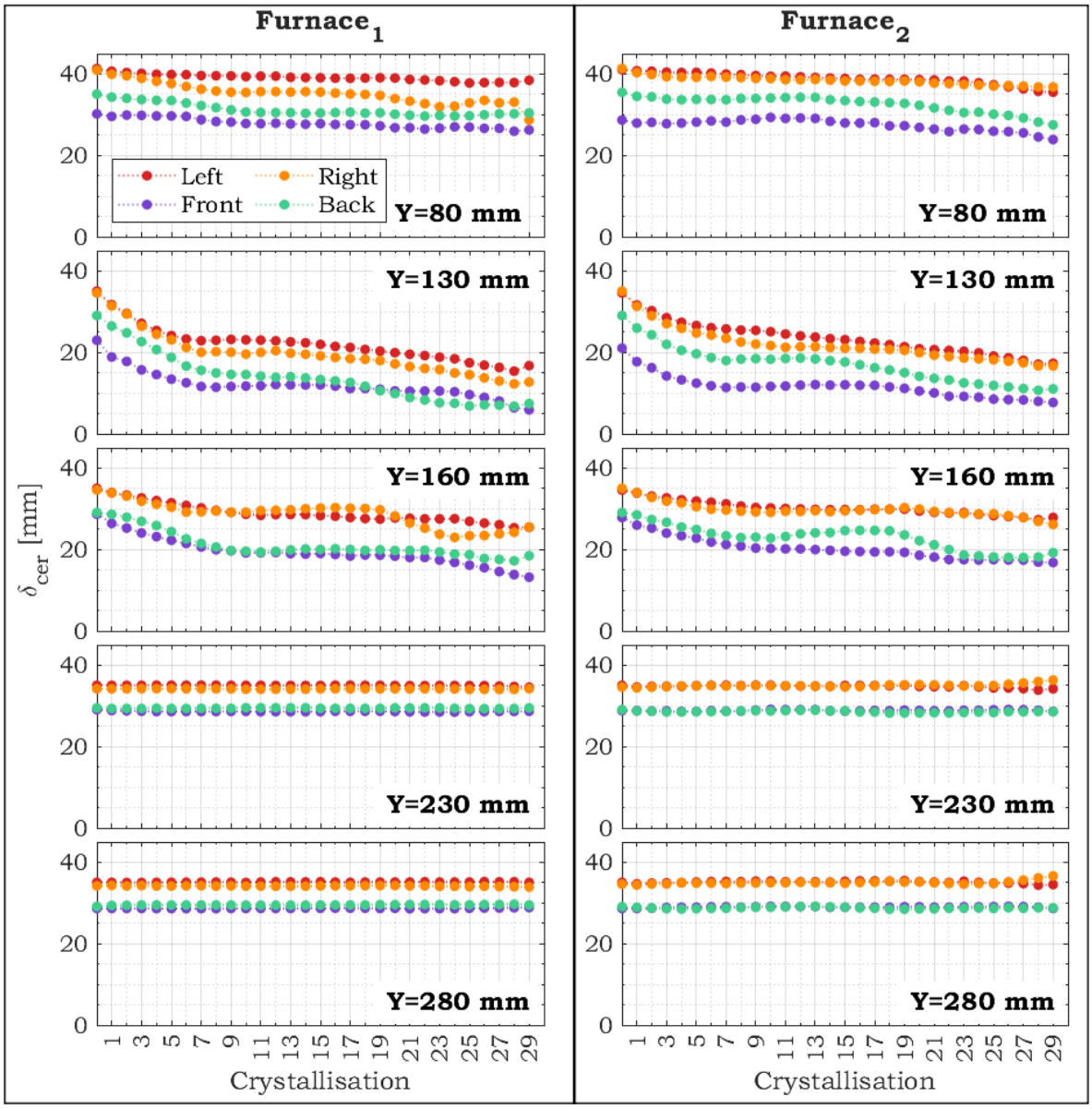

Figure 1.17: Ceramic Thickness Evolution, δ_{cer}

Figure 1.18 illustrates the complete profiles of for crystallisation cycles No.1, No.7, No.15 and No.29. *Furnace 1* insulation shows more substantial damage over the ceramic insulation life time, specially for the first crystallisations. The study shows that the ceramic thickness does not change significantly between CT No.7 and No.15, for almost all the sides except for the right side. This event is probably related to an inadequate positioning of the ceramic insulation. Moreover, the most significant degradation are observed between the Y-positions Y=70mm and Y=180mm. The encounter point between the crystal boule and the flame is located within this zone. The flame flow deviates some of the

Cette thèse est accessible à l'adresse : http://theses.insa-lyon.fr/publication/2022LYSEI044/these.pdf
© [K. Utria Salas], [2022], INSA Lyon, tous droits réservés

crystalline alumina towards the ceramic internal surface, causing a major accumulation of the material in this area which obliges the operators to remove part of the ceramic insulation. The back and the front reported the thinnest ceramic thickness, due to the initial geometric of the ceramic. The most remarkable degradation is observed for the front side where the ceramic window is located. It is important to point out that the flame seeded with crystallised alumina touches directly this zone, hence there is a higher quantity of crystallised material accumulated during a crystallisation cycle.

The impact of the ceramic thickness on the temperatures is analysed in section 2.2 and their interaction with the other quality parameters are analysed in chapter 2.

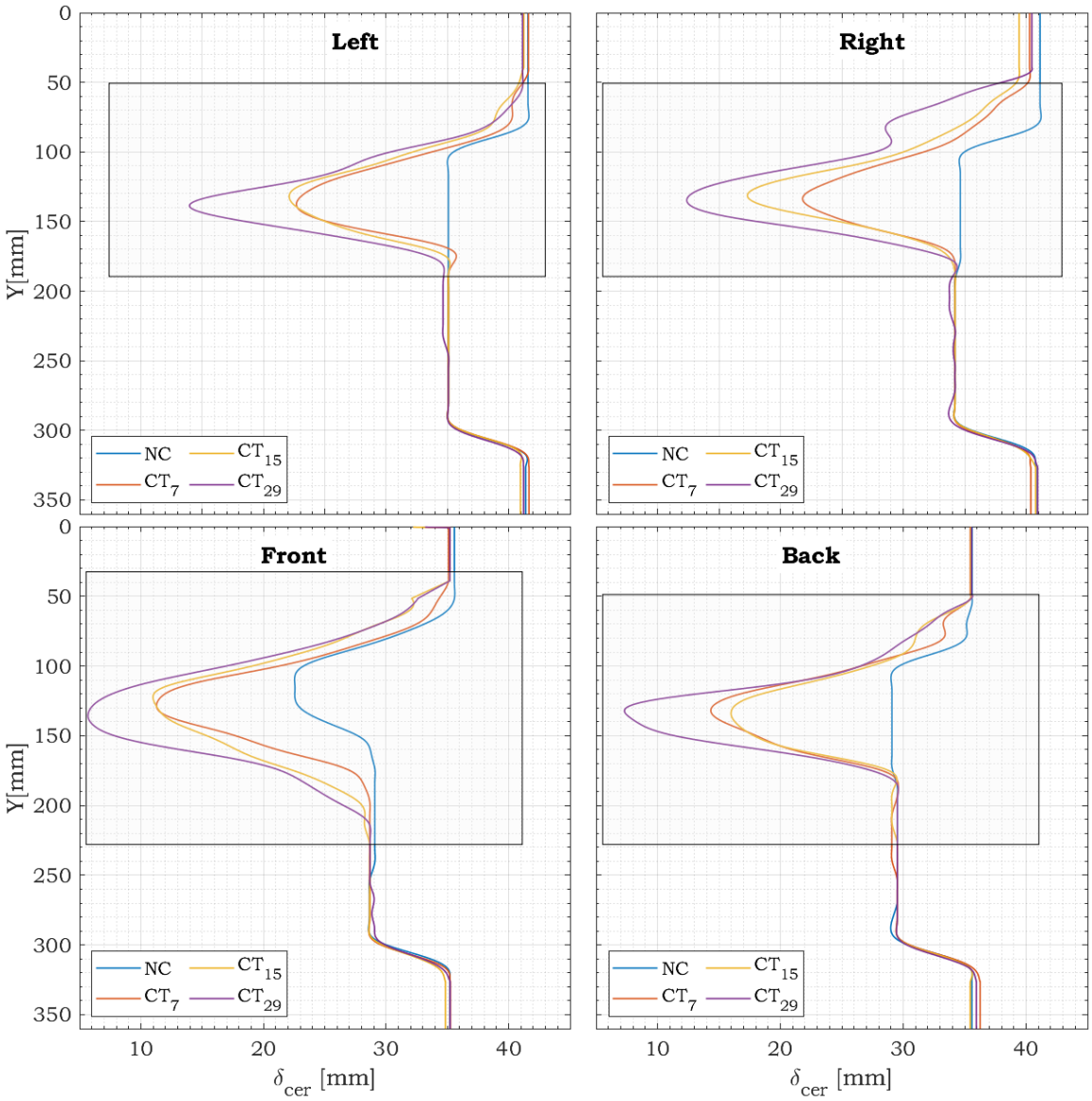

Figure 1.18: Ceramic Thickness (δ_{cer}) Evolution for crystallisation cycles [NC,7,15,29] in *Furnace 1.* *NC (No Crystal)

Cette thèse est accessible à l'adresse : http://theses.insa-lyon.fr/publication/2022LYSEI044/these.pdf
© [K. Utria Salas], [2022], INSA Lyon, tous droits réservés

Thermal thickness evolution

The thermal thickness, δ_{therm}, is a crucial parameter that indicates the area of heat transfer in the crystal growth environment (convection and radiation). This region is defined as the distance between the external surface of the crystal and the internal surface of the ceramic (see figure 1.13). This distance also corresponds to the flow flame development zone and defines the gradient temperature between the crystal and the insulation. However, defining the heat transfer equation is a challenging process due to the complex configuration of the furnace. δ_{therm} is a parameter that influence the environment, hence the temperature gradient. Due to the fact, that this parameter defines the thermal resistance, R_{therm}, see figure 1.19:

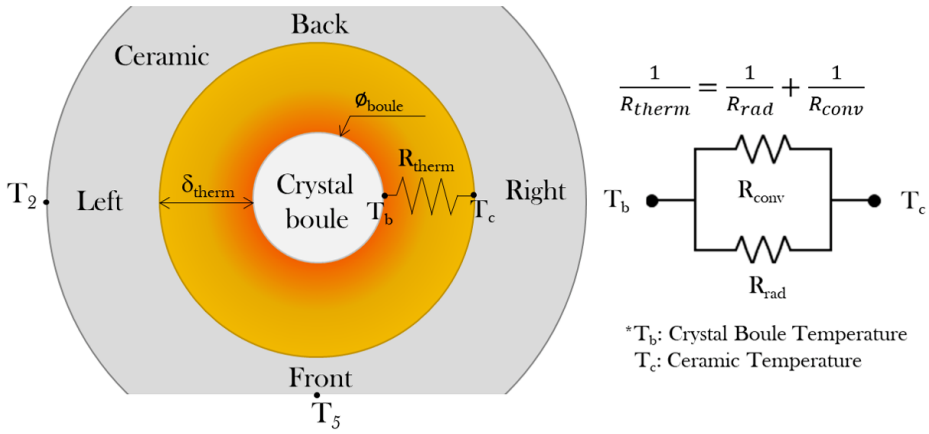

Figure 1.19: Scheme thermal resistance

R_{therm} is not an easy parameter to define, because this depends on convective and radiative heat transfer coefficients which in turn depend on the combustion conditions that are changing over time and along Y-axe owing the crystal growth. The system can be considered in steady state after $\sim$ 3 hours of operation, as observed in figure 1.10. This means that the analogy of thermal resistance can be used for small sections along Y-axis, Δy, to indicate the radial heat flow rate during the crystallisation. The steady radial heat flux, $\widehat{Q}_r$, between the external surface of the crystal and internal ceramic surface is given by:

$$\widehat{Q}_r = \frac{T_c - T_b}{R_{therm}} \tag{1.9}$$

Thermal resistances are determined by:

- Convection: The thermal resistance for convection for the small section is given by:

$$R_{conv} = \frac{1}{h_{conv} d\Lambda} \tag{1.10}$$

where h_{conv} is the convective heat transfer coefficient. Its value depends on the

Cette thèse est accessible à l'adresse : http://theses.insa-lyon.fr/publication/2022LYSEI044/these.pdf
© [K. Utria Salas], [2022], INSA Lyon, tous droits réservés

conditions at the surface layer between the solid and the fluid. It is influenced by the surface geometry, the nature of the fluid motion, and a variety of other thermodynamic parameters and

Λ is area. $d\Lambda = 2\pi r_{cer} dy = \pi(\oslash_{boule} + 2\delta_{therm})dy$

- Radiation: The thermal resistance for radiation is given by:

$$R_{rad} = \frac{1}{h_r d\Lambda} \tag{1.11}$$

where h_r is an effective radiation heat transfer coefficient. Between two gray diffuse surfaces, it is given by

$$h_r = \frac{1}{\varepsilon\sigma\Lambda(T_1^2 + T_2^2)(T_1 + T_2)} \tag{1.12}$$

where ε is emissivity

σ is Stefan Boltzmann constant [kg s^{-3} K^{-4}]

T ([K]) is temperature. The sub-indexes 1 and 2 refers to surface 1 and 2, respectively. For this particular case, 1 is the crystal boule and 2 is the internal surface of the ceramic insulation, hence:

$$h_r = \frac{1}{\varepsilon\sigma\Lambda(T_b^2 + T_c^2)(T_b + T_c)} \tag{1.13}$$

Hence R_{therm} is defined as:

$$\frac{1}{R_{therm}} = \pi(\oslash_{boule} + 2\delta_{therm})dy\,(h_{conv} + h_{rad}) \tag{1.14}$$

As observed, the thermal resistance decreases with higher δ_{therm}.

and $d\widehat{Q}_r$:

$$d\widehat{Q}_r = \pi(\oslash_{boule} + 2\delta_{therm})dy\,(h_{conv} + h_{rad})\,dT \tag{1.15}$$

where dT, represents the temperature gradient between the external surface of the crystal boule and the internal surface of the ceramic insulation. In figure 1.16, it was shown that the radial heat loss rate diminishes, when δ_{cer} decreases (increasing δ_{therm} with constant $\oslash_{boule}$). Thus, dT decreases with higher δ_{therm} due to higher thermal resistances (see equation 1.14) and lower heat loss rate.

Hence, external and internal defects might increase due to the inadequate thermal gradients in the confinement. In light of this, the accurate control of this parameter would contribute to improve the crystal quality.

Cette thèse est accessible à l'adresse : http://theses.insa-lyon.fr/publication/2022LYSEI044/these.pdf
© [K. Utria Salas], [2022], INSA Lyon, tous droits réservés

Figure 1.20 shows the δ_{therm} evolution throughout an insulation life cycle. The missing data corresponds to the crystallisations where the boule was broken or was not considered by the quality department. Three Y-positions were exposed:

- Y=130mm position where the crystal is located
- Y=160mm and Y=230mm positions where the the thermocouples are located, T_2 and T_3, respectively.

The complete profiles for the first six crystallisations are found in appendix A.3 in figure A.5. These changes in δ_{therm} are mainly the result of the removing process of the crystallised alumina performed by the production operators at the end of each crystallisation.

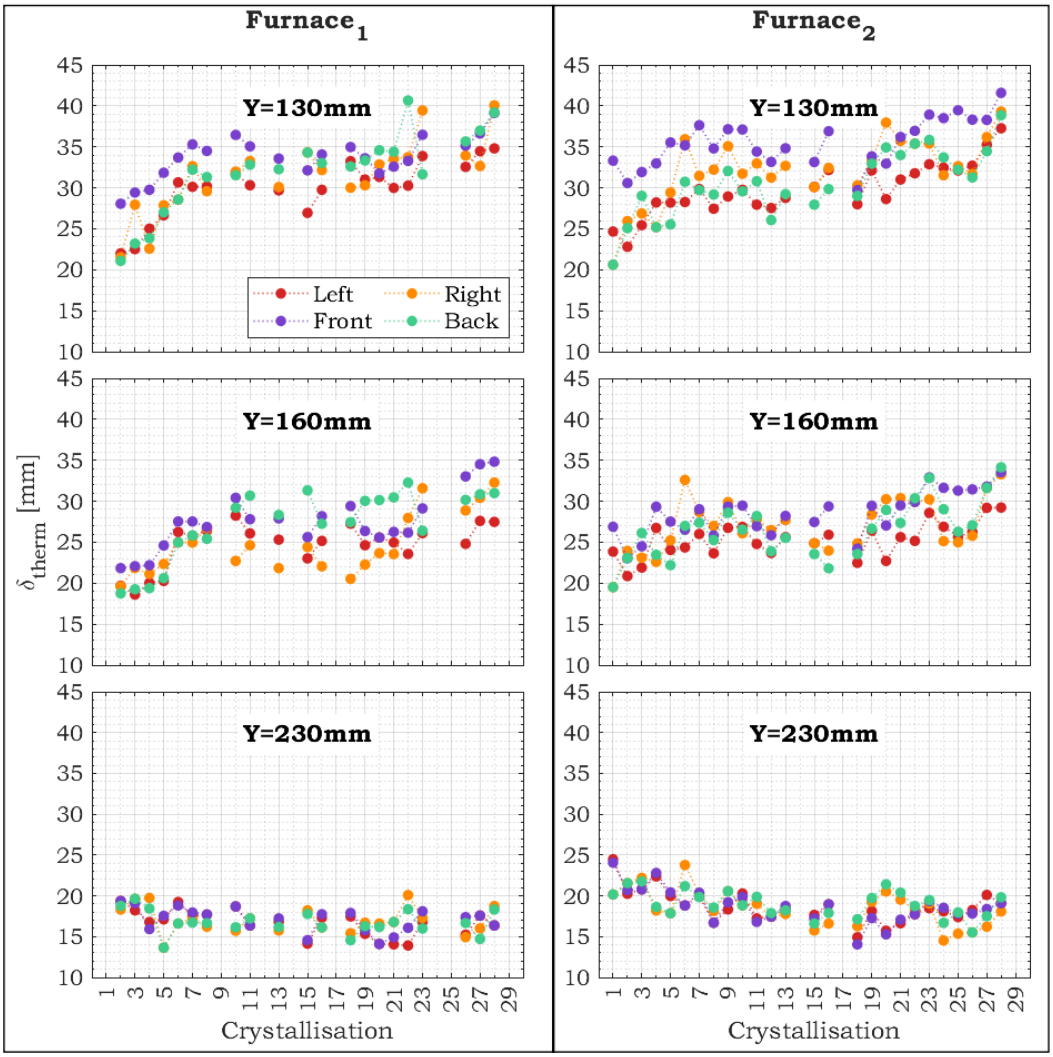

Figure 1.20: Thermal Thickness Evolution

In figure 1.20, it can be observed that for the first nine crystallisations the increase on δ_{therm} is more significant than the rest of the crystallisations. This behaviour occurs

Cette thèse est accessible à l'adresse : http://theses.insa-lyon.fr/publication/2022LYSEI044/these.pdf
© [K. Utria Salas], [2022], INSA Lyon, tous droits réservés

because of the rapid increase in the boule diameter (figure 1.21), causing a significant accumulation of crystallised alumina powder on the internal walls of the ceramic insulation, which obliged the operator to perform a removing process of this material. Its evolution and influence on crystal features are analysed in subsection 1.3.1.1.

The findings show the dynamic conditions of the crystal growth environment. It could be observed that the ***Furnace 2*** *presented a more homogeneous temperature distribution which means that the temperature gradients for this position are lower than in position 1, where a more significant difference was observed between the ceramic temperatures. Furthermore,* ***Furnace 2*** *also showed a lower degradation of the insulation ceramic that contributes to maintaining adequate temperatures gradients. This behaviour affects the thermal conditions in the crystal growth environment directly. The thermal thickness is a helpful parameter to define the thermal conditions of this complex system.*

Cette thèse est accessible à l'adresse : http://theses.insa-lyon.fr/publication/2022LYSEI044/these.pdf
© [K. Utria Salas], [2022], INSA Lyon, tous droits réservés

1.3 Crystal quality parameters

The crystal quality parameters are divide into three main groups: geometrical features, external defects and internal defects. These parameters define the geometrical and internal quality of the crystal, subsequent the evolution of all these features are shown:

1.3.1 Geometrical features

The geometrical features of the crystal are mainly correlated with the inlet flow rates, that are changing during a crystallisation cycle and during a insulation life cycle, as it could be seen section 1.2.1. Thence, it is necessary to measure their influence on crystal geometrical features as diameter, length and ovalisation index. Following, these aspects are examined:

1.3.1.1 Boule diameter and length evolution

Figure 1.21 shows the evolution of the diameter for the different crystallisation during the insulation life cycle. The *boule diameter*, $\oslash_{boule}$, represents the diameter of the cylinder inscribed in the crystal boule. As mentioned in section 1.2.1 for the first crystallisations, the objective diameters are the smallest, around 32 mm, as well as the first flow rates are the lowest of the cycle. It can be observed the diameter augmentation for these crystallisations. However, diameter values in crystallisation No.5 are excessively high compared to the objective. Consequently, in crystallisation No.6 the objective is decreased by reducing the flow rates as shown in figure 1.7. This procedure is repeated each time the diameter is highly elevated.

The interactions between the $\oslash_{boule}$ and flow rates affect the other parameters of the crystalline growth environment as ceramic temperatures and thermal thickness, δ_{therm}. As observed, the first seven crystallisations reported the most significant changes in these parameters, after this period the evolution is less important.

Regarding the temperatures, between crystallisation No.1 and No.7, the ceramic surface acquired $\sim 100°C$, at the same time $\oslash_{boule}$ increased 7 mm, and flow rates increased in 10%. It is important to mention that the ceramic temperature is also affected by δ_{cer} which lose more than 10mm of thickness at Y=130mm between these two crystallisations.

On the other hand, the thermal thickness increased 8 mm, increasing the temperature gradient between the ceramic and the crystal, hence the furnace heat loss rate. Their impact on crystal quality is analysed in section 1.3.2.

Cette thèse est accessible à l'adresse : http://theses.insa-lyon.fr/publication/2022LYSEI044/these.pdf
© [K. Utria Salas], [2022], INSA Lyon, tous droits réservés

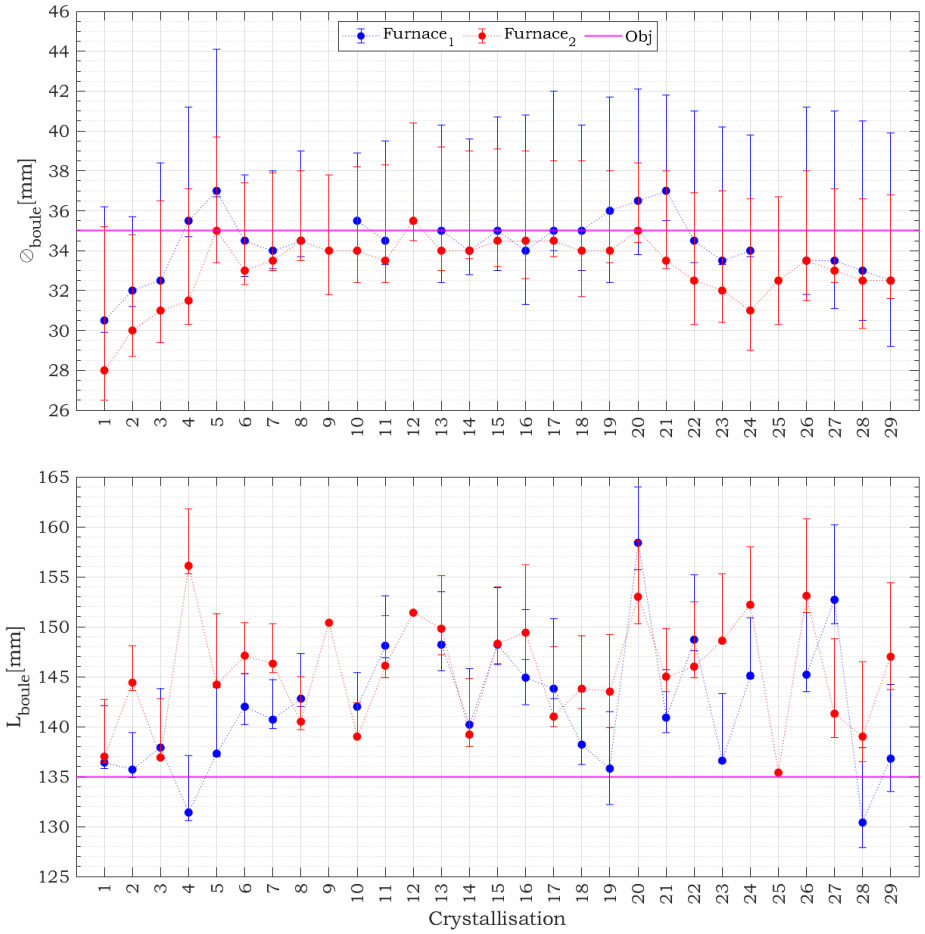

Figure 1.21: Diameter and Length Evolution (Obj: objective)

In the case of the boule length trends are difficult to find according to the results. This parameter is changing constantly.

1.3.1.2 Ovalisation index

One of the features that is taken into count to define the geometrical quality of the crystal is the *Verneuil boule* ovalisation index, "O_{in}". With the objective to calculate the ovalisation index an image acquisition is performed for each crystal considering an optical axis perpendicular to the Verneuil boule axis. Thus 100 geometric profiles of the crystal are obtained by rotating the latter on its axis (see below the principle diagram - top view).

Cette thèse est accessible à l'adresse : http://theses.insa-lyon.fr/publication/2022LYSEI044/these.pdf
© [K. Utria Salas], [2022], INSA Lyon, tous droits réservés

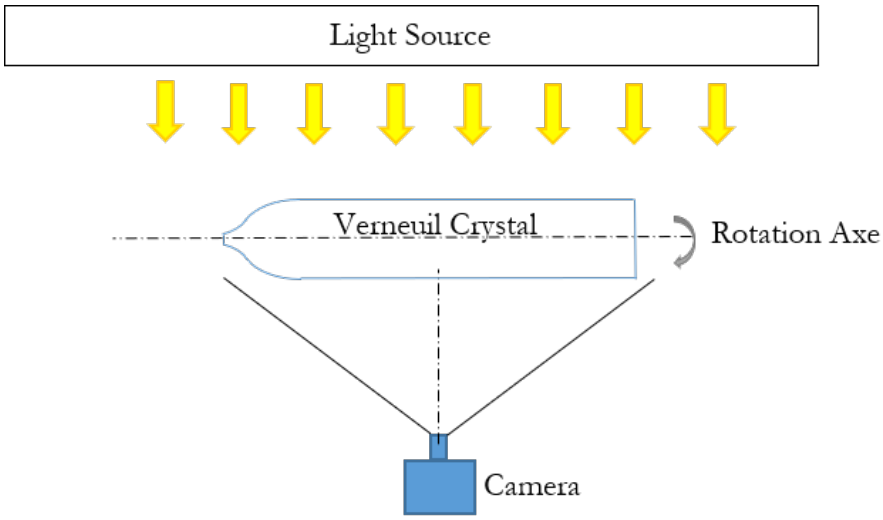

Figure 1.22: Definition of the Ovalisation Index

In order to calculate the ovalisation index (see figure 1.22), for each section "i" of the cylindrical part (i = 1 to n depending on the length of the cylindrical part), 100 diameters (j = 1 to 100) are calculated from the images. It is thus obtained the variable $\oslash_{i,j}$ with j = 1 to 100 and i = 1 to n.

$$O_{in} = \frac{\oslash_{i,j\ max} - \oslash_{i,j\ min}}{\frac{\sum_{j=1}^{100} \oslash_{i,j}}{100}} \tag{1.16}$$

Finally, a global ovalisation index "O_{in}" is acquired over the whole of the cylindrical section by: Thus for each section "i" we have an ovalisation index O_{in} whose calculation is as follows:

$$O_{in} = \frac{\sum_i O_i}{n} \tag{1.17}$$

Ovalisation is mainly due to the thermal conditions of the crystalline growth environment. The temperature gradient is a critical parameter that affects the ovalisation index. From empirical knowledge acquired through observation, RSA production team has stated that the probability of finding high ovalisation index increases with lower temperature gradients, the crystal boule can growth in any direction causing the oval shape of the boule. However, there are not quantity study to prove this hypothesis. As observed in subsection 1.2.2.2, the temperature gradients are related to the thermal thickness (δ_{therm}), therefore this parameter is used to analyse the ovalisation index.

In figure 1.23 crystallisation No.5 presents an elevated ovalisation index, owing the high value of δ_{term} (low temperature gradient). *Furnace 1* also presents a higher ovalisation index due to the crystalline growth conditions. The heat lost rate is lower for this furnace as observed in figures 1.10 and 1.12, where the external temperatures of the ceramic

Cette thèse est accessible à l'adresse : http://theses.insa-lyon.fr/publication/2022LYSEI044/these.pdf
© [K. Utria Salas], [2022], INSA Lyon, tous droits réservés

insulation were lower for this furnace. Although *Furnace 2* also loses significant insulation, its ovalisation index keeps lower than 4%, which is the maximum accepted. These values are obtained due to the confined conditions given by the other furnaces around, generating more adequate temperature gradients. At the end of the insulation cycle, *Furnace 1* ovalisation index is extremely high due to the loss of the ceramic insulation, caused by the low temperature gradients. Ensuing their influence on crystal defects is analysed.

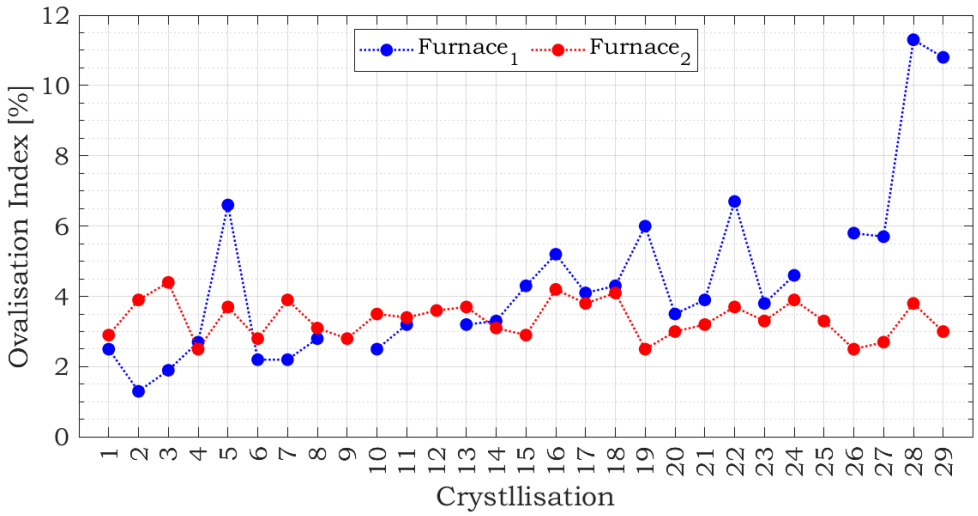

Figure 1.23: Ovalisation index evolution

1.3.2 Crystal defects

This section shows the crystal defects obtained during the cycle analysed. They are classified as external defects and internal defects.

1.3.2.1 External defects

External defects are related to the geometrical appearance of the crystal boule. These defects are causes for difference reasons as.

- Bad position of the germ at the beginning of the cycle
- Inadequate alumina powder frequency injection.
- Accumulation of crystallised alumina powder on the internal ceramic walls

Figure 1.24 shows some of the geometrical type of defects that can be found. Although there are other defects that can be present, during this study they were not found:

Cette thèse est accessible à l'adresse : http://theses.insa-lyon.fr/publication/2022LYSEI044/these.pdf
© [K. Utria Salas], [2022], INSA Lyon, tous droits réservés

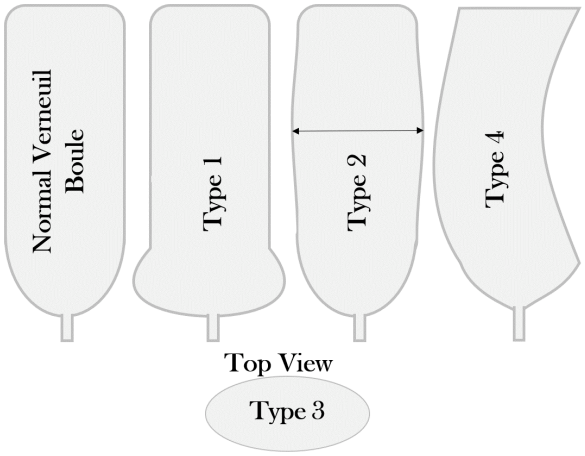

Figure 1.24: Type of external defects

- Type 1: The base of the boule is larger than than the rest of the boule, this defects occurs during the formation and is due to the germ position at the beginning of the cycle.
- Type 2: There is at least one transversal area along the boule with a diameter superior to 4 mm to the mean boule diameter. One of the causes is the inadequate powder frequency injection.
- Type 3: Ovalisation when the percentage of ovalisation is superior a 4%, see previous section (1.3.1.2).
- Type 4: One of the boule side is not straight and has a curve, this is present when the powder sticks to the internal ceramic wall and the space of crystal growth is not enough.

In figure 1.25, type 0 refers to the crystal boule without defects. It is apparent that crystal boules for *Furnace 2* presents fewer geometrical defects than *Furnace 1*. At the beginning of the cycle, it can be observed that both furnaces present type 2 defects, which is probably related with a inadequate powder frequency injection. Between crystallisation cycle No.6 and cycle No.14 there is no presence of defects. Moreover, at the end of the cycle in *Furnace 1* defects type 2 and 3 are more recurrent, which are probably present due to an increase in the temperature gradient.

Cette thèse est accessible à l'adresse : http://theses.insa-lyon.fr/publication/2022LYSEI044/these.pdf
© [K. Utria Salas], [2022], INSA Lyon, tous droits réservés

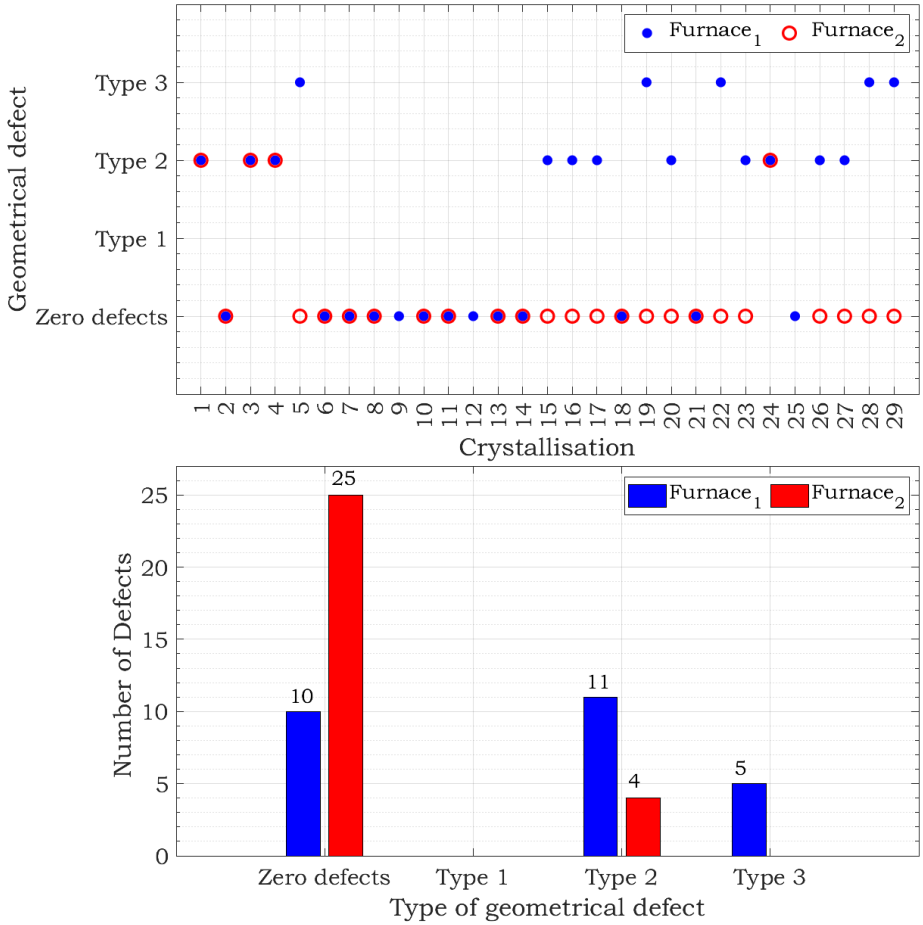

Figure 1.25: Geometrical defects evolution

1.3.2.2 Internal defects

Sapphire, Alpha (α)-alumina crystal, is the most common form of crystalline aluminium oxide and has a corundum structure, mainly composed of atoms of aluminum (Al^{3+}) and oxygen (O^{2-}) (Dienes et al., 1975). These atoms are packed according to a determined geometry (hexagonal packing), as shown in figure 1.26. The use of the Verneuil method for industrial sapphire growth can present different internal defects. They are related to the crystalline structure which determines the mechanical and optical properties of the crystal.

Corundum crystals belong to the ditrigonal-scalenohedral class of the trigonal symmetry with symmetry elements. Sapphire can be expressed both as a hexagonal as well as a rhombohedral unit cell, due to hexagonal structure of the space group D^3d^6 (R3c) (Dobrovinskaya et al., 2009). The basic structure consists of hexagonal close-packed planes of oxygen intercalated with aluminum planes. The aluminum planes arrangement has 1/3 of the sites vacant, resulting in an Al/O ratio of 2/3 as represented in figure1.26. Each Al

Cette thèse est accessible à l'adresse : http://theses.insa-lyon.fr/publication/2022LYSEI044/these.pdf
© [K. Utria Salas], [2022], INSA Lyon, tous droits réservés

atom is coordinated by 6 oxygen atoms, and each oxygen atom has 4 Al neighbours. The vacancies are aligned on the R-planes, giving sapphire the ability to cleave along these rhombohedral planes (Dienes et al., 1975).

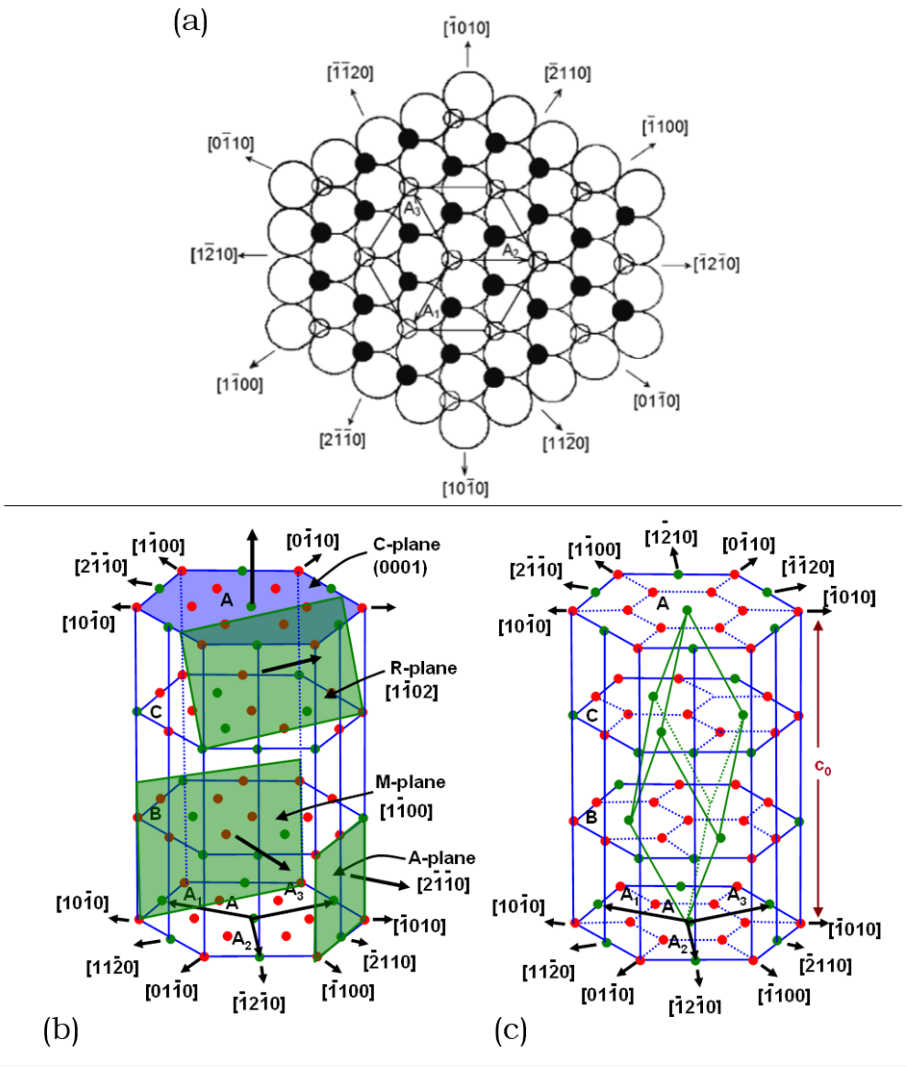

Figure 1.26: Structure of Sapphire: (a) Schematic of the arrangement of Al^{3+} (black circles) and octahedral hollows (small light circles) between two layers of O^{2-}(large light circles) in the basal plane (the upper O^{2-} layer is not shown). A_1 , A_2 , and A_3 are $\langle 11\bar{2}0\rangle$ translational vectors of the hexagonal sapphire cell for the basal plane. Printed from Dobrovinskaya et al. (2009). (b) A-, M-, R-, and C-planes of the crystal; (b) Schematic illustration of the aluminum planes, printed from Liao (2007).

The crystalline structure can be perturbed significantly within the vacancies by using Verneuil method to fabricate the industrial sapphire. The potential defects generated by this technology are called Bubbles and Foils. These defects are usually formed during the last quarter of the crystallisation cycle at high-temperature gradients.

Cette thèse est accessible à l'adresse : http://theses.insa-lyon.fr/publication/2022LYSEI044/these.pdf
© [K. Utria Salas], [2022], INSA Lyon, tous droits réservés

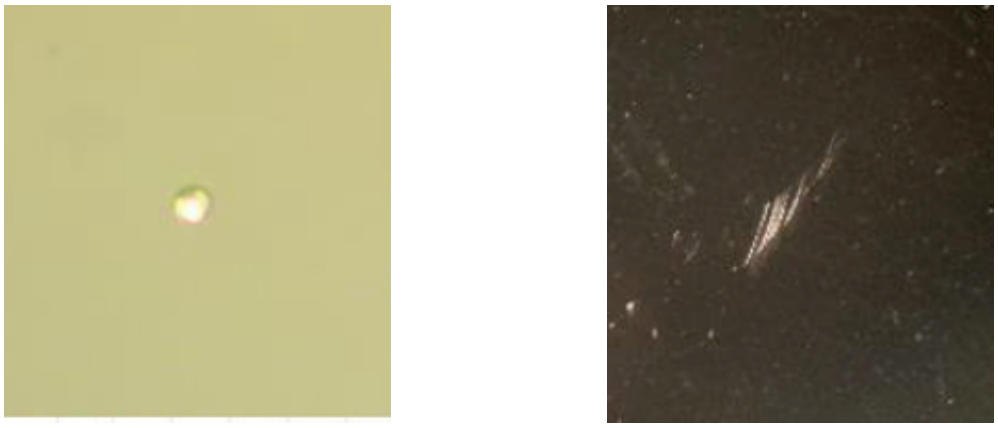

(a) Bubbles (b) Foils

Figure 1.27: Defects of structure crystalline

- **Bubbles** are gas inclusions linked either to stabilisation of the crystallisation front (growth rate too high) or degassing of a chemical element at low evaporation temperature (figure 1.27a).
- **Foils** are low-angle grain boundary or sub-grain boundary decorations that are the result of small bubbles (μm) clusters in the grain boundaries present in the material (figure 1.27b). For instance, interstitial H_2 within the grain boundary is detected by highlighting O-H bonds (using IR spectrometry).

  A sub-grain boundary is the interface between two grains with a misorientation less than 15° in a single-crystal. These misorientations are the results of the temperature gradient between the top and bottom surface of the *Verneuil boule* during crystallisation. High temperature gradients cause a stress relaxation that move the plans of the crystalline structure to counter the elevated temperature difference and produce the dislocations. These defects in the crystal structure tend to decrease the electrical and thermal conductivity of the material.

The crystal defects are detected through the optical properties of the sapphire, using different techniques as cross-polarisation. This technique, with regard to visible light, is a process wherein two polarisers with perpendicular orientation to one another are used on the incident and reflected lights.

Figure 1.28: Birefringence (Auctions, 2019)

One of the optical properties is the birefringence, Δn (equation 1.18), which is defined as the double refraction of light in a transparent, molecularly ordered material, which is manifested by the existence

Cette thèse est accessible à l'adresse : http://theses.insa-lyon.fr/publication/2022LYSEI044/these.pdf
© [K. Utria Salas], [2022], INSA Lyon, tous droits réservés

of orientation-dependent differences in refractive index. When a ray luminous passes through a crystal it is divided into two part-rays: ordinary and extraordinary, possessing signs of different refraction. The ordinary ray passes through the object in a straight line and the extraordinary ray suffers parallel displacement. An example to through a calcite crystal is presented in figure 1.28. As they pass through the crystal, the two rays have neither the same polarisation nor the same speed of propagation (Patzelt, 1974).

$$\Delta n = n_e - n_0 \tag{1.18}$$

where n_e is the angle of the extraordinary ray and n_o is the angle of the ordinary ray.

The sapphire is a trigonal crystal, which means that it presents properties of uniaxial negative birefringence. This property allows its observation in crossed polarisation. Indeed, the crystal crossed by initially polarised light transmits two beams whose polarisations are orthogonal, as shown in figure 1.29. By placing a polarised filter perpendicular to the other side of the crystal, a light signal is obtained which depends the orientation of the crystal. This easy-to-implement technique makes it possible to quickly know the orientation of crystals.

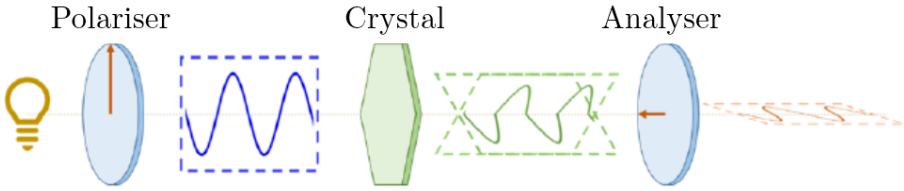

Figure 1.29: Cross Polarisation. Printed from Muzy (2021)

An extinction condition for cross-polarised sapphire occurs when the $\overrightarrow{c}$ (see figure 1.30) axis is parallel to the direction polarisation of the analyser or polariser. When this is achieved, if the crystals possess domains showing disorientation greater than 1/10°, they can be observed.

Cette thèse est accessible à l'adresse : http://theses.insa-lyon.fr/publication/2022LYSEI044/these.pdf
© [K. Utria Salas], [2022], INSA Lyon, tous droits réservés

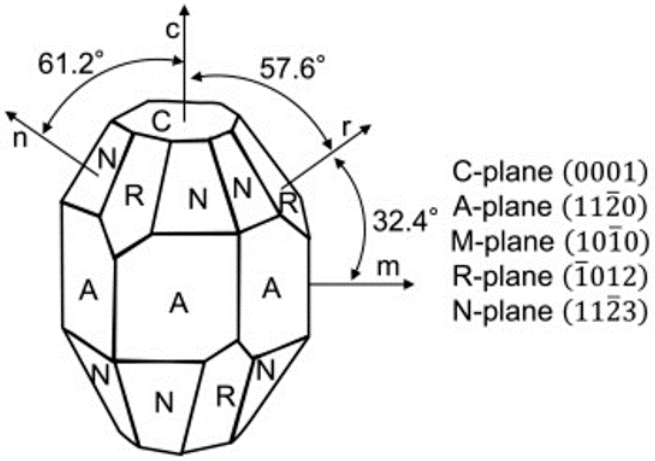

Figure 1.30: Crystallographic structure with the common nomenclature of crystal planes for the structural unit cell. Capital letters denote planes and small letters indicate a crystallographic axis or the corresponding plane normal. Printed from Dobrovinskaya et al. (2009)

In figure 1.31, the polarisation photography of a crystal is shown. This is composed of several grains slightly disoriented with respect to each other. Since they can not be all simultaneously observed in one extinction condition (some appear brighter than others that are more opaque). This technique allows quickly identifying the different grains of a crystal as well as the zones slightly disoriented from a single crystal.

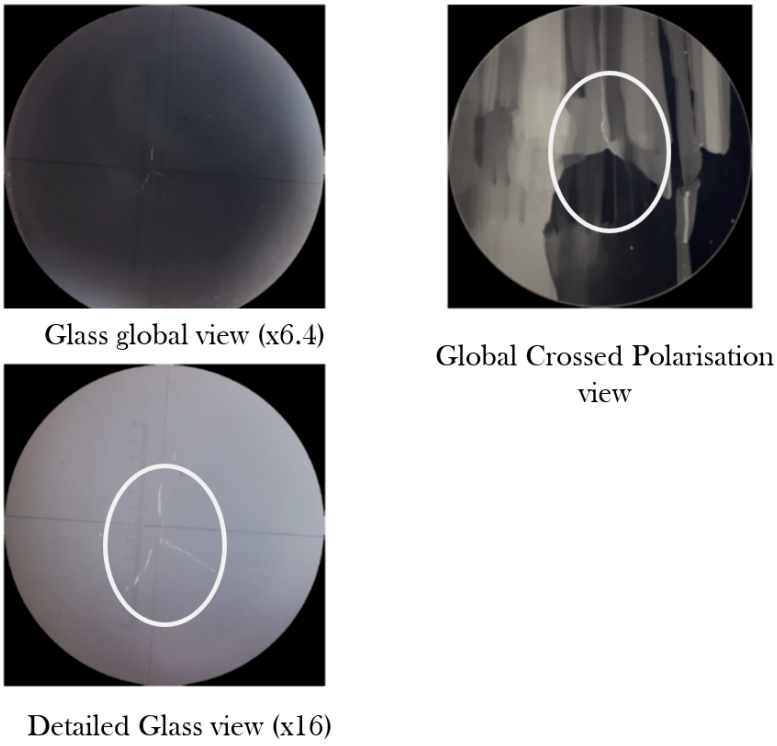

Figure 1.31: Foils detection through crossed polarisation

Cette thèse est accessible à l'adresse : http://theses.insa-lyon.fr/publication/2022LYSEI044/these.pdf
© [K. Utria Salas], [2022], INSA Lyon, tous droits réservés

Furthermore, another technique used to detect the bubbles and the foils inside the crystalline structure is the tomography. This is performed for each crystal boule produced. The Vernueil boules are submerged inside a liquid solution, and the foils and bubbles are revealed as shown in figure 1.33.

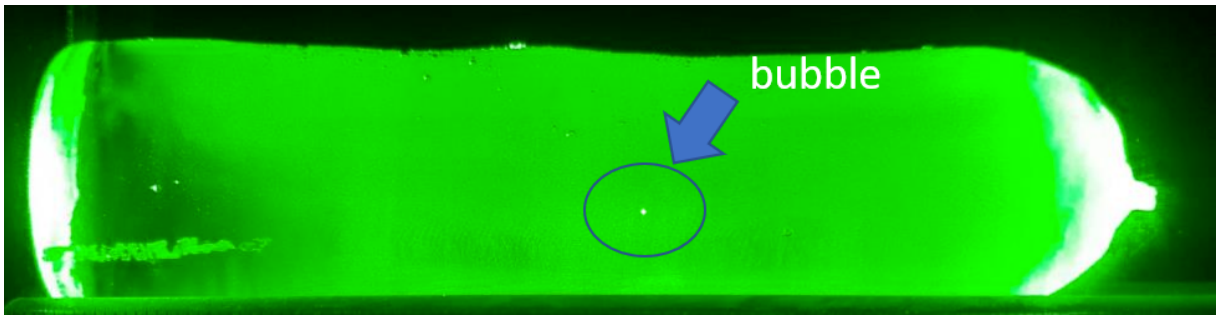

Figure 1.32: Tomography performed during the quality control to detect Bubbles and Foils. A bubble was detected during this test

The objective of this technique is to observe the internal defects in the crystal by visualising them through a laser slice—particularly the bubbles by light scattering (Mie Scattering). The crystal rotates on its axis to the laser plane "sweeps" the entire volume of the *Verneuil boule*. However, this technique presents a risk for the observer. When the laser beam passes through the crystal, it causes a reflection (the beam is not always normal to the surface of the crystal; otherwise, there would be no reflection). This reflection is particularly troublesome or even dangerous for the observer. In order to (partially) overcome this reflection, the crystal is immersed in a liquid (CH_2I_2). This liquid has the following properties:

- It has a refractive index close to that of sapphire. The solid/liquid interface then "disappears", and consequently, there is no longer any reflection at the interface.
- It has good wettability on sapphire, allowing the liquid to contact the crystal very well. Thus, the surface roughness "disappears", and it gives the impression of a fully polished crystal.

Figure 1.33 illustrates the bubbles and the foils detected in this study. As observed there are not apparent tendency along the crystallisation cycles. Bubbles seem to be more present in *Furnace 2*. The influence and correlation of the other parameters are analysed on the next chapter.

Cette thèse est accessible à l'adresse : http://theses.insa-lyon.fr/publication/2022LYSEI044/these.pdf
© [K. Utria Salas], [2022], INSA Lyon, tous droits réservés

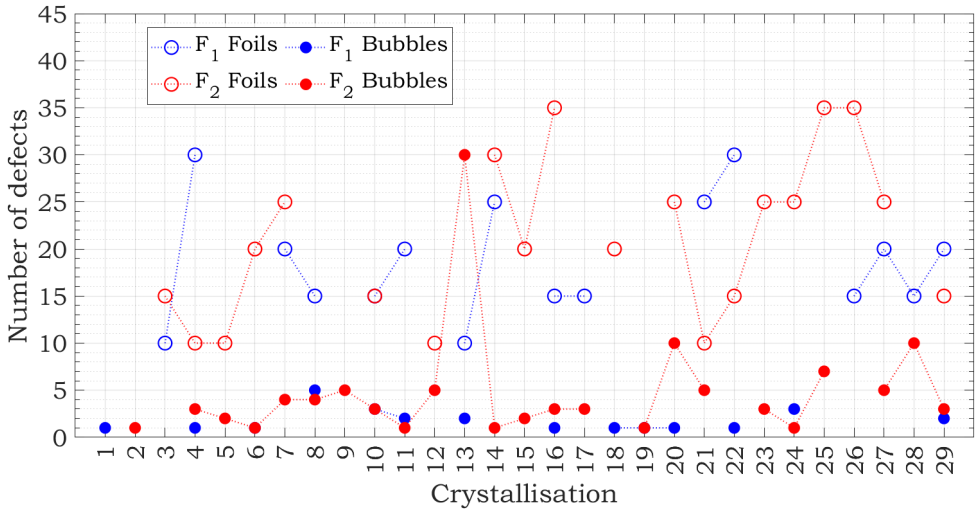

Figure 1.33: Internal defects evolution

As observed, the crystal growth environment, determined by the injection flow rates and insulation conditions, affects considerably the quality of the crystal. These parameters determine whether the Verneuil boule exhibits the desirable geometry and the internal quality. The results of this section are not enough to find tendencies and correlations between the crystal growth environment and the quality of the crystal. Therefore, an statistical study is performed later on.

Cette thèse est accessible à l'adresse : http://theses.insa-lyon.fr/publication/2022LYSEI044/these.pdf
© [K. Utria Salas], [2022], INSA Lyon, tous droits réservés

1.4 Conclusions

The evolution of crystal growth parameters were observed for an insulation life cycle. The flow rates along the cycle fluctuated regarding the objective boule diameters and the insulation conditions of the confinement. These adjustments affected the ceramic temperatures at first instance. Nevertheless, these temperatures are also dependent of other parameters as δ_{cer} and $\oslash_{boule}$, which were also changing. δ_{cer} reported a decreased between two crystallisation cycles in a row, which can be detected in the increase of the temperatures of the ceramic external surface. δ_{term} increased at the beginning of the cycle, to then stabilised; however finding a tendency was challenging.

In addition, the evolution of the crystal features in terms of quality parameters were also studied during the insulation life cycle. The study highlighted the necessity to find correlations between the controlled and the quality parameters of the crystallisation process. Due to the complexity of the system the direct correlations and trends are difficult to establish. Therefore, in the next chapter a statistical study is performed.

Finally, it could be observed that the crystal boules obtained between crystallisation cycle No.7 and No.19 presented the best crystal features. Thus, in chapter 7 of part III another study was carried out with a new ceramic insulation geometry, in order to analyse their influence on crystal features. Moreover, as observed flow rates are the controlled variables that are regulated to have the desired crystal. In chapter 8 the flow rates of this chapter were the base to study the impact of the crystal presence in the development of the flame and flow structure.

Cette thèse est accessible à l'adresse : http://theses.insa-lyon.fr/publication/2022LYSEI044/these.pdf
© [K. Utria Salas], [2022], INSA Lyon, tous droits réservés

Chapter 2 | Statistical Correlations

During the study carried out at the factory, many data were collected from the different parameters analysed. Twenty-nine crystallisations for two furnaces were analysed. Each crystallisation has four different phases the initial formation (F_i), the final formation (F_f), the initial growth and the final growth (G_i and G_f, respectively), which correspond to four values of H_2 and O_2 flow rates (eight in total). At the same time, the evolution of the ceramic insulation temperature for five vertical positions were collected with the geometrical dimensions of the ceramic internal surface. Besides, the external and internal qualities of the crystal were also taking into count. All these parameters represent in total 1392 values (see table 2.1), which are dependent of one another.

Description	**Number of variables**
Crystallisations	29
Furnaces	2
External parameters	7
Internal parameters	2
Temperatures	5
Ceramic Insulation geometry (sides)	2
Flow rates	8
Total	**1392**

Table 2.1: Total of Variables analysed during the production study

Therefore, finding the correlations between them became a complex process. Hence, a widespread statistical tool that describes complex relations among variables called Analysis of Variance (ANOVA) was used. First of all, the statistical tools and the parameters used are exposed. Several preliminary studies were carried out to identify correlations, but not all the links between these parameters could be established. Hence, this chapter only shows the statistically significant factors.

2.1 Statistical Techniques

Statistician Ronald Fisher developed this analysis at the beginning of the twenty century, which is a collection of statistical models and their associated estimation procedures (Fisher, 1919). They are used to determine whether there are any statistically significant

Cette thèse est accessible à l'adresse : http://theses.insa-lyon.fr/publication/2022LYSEI044/these.pdf
© [K. Utria Salas], [2022], INSA Lyon, tous droits réservés

differences between the means of three or more independent (unrelated) groups. Depending on the number of parameters analysed and correlated, the ANOVA can be classified as one-way ANOVA, two-way ANOVA and N-way ANOVA, the next two sections explain their principles.

2.1.1 One-way ANOVA

The one-way ANOVA compares the means between two or more groups and determines whether any of those means are statistically significant from each other by using the null hypothesis (Miller, 1997):

$$H_0 : \mu_{m,1} = \mu_{m,2} = \mu_{m,3} = ... = \mu_{m,k} \tag{2.1}$$

where μ_m is the group mean and k is the number of groups.

With this equation the alternative hypothesis, H_1, is evaluated. H_1 affirms that there are at least two group means that are statistically significant from each other. If one-way ANOVA returns a statistically significant result, H_1 is accepted. One-way ANOVA can determine only that at least two groups were statistically significant. To specify which group differed from each other a post hoc test is needed. Post hoc analysis (from Latin post hoc, "after this") consists of statistical analyses that are specified after the data were seen. The most common post hoc tests are:

- Tukey's honest significance test, or Tukey's HSD (honestly significant difference) test (Ott and Longnecker, 2016)
- Bonferroni Procedure (Ott and Longnecker, 2016)
- Duncan's new multiple range test (MRT) (Duncan, 1955)
- Dunn's Multiple Comparison Test (Dunn, 1961)
- Fisher's Least Significant Difference (LSD) (Fisher, 1992)
- Holm-Bonferroni Procedure (Holm, 1979)
- Newman-Keuls (Newman, 1939)
- Rodger's Method (Roberts, 2011)
- Scheffe's Method (Ott and Longnecker, 2016)

The principle of ANOVA is based on the dispersion of the data (i.e the spacing of the data around the mean). According to one-way ANOVA the data dispersion has two origins:

Cette thèse est accessible à l'adresse : http://theses.insa-lyon.fr/publication/2022LYSEI044/these.pdf
© [K. Utria Salas], [2022], INSA Lyon, tous droits réservés

1. Dispersion or variability: this corresponds to the effect of the factor studied, and it is called factor variability or inter-class variability .

2. The intrinsic variability. This variability is also called residual variability, because it is the part of variability that remains when the factor variability is subtracted from the total variability. This corresponds to the part of dispersion which is not explained, and considered as the noise of the data.

The objective of ANOVA is to determine, using a statistical test, whether the part of dispersion attributable to the factor studied is significantly greater than the residual part. If the factorial dispersion is significantly greater than the residual dispersion, then this means that the dispersion of the data, around the means of each modality, is low compared to the dispersion of the means around the general average. And if the means for each modality are very dispersed, at the same time as the intra-class variability is low, then this means that the means are globally different. Conversely, if the factorial dispersion is of the same order of magnitude as the residual dispersion, then this means that the means are not globally different. The calculation of the ANOVA process is summarised in figure 2.1.

It is important to mention that the ANOVA is a linear regression model which assumes a mean by modality of the factor studied. It is written:

$$y_{ij} = \overline{y_i} + e_{ij}$$

e_{ij} correspond to the residuals (the differences between the observations and the means of the groups to which they relate). It is on these residuals that the validity hypotheses of the F test are evaluated. The results of the F test are valid, if:

- the residuals are independent
- the residuals follow a normal distribution with mean 0 and *variance = residual variance*
- the residues are homogeneous.

This is verified with a regression diagnosis and / or the use of adequate statistical tests. If these assumptions are not verified, it is always possible to apply a transformation at the response level (log for example), or to use a non-parametric ANOVA (Kruskal-Wallis test), or to perform a ANOVA based on permutation tests.

Cette thèse est accessible à l'adresse : http://theses.insa-lyon.fr/publication/2022LYSEI044/these.pdf
© [K. Utria Salas], [2022], INSA Lyon, tous droits réservés

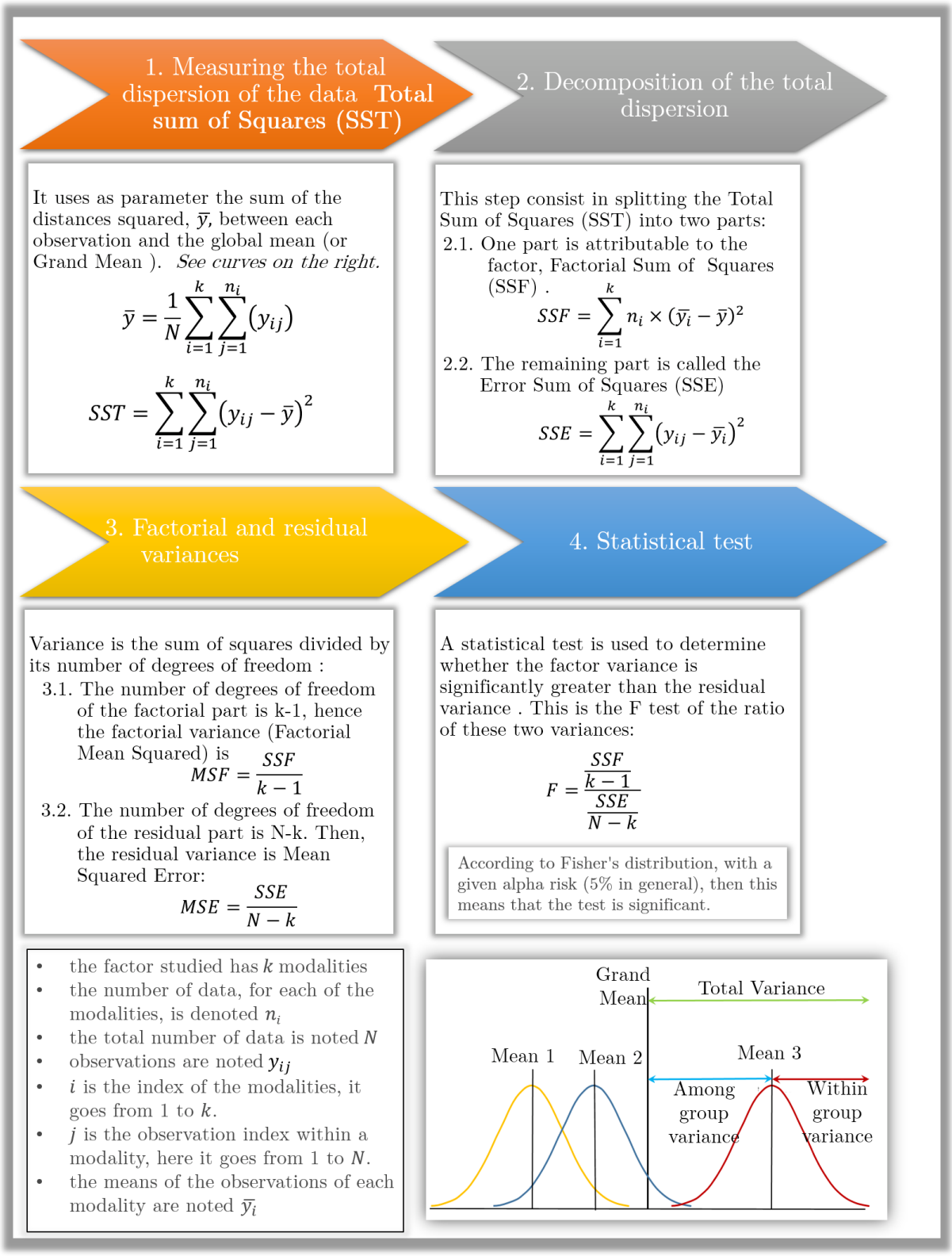

Figure 2.1: Detailed one-way ANOVA Process (RAInBOV internal documentation).

Cette thèse est accessible à l'adresse : http://theses.insa-lyon.fr/publication/2022LYSEI044/these.pdf
© [K. Utria Salas], [2022], INSA Lyon, tous droits réservés

2.1.2 Two-way ANOVA

The two-way ANOVA is an extension of the one-way ANOVA. It evaluates the effects of two factors on a response variable, no longer of a categorical variable (or factor), but of two categorical variables, on a response. These two factors can be independent, and have no interaction effect, or the impact of one factor on the response variable can depend on the group (level) of the other factor. If the two factors have no interactions, the model is called an additive model (Miller, 1997).

Two-way ANOVA is typically used to analyse the results of an experiment. The experimental units are exposed, in a random (randomized) fashion, to one of the combinations (or crosses) of the modalities of the two categorical variables. We then speak of a factorial plan , 2×2 if the categorical variables have two modalities each, or 2×3 for example if one of the variables has two modalities and the other three modalities, etc ...

The number of observations within each condition (crossing of the modalities) is generally identical, one speaks of "balanced" factorial plan.

In a factorial experiment, the categorical variables are said to be controlled, because it is the experimenter who chooses their modalities (or levels). Besides, randomization makes it possible to erase, on average the effects of variables not studied.

The factorial experimental design makes it possible to limit the number of experimental units used (compared to a study carried out with each of the variables separately), but above all it makes it possible to assess whether the two categorical variables act jointly on the response variable, or not. This is called interaction. If the evolution of the response according to the different modalities of the first categorical variable does not depend on the modalities of the second categorical variable, then there is no interaction between the two variables. If, on the contrary, we observe a modification of this evolution, either by an increase in the effect of the first variable, or by a decrease, then there is an interaction.

Similar to one-way ANOVA, the principle of two-factor ANOVA is based on the total dispersion of data, and its breakdown into four origins :

- the part attributable to the first factor
- the part attributable to the second factor
- the part attributable to the interaction of the 2 factors
- the unexplained or residual part .

Two-way ANOVA is a special case of the linear model. Following, the two-way ANOVA

Cette thèse est accessible à l'adresse : http://theses.insa-lyon.fr/publication/2022LYSEI044/these.pdf
© [K. Utria Salas], [2022], INSA Lyon, tous droits réservés

form of the model calculated by MATLAB (2021):

$$y_{ijr} = \mu_m + \alpha_i + \beta_j + (\alpha\beta)_{ij} + \epsilon_{ijr} \tag{2.2}$$

where,
y_{ijr} is an observation of the response variable.
i represents group i of row factor A, $i = 1, 2, ..., I$.
j represents group j of column factor B, $j = 1, 2, ..., J$.
r represents the replication number, $r = 1, 2, ..., R$.

There are a total of $N = I \times J \times R$ observations. μ_m is the overall mean.

α_i are the deviations of groups defined by factor A from the overall mean μ_m . The values of α_i sum to 0.

$$\sum_{i=1}^{I} \alpha_i = 0. \tag{2.3}$$

β_j are the deviations of groups defined by factor B from the overall mean μ_m. The values of β_j sum to 0.

$$\sum_{j=1}^{J} \beta_j = 0. \tag{2.4}$$

$(\alpha\beta)_{ij}$ are the interactions. The values in each row and in each column of $(\alpha\beta)_{ij}$ sum to 0.

$$\sum_{i=1}^{I} (\alpha\beta)_{ij} = \sum_{j=1}^{J} (\alpha\beta)_{ij} = 0. \tag{2.5}$$

ϵ_{ijr} are the random disturbances. They are assumed to be independent, normally distributed, and have constant variance.

Two-way ANOVA tests hypotheses about the effects of factors A and B, and their interaction on the response variable y. The hypotheses about the equality of the mean response for groups of row factor A are:

$$H_0 : \alpha_1 = \alpha_2 = \alpha_3 = ... = \alpha_I \tag{2.6}$$

H_1: at least one α_i is different, $i = 1, 2, ..., I$. The hypotheses about the equality of the mean response for groups of column factor B are

$$H_0 : \beta_1 = \beta_2 = \beta_3 = ... = \beta_J \tag{2.7}$$

H_1: at least one β_j is different, $j = 1, 2, ..., J$.

Cette thèse est accessible à l'adresse : http://theses.insa-lyon.fr/publication/2022LYSEI044/these.pdf
© [K. Utria Salas], [2022], INSA Lyon, tous droits réservés

The hypotheses about the interaction of the column and row factors are

$$H_0 : (\alpha\beta)_{i,j} = 0 \tag{2.8}$$

H_1: at least one $(\alpha\beta)_{ij} \neq 0$

2.1.3 Application to the study

As mentioned, different parameters were analysed, such as: injection flow rates, ceramic insulation thickness, ceramic external temperatures, boule diameter and length, internal and external defects. In total 1392 values were used to performe the analysis. The correlations between all these parameters were found by using one-way and two-way ANOVA. The study used the MATLAB Statistics and Machine Learning Toolbox to find the correlations between the parameters, the general results given by MATLAB are shown in tables 2.2 and 2.3. As post-hoc analysis the study uses a widespread method, the Tukey's range test.

Tukey's range test, also known as Tukey's test, Tukey method, Tukey's honest significance test, or Tukey's HSD (honestly significant difference) test, is a single-step multiple comparison procedure and statistical test. It can be used to find means that are significantly different from each other. Named after John Tukey, this method compares all possible pairs of means, and is based on a studentised range distribution (q) (this distribution is similar to the distribution of t from the t-test (Kutner et al., 1975)). This method rejects the null hypothesis, $H_0 : \alpha_i = \alpha_j$, if (MATLAB, 2021):

$$|t| = \frac{|\overline{y}_i - \overline{y}_j|}{\sqrt{MSE\left(\frac{1}{n_i} + \frac{1}{n_j}\right)}} > \frac{1}{\sqrt{2}} q_{\alpha,k,N-k}, \tag{2.9}$$

where $q_{\alpha,k,N-k}$ is the upper $100 * (1-\alpha)$th percentile of the studentised range distribution with parameter k and $N-k$ degrees of freedom. k is the number of groups (treatments or marginal means) and N is the total number of observations.

In addition, the covariance between the parameters was also analysed. Probability theory and statistics define covariance as a measure of the directional relationship between the returns on two random variables. This measure evaluates how one variable will change regarding the other. The covariance is positive when the variables tend to behave similarly. In other words, the greater values of one variable correspond with the greater values of the other variable, as in for the lesser values. In contrast, for cases where the covariance is negative, the greater values of one variable correspond principally to the lesser values of

Cette thèse est accessible à l'adresse : http://theses.insa-lyon.fr/publication/2022LYSEI044/these.pdf
© [K. Utria Salas], [2022], INSA Lyon, tous droits réservés

the other, which denotes that the variables tend to show opposite behaviour. Moreover, cases with covariance equal to zero refer to the variables that are not correlated (Rice, 1995).

For two random variable vectors A and B, the covariance is defined as (MATLAB, 2021):

$$cov(A, B) = \frac{1}{N-1} \sum_{i=1}^{N} (A_i - \mu_{m,A}) * (B_i - \mu_{m,B}) \tag{2.10}$$

where $\mu_{m,A}$ is the mean of A, $\mu_{m,B}$ is the mean of B, and * denotes the complex conjugate. The covariance matrix of two random variables is the matrix of pairwise covariance calculations between each variable,

$$C = \begin{pmatrix} cov(A, A) & cov(A, B) \\ cov(B, A) & cov(B, B) \end{pmatrix}$$

For a matrix A whose columns are each a random variable made up of observations, the covariance matrix is the pairwise covariance calculation between each column combination. In other words, $C(i, j) = cov(A(:, i), A(:, j))$.

Cette thèse est accessible à l'adresse : http://theses.insa-lyon.fr/publication/2022LYSEI044/these.pdf
© [K. Utria Salas], [2022], INSA Lyon, tous droits réservés

Source	**SS**	**df**	**MS**	**F**	**P-value**
Group(Between)	SSF	$k-1$	MSE=SSF/$(k-1)$	MSE/MSF	$P(F_{k-1\,N-k})$>F
Error(Within)	SSE	$n-K$	MSE=SSE/$(N-k)$		
Total	SST	$n-1$			

Column	**Definition**
Source	Source of the variability.
SS	Sum of squares due to each source.
df	Degrees of freedom associated with each source. N is the total number of observations and k is the number of groups. $N-k$ is the within-groups degrees of freedom (Error) $k-1$ is the between-groups degrees of freedom (Columns), $N-1$ is the total degrees of freedom: $N-1=(N-k)+(k-1)$.
MS	Mean squares for each source, which is the ratio SS/df
F	F-statistic, which is the ratio of the mean squares.
Prob>F	p-value, which is the probability that the F-statistic can take a value larger than the computed test-statistic value. one-way ANOVA derives this probability from the cdf of the F-distribution.

Row (Source)	**Definition**
Groups or Columns	Variability due to the differences among the group means (variability between groups)
Error	Variability due to the differences between the data in each group and the group mean (variability within groups)
Total	Total variability

Table 2.2: MATLAB (2021) presentation of the results. The standard one-way ANOVA table

Cette thèse est accessible à l'adresse : http://theses.insa-lyon.fr/publication/2022LYSEI044/these.pdf
© [K. Utria Salas], [2022], INSA Lyon, tous droits réservés

Source	SS	df	MS	F	P-value
Columns	SS_A	$k-1$	MS_A	MS_A/MSE	$P(F_{k-1,:\ mk(R-1)})$>F
Rows	SS_B	$m-1$	MS_B	MS_B/MSE	$P(F_{m-1,:\ mk(R-1)})$>F
Interaction	SS_{AB}	$(m-1)(k-1)$	MS_{AB}	MS_{AB}/MSE	$P(F_{(m-1)(k-1),:\ mk(R-1)})$>F
Error	SSE	$mk(R-1)$	MSE		
Total	SST	$mkR-1$			

Row (Source)	Definition
Columns	Variability due to the column factor
Rows	Variability due to the row factor
Interaction	Variability due to the interaction of the row and column factors
Error	Variability due to the differences between the data in each group and the group mean (variability within groups)
Total	Total variability

Table 2.3: MATLAB (2021) presentation of the results. The standard two-way ANOVA table, k : modalities Factor A and m : modalities factor B, R number of replications

One of the crucial part to use ANOVA is the definition of the parameters. In table 2.4 the parameters are summarised. The factors used were according to the controlled and response parameters of the crystallisation process, already exposed in figure 1.2. As independent variables are found the reactive flow rates, which likewise are divided in different levels as initial formation cycle, final formation cycle, initial crystal growth cycle and final crystal growth cycle. The furnace position was also evaluated as independent variable, to recall one furnace is located at one extreme of the production line and the other furnace is found at the centre (see figure 1.3). Geometrical and internal crystal characteristic are defined as response variables. As well as the thermal thickness and ceramic temperatures. However, later on they are categorised and used as independent variables to analyse their impact on the crystal quality parameters.

Ceramic temperature was measured in five different positions which are indicated as modalities of this variable.

Furthermore, the crystal quality parameters are divided into four factors:

- Verneuil boule diameter, $\oslash_{boule}$.
- Index Ovalisation, O_{in}
- Geometrical or external defects that are divided in four different types, exposed in section 1.3.2.1.

Cette thèse est accessible à l'adresse : http://theses.insa-lyon.fr/publication/2022LYSEI044/these.pdf
© [K. Utria Salas], [2022], INSA Lyon, tous droits réservés

- Internal Defects: This response has two categories that are foil and bubbles defects, explained previously in section 1.3.2.2 .

Independent Variables			
Parameters	**Factors (or groups)**		**Modality**
Thermal and flame combustion parameters	Flow rates	Initial Formation, F_i Final Formation, F_f Initial Growth, G_i Final Growth, G_f	H_2 O_2
Production process	Furnace Position		Furnace 1 (F_1) Furnace 2 (F_2)

Response Variables			
Thermal and flame combustion parameters	Ceramic temperature	Initial Formation, F_i Final Formation, F_f Initial Growth, G_i Final Growth, G_f	T_1 T_2 T_3 T_4 T_5
	Thermal thickness (δ_{therm}) Ceramic insulation thickness (δ_{cer})		
Crystal geometrical parameters	Verneuil boule diameter Ovalisation index		
Quality parameters	Internal Defects		Foils Bubbles

Table 2.4: Syntheses of the parameters analysed

Cette thèse est accessible à l'adresse : http://theses.insa-lyon.fr/publication/2022LYSEI044/these.pdf
© [K. Utria Salas], [2022], INSA Lyon, tous droits réservés

2.2 Correlations of thermal and flame combustion parameters

As discussed in section 1.2.1, a crystallisation has four crucial moments: the beginning of the cycle, which corresponds to the crystal initial formation phase F_i, the final formation phase F_f, the beginning of the crystal growth G_i and the end of the crystal growth G_f, each of them with specific flow rates reported in figure 1.7. An one-way ANOVA was performed to compare the effect of flow rates on ceramic temperatures. It was determined whether there is or not a difference in the mean ceramic temperatures between the four groups. The temperature in position 2 was analysed which corresponds to the closest location of the stagnation point between the flame and the crystal boule. In table 2.5, the factor and response variable are described. The factor chosen to be observed was the hydrogen flow rates, since the ratio between hydrogen and oxygen most be maintained, ν_{O_2} is dependent on ν_{H_2}.

Factor	**Modality (k)**	**Response**
Flow rates	F_i	Temperature Position 2
ν_{H_2}	F_f	
	G_i	
	G_f	

Table 2.5: Variables of the one-way ANOVA

The results are depicted with one-way ANOVA tables (refer to tables 2.2 and 2.3), and Tukey's test tables, the latter are shown in appendix A.3. The dispersion data is illustrated with Box-and-Whisker charts, described in figure 2.2. This is a useful graph that provides a visual representation of statistical data based on the minimum, first quartile, median, third quartile, and maximum. Outliers are plotted as individual points (du Toit et al., 1986). The data is represented in graph that looks like a rectangle (box) with lines extending from the top and bottom (whisker). The distances between different box parts represent the degree of data dispersion and data asymmetry to identify outliers.

Cette thèse est accessible à l'adresse : http://theses.insa-lyon.fr/publication/2022LYSEI044/these.pdf
© [K. Utria Salas], [2022], INSA Lyon, tous droits réservés

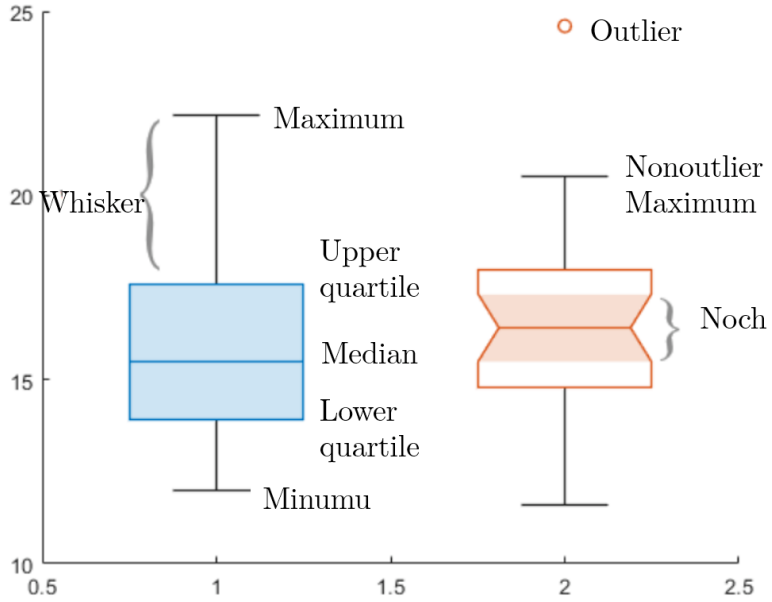

Figure 2.2: Box-and-Whisker Chart, printed from MATLAB (2021)

Tables 2.6 and 2.7 show the results of the one-way ANOVA and with the Tukey post-hoc multiple comparisons table, respectively. In figure 2.3 shows a box-and-whisker chart, which indicates the distribution of the data into quartiles, highlighting the median and outliers. For the case of initial formation cycle, F_i, three outliers were reported, for the other cycle the data is within the maximum and minimum nonoutliers. Besides, for this cycle the median is the lowest and the dispersion of the data seems to be more significant at the upper part compared to the other cycles.

Source	**SS**	**df**	**MS**	**F**	**Prob>F**
Group(Between)	1.1E+07	3	3.7E+06	38.61	2.4E-20
Error(Within)	2.3E+07	236	9.7E+04		
Total	3.4E+07	239			

Table 2.6: Results one-way ANOVA Temperatures vs. Flow rates

Cette thèse est accessible à l'adresse : http://theses.insa-lyon.fr/publication/2022LYSEI044/these.pdf
© [K. Utria Salas], [2022], INSA Lyon, tous droits réservés

I (technique)	J (technique)	Mean Difference (I-J)	95% Confidence Interval Lower Bound	Upper Bound	p-value
F_i	F_f	-639.3	-487.8	-336.3	0
F_i	G_i	-652.6	-501.1	-349.7	0
F_i	G_f	-662.4	-510.9	-359.4	0
F_f	G_i	-164.8	-13.3	138.1	1
F_f	G_f	-174.6	-23.1	128.4	1
G_i	G_f	-161.2	-9.8	141.7	1

Table 2.7: Multiple Comparisons Tukey's test Temperatures vs Flow rates

The one-way ANOVA revealed that there was a statistically significant difference in temperatures between at least two groups ($F(3, 236) = [38.6], p = 2.4E - 20$).

The numbers in table 2.7 indicate that the mean of the group F_i minus the mean of the group F_f is estimated to be -639.3, and a 95% confidence interval for the true difference of the means is [-487.8, -336.3]. The $p - value$ for the corresponding hypothesis test that the difference of the means of groups F_i and F_f is significantly different from zero is 0. The confidence interval does not contain 0, so the difference is significant at the 5% significance level. If the confidence interval did contain 0, the difference would not be significant. The p-value of 0 also indicates that the difference of the means of groups F_i and F_f is significantly different from 0.

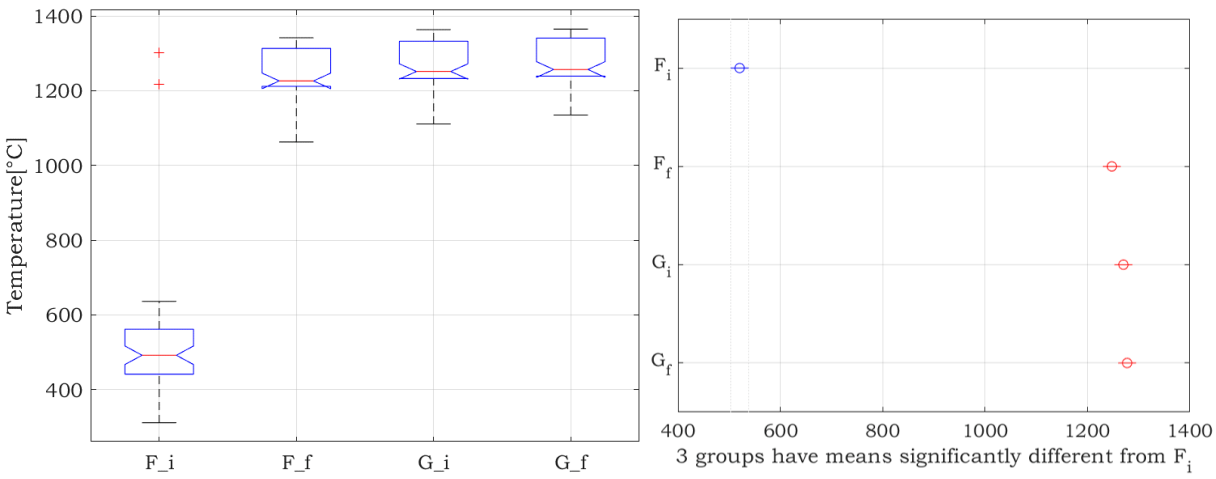

(a) Box-and-Whisker Chart (b) Tukey's test results

Figure 2.3: One-way ANOVA Results. Flow rates versus ceramic temperatures.

These results show that the temperatures are significantly different for the formation initial phase. For the other phases, the temperatures are close and $p > 0.05$, which denotes they are not statistically significant.

In section 1.2.2.1 the evolution of the temperature along the ceramic life cycle was de-

Cette thèse est accessible à l'adresse : http://theses.insa-lyon.fr/publication/2022LYSEI044/these.pdf
© [K. Utria Salas], [2022], INSA Lyon, tous droits réservés

scribed for two furnaces. It could be observed that *Furnace 2* presented the highest temperatures. Ensuing, the influence of furnace position on the ceramic temperature was analysed through an one-way ANOVA, see table 2.8.

Factor	**Modality (k)**	**Response**
Furnace Position	Furnace 1 (extreme of the production line) Furnace 2 (centre of the production line)	Temperature Position 2 (Y=160mm, G_i)

Table 2.8: Variables of the one-way ANOVA

In figure 2.4 the box and whisker chart is shown for temperatures at Y=160mm for the G_i phase, which corresponds to the highest temperatures of the crystallisation cycle. The chart shows that the temperature medians of the two furnaces are $1236°C$ and $1363°C$, respectively, and each furnace has three outliers. The $p - value < 0.05$ in table 2.9 indicates that the furnace position is an important factor that influence the temperature.

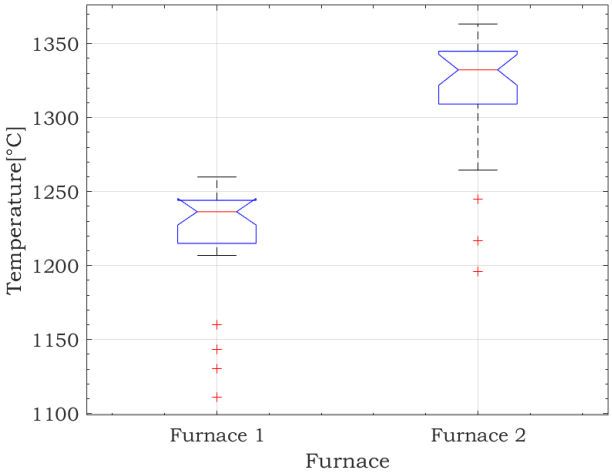

Figure 2.4: One-way ANOVA Results Temperature vs. Furnace Position

Source	**SS**	**df**	**MS**	**F**	**Prob>F**
Groups	1.3E+05	1	1.3E+05	81.1	2.8E-12
Error	8.6E+04	53	1.6E+03		
Total	2.2E+05	54			

Table 2.9: Results one-way ANOVA Temperature vs Furnace Position

Furthermore, it could be observed the increase in temperature along the crystallisation cycles in section 1.2.2.1. In contrast, the ceramic thickness decreased over time, figure 1.17. In order to understand how δcer regulates the temperature, an one-way ANOVA

Cette thèse est accessible à l'adresse : http://theses.insa-lyon.fr/publication/2022LYSEI044/these.pdf
© [K. Utria Salas], [2022], INSA Lyon, tous droits réservés

was performed to analysed the effect of the ceramic thickness on the temperature, see table 2.10.

Factor	Modality (k)	Response
δ_{cer}	25 26 27 28 29 30 31 32 33 34 35	Temperature Position 2 (Y=160mm, G_i)

Table 2.10: Variables of the one-way ANOVA

In figure 2.5a the dispersion values of the temperature versus the ceramic thickness and in figure 2.5b the box and whisker chart. The ceramic left side thickness was chosen to be analysed because the temperature were measured on this side. At the same time, it was decided that the best position to be analysed in Y was at 160 mm which reported the maximum temperatures. Besides, the crystal and the flame encounter around this point.

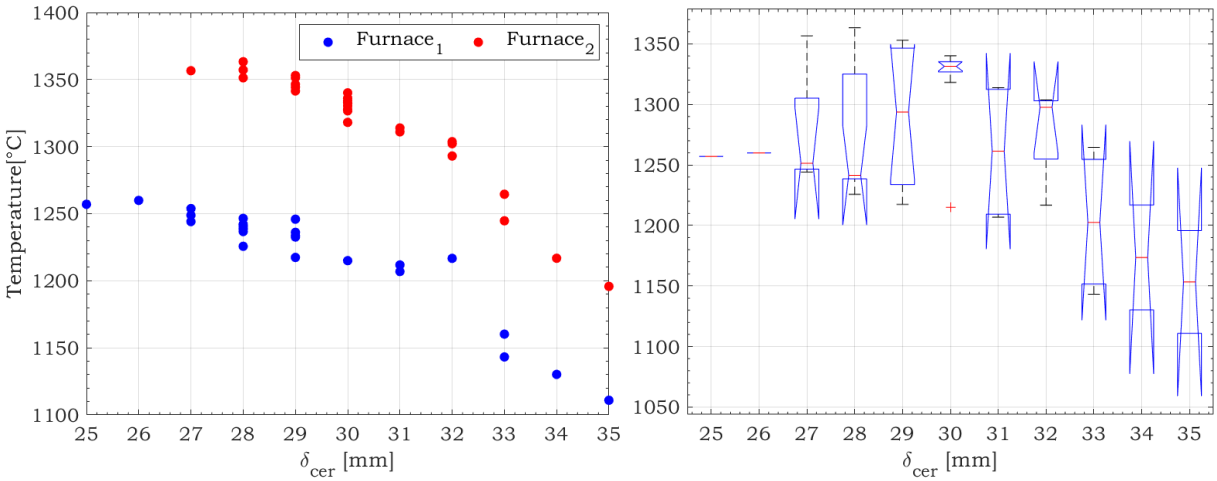

(a) Dispersion data

(b) Box and whisker chart.

Figure 2.5: Temperature Vs. δ_{cer}

Source	SS	df	MS	F	Prob>F
Groups	1E+05	10	1E+04	3.7	1.2E-03
Error	1.2E+05	44	2.7E+03		
Total	2.2E+05	54			

Table 2.11: Results one-way ANOVA Temperatures vs. δ_{cer}

The one-way ANOVA results in table 2.11 revealed that there was a statistically significant difference in temperatures between at least two groups ($F(10, 54) = [3.69], p = 1.2E-03$).

Cette thèse est accessible à l'adresse : http://theses.insa-lyon.fr/publication/2022LYSEI044/these.pdf
© [K. Utria Salas], [2022], INSA Lyon, tous droits réservés

The post hoc analysis showed that the $p-values$ for $\delta_{cer} = 30, 33, 34, 35$ were lower than 0.05 which denotes that they are statistically significant (table A.1 on appendix A.3).

The resulting covariance matrix between these two parameters is:

$$C_{T,\delta_{cer}} = \begin{pmatrix} 1583 & -95.1 \\ -95.1 & 6.4 \end{pmatrix}$$

where 1583 is the variance for the ceramic temperatures, and -95.1 is the covariance between the two parameters. The negative value means that a decrease in δ_{cer} increases the ceramic temperature.

Furthermore, one-way ANOVA was also performed to analyse the influence of $\oslash_{boule}$ on the temperature. The variables analysed are depicted in table 2.12.

Factor	**Modality (k)**	**Response**
$\oslash_{boule}$	31 32 33 34 35 36 37	Temperature Position 2

Table 2.12: Variables of the one-way ANOVA

In figure 2.6a on the left the dispersion values and on the right the box and whiskers char.

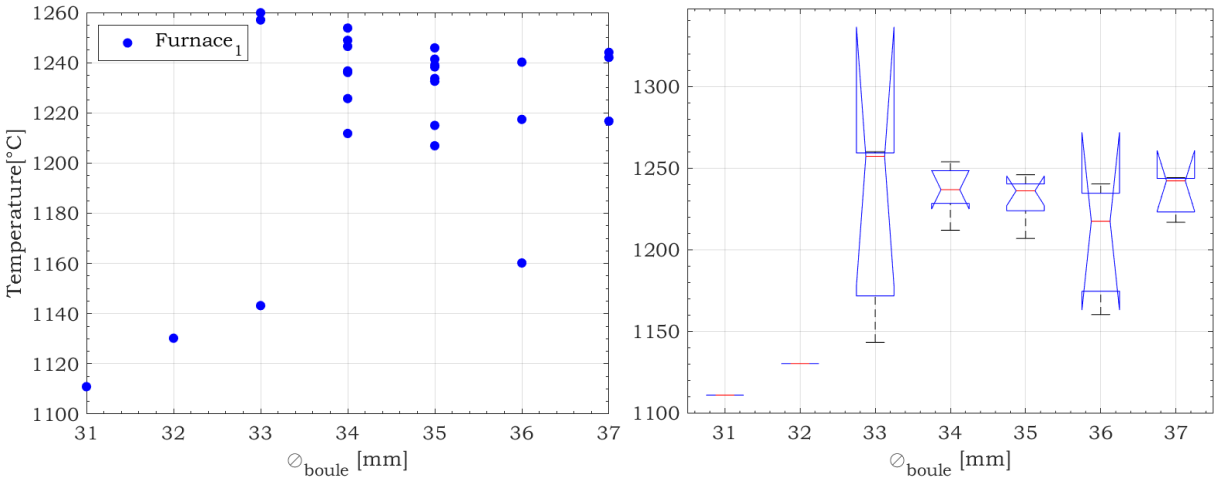

(a) Dispersion data

(b) Box and whisker chart.

Figure 2.6: Temperatures vs. $\oslash_{boule}$

Cette thèse est accessible à l'adresse : http://theses.insa-lyon.fr/publication/2022LYSEI044/these.pdf
© [K. Utria Salas], [2022], INSA Lyon, tous droits réservés

Source	SS	df	MS	F	Prob>F
Groups	2.4E+04	6	4E+03	5.03	3.1E-03
Error	1.5E+04	19	804.8		
Total	3.9E+04	25			

Table 2.13: Results one-way ANOVA Temperatures vs. $\oslash_{boule}$

Table 2.13 shows that there was a statistically significant difference in temperatures between at least two groups ($F(6, 25) = [5], p = 3.1E - 03$).

The resulting covariance matrix between these two parameters is:

$$C_{T,\oslash_{boule}} = \begin{pmatrix} 1583 & 27.3 \\ 27.3 & 2.3 \end{pmatrix}$$

The positive value of the covariance between the two parameter means that the temperatures increases with $\oslash_{boule}$

The effects of the interaction between these two parameters δ_{cer} and $\oslash_{boule}$ on the temperature were analysed through a two-way ANOVA in table 2.14. As seen, the two factors are significant different $p - values$ are lower than 0.05. However the interaction between the two factors was difficult to assess.

Source	SS	df	Mean Sq.	F	Prob>F
δ_{cer}	1.5E+04	8	1.9E+03	3.7182	1.1E-01
$\oslash_{boule}$	1.2E+03	4	293.6	0.6	6.7E-01
Error	2E+03	4	512.4		
Total	3.2E+04	17			

Table 2.14: Results two-way ANOVA Temperature vs $\delta_{cer}/\oslash_{boule}$

From these results, it could be concluded that the thermal conditions inside the confinement depend on the injection flow rates, the geometry of the ceramic insulation and the Verneuil boule diameter. Furthermore, these dependencies were corroborated statistically, finding that the temperatures for the final formation and growth phases are not significant different from each other

Cette thèse est accessible à l'adresse : http://theses.insa-lyon.fr/publication/2022LYSEI044/these.pdf
© [K. Utria Salas], [2022], INSA Lyon, tous droits réservés

2.3 Geometrical features correlations

Following the influence of flow rates, furnace position, ceramic temperature and thickness on the geometrical features that define the quality appearance of the Verneuil boule are analysed through ANOVA.

2.3.1 Boule diameter

In this section, the effects of flow rates on *Verneuil boule* diameter were corroborated through a two-way ANOVA. The analysis focuses on the influence of the interaction between the flow rates of the hydrogen and oxygen for the initial growth phase (G_i), as shown in table 2.15. At this moment, the crystal boule achieves the objective diameter.

Factor	**Modality (k)**	**Response**
Flow rates $\overline{\nu}_{H_2}$ and $\overline{\nu}_{O_2}$	G_i	$\oslash_{boule}$

Table 2.15: Variables of the one-way ANOVA

In order to analyse the influence of the flow rates on the boule diameter, the flow rates were classified in different categories:

Category	H_2	O_2
1	≤ 0.9	≤ 0.13
2	$0.9 < \overline{\nu}_{H_2} \leq 0.94$	> 0.13
3	> 0.94	

Table 2.16: Category of the variables of the one-way ANOVA

In figure 2.7, the dispersion data along with its box and whisker chart shown the behaviour of the $\oslash_{boule}$. The results obtained through the ANOVA can be found in table 2.17.

Cette thèse est accessible à l'adresse : http://theses.insa-lyon.fr/publication/2022LYSEI044/these.pdf
© [K. Utria Salas], [2022], INSA Lyon, tous droits réservés

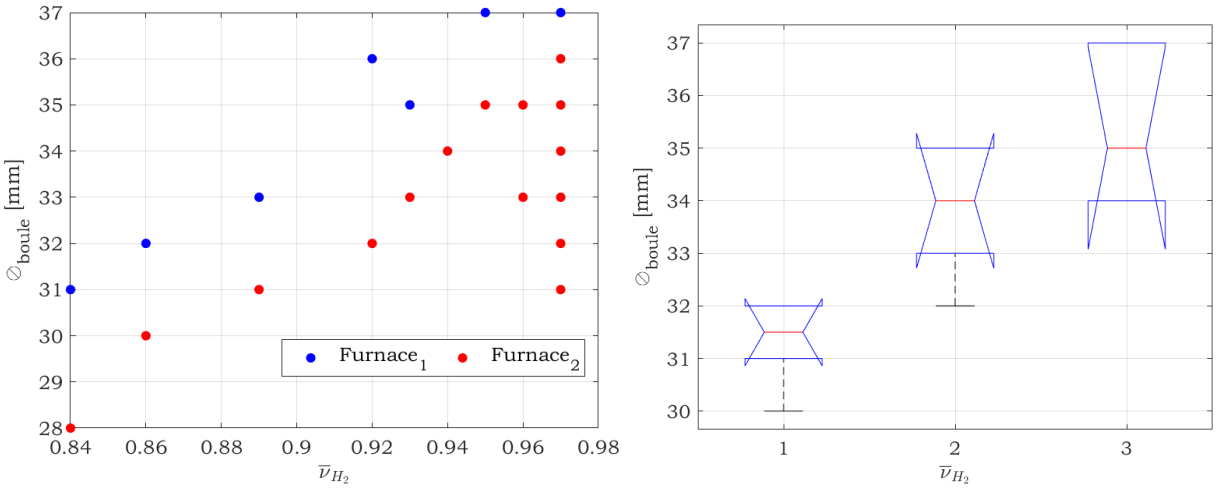

(a) Dispersion data

(b) Box and whisker chart.

Figure 2.7: $\oslash_{boule}$ vs. $\overline{\nu}_{H2}$

Source	SS	df	Mean Sq.	F	Prob>F
H_2	49	2	24.5	147	3.6E-09
O_2	20.1	1	20	120	1.3E-07
$H_2 * O_2$	1.4	2	0.7	4.3	3.8E-02
Error	2	12	1.7E-01		
Total	72.5	17			

Table 2.17: Results two-way ANOVA $\oslash_{boule}$ vs. $\overline{\nu}_{H2}$ and $\overline{\nu}_{O2}$

The two-way ANOVA results in table 2.17 shows that there was a statistically significant difference in $\oslash_{boule}$ between at least two groups of H_2 flow rates ($F(2, 72.5) = [147], p = 3.6E-09$). Likewise, for O_2 flow rates and for the interaction between these two parameters.

According to the results, although the diameter depends on both flow rates, the influence of the $\overline{\nu}_{H2}$ is more important, because the $p-value$ is lower. Moreover, the post hoc analysis for $\overline{\nu}_{H_2}$ shows that all the categories are significant difference from each other (table A.3 on appendix A.3).

Covariance matrix between $\overline{\nu}_{H2}$ and $\oslash_{boule}$ is:

$$C_{\overline{\nu}_{H2},\oslash_{boule}} = \begin{pmatrix} 1.1 & 0.9 \\ 0.9 & 2.3 \end{pmatrix}$$

where 1.1 is the variance for $\overline{\nu}_{H2}$, and 0.9 is the covariance between the two parameters. **This means that the increase in $\overline{\nu}_{H2}$ increases the $\oslash_{boule}$.**

Cette thèse est accessible à l'adresse : http://theses.insa-lyon.fr/publication/2022LYSEI044/these.pdf
© [K. Utria Salas], [2022], INSA Lyon, tous droits réservés

2.3.2 Ovalisation index

The first analysed was performed to determine the dependency of the ovalisation index regarding the furnace position, as shown in table 2.18.

Factor	Modality (k)	Response
Furnace position	Furnace 1 Furnace 2	Ovalisation index "O"

Table 2.18: Variables of the one-way ANOVA

In figure 2.8 the box and whisker chart is shown. As can be seen, the ovalisation index median for *Furnace 1* is 3.85% and two outliers were found, for *Furnace 2* is 3.3%.

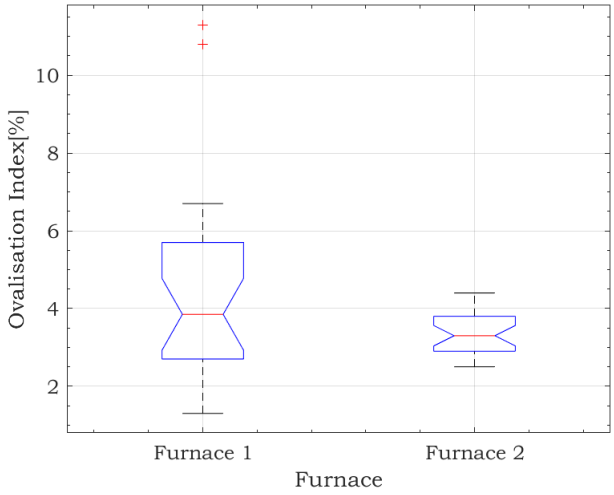

Figure 2.8: One-way ANOVA Results Ovalisation Index vs Furnace Position

Source	SS	df	MS	F	Prob>F
Groups	14.4	1	14.4	4.8	0.03
Error	158.3	53	3.0		
Total	172.6	54			

Table 2.19: Results one-way ANOVA Ovalisation Index vs Furnace Position

From the table 2.19 above we can see that the $p - value < 0.05$, which means that the ovalisation index for *Furnace 1* are significant different from *Furnace 2*. In other words, the ovalisation index for *Furnace 1* will be higher than in *Furnace 2*.

The second analysed was carried out for the influence of the ceramic temperature on the ovalisation index. In order to conduct the analyse, the temperatures were categorised

Cette thèse est accessible à l'adresse : http://theses.insa-lyon.fr/publication/2022LYSEI044/these.pdf
© [K. Utria Salas], [2022], INSA Lyon, tous droits réservés

according to the occurrence frequency at the position No.2 (location of the crystal top face, Y=160mm) and at the beginning of the initial growth cycle ($t_{cycle} = 2.5h$), when the crystal has achieved its objective diameter. In figure 2.9, the histogram created from the dispersion data is shown, and the factor and modalities are described in table 2.20. Five groups stand out from the results:

- Category 1: 1100-1150°C
- Category 2: 1150-1200°C
- Category 3: 1200-1250°C
- Category 4: 1250-1300°C
- Category 5: > 1300°C

Factor	**Modality (k)**	**Response**
Ceramic external surface temperature	Category 1: 1100-1150°C Category 2: 1150-1200°C Category 3: 1200-1250°C Category 4: 1250-1300°C Category 5: > 1300°C	Ovalisation index "O"

Table 2.20: Variables of the one-way ANOVA

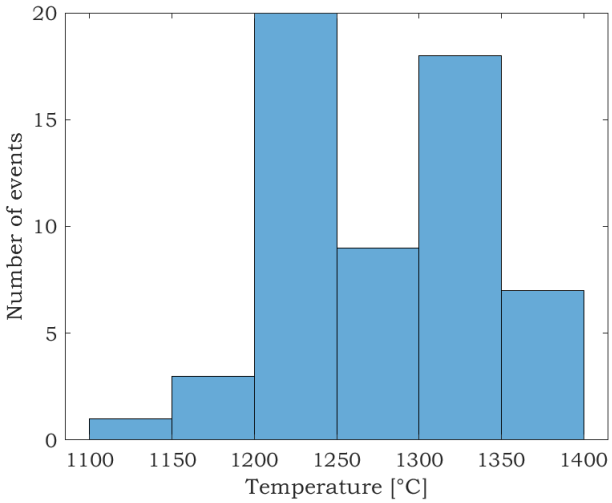

Figure 2.9: Histogram of ceramic temperatures, furnaces 1 and 2

As mentioned, the temperature depends on the furnace position. Hence, the analysed was only performed for *Furnace 1* which presented the highest ovalisation index, and most of

Cette thèse est accessible à l'adresse : http://theses.insa-lyon.fr/publication/2022LYSEI044/these.pdf
© [K. Utria Salas], [2022], INSA Lyon, tous droits réservés

the Verneuil boules with ovalisation index > 4% which is the critical value to consider a boule with type "O_{in}" geometrical defect. Figure 2.10 illustrates the results obtained for the ovalisation index with respect to the ceramic temperatures. It is apparent that the ovalisation index median increases with the temperature, being the the highest for category 4, the other categories maintain ovalisation index lower than 4% which are the maximum accepted. It is important to mention that for *Furnace 1*, temperatures higher than 1300°C were not found.

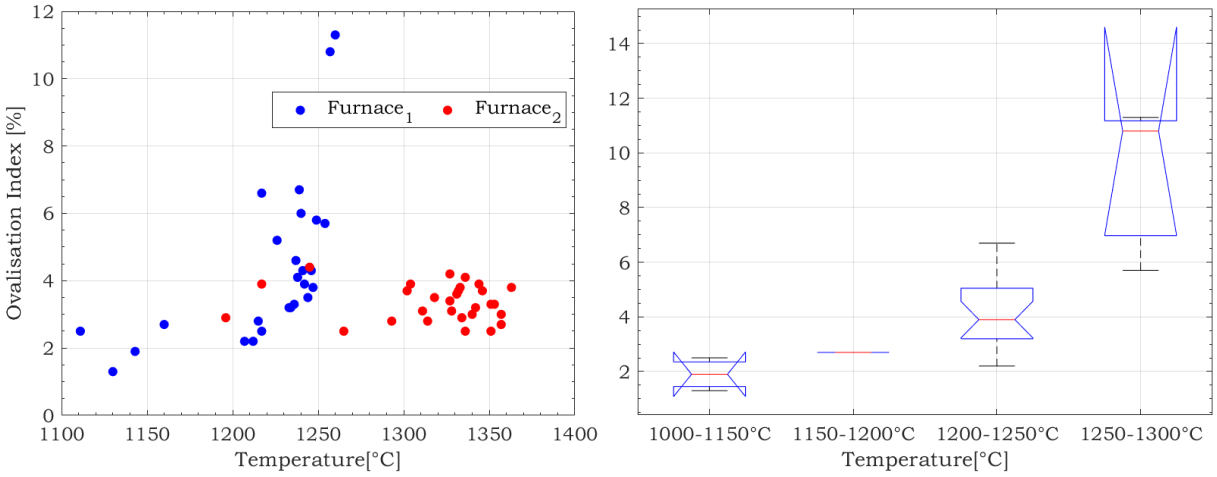

(a) Dispersion Data

(b) Box and whisker chart

Figure 2.10: Ovalisation Index Vs Temperature

Furthermore, the probability that type 3 (section 1.3.1.2) geometrical defect is present in *Furnace 1* is 40% and for *Furnace 2* is of 10%, according to equation 2.11. For category 4 ($1200°C < T_{cer} < 1250°C$) is 34 % in *Furnace 1* and 15% for *Furnace 2*.

$$P(O_{in}) = \frac{\text{Number of Verneuil boules with O} > 4\%}{\text{Total of Verneuil boules}} \tag{2.11}$$

where $P(O_{in})$ probability of defect type 3 occurs.

The one-way ANOVA results in table 2.21 reveal the statistically significant difference between the different categories ($F(3, 25) = [12.5], p = 5.5E - 05$).

Source	SS	df	MS	F	Prob>F
Groups	9.4E-03	3	3.1E-03	12.5	5.5E-05
Error	5.5E-03	22	2.5E-04		
Total	0.01	25			

Table 2.21: Results one-way ANOVA Ovalisation Index vs Temperature

Cette thèse est accessible à l'adresse : http://theses.insa-lyon.fr/publication/2022LYSEI044/these.pdf
© [K. Utria Salas], [2022], INSA Lyon, tous droits réservés

The Tukey's test (table A.4) shows that the category 4 is statistically significant from categories 1, 2 and 3, with a $p - value = 5.5E - 05$, for categories 1 and 3, and $p = 0.01$ for category 2.

The covariance matrix between these two parameters is:

$$C_{O,T} = \begin{pmatrix} 1583 & 0.6 \\ 0.6 & 1E-03 \end{pmatrix}$$

The covariance between the temperature and the ovalisation index results as 0.6, which means that there is a direct dependency between the two parameters. The highest the ceramic temperature, the highest the ovalisation index. However, this statement is true taking into count the confinement conditions, e.g. furnace position and ceramic insulation conditions. It is known from RSA experience that the ovalisation index is higher at the end of the cycle, when the ceramic insulation has lost considerable material. The ceramic thickness in turn is related to the ceramic temperature, that increases with the diminution of δ_{cer}. Therefore, in order to determine this dependency, it is necessary to analyse the impact of the ceramic thickness on the ovalisation index.

The influence of the ceramic thickness, δ_{cer}, on the ovalisation index is analysed according to table 2.22.

Factor	**Modality (k)**	**Response**
δ_{cer}	25 26 27 28 29 30 31 32 33 34 35	Ovalisation index "O"

Table 2.22: Variables of the one-way ANOVA

Figure 2.11 presents the dispersion data and the box and whisker chart for the ovalisation index with respect to the ceramic thickness, δ_{cer}.

Cette thèse est accessible à l'adresse : http://theses.insa-lyon.fr/publication/2022LYSEI044/these.pdf
© [K. Utria Salas], [2022], INSA Lyon, tous droits réservés

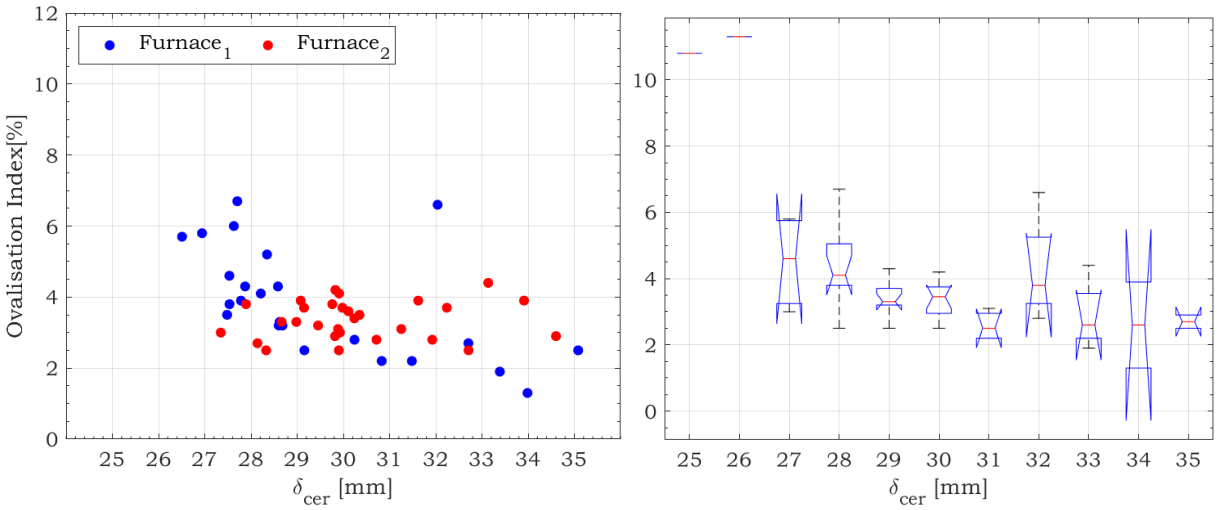

(a) Dispersion data (b) Box and whisker chart.

Figure 2.11: Ovalisation Index vs δ_{cer}

Source	SS	df	MS	F	Prob>F
Groups	129.4	10	12.9	13.2	2.9E-10
Error	43.2	44	1.0		
Total	172.6	54			

Table 2.23: Results one-way ANOVA Ovalisation Index vs δ_{cer}

It was found that the ovalisation index is dependent on the ceramic thickness, δ_{cer}, regarding the results obtain through the one-way ANOVA ($F(10, 54) = [13.2], p = 2.9E - 10$). The highest ovalisation index were found at the lowest δ_{cer} which indicates that they are significant different from the others δ_{cer}, see table A.5.
The covariance matrix between the two parameters is:

$$C_{O,\delta_{cer}} = \begin{pmatrix} 4.9 & -2.1E-03 \\ -2.1E-03 & 3.2E-02 \end{pmatrix}$$

The covarience between the ovalisation index and δ_{cer} of -2.1E-03 means that the ovalisation index increases with the diminution of δ_{cer}.

The two-way ANOVA was performed to analyse the interaction and influence of the ceramic temperature and thickness on the ovalisation index. As shown, in table 2.24, all the groups are significant statistically, including the groups formed by the two factors. Moreover, the means and standard error of the groups are shown in table 2.25. The group 2 that presents the highest temperatures and one of the lowest ceramic thickness is significantly different from 8 groups, the p-values are lower than 0.05 and are also shown

Cette thèse est accessible à l'adresse : http://theses.insa-lyon.fr/publication/2022LYSEI044/these.pdf
© [K. Utria Salas], [2022], INSA Lyon, tous droits réservés

in table 2.25. This group also presents the highest ovalisation index mean. The missing *p-value* are due to the missing of data of the group.

Source	**SS**	**df**	**Mean Sq.**	**F**	**Prob>F**
Temperature	92.3	2	46.2	49.6	0
δ_{cer}	45	10	4.5	4.8	5E-03
Temperature*δ_{cer}	0	0	0	0	0
Error	12.1	13	0.9		
Total	149.4	25			

Table 2.24: Results two-way ANOVA Ovalisation Index vs Temperature /δ_{cer}

Group	Interaction of the factors	Ovalisation Index [%]	% Error	p-value
1	Category 4,δ_{cer}=25	10.8	1.0	
2	Category 4,δ_{cer}=26	11.3	1.0	
3	Category 3,δ_{cer}=27	4.7	0.7	3.3E-02
4	Category 4,δ_{cer}=27	5.7	1.0	
5	Category 3,δ_{cer}=28	4.8	0.3	
6	Category 3,δ_{cer}=29	3.3	0.4	2.1E-03
7	Category 3,δ_{cer}=30	2.8	1.0	1.2E-02
8	Category 3,δ_{cer}=31	2.2	0.7	1.7E-03
9	Category 3,δ_{cer}=32	6.6	1.0	
10	Category 1,δ_{cer}=33	1.9	1.0	4.8E-03
11	Category 2,δ_{cer}=33	2.7	1.0	1.1E-02
12	Category 1,δ_{cer}=34	1.3	1.0	2.6E-03
13	Category 1,δ_{cer}=35	2.5	1.0	9.0E-03

Table 2.25: Total results two-way ANOVA Ovalisation Index vs Temperature /δ_{cer}

This section has shown statistically the dependency of the geometrical parameters on the thermal and flame combustion conditions. Furthermore, this study has corroborated the empirical knowledge of RSA regarding the importance of the thermal gradients on the geometry quality of the Veneuil boules. The probability of an ovalisation index > 4% is 34% for ceramic temperatures between 1200 and 1250°C. Furthermore, the highest ovalisation index are present for temperature between 1200 and 1250°C with a ceramic thickness of 26 mm.

Cette thèse est accessible à l'adresse : http://theses.insa-lyon.fr/publication/2022LYSEI044/these.pdf
© [K. Utria Salas], [2022], INSA Lyon, tous droits réservés

2.4 Crystal defects correlation

The crystal quality is measured regarding their defects, as mentioned in chapter 1. They are classied into two kinds: geometrical or external and internal defects. Succeeding the effects of the ceramic thickness and temperature on their quantity are analysed.

2.4.1 External defects

As described in section 1.3.2.1 there are different types of external defects which are related to the geometry appearance of the crystal boule. One of the factor that affect them is the internal geometry of the ceramic insulation. Following, the one-way ANOVA was used to observed their apparition with respect to the ceramic geometry, see table 2.26.

Factor	Modality (k)	Response
Geometrical defects	Zero defects	δ_{cer}
	Type 2	
	Type 3	

Table 2.26: Variables of the one-way ANOVA

Figure 2.12 illustrates the geometrical defects regarding the quantity for each δ_{cer}. It can be noticed that during this study only defects type 2 and 3 were found (see figure 1.25).

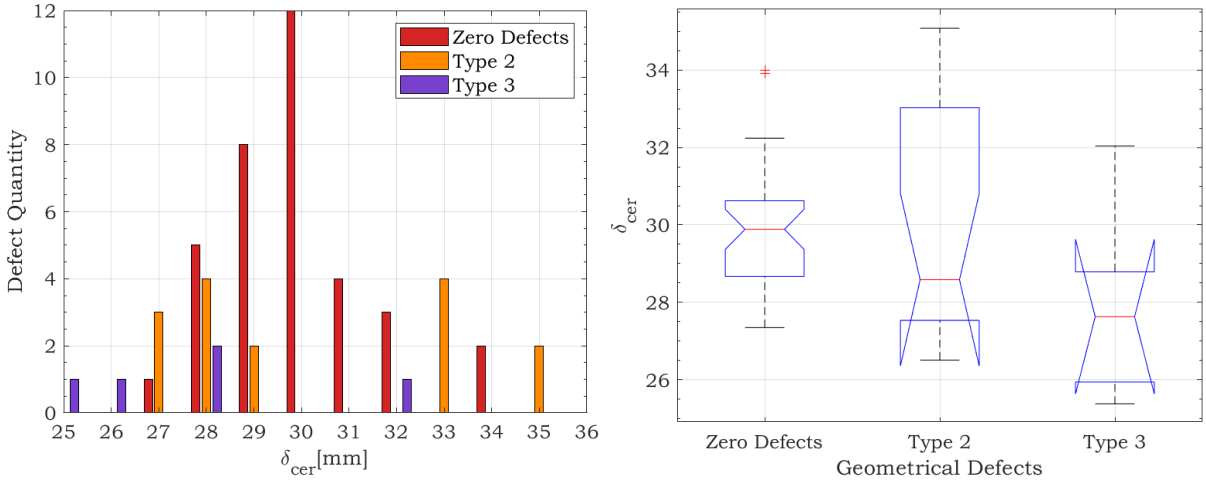

(a) Global Data (b) Box and whisker chart

Figure 2.12: Geometrical defects vs δ_{cer}

In figure 2.12b, it is apparent that most of the crystal without geometrical defects are

Cette thèse est accessible à l'adresse : http://theses.insa-lyon.fr/publication/2022LYSEI044/these.pdf
© [K. Utria Salas], [2022], INSA Lyon, tous droits réservés

obtained with a $\delta_{cer} = 30\ mm$. The one-way ANOVA shows in table 2.27 that each δ_{cer} has a kind of different defect ($p - value < 0.05$). For instance, defect type 3 is usually obtained with a δ_{cer} around 28 mm. For type 2, the δ_{cer} is around 27 mm.

Source	SS	df	MS	F	Prob>F
Groups	32.4	10	3.2	4	6.3E-04
Error	35.7	44	0.8		
Total	68.2	54			

Table 2.27: One-way ANOVA Results Geometrical defects vs δ_{cer}

The Turkey's test in table A.6 revealed that the $\delta_{cer} = 30\ mm$ which reported the fewest defects is significantly different from $\delta_{cer} = 25\ mm$ and $\delta_{cer} = 33\ mm$. The latter presented most of the type 2 defects.

2.4.2 Internal defects

As a reminder, internal defects are related to the crystalline structure of the crystal boule, as explained in section 1.3.2.2. This seems to be affected by two major parameters, the ceramic temperature and ceramic thickness. Owing the ceramic temperature is dependent on δ_{cer} and $\oslash_{boule}$ (hence, δ_{therm}), following the ANOVA is performed to analyse how the temperature influences the apparition of the internal defects.

2.4.2.1 Foils

Foils, the sub-grain boundaries, are mostly generated due to the temperature gradients inside the confinement. Thence, their interactions are analysed through an one-way ANOVA. In figure 2.13a the dispersion data of the number of grain boundaries versus the temperatures are presented. As in section 2.3.2, the ceramic temperatures in position No.2 (Y=160mm) at the beginning of the initial growth phase G_i) were classified in categories. The categories were obtained with the temperatures and the quantity of foils found in each Verneuil boule, finding the most adequate ranges when the temperatures presented similar quantity of foils:

- Category 1: < 1250°C
- Category 2: 1250-1350°C
- Category 3: > 1350°C

Cette thèse est accessible à l'adresse : http://theses.insa-lyon.fr/publication/2022LYSEI044/these.pdf
© [K. Utria Salas], [2022], INSA Lyon, tous droits réservés

In table 2.28 the variables analysed are shown:

Factor	Modality (k)	Response
Ceramic internal surface temperature	Category 1: < 1250°C Category 2: 1250-1350°C Category 3: > 1350°C	Number of foils

Table 2.28: Variables of the one-way ANOVA

The dispersion data and the box-and-whisker chart are depicted in figure 2.13. From the latter, it can be observed that most of the foils are presented in category 2, which correspond to the range of temperatures between 1250 to 1350°C. 46 from a total of 55 Verneuil boules presented this defect for category 2 and 6 Verneuil boules for category 3, with a median of 15 and 25 foils, respectively. The probability according to equation 2.11 that this defect appears is 29% for category 4 and 10% for category 3. For *Furnace 1* most of the foil are found between temperatures of 1200 and 1250°C, in the case of *Furnace 2* most of the foils are obtained with temperatures within the range from 1300 to 1350°C.

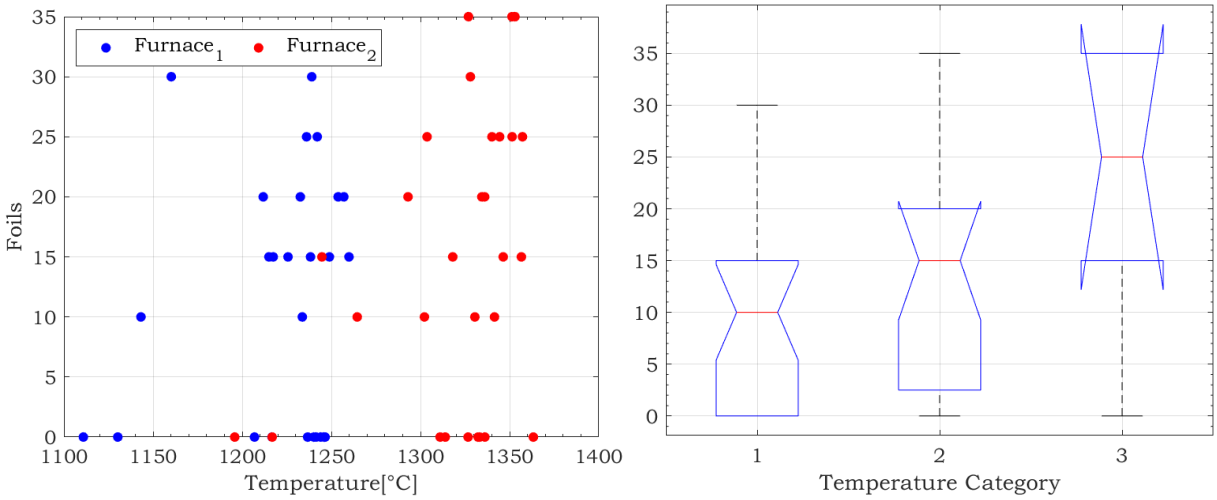

(a) Dispersion Data (b) Box and whisker chart

Figure 2.13: Foils vs Temperature

In table A.7, the one-way ANOVA shows that $F(2, 52) = [3.4]$, $p = 4.1E - 02$, which implies that the means for each category are significant different. Furthermore, the Tukey's test revealed that the mean for temperatures > 1350°C is significant different from means of temperatures < 1250°C (see table A.7).

Cette thèse est accessible à l'adresse : http://theses.insa-lyon.fr/publication/2022LYSEI044/these.pdf
© [K. Utria Salas], [2022], INSA Lyon, tous droits réservés

Source	SS	df	MS	F	Prob>F
Groups	800	2	400	3.4	4.1E-02
Error	6.2E+03	52	119		
Total	7.0E+03	54			

The covariance matrix between the two parameters is:

$$C_{Foils,T} = \begin{pmatrix} 4074 & 197.8 \\ 197.8 & 129.2 \end{pmatrix}$$

The positive number in the covariance means that the number of foils increases with the temperature on the ceramic surface.

2.4.2.2 Bubbles

Bubbles are the gas inclusions in the crystalline structure. Their apparition regarding the ceramic temperature is analysed on figure 1.33. The temperatures were categorised according to their occurrence and the quantity of bubbles, the next categories summarised the results obtained:

- Category 1: 1100-1150°C
- Category 2: 1150-1200°C
- Category 3: 1200-1300°C
- Category 4: $>$ 1300°C

In table 2.29 the variables analysed with the one-way ANOVA are shown:

Factor	Modality (k)	Response
Ceramic internal surface temperature	Category 1: 1100-1150°C Category 2: 1150-1200°C Category 3: 1200-1300°C Category 4: $>$ 1300°C	Number of bubbles

Table 2.29: Variables of the one-way ANOVA

Cette thèse est accessible à l'adresse : http://theses.insa-lyon.fr/publication/2022LYSEI044/these.pdf
© [K. Utria Salas], [2022], INSA Lyon, tous droits réservés

From the box-and-whisker chart, it can be observed that most of the bubbles are presented for the ceramic temperatures between 1200 and 1350°C (category 3 and 4), 49 from a total of 55 Verneuil boules presented this defect at this range of temperature. The median for category 3 is 1 bubbles and category 4 is 3 bubbles, *Furnace 2* presented the highest quantity of this type of defect. The probability according to equation 2.11 that this defect appears is 73% in *Furnace 1* for category 3 with a median of 1, and 82% in *Furnace 2* for category 4 with a median of 3 bubbles.

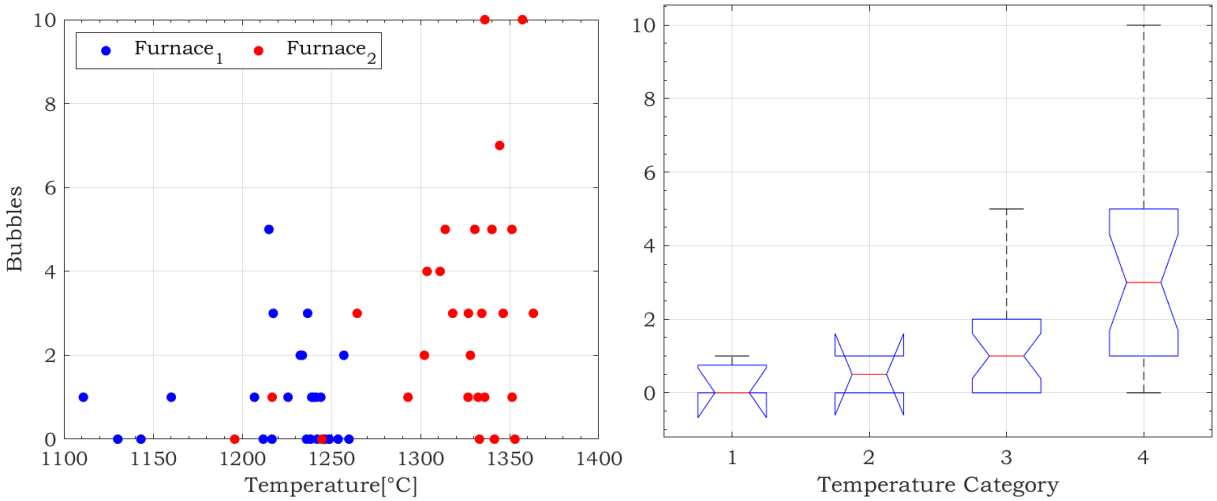

(a) Dispersion Data (b) Box and whisker chart

Figure 2.14: Bubbles vs Temperature

The one-way ANOVA results in table 2.30 reveal that the means are statistically significant ($F(3, 50) = [6.1], p = 1.3E - 03$), which indicates that the means for each category are significant different. Furthermore, the Tukey's test showed that the mean for temperatures > 1300°C (category 4) is significant different from means of temperatures $1100 - 1150$°C (category 1) and $1200 - 1300$°C (category 3), see table A.8.

Source	SS	df	MS	F	Prob>F
Groups	79.5	3.0	26.5	6.1	1.3E-03
Error	216.5	50.0	4.3		
Total	296.0	53.0			

Table 2.30: Results one-way ANOVA Bubbles vs Temperature

The covariance matrix between ceramic temperatures and number of bubbles:

$$C_{Bubbles,T} = \begin{pmatrix} 5.6 & 70.8 \\ 70.8 & 4014.9 \end{pmatrix}$$

Cette thèse est accessible à l'adresse : http://theses.insa-lyon.fr/publication/2022LYSEI044/these.pdf
© [K. Utria Salas], [2022], INSA Lyon, tous droits réservés

As in foils, the positive number in the covariance indicates that the number of bubbles increases with the temperature on the ceramic.

From this section, it can be concluded that the most adequate δ_{cer} to avoid geometrical defect is $\delta_{cer} = 30mm$. Moreover, the direct dependency of the internal defects on the temperature gradients is also corroborated, most of the internal defect are found for ceramic temperature range 1200 - 1250° C for ***Furnace 1*** *and for* ***Furnace 2*** *the temperature are from 1300 to 1350 ° C .*

In table 2.31 the dependencies between the difference parameters are summarised along with the covariances. The first column represents the factor evaluated, the response variable is found in the second column, the third column corresponds to whether the ANOVA found that a factor is significant statistically with respect to the other, showing a dependency between them, in the last column the covariance is shown, in order to illustrate if this dependency is positive or negative.

Cette thèse est accessible à l'adresse : http://theses.insa-lyon.fr/publication/2022LYSEI044/these.pdf
© [K. Utria Salas], [2022], INSA Lyon, tous droits réservés

Factor	**Modality**	**Response**	**Statistically significant**	**Covariance**
Injection Flow rates ν_{H_2}	F_i: Initial formation phase F_f: Final formation phase G_i: Initial growth phase G_f: Final growth phase	Temperature Position 2 (T_2) (Y=160mm)	Yes	Positive
Furnace position	Furnace 1 (extreme production line) Furnace 2 (centre production line)	T_2 (G_i)	Yes	
Ceramic thickness (δ_{cer})	25 26 27 28 29 30 31 32 33 34 35	T_2 (G_i)	Yes	Negative
Boule diameter ($\oslash_{boule}$)	31 32 33 34 35 36 37	T_2	Yes	Positive
Flow rates	$\overline{\nu}_{H_2}$ $\overline{\nu}_{O_2}$ Category 1: ≤ 0.9 Category 1: ≤ 0.13 Category 2: Category 2: > 0.13 $0.9 < \overline{\nu}_{H_2} \leq 0.94$ Category 3: > 0.94	$\oslash_{boule}$	Yes	Positive
Furnace position	Furnace 1 (extreme production line) Furnace 2 (centre production line)	Ovalisation index "O_{in}"	Yes	
Ceramic external surface temperature (G_i)	Category 1: 1100-1150°C Category 2: 1150-1200°C Category 3: 1200-1250°C Category 4: 1250-1300°C Category 5: > 1300°C	Ovalisation index "O_{in}"	Yes	Positive
Geometrical defects	Zero defects Type 2 Type 3	δ_{cer}	Yes	
Ceramic external surface temperature (G_i)	Category 1: < 1250°C Category 2: 1250-1350°C Category 3: > 1350°C	Number of foils	Yes	Positive
Ceramic external surface temperature (G_i)	Category 1: 1100-1150°C Category 2: 1150-1200°C Category 3: 1200-1300°C Category 4: > 1300°C	Number of bubbles	Yes	Positive

Table 2.31: Summary of the results obtained with the ANOVA analysis in the Verneuil production parameters.

Cette thèse est accessible à l'adresse : http://theses.insa-lyon.fr/publication/2022LYSEI044/these.pdf
© [K. Utria Salas], [2022], INSA Lyon, tous droits réservés

2.5 Conclusions

The influence of the thermal field in the area of crystal growth was analysed through a statistical study. The crystal growth conditions under a given crystal geometry were analysed under real production conditions. The parameters that control the final process of sapphire crystallisation were identified, and their relative importance was assessed. Furthermore, the relevant parameters of a crystallisation cycle were evaluated and the correlations between them were found, as well as their importance in the growth crystal environment and quality criteria during a insulation life cycle.

The one-way ANOVA was used to find whether certain parameters were significant statistically or not. A Tukey's test was each time performed in order to analyse which factors were more statistically significant. Furthermore, the covariances between the parameters were calculated. The following conclusions can be drawn from the present study :

- Ceramic temperature depends on the flow rates, $\oslash_{boule}$ and δ_{cer}. The factor with the most relevance seems to be the δ_{cer}, which presented the lowest $p - value$.
- The results showed that $\oslash_{boule}$ depends principally on $\overline{\nu}_{H2}$.
- Ovalisation index is principally dependent on the ceramic thickness, which likewise determines the ceramic temperature. The lowest value are found for the highest δ_{cer}.
- The geometrical defects type 2 and 3 are more probably found in $\delta_{cer} < 30\ mm$.
- The internal defects are statistically significant for each temperature. Most of the defects are found at ceramic temperatures between 1250-1300°C and temperatures $> 1300°C$ for *Furnace 1* and *Furnace 2*, respectively.

These conclusions lead us to carry out a more detailed study of the conditions of the crystal growth medium. The following part analyses the influence of injection conditions on the characteristics of the flame, which in turn will define the boule diameter, the temperatures and the external and internal quality of the crystal. Furthermore, they show that the geometry of the ceramic insulation is an essential parameter that defines de thermal conditions of the crystalline growth environment which later on determines the external and internal quality of the crystal.

Cette thèse est accessible à l'adresse : http://theses.insa-lyon.fr/publication/2022LYSEI044/these.pdf
© [K. Utria Salas], [2022], INSA Lyon, tous droits réservés

Therefore, a new geometry was defined according to ceramic geometry obtained in this part with which the best geometric features and crystalline structure were found, this geometry will be analysed in chapter 8.

Cette thèse est accessible à l'adresse : http://theses.insa-lyon.fr/publication/2022LYSEI044/these.pdf
© [K. Utria Salas], [2022], INSA Lyon, tous droits réservés

Part II

H_2/O_2 downward inverse diffusion flames

The previous part revealed the necessity to better understand the aerothermodynamic behaviour of the flame under different injection flow rates conditions. This part is divided in four chapters. Chapter 3 shows a literature review of inverse diffusion flames that correspond to the theoretical configuration of the flame produced by a *Verneuil burner*. In chapter 4 the experimental bench used to characterise the flame is described. Chapter 5 is about the flame structure characteristics and the OH^* emission intensities of the flame. Finally chapter 6 is related to the aerothermodynamic behaviour of the flow. The principal objectives of this part are to understand the overall thermal operation of the *Verneuil furnace* and to identify the parameters that can modify the thermal behaviour of the crystal growth environment.

Cette thèse est accessible à l'adresse : http://theses.insa-lyon.fr/publication/2022LYSEI044/these.pdf
© [K. Utria Salas], [2022], INSA Lyon, tous droits réservés

Cette thèse est accessible à l'adresse : http://theses.insa-lyon.fr/publication/2022LYSEI044/these.pdf
© [K. Utria Salas], [2022], INSA Lyon, tous droits réservés

Contents

Cette thèse est accessible à l'adresse : http://theses.insa-lyon.fr/publication/2022LYSEI044/these.pdf
© [K. Utria Salas], [2022], INSA Lyon, tous droits réservés

Cette thèse est accessible à l'adresse : http://theses.insa-lyon.fr/publication/2022LYSEI044/these.pdf
© [K. Utria Salas], [2022], INSA Lyon, tous droits réservés

Chapter 3 | Literature review

The *Verneuil furnace* is a particular configuration that involves different aerothermodynamic and chemical mechanisms. This unique system has been poorly study, the closest academical configuration is a downward inverse diffusion burner. This chapter focuses in reviewing de current available literature in order to better understand the different interactions in the crystal growth environment. The review begins with the general concepts of a diffusion flame to the different studies developed to comprehend the structure, stabilisation mechanisms and appearance of this kind of flame, as well as the flow structure.

Different practical combustion systems use diffusion flames widely due to their safety and wide operating range compared to premixed combustion (Mahesh and Mishra, 2010). Diffusion flames can be classified as normal diffusion flames (NDF), where oxidiser jet surrounds the fuel jet, and inverse diffusion flames (IDF). Diffusion flames are also divided into coflow flames and counter-flow flames.

In coflow normal diffusion flames, the burning or fuel consumption rate is determined by the rate at which the fuel and oxidiser are brought together in proper proportions for reaction (Glassman and Glumac, 2015). The shape of the burning laminar fuel jet depends on the mixture strength (see figure 3.1). According to their appearance they can be classified as:

- Overventilated:
  The volumetric flow rate of air flowing in the outer annulus is in excess of the stoichiometric amount required for the volumetric flow rate of the inner fuel jet, the flame that develops takes a closed, elongated form.
- Underventilated:
  The air supply in the outer annulus is reduced below an initial mixture strength corresponding to the stoichiometric required amount, a fan-shaped.

Cette thèse est accessible à l'adresse : http://theses.insa-lyon.fr/publication/2022LYSEI044/these.pdf
© [K. Utria Salas], [2022], INSA Lyon, tous droits réservés

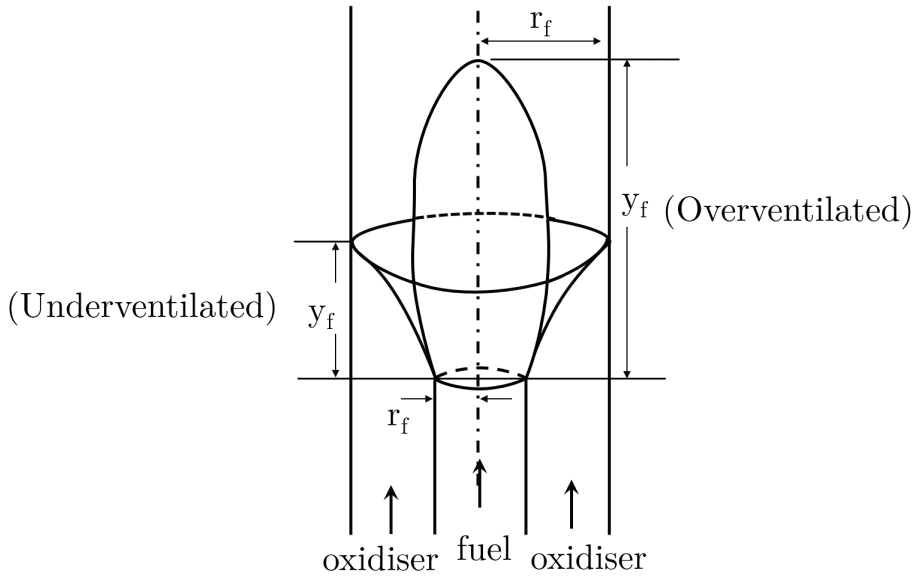

Figure 3.1: Coflow normal diffusion flames types. y_f: flame height r_f: flame radius (Glassman and Glumac, 2015)

On the other hand, inverse diffusion flames are characterised by an oxidiser jet located in the centre of the flame and surrounded by fuel jets. This configuration enables different advantages such as a cleaner combustion (Sze et al., 2004, 2006), adjustable flame lengths (Miao et al., 2016), improvement of flame stability and, compared to premixed flames, a larger flammability range (Sze et al., 2006). Given these advantages, their use for industrial or domestic burners is of greatest interest. Most of the studies in this kind of flames have been in hydrocarbons and have shown that IDF have different flame structure types and characteristics that depend on fuel and oxidiser flow rates, fuel-to-oxidiser momentum ratio and the geometry of the burner (Wu and Essenhigh, 1984; Sobiesiak and Wenzell, 2005; Bindar and Irawan, 2012). In the next section the conducted efforts to understand IDF behaviour are described.

Cette thèse est accessible à l'adresse : http://theses.insa-lyon.fr/publication/2022LYSEI044/these.pdf
© [K. Utria Salas], [2022], INSA Lyon, tous droits réservés

3.1 Structure of inverse diffusion flames

Inverse diffusion flames have shown different types of flame structure depending on fuel and oxidiser flow rates (Wu and Essenhigh, 1984; Sobiesiak and Wenzell, 2005; Bindar and Irawan, 2012). Several researches have analysed this dependency (Sze et al., 2004, 2006; Miao et al., 2016; Kapusta et al., 2020; Elbaz and Roberts, 2014; Miao et al., 2013), as well as their thermal behaviour (Sze et al., 2004; Dong et al., 2007; Ng et al., 2007; Badiger et al., 2020; Zhen et al., 2012) and NOx production (Stansel et al., 1995; Sobiesiak et al., 1998; Sze et al., 2006; Zhen et al., 2012).

Thus, Wu and Essenhigh (1984) were the first to map out six different types of IDF according to their appearance and stability. They found that the IDF appearance is similar to a premixed flame developed in a confined laminar flow, consisting of a bell-shaped bluish reaction zone stabilised on the air jet. In figure 3.2 the boundaries of the different flame types are identified according to fuel and air velocity, the description of the flames obtained are exposed in table 3.1. Figure 3.3 illustrates the zone found in a flame type III which corresponds to the flame structure mostly found by these authors. Zone 1 i a parabolic cap that constitutes the main blue combustion zone. In zone 2, a faint yellow zone is observed, it starts about 1/3 of the way up the side of the blue zone, and is a tapered truncated annulus, open at the top and thus enclosing a dark zone, 3, above the top of the blue zone.

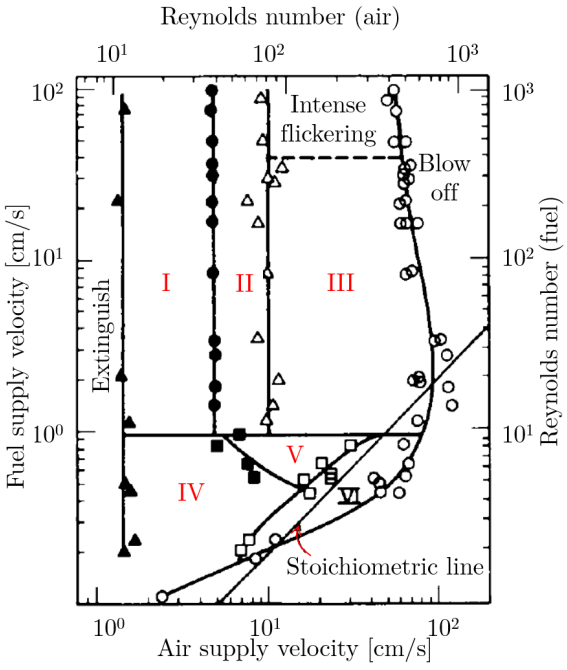

Figure 3.2: Map of flame types of inverse diffusion flames of methane (air port 11 mm; flame tube 28 mm). Printed from Wu and Essenhigh (1984)

Cette thèse est accessible à l'adresse : http://theses.insa-lyon.fr/publication/2022LYSEI044/these.pdf
© [K. Utria Salas], [2022], INSA Lyon, tous droits réservés

Type	Principal Characteristics
	Stables flames: Fuel velocity > 1cm/s
I	Weak blue; recessed: fuel must diffuse down against upflowing combustion products. Insensitive to fuel velocity. Non-existent with porous plug burners
II	Blue with faint orange-yellow cap; clear boundaries between blue and yellow zones.
III	Most representative: Stronger than type II; more intense blue; larger, more intense yellow zone. Zone demarkations fuzzy (see figure 3.3).
	Unstable flames: Fuel velocity < 1cm/s. Buoyancy sensitive
IV	Weak blue: flames cap tube. Instability frequency of 1-2Hz. Similar to Barr's "lambent" flames.
V	Weak blue with yellow cap; combine characteristics of type III and IV. Blue and yellow zones with independently unstable
VI	Blue. Only overventilated flame type. Attaches at a variable point on the burner rim.

Table 3.1: Summary of flame type characteristics. Printed from Wu and Essenhigh (1984)

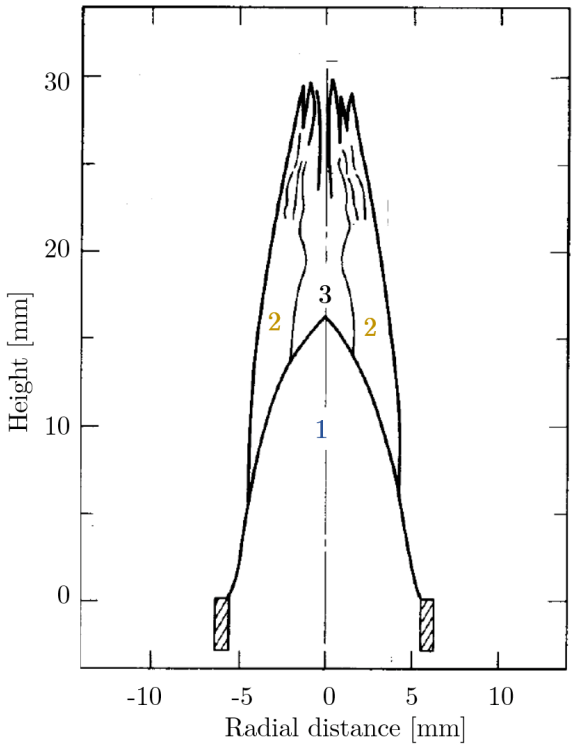

Figure 3.3: Type III flame profile according to Wu and Essenhigh (1984). 1: Volume enclosed by blue zone. 2: Orange yellow cap. 3: Dark zone

Cette thèse est accessible à l'adresse : http://theses.insa-lyon.fr/publication/2022LYSEI044/these.pdf
© [K. Utria Salas], [2022], INSA Lyon, tous droits réservés

The later work of Bindar and Irawan (2012) did not confirm these different flame shapes. They found only five types of IDF mainly controlled by inlet air and fuel momentums in a confined case and at high level of fuel excess, see figure 3.4. At low air jet velocities, they observed similar flame shapes to NDF (type I), but when the air velocity was 5–16 times higher than inlet fuel velocity, the appearance changed (type II to type V). Two distinct regions then appear: a wide flame base and a thinner shape flame on top of the base (downstream), which increased when the air flow rate increased (figure3.4a). The different types of flame shape are depicted in figure 3.4b according to fuel-to-air momentum ratio. They also showed that the highest temperature zone was located at the centre of the flame and shifted closer to the flame tip (downstream) as the fuel fraction increased.

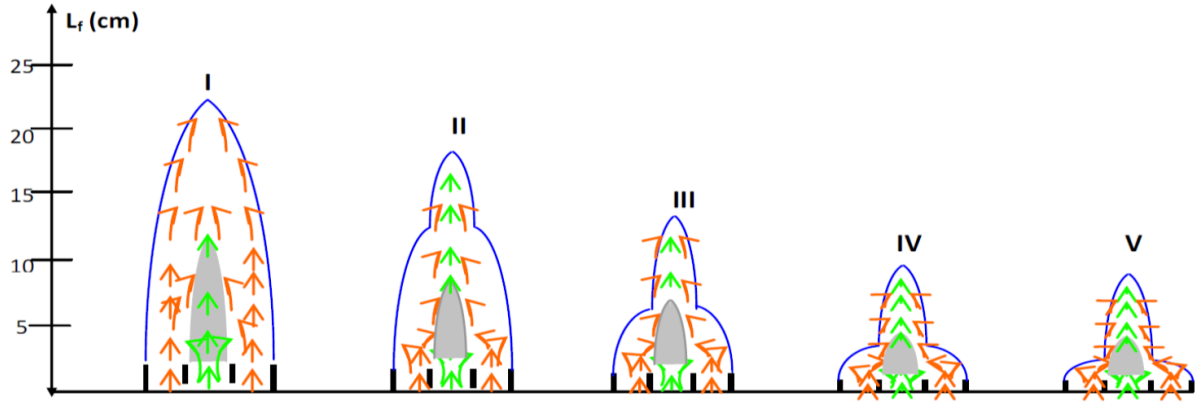

(a) Visualisation of the inverse diffusion flame shape development for hydrogen fuel

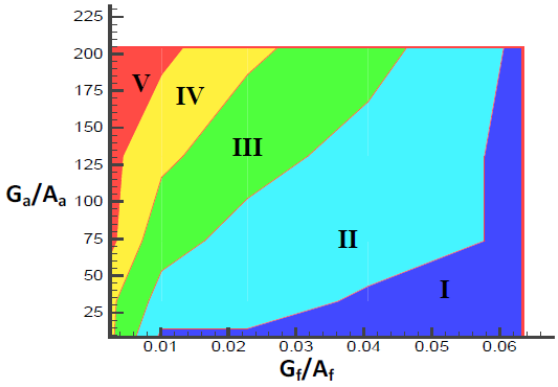

(b) The shape-map for inverse diffusion flames of Hydrogen fuel. G_a: air momentum, G_f fuel momentum (hydrogen momentum). A_a crossed section area of the air inlet and A_f crossed section of fuel inlet area.

Figure 3.4: Types of flame. Printed from Bindar and Irawan (2012)

To improve IDF efficiency and limiting pollutant emissions further studies have focused on a new configuration called Multi-jet Inverse Diffusion Flames (MIDF) (Sze et al., 2004, 2006; Miao et al., 2013; Elbaz and Roberts, 2014; Dong et al., 2007; Zhen et al., 2011). This device consists of a larger central circular oxidiser jet circumferentially surrounded

Cette thèse est accessible à l'adresse : http://theses.insa-lyon.fr/publication/2022LYSEI044/these.pdf
© [K. Utria Salas], [2022], INSA Lyon, tous droits réservés

by several smaller circular fuel jets. Compared to the traditional IDF burner, Sze et al. Sze et al. (2004, 2006) found that the MIDF set-up ensures the stability of the flame at Reynolds numbers lower than 1000. This stability mainly lies in the enhanced fuel entrainment associated with a more intense air/fuel mixing, occurring in the annular distance separating the central air jet from the annular fuel jets and the bluff body effect by this area (Elbaz and Roberts, 2014). Furthermore, they reported that the mixing air/fuel is more intense. In this case, concerning their appearance, they observed a blue flame with short mixing and combustion zone at low ϕ, and a yellowish flame with long mixing and combustion zone at high ϕ. The change from blue to yellow indicates a transition from fuel-rich to fuel-lean conditions. In the same time, an increase in Re_{air} also increased the mixing and combustion zone length. The entrainment zone length was not much affected by either Re_{air} or ϕ. Dong et al. (2007) also examined the influences of the air-jet Reynolds number and overall equivalence ratio on the local and average heat flux of a MIDF. The flame shape and structure mainly depended on the air jet velocity and the air/fuel velocities ratio. The area-averaged heat flux increased with either Re_{air} or ϕ; however, the heat transfer efficiency decreased. To better understand the role of mixing and entrainment in these flames, and their spatial flame structure, Elbaz and Roberts (2014) investigated the effect of the air flow rate in terms of air Reynolds number with a constant fuel flow rate. Three types of structures in IDF flame were identified: breaks, closures, and growing kernels, see figure 3.5. The results showed that increasing the velocity ratio (oxidiser to fuel) enhances the fuel entrainment toward the air jet, improving the mixing between the fuel and air jets.

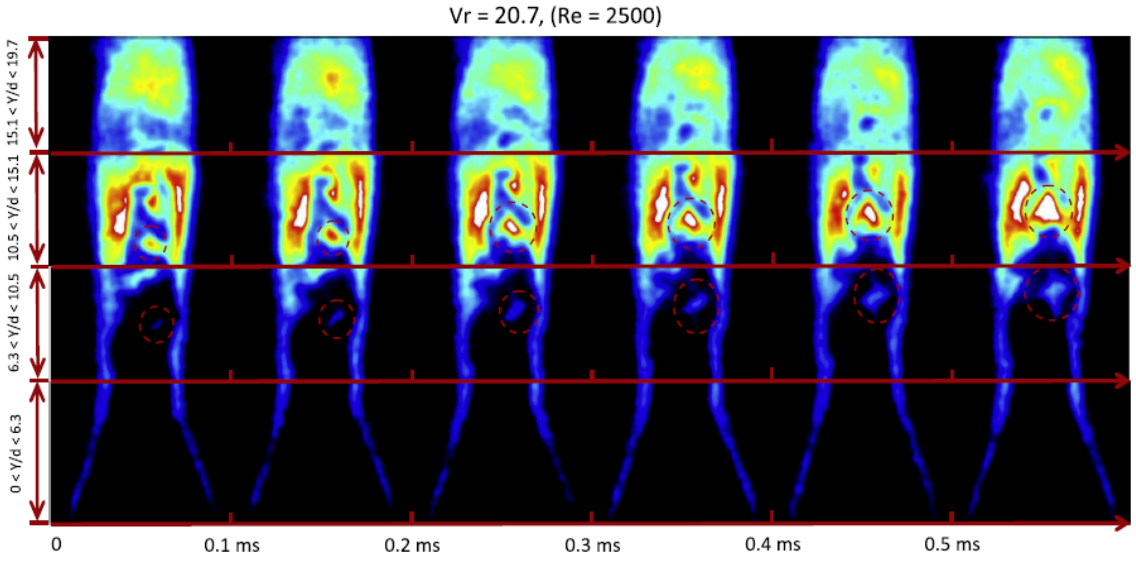

Figure 3.5: Selected sequences of OH-PLIF images collected at various axial locations in flame with Vr = 20.7 (Re = 2500). 'Breaks', 'Closures' and 'Growing Kernels' are represented by dashed arrows, dashed squares and dashed circles respectively. Printed from Elbaz and Roberts (2014)

Cette thèse est accessible à l'adresse : http://theses.insa-lyon.fr/publication/2022LYSEI044/these.pdf
© [K. Utria Salas], [2022], INSA Lyon, tous droits réservés

3.2 Flame appearance

The morphology and appearance of an IDF are highly dependent on the burner design (Sze et al., 2006; Zhen et al., 2011), and the fuel and the oxidiser flow rates (Sze et al., 2006; Wu and Essenhigh, 1984; Bindar and Irawan, 2012). These rates determine the overall equivalence ratio and the ratio between the jets' momentums.

The equivalence ratio, ϕ is defined as:

$$\phi = \frac{\dot{m}_{H_2}/\dot{m}_{O_2}}{(\dot{m}_{H_2}/\dot{m}_{O_2})_{stoic}} \tag{3.1}$$

where $\dot{m}_{H_2}$ is hydrogen mass flow in $[kg/s]$ and $\dot{m}_{O_2}$ is oxygen mass flow.

and oxidiser to fuel momentum ratio, G_O/G_f, is:

$$G_O/G_f = \frac{\rho_{H_2} U_{H_2}^2}{\rho_{O_2} U_{O_2}^2} \tag{3.2}$$

where U_{H2} in $[m/s]$ is the inlet velocity of H_2 per jet, U_{O2} is the inlet velocity of O_2 and ρ is the density in [kg/m^3] at 300K.

In the case of hydrogen–air flames, the most notable emission features are from OH* radicals in the ultraviolet wavelength range and from vibrationally excited H_2O molecules in the infrared region. In the infrared region, H_2O has strong emission bands at 1800, 2700 and 6300 nm. Flame emission from the infrared region dominates the total radiative emission from hydrogen flames. Schefer et al. (2009) found that the appearance of H_2/air NDF exhibits blue and red/orange as predominant colours for rich fuel conditions. The downstream region appears red for rich conditions, and on leaner flames, the red downstream area is less visible due to the lower gas temperatures. A continuous blue emission region is observed next to the long-wavelength side of the OH peak in figure 3.6, this is relatively weak and is attributed to the interaction of flame radical species such as OH* and H* that combine to produce H_2O (Schefer et al., 2009; Gaydon, 1942; Padley, 1960).

The proposed emission mechanisms are described in equations 3.3 and 3.4; however, they still appear to be controversial and discussed in Schefer et al. (2009).

$$OH^* + OH^* \rightarrow H_2O_2 + h_c v \tag{3.3}$$

Cette thèse est accessible à l'adresse : http://theses.insa-lyon.fr/publication/2022LYSEI044/these.pdf
© [K. Utria Salas], [2022], INSA Lyon, tous droits réservés

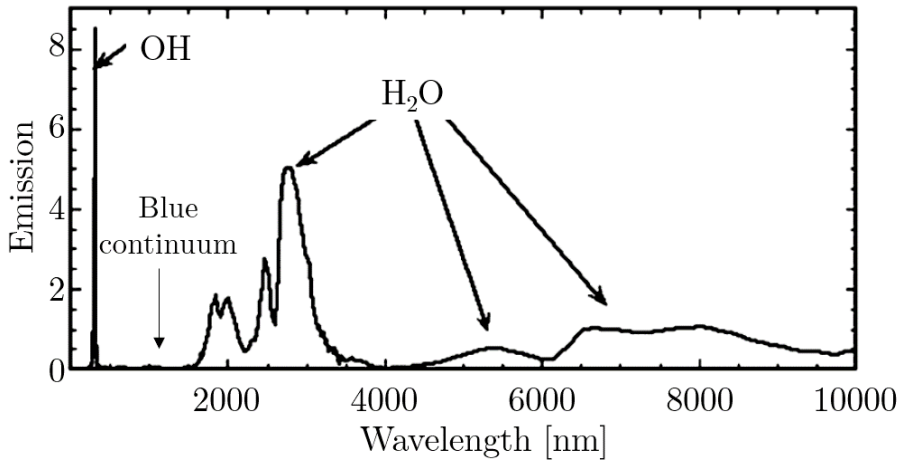

Figure 3.6: Emission spectra in typical hydrogen–air diffusion flames $[kw/m^2\mu m/sr]$(Schefer et al., 2009)

and

$$OH^* + H^* \rightarrow H_2O + h_c v \tag{3.4}$$

h_c: Planck constant, v: photon frequency

The red is related to the high vibrational excitement of H_2O, that is produced in the wavelength range from 600 to about 900 nm Gaydon (1942). The vibration-rotation spectrum of water is connected to thermal features of H_2/O_2 flames where the excess of H_2 colds out the flame in the outer layer due to a fast flow of hydrogen with a high thermal conductivity (Gaydon, 1942). The yellow colour on H_2/air flame is related to the impurities in the air such as sodium, potassium or dust (Gaydon and Egerton, 1948; Gaydon, 1974). It has spectral lines of 589 nm and 589.6 nm in the visible range which explains the red/orange colour observed on these flames.

Nitrogen chemistry can also lead to visible emission in H_2/air flames. Previous studies have cited the observation of green emission from the $NO + O \rightarrow NO_2 + h_c v$ reaction (Gaydon and Egerton, 1948; Vanpee and Mainiero, 1979).

Unlike premixed flames, which have a very narrow reaction zone, diffusion flames have a wider region over which the composition changes and chemical reactions occur. These changes are principally due to some interdiffusion of reactants and products (Glassman and Glumac, 2015). In order to discuss the features previously described, direct visualisation was recorded and analysed.

Cette thèse est accessible à l'adresse : http://theses.insa-lyon.fr/publication/2022LYSEI044/these.pdf
© [K. Utria Salas], [2022], INSA Lyon, tous droits réservés

3.3 Stabilisation mechanisms of inverse diffusion flames

The stabilisation mechanisms of jet diffusion flames have been extensively studied (Lyons, 2007; Lawn, 2009). Several studies have shown that their stabilisation depends strongly on the aerodynamics of the jet (Gollahalli et al., 1988; Lawn, 2009; Wyzgolik and Baillot, 2007), and on the shape of the jet burner (Takahashi and Schmoll, 1991). For the case of a laminar diffusion flame, Borghi and Destriau (1995) established that this regimen of stabilisation is present when a spontaneous reaction of the two gases at the temperature of injection is produced, which is not possible for this case since the mixture $H_2 - O_2$ do not present spontaneous combustion despite the fast kinetics chemistry. Other researches support the theory of triple flame structure as the cause of the flame stabilisation mechanisms (Chung, 2007). The triple flame structure consists of lean and rich premixed wings followed by a trailing diffusion flame (see figure 3.7). The triple flame enables stabilisation of the lifted flame, which is determined by the state of the dynamic equilibrium of the propagation speed of the triple flame and the local flow speed. This triple flame structure was first observed experimentally by Phillips (1965), followed by substantial studies as reviewed in Chung (2007) and Wu et al. (2006).

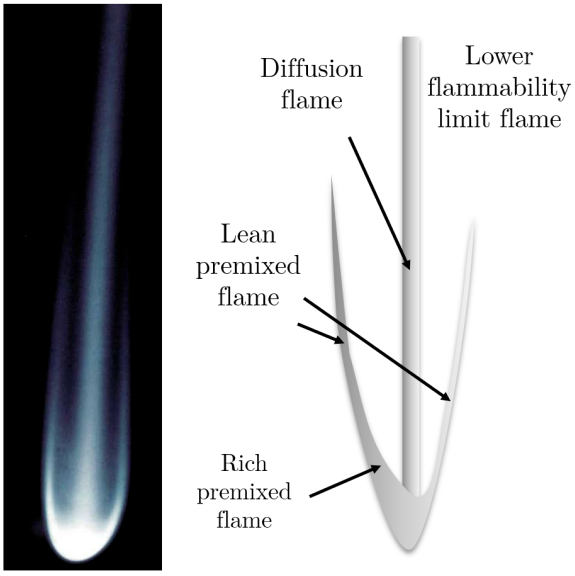

Figure 3.7: Typical photograph of a stationary triple flame in a coflowing stream, printed from Kioni et al. (1993)

Jeon and Kim (2017) also conducted an experimental and analytical study of a stably lifted flame burning propane as the fuel. They proposed that a lifted flame can only be stabilised when the Schmidt number is within a range of either $Sc > 1$ or $Sc < 0.5$. The Schmidt number(Sc) is a dimensionless number used to characterise the relative thickness of the hydrodynamic layer and mass transfer boundary layer for fluid flows that presents

Cette thèse est accessible à l'adresse : http://theses.insa-lyon.fr/publication/2022LYSEI044/these.pdf
© [K. Utria Salas], [2022], INSA Lyon, tous droits réservés

simultaneously momentum and mass diffusion convection process (Incropera et al., 2015):

$$Sc = \frac{v}{D} = \frac{\mu}{\rho D} = \frac{\text{viscous diffusion rate}}{\text{molecular(mass) diffusion rate}} \tag{3.5}$$

Chaudhuri et al. (2010) performed a detailed numerical simulation of both isothermal and reactive flow field of a propane jet flame, and adopted two stabilisation mechanisms for explaining lifted diffusion flame base, i.e. "propagation mechanism" and "Damköhler mechanism" were examined. Their results showed that the propagation mechanism which is based on a triple flame concept failed in several cases where the Damköhler mechanism is valid.

Labor (2003) suggested a flame stabilisation hypothesis in a *Verneuil burner*. The author proposed that the stabilisation mechanism for this type of burner is due to the presence of a recirculation core located at the lip of the injector. The tube separating the flows has a sufficient thickness to generate this core in which combustion stabilises. Sutton and Driscoll (2007) studied non-premixed jet flames and confirmed that these are located along the stoichiometric contour. They established that the combustion characteristics and stabilisation mechanisms of non-premixed flames depend on the location of the flame base that belongs to the stoichiometric contour of the flame. This base is located where the gas and flame burning velocities are balanced, and has premixed flame characteristics since the fuel and oxidiser are locally premixed at this zone. Although the fuel is initially non-premixed with an oxidiser.

In addition, Kim et al. (2019) studied the flame stabilisation mechanisms of H_2/O_2 inverse diffusion flames through the analysis of the turbulence-chemistry interactions. They used as parameter a modified Damkohler number (D_a) which is classically defined as the ratio of the characteristic flow time to the characteristic chemical time (τ_{ch}). In general, the integral time scale (τ_o) is used as the characteristic flow time. Therefore, Da can be defined as follows:

$$D_a = \frac{\tau_o}{\tau_{ch}} \tag{3.6}$$

The new suggested method calculates the D_a based on the flame length (y_d) and fuel injection velocity (u_F), due to the difficulty to calculate τ_o caused by the high temperatures of H_2/O_2 flames (adiabatic temperature $> 3000K$).

In inverse jet flames when the oxidiser and fuel are injected, mixing occurs behind the injector lip and then flame is established. For this kind of flames the mixing time is insufficient and quenching on the lip appears, locating the flame below the injector lip regardless the oxidiser-rich or fuel-rich condition. The highest OH^* intensity is expected to be located along the well-mixed region in the shear layer since the nonpremixed flames

Cette thèse est accessible à l'adresse : http://theses.insa-lyon.fr/publication/2022LYSEI044/these.pdf
© [K. Utria Salas], [2022], INSA Lyon, tous droits réservés

are located at the stoichiometric contour. Moreover, the local burning velocity is sufficient to maintain the flame position and thus L_f is affected only by the mixing rate of O_2 and H_2. Based on these observations, Kim et al. (2019) defined the characteristic flow time as:

$$\tau_o = \frac{L_f}{u_F} \tag{3.7}$$

Also, using the laminar burning velocity S_L at the stoichiometric and corresponding pressure condition and $\overline{\delta}_{OH}$ which is measured at $x = L_f$, the characteristic chemical time can be defined as follows:

$$\tau_{ch} = \frac{\overline{\delta}_{OH}}{S_L} \tag{3.8}$$

With these parameters they identified two regions in an inverse diffusion flame of H_2/O_2: a connected reaction zone where the local flame extinction is not observed, which corresponds to the condition of $D_a > D_{a,ext}$ (local extinction D_a), and a broken reaction zone where the local flame extinction occurs, which corresponds to the condition of $D_a < D_{a,ext}$.

Cette thèse est accessible à l'adresse : http://theses.insa-lyon.fr/publication/2022LYSEI044/these.pdf
© [K. Utria Salas], [2022], INSA Lyon, tous droits réservés

3.4 Flow structure

Labor (2003) studied the aerothermodynamic behaviour of a *Verneuil burner* configuration with similar geometries. They analysed the two jets individually and the coaxial behaviour for non-reactive and reactive conditions. The author observed that the flow structure is divided into two zones of different evolution:

- Zone 1. Located in the upper containment (burner nozzle). The two coaxial jets were identified for this zone on both the mean axial velocity and turbulence intensity profiles.
- Zone 2. Further downstream, where the flow evolved into a single jet structure. The presence of coaxial flow is manifested due to the buoyancy effects generated by the hydrogen ($Froude\ number > 0$, see section 6.2.2.1). This transition from a structure of two coaxial jets to that of a single jet is explained by a significant decay in the mean axial velocity of hydrogen flow. The entrainment phenomenon of the hydrogen flow from the central jet was not relevant since the aerodynamic expansion measured on the central jet had a very low slope in the entire explored area.

On the other hand, this study confirmed the laminar nature of the flow and found that the initial Reynolds number of central jet corresponds to that of a laminar jet that may present a transition to turbulence. The intensity of turbulence on the axis, although slightly high (2%), maintained a constant level along the entire length of the confinement. Furthermore, the lengthening of the laminar zone was linked to the coaxial flow configuration, supported by significant buoyancy effects occurring in the development of the jet.

This research also found auto-similarity between the velocities of the non-reactive flow and the reactive flow of 1.2 ($\overline{U_R}/\overline{U}_{NR} \cong 1.2$). Therefore, the non-reactive flow for the present research is analysed in chapter 6 through the implemantation of a LDA system.

Cette thèse est accessible à l'adresse : http://theses.insa-lyon.fr/publication/2022LYSEI044/these.pdf
© [K. Utria Salas], [2022], INSA Lyon, tous droits réservés

Chapter 4 | Experimental test bench

4.1 Laboratory setup

In order to study the behaviour of the hydrogen-oxygen inverse diffusion flame produce by a *Verneuil burner*. An academical arrangement was set up at the laboratory. Although the upper system configuration was not modified, certain modifications were done to have optical access to the reaction zone at the outlet of the burner. The ceramic tube that surrounds the O_2 and H_2 jets (see figure1), was replaced by a transparent tube of quartz with the same geometries. The insulation confinement of the flame was also replaced by a transparent quartz tube as shown in figure 4.1. The quartz tube had a diameter of 120 mm by a length of 250 mm and a thickness of 3 mm.

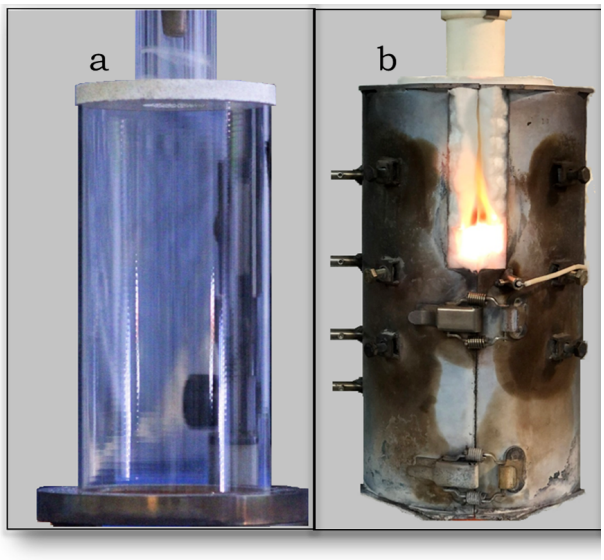

Figure 4.1: Verneuil Burners H_2/O_2: a. Academical approach. b. Industrial setup

Cette thèse est accessible à l'adresse : http://theses.insa-lyon.fr/publication/2022LYSEI044/these.pdf
© [K. Utria Salas], [2022], INSA Lyon, tous droits réservés

4.2 Measurement techniques

One of the difficulties of the study is the implementation of measurement techniques due to complex operating conditions (e.g. restricted optical access, very high temperatures due to the oxycombustion, high radiative environment). Consequently, the thermal approach is mainly experimental and uses visualisation techniques, allowing to highlight the qualitative aspects of the flame. These techniques are principally based on images of the emission of the naturally excited OH^* radicals (spontaneous chemiluminescence) as well as direct visualisations of the flame. In addition, temperature measurements were acquire to have preliminary quantitative results. Classical laser diagnostics as Laser Doppler Anemometry were used to aerodynamically analyse the flame flow. Figure 4.2 shows the laboratory setup.

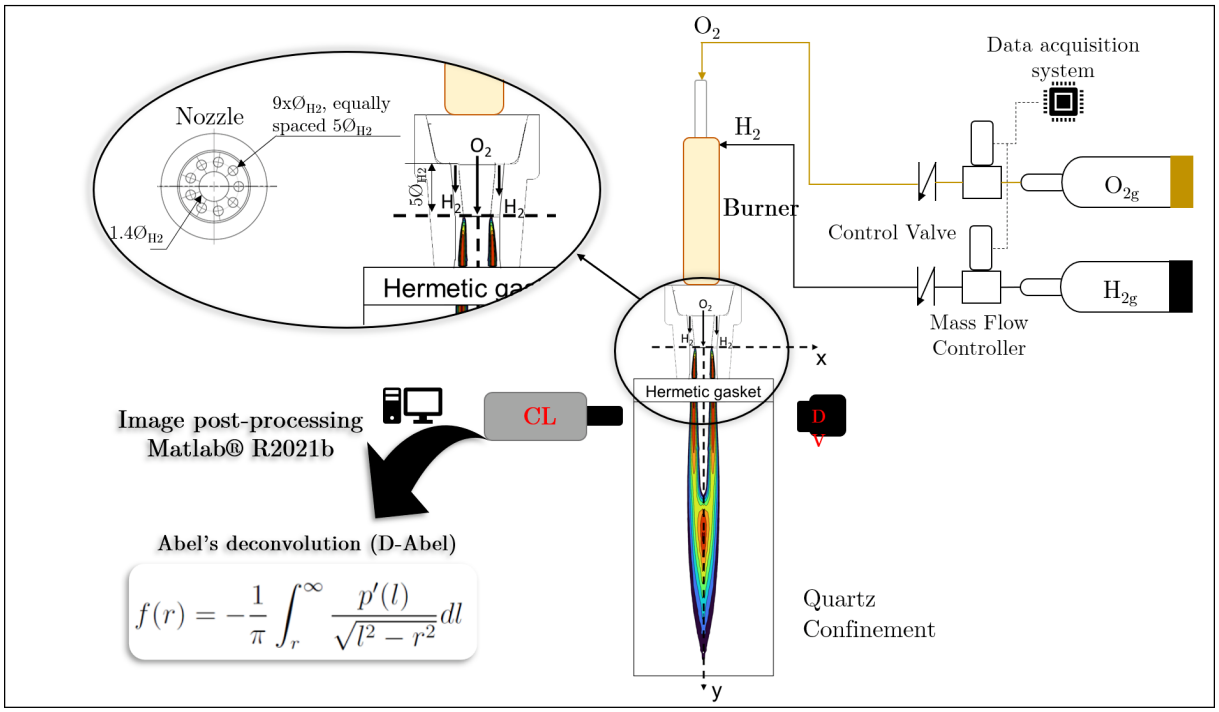

Figure 4.2: Laboratory setup

4.2.1 Direct visualisation

Direct Visualisation (DV) is a technique used to qualitatively observe the overall behaviour of the flame. During combustion, the reaction zones are characterised by an intense emission of light, by which the naked eye can see them. This light emission comes from excited species that are produced from elementary chemiluminescence processes, and the hot gas. In which, all or part of the reaction heat retained by one of the molecules is produced

Cette thèse est accessible à l'adresse : http://theses.insa-lyon.fr/publication/2022LYSEI044/these.pdf
© [K. Utria Salas], [2022], INSA Lyon, tous droits réservés

in the form of an excitation energy, which subsequently is emitted in a characteristic spectrum (Labor, 2003).
Observation of the light emitted by a flame in the visible spectrum constitutes the first and simplest technique to investigate the overall characteristics of the flame. We can obtain qualitative information, by which we can determine the global topology of the flame, the visible colors and deduce its characteristic dimensions, among others (Lamige, 2014).

Application to the study
The whole flame shape and appearance are obtained from the direct images using a digital camera, Nikon D7500. Which has a 20.9-megapixel APS-C[1] CMOS[2] sensor with a focal length multiplier (or "crop factor") of about 1.5x. Its resolution is 5568 x 3712 pixels and a lens $AF-S$[3] Nikkor, with a focal length of 85 mm and a maximum aperture of f/1.8. This approach also gives information about the equivalence ratio, thus the mixing during the combustion and about the chemistry through the colours emitted by the flames reported by this technique.

4.2.2 Chemiluminescence OH*

The reaction zone's features can be analysed and quantified by using OH^* chemiluminescence emission recording. This technique can also be used to obtain OH^* intensity distribution, which can describe the OH^* concentration distribution qualitatively (He et al., 2019). Furthermore, OH^* chemiluminescence is an indirect measurement of the heat release (Lauer, 2011).
Chemiluminescence (CL) is a particular direct visualisation, for which we will only collect, by filtering, part of the flame emission. This filtering helps detect areas in which a specific species is present. In an O_2/H_2 flames, OH^* is the predominant emitter of chemiluminescence (see figure 4.3). The emissions of OH^* are related to the heat release rate of the flame because the emission spectrum of the hydroxyl radical results from its energetic structure.

During combustion, different reactions and the formation of different atoms or molecules in an electrically excited state are present. Subsequently, for any two species A and B, their reaction is written:

$$A + B \rightarrow D^* \tag{4.1}$$

D : excited species

[1]APS-C: Advanced Photo System type C
[2]CMOS: Complementary Metal Oxide Semiconductor
[3]AF-S: Autofocus Silent Focusing

Cette thèse est accessible à l'adresse : http://theses.insa-lyon.fr/publication/2022LYSEI044/these.pdf
© [K. Utria Salas], [2022], INSA Lyon, tous droits réservés

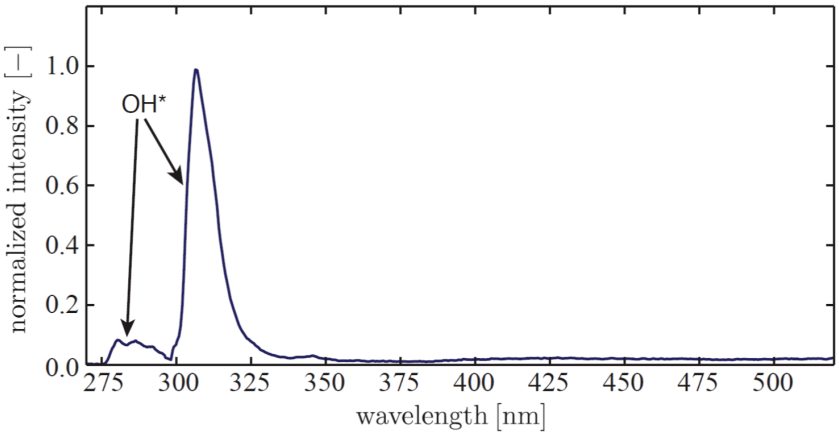

Figure 4.3: Typical chemiluminescence spectrum of an atmospheric hydrogen-air flame OH* is the only chemiluminescence emitter. (Lauer, 2011)

D passes from an excited state 1 of energy E_1 to a ground state 0 of energy E_0. When D emits a photon of frequency v in the visible or UV spectrum, the mechanism of spontaneous emission or chemiluminescence appears as:

$$D^* \rightarrow D + h_c v \tag{4.2}$$

$$h_c v = E_0 - E_1 \tag{4.3}$$

h_c: Planck constant (6.62607004x10^{-34} [m^2 kg/s]) and v the frequency of the emitted photon [s^-1]. For hydroxyl radical, this corresponds to the frequency $v = c/\lambda$ where the wavelength $\lambda = 306.6\,nm$ lies in the ultraviolet OH band (Marchese et al., 1996) and c is the speed of the light. The intensity emitted by species D (I_e) is isotropic and proportional to the population N_1 of level 1. It is defined as: $I_e \propto A_{10} N_1 h_c v$ (A is the Einstein coefficient (1.86×10^6 [s^{-1}]).

Several studies have measured OH* chemiluminescence signals to relate the OH* intensities with heat release rate (Clark and Bittker, 1954; Hardalupas and Orain, 2004; Ayoola et al., 2006; De Leo et al., 2007; Lauer, 2011). Clark and Bittker (1954) were the first to study the relation between OH* chemiluminescence measurement and integrated heat release rate. They found a linear dependency of measured chemiluminescence signals on fuel-flow rate at constant equivalence ratios and a decrease of the intensity with decreasing equivalence ratio. Ayoola et al. (2006) studied the heat release rate in turbulent premixed flames. They successfully characterised OH* chemiluminescence as a measure for spatially resolved heat release rate for counterflow flames. Their study uses the heat release rate imagining technique, which consists in determine a heat release rate from OH* and CH_2O PLIF images. They compared these results with OH* chemiluminescence

Cette thèse est accessible à l'adresse : http://theses.insa-lyon.fr/publication/2022LYSEI044/these.pdf
© [K. Utria Salas], [2022], INSA Lyon, tous droits réservés

measurements and found that the two techniques have similar behaviours when the strain rate was varied. Further, De Leo et al. (2007) investigated diffusion flames at atmospheric pressure by analysing OH* emission methane/oxyflames. They used GRI-Mech 3.0 kinetics scheme coupled with additional reactions, and validated through experimental results. They compared temperature profiles with OH* and CH* concentration profiles, and found that the latter showed the sharpest. For high oxygen fractions, both the temperature and the OH peaks become wider, but not CH peaks. Moreover these peaks are within 1.5 mm of temperature maximum. Therefore, they suggest that OH is a good tracer of heat release position, specially in oxy-flames. In addition, Lauer (2011) used chemiluminescence imaging to determinate the heat release distribution in turbulent flames by developing a correction model of the chemiluminescence signals. This model correct the measured OH signals in a way that they exhibit heat release rate proportional intensities. They took into count the effect of turbulence on OH intensity and heat release rate. The correction method is based on a statistical model describing the pdfs of turbulence induced straining of flamelets. For lean flames, the corrected OH intensities are in very good agreement with the heat release rate distribution determined with the reference method. This reference method is based on the first law of thermodynamics, this technique assumes that the local net heat release rate of the flame is balanced by the increase of the fluid's sensible enthalpy due to combustion. For evaluation of this energy balance, measurement data from chemiluminescence, PIV, and OH-PLIF were required.

Furthermore, He et al. (2019) suggested a correlation (equation 4.4) between the intensity and the concentration of OH*. This correlation was used to find a correlation between the integrated OH* concentration and the integrated heat release rate for diffusion flames.

$$I_{OH^*} = \frac{1}{4\pi}\tau K A V_{em} \cdot [OH^*] \tag{4.4}$$

where $[OH^*]$ is the concentration of OH*, A is the Einstein coefficient ($1.86 \times 10^6\ 1/s$), τ is the exposure time, V_{em} is the pixel volume, and K is a constant associated with the parameters of the camera.

Therefore the present study focuses on analysing the distribution and intensities of OH* emissions to use it as a qualitative indicator of the local heat release rate.

Application to the study

The OH* chemiluminescence images were obtained by using a Photon SA4 Fast Camera and an OH* FWHM filter of 310 nm ± 50 nm (transmission curve figure 4.4). A single image of OH* chemiluminescence is obtained by averaging 60 images with an exposure time of 10 ms and a frame rate of 50 images/second. The flow exhibits a laminar behaviour and the deviation standard of the intensities (defined in equation 4.5) between the samples

Cette thèse est accessible à l'adresse : http://theses.insa-lyon.fr/publication/2022LYSEI044/these.pdf
© [K. Utria Salas], [2022], INSA Lyon, tous droits réservés

is <0.01. In order to analyse the heat release rate, the OH* chemiluminescence images directly obtained are converted into the planar chemiluminescence images using Abel inversion transform (see section 4.2.3).

The emission intensities were normalised and represented as:

$$I_{N,OH^*} = \frac{I}{I_{max}} \tag{4.5}$$

where I is the local intensity of OH* and I_{max} is the OH* maximum intensity of all the images.

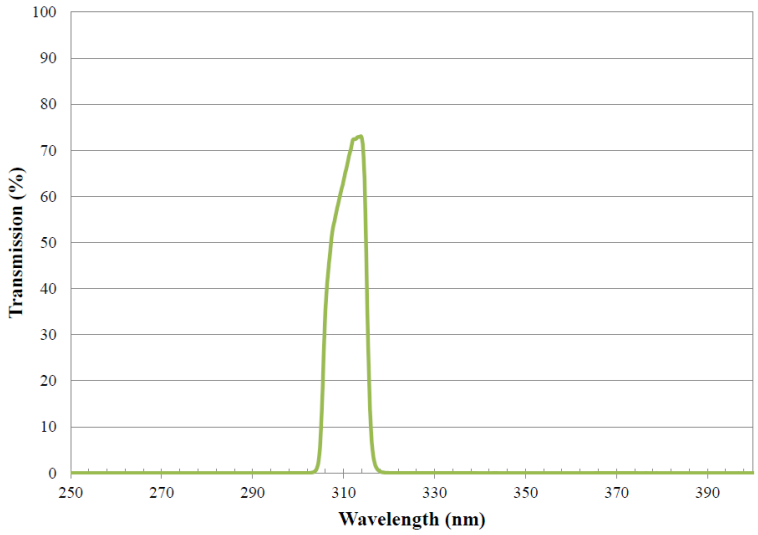

Figure 4.4: Coating Curve: 310 nm CWL TECHSPEC 10nm OD4 Bandpass Filter

4.2.3 Abel transform

The OH* chemiluminescence technique generates line-of-sight (LOS) projections of the OH* emission intensities. To reconstruct the spatial field, these projections need to be deconvoluted. The flame is considered axisymmetric, for which commonly used deconvolution methods include the Abel transform, the onion peeling method and the two-dimensional Fourier transform. During this research the Abel transform was performed, in order to avoid the derivative calculation of the projection data.

Yuan (2003) stated that the Abel transform is an exact method and the simplest among the commonly used methods. Figure 4.5 illustrates the relation between the projection and the spatial distribution of a flame property in a plane normal to the streamwise axis of an axisymmetric flame. The projection function $p(l)$ is related to the line-of-sight

Cette thèse est accessible à l'adresse : http://theses.insa-lyon.fr/publication/2022LYSEI044/these.pdf
© [K. Utria Salas], [2022], INSA Lyon, tous droits réservés

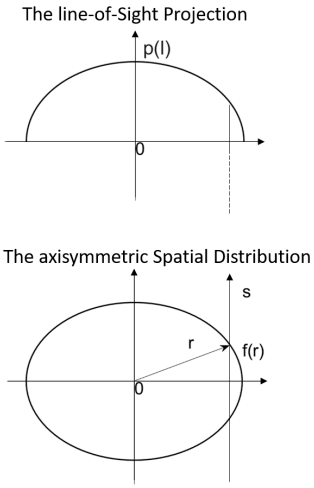

Figure 4.5: The line-of-sight integration of an axisymmetric spatial distribution (Yuan, 2003)

integration of the flame property $f(r)$ by the following equation:

$$p(l) = \int_{-\infty}^{\infty} f(r)ds \tag{4.6}$$

The reconstruction or deconvolution has as objective to find the spatial distribution $f(r)$ based on the given projection $p(l)$. In figure 4.5 the radius r can be expressed in terms of l and s as $\sqrt{l^2 + s^2}$. The equation is written:

$$p(l) = 2\int_{l}^{\infty} \frac{rf(r)}{\sqrt{r^2 - l^2}}dr \tag{4.7}$$

A well-known analytical inverse is the Abel transform

$$f(r) = -\frac{1}{\pi}\int_{r}^{\infty} \frac{p'(l)}{\sqrt{l^2 - r^2}}dl \tag{4.8}$$

However, the direct application of this equation is noisy because it requires to calculate the derivative of projection data $p(l)$. Moreover, it depends mainly of the scheme for approximation the numerical derivative. A more advantageous method is suggested by (Kasim et al., 2015), the modified 3-points Abel inversion.

Modified 3-points Abel transformation

Kasim et al. (2015) uses the definition of the classical Abel transformation (equation 4.8), excepts that it contains a cosine factor in the integral. Another difference between normal Abel inversion and modified Abel inversion is that the latter takes into account if

Cette thèse est accessible à l'adresse : http://theses.insa-lyon.fr/publication/2022LYSEI044/these.pdf
© [K. Utria Salas], [2022], INSA Lyon, tous droits réservés

the object is moving to longitudinal direction and/or the probe is not crossing the object perpendicularly.

$$\tilde{f}(r,y) = -\frac{1}{\pi}\int_r^\infty \frac{\partial \tilde{F}}{\partial y}(y,k)\frac{cosh(ka\sqrt{y^2-r^2})}{\sqrt{y^2-r^2}}dy \tag{4.9}$$

Where the variable $\tilde{F}(y,k)$ represents the Fourier transformation of measured property in axes x, y and z (figure 4.6). $a \equiv [(cos\theta - u_p/v_g)/sin\theta]$. For our case $a = 0$, because the object is not moving. It was used by Kasim et al. (2015) for plasma wakefield diagnostics. The laser pulse propagates with angle θ and speed v_g, and crosses the wakefield which propagates in the z-direction with speed u_p.

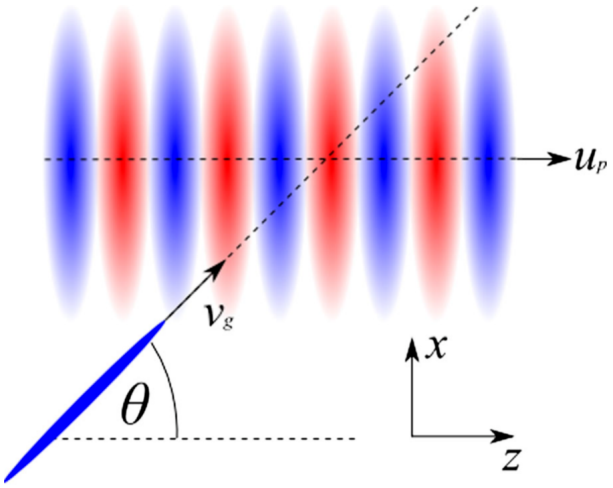

Figure 4.6: The configuration considered: the laser probe pulse crosses the wakefield at an arbitrary oblique angle. The y-axis is pointed out of the page. By obtaining the phase or frequency modulation of the pulse, one can obtain the density modulation profile of the wakefield at the crossing point. Printed from Kasim et al. (2015)

Equation 4.9 is solved splitting the integral therm into several integral with spacing Δr:

$$f(r_j) = -\frac{1}{\pi}\sum_{i\geq j}\int_{y_{i0}}^{y_{if}} F'(y)\frac{1}{\sqrt{y^2-r_j^2}}dy \tag{4.10}$$

where $r_j = j\Delta r$, $y_{if} = i\Delta r + \Delta r/2$, $y_{i0} = i\Delta r + g_{ij}\Delta r$ and

$$g_{ij} = \begin{cases} 0 & \text{if i=j} \\ -1/2 & \text{otherwise.} \end{cases} \tag{4.11}$$

Cette thèse est accessible à l'adresse : http://theses.insa-lyon.fr/publication/2022LYSEI044/these.pdf
© [K. Utria Salas], [2022], INSA Lyon, tous droits réservés

Resolving equation 4.10 the final expression is:

$$f(r_j) = -\frac{1}{\pi\Delta r}\sum_{i\geq j}\left\{F_i\left[-2C_{ij}B_{ij}^{(1)}\right] + F_{i-1}\left[-\frac{1}{2}B_{ij}^{(0)} + B_{ij}^{(1)}\right] + F_{i+1}\left[\frac{1}{2}B_{ij}^{(0)} + B_{ij}^{(1)}\right]\right\} \tag{4.12}$$

where $F_i = F(i\Delta r)$, and it represents the discrete Fourier transform of the property measured.

$$B_{ij}^{(0)} = \begin{cases} 0 & ; i = j = 0 \; i < j \\ ln\left[\frac{2i+1+\sqrt{(2i+1)^2-4j^1}}{2i}\right] & ; i = j \neq 0 \\ ln\left[\frac{2i+1+\sqrt{(2i+1)^2-4j^1}}{2i-1+\sqrt{(2i+1)^2-4j^1}}\right] & ; i > j. \end{cases} \tag{4.13}$$

$$B_{ij}^{(1)} = \begin{cases} 0 & ; i = j = 0 \text{ or } i < j \\ D_{ij}^{+} - iB_{ij}^{(0)} & ; i = j \neq 0 \\ D_{ij}^{+} - D_{ij}^{-} - iB_{ij}^{(0)} & ; i > j, \end{cases} \tag{4.14}$$

with $D_{ij}^{\pm} \equiv \sqrt{(i \pm 1/2)^2 - j^2}$

Application to the study

The Abel deconvolution is performed in order to analyse quantitatively the image obtained by the use of the OH^* chemiluminescence. The two methods explained in previous section are used. Figure 4.7 illustrates the comparison done by this research with the objective to choose the most adequate method to be implemented. *Abel 1* is the results obtained by the algorithm developed by the current study using equation 3.3 directly. *Abel 2* uses the algorithm developed by Kasim et al. (2015) (Abel 2). The Gaussian noise is used as selection criteria which represents the image unwanted information. The Gaussian noise of the image obtained with each method is calculated base on equation 4.15.

$$P(g) = \sqrt{\frac{1}{2\phi\sigma_s^2}}e^{-\frac{(g-\mu)}{2\sigma_s^2}} \tag{4.15}$$

where P is the Gaussian noise which characteristics by its probability density function (PDF) (normalises with respect to gray value (g)), μ is the mean and σ_s the standard deviation (Boyat and Joshi, 2015).

Cette thèse est accessible à l'adresse : http://theses.insa-lyon.fr/publication/2022LYSEI044/these.pdf
© [K. Utria Salas], [2022], INSA Lyon, tous droits réservés

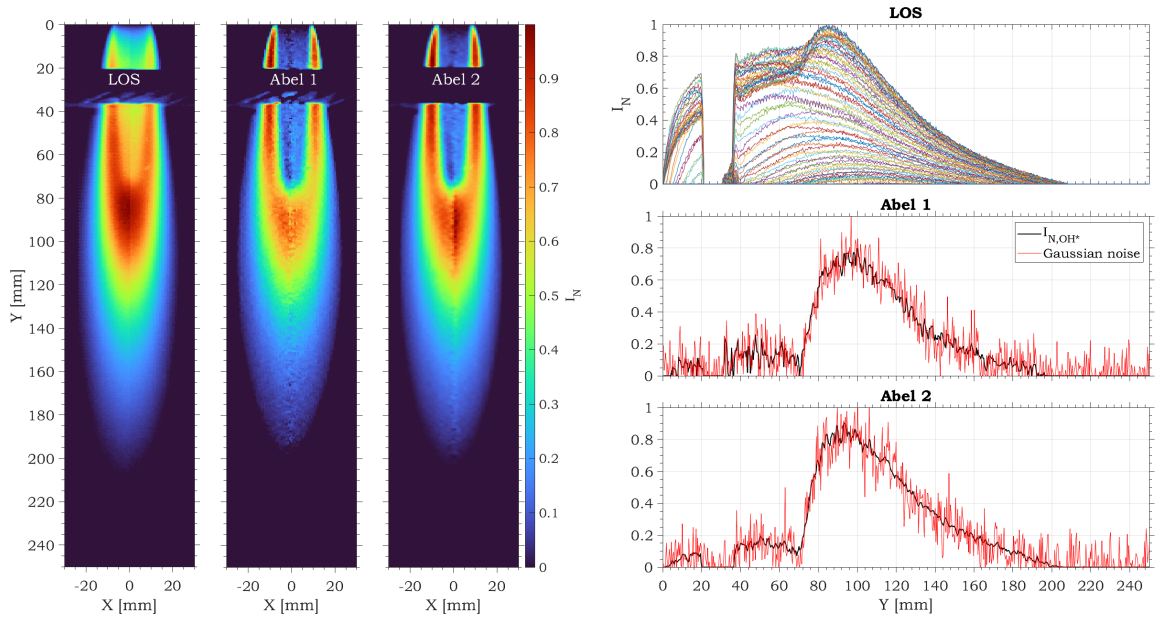

Figure 4.7: Comparison of traditional Abel transform (Abel 1) and 3-points Abel transform (Abel 2)(flame injection conditions: $\phi = 1.5$ $Re_{O_2} = 1500$). Left: Ligth-of-Sight (LOS) image obtained from instant chemiluminescence image. Right: Up(direct intensities of the LOS image), center and down (Normalised intensities and Gaussian noise along the central axe (X=0mm)).

Although the noise reported by the two methods is similar, the results of 3-points method (Abel 2) seem to be more adapted to the present research, since the values at the axe central obtained by the direct application of the Abel transform reported slight higher Gaussian noise. Therefore, all the analysed flames using the chemiluminescence images are done by applying the method called Abel 2.

4.2.4 Laser Doppler Anemometry (LDA)

Laser Doppler Anemometry (LDA), also known as Laser Doppler Velocimetry (LDV), is an non-intrusive optical technique ideal to measure velocity and turbulence distribution in free flows and internal flows. The technique is based on the Doppler effect which indicates that the frequency shift generated by a wave emitted or reflected from a moving source is related with its relative velocity (Russo, 2011). The LDA sends usually a monochromatic laser beam toward a particle and collects the reflected radiation. The velocity of the particle can be found by measuring the change in wavelength of the reflected laser light (Hennessy, 2005). In other words, the LDA calculates the velocity from the difference in frequency between the light that strikes the moving particle and that is scattered and seen by an observer. The measurement can be performed by producing an interference fringe pattern (pattern of light and dark stripes) by superimposing the original and reflected signals (Hennessy, 2005).

Cette thèse est accessible à l'adresse : http://theses.insa-lyon.fr/publication/2022LYSEI044/these.pdf
© [K. Utria Salas], [2022], INSA Lyon, tous droits réservés

The Laser Doppler Anemometer (LDA) is a technique that has been widely used in combustion. It is specially useful for applications where physical sensors usually are difficult or impossible to use (e.g. reversing flow, chemically reacting or high-temperature media, and rotating machinery). The directional sensitivity and non-intrusiveness of LDA overcome the mentioned constraints. However, this technique requires tracer particles in the flow (Hennessy, 2005). Its implementation also brings several issues in combustion applications due to the optical access need. The reactive environment generates high temperatures and pressures in transparent confinement conditions, this confinement must be high temperature resistant. Besides, the particles use to track the flow can produce some optical perturbations, due to incandescent radiation (White, 2010).

The crossed-beam (or interference) LDA system is a LDA technique where the moving particle is illuminated by two light beams of equal intensity (see figure 4.8) obtained from splitting one laser beam. The particle scatters the light from each of the two beams: from beam 1, with wavelength λ_1 and frequency fs_1, and from beam 2, with wavelength λ_2 and frequency fs_2.

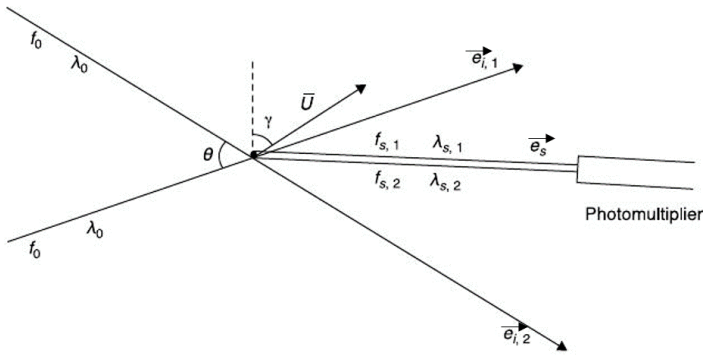

Figure 4.8: Schematic crossed-beams LDA (Russo, 2011).

The variable part of the photomultiplier signal is only due to the difference of the frequencies, the Doppler frequency, is defined as:

$$f_D = f_{s2} - f_{s1} = f_0 + \frac{\overrightarrow{U}}{\lambda_0} \cdot (\overrightarrow{e_s} - \overrightarrow{e_{i2}}) - \left(f_0 + \frac{\overrightarrow{U}}{\lambda_0} \cdot (\overrightarrow{e_s} - \overrightarrow{e_{i1}}) \right) = \frac{\overrightarrow{U}}{\lambda_0} \cdot (\overrightarrow{e_{i1}} - \overrightarrow{e_{i2}}) \quad (4.16)$$

Another approach to analyse the crossed-beam system is by using the interference principle. The laser light produces two beams that intersect at an area as shown in figure 4.9. They come from the same source coherent and with the same wavelength, λ, and the same intensity $I_1 = I_2 = I$, the intensities sum of the interfering beams is:

$$I_{1+2} = 2I[1 + cos(\alpha_1 - \alpha_2)] = 2I \left[1 + cos\frac{2\pi}{\lambda}(l_1 - l_2) \right] \quad (4.17)$$

Cette thèse est accessible à l'adresse : http://theses.insa-lyon.fr/publication/2022LYSEI044/these.pdf
© [K. Utria Salas], [2022], INSA Lyon, tous droits réservés

where $\alpha = \dfrac{2\pi l}{\lambda}$, and l is the optical path.

Two extreme cases could appear at calculating the light intensity sum of the interfering beams:

- the difference in path lengths is equal to a multiple of the wavelength, $l_1 - l_2 = N\lambda(N = 0, \pm1, \pm2....)$: the resulting light intensity is $I_{1+2} = 4I$
- the difference in path lengths is equal to an odd multiple of half wavelengths, $l_1 - l_2 = (2N + 1)\lambda/2$: the resulting light intensity is zero, $I_1 + 2 = 0$.

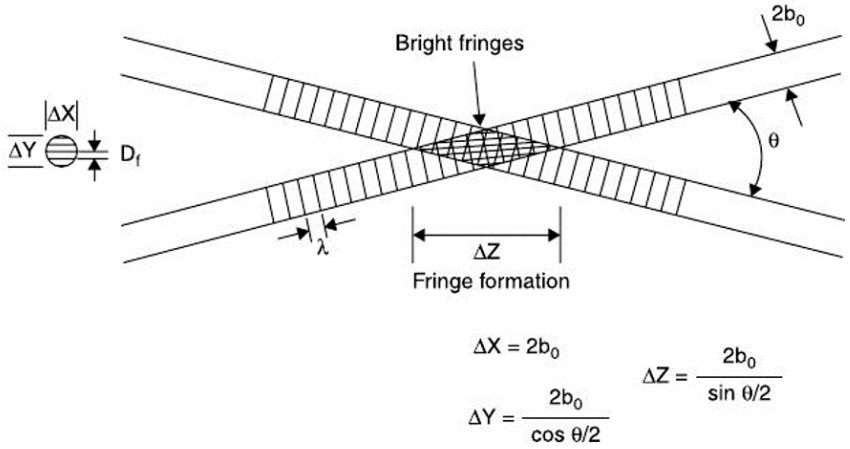

Figure 4.9: Formation of interference fringes in the measuring volume of a crossed-beams LDA (Russo, 2011).

In figure 4.9, we can observe a series of parallel interference fringes that are generated in the area of intersection of the two laser beams, which is the measurement volume. The velocity component normal to the fringes can be calculated by measuring the Doppler frequency and the distance between the fringes, as follows.

The the distance between two consecutive fringes is:

$$D_f = \frac{\lambda}{2sin\left(\dfrac{\theta}{2}\right)} \tag{4.18}$$

Each particle passing in this network of fringes diffuses or not the light while crossing alternately light and dark bangs. The Doppler frequency of the light variable that illuminates the crossing particles as:

$$f = \frac{Ucos\gamma}{D_f} = 2sin\left(\frac{\theta}{2}\right)\frac{Ucos\gamma}{\lambda_0} \equiv f_D \tag{4.19}$$

Cette thèse est accessible à l'adresse : http://theses.insa-lyon.fr/publication/2022LYSEI044/these.pdf
© [K. Utria Salas], [2022], INSA Lyon, tous droits réservés

where γ is the direction of the particle velocity as illustrated in 4.8.

The particles emit light according to Mie Scattering, since the laser beam has a Gaussian intensity distribution of light. The trace on an oscilloscope of a typical signal is shown in Figure 4.10.

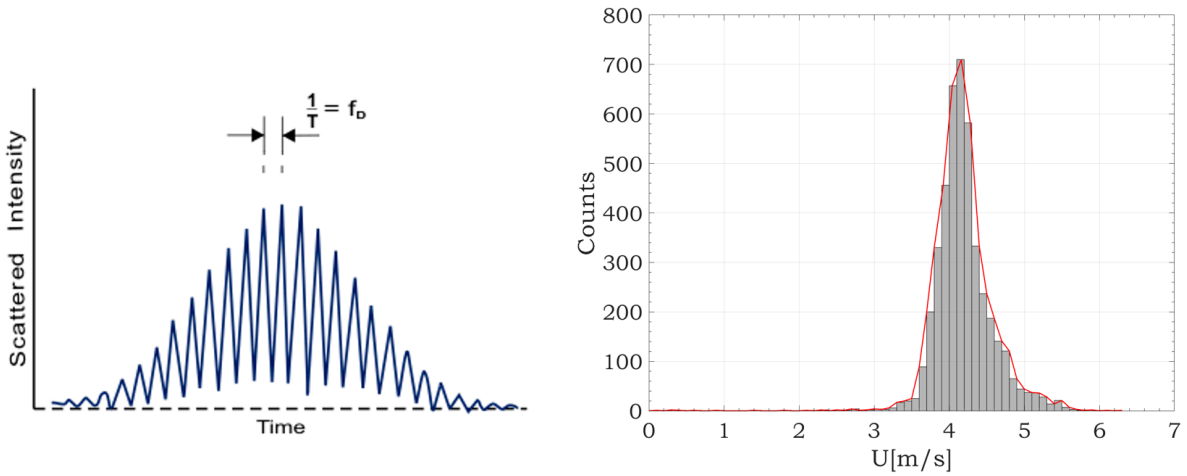

Figure 4.10: Left: A typical signal of a LDA on an oscilloscope (Russo, 2011). Right: The calculated velocity

The measurement accuracy of the distance between the fringes, determines the precision with which the velocity of the particle can be measured using the Doppler frequency. For turbulent flows, this could be an issue, since speed can be null or of unknown direction (zone of separation, wakes,etc.). The zero speed is not recognized because there is no output signal from the photo detector, the direction of the velocity component cannot be inferred from Equation 4.19.

To eliminate the ambiguity that the Doppler frequency does not depend on the sign of the velocity component, one of the laser beam is passed through a Bragg Cell. This consist in an acoustic-optical modulator (Figure 4.11), a crystal or a liquid, transparent. A vibrator (a piezoelectric transducer) sends a pressure wave to the modulator, and then a wave of an index of refraction with a constant frequency, changing the optical path of the laser beam passing through the cell with the same frequency of the vibrator.

The principle of laser Doppler anemometry has been briefly exposed, let us now see how the two-component assembly is carried out which allows simultaneous measurement of the velocity in two directions of flow.

Application to the study

The present research used a commercial LDA acquisition system, the FlexLDA system shown in figure 4.12. This is a system DANTEC full featured turn-key solution for working distances up to 500 mm and velocities up to 68 m/s. It uses compact lasers and

Cette thèse est accessible à l'adresse : http://theses.insa-lyon.fr/publication/2022LYSEI044/these.pdf
© [K. Utria Salas], [2022], INSA Lyon, tous droits réservés

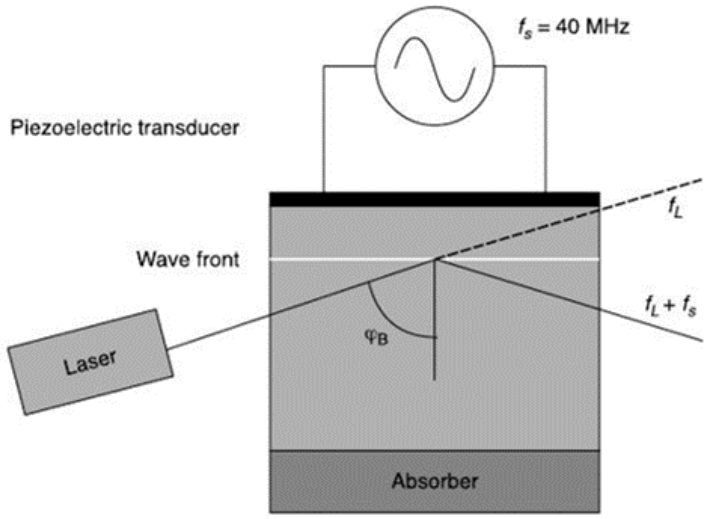

Figure 4.11: A Bragg Cell (Russo, 2011).

Bragg cells integrated into the stable and robust design. Signal processing is done by the well proven BSA (Burst Spectrum Analyzer) using robust real time FFT (Fast Fourier Transform) processing. The calibration data are loaded into the BSA Flow software package providing the most accurate results directly in velocity units (m/s or ft/s).

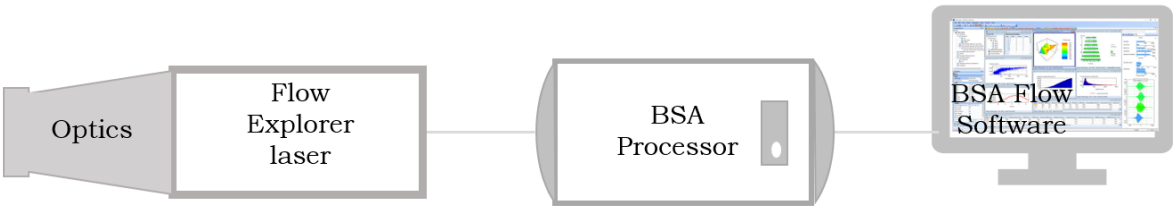

Figure 4.12: Scheme of LDA acquisition system.

Inside the FlowExplorer, a laser beam is split in two and then focused to a point to form a measurement volume. The Doppler-shifted scattered light of each particle passing the measurement volume is collected and then sent to the signal processor to determine their velocity. The main benefits of LDA over other flow velocity measurement methods include: the optical technique does not disturb the flow, the transfer function is linear and can be determined to high accuracy, small measurement volumes are possible, high frequency response is possible in well-seeded flows, and the absolute accuracy of the measurement results are unmatched due to calibrated optics and signal processor performance.The solution is based on three core components: optics, signal processor, and software. The system is used to analysed two component measurements. Table 4.1 show the specifications of the system.

Cette thèse est accessible à l'adresse : http://theses.insa-lyon.fr/publication/2022LYSEI044/these.pdf
© [K. Utria Salas], [2022], INSA Lyon, tous droits réservés

Optics	
FlowExplorer	
Laser	Diode
Laser power	70 mW
Laser wavelength	660/785 nm
Focal length	500 mm
Measurement volume dimensions	0.15 x 0.15 x 2.55 mm^3 (500 mm focal length)
Processor	
BSA F100	
Max. Velocity	>68 m/s (500 mm focal length)
Data rate	>100,000 bursts/sec
Accuracy	1%
Resolution	>16 bits

Table 4.1: LDA Technical Specifications

For the statistical processing of the data obtained through the BSA, a number of 5000 "bursts' was chosen for each measurement point after different tests. This value mainly depends on the nature of the flow (laminar, turbulent). Thus, for turbulent configurations it is necessary to increase the number of samples to characterise all the flow frequencies. In this study, the choice of 5000 "bursts" showed that the average velocities had become constant asymptotically and that it was unnecessary to increase the number of achievements. A multiple axes controller was used to move the optics (IMC-S8, isel). This is controlled by computer, and allows movements along the three axes X, Y and Z shown in Figure 4.13. These different axes and their names will be those used systematically throughout the report. In order to avoid beam deviations when crossing the transparent confinement, the measurements will be carried out systematically according to the light scattering source. Thus, the transversal axis will be the X-axis and the collected transverse velocity component will be W and not that characterises the flow's development (V). In the case of axisymmetric laminar flow , this component W should be negligible.

Cette thèse est accessible à l'adresse : http://theses.insa-lyon.fr/publication/2022LYSEI044/these.pdf
© [K. Utria Salas], [2022], INSA Lyon, tous droits réservés

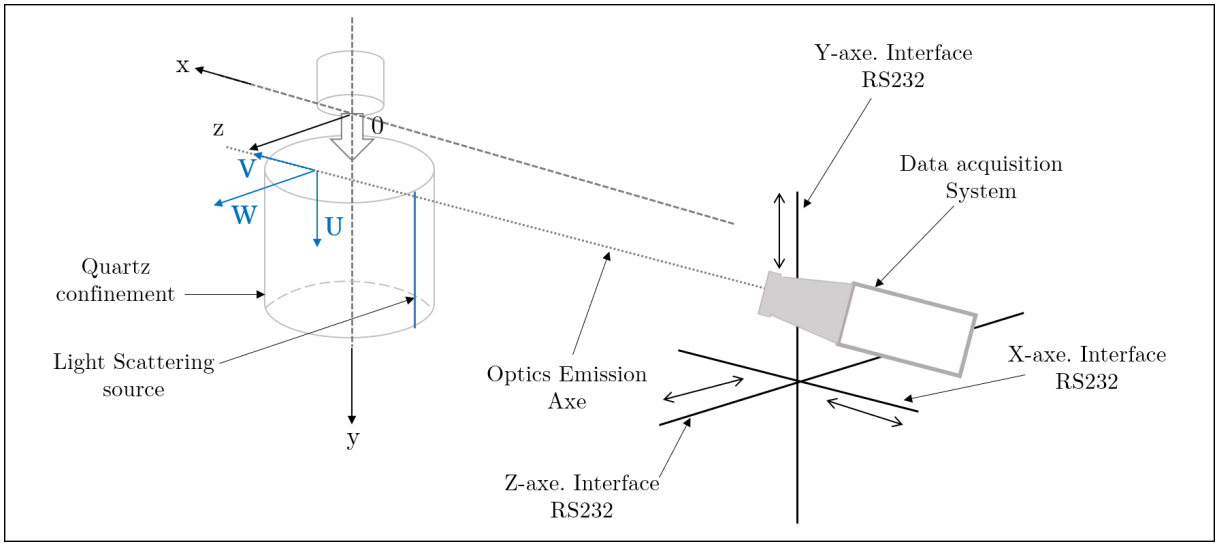

Figure 4.13: Displacement device

Cette thèse est accessible à l'adresse : http://theses.insa-lyon.fr/publication/2022LYSEI044/these.pdf
© [K. Utria Salas], [2022], INSA Lyon, tous droits réservés

4.3 Analysis methods

The principal objective of this part is to understand the thermal behaviour of the *Verneuil furnace*. In order to achieve this objective, it is necessary to characterise the flame. Furthermore, it is also essential to understand the parameters that influence the thermal conditions of the crystal growth environment. The fuel and oxidiser injection conditions impact it considerably, as observed previously (see section 1.2.1). Within this in mind, this part analyses the influence of different aerodynamics and chemistry conditions. Main parameters studied as Reynolds numbers of fuel and oxidiser were used, as well as their momentum ratios and equivalence ratio. As the literature indicated in chapter 3 these parameters are helpful to identify flame structure shapes, determine flame structure characteristics and OH^* emissions (related to the heat transfer release).

The analysis is divided into three cases. The first case analyses the influence of the fuel injection conditions, and the second case the oxidiser injection conditions, the third case assess the importance of the parameters used to characterise the flame. The operating conditions are depicted in table 4.2. The Reynolds numbers chosen were within the stable zone of H_2/air inverse diffusion flames suggested by (Bindar and Irawan, 2012). Some of these points also correspond to actual industrial conditions of the *Verneuil growth method*.

Case 1

Case 1 corresponds to the study of fuel momentum influence. A laminar fixed Re_{O_2} of 1500 was used while the overall equivalence ratio was varied from 0.8 to 1.7. Although the oxidiser and fuel jets are initially separated, the concept of equivalence ratio might not be applicable to an IDF; this indicates the relative strength of the O_2 and fuel supply concerning the stoichiometric oxidiser/fuel ratio and denotes the oxidiser-fuel ratio momentum. For this case the oxidiser momentum is constant and the oxidiser-fuel momentum ratio decreases while the overall equivalence ratio increases.

Case 2

In case 2, the influence of oxygen momentum was analysed. From case 1, the condition with the maximum hydrogen Reynolds number was chosen to study a wide range of injection conditions varying oxygen Reynolds number. At fixed laminar fuel flow rate ($Re_{H_2} = 140$), the Re_{O_2} was varied from 1500 to 3200, from laminar ($Re_{O_2} < 2000$) to critical ($2000 < Re_{O_2} < 3200$) regimen (see appendix B.1, in order to obtain equivalence ratio from 1.7 to 0.8. The oxidiser-fuel momentum ratio increases for this case while the

Cette thèse est accessible à l'adresse : http://theses.insa-lyon.fr/publication/2022LYSEI044/these.pdf
© [K. Utria Salas], [2022], INSA Lyon, tous droits réservés

equivalence ratio decreases.

Case 3

In order to analyse the most significant parameter on the studied features, case 3 compared the variation on Re_{O_2} and Re_{H_2} at constant global equivalence ratios, three representative flame structure shape were chose to effectuate the evaluation.

	U_{0,H_2} [m/s]	U_{0,O_2} [m/s]	ϕ	Re_{H_2}	Re_{O_2}	G_f [kg m/s]	G_O[kg m/s]	G_O/G_f
Case 1. Influence of fuel momentum, Re_{O_2} constant								
1	1.43	4.09	0.8	66	1500	1.5	21.5	14.5
2	1.60	4.09	0.9	74	1500	1.9	21.5	11.5
3	1.78	4.09	1.0	82	1500	2.3	21.5	9.3
4	1.96	4.09	1.1	91	1500	2.8	21.5	7.7
5	2.14	4.09	1.2	99	1500	3.3	21.5	6.4
6	2.32	4.09	1.3	107	1500	3.9	21.5	5.5
7	2.50	4.09	1.4	115	1500	4.5	21.5	4.7
8	2.67	4.09	1.5	123	1500	5.2	21.5	4.1
9	2.85	4.09	1.6	132	1500	5.9	21.5	3.6
10	3.03	4.09	1.7	140	1500	6.7	21.5	3.2
Case 2. Influence of oxidiser momentum, Re_{H_2} constant								
1	3.03	8.70	0.80	140	3188	6.7	97.1	14.5
2	3.03	7.73	0.90	140	2833	6.7	76.7	11.5
3	3.03	6.96	1.00	140	2550	6.7	62.2	9.3
4	3.03	6.33	1.10	140	2318	6.7	51.4	7.7
5	3.03	5.80	1.20	140	2125	6.7	43.2	6.4
6	3.03	5.35	1.30	140	1962	6.7	36.8	5.5
7	3.03	4.97	1.40	140	1821	6.7	31.7	4.7
8	3.03	4.64	1.50	140	1700	6.7	27.6	4.1
9	3.03	4.35	1.60	140	1594	6.7	24.3	3.6
10	3.03	4.09	1.70	140	1500	6.7	21.5	3.2
Case 3. Influence of momentum ratio								
1	1.43	4.09	0.8	66	1500	1.5	21.5	14.5
2	2.38	6.82	0.8	110	2500	4.1	59.7	14.5
3	2.14	4.09	1.2	99	1500	3.3	21.5	6.4
4	3.57	6.82	1.2	165	2500	9.3	59.7	6.4
5	2.67	4.09	1.5	123	1500	5.2	21.5	4.1
6	4.46	6.82	1.5	206	2500	14.5	59.7	4.1

Table 4.2: Operating conditions

Cette thèse est accessible à l'adresse : http://theses.insa-lyon.fr/publication/2022LYSEI044/these.pdf
© [K. Utria Salas], [2022], INSA Lyon, tous droits réservés

4.3.1 Structure flame characteristics

In order to describe the flame characteristics four thresholds of the OH* emission images were determined based on the image histogram (see figure 4.14). Threshold 1 is the outer layer of the flame which will be useful to describe flow aerodynamic development (in subsection 6.2.2.3, page 152), threshold 2, 3 and 4 are used to determine flame structure characteristics in section 4.3.1.

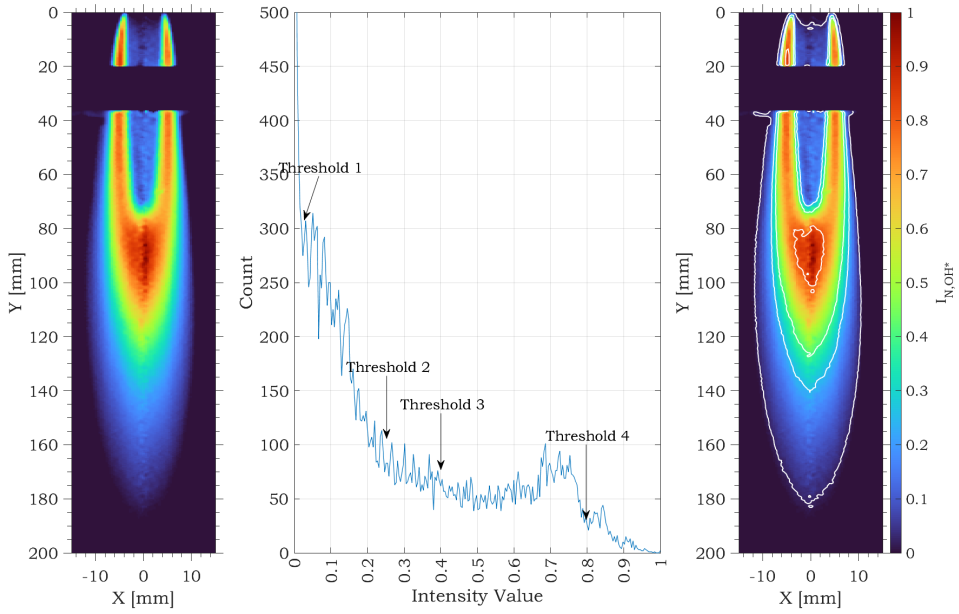

Figure 4.14: Threshold settings

Figure 4.15 defines the analysed characteristics of the structure flame. This research defined four heights to characterise the flame:

- y_f: the distance between the nozzle outlet and the OH* maximum emission intensity. These heights indicate where the maximum emission in the central reaction zone is located and where the stoichiometric oxygen to fuel mass ratio region begins (Kim et al., 2019).

- y_d: Length between the nozzle outlet and the maximum OH* emission intensity on the sides. This parameter was calculated at x=-5mm, at which the flame side front is found. The study has considered the flame symmetrical; hence, the results reported are for the left side of the flame and assumed to be the same for the right side. The maximum intensity threshold was defined as 90% of the maximum intensity of each flame (Kim et al., 2019).

- y_T: total length of the flame calculated at a threshold of 20% of the maximum OH* intensity. As its name indicates, this parameter is an indicator of the total extension

Cette thèse est accessible à l'adresse : http://theses.insa-lyon.fr/publication/2022LYSEI044/these.pdf
© [K. Utria Salas], [2022], INSA Lyon, tous droits réservés

of the visible flame (Sze et al., 2004, 2006).

- y_j: Length between the nozzle outlet and the closing point of the reaction zone, which determines the end of the diffusion mode upstream and the appearance of the reaction zone in the centre of the flame, a threshold of 40% was used to define this parameter (Sze et al., 2004, 2006).

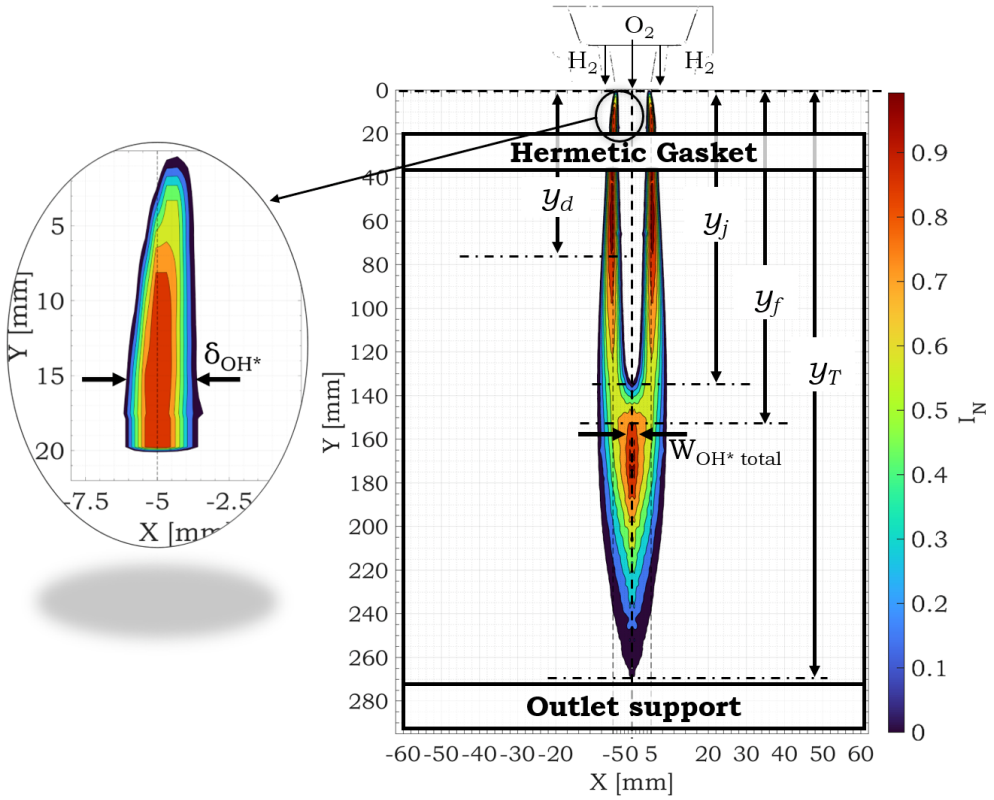

Figure 4.15: Structure flame characteristics

Furthermore, 25% of the flame maximum emission intensity was chosen as a threshold to calculate the flame thickness. δ_{OH^*} corresponds to pure diffusion mode (Kim et al., 2019). This parameter is linked to the quantity of fuel burning in diffusion mode until y_j (upstream). Downstream, from y_j, the flame thickness denotes half of the flame total width. As mentioned, δ_{OH^*} is shown for the left side and assumed to be the same for the right side. Simultaneously, at 80% of the OH* flame maximum intensity, $W_{OH^*,max}$ is defined. This term is indicative of the quantity of fuel burning in the central reaction zone and the extension of the stoichiometric oxygen to fuel mass ratio region.

The next chapter analyses the characteristics of H_2/O_2 inverse diffusion flames taking into count the methodology described in this section.

Cette thèse est accessible à l'adresse : http://theses.insa-lyon.fr/publication/2022LYSEI044/these.pdf
© [K. Utria Salas], [2022], INSA Lyon, tous droits réservés

Chapter 5 | Characteristics of inverse diffusion flames

This chapter analyses the flame structure characteristics and OH^* emission distribution under different Reynolds numbers and equivalence ratios [1]. The first section describes the flame structure, following section examines the influence of the peripheral jets on flame structure (parameters as flame length and thickness are studied, described in figure 4.15) and OH^* emission distribution, later on the influence of the central jet and finally the impact of the two parameters are compared to asses their impacts on the flame structure.

5.1 Flame structure and topology

The analysis of the flame structure and topology is based on the study of the OH^* radicals and direct light emissions from the reactive zone. For the present test conditions, only stabilised slightly lifted flames located close to the O_2 injector are observed, as show in figure 5.1.

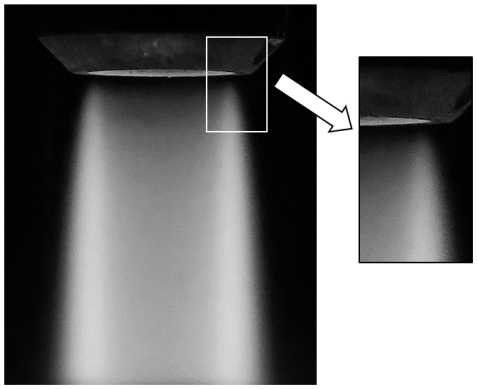

Figure 5.1: Flame stabilisation mechanism, direct visualisation of the flame

According to Kim et al. (2007), this small lift is mainly due to the correct mixing rates achieved by the injection conditions of this study owing the thickness of the O_2 lip injector, this is corroborated with the analysis of flame structure characteristics and aerodynamic behaviour development.

During this study three types of inverse diffusion flame were identified by means of OH^* chemiluminescence maps: type I, type II, and type III, shown in figure 5.2. Ensuing the characteristics of each flame structure are described.

[1] This chapter is based on the results published in Utria et al. (2022)

Cette thèse est accessible à l'adresse : http://theses.insa-lyon.fr/publication/2022LYSEI044/these.pdf
© [K. Utria Salas], [2022], INSA Lyon, tous droits réservés

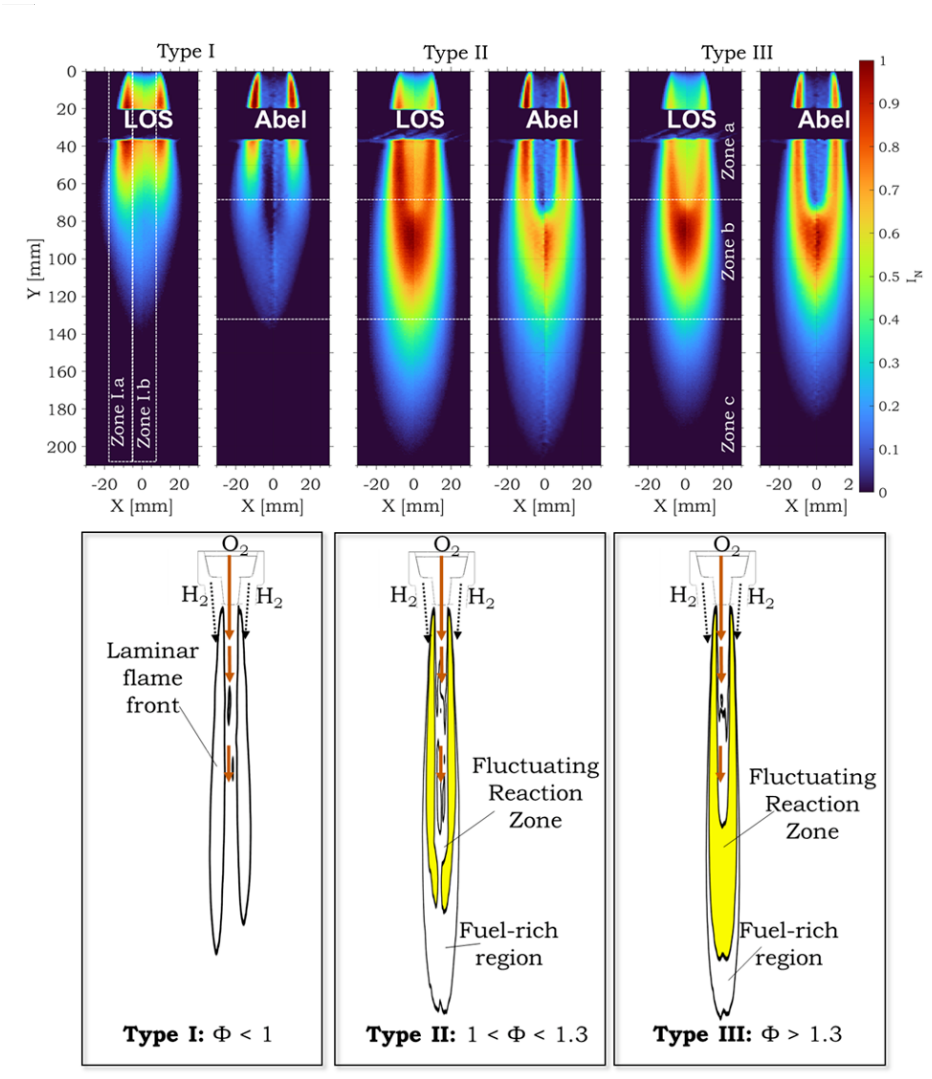

Figure 5.2: OH* Chemiluminescence, I_{N,OH^*} and type of flames found

Type I: For $\phi < 1.0$

Type I is observed at the lowest equivalence ratios. This type of flame exhibits an over-ventilated NDF shape (Glassman and Glumac, 2015). In figure 5.4up, a hollow dark blue structure is observed upstream at the centre of the flame. This effect is created by the O_2 jet. This result indicates that the H_2 is all consumed on the sides, where a pale blue flame is observed. This blue zone indicates the reaction among OH* and H* radicals to produce H_2O, since this study use O_2 pure (Kim et al., 2018; Schefer et al., 2009). The flame tips have an orange-yellow colour. They seem to disappear at lower ϕ, indicating fuel-lean conditions Schefer et al. (2009), hence lower gas temperatures. As mentioned before, the yellow on the flame suggests impurities in the air that surrounds the flame (Gaydon, 1942). This yellow colour can also be observed due to the radiation emitted by the material of the hermetic gasket when the flame passes through. The flame shape implies that the O_2 jet mainly coflows with the H_2 jets. Some of the fuel is entrained into the O_2 jet. As a consequence, the H_2 is burning in pure diffusion mode. As illustrated in

Cette thèse est accessible à l'adresse : http://theses.insa-lyon.fr/publication/2022LYSEI044/these.pdf
© [K. Utria Salas], [2022], INSA Lyon, tous droits réservés

figure 5.2, the OH* chemiluminescence images enable us to draw two zones for this flame type, "zone I.a" and "zone I.b". The former corresponds to the reaction zone located on the sides, which indicates the diffusion mode. The zone I.b represents the O_2 jet; this is the hollow at the centre. The OH* intensities are very low downstream within this zone. Additionally, a laminar flow is observed for this type of flame with a $Re_{H_2} < 100$.

Type II: For $1.0 < \phi < 1.3$

At or close to stoichiometric conditions, the hollow flame structure begins to disappear downstream. A visible pale blue reaction zone at the centre of the flame is formed. This phenomenon is related to reaction of OH* and H* radical species. These findings suggest that the ratio G_O/G_f is small enough to entrain some fuel jets to close the flame on the bottom. As can be seen in figure 5.2, for type II, pure diffusion is predominant on the sides upstream as in type I, and shown as "zone a". On the other hand, the "zone b" in figure 5.2 represents the central reaction zone. This zone is formed due to the excess of H_2, after the upstream diffusion mode. Some fuel jets find the jet of O_2 to react and create a central reaction zone. This effect occurs because the momentum of H_2 is higher as compared to that of leans conditions. The central reaction zone encloses the expansion of O_2 jet. This reaction zone has a predominant diffusion mode, but also some zones in premixed mode. These two zones are present when the oxidiser jet velocity is high enough that it entrains the outer fuel jets inward, mixing to form a partially premixed flame that enlarges the reaction zone (Sobiesiak and Wenzell, 2005; Zhang et al., 2010).

Downstream, the flame tips determine the beginning of "zone c" (see figure 5.2). Within this zone, the fuel-rich region, the excess of fuel is burning in normal diffusion mode with the surrounding air. On the other hand, flames tips are brighter and show a darker red, related to the high vibration of the excited H_2O and the cooling from H_2. The colour also indicates higher temperatures to that of leaner conditions (Schefer et al., 2009).

Type III: For $\phi > 1.3$

Figure 5.2 shows that the central reaction has stronger OH* intensities at higher fuel flow rates. As a consequence, the flame closing is stronger ("zone b"). The result is a brighter sheet shape that encloses the jet of O_2. A possible explanation for this might be that the difference between the two jet momentums is significant enough to entrain some fuel into the central O_2 jet. In "zone b", the increase in the H_2 momentum creates a larger reaction zone at the centre of the flame; because more fuel is mixing with the central O_2 jet and burning in the premixed mode. The excess of fuel is also present in "zone c" and reacts with the external air.

Cette thèse est accessible à l'adresse : http://theses.insa-lyon.fr/publication/2022LYSEI044/these.pdf
© [K. Utria Salas], [2022], INSA Lyon, tous droits réservés

The main difference between type II and type III is that whereas for type II the highest intensities of OH radicals are on the side reaction zone; for type III, these intensities are found in the central reaction.*

The evolution of the flame shape according to ϕ and Re is resumed in figure 5.3. Different fixed Re_{H_2} changing Re_{O_2}, and vice-versa were used to illustrate the flame typologies. As observed, low Re_{H_2} with high Re_{O_2} will show the type I topology. The Re_{H_2} range to obtain type II topology is dependent on Re_{O_2} values. The higher it is, the range will increase. Flames will present type III topology for higher Re_{H_2} and Re_{O_2}.

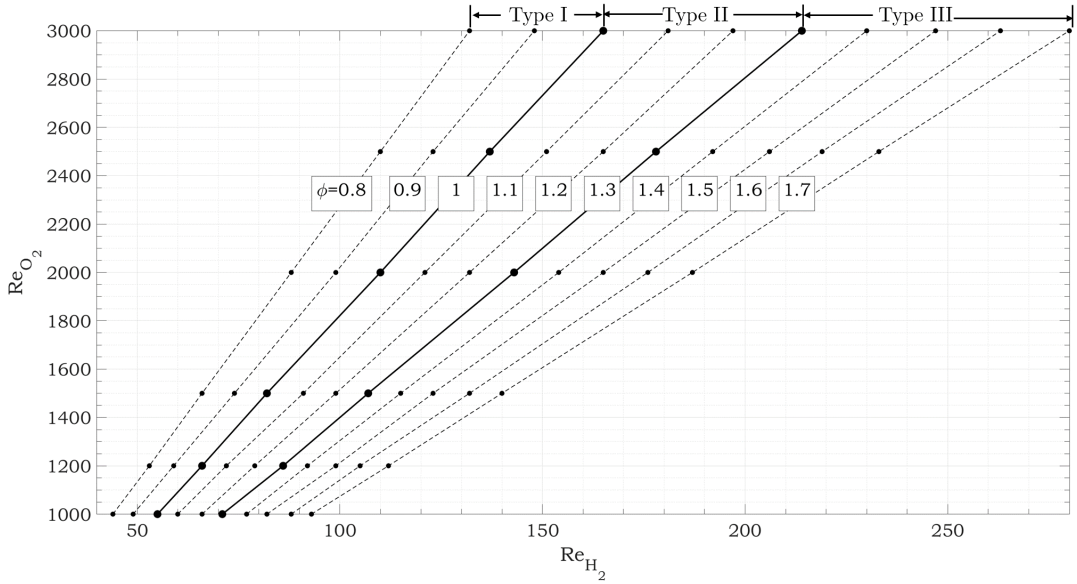

Figure 5.3: Mapping of flame types according to their morphology and topology

Following sections study the influence of fuel and oxidiser momentums on flame appearance, topology and OH* emission distribution to better understand the thermal conditions in the crystal growth environment.

Cette thèse est accessible à l'adresse : http://theses.insa-lyon.fr/publication/2022LYSEI044/these.pdf
© [K. Utria Salas], [2022], INSA Lyon, tous droits réservés

5.2 Influence of the fuel jet momentum

At fixed Reynolds number of oxygen, the fuel flow rate and the fuel jet Reynolds are increased. Consequently, the jet momentum and thus the overall equivalence ratio and momentum ratio oxidiser to fuel are also augmented. Figure 5.4 shows the influence of H_2 momentum on flame appearance and OH* emissions. Upstream the flames are always divided into two structures and characterised by an intense blue, representing the reaction of OH* and H* radicals. The brightness of the flames increases as G_f increases. The central pale blue region also seems to be brighter. This effect could be explained by observing the OH* image (figure 5.4 down), in which the OH* radical intensities increase with ϕ.

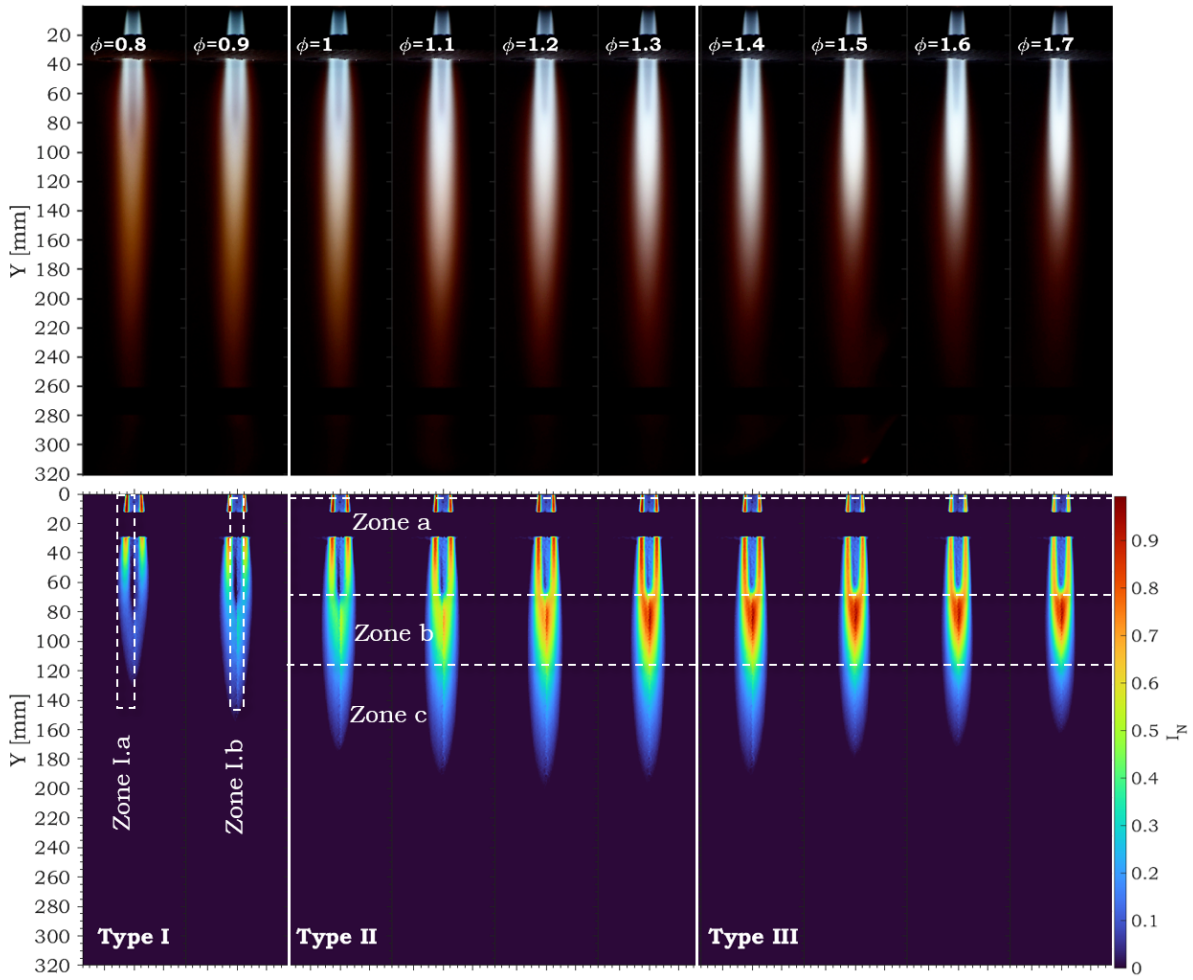

Figure 5.4: Case 1. Evolution of the flames at constant G_O, $Re_{O_2} = 1500$. Up: Instant images of Direct Visualisation. Down: Abel OH* Chemiluminescence

The shape evolution and appearance of the flames was according to figures 5.2 and 5.3, and described in figure 5.4. As mentioned before, depending on flame shape type, the flame splits into different zones, with the OH* chemiluminescence, the three types of flames,

Cette thèse est accessible à l'adresse : http://theses.insa-lyon.fr/publication/2022LYSEI044/these.pdf
© [K. Utria Salas], [2022], INSA Lyon, tous droits réservés

and the zones appear clearly (figure 5.2 down). The distribution of the OH* emissions along Y-axis is analysed in figure 5.5. These curves represent the OH* emission intensities on the central reaction zone (X=0) and on the side reaction zone (X=-5mm), which represents the diffusion mode on the flame, see figure 4.15), respectively. The different kind of flames and zones found by this study are described in the following:

Type I : For $\phi < 1.0$

- Zone I.a: This region is the pure diffusion mode of the flame and shows a laminar flow structure(Re_{H_2} and Re_{O_2} lower than 2000). The strongest OH* emission intensities are found on the sides, comparing the intensities in figure 5.5, which is the blue colour observed in figure 5.4 (up). The diffusion zone extends with the increase of G_f, as observed in figure 5.6 and represented by y_d. This is higher with the increase of ϕ, more fuel is entrained and reacting with the O_2 jet.
- Zone I.b: The lowest intensity of OH* emissions are found in this zone (figure 5.5). They are lower than 25% of the maximum intensity. For these flames, the O_2 central jet coflows with the H_2. They begin to be sharper downstream with the increase of H_2 momentum. Consequently, the entrained H_2 enhancement by the O_2 jet leads to a slightly bigger reaction zone.

The unused O_2 and the air surrounding the flame react with the end of the fuel jets, which is the orange colour in figure 5.4 at 50mm. It can be observed, at $\phi < 1$, the central reaction zone is almost absent for type I, figure 5.5. Then, the OH* emissions decrease rapidly after the upstream diffusion front at X=-5mm (figure 5.5).

Type II and III:

Type II: For $1.0 < \phi < 1.3$

Type III: $\phi > 1.3$

For $\phi > 1$, flames report a blue more intense (figure 5.4 up), which denotes an increase in the production of OH*. This increase is illustrated in figure 5.5. Following the zones obtained for this type of flame through OH* chemiluminescence are describe:

- Zone a: This zone is in diffusion mode. High OH* intensities are observed and divided into two parts (left and right) as in type I. The increase of G_f, generates

Cette thèse est accessible à l'adresse : http://theses.insa-lyon.fr/publication/2022LYSEI044/these.pdf
© [K. Utria Salas], [2022], INSA Lyon, tous droits réservés

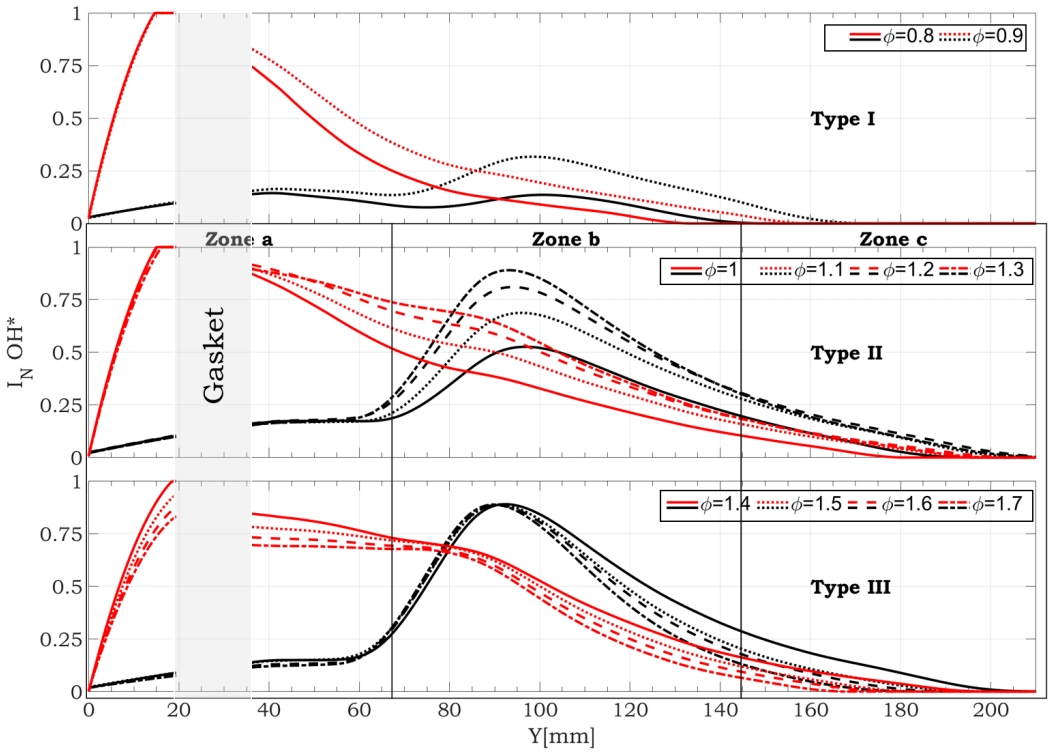

Figure 5.5: Case 1 $Re_{O_2} = 1500$: OH* Emissions along Y-axis at X=0 (black) and X=-5mm (red)

an increase in the fuel reacting with the O_2 jet as observed in figure 5.5 at X=-5mm. The decrease on G_O/G_f by increasing H_2 decreases the reaction "zone a", represented in figure 5.6 by y_j. This change also affects the intensities within this zone. For type II, these increases with ϕ. When the flame is at type III range, the intensities decrease continuously.

- Zone b: The location of this zone is defined by y_j. This height determines the flame closing and the apparition of the central reaction zone. This phenomenon occurs because of the increase in H_2 momentum. The entrainment of the H_2 jets with O_2 jet is stronger for this type, and more fuel is burning. Consequently, the diffusion zone extends to find the central reaction zone downstream. This extension could also be explained as a result of the high diffusivity of the H_2.

In figures 5.4 (down) and 5.5, Abel OH* chemiluminescence results show that the diffusion fronts (stoichiometric zone) in the centre extend for $\phi > 1.0$, meaning the mixing in the centre is stronger between O_2 and H_2 jets finding its optimal at $\phi = 1.4$. $\phi > 1.3$, flames type III, show stronger emissions intensities on the central reaction zone. However, the OH* intensities decrease on the sides (figure 5.5, X=-5mm), which implies that more fuel is burned at the centre of the reaction zone downstream (figure 5.5, X=0). The increase in the intensities of OH* denotes

Cette thèse est accessible à l'adresse : http://theses.insa-lyon.fr/publication/2022LYSEI044/these.pdf
© [K. Utria Salas], [2022], INSA Lyon, tous droits réservés

a stronger mixing of fuel-oxidiser. These intensities also indicate that the G_O is too low to burn all the H_2 in diffusion mode on the sides. In this case, the excess reacts with the end of O_2 jet and forms the central reaction zone.

- Zone c: This zone is formed due to the fuel-rich conditions, and it is the excess of H_2 that reacts in diffusion mode with the ambient air inside the confinement. For type II,"zone c" gets larger with the increase of H_2. The entrainment upstream diminishes due to the decrease in G_O/G_f, and the G_f is low enough to entrain the ambient air that surrounds the external layer of the flame. In contrast, for type III flames the size of this zone decreases with the increase of G_f. This result indicates that the G_f is elevated and decreases the entrainment of the ambient air and the production of OH* radicals. For these flames the fuel is burning principally in "zone a" and "zone b". It can thus be suggested that the G_O/G_f ratios for $1 \leq \phi \leq 1.4$ are good enough to enhance the mixing and burning of the fuel upstream, decreasing the unburned H_2 in "zone c". The red observed within this zone is darker with the increase of Re_{H_2} and covers up all the downer pale blue zone. The increase of the red flame brightness is an indicator of more fuel burning in the flame due to the H_2 momentum increase (Schefer et al., 2009). The darker red colour at $\phi > 1$ indicates that the vibration-rotation spectrum of H_2O is stronger, thus higher temperatures on the flame tail Gaydon (1942). The visible red zone starts to be smaller at $\phi = 1.5$, due to the increase of H_2O production.

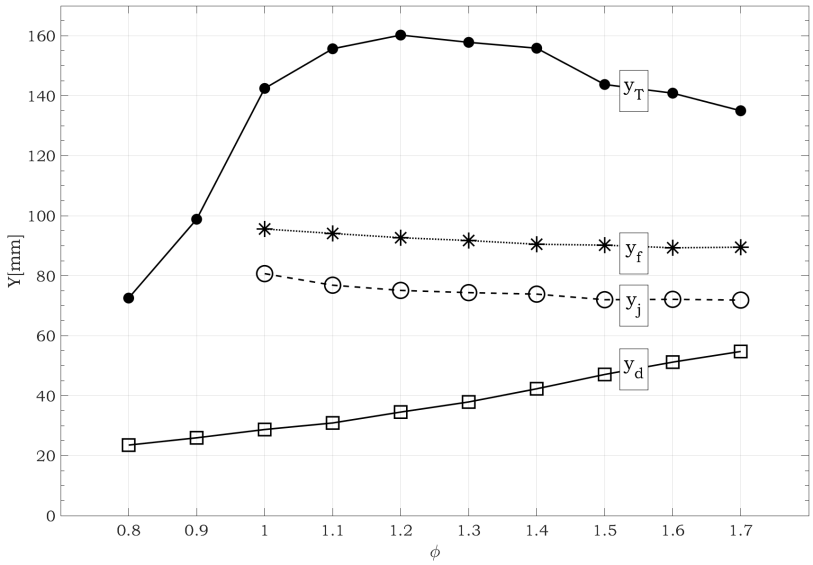

Figure 5.6: Case 1 $Re_{O_2} = 1500$: Flame heights (y_d, y_j, y_f ,y_T defined in section 4.3.1)

Figure 5.6 shows that for type II, y_j is decreasing with the increase of H_2 momentum. The maximum value of y_j is observed at $\phi = 1.0$. The highest OH* intensities are found on

Cette thèse est accessible à l'adresse : http://theses.insa-lyon.fr/publication/2022LYSEI044/these.pdf
© [K. Utria Salas], [2022], INSA Lyon, tous droits réservés

flame sides for these flames, which is in pure diffusion mode (figure 5.5, X=-5mm). These intensities are stronger when G_O/G_f is lower. Furthermore, the decrease of y_j reduces as the flame approaches to type III shape, the central reaction zone has stronger intensities. It can thus be suggested that mixing within this zone is stronger. Once $\phi > 1.3$, there is not significant change in y_j associated with the increase of H_2 momentum with constant G_O. Conversely, the maximum intensity length of the upstream diffusion mode, y_d (figure 5.6), increases with ϕ. Therefore, it can be assumed that H_2 momentum in "zone a" determines the diffusion mode's intensity and length of the stoichiometric zone. Furthermore y_f (location of maximum emissions of OH*) maintained constant in the range of ϕ studied.

The visible reaction zone of the flame is analysed with the total flame length, y_T (see figure 5.6). The maximum value is reached at $\phi = 1.2$. It can be seen that with an increase in G_f, the entrainment of O_2 jet becomes stronger on the sides at $\phi < 1.2$, leading to more fuel to be burned in pure diffusion mode, hence longer flames. At $\phi > 1.2$ shorter flames indicates more H_2 flows to the central O_2 jet to create a stronger central reaction zone (figure 5.5). Moreover, the total reaction zone seems smaller for $\phi > 1.4$ with constant O_2 momentum. Long flame lengths are defined by the laminar-flame behaviour and reduced residence time for mixing H_2 and O_2 jets. Increasing Re_{H_2} enhances the mixing (Choi et al., 2017); thus, y_T gets smaller due to the stronger burning in "zone a" and "zone b". In figure 5.4, this result is confirmed; the highest intensities extend almost all over the "zone a" and " zone b".

In order to study the maximum emission zone, the reaction zone width, $W_{OH^*,max}$ is analysed in figure 5.7. As it can be seen, $W_{OH^*,max}$ has two zones, "zone a": pure diffusion, and has the same value upstream for $\phi < 1.4$. It decreases at the confinement inlet. Wider flames are found with the G_f increase. The maximum is found at $\phi > 1.2$. $W_{OH^*,max}$ is zero for higher ϕ, which suggests that the heat released within this zone is low compared to that of the centre.

In "zone b", $W_{OH^*,max}$ is not impacted significantly by Re_{H_2} increase. The lowest equivalence ratios ($\phi < 1$) do not present this zone. The maximum is found at $\phi = 1.5$. This suggests that the stoichiometric zone is wider; however, for $\phi > 1.4$ its extension do not show significant increment with ϕ.

Contrarily to y_T, the flame thickness, δ_{OH^*} (which represents the diffusion mode) analysed in 5.7, showed not to be significantly influenced by G_f, on the upstream zone ($y < y_j$). No difference greater than 0.5 mm is observed for the maximum δ_{OH^*}. However, downstream it can be seen that the maximum thickness extends with ϕ for type II flames. Contrarily,

Cette thèse est accessible à l'adresse : http://theses.insa-lyon.fr/publication/2022LYSEI044/these.pdf
© [K. Utria Salas], [2022], INSA Lyon, tous droits réservés

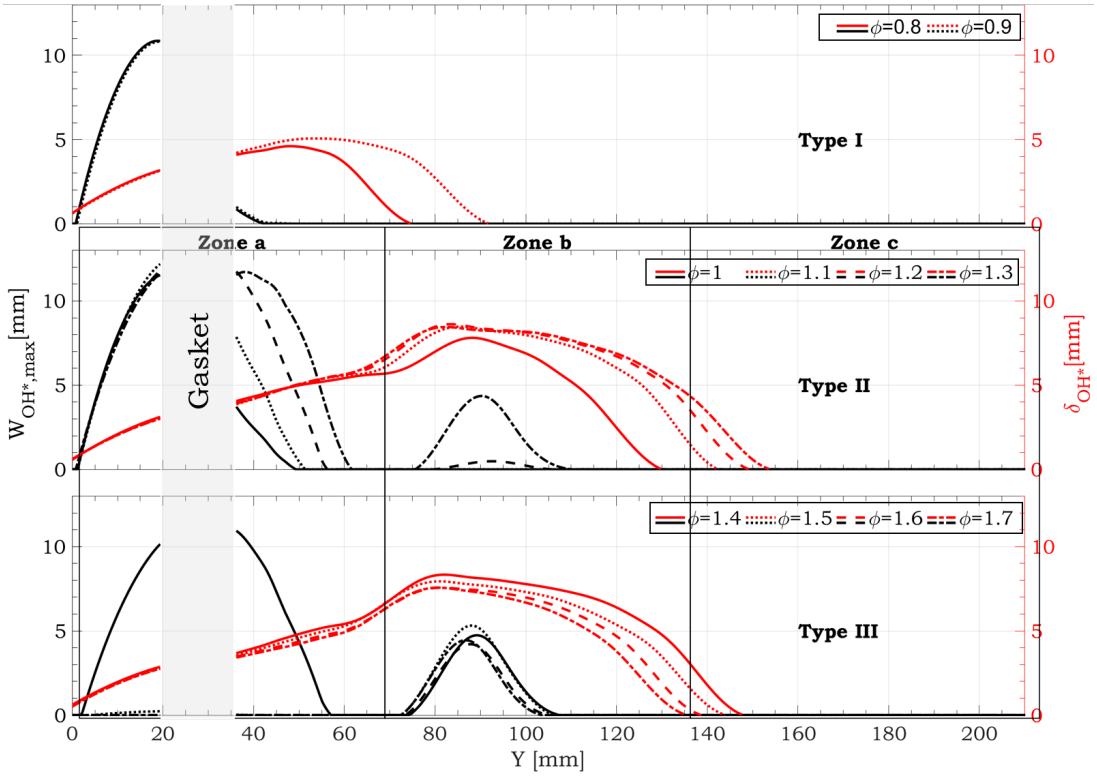

Figure 5.7: Case 1 $Re_{O_2} = 1500$: Flame Width, $W_{OH^*,max}$(black) and thickness δ_{OH^*}(red)

for type III the extension reduces with ϕ.

To conclude, at constant Re_{O_2}, H_2 momentum (G_f) affects the OH intensities for $\phi < 1.4$. Its modification also changed the side diffusion mode maximum intensities and their length (y_d). Moreover, the extension of the maximum intensities in the central reaction zone also shows dependency (W_{OH^*}). By contrast, the maximum intensity locations within this region do not show to be affected by G_f. y_f seems to be mainly impacted by the central jet (O_2) momentum, as well as the position of the flame closure (y_j). No significant changes are observed with the increase of G_f. Contrarily, the total flame length changed with the increase of G_f finding its maximum at $\phi = 1.2$. From these results, it is possible to hypothesise that the O_2 momentum defines the location of the maximum heat release rate, analysed in the next section.*

Cette thèse est accessible à l'adresse : http://theses.insa-lyon.fr/publication/2022LYSEI044/these.pdf
© [K. Utria Salas], [2022], INSA Lyon, tous droits réservés

5.3 Influence of the oxidiser jet momentum

The fuel Reynolds number is now fixed, and the oxidiser fuel flow is changed to study the oxidiser jet momentum influence. An increase in the oxygen flow rate decreases the overall equivalence ratio but increases the ratio of oxygen jet momentum to hydrogen jet momentum. Figure 5.8 (up) shows that the colour of the flames changes from blue and red to blue and red/yellow, indicating a change from fuel-rich to fuel-lean conditions. At higher Re_{O_2}, the lower overall ϕ would be, hence the G_O/G_f increases. As mentioned before, the blue continuum is related to the reaction of the species OH^* and H^*. A more significant blue zone means more fuel burning (under fuel-rich conditions). For type III flames, the blue and the red zones increase with Re_{O_2}. Therefore, the total flame length is longer when G_O is higher. For type II, the extensions of both the blue and the red zone seem to be constant.

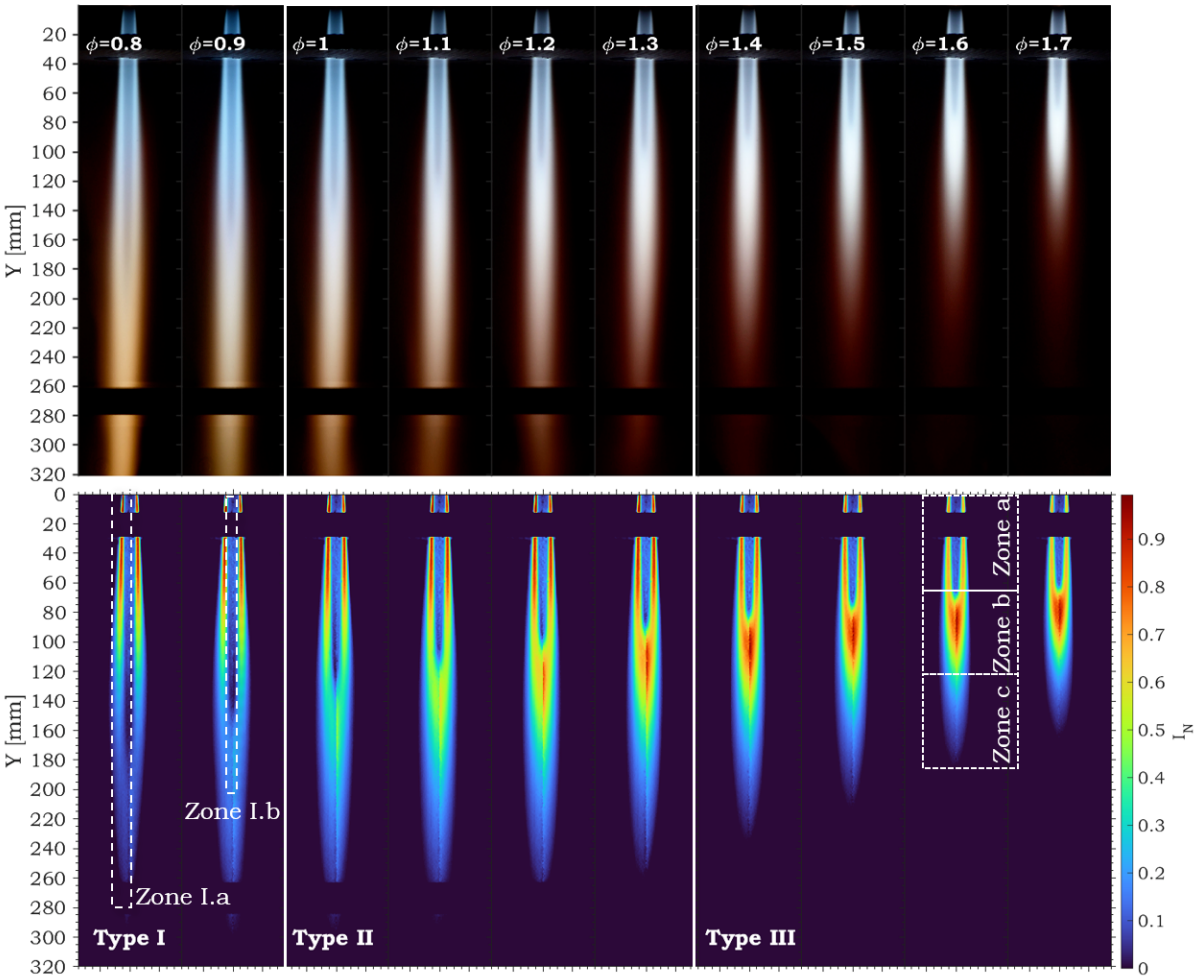

Figure 5.8: Case 2 Evolution of the flames at constant G_f, $Re_{H_2} = 140$. Up: Instant images of Direct Visualisation. Down: Abel OH^* Chemiluminescence

As observed in case 1, the flame has the same evolution according to ϕ, finding type I for

Cette thèse est accessible à l'adresse : http://theses.insa-lyon.fr/publication/2022LYSEI044/these.pdf
© [K. Utria Salas], [2022], INSA Lyon, tous droits réservés

the lowest equivalence ratios ($\phi < 1$), type II at the range $1 < \phi < 1.3$, and type III for $\phi > 1.3$. In figure 5.8 (down), the three zones in the flame can be identified for type II and type III:

- Zone a: We can observe that the highest OH* emission zone in the diffusion mode, which is determined by y_d, does not change significantly for types I and II. This implies that the length of this zone is determined by H_2 momentum. However, for type III flames, this zone increases with ϕ. These results suggest that the H_2 defines the extension of the stoichiometric zone in the diffusion mode upstream.

- Zone b: The location of this zone moves with the oxygen momentum. Higher G_O increases the amount of fuel burning in diffusion mode on the sides. More fuel is entrained by the O_2 jet to burn in this mode, generating longer flames. Consequently, the central reaction zone is located farther from the nozzle, and the intensities diminish.

- Zone c: As in case I, this zone decreases at fuel-rich conditions, the value of G_O/G_f is adequate to enhance the burning of the fuel in "zone a" and "zone b". This enhancement also means that the premixed mode zone in the central reaction zone enlarges.

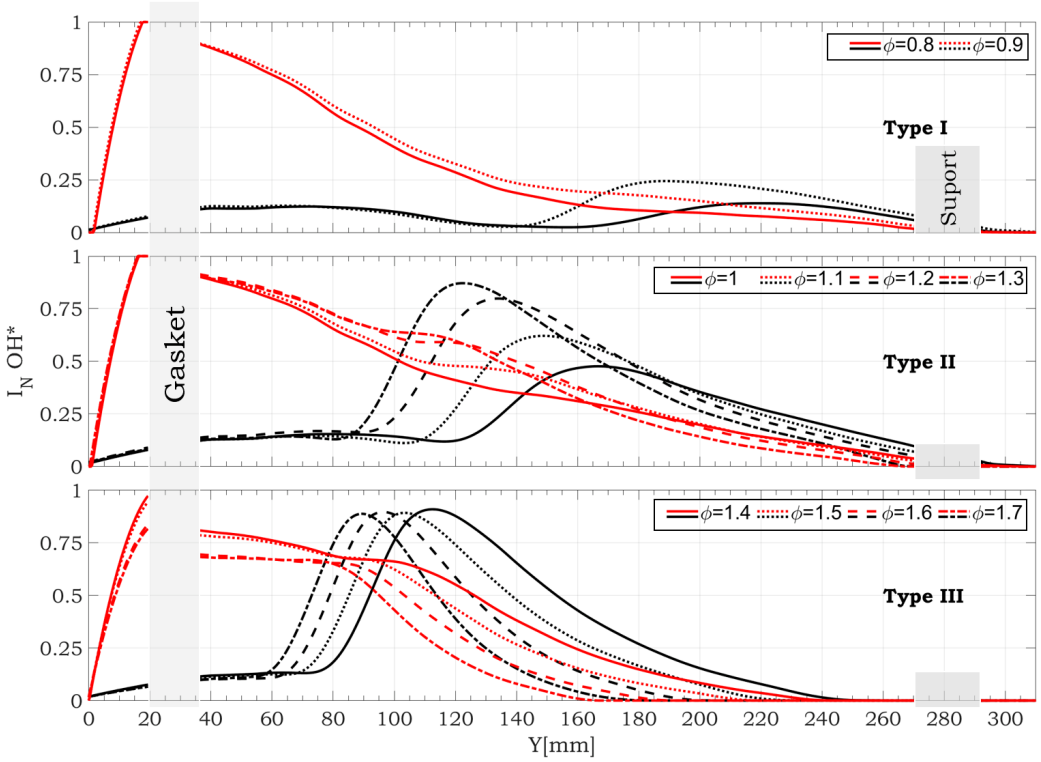

Figure 5.9: Case 2 $Re_{H_2} = 140$: OH* Emissions along Y-axis at X=0 (black) and X=-5mm (red)

Cette thèse est accessible à l'adresse : http://theses.insa-lyon.fr/publication/2022LYSEI044/these.pdf
© [K. Utria Salas], [2022], INSA Lyon, tous droits réservés

For this case, the distribution, the location, and the intensity of the maximum are changing, which means that they depend on the G_O momentum (figure 5.9). Lower momentum oxidiser to fuel increases the mixing between H_2 and O_2 in the central reaction zone, hence the production of OH*. The maximum is found at $\phi = 1.4$, as in case 1. For higher ϕ, the intensity level does not change at all. This result indicates that this G_O/G_f ratio is an optimal operating point (figure 5.9) in terms of OH* emissions. The high production of OH* emissions is an indicator of elevated heat release rate (Hardalupas and Orain, 2004; He et al., 2019), these can be use to obtain adequate thermal gradients for the production of *Verneuil boules*.

In the other hand, the stronger the O_2 momentum, the stronger the entrainment with the peripheral H_2 jets upstream, then the local premixed mode in the diffusion zone ("zone a") is larger (see figure 5.9 red). The G_O/G_f ratio is high enough to mix and burn all the H_2 within this region.

Consequently, the central maximum of OH* production (the stoichiometric line) is farther from the nozzle outlet. The diffusion mode has more OH* production at lower ϕ and increases with G_O momentum. For $\phi > 1.1$, this increase also expands the central reaction zone and the stoichiometric region until $\phi = 1.4$ (figure 11 black).

Figure 5.9 also shows the same behaviour as in case 1 for type I and type II; the maximum of the emissions are on the sides of the flame. The emissions in the central reaction zone increase with the decrease of G_O. For $\phi < 1.4$, there is not a significant change in the upstream reaction zone. In figure 5.10, this behaviour can also be noticed by observing y_d. The decrease in G_O/G_f by diminishing Re_{O_2} does not significantly impact y_d, as much as it does when changing H_2 momentum in case 1; nonetheless, the OH* emissions increase. In contrast, for $\phi > 1.4$ the emissions increase on the sides with lower G_O, less fuel is burned in the centre of the reaction zone downstream (figure 5.9 in red). As observed in case 1, the G_O is too low to burn all the O_2 with the H_2 in diffusion mode. Therefore, there is more fuel to be burned in the central reaction zone, intensifying the OH* emissions, thus enlarging y_d (figure 5.10).

The evolution of y_j, y_f and y_T with respect to G_O is observed in figure 5.10. The decrease in Re_{O_2} impacts all the heights analysed. As mentioned before, with lower Re_{O_2} less fuel is burned on the sides in diffusion mode (figure 5.9) and entrained by the O_2 jet, as a consequence lower y_T are found. This effect also impacts the other heights that diminish with the decrease in G_O. At $\phi = 1$, y_j, y_f and y_T find their maximum. This behaviour implies that close to the stoichiometric injection conditions, the entrainment of the fuel jets is better, the value of G_o is lower than for the other ϕ conditions.

Cette thèse est accessible à l'adresse : http://theses.insa-lyon.fr/publication/2022LYSEI044/these.pdf
© [K. Utria Salas], [2022], INSA Lyon, tous droits réservés

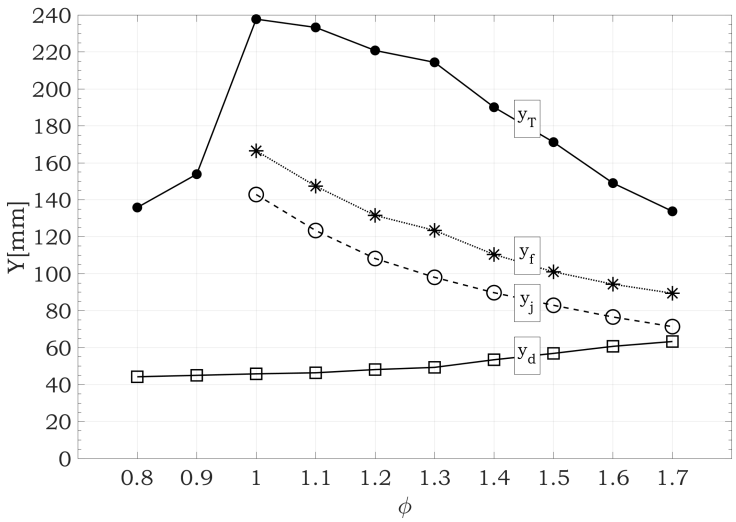

Figure 5.10: Case 2 $Re_{H_2} = 140$: Flame heights (y_d,y_j, y_f ,y_T)

In figure 5.11, the largest maximum reaction zone is found at $\phi = 1.7$, which has the lowest extension (shorter flames). The maximum extension of $W_{OH^*,max}$ region is found at $\phi = 1.4$, which corresponds to the largest reaction zone in the centre (Hardalupas and Orain, 2004). This result could be interpreted as the highest integrated OH* emission, thus high heat release rate. On the other hand, the extension of the diffusion mode decrease by decreasing Re_{O_2}. The maximum, δ_{OH*} is found at $\phi = 1.4$. This parameter enlarges for type III with G_O increase, whereas it decreases for type II.

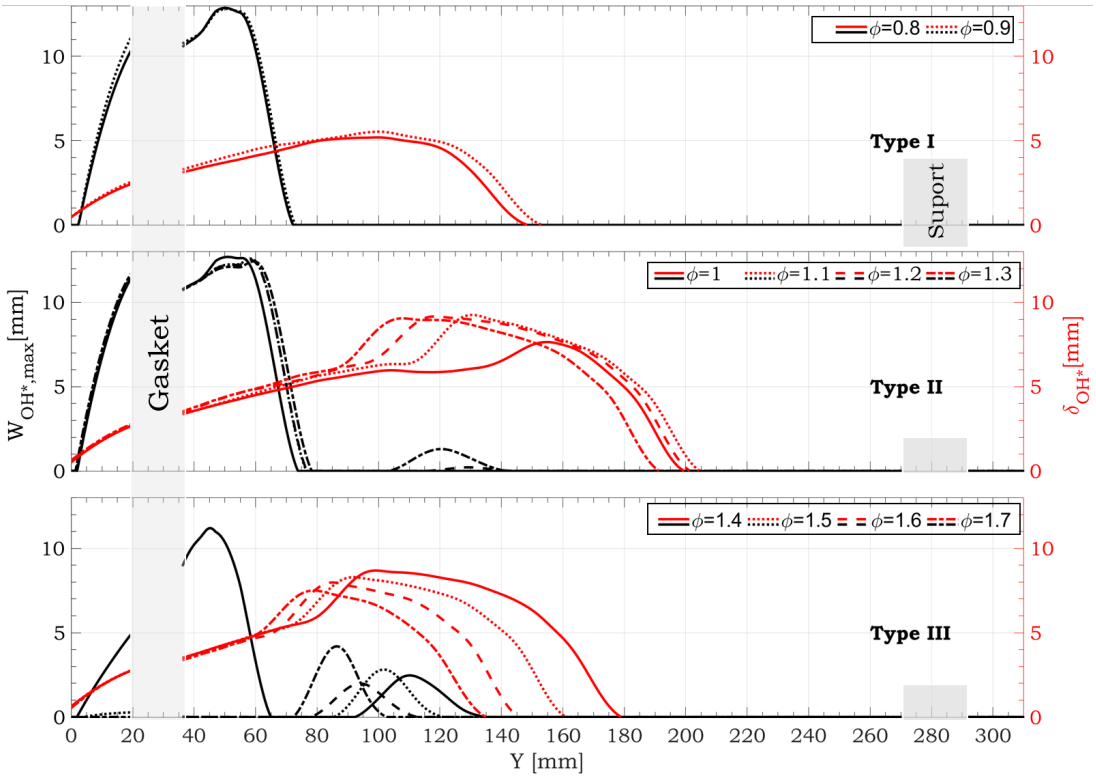

Figure 5.11: Case 2 $Re_{H_2} = 140$ Flame Width, $W_{OH^*,max}$(black) and thickness δ_{OH^*}(red)

Cette thèse est accessible à l'adresse : http://theses.insa-lyon.fr/publication/2022LYSEI044/these.pdf
© [K. Utria Salas], [2022], INSA Lyon, tous droits réservés

As a conclusion of this section: oxidiser momentum defines the size of reaction zones and the location of the stoichiometric zone. Furthermore, it was found that the variation of O_2 Reynolds from laminar to critical regimen affects mainly the flame tips. They start to flicker with the transition from laminar to critical regime. Shu et al. (1997) attributed this phenomenon to the effect of buoyant acceleration of hot gases outside the diffusion outer flame layer, which causes shear-layer rollup, leading to the formation of toroidal vortex rings in this zone.

Cette thèse est accessible à l'adresse : http://theses.insa-lyon.fr/publication/2022LYSEI044/these.pdf
© [K. Utria Salas], [2022], INSA Lyon, tous droits réservés

5.4 Impact of the momentum ratio

At a fixed overall equivalence ratio, the oxidiser to fuel momentum ratio is constant, and vice versa. Following flames at the same global equivalence ratio were analysed. Different Re_{H_2} jets and Re_{O_2} were used to study the momentum ratio effect on flame appearance. Three ϕ were chosen to be analysed; each one represents a flame type. The influence of R_{O2} on flame lengths is observed in figure 5.12. At higher the R_{O2}, longer flames are observed for the same equivalence ratio. The flame shape does not change with the increase in flow rates. The flames reported higher light intensities with the increase of Re (H_2 and O_2) due to the intensified burning and higher temperatures. A yellow flame is always observed at $\phi = 0.8$ at the tip of the flame, when R_{O_2} the tip is more yellow because there is more unused O_2. For type II and III flames brighter and wider central reaction zone is observed. On type III, the red outer layer is firmer, indicating more vibration of the excited H_2O.

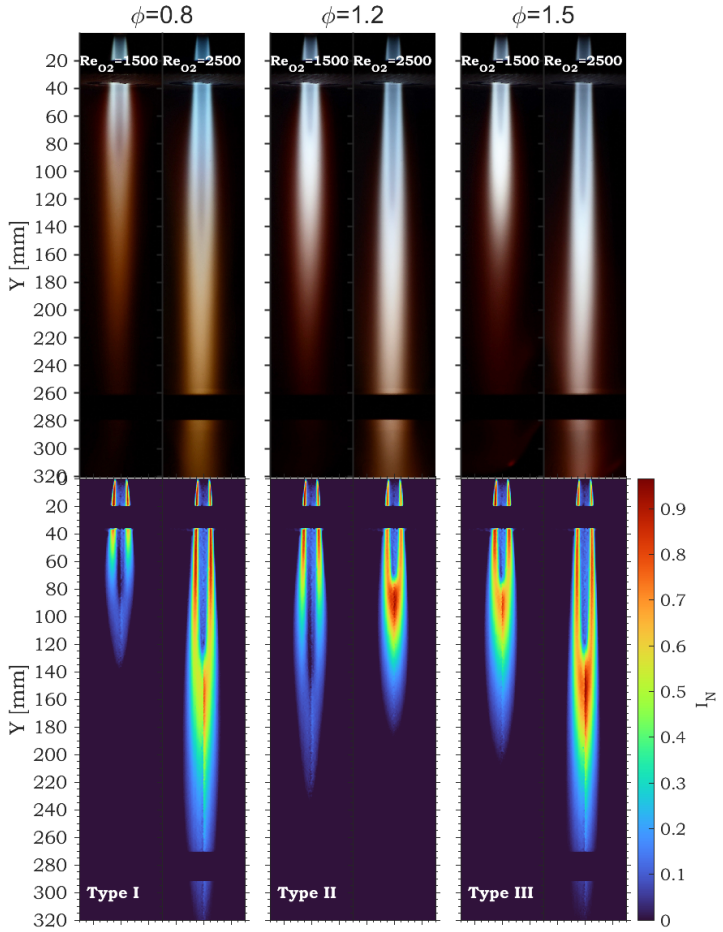

Figure 5.12: Case 3. Constant ϕ varying oxygen momentum and fuel momentum: Up. Images of Direct Visualisation. Down. Abel OH* Chemiluminescence

In figure 5.13, the fuel and oxidiser Reynolds effect with constant momentum ratio is observed. The OH* maximum intensities do not seem to increase with Re. It can therefore

Cette thèse est accessible à l'adresse : http://theses.insa-lyon.fr/publication/2022LYSEI044/these.pdf
© [K. Utria Salas], [2022], INSA Lyon, tous droits réservés

be assumed that the intensities depend on the momentum ratio, hence ϕ. In contrast, it affects maximum intensity location, the extension of the reaction zones and the stoichiometric zones.

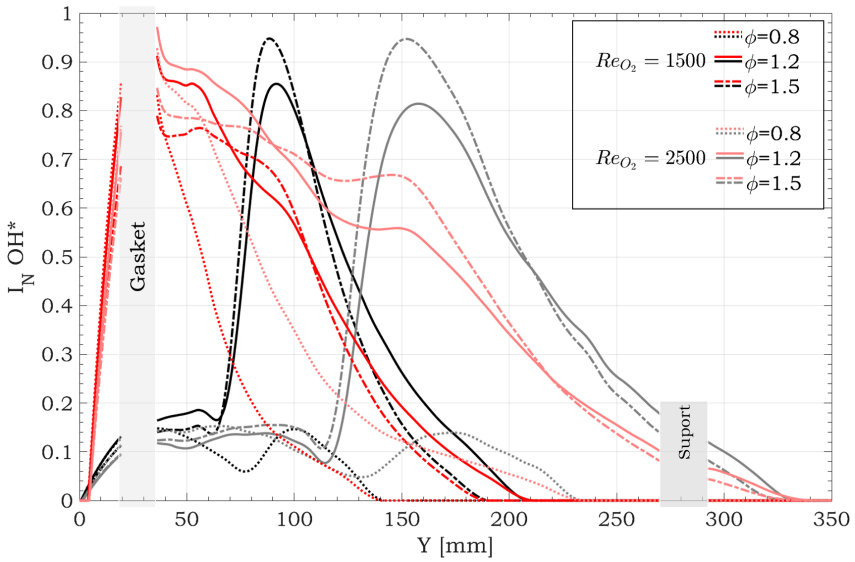

Figure 5.13: Case 3 Constant ϕ varying oxygen momentum and fuel momentum: OH* Emissions along Y-axis at X=0 (black) and X=-5mm (red)

The stronger the momentum of O_2, the better the entrainment with the peripheral H_2 jets in "zone a" enlarging the local premixed zones. Downstream, this effect increases the flame lengths. As a result, the maximum OH* production at the centre is found farther from the nozzle outlet.

The enhanced entrainment due to the increase in fuel and oxidiser momentum, with a constant G_O/G_f ratio, also expands the stoichiometric region at the central reaction zone, enlarging the latter. It was found by Dong et al. (2007) that in the case where Re_{O_2} is lower than 3000 (laminar/transition regime), the flame lengths are highly dependent of this parameter, which is confirmed by this study. In addition, the extension of the side reaction zone seems to be more significantly impacted by Re_{O_2} than the central reaction zone. On the other hand, at $\phi = 1.2$ a decrease in the OH* emission can be observed with the increase on R_{O_2}.

In figure 5.14, the impact of ϕ and Re is analysed on flame heights. Flame length results (y_f) at different Re_{O_2} and Re_{H_2}, suggest that they depend principally on Re_{O_2}. The optimal conditions for the highest heights are found at $\phi = 1.2$. The upstream diffusion mode (y_j) shows to be dependent on Re_{O_2}, this is higher for higher Re_{O_2}. Because y_f depends on y_j, the higher y_j means that the stoichiometric zone is located farther from the outlet nozzle for higher Re_{O_2}.

In figure 5.15, flame width distribution ($W_{OH^*,max}$) is studied. With constant ϕ the

Cette thèse est accessible à l'adresse : http://theses.insa-lyon.fr/publication/2022LYSEI044/these.pdf
© [K. Utria Salas], [2022], INSA Lyon, tous droits réservés

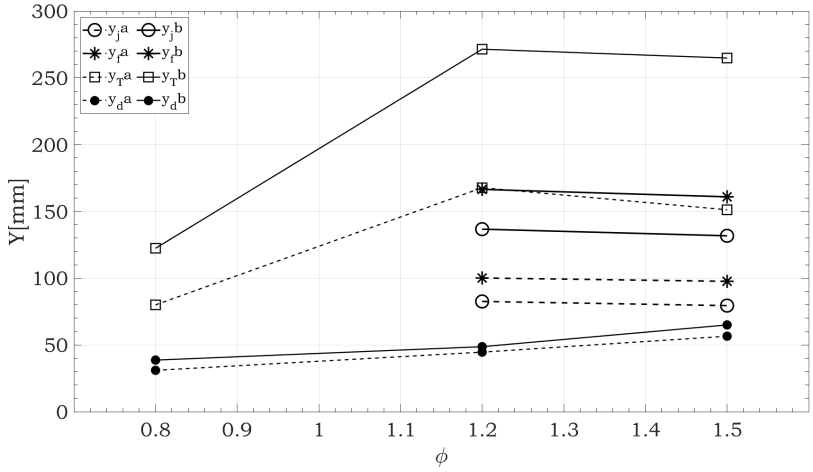

Figure 5.14: Case 3 Constant ϕ, Re_{O_2}: a = 1500, b = 2500. Flame heights (y_j, y_f ,y_T), y_d

increase in Re_{O_2} and R_{H_2} expands the diffusion mode upstream. This result agrees with y_d in figure 5.14, in which this height increases with Re. It can also be observed that whereas the stoichiometric region in the central reaction zone increases, the maximum $W_{OH^*,max}$ decreases. Moreover, at higher equivalence ratios, $W_{OH^*,max}$ decreases. This parameter is impacted the most by Re_{O_2}, as observed in case 2.

On the other hand, in figure 5.15 flame thickness (δ_{OH^*}) is analysed. The maximum δ_{OH^*} enlarges with higher Re and lower ϕ being more significant by the increase in Re_{O_2}. The δ_{OH^*} distribution for constant ϕ behaves in the same way when increasing Re_{O_2}, it expands with Re_{O_2} because flames are larger, due to more fuel entrained by the O_2 jet. The maximum thickness of the upstream reaction zone is not significantly affected either by Re_{O_2} or Re_{H_2}. However, downstream an increase in Re_{O_2} enlarges δ_{OH^*}. In contrast, the increase on the ϕ decreases the thickness.

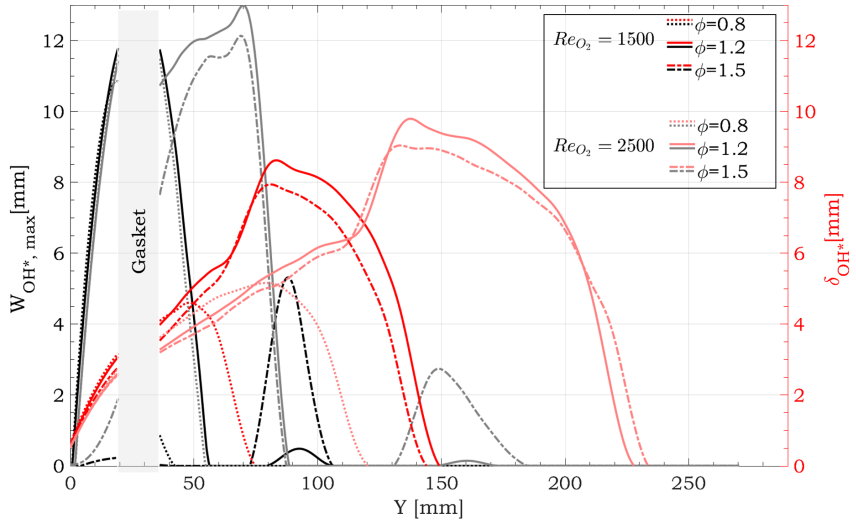

Figure 5.15: Case 3 Constant ϕ, Re_{O_2}: a = 1500, b = 2500. Flame Width $W_{OH^*,max}$ (black) and thickness δ_{OH^*}(red)

Cette thèse est accessible à l'adresse : http://theses.insa-lyon.fr/publication/2022LYSEI044/these.pdf
© [K. Utria Salas], [2022], INSA Lyon, tous droits réservés

This section concludes that the ratio oxidiser to fuel momentum determines the OH^* intensities of the flame. Therefore, the strength of the fuel-oxidiser mixing in the reaction zones creates or not the central reaction zone.

The present research results are different from those obtained in Sze et al. (2006); Wu and Essenhigh (1984); Bindar and Irawan (2012). This could be explained by the fact that the burner configuration used does not create an entrainment zone. The different heights of the H_2 and O_2 outlets avoid this zone to be present. The entrainment zone is a broad area where the fuel is mixing with the oxidiser. The flame presented begins in diffusion mode, and with a sufficient high G_O/G_f, the reaction zone becomes a closed sheet. They found that with more elevated Re_{O_2}, the entrainment is enhanced, and then the premixed mode is more prevalent. However, it occurs just with rich fuel conditions. In lean fuel conditions, the flame is always pure diffusion. This is placed on the sides. For $\phi > 1$, we can observe the formation of some premixed zones that expand the flame's stoichiometric zone. The central reaction zone increases by increasing Re_{O_2}, as was observed in this study.

Cette thèse est accessible à l'adresse : http://theses.insa-lyon.fr/publication/2022LYSEI044/these.pdf
© [K. Utria Salas], [2022], INSA Lyon, tous droits réservés

5.5 Conclusions

The purpose of this chapter was to analyse the aerodynamics and chemistry interactions that affect the flame appearance, structure characteristics, and heat release distribution of H_2/O_2 downward coflow multi-fuel-jet inverse diffusion flames. Different fuel and oxidiser Reynolds numbers were used, under fixed fuel momentum, fixed oxidiser momentum and constant oxidiser to fuel momentum (overall equivalence ratio).

Furthermore, since the intensity of the OH^* radical emissions are good marker of the heat release, this was analysed through the implementation of OH^* chemiluminescence.

The following conclusions can be drawn from the present study:

According to their morphology and appearance, H_2/O_2 inverse diffusion flames can be classified into three types, which are defined principally by the fuel/oxidiser momentum ratio. Two reaction zones characterised the flames: an upstream reaction zone and a central reaction zone. The upstream zone was always found and behaved as a classical diffusion flame. This zone was divided into two parts. The central reaction zone appeared for momentum ratios smaller than 9.

The results found indicate that the oxidiser momentum affects the flame structure characteristics. This parameter determines the flame heights (e.g. the flame length) and the extension of the diffusion mode upstream, hence the location of the central reaction zone. Furthermore, oxidiser momentum also defined the extension of the stoichiometric zone downstream.

Regarding the production of OH^*, the fuel momentum and the ratio G_O/G_f impacts the OH^* emission intensities, hence the OH^* concentration. For flames with injection conditions between $\phi = 1$ and $\phi = 1.4$, the higher the fuel momentum, the higher the production of OH^*. This result suggests that the mixing fuel/oxidiser is strong. Consequently, brighter reaction zones are observed. This behaviour can be interpreted as a higher heat release rate. For higher ϕ the decrease in G_O/G_f diminishes the production of OH^* due to the decrease in the enhancement of the H_2 jets.

Cette thèse est accessible à l'adresse : http://theses.insa-lyon.fr/publication/2022LYSEI044/these.pdf
© [K. Utria Salas], [2022], INSA Lyon, tous droits réservés

These results enhance the understanding of H_2/O_2 inverse diffusion flames. Hence, to identify adequate injection flow rates that lead to accurate thermal conditions of the crystal growth environment. This study shows that the aerodynamics condition determines upstream the size of the diffusion mode. The central reaction zone depends highly on the G_O/G_f ratio, hence on the aerodynamics and chemistry interactions. Further studies on flow velocity profiles carried out in the next chapter improves the comprehension of these interactions.

Cette thèse est accessible à l'adresse : http://theses.insa-lyon.fr/publication/2022LYSEI044/these.pdf
© [K. Utria Salas], [2022], INSA Lyon, tous droits réservés

Cette thèse est accessible à l'adresse : http://theses.insa-lyon.fr/publication/2022LYSEI044/these.pdf
© [K. Utria Salas], [2022], INSA Lyon, tous droits réservés

Chapter 6 | Aerothermodynamic behaviour of reactive flow

The following chapter focuses on the flow structure and on the different physical mechanisms involved in the mixing and the combustion obtained with a *Verneuil burner* for different flame structures. Moreover, this study outlines the aerodynamic mechanisms participating in this very particular configuration. The unusual burner configuration should be mentioned since the coaxial flow is directed downwards and has an inverse diffusion arrangement. This configuration is poorly described in the literature. However, an extensive study of the non-reactive and reactive flow structure for this type of burner with different geometries was carried out by Labor (2003). They focused principally on the influence of the burner geometry in flow development. Following a non-reactive and reactive flow approach is described to study the influence of the initial conditions for this type of burner. The results are compared with the classic jet literature and the findings of Labor (2003). The first part focused on the influence of the peripheral jets (H_2) and the second part on the central jet (O_2). At the end of the chapter, an exploration of flame temperatures is described in order to have quantitative values of the temperature gradients inside the crystal growth environment.

6.1 Analysis methods

To understand the flow structure and the different physical mechanisms involved in the mixing and the combustion obtained with a *Verneuil burner* for different flame structures, it is necessary to characterise the flow development. Furthermore, it is also essential to understand the parameters that influence the aerodynamics conditions of the crystal growth environment. The fuel and oxidiser injection conditions impact it considerably, as observed previous chapter (see chapter 5). Within this in mind, this part analyses the influence of different aerodynamics and chemistry conditions. Parameters as Reynolds numbers of fuel and oxidiser were used, as well as their momentum ratios and equivalence ratio. The analysis is divided into two cases. The first case analyses the influence of the fuel injection conditions, and the second case the oxidiser injection conditions. The operating conditions are depicted in table 4.1. Some of these points also correspond to actual industrial conditions of the *Verneuil growth method*. The results were obtained through Laser Doppler Anemometry (see section 4.2.4) using as seeding powder the Zirconium dioxide (ZrO_2). The analysis carried out was based on the results obtained by Labor (2003) (see section 3.4). Velocity and turbulence intensity measurements of the

Cette thèse est accessible à l'adresse : http://theses.insa-lyon.fr/publication/2022LYSEI044/these.pdf
© [K. Utria Salas], [2022], INSA Lyon, tous droits réservés

non-reactive flow and reactive flow were performed. In the case of the non-reactive flow only the O_2 jet was present. For the reactive case, the seeded jet was also only O_2.

Case 1

Case 1 corresponds to the study of fuel momentum influence. A laminar fixed Re_{O_2} of 1500 was used while the overall equivalence ratio were [0.8, 1.2, 1.5]. For this case the oxidiser momentum is constant and the oxidiser-fuel momentum ratio decreases while the overall equivalence ratio increases.

Case 2

In case 2, the influence of oxygen momentum was analysed. At fixed laminar fuel flow rate ($Re_{H_2} = 140$), the Re_{O_2} was varied [3200, 2125, 1700], from laminar ($Re_{O_2} < 2000$) to critical ($2000 < Re_{O_2} < 3200$) regimen (see appendix B.1), in order to obtain equivalence ratio from [0.8, 1.2, 1.5].

	U_{0,H_2} [m/s]	U_{0,O_2} [m/s]	ϕ	Re_{H_2}	Re_{O_2}	G_f [kg m/s]	G_O[kg m/s]	G_O/G_f
Case 1. Influence of fuel momentum, Re_{O_2} constant								
1	1.43	4.09	0.8	66	1500	1.5	21.5	14.5
2	1.60	4.09	0.9	74	1500	1.9	21.5	11.5
3	1.78	4.09	1.0	82	1500	2.3	21.5	9.3
4	1.96	4.09	1.1	91	1500	2.8	21.5	7.7
5	2.14	4.09	1.2	99	1500	3.3	21.5	6.4
6	2.32	4.09	1.3	107	1500	3.9	21.5	5.5
7	2.50	4.09	1.4	115	1500	4.5	21.5	4.7
8	2.67	4.09	1.5	123	1500	5.2	21.5	4.1
9	2.85	4.09	1.6	132	1500	5.9	21.5	3.6
10	3.03	4.09	1.7	140	1500	6.7	21.5	3.2
Case 2. Influence of oxidiser momentum, Re_{H_2} constant								
1	3.03	8.70	0.80	140	3188	6.7	97.1	14.5
2	3.03	7.73	0.90	140	2833	6.7	76.7	11.5
3	3.03	6.96	1.00	140	2550	6.7	62.2	9.3
4	3.03	6.33	1.10	140	2318	6.7	51.4	7.7
5	3.03	5.80	1.20	140	2125	6.7	43.2	6.4
6	3.03	5.35	1.30	140	1962	6.7	36.8	5.5
7	3.03	4.97	1.40	140	1821	6.7	31.7	4.7
8	3.03	4.64	1.50	140	1700	6.7	27.6	4.1
9	3.03	4.35	1.60	140	1594	6.7	24.3	3.6
10	3.03	4.09	1.70	140	1500	6.7	21.5	3.2

Table 6.1: Operating conditions highlighted in blue

Cette thèse est accessible à l'adresse : http://theses.insa-lyon.fr/publication/2022LYSEI044/these.pdf
© [K. Utria Salas], [2022], INSA Lyon, tous droits réservés

6.2 Influence of hydrogen jet

This section analyses the influence of hydrogen jets on flow development by varying the injection velocity, U_{0,H_2}, with constant U_{0,O_2}. The three chosen operation conditions represent the three types of flame topology observed in the previous chapter. The LDA measurements were conducted to characterised the non-reactive flow and reactive flow. Due to safety issues the non-reactive case was performed with a single O_2 jet.

Figure 6.1 shows the seeded particles to study the aerodynamic behaviour of the flame. These particles highlight the structure of the different flames and, the trajectory of the flow can be observed, which is discussed posteriorly.

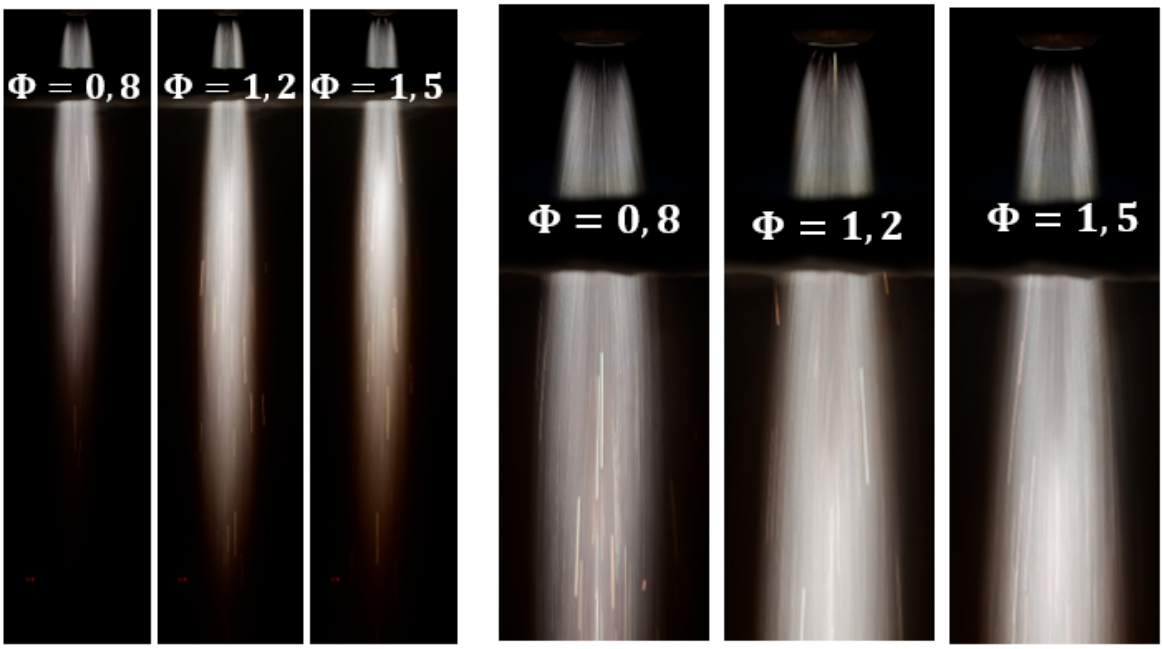

Figure 6.1: Flames during LDA with constant U_{0,O_2} and varying ϕ (on the right close-up of the flames)

6.2.1 Initial characteristics

Combustion affects the structure of the flow and its initial aerodynamic characteristics significantly. In this context, this section focuses on the initial characteristics of the two jets (H_2 and O_2), as reminder the nozzles do not locate at the same Y-position. They are observed at the crossed plane Y=0, which corresponds to the face outlet of the central oxygen jet. It is important to note that, at the injection in non-reactive conditions, the central jet analysed has semi-turbulent jet characteristics, $Re_{O_2,0} = 1500$, according to the literature in appendix B.1.

Cette thèse est accessible à l'adresse : http://theses.insa-lyon.fr/publication/2022LYSEI044/these.pdf
© [K. Utria Salas], [2022], INSA Lyon, tous droits réservés

Figure 6.2 illustrates on the left, the evolution of the mean velocity for the crossed plane at Y=0, for one side of the flame, as the central jet is axisymmetric (Labor, 2003). Figure 6.2 on the right compares the axial mean velocity profiles, rendered dimensionless by the maximum centreline velocity, $\overline{U}_{C,0}$ with a Power-law $n = 7$ for turbulent jets and, a law resulting from a parabolic equation for laminar jets. It can be inferred from the non-reactive case results that the profile velocity disagrees with any of the two theoretical profiles. This can be explained by the fact that the internal surface of the O_2 nozzle has a complex geometry that integrates a slight contraction at the nozzle exit that can modify the outlet flow. This effect is consistent with the geometries used for the jets generation for which the velocity profiles are uniform (Antonia and Bilger, 1973).

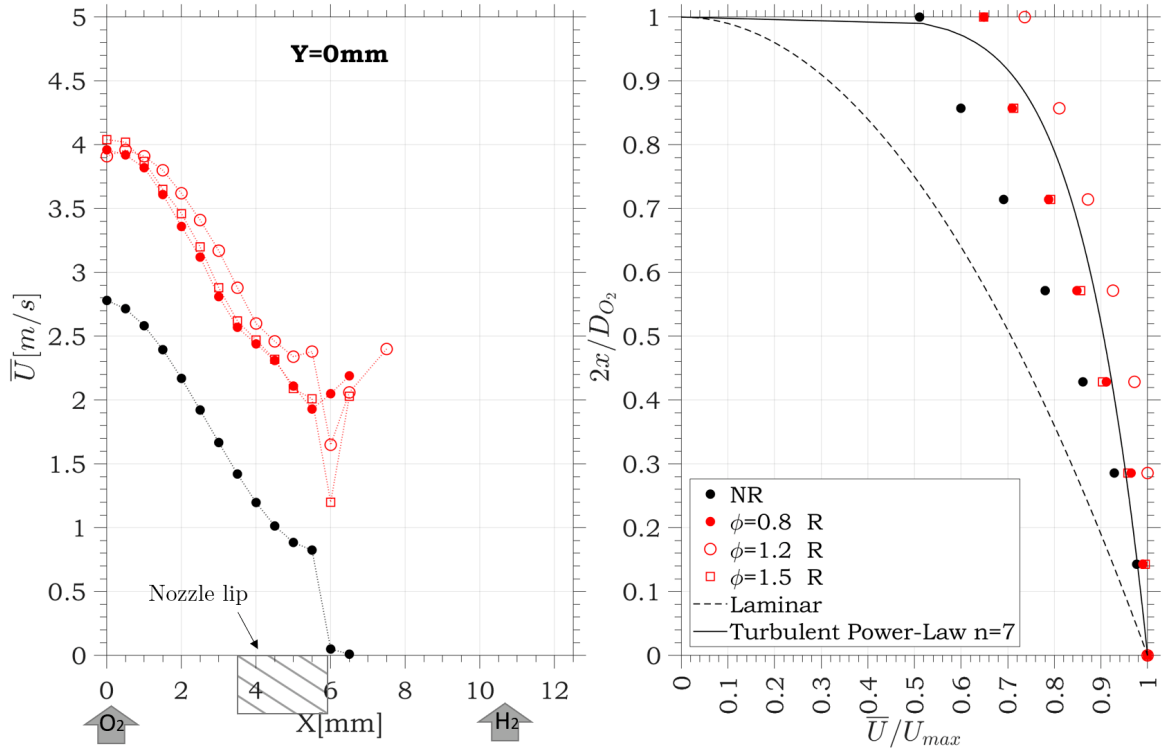

Figure 6.2: Profiles of velocity along X-axis for constant U_{0,O_2} at Y=0, non-reactive and reactive flow

Moreover, the comparison between the non-reactive (NR) and reactive flows (R) indicates higher velocity levels for the reactive case with identical initial mass flow conditions. According to Takagi et al. (1981), this increase in velocity ($\cong$ 1.2 m/s) is related to the expansion of gases caused by temperature rise. As observed, there is also a velocity decrease for both cases on the edges of the central flow related to the development of the boundary layer along the wall (Antonia and Bilger, 1973). The influences of the H_2 peripheral jets can be observed with the increase in the velocity for the $x >$ 6mm.

As mentioned, the velocity profiles of the reactive case were similar to the turbulent Power-

Cette thèse est accessible à l'adresse : http://theses.insa-lyon.fr/publication/2022LYSEI044/these.pdf
© [K. Utria Salas], [2022], INSA Lyon, tous droits réservés

Law (n=7). This means that at the outlet the flow can present turbulent characteristics. However, in figure 6.3, the overall turbulence intensities are lower than 10%, which indicates the semi-turbulent characteristics close to the O_2 nozzle. In addition, the relative turbulence intensities, $\sqrt{\overline{u'^2}}/\overline{U_C}$ are lower than 0.2 for the central jet and increase at the jets shear layer to then decrease (figure 6.4). These results indicate that the central jet has laminar characteristics and at the shear layer the flow becomes semi-turbulent.

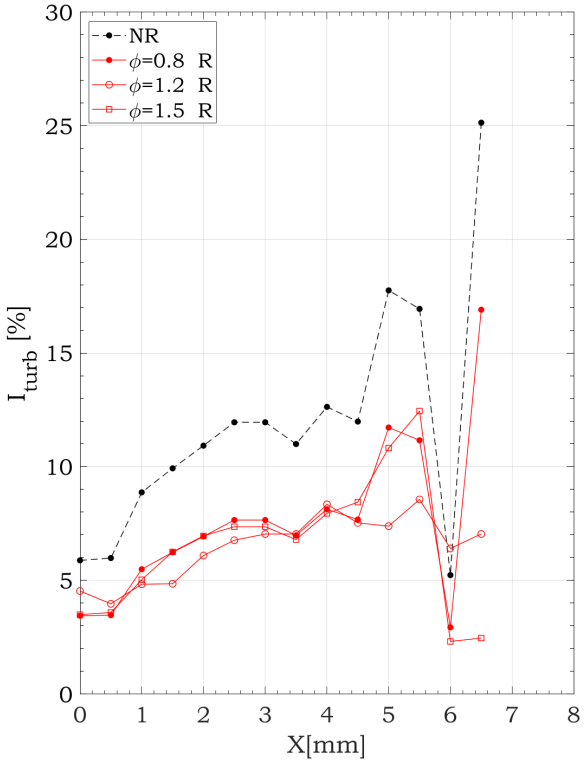

Figure 6.3: Overall Turbulence Intensity along X-axis at Y=0

In figure 6.4, it can be observed that the velocity is higher for the axial component, and the transversal component is almost zero, being more significant at the shear layer for both cases. On the other hand, it can be observed that the relative turbulence intensities in reactive case do not reach the levels as in non-reactive flow. This is a classic effect of the kinematic viscosity increase due to higher temperatures.

Cette thèse est accessible à l'adresse : http://theses.insa-lyon.fr/publication/2022LYSEI044/these.pdf
© [K. Utria Salas], [2022], INSA Lyon, tous droits réservés

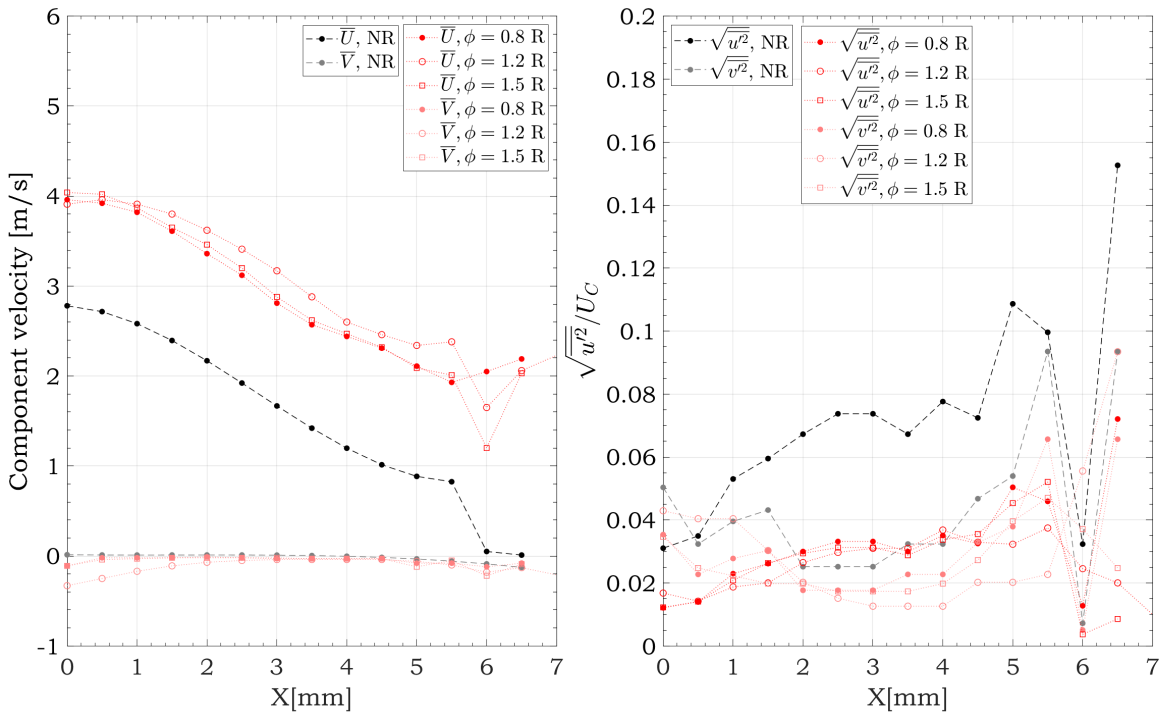

Figure 6.4: Components turbulence fluctuations, along X-axis at Y=0

The observation of the shearing evolution through the gradient of the mean axial velocity, $\frac{dU}{dX}$ is illustrated in figure 6.5. It was observed similar jets shearing for both cases, finding a high level in the shear layer ($X = 6$mm). Although the velocities increased with the reaction zone apparition, the constant shearing can be explained because a smaller velocity deficit is present, causing less shearing at these velocities, thus a lower turbulence intensity. In addition, the laminar jet features present in the area of chemical reaction at high temperature contributes to the decrease in turbulence intensity values, as illustrated in figure 6.3.

In addition, it can also be observed for the reactive flow that an increase in the injection velocity of H_2 produces higher shearing between the two jets in the reactive case. As seen, for type 1 flame structure, the shearing between the two jets is the lowest. This phenomenon can be explained because the near-field flow characteristics are imposed by r_u (see appendix B.1.3 on page 278), which are 0.25, 0.57 and 0.65 for $\phi = 0.8$, $\phi = 1.2$ and $\phi = 1.5$, respectively. These characteristics are governed by competing wake and shear instabilities (Dahm et al., 1992) (see figure B.4 in page 279). The latter results from the velocity jump between the inner and the outer jet, (U_i and U_o) (inner shear instabilities), and that between the outer jet, U_o (outer shear instabilities). Wake-like instabilities can always be found even conditions of $r_u = 1$, characterised by opposite sign vortices, they result from the finite lip thickness. For conditions close to $r_u = 1$, the wake-like instabilities are visible the inner shear instabilities are weak. Dahm et al. (1992) indicated that when $r_u < 0.6$, outer shear instabilities are governed, and inner shear layer

Cette thèse est accessible à l'adresse : http://theses.insa-lyon.fr/publication/2022LYSEI044/these.pdf
© [K. Utria Salas], [2022], INSA Lyon, tous droits réservés

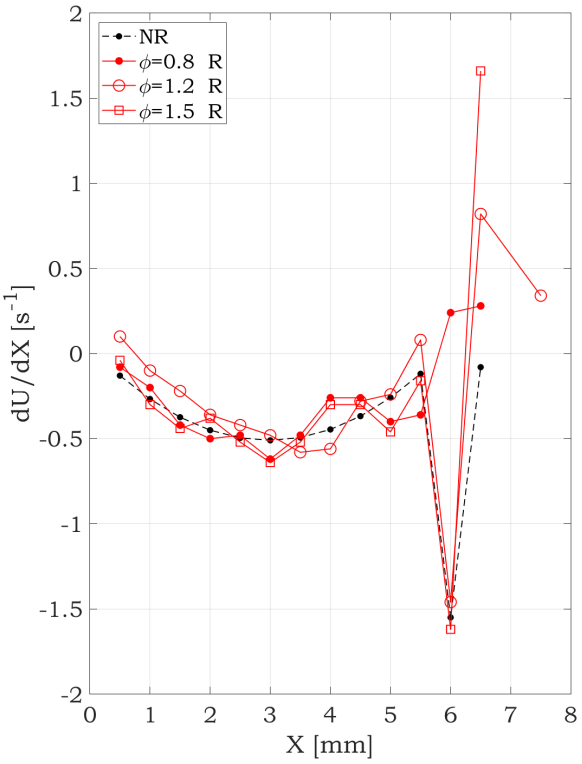

Figure 6.5: Velocity gradients at the crossed-plane Y=0

instabilities are suppressed, which would be the study conditions $\phi = 0.8$ and $\phi = 1.2$. In the range $0.6 < r_u < 0.9$ ($\phi = 1.5$), the inner shear instability become important while weak wake instabilities could also be discerned. Hence, the outer shear will also impact the flow field downstream. This means that the instabilities observed increased due to higher r_u.

Furthermore, results also revealed that the trends are similar for the non-reactive and reactive case, which means that a self-similarity can be estimated from the non-reactive. Therefore, if the flow development is considered of the same type, it can be assumed that the relation between flow rate and velocity on the centreline is identical for both cases (Labor, 2003). Besides, Blevins (1984) showed that the expressions for laminar and turbulent flows have a linear dependency. Using the non-reactive case where the injection velocity and the longitudinal velocity on the axis are known, the expression is:

$$\frac{U_C}{U_{0,O_2}} = 0.66 \tag{6.1}$$

This expression is useful to determine the laminar or turbulent characteristics of the flow in the reactive case. Within this context, the Reynolds number also depends on the viscosity which likewise is dependent of the temperature. Previous measure of the temperature at the O_2 showed that this is $418K$ (Labor, 2003). The dynamic viscosity at temperature

Cette thèse est accessible à l'adresse : http://theses.insa-lyon.fr/publication/2022LYSEI044/these.pdf
© [K. Utria Salas], [2022], INSA Lyon, tous droits réservés

T is giving by the equation:

$$\frac{\mu}{\mu_0} = \frac{(T/T_0)^{3/2}(T_0 + S)}{T + S} \tag{6.2}$$

where T is the temperature of the reactive flow and T_0 is the temperature of the known viscosity, S is an experimental constant at $O_2 = 139K$ (White, 2010).

Another expression to calculate the kinematic viscosity is (Borghi and Champion, 2000):

$$\frac{v}{v_0} = \frac{(T/T_0)^{5/2}(T_0 + S)}{T + S} \tag{6.3}$$

Table 6.2 provides the calculated initial conditions of the reactive flow:

Parameter	**Non-Reactive**	**Reactive**
$U_{O_2,c}$ [m/s]	4.09	5.84
U_C [m/s]	2.72	3.9
T(K)	300	418
ρ $[kg/m^3]$	1.284	0.93
v $[m^2/s]$	1.61 E-5	2.91E-05
Re	1500	1400
Re_c	≅1000	≅950

Table 6.2: Initial conditions of the O_2 central jet

Re values indicate that the flow conserves its laminar behaviour due to the increase of the kinematic viscosity with the temperature, resulting in a decrease in the turbulence fluctuations for the reactive case.

Furthermore, it is necessary to examine the development of the flow according to the density ratio, owing to the use of two gases that present very distant densities. McNaughton and Sinclair (1966) realised the effect of the gas densities different in the flow development. They used a tracer to perform visualisations that introduced minor modifications in the flow density and noted a large laminar zone caused by a force of buoyancy directed in the same flow direction. For the current study, the density ratio $R_\rho(= \rho_{H_2}/\rho_{O_2})$ is 0.063, which may suggest significant changes in flow development. As for the influence of the initial velocity profiles, Richards and Pitts (1993) observed that the initial conditions on the densities did not affect the self-similar behaviour once the flow was fully developed. Papadopoulos and Pitts (1999) also studied the influence of initial conditions extensively. They showed that the axial decay rates and the fully developed flow zone are independent of density ratio, velocity profile and turbulence level. Nevertheless, they pointed out that

Cette thèse est accessible à l'adresse : http://theses.insa-lyon.fr/publication/2022LYSEI044/these.pdf
© [K. Utria Salas], [2022], INSA Lyon, tous droits réservés

for the cases where $x/Di < 30$, the initial injection conditions will play a significant role in the flow behaviour in the near region.

Summarising the initial conditions: the axial mean velocity profile and its non-uniform character indicate that the oxygen jet's initial development strongly affects the flow development. Reynolds number values reveal a laminar flow that can present a transition to turbulent flow. In addition, the position at which this is observed can be significantly modified by the density ratio and the aerodynamic effect of the coaxial flow. These observations can give some explanations of the flow development characteristics.

6.2.2 Flow development

This section analyses the flow development at the three mentioned conditions. Figure 6.6 depicts on the left the velocity profiles at the centreline along Y-axis, and on the right, the overall turbulence intensities, I_{turb}, are represented. It can be observed that the maximum velocity is found at Y=60mm for the three reactive conditions, as in for the non-reactive case (single O_2 jet) the maximum is found at Y=40mm.

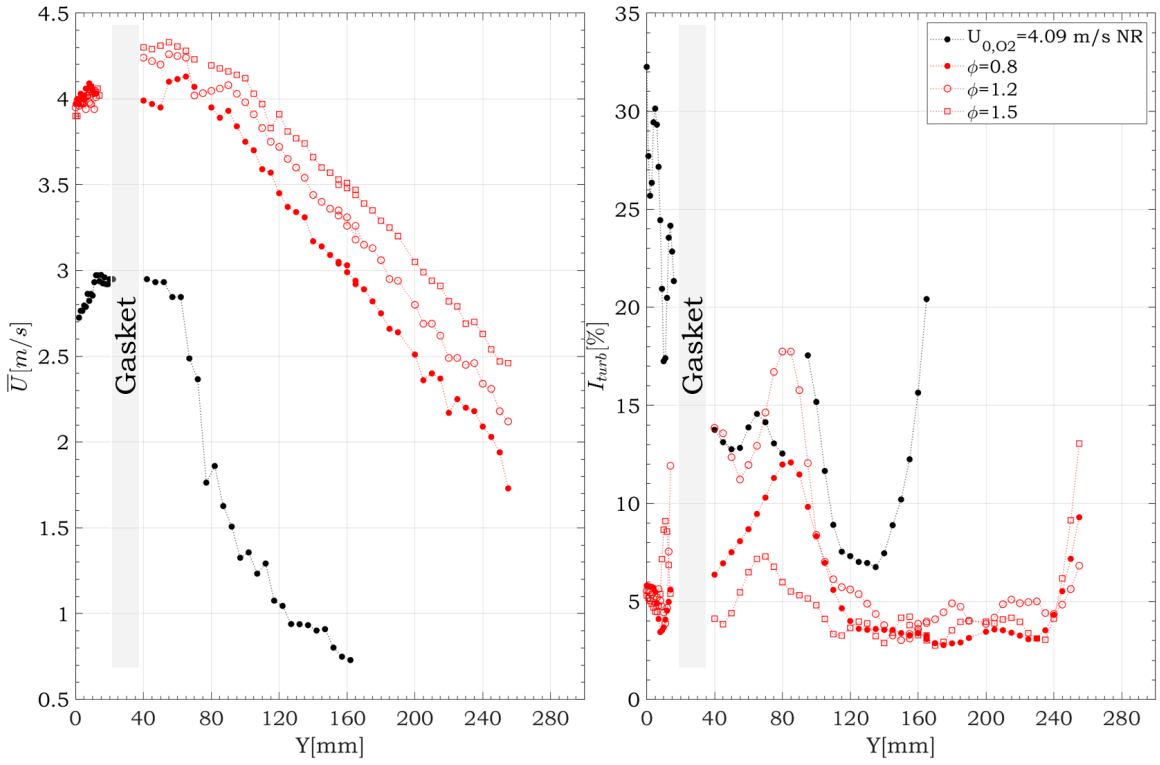

Figure 6.6: Profiles of the mean velocity along the centreline Y-axis for constant U_{0,O_2} at $X = 0$

Cette thèse est accessible à l'adresse : http://theses.insa-lyon.fr/publication/2022LYSEI044/these.pdf
© [K. Utria Salas], [2022], INSA Lyon, tous droits réservés

As observed, the peripheral hydrogen jets affect the flow development significantly. The turbulence intensity at the upper part of the flow is high; this indicates the turbulence character of the flow close to the O_2 nozzle, especially in the non-reactive case.

In contrast, the reactive case shows lower I_{turb}; as mentioned, the increase in the temperature relaminarise the flow as the kinematic viscosity increases. Downstream, different peaks are observed, and the first one is reported at the region with the highest mean velocities. The mechanisms that cause this flow development are explored in the following. It is important to mention that a smooth filter were performed to the curves to find tendencies, this treatment has a maximal relative error of 15% ($\phi = 0.8$) for one experimental point, the others values were around 6%.

The relative error is calculated as:

$$error[\%] = abs\left(\frac{\text{real value} - \text{theorical value (smooth)}}{\text{real value}}\right) \times 100\% \tag{6.4}$$

At first, the centreline dimensionless velocity decay has been analysed in figure 6.7. The flow velocity for the single oxygen jet in non-reactive case exhibits a constant maximum until $9D_{O_2}$. From this position, the flow begins to have turbulent characteristics as observed in the overall turbulence intensity. Compared to the theory, this could be the potential core; nevertheless, other mechanisms are present in the flow and analysed posteriorly. For the three reactive cases, the trend is the same: the zone of the maximum $\overline{U}_C/\overline{U}_{C,0}$ is found until $12D_{O_2}$. The smooth filter was only performed to the non-reactive case which presented the highest turbulence intensities with a relative error of 2%.

Moreover, the laminar behaviour along the centreline is observed for $\phi = 1.2$ and $\phi = 1.5$, since the relative turbulences are lower than 10%. The increase at the end of the confinement is due to the jet instabilities at the furnace outlet. Contrary, the non-reactive case shows more turbulence instabilities, particularly close to the O_2 nozzle and at $16D_{O_2}$.

Cette thèse est accessible à l'adresse : http://theses.insa-lyon.fr/publication/2022LYSEI044/these.pdf
© [K. Utria Salas], [2022], INSA Lyon, tous droits réservés

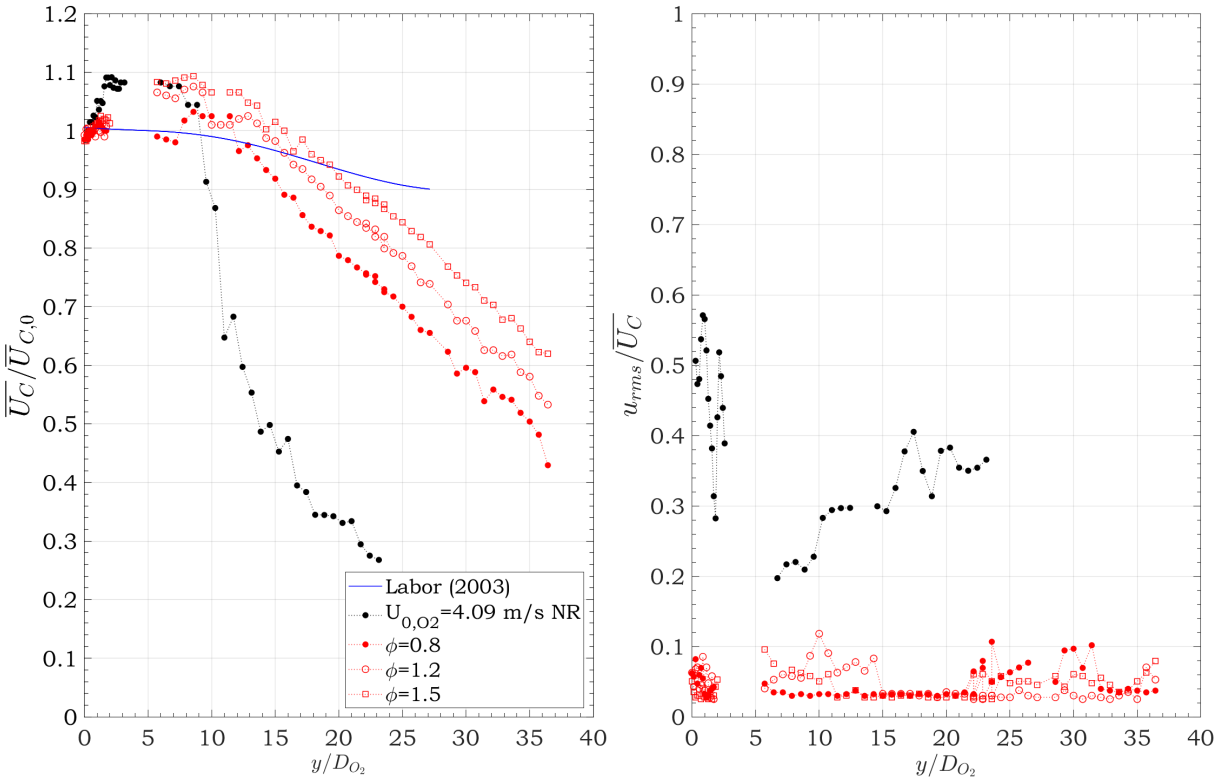

Figure 6.7: Decay of centreline mean velocity for constant U_{0,O_2} at $X = 0$

In addition, it was found that the decay rate is higher for this case. This effect is because, in the non-reactive case, there was only the O_2 jet present. As Labor (2003) observed, for a coaxial non-reactive flow (in blue), the hydrogen jets contribute to the buoyancy effects, causing a decrease in the decay rate at the centreline. Furthermore, in the reactive case, the decay rate increases compared to the non-reactive coaxial flow results. Regarding the increase in the velocity of the hydrogen jets, the results show a decrease in the decay rate.

In order to understand the mechanisms that affect the flow development, it is necessary to analyse the different effects present in this configuration. There is the influence of the coaxial flow and the buoyancy forces within them. The coaxial flow modifies the shear layer, and downstream, different buoyancy forces are present due to fluid density changes. These two effects are difficult to separate in the context of this study since the coaxial flow generates the hydrogen environment. Their influence on flow development is covered separately to determine which of the two mechanisms impact the most. The direct consequence of buoyancy is analysed first, and then the shear effect is treated (coaxial flow).

6.2.2.1 Buoyancy Effects

Labor (2003) compared his results with the conventional theory of potential core length.

Cette thèse est accessible à l'adresse : http://theses.insa-lyon.fr/publication/2022LYSEI044/these.pdf
© [K. Utria Salas], [2022], INSA Lyon, tous droits réservés

The author realised that the distance with this burner configuration was more elevated than the values found in the literature for classic jets (McNaughton and Sinclair, 1966). Since Labor (2003) studied the oxygen jet separately, the only explanation for the potential core's increase was the buoyancy effects. From the current study, a relatively large elongation is found when comparing the results of the decay evolution at the centreline of the non-reactive case with the conventional potential core length ($\cong 5D_i$) (see figure 6.7). Moreover, considering the jet as semi-turbulent, the laminar jet zone for this study should be located between 2.5 and $4.5D_i$ depending on the confinement size (McNaughton and Sinclair, 1966). As noted, regardless of the jet development approach, the distance found by the current study is elevated.

The buoyancy effects are widely described by the used of the Froude number, defined by equation 6.5. This is a dimensionless parameter commonly used to characterise variable-density flows and represents the ratio between the forces of inertia and those due to the gravity.

$$Fr = U_{i,0}^2 \frac{1}{gD_i} \frac{\rho_{i,0}}{\rho_o - \rho_{i,0}} \tag{6.5}$$

with $U_{i,0}$ the initial flow velocity of the central jet, D_i the outlet diameter of the central jet, $\rho_{i,0}$ the initial density of the central jet and ρ_o the density of the surrounding fluid.

There are different authors that analysed experimentally and numerically the influence of the densities difference in the flow development (Chen et al., 1980; Sautet, 1992; Pagé et al., 1998, 1999; Harran et al., 1996). Chen et al. (1980) were the first to propose an expression to determine the different region of a flow submitted to the buoyancy effects. They defined a dimensionless parameter ($\hat{y}$) in function of the Froude number, Fr, and the initial density ratio:

$$\hat{y} = Fr^{1/2} \left(\frac{\rho_{i,0}}{\rho_o} \right)^{-1/4} \frac{y}{D_i} \tag{6.6}$$

Chen et al. (1980) proposed that at $\hat{y} = 0.5$, the effects of the buoyancy affect the flow development for ascendant flows. With this parameter, the distance for the configuration of this study is $Y = 32D_i$. Nevertheless, Labor (2003) proposes to inverse the density ratio due to the buoyant flow configuration, resulting in $Y = 8D_i$. For the non-reactive case of this study (single central jet), $F_r = -9095$ indicates that the jet has negative buoyancy according to the literature of ascendant jets. Nevertheless, the buoyancy forces follow the same direction of the inlet velocities due to the downward configuration, indicating that the jet is a buoyant flow ($Fr > 0$).

Moreover, Sautet (1992) established a relation between the potential core, Y_p, and the

Cette thèse est accessible à l'adresse : http://theses.insa-lyon.fr/publication/2022LYSEI044/these.pdf
© [K. Utria Salas], [2022], INSA Lyon, tous droits réservés

density ratio for an ascending jet:

$$\frac{Y_p}{D_i} \cong 5.4\sqrt{\frac{\rho_{i,0}}{\rho_o}} \tag{6.7}$$

where ρ_i and ρ_o, correspond to the densities of the inner and outer flows, respectively. He found that for a Froude number between 1510 and 6700, the transition region towards the pure plume flow ($\hat{y} = 0.5$, is respectively between $Y = 10D_i$ and $Y = 30D_i$).

Likewise, Pagé et al. (1998, 1999) and Harran et al. (1996) evaluated Y_p and found a particular position where the turbulent kinetic energy is maximum. Furthermore, Pitts (1991) studied the influence of density effects on this position and showed that this corresponds to the end of the potential cone for which the intensities of longitudinal and transverse turbulence are maximum. Table 6.3 and figure 6.8 summarise these expressions with the values for this study.

Author	Equation	Present Study
Sautet (1992)	$\frac{Y_p}{D_i} \cong 5.4\sqrt{\frac{\rho_{i,0}}{\rho_o}}$	21 D_{O_2}
Harran et al. (1996)	$\frac{Y_{k,max}}{D_i} = 10.3978 * R_\rho^{-0.4096}$	24 D_{O_2}
Pagé et al. (1998)	$\frac{Y_{k,max}}{D_i} = 5 + 5 * R_\rho^{-0.5}$	32 D_{O_2}

Table 6.3: Evolution of the core potential length(Y_p) for different authors

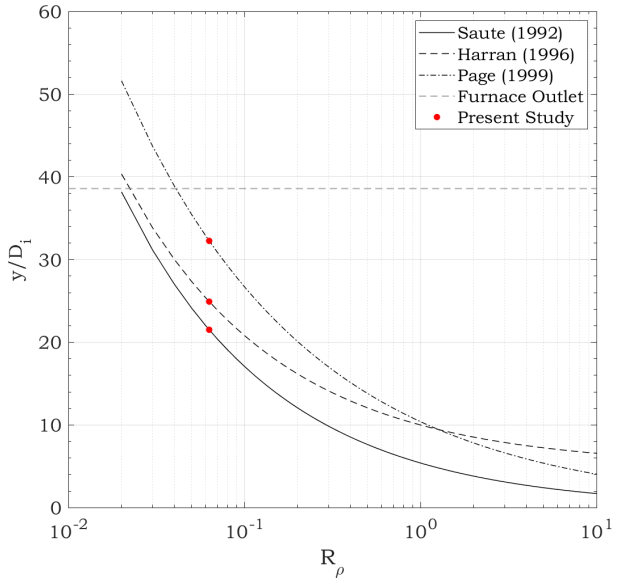

Figure 6.8: Evolution of the core potential length in function of the densities ratio,R_ρ

In order to compare the present experimental results with the theoretical models, the turbulent kinetic energy at centreline has been plotted in figure 6.9. Analysing the non-

Cette thèse est accessible à l'adresse : http://theses.insa-lyon.fr/publication/2022LYSEI044/these.pdf
© [K. Utria Salas], [2022], INSA Lyon, tous droits réservés

reactive case: a first peak located at the O_2 nozzle is observed. This is related to the establishment of the jet. Further downstream, a peak is observed around $Y = 22D_{O_2}$. This phenomenon is linked to the appearance of a transition to turbulence, consistent with the values provided by the different expressions gathered in table 6.3 and figure 6.8. This effect could be also related to the jet instabilities at the furnace outlet due to the geometry change in crossed section.

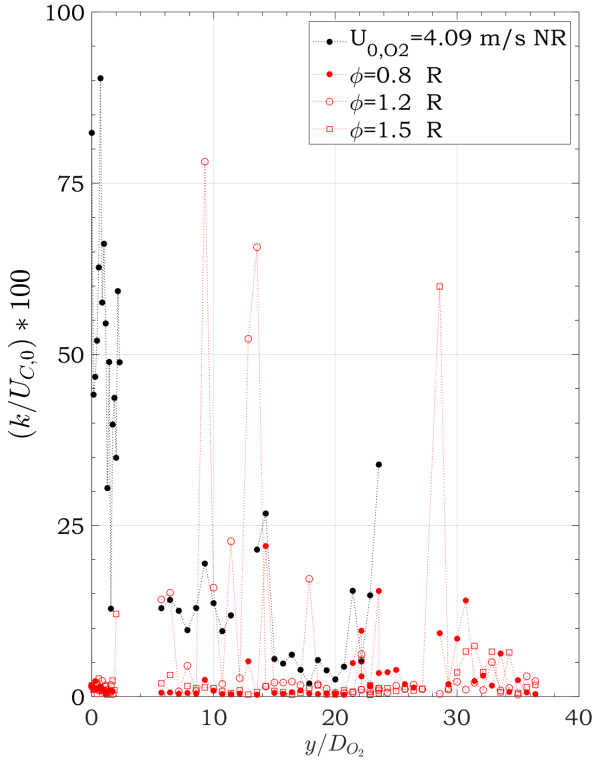

Figure 6.9: Evolution of the turbulent kinetic energy at the centreline, $k = \frac{1}{2}\left(\overline{u'}^2 + \overline{v'}^2\right)$

The examination of the non-reactive flow revealed the important role of buoyancy effects in the development of the central jet. In the reactive case, the buoyancy effects are also significant due to the nature of the initial gases present and the temperature variation. Takagi et al. (1981) studied flame temperature profiles and found that gas densities evolve as the inverse of temperature. The minimum density appears on the axis in the reactive zone, which differs from the non-reactive flow, where this conserves permanently if the central jet gas is of lower density than the environment. In addition, the 'hot' combustion products formed in the proximity of the reaction zone also influence the overall flow density. For this study, these products are mainly water vapour. In figure 6.10, the density evolution is illustrated in function of the temperature. The buoyancy effects behave similarly as in the non-reactive case since H_2 is outside the range. Moreover, the density ratios ($R_\rho = \rho_{H_2}/\rho_{O_2}$ or ρ_{H_2}/ρ_{H_2O}) remains less than one regardless of the temperature.

In addition, Sacadura (1997) calculated the density of $H_2 - O_2$ mixture through a Chemkin

Cette thèse est accessible à l'adresse : http://theses.insa-lyon.fr/publication/2022LYSEI044/these.pdf
© [K. Utria Salas], [2022], INSA Lyon, tous droits réservés

code and found similar characteristics. Figure 6.11 depicts the evolution of the density of the mixture $H_2 - O_2$ as a function of temperature. It seems that significant buoyancy effects can appear in the reactive flow as in the non-reactive flow and modify the flame development. In figure 6.9 in the reactive case for $\phi = 0.8$ and $\phi = 1.5$ the turbulent kinetic energy is low, a peak is observed at $26D_{O_2}$ for the latter. For $\phi = 1.2$ peaks are found between 10 and $12D_{O_2}$, which are related to the reaction zone that is located within this region, examined in subsection 6.2.2.3. The laminar characteristics of the studied flow are related to the buoyancy effects described by Sautet (1992); Harran et al. (1996); Pagé et al. (1999).

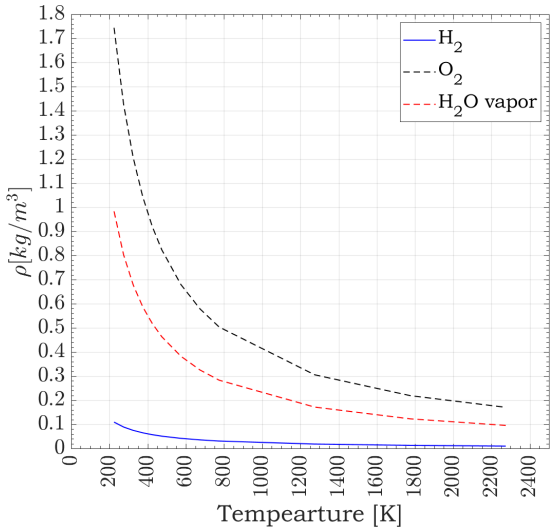

Figure 6.10: Evolution of density for H_2, O_2 and H_2O at different temperatures (Cengel, 1997)

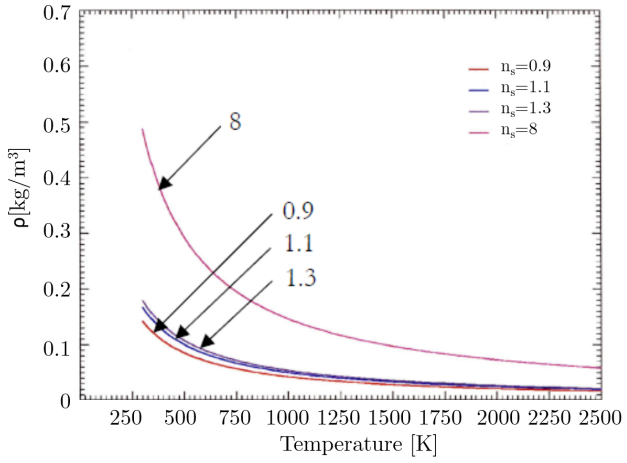

Figure 6.11: Evolution of the density for the mixture $H_2 - O_2$ as a function of the temperature and for different values of the mass coefficient $n_s = nM_{O_2}/M_{H_2}$ (n stoichiometric coefficient)

Nevertheless, another important parameter that influences the laminar or turbulent nature

Cette thèse est accessible à l'adresse : http://theses.insa-lyon.fr/publication/2022LYSEI044/these.pdf
© [K. Utria Salas], [2022], INSA Lyon, tous droits réservés

of the flow is the kinematic viscosity, which varies with temperature. Figure 6.12 shows the evolution of this for the different gases present in this study. An increase in kinematic viscosity with temperature may have consequences on flow development. The laminar character is conserved if the velocity increment due to the heat released is insufficient compared to viscous effects. The aerodynamic evolution analysis will determine which of these two effects is predominant. Moreover, it can be observed that regardless of the temperature, the oxygen viscosity is weaker than that of the hydrogen. This indicates that the flow may develop differently depending on the side of the reaction zone observed. Figure 6.13 shows similar results for the $H_2 - O_2$ mixture calculated by Sacadura (1997).

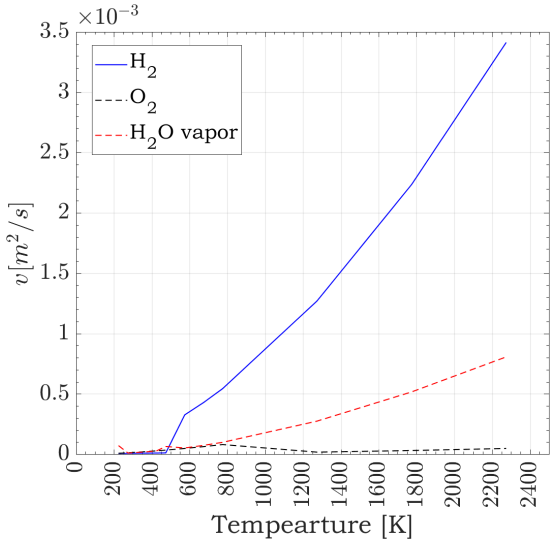

Figure 6.12: Temperature influence in kinematic viscosity, v, of different species (Cengel, 1997).

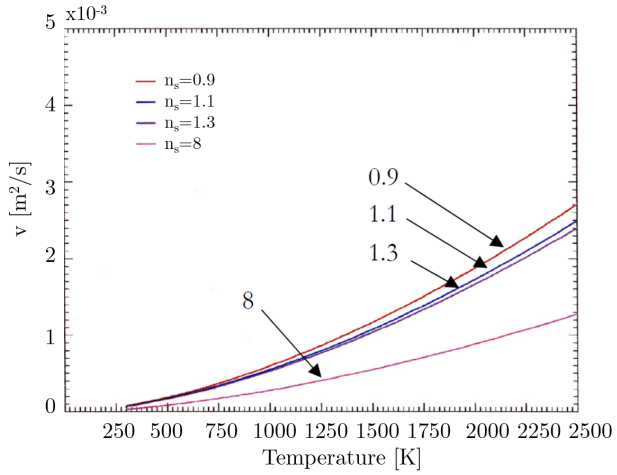

Figure 6.13: Evolution of the kinematic viscosity, v of the mixture as a function of the temperature and for different values of the mass coefficient $n_s = nM_{O_2}/M_{H_2}$ (n stoichiometric coefficient)(Sacadura, 1997)

Cette thèse est accessible à l'adresse : http://theses.insa-lyon.fr/publication/2022LYSEI044/these.pdf
© [K. Utria Salas], [2022], INSA Lyon, tous droits réservés

6.2.2.2 Coaxial flow influence

The other mechanism present in this configuration is the coaxial flow. It is important to note that the current configuration studied does not correspond to a classic coaxial case. The geometry of the burner is particular, the H_2 nozzle exit is located $7D_{H_2}$ above the O_2 outlet. Nevertheless, the available literature helps to better understand this mechanisms on this particular configuration.

Labor (2003) reported that the influence of the coaxial flow are observed until $Y = 8D_{O_2}$ for a *Verneuil furnace*, downstream the effects of the coaxial flow are not found and the flow behaves as a single jet. In figure 6.14 the evolution of the mean velocity at different Y-positions for the axial component are depicted, as well as the turbulence fluctuations.

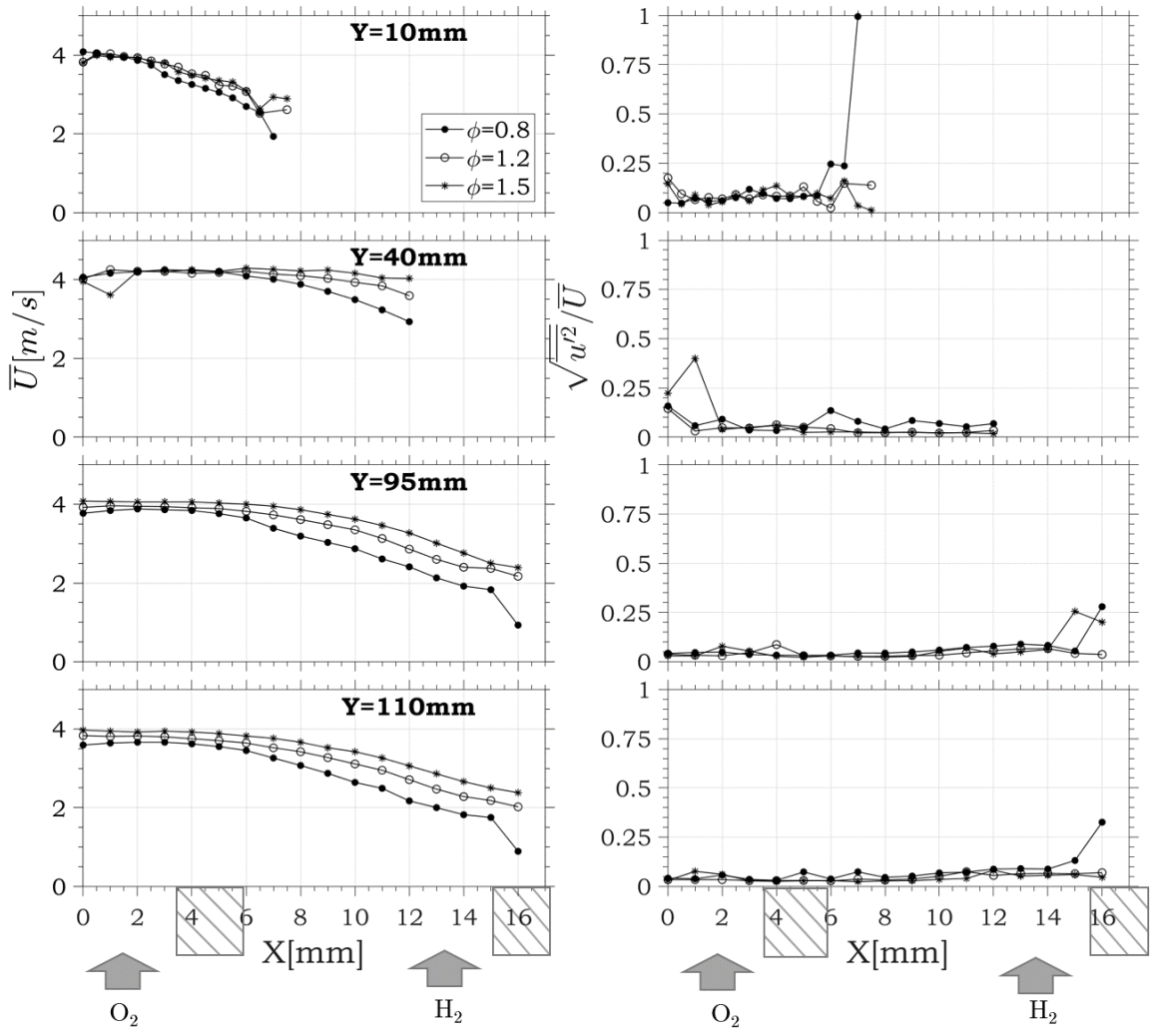

Figure 6.14: Profiles of the mean longitudinal velocity along X-axis for constant U_{0,O_2} at crossed-planes, Y=10, 40, 95, 110 mm

At Y=10mm the coaxial flow can be perceived for the highest U_{0,H_2}, which means that

Cette thèse est accessible à l'adresse : http://theses.insa-lyon.fr/publication/2022LYSEI044/these.pdf
© [K. Utria Salas], [2022], INSA Lyon, tous droits réservés

the r_u increases. For the other condition, the coaxial flow is not observed, however the shear layer presents high turbulence fluctuation. These results are concordant with the observations in Labor (2003). Stream-wise at Y=40mm ($\cong 6D_{O_2}$), the flow shows a widening, specially for the highest r_u, this confirms that the flow development is affected by the hydrogen jet. In contrast, the turbulence fluctuations of the shear layer are not observed. The spreading of the central jet at this position could be explained by the sudden widening present between the upper part (the burner nozzle) and the confinement (furnace) can influence the development of the external flow, hence its interaction with the central jet, resulting in the spread of the flow. At Y>40mm the influence of the peripheral jets are not observed and the flow width seems to diminish as well as the turbulence fluctuation at the shear layer.

In figure 6.15 the evolution of the mean velocity is analysed for the axial component at X=5mm, which corresponds to the shear layer position. As observed, the outer potential core is obtained at $Y = 9D_{O_2}$, where the mean longitudinal velocity decreases.

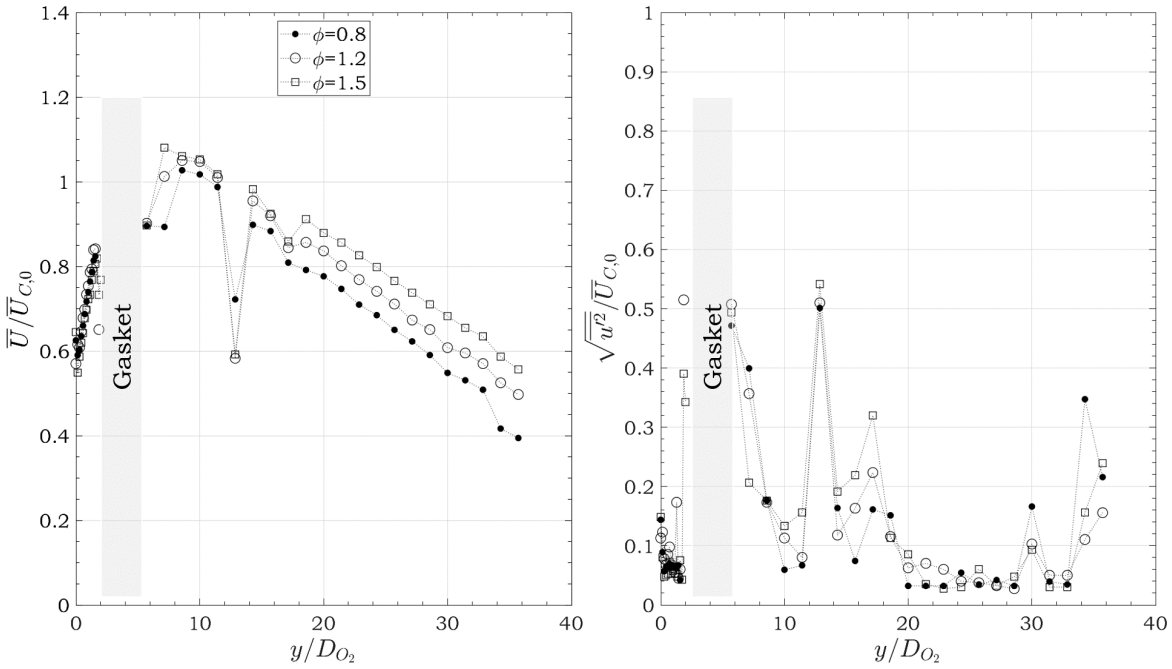

Figure 6.15: Profiles of the mean longitudinal velocity along Y for constant U_{0,O_2} at X=5mm

The increase in the velocity is due to the O_2 entrainment of H_2 jets which is enhanced with the increase of the H_2 inlet velocity. The flow begins its axisymmetric free jet behaviour at $Y \cong 19D_{O_2}$, where the turbulence fluctuations decrease significantly which means that the jet shear layer is not present. The decrease in the velocity at $9D_{O_2}$ is owing the end of the outer core, a diminution on the fluctuation is also observed. Between $11D_{O_2}$ and $18D_{O_2}$ the flow is at the intermediated merging region, where the intensity fluctuation are

Cette thèse est accessible à l'adresse : http://theses.insa-lyon.fr/publication/2022LYSEI044/these.pdf
© [K. Utria Salas], [2022], INSA Lyon, tous droits réservés

considerably high.

The increase in the turbulence fluctuations at the end of the flow is related to the jet instabilities at the furnace outlet. Regarding the increase in the H_2 inlet velocity, it can be observed that the rate decay decreases with it.

Nevertheless, the outer potential core length does not seem to be affected. As compared to classic coflow jets, the potential core obtained for this study is lower since the outer potential core length is equal about eight times the annular gap size, i.e., $8(D_o - (D_i + 2t))/2$ (Hout et al., 2021). These results are due to the geometry of the burner since the H_2 nozzle exit is located $7D_{H_2}$ above the O_2 outlet.

6.2.2.3 Effects of the reaction zone apparition

In figure 6.16 the influence of the chemical reaction in the flow development is analysed. As observed, for $\phi = 0.8$ and $\phi = 1.2$ within the central reaction zone ($10D_{O_2} < Y < 14D_{O_2}$), the flow shows turbulent characteristics due to the increase in the shearing on the transversal component, shown in figure 6.16b with the velocity gradient along X-axis. Although the transversal component is low along the axis, the turbulence fluctuations upon this zone are significant, and the traversal component reports the highest values; this means that the reaction zone affects this component considerably. Besides, the highest values are obtained close to the centreline (figure 6.16b).

As mentioned, the inner potential core is at Y$\cong 11D_{O_2}$, and the highest emissions of OH* are obtained at $Y \cong 14D_{O_2}$. At this position, the turbulence fluctuations are close to zero, which can indicate high temperatures. Downstream the central reaction zone ends, and the decay rate increases. With the increase of H_2 inlet velocity, the entrainment is enhanced, decreasing the decay rate.

Cette thèse est accessible à l'adresse : http://theses.insa-lyon.fr/publication/2022LYSEI044/these.pdf
© [K. Utria Salas], [2022], INSA Lyon, tous droits réservés

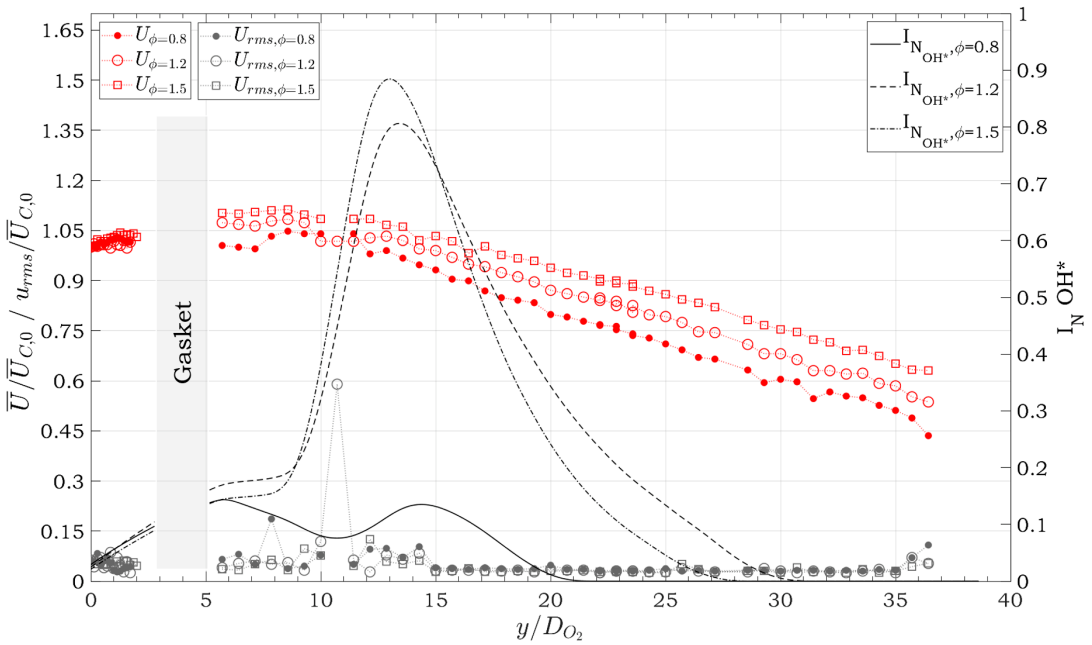

(a) Profiles of the mean longitudinal velocity and OH* emission intensities

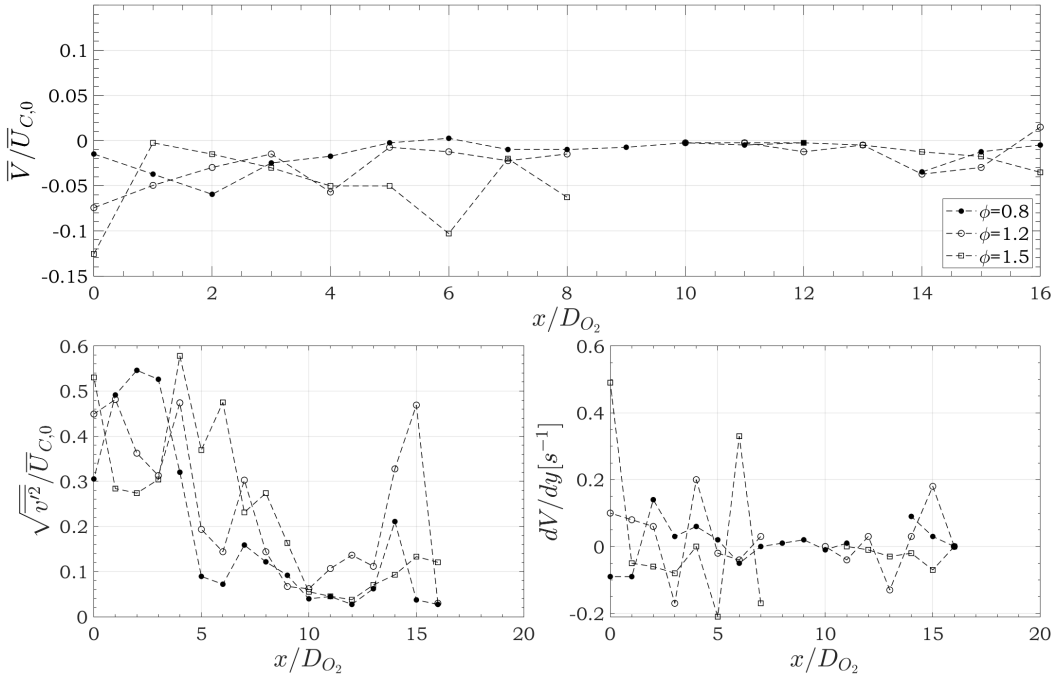

(b) Profiles of the mean transversal velocity along X-axis at $Y = 13D_{O_2}$ and OH* emission intensities

Figure 6.16: Analysis of the reaction zone influence on the flow development for constant U_{0,O_2} at $X = 0$

The closure of the flame, y_j, is located at $Y \cong 11D_{O_2}$. At this position, for $\phi = 1.2$, the transversal and longitudinal components and their turbulence fluctuations are the highest, this can be interpreted as an indicator of the end of the buoyancy effects. The closure of the flame can be interpreted as the beginning of the momentum controlled flame

Cette thèse est accessible à l'adresse : http://theses.insa-lyon.fr/publication/2022LYSEI044/these.pdf
© [K. Utria Salas], [2022], INSA Lyon, tous droits réservés

structure (Dong et al., 2007). For momentum controlled IDF, the oxidiser velocity is large enough to produce large enough negative pressure, and the velocity difference between the oxidiser/fuel jets is large enough to create sufficient pressure difference between the fuel and oxidiser to redirect the fuel jets towards the oxidiser jet, causing an intense mixing. When ϕ is increased, there is unburned fuel reaching the end of the upstream diffusion flame and mixes there with the central oxidiser jet. The mixed fuel and oxidiser will march downstream as a partially premixed flame (Dong et al., 2007), in the case of type II flames. A complete premixed flame appearance is exhibited when more fuel is provided after ϕ exceeds 1.3, flame type III. The momentums of fuel and oxidiser are the responsible of this dual-structure flame with a diffusion flame base and a premixed flame torch downstream exhibited by these flames.

On the other hand, at the jet shear layer in figure 6.17 the decay rate is analysed to highlight the influence of the reaction zone. Within this zone, the decrease in r_u, which corresponds to an increase of the OH* intensities, seems to affect the flow development. The longitudinal mean velocity follows the same trends as I_{NOH^*}.

From $17D_{O_2}$, I_{N,OH^*} is lower than 0.5, the velocity drops quickly. The decay is less significant for the higher ϕ, which have a more elevated temperature, resulting in laminar behaviour. Furthermore, it can be observed that for $14D_{O_2}$ (highest I_{N,OH^*}), the turbulence fluctuations are highly significant, being greater than one and, at the furnace outlet, these are related to the jet oscillations at this position.

Moreover, at $Y \cong 11D_{O_2}$ the flame thickness is the highest and downstream the flame ends. The longitudinal velocity showed turbulence fluctuations lower than one, which means that the transversal component is significant within this zone (figure 6.17b).

As mentioned, figure 6.17b depicts the evolution of the transversal component at X=5mm. The results show that the component is almost zero along Y-axis and does not appear to change along the axis. This effect indicates that the reaction zone affects the direction of the velocity, being $\phi = 0.8$ the most affected since the transversal component reported value closer to zero. For $\phi = 1.2$ ad $\phi = 1.5$ the values are slightly higher but continue to be small, they did not change with the increase in ϕ .

In contrast, the turbulence intensities for the transversal component, v' are not negligible at the change of crossed-section $Y = 6D_{O_2}$, downstream this reaches the lowest values between $14D_{O_2}$ and $29D_{O_2}$. At this region, the OH* intensities are lower than 0.5. Streamwise at $Y > 29D_{O_2}$, the turbulence fluctuations begin to increase, at this point the flame ends, decreasing the temperature, hence the kinematic viscosity augments.

Cette thèse est accessible à l'adresse : http://theses.insa-lyon.fr/publication/2022LYSEI044/these.pdf
© [K. Utria Salas], [2022], INSA Lyon, tous droits réservés

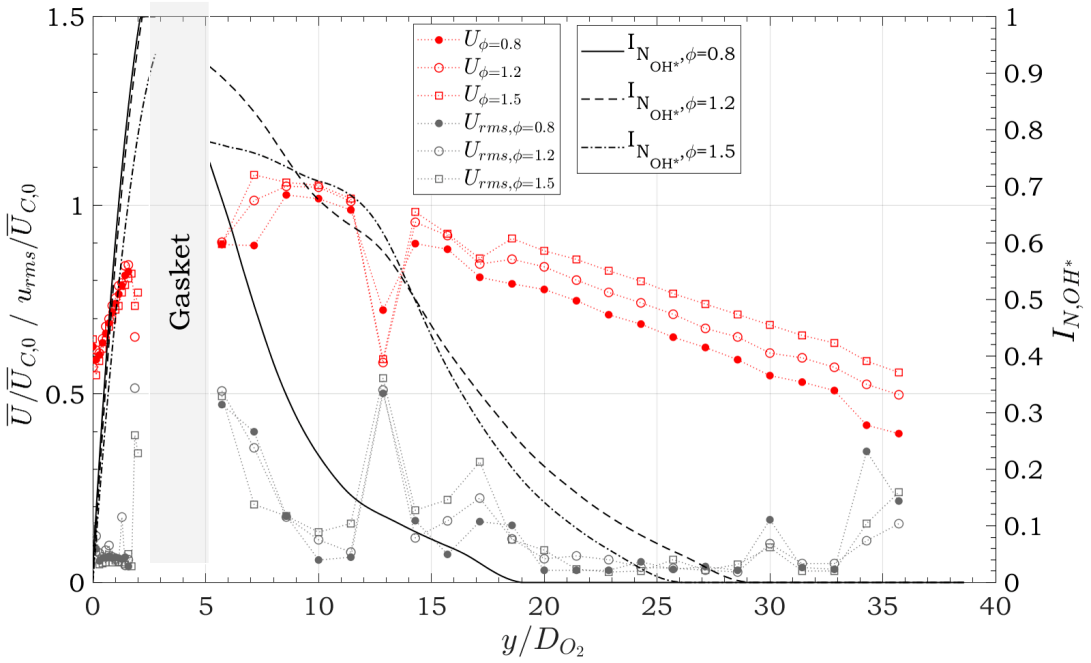

(a) Profiles of the mean longitudinal velocity and OH* emission intensities

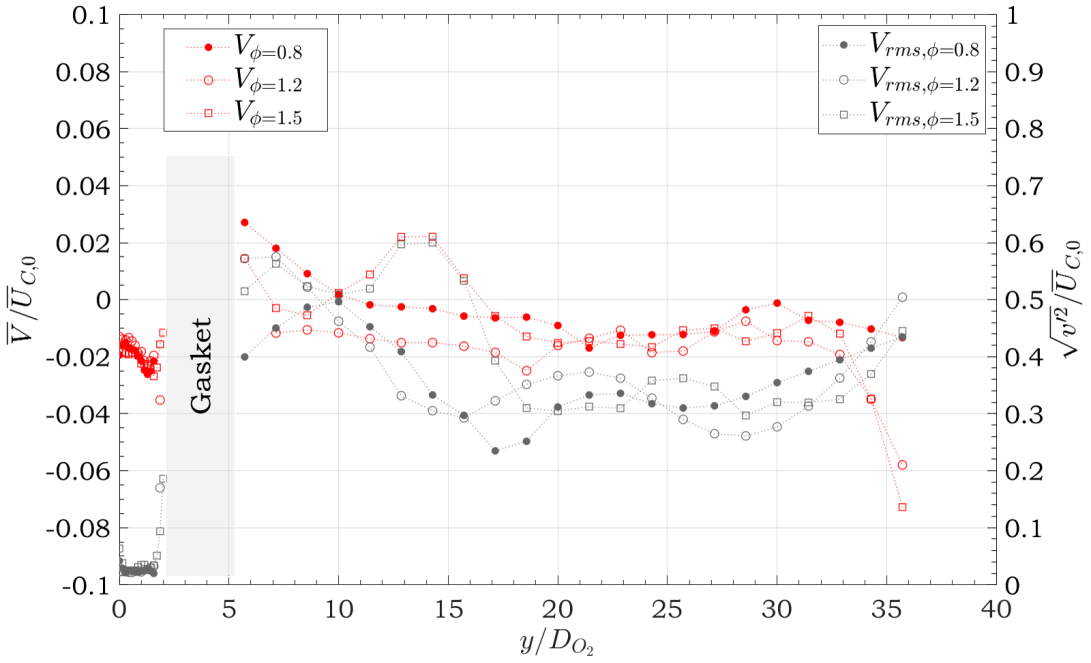

(b) Profiles of the mean transversal velocity and OH* emission intensities

Figure 6.17: Analysis of the reaction zone influence on the flow development for constant U_{0,O_2} at X=5mm

In addition, the trajectories of the velocity vectors are highlighted in figure 6.18. As seen, the changes in the average longitudinal velocity along the axis also affect the jet aerodynamic development. It is shown qualitatively on the trajectory generated from the direct visualisation of the seeded flow. The transversal component of the velocity is more significant close to the O_2 nozzle, especially at the edges. Downstream with U_c decay, the

Cette thèse est accessible à l'adresse : http://theses.insa-lyon.fr/publication/2022LYSEI044/these.pdf
© [K. Utria Salas], [2022], INSA Lyon, tous droits réservés

flames appear to spread, and the component v becomes zero except at the flame edges.

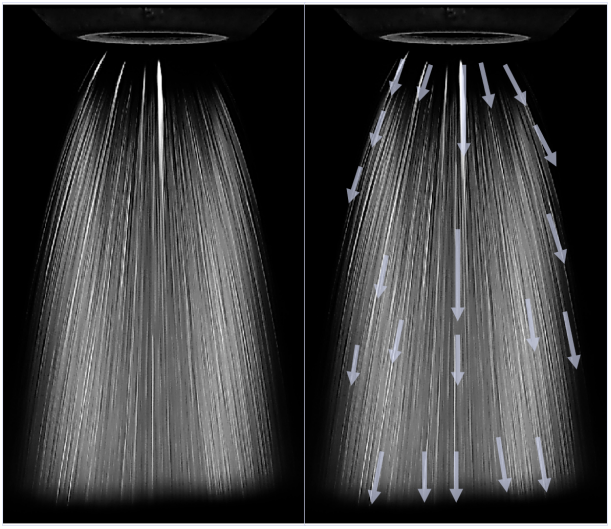

Figure 6.18: Visualisation of the seeded flow

These results show that the location of the reaction zones plays an important role in the evolution of the aerodynamic quantities. In order to define more precisely its influence, the longitudinal length evolution of various variables has been examined to characterise the jet development.

The self-similarity is analysed in figure 6.19. The aerodynamic development of the flow is described through the longitudinal evolution of the value of $X_{0.5}$, which represents the value of X for which the longitudinal velocity is equal to half of that measured on the axis. At the burner nozzle, the jet establishment can be observed. $X_{0.5}$ spreads for the higher ϕ which have the highest injection velocities of H_2. It can also be observed that the self-similarity is achieved at $Y = 6D_{O_2}$ for $\phi = 0.8$ and $\phi = 1.2$, with the increase in U_{0,H_2} the self-similarity is shifted to $Y = 14D_{O_2}$. Moreover, at the centre, the profiles overlap perfectly with the classic Gaussian curve ($\alpha = 2$), even for $Y < 6D_{O_2}$, describing the flows in auto-similarity. However, there are some differences, especially on the edges, which can be explained by the buoyancy effects induced by combustion. Thus, for the first profiles Y=10mm ($1D_{O_2}$) an outward deviation is observed, in accordance with that reported by Muñiz and Mungal (2001) and also attributed to buoyancy effects. For the profiles Y=40mm ($6D_{O_2}$), these differences are due to the influence of the sudden widening of crossed-section between the nozzle burner and the confinement. The increase in H_2 inlet velocity affects the flow development due to the increment in the impact of the coaxial jets, as observed in the coaxial flow analysis.

Cette thèse est accessible à l'adresse : http://theses.insa-lyon.fr/publication/2022LYSEI044/these.pdf
© [K. Utria Salas], [2022], INSA Lyon, tous droits réservés

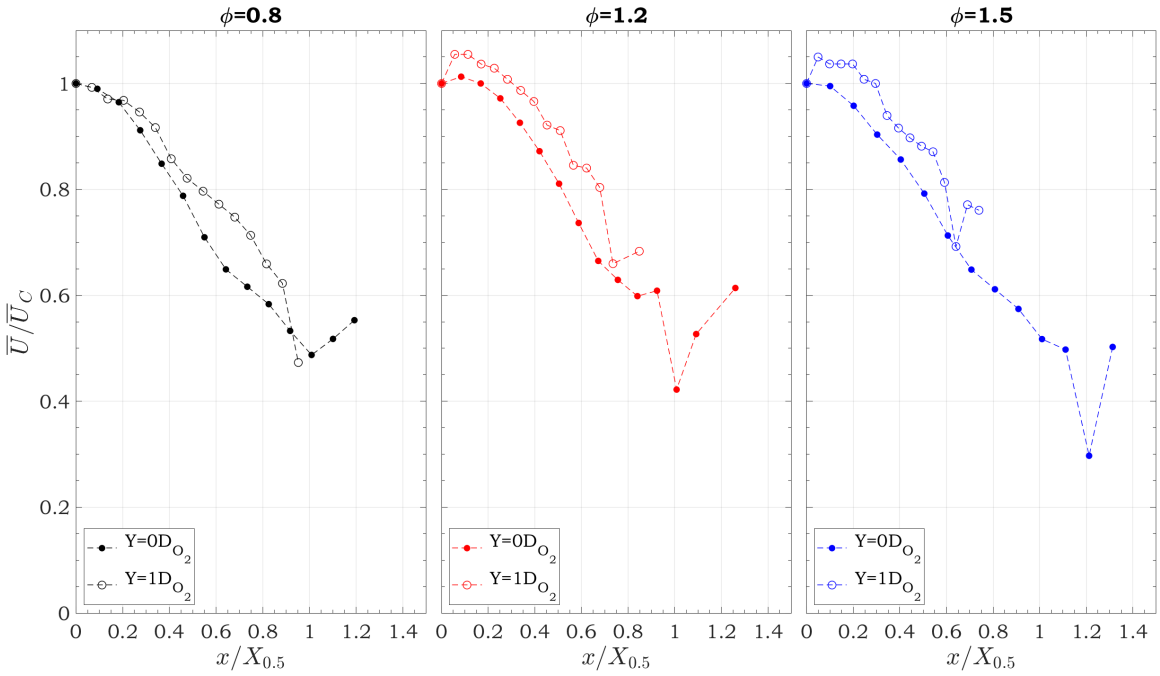

(a) $X_{0.5}$ at the burner nozzle

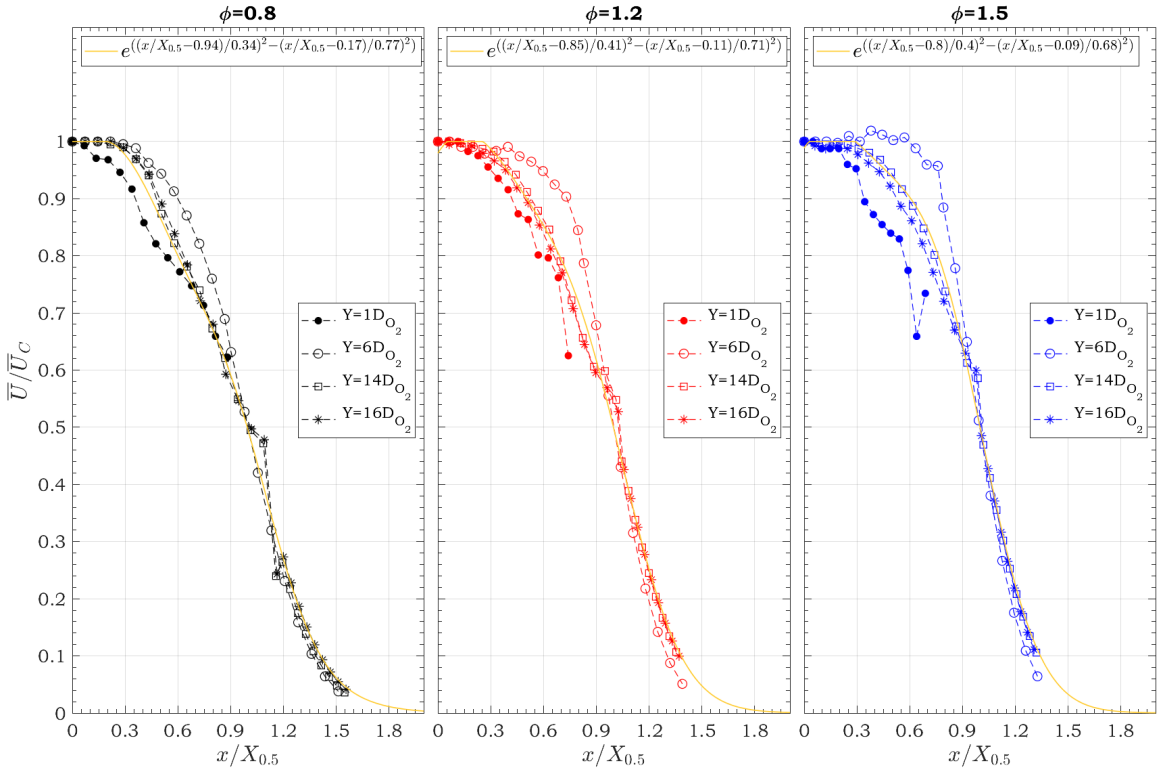

(b) $X_{0.5}$ at the confinement

Figure 6.19: Crossed section profiles of the longitudinal velocity at the secondary development zone

Comparing the current results with previous research, the self-similarities are reached before certain studies, but others agree with the findings. Wygnanski and Fiedler (1969) established that the mean velocity and the axial fluctuations become self-similar at $y/D_i =$

Cette thèse est accessible à l'adresse : http://theses.insa-lyon.fr/publication/2022LYSEI044/these.pdf
© [K. Utria Salas], [2022], INSA Lyon, tous droits réservés

20 and $y/D_i = 40$ respectively, contrary the transverse fluctuations only obtain such behaviour for $y/D_i = 70$, being the latter the point of actual self-similarity. This can be explained because the combustion contributes to the self-similarity for the axial mean velocity by accelerating the transformation of two coaxial jets in a single jet (Labor, 2003). Furthermore, Cheng et al. (1992) also observed the current self-similarity behaviour for the mixture fraction on a lifted air/hydrogen diffusion flame. Drake et al. (1986) proposed equivalent results for a non-lifted flame. Regarding the turbulence fluctuations the self-similarity is not observed in figure 6.20.

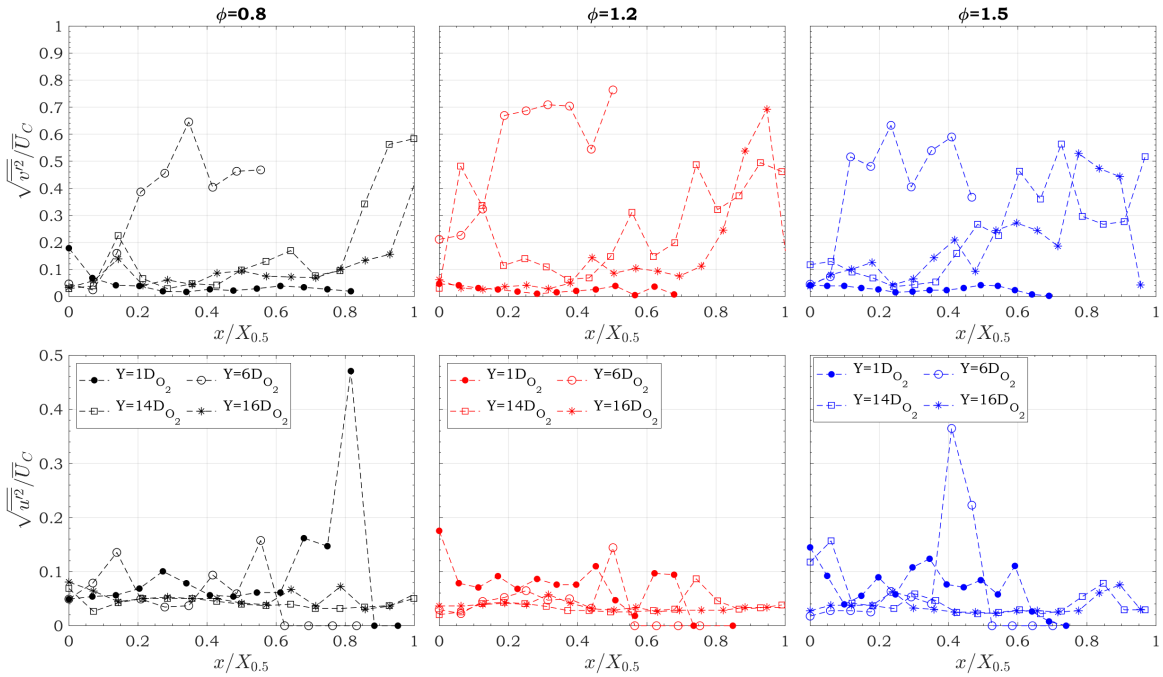

Figure 6.20: Crossed section profiles of turbulence relative intensities at the secondary development zone

To describe more globally the flow development, figure 6.21 describes the aerodynamic development of the flow through the longitudinal evolution of the value of $X_{0.5}$ which is compared with the non-reactive and reactive case found by Labor (2003). The self-similarity is used to calculated $X_{0.5}$ for the point not measured experimentally.

As observed, the flow development follows similar trends as for Labor (2003), and depends on the analysed zone: Upstream ($x/D_{O_2} < 5$) $X_{0.5}$ is close to a linear evolution with a slope of 0.44, and downstream, the development decay rate is lower and close to that of the non-reactive case (slope 0.04). For the first zone (**zone 1**), in table 6.4 can be observed that the slope increases with ϕ, being $\phi = 0.8$ the closest to the results obtained by Labor (2003). In zone 2, the slopes are the same for $\phi = 1.2$ and $\phi = 1.5$, and they are slighty higher than the values found by Labor (2003). As observed, in the entire explored area ($35D_{O_2}$), the slope is close to that corresponding to the development of a laminar jet Labor (2003). However, the theoretical expression proposed values of $X_{0.5}$

Cette thèse est accessible à l'adresse : http://theses.insa-lyon.fr/publication/2022LYSEI044/these.pdf
© [K. Utria Salas], [2022], INSA Lyon, tous droits réservés

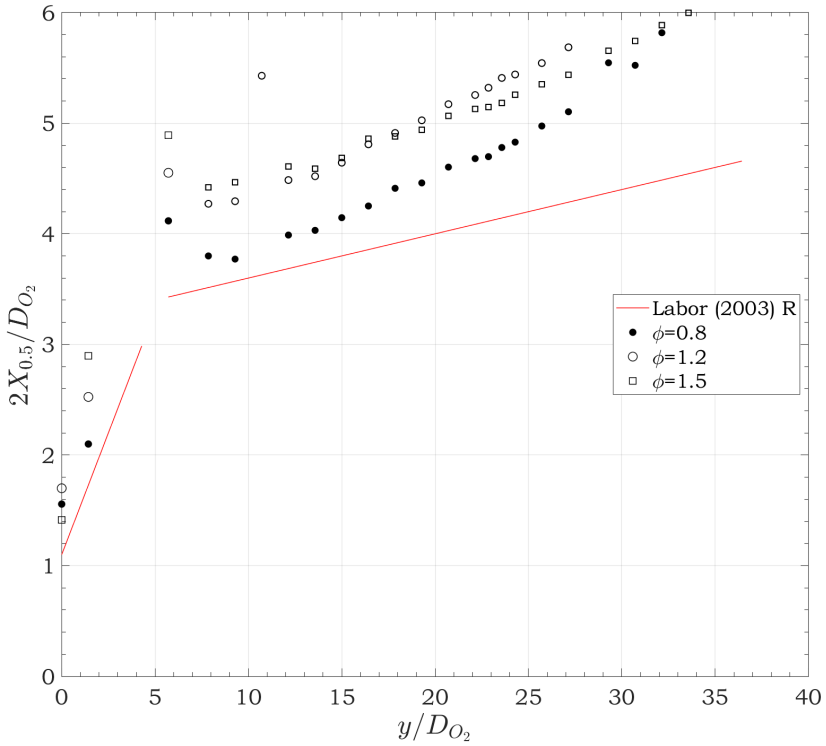

Figure 6.21: Longitudinal evolution of the value of $X_{0.5}$

(Schlichting and Gersten, 2016) are significantly lower than those measured by this study. Likewise, the slope values are lower than that calculated for a turbulent jet developing in a stationary fluid (Hinze, 1975), lower than the values proposed for coaxial and variable density jets (Sautet, 1992). Most of these theories concern developed areas, therefore, exhibit a turbulent character over the entire section. Nevertheless, for the very specific configuration studied here, it can be said that the transition to a fully turbulent flow is not reached.

	Zone 1		**Zone 2**	
ϕ	Flow Establishment		Self-similarity zone	
	a	b	a	b
0.8	0.45	1.51	0.08	2.95
1.2	0.49	1.75	0.06	3.87
1.5	0.58	1.70	0.06	3.81

Table 6.4: Linear Equation of $X_{0.5}$ ($2X_{0.5}/D_{O_2} = ay/D_{O_2} + b$)

To support the analysis of the reaction zone influence in the flow development, the secondary flow development is compared to that of the OH* emissions obtained from chemiluminescence measurements, using threshold 1 depicted in figure 4.14 (see section 3.1). As observed in figure 6.22, threshold 1 (isolevel of normal intensity 0.023) helps to describe the flow development. Although the comparison seems to be complex, it can be

Cette thèse est accessible à l'adresse : http://theses.insa-lyon.fr/publication/2022LYSEI044/these.pdf
© [K. Utria Salas], [2022], INSA Lyon, tous droits réservés

inferred that the development of $X_{0.5}$ is found outside the reaction zone. This occurs for two reasons: (i) is due to the cold hydrogen jets that surround the reaction zone and, (ii) the high temperatures keep the velocity in the reaction zone high. As observed for the $\phi = 0.8$ the development of the flame at **zone 1** follows the threshold 1. The development for this condition is a slightly higher regarding the slope, the reaction zone ends before the other conditions. This is also observed at the OH* emissions, where the reaction zone spreads more significantly with the increase in ϕ. These results confirm the impact of the reaction zone size in the flow development.

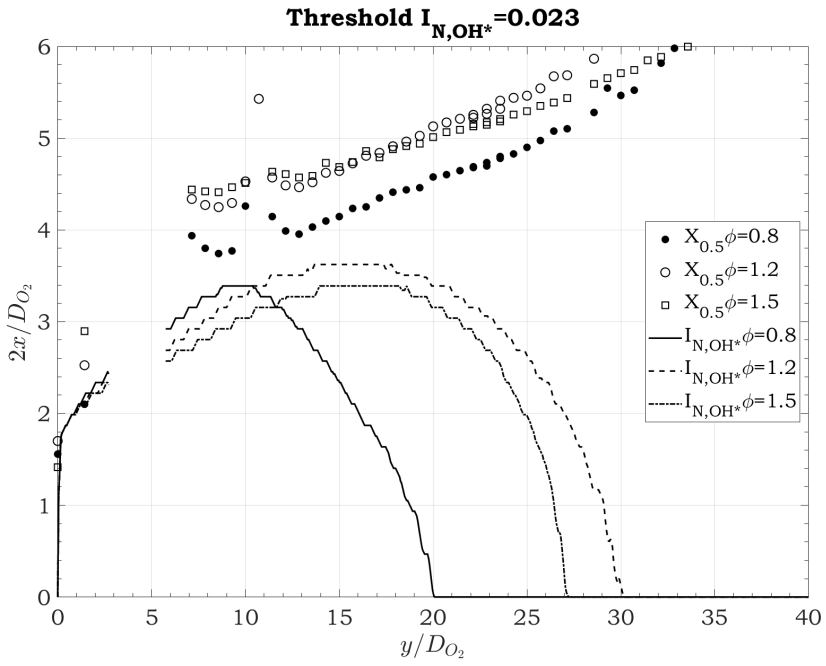

Figure 6.22: Secondary flow development vs OH* emission intensities

Different physical mechanisms affect the flow development, the next section summarised the effects of the central jet of oxygen.

Cette thèse est accessible à l'adresse : http://theses.insa-lyon.fr/publication/2022LYSEI044/these.pdf
© [K. Utria Salas], [2022], INSA Lyon, tous droits réservés

6.2.3 Conclusions

The influence of the peripheral jets of hydrogen on the flow development were studied varying the inlet fuel velocity with constant oxygen velocity for non-reactive and reactive cases. The results in this section indicate that the flow development depends on different mechanisms, principally:

- The coflow mechanism affects the structure of the flow until $8D_{O_2}$, the variation of the H_2 inlet velocity does not affect significantly this value. The shear layer fluctuations due to the peripheral hydrogen jets are observed for different Y-positions, these effects diminish with the reaction zone presence and with the increase of ϕ, due to the high temperatures in the reactive flow decreasing the velocity difference owing the higher viscosities.
- The buoyancy forces influence until $21D_{O_2}$ and the reaction zone increases the fluctuations at the centreline within the central reaction zone, located between $12D_{O_2}$ and $15D_{O_2}$. The increase of the hydrogen inlet velocity decreases the decay rate and influences significantly the flow development.
- The combustion increases the buoyancy effects on the flow and affects the transversal component of the mean velocity especially. In addition, the self-similarity is reached before due to the presence of the reaction zone, which accelerates the transformation from coaxial jet to single jet. The flame closure increases the turbulence intensities.
- The increase of the hydrogen inlet velocity does not seem to affect the laminar behaviour of the flame since this is smaller than the oxygen velocity inlet ($ru < 1$). This also indicates that the viscosity effects due to the high temperatures are more relevant than the changes in the fuel velocities for this specific configuration.

Cette thèse est accessible à l'adresse : http://theses.insa-lyon.fr/publication/2022LYSEI044/these.pdf
© [K. Utria Salas], [2022], INSA Lyon, tous droits réservés

6.3 Influence of oxygen jet

From previous section the aerodynamics flow development seems to be highly impacted by the injection velocity of the central jet. Its influence is detailed in the following. As before, three operating conditions which correspond to three flame topologies were chosen to be the study of interest. Non-reactive flow and reactive flow were analysed. In addition, the non-reactive flow measurement were performed for single O_2 jets.

Figure 6.23 shows the flame seeded with the particles used to carry out the LDA measurements for the reactive flow.

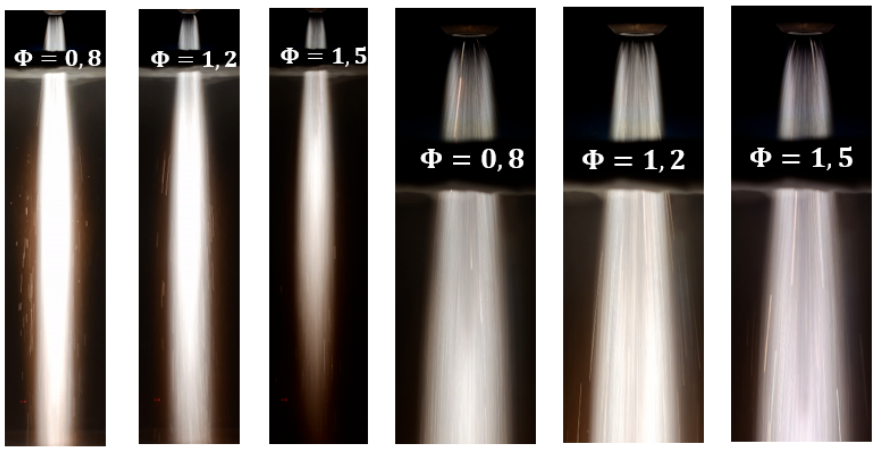

Figure 6.23: Flames during LDA with constant U_{0,H_2} and varying ϕ, on the right a close up of the image is shown

6.3.1 Initial characteristics

As in the previous section, the first examination performed is for the initial conditions at the O_2 nozzle outlet crossed-section.

Figure 6.24 represents the different conditions tested for the central jet. As observed, the increase in U_{0,O_2} approaches the flow to the turbulence Power-law n=7, specially for the reactive case. The results denote the presence of jet turbulence characteristics at the O_2 nozzle. Despite the increase in the velocity, the overall turbulence intensity is lower than 16% for the reactive case, which means that the conditions remain semi-turbulent (figure 6.25). For the non-reactive case they are slightly more elevated. The increase in the velocity due to the apparition of the reaction zone is $\cong 1m/s$.

Cette thèse est accessible à l'adresse : http://theses.insa-lyon.fr/publication/2022LYSEI044/these.pdf
© [K. Utria Salas], [2022], INSA Lyon, tous droits réservés

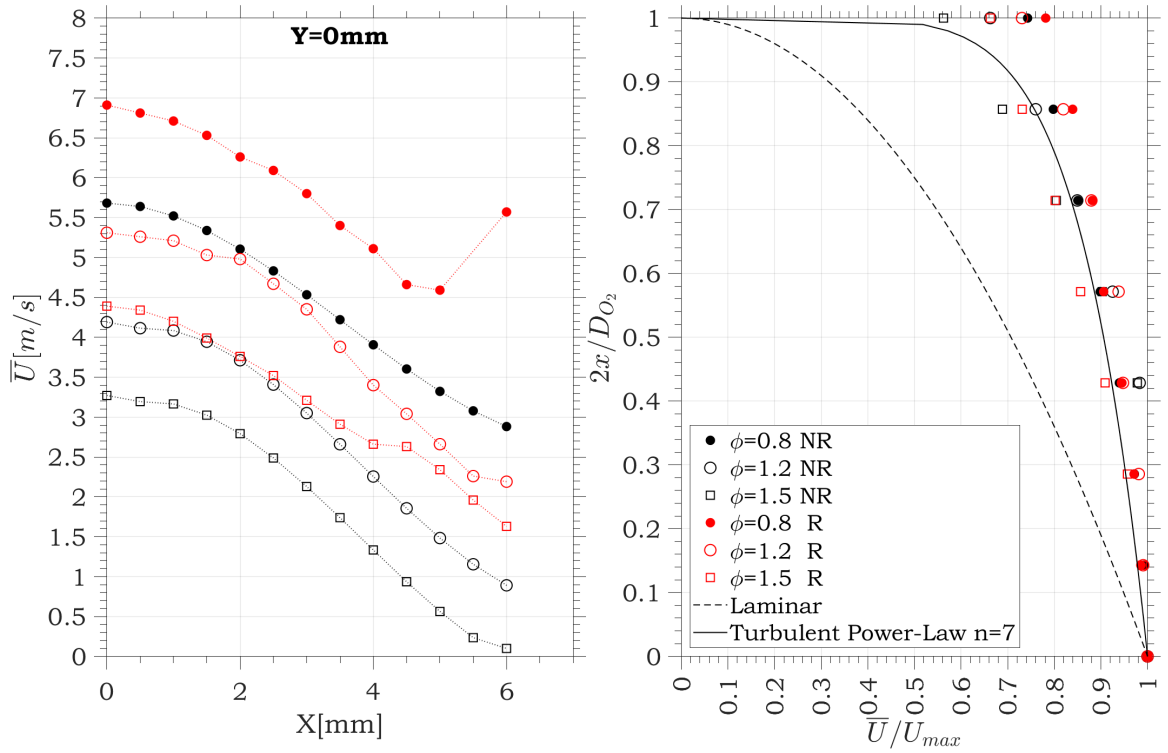

Figure 6.24: Profiles of velocity along X-axis for constant U_{0,H_2} at Y=0, non-reactive and reactive flow

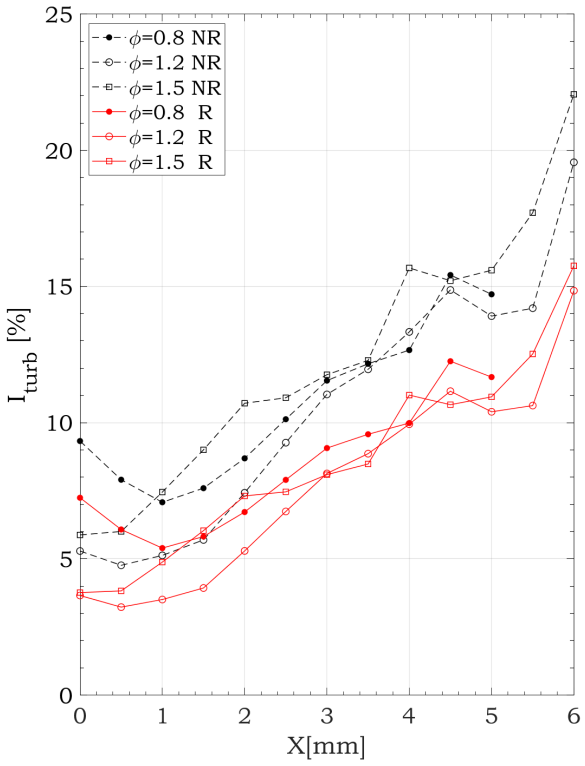

Figure 6.25: Overall turbulence intensity along X-axis at Y=0

Cette thèse est accessible à l'adresse : http://theses.insa-lyon.fr/publication/2022LYSEI044/these.pdf
© [K. Utria Salas], [2022], INSA Lyon, tous droits réservés

In figure 6.26 the transversal and longitudinal components are analysed. The influence of the peripheral jets is accentuated with the decrease of U_{0,O_2}. The turbulence fluctuations continue to have low values for the three conditions, being higher for the non-reactive case. An increase in the transversal turbulent fluctuations, $\overline{v'}$ is distinguished at $X = 6$mm for $\phi = 0.8$, which corresponds to the shear layer and the highest velocity difference between the two flow velocities. Transversal components are almost null for the three conditions. The longitudinal turbulence fluctuation is higher for the higher U_{0,O_2}.

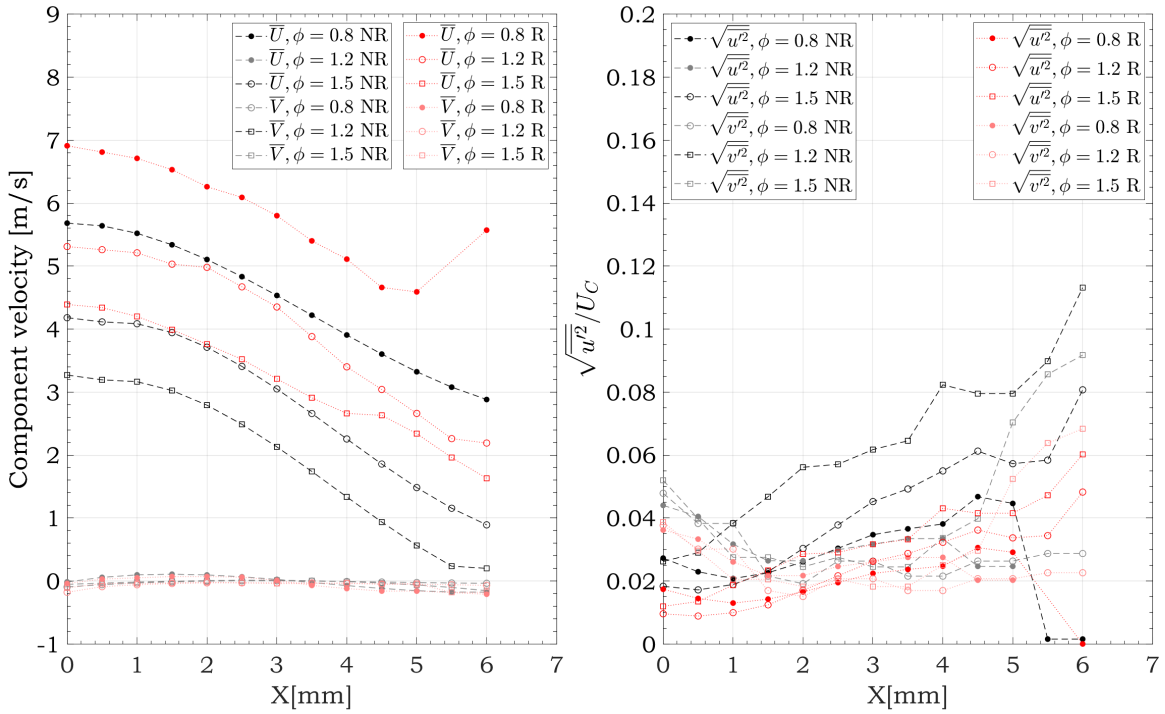

Figure 6.26: Components turbulence fluctuations, along X-axis at Y=0

The shearing distribution is depicted in figure 6.27, in order to find tendencies a smooth filter was performed for the experimental results and the relative errors are also depicted. At the centreline all the case reported similar velocity gradients. It was also found that close to the shear layer (X= 4 mm) the longitudinal velocity gradient increases and its value depends on the Re_{O_2}, r_u and ϕ, in the case of the reactive flow. The differences between the shearing distributions are more significant changing U_{0,O_2} than changing U_{0,H_2} (see figure 6.5).

The values of the shearing in the reactive flow are higher than in non-reactive flow because for these points the H_2 jets were not present.

For the non-reactive flow, it can be observed that for $\phi = 0.8$ reported lower $\frac{dU}{dX}$ than $\phi = 1.2$, due to the characteristics of turbulent and semi-turbulent jets, respectively. The diminution of the inlet velocity decreases the flow development in X, thinner profiles are

Cette thèse est accessible à l'adresse : http://theses.insa-lyon.fr/publication/2022LYSEI044/these.pdf
© [K. Utria Salas], [2022], INSA Lyon, tous droits réservés

observed in figure 6.24, hence the static condition is achieved faster for lower U_{0,O_2}. In the case of $\phi = 1.5$, Re_{O_2} has been decreased showing a laminar behaviour (see figure 6.3), decreasing the shearing along X. Furthermore, the velocities difference between the central jet and the static air decreases considerably and therefore also the velocity gradients.

In the reactive flow, the temperature of the reaction zone affects the shearing distribution and values. Temperatures increase with ϕ and the velocity deficit decreases. For the regime $r_u < 0.6$ ($\phi = 0.8$ and $\phi = 1.2$), the shearing increases in the central jet zone with ϕ, but it decreases at the jet shear layer. For $\phi = 1.5$ ($0.6 < ru < 0.9$), the shearing does not change considerably due to the effect of the viscosity (higher temperatures) and the Reynolds number of the outer jets (Re_{H_2}<1000). These observations are analysed next with the calculation of the initial conditions for the reactive case (see table 6.5).

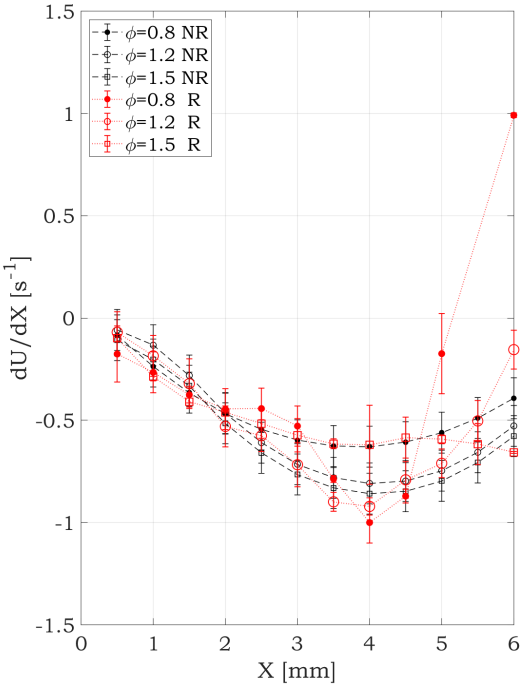

Figure 6.27: Velocity gradients at the crossed-plane Y=0

Table 6.5 provides the initial conditions calculated based on the self-similarity between the non-reactive and reactive cases. The ratio between flow rate and velocity on the centreline ($U_{0,O_2}/U_C$) is considered identical for both cases. It is confirmed the laminar jet characteristics for $\phi = 1.2$ and $\phi = 1.5$. $\phi = 0.8$ shows a behaviour closer to turbulent jet regime. It is apparent that the increase in the temperature due to the increase in ϕ decreases Re, which relaminarise the jet as in section 6.2. Therefore, the turbulence fluctuations and the shearing decreases with the increase on ϕ. In the next section the flow development along Y-axis is analysed to study the influence of the central jet on the flow development.

Cette thèse est accessible à l'adresse : http://theses.insa-lyon.fr/publication/2022LYSEI044/these.pdf
© [K. Utria Salas], [2022], INSA Lyon, tous droits réservés

Parameter	Non-Reactive	Reactive
	8.7	10.02
$U_{O_2,c}$ [m/s]	5.8	7.33
	4.64	5.80
	6	6.91
U_C [m/s]	4.2	5.31
	3.2	4
T(K)	300	418
ρ $[kg/m^3]$	1.284	0.93
v $[m^2/s]$	1.61E-05	2.91E-05
	4856.87	2241.48
Re	3200	1700
	2600	1300
	3349.57	1545.85
Re_C	2400	1200
	1800	900

Table 6.5: Initial conditions of the O_2 central jet

Changing the inlet velocity of the central jet (U_{0,O_2}) influences more considerably the initial conditions as compared to the results of constant U_{0,O_2}. The instabilities at the nozzle outlet depend on the Reynolds numbers, the equivalence ratio (in the case of reactive flow) and the parameters of the coaxial flow. Higher temperatures due to the increase in ϕ decreases Re, which relaminarise the jet, decreasing the turbulence fluctuations and the shearing between the fuel and oxidiser jets.

6.3.2 Flow development

The mean velocity has been analysed at the centreline for the three operation conditions in non-reactive flow and reactive flow, and their behaviours are depicted in figure 6.28. For the non-reactive case, the highest velocities are found for Y<20mm with $\phi = 0.8$. The extension of the maximum velocity level increases with the decrease of U_{0,O_2}, indicating that the buoyancy effects are more significant with low injection velocities of the central jet. For the reactive case, the maximum velocity is constant until $Y \cong 80$mm ($\cong 15D_{O_2}$).

The decay rate seems to be the same for $\phi = 1.2$ and $\phi = 1.5$. As observed on the right, the laminar behaviour is spread for the reactive case ($\phi = 1.2$ and $\phi = 1.5$), due to two reasons:
(i) As for the previous case, the coaxial jet spreads the laminar behaviour of the flame

Cette thèse est accessible à l'adresse : http://theses.insa-lyon.fr/publication/2022LYSEI044/these.pdf
© [K. Utria Salas], [2022], INSA Lyon, tous droits réservés

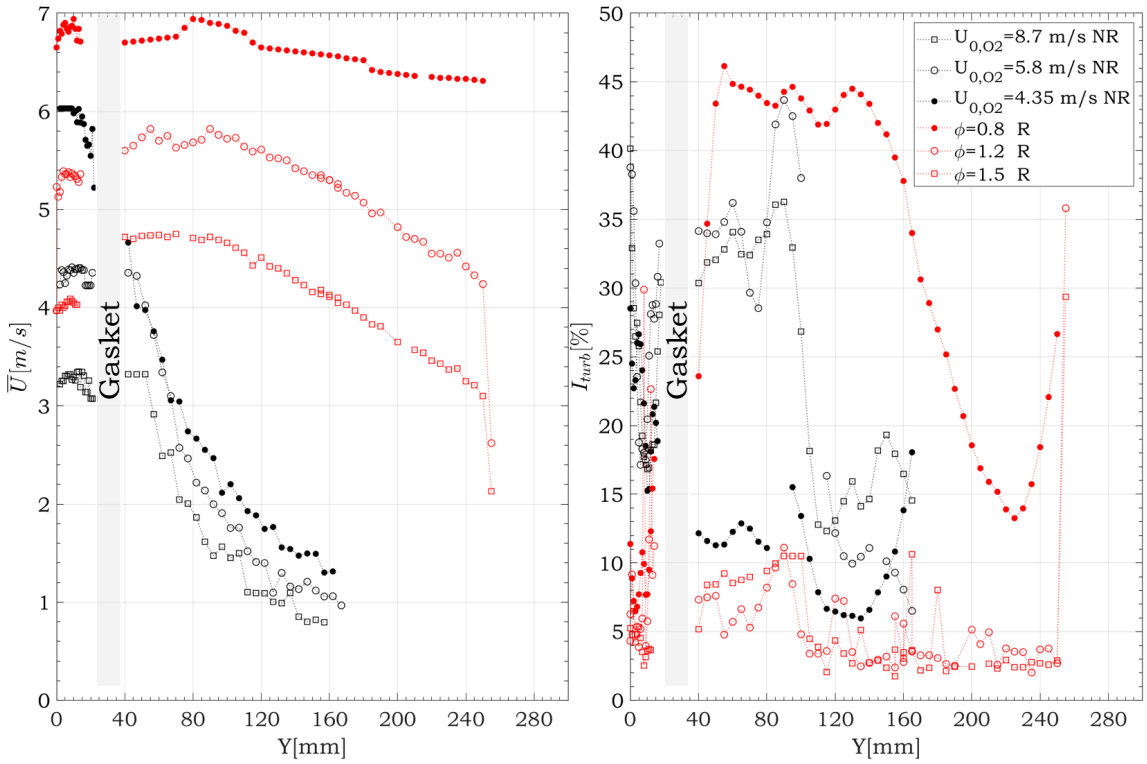

Figure 6.28: Profiles of the mean velocity along the centreline Y-axis for constant U_{0,H_2} at $X = 0$

and,
(ii) the high temperatures increase the kinematic viscosity hence the Reynolds numbers diminish.

In addition, the dimensionless longitudinal velocities at the centreline have been analysed in figure 6.29. As before, a smooth filter was performed to the curves on the right for the non-reactive case and $\phi = 0.8$, the results have a relative error of 6%.

As observed, the non-reactive flows behave similarly, and after $12D_{O_2}$ the curves overlap. In contrast, for the reactive case, $\phi = 0.8$ agrees with the classical coaxial jet behaviour obtained by Labor (2003) (curve in blue). As for $\phi = 1.2$ and $\phi = 1.5$, the decay rate increases with the increase in ϕ.

For the non-reactive case, the flow behaves as a turbulent jet after $9D_{O_2}$ where the relative turbulences increases faster for the three conditions, this result corresponds to self-similarity.

For the reactive flow, the turbulence fluctuations on the right show the turbulent jet characteristics of $\phi = 0.8$ and the laminar behaviour of $\phi = 1.2$ and $\phi = 1.5$ after $15D_{O_2}$ the turbulence fluctuations are the same. Although, the temperature increases the turbulent behaviour for $\phi = 0.8$ is the results of the high central inlet velocity ($Re > 3000$),

Cette thèse est accessible à l'adresse : http://theses.insa-lyon.fr/publication/2022LYSEI044/these.pdf
© [K. Utria Salas], [2022], INSA Lyon, tous droits réservés

the effects of the viscous forces under these injection conditions are less significant than the aerodynamic effects of the coflow. At $Y = 20D_{O_2}$, the turbulence intensities decreases (this is analysed in the following) until $Y = 35D_{O_2}$ where an increase in the turbulence can be observed. This effect is related to jet oscillations at the confinement outlet and the lower temperatures of these zones.

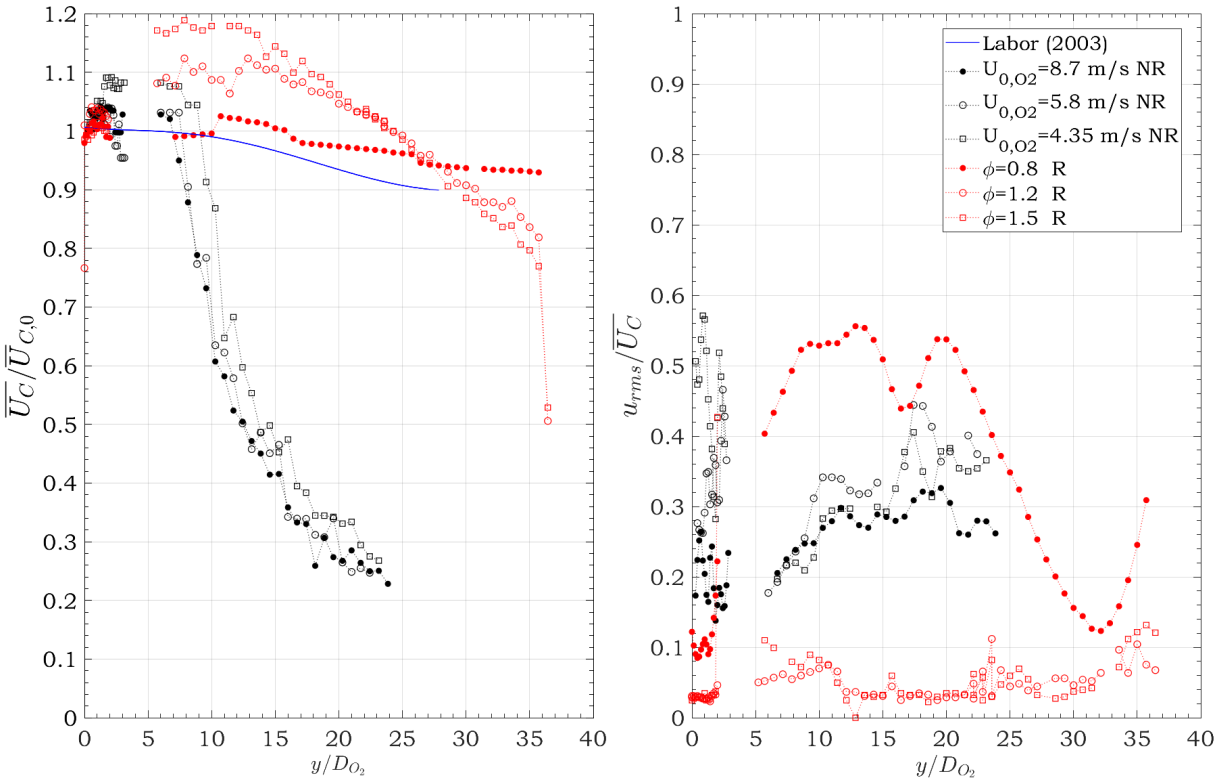

Figure 6.29: Decay of centreline mean velocity for constant U_{0,H_2} at $X = 0$

The buoyancy effects are analysed accordingly the turbulent kinetic energy in figure 6.30. The non-reactive case shows similar behaviour for all the three conditions. As expected, the results are in agreement with the theory analysed in the previous section (see section 6.2.2.1), which indicates that the buoyancy forces affect the flow development until the maximum turbulent kinetic energy (Y=$5D_{O_2}$) (Sautet, 1992; Pagé et al., 1998, 1999; Harran et al., 1996).

As for the reactive case, the flow development is impacted by the buoyancy effects at the highest ϕ, which have the lowest U_{O_2}. These conditions also reported the highest I_{OH^*} which indicates a higher local heat release rate. $\phi = 0.8$ shows a region of high turbulent kinematic energy that decreases at $Y \cong 20D_{O_2}$, the velocities are lower from this Y-position and the buoyancy effects can influence in the flow development.

Furthermore, a peak at $Y \cong 21D_{O_2}$ is observed for the $\phi = 1.2$ and $\phi = 1.5$ which confirms the impact of the buoyancy effects before the maximum turbulent kinetic energy. The

Cette thèse est accessible à l'adresse : http://theses.insa-lyon.fr/publication/2022LYSEI044/these.pdf
© [K. Utria Salas], [2022], INSA Lyon, tous droits réservés

peak a $Y \cong 10D_{O_2}$ is related to the flame closure (y_i) and it is analysed in the influence of the reaction zone.

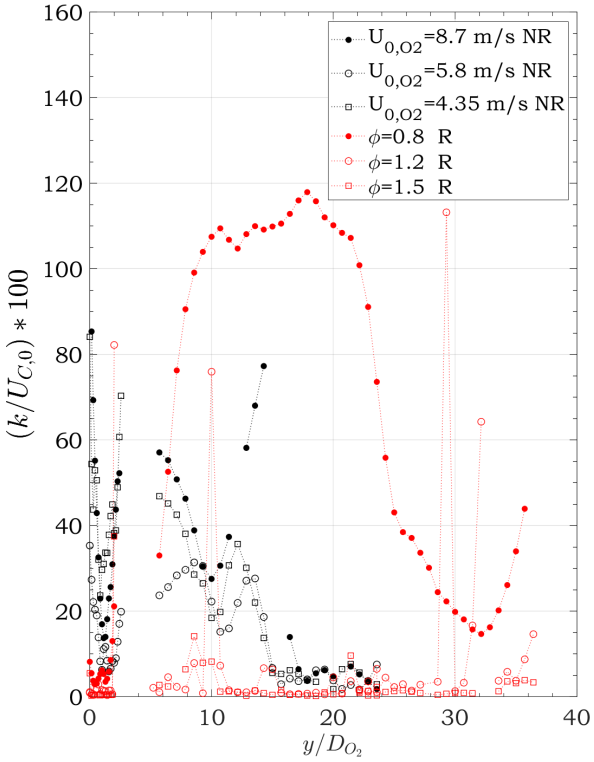

Figure 6.30: Evolution of the turbulent kinetic energy at the centreline, $k = \frac{1}{2}\left(\overline{u'}^2 + \overline{v'}^2\right)$

The impact of the peripheral jets is analysed in figure 6.31. The profiles of the longitudinal mean velocities at different crossed-section are provided. The effect of the coaxial flow seems to be less present in the flow structure. For Y=10mm, the coaxial flow is only observed for $\phi = 1.5$, corresponding to the lowest O_2 inlet velocity. For the rest of the conditions, the flow appears to be a single jet. The turbulence fluctuations present low values at the burner nozzle on the left.

Contrarily, at Y=40mm there are the highest levels. This position corresponds to the change of crossed-section geometry, causing this increase in turbulence fluctuations. These are more relevant in the flow edges downstream (in the confinement) for $\phi = 0.8$, related to the shear layer between the hot gas and the stagnant cold air surrounding the flame. For $\phi = 1.2$, this effect is observed at Y=95mm downstream the values are not significant. For $\phi = 1.5$, this behaviour is not found owing to the high temperatures and viscosities that contribute to the laminar behaviour. There is a peak at Y=40mm, which should be related to the change on the crossed section.

Cette thèse est accessible à l'adresse : http://theses.insa-lyon.fr/publication/2022LYSEI044/these.pdf
© [K. Utria Salas], [2022], INSA Lyon, tous droits réservés

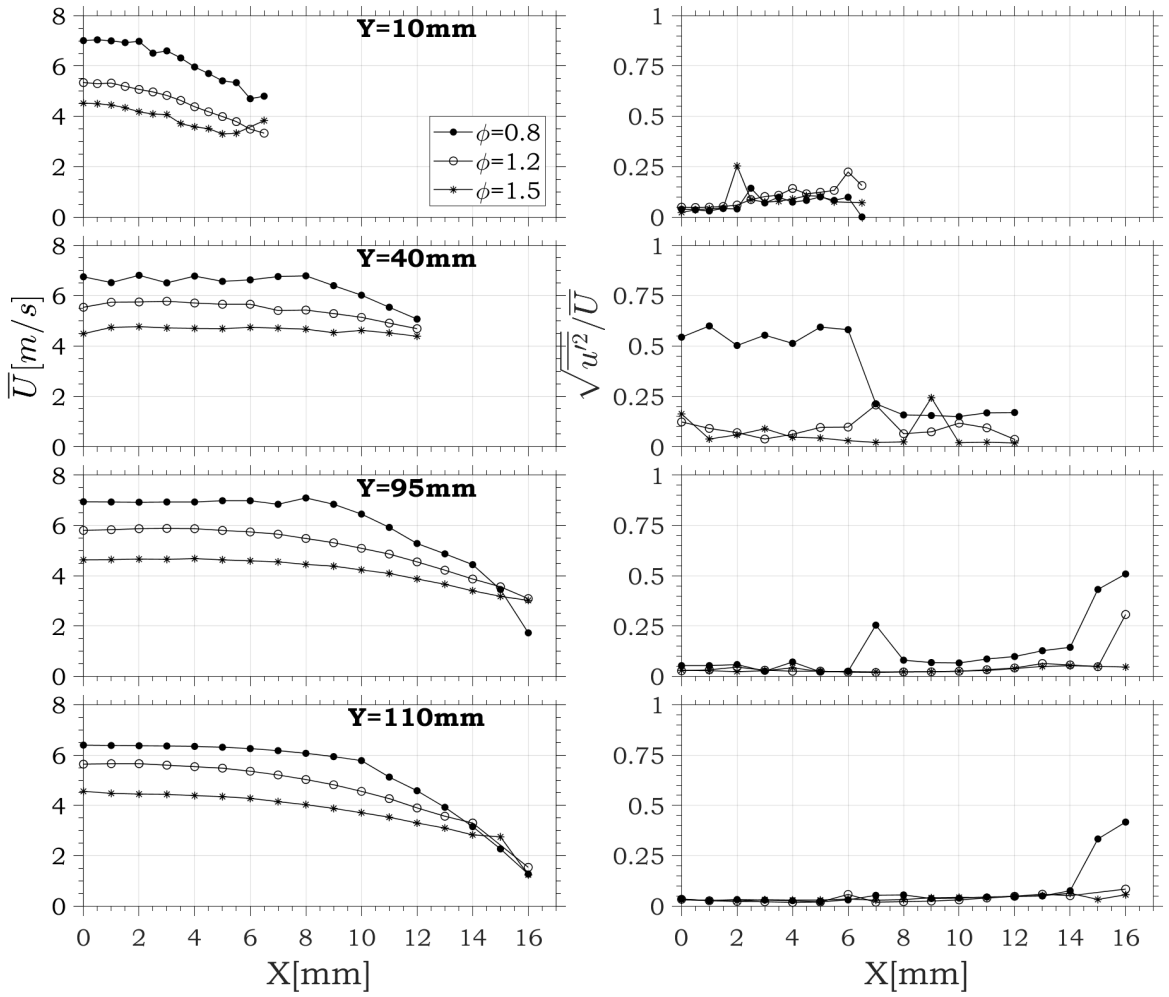

Figure 6.31: Profiles of the mean longitudinal velocity along X-axis for constant U_{0,H_2} at crossed-planes, Y=10, 40, 95, 110 mm

In figure 6.32 the flow development is analysed for the position X=5 mm (the jet shear layer). A significant diminution on the jet velocity is observed at $Y = 12D_{O_2}$ for $\phi > 1$, which could indicate the reverse flow that can be found in coaxial flow at the intermediate merging zone. Because in $\phi = 0.8$ the central jet velocity is higher, this position is found downstream, $Y = 15D_{O_2}$. At these positions the turbulent fluctuation levels start to increase, indicating in the case of $\phi = 0.8$ the transition to a turbulent flow. Velocities do not decrease along Y-axis at this X-position, due to the presence of the reaction zone, analysed in the following. The increase in the turbulent fluctuation for $\phi > 1$ are also related to the end of the reactive flow.

Cette thèse est accessible à l'adresse : http://theses.insa-lyon.fr/publication/2022LYSEI044/these.pdf
© [K. Utria Salas], [2022], INSA Lyon, tous droits réservés

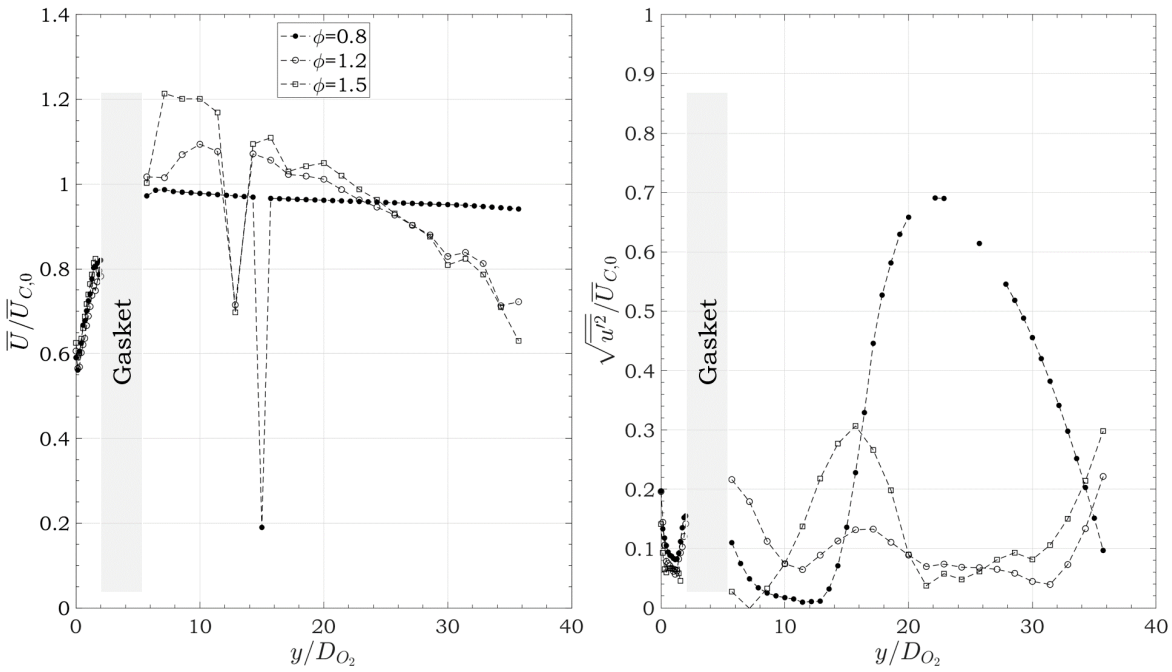

Figure 6.32: Profiles of the mean longitudinal velocity along Y for constant U_{0,H_2} at X=5mm

The OH* emissions intensities, longitudinal mean velocities and the turbulence fluctuations at the centreline (X=0) are depicted in figure 6.33 in order to analyse the effect of the reaction zone on the flow development. As observed, the low intensities for $\phi = 0.8$ report high turbulence fluctuations and constant high velocities. As mentioned, the effect of the coaxial jets and the buoyancy effect seems to be the explication for this phenomenon. Due to the high turbulent fluctuations reported, the coaxial flow is more significant for this operating condition. Since the central reaction zone is not present for this condition, the temperatures are lower. Unlikely, for the highest ϕ, the reaction zone presence seems to decrease the turbulence intensities due to the buoyancy effects and temperature augmentation.

Furthermore, the central reaction zone position change does not seem to affect the flow structure; no significant changes are reported in the longitudinal velocity or the turbulence fluctuations. Besides, the transversal component is close to zero. This indicates that the reaction zone promotes the vertical flow trajectory; the relative turbulence is almost null for $\phi > 1$ and this is lower than 10% for $\phi = 0.8$, confirming that the reaction zone contributes to the vertical flow structure. At the same time, the point of the flame closure increases the turbulence fluctuations ($\overline{v'}/\overline{U}_{C,0}$) for $\phi = 1.2$ ($Y = 14D_{O_2}$) and $\phi = 1.5$ ($Y = 9D_{O_2}$). There is also a peak at $Y = 2D_{O_2}$ which is related to the change on the crossed section.

Cette thèse est accessible à l'adresse : http://theses.insa-lyon.fr/publication/2022LYSEI044/these.pdf
© [K. Utria Salas], [2022], INSA Lyon, tous droits réservés

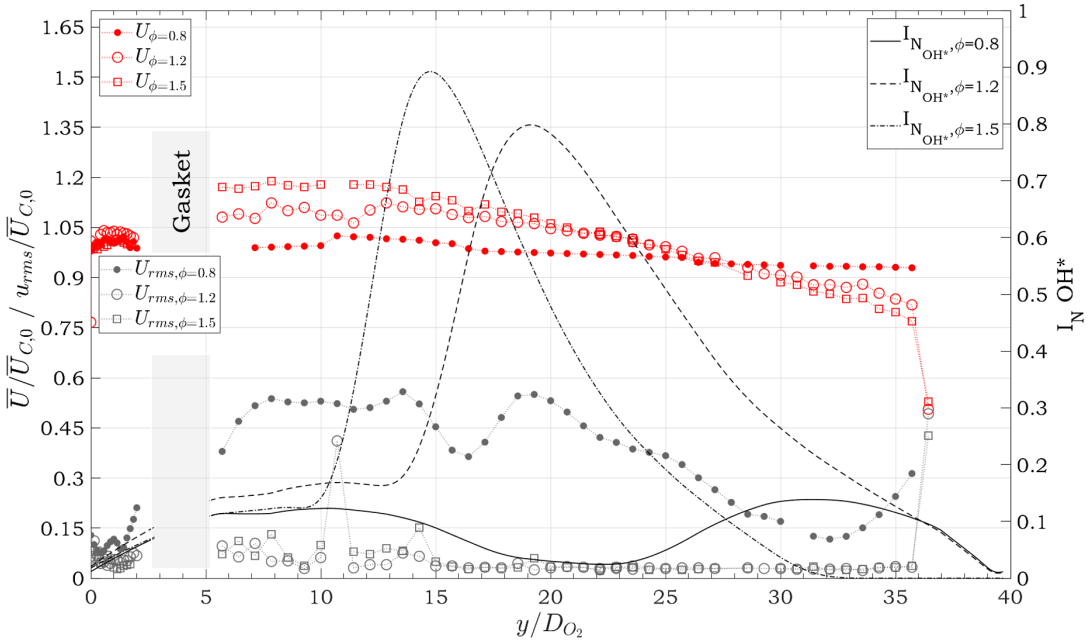

(a) Profiles of the mean longitudinal velocity and OH* emission intensities

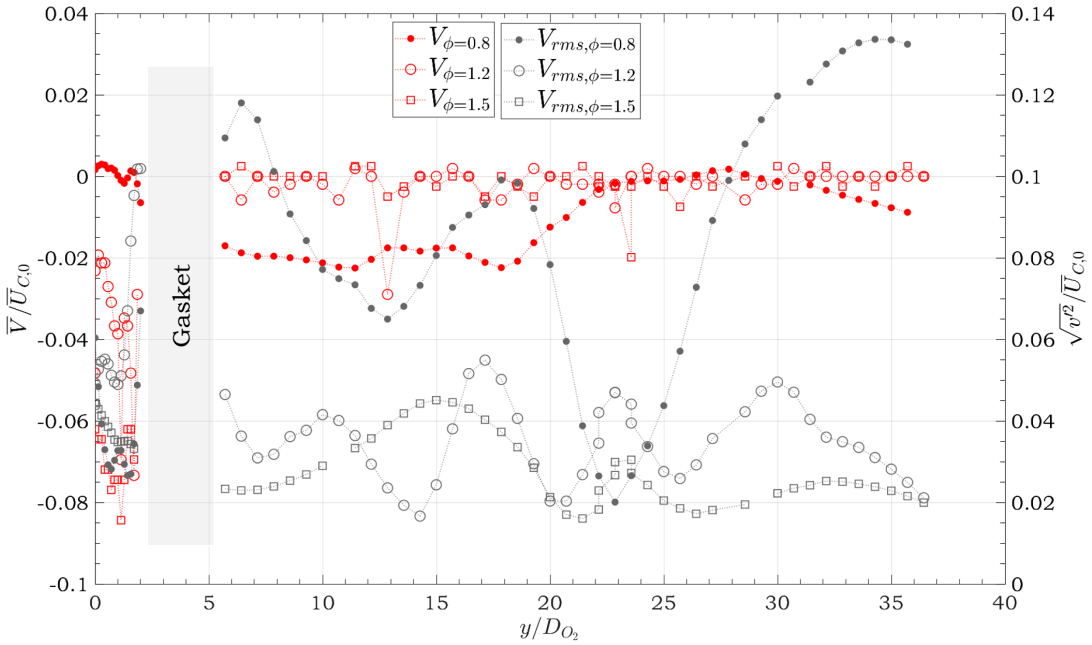

(b) Profiles of the mean transversal velocity and OH* emission intensities

Figure 6.33: Analysis of the reaction zone influence on the flow development for constant U_{0,H_2} at $X = 0$

In figure 6.34, the reaction zone on the sides reported the same behaviour as in section 6.2. The high temperatures in the reaction zone cause the high-velocity levels at this position. Within the reaction zone for $\phi > 1$, the turbulence intensities are low, which increase for $I_{N,OH^*} < 0.5$, confirming the influence of combustion in the transformation from coaxial jet to single jet behaviour and the influence of the high temperatures. At this Y-position ($I_{N,OH^*} = 0.5$) for $\phi > 1$, the longitudinal velocity decreases.

Cette thèse est accessible à l'adresse : http://theses.insa-lyon.fr/publication/2022LYSEI044/these.pdf
© [K. Utria Salas], [2022], INSA Lyon, tous droits réservés

Contrarily $\phi = 0.8$ depicts high-velocity levels farther downstream, as well as turbulence intensities due to its coaxial jet characteristics. This behaviour can be explained because the combustion is not as strong as for $\phi > 1$, since the OH* intensities observed are lower for this condition.

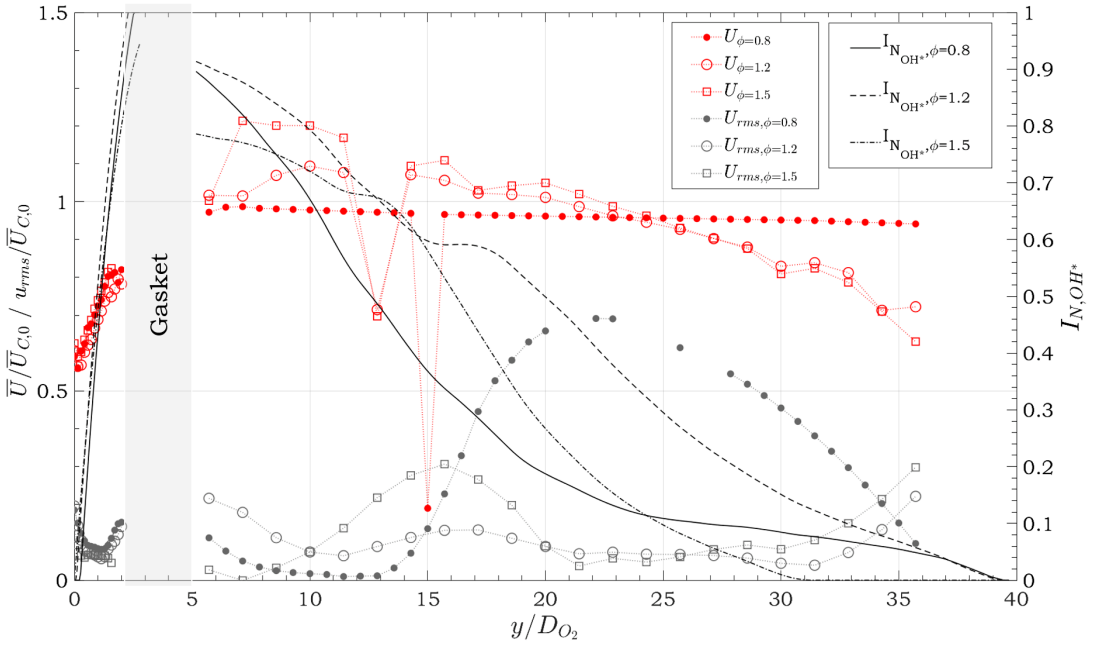

Figure 6.34: Analysis of the reaction zone influence on the flow development for constant U_{0,H_2} at X=5mm. Profiles of the mean longitudinal velocity

Regarding the self-similarity, this is achieved at $Y = 1D_{O_2}$ for the mean longitudinal velocity, at the central part (see figure 6.35). As before, there are some differences at the edges, related to the buoyancy effects, as mentioned the reaction zone increases the effect of buoyancy, the increase in ϕ show major difference with the Gaussian behaviour of the self-similarity. Moreover, at the burner nozzle, these differences are related to the change on the crossed-section. In contrast, the turbulence fluctuations do not seem to show the self-similarity for the range observed, figure 6.36.

Cette thèse est accessible à l'adresse : http://theses.insa-lyon.fr/publication/2022LYSEI044/these.pdf
© [K. Utria Salas], [2022], INSA Lyon, tous droits réservés

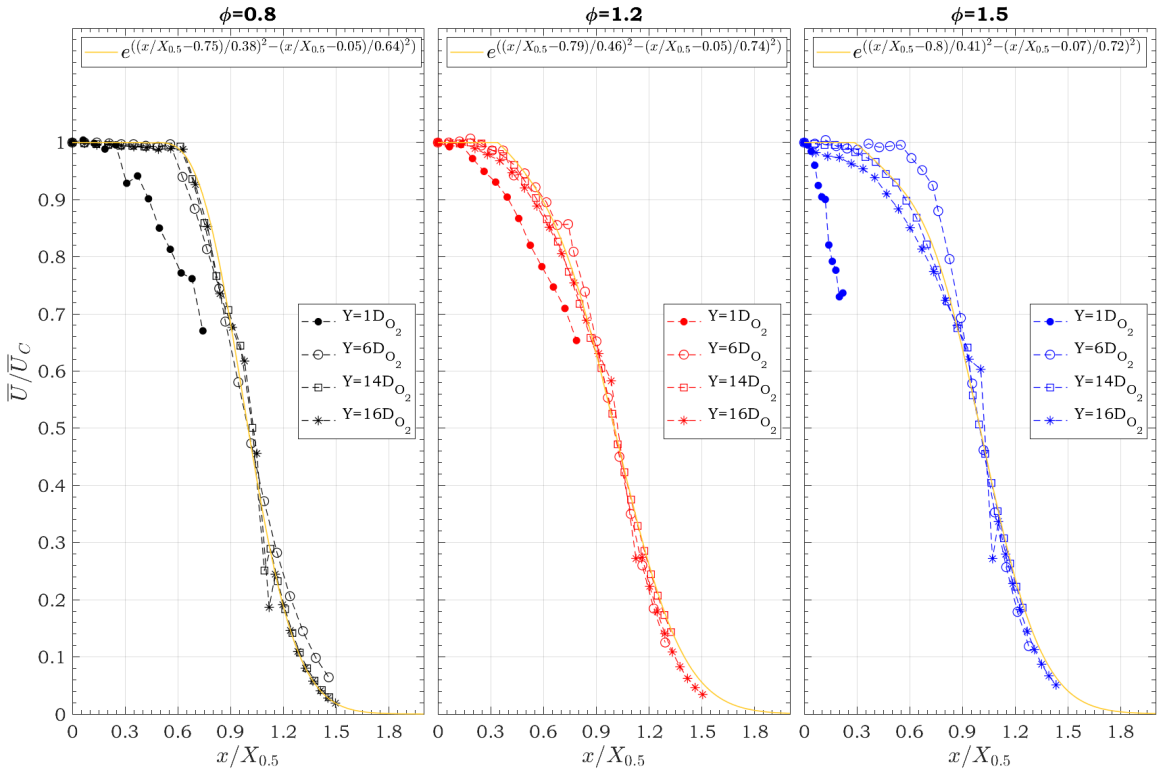

Figure 6.35: Longitudinal evolution of the value of $X_{0.5}$ at the confinement

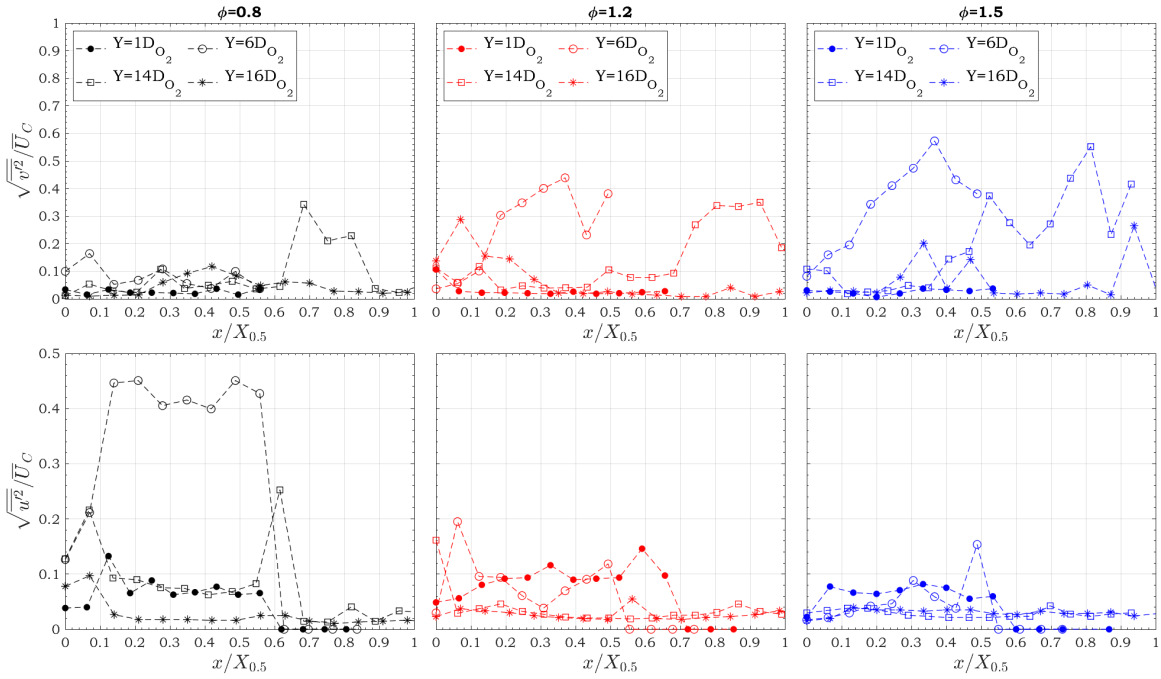

Figure 6.36: Crossed section profiles of turbulence relative intensities at the secondary development zone

In addition, higher $X_{0.5}$ are found for these cases. The increase in ϕ enhances the development of the secondary flow as observed in figure 6.37. In **zone 1**, $\phi = 0.8$ shows values close to the obtain by Labor (2003). For $\phi > 1.2$ the values are similar, and are almost the

Cette thèse est accessible à l'adresse : http://theses.insa-lyon.fr/publication/2022LYSEI044/these.pdf
© [K. Utria Salas], [2022], INSA Lyon, tous droits réservés

same as observed in table 6.6. In **zone 2**, for $\phi = 0.8$ the flow behaves as a pure coflow jet and the position of $X_{0.5}$ does not seem to evolve. For $\phi = 1.2$ and $\phi = 1.5$ after the change on the crossed-section the flow develops in parallel. $\phi = 1.2$ reports slope values close to the results obtained by Labor (2003) (see table 6.6).

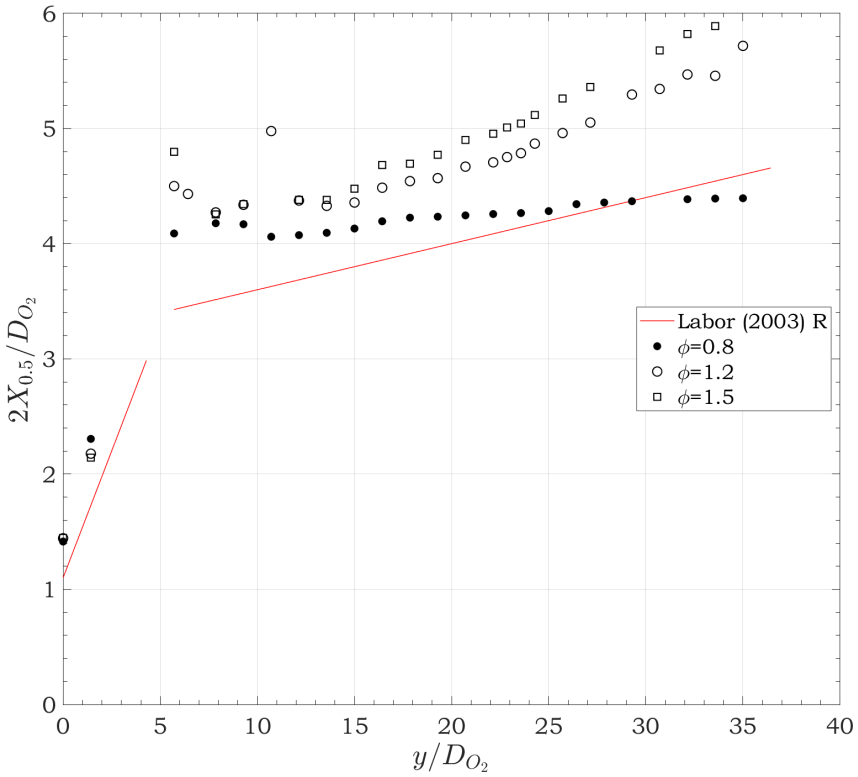

Figure 6.37: Longitudinal evolution of the value of $X_{0.5}$

	Zone 1		**Zone 2**	
ϕ	Flow Establishment		Self-similarity zone	
	a	b	a	b
0.8	0.46	1.52	0.01	3.99
1.2	0.54	1.43	0.04	3.89
1.5	0.59	1.38	0.07	3.57

Table 6.6: Linear Equation of $X_{0.5}$ $(2X_{0.5}/D_{O_2} = ay/D_{O_2} + b)$

Figure 6.38 shows the influence of the reaction zone on the secondary flow development. As observed, $X_{0.5}$ is impacted by the size of the reaction zone, at **zone 1** (flow establishment), the value of $X_{0.5}$ follows the I_{N,OH^*} contour of 0.023. The values are higher for $\phi = 1.5$, as observed this conditions reports the smallest reaction zone. It can also be observed that there is an overlapping for both $X_{0.5}$ and OH* emissions until $Y = 12D_{O_2}$.

Cette thèse est accessible à l'adresse : http://theses.insa-lyon.fr/publication/2022LYSEI044/these.pdf
© [K. Utria Salas], [2022], INSA Lyon, tous droits réservés

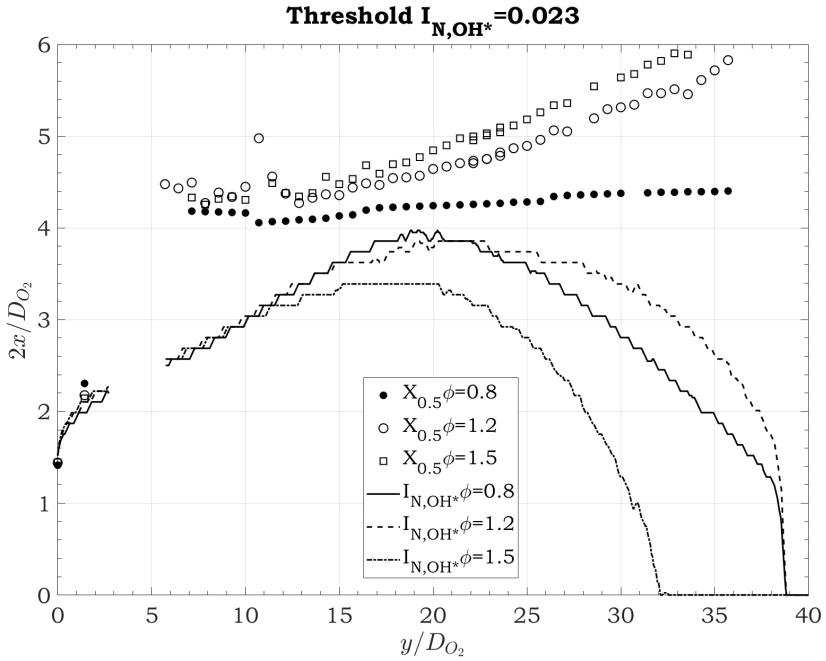

Figure 6.38: Secondary flow development vs OH* emission intensities

6.3.3 Conclusions

The impact on the flow development varying the O_2 inlet velocity was analysed. The different mechanisms that affect the flow development were exposed. Finding that the type I flame presents turbulent characteristics and coaxial jet behaviour. The two other types are more influenced by the mechanisms involved during the combustion, showing laminar jet characteristics.

Furthermore, the longitudinal velocity gradient increased with U_{O_2}; this increase is more significant compared to that observed in the variation of U_{H_2}.

The buoyancy effects are more significant with low injection velocities of the central jet, higher equivalence ratios. This phenomenon was also exposed with the self-similarity found faster than expected (at $Y = 6D_{O_2}$), but according to other researches.

In addition, the position of the reaction zone does not seems to affect the flow structure. There are not significant changes reported neither in the longitudinal velocity nor the turbulence fluctuations. Nonetheless, the point of the flame closure increases the turbulence fluctuations for $\phi = 1.2$ and $\phi = 1.5$.

Cette thèse est accessible à l'adresse : http://theses.insa-lyon.fr/publication/2022LYSEI044/these.pdf
© [K. Utria Salas], [2022], INSA Lyon, tous droits réservés

6.4 Heat release distribution in a Verneuil furnace

In order to have a more global comprehension of the heat transfer influence, temperature measurements of the flame were carried out. Their characterisation provides important data regarding the understanding of the phenomena developing in the flow and in the reaction zone.

However, the means of investigation are limited to intrusive techniques (e.g. thermocouples). Indeed, the limitations are significant because the oxygen/hydrogen diffusion flame generates very high temperatures in the reaction zone. Gaydon and Wolfhard. (1953) proposes an adiabatic temperature value for a 3083K (2810°C) hydrogen/oxygen stoichiometric mixture. Nonetheless, Takagi et al. (1996) compared the temperatures between NDF and IDF and found that the latter have higher temperatures than the adiabatic equilibrium.

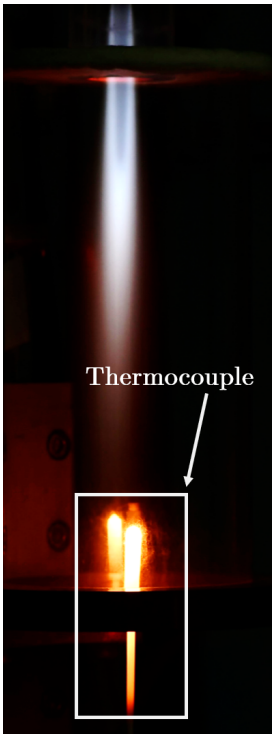

Figure 6.39: Thermocouple used to temperature measurements

Due to the high levels of temperatures (>2800°C), the measurements are complex. Therefore, this study measured temperature at the edge of the centreline of the flame as show in figure 6.39 using coated thermocouple type R (Platinum Rhodium-13% and Platinum), the wire diameter was 0.5 mm. A system of data acquisition using LabView was developed to record the average temperature acquired with a frequency of 1000 sample/s. The experimental temperatures reported correspond to the mean value of the samples (T_m), that were performed 5 times with a standard deviation of $\pm 1°C$.

6.4.1 Temperature distribution in IDF

The centreline temperature in IDF usually increases rapidly with the increase in the axial position, indicating that the downstream high-temperature combustion zone gradually heats the cold oxidiser inside the potential core. According to Zhen et al. (2013) the flame structure of the IDF comprises four zones regarding the temperature distribution (see figure 6.40):

Cette thèse est accessible à l'adresse : http://theses.insa-lyon.fr/publication/2022LYSEI044/these.pdf
© [K. Utria Salas], [2022], INSA Lyon, tous droits réservés

- Zone 1 is a base zone in which a high-velocity central oxidiser entrains the fuel jet. The fuel entrainment occurs at low temperatures due to the lack of chemical reactions. Besides, within this zone, a cool core with temperatures below 200°C is found, this corresponds to the potential core of the oxidiser jet.
- Zone 2 is a mixing zone where the mixing of fuel and air is completed. As chemical reactions evolve above the entrainment region and in the mixing zone, the flame temperature gradually increases, in contrast the temperature at the center of the flame is still the lowest due to the oxidiser excess near the flame axis. Finally , the mixing process of supplied oxidiser and fuel is completed before the flame reaches the main reaction zone.
- Zone 3 is a reaction zone (central reaction zone) with the highest flame temperature due to the intense heat released by the reaction.
- Zone 4 is a post-combustion zone associated with the cooling of hot gases due to the entrainment of ambient air. As the axial distance ascends into the post-combustion region, the heat released becomes less and simultaneously, entrained cold ambient air dilutes and cools the combustion products.

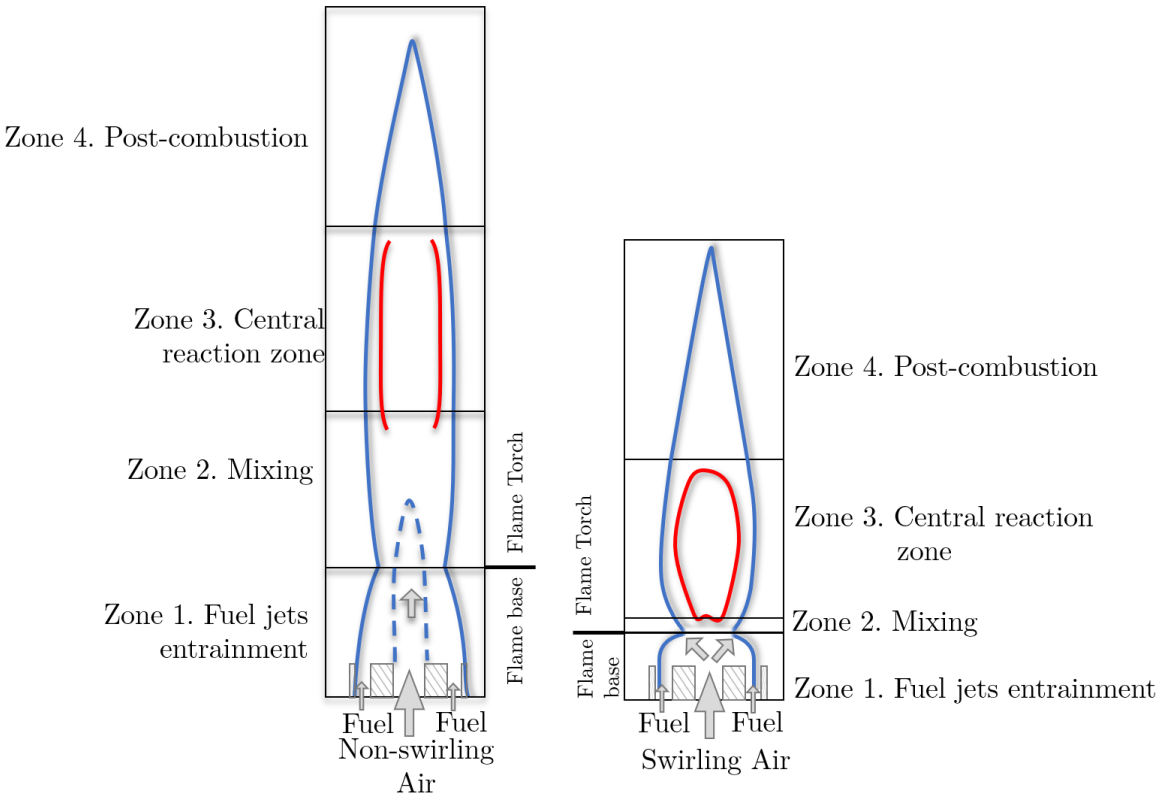

Figure 6.40: Temperature distribution in classic IDF, based on the results in Zhen et al. (2013)

Cette thèse est accessible à l'adresse : http://theses.insa-lyon.fr/publication/2022LYSEI044/these.pdf
© [K. Utria Salas], [2022], INSA Lyon, tous droits réservés

Zhen et al. (2013) and Patel and Shah (2019) compared IDF with non-swirl and swirl. They found that for both cases, the temperature follows the same trends. However, the maximum temperature shifted closer to the burner nozzle for swirl jets due to the recirculation at the outlet. The swirl configuration increases the mixing between the surrounding fluid and breaks the inner potential core. In the case of non-swirl, the high-temperature zone is spread and behaves as a premixed flame (Zhen et al., 2013). In addition, Zhen et al. (2011) also observed that the length of the nozzle impact considerably the distribution of the temperature. For a shorter nozzle, the temperature at the post-combustion region decreases faster than for a longer nozzle (Zhen et al., 2011).

Furthermore, Sze et al. (2006) found that temperatures for multi-fuel-jet flames are higher than 170°C compared to single fuel jet flames. The former have premixed and non-premixed features, the latter presents non-premixed characteristics principally, and the maximum temperatures are found on the sides of the flame. Within this context, the temperature distribution for the current configuration is underlined by certain characteristics of the exposed above. The effect of recirculation due to the difference in the heights of the fuel and oxidiser outlet will impact temperature distribution. Furthermore, the characteristic of high combustibility of hydrogen promotes exothermic reaction that expands the combustion products speedily. Therefore, a large amount of heat energy is expected to be release during combustion, enhancing the flow velocity and reducing the recirculation flow in the internal recirculation zone.

Another parameter that influences the temperature distribution is the Lewis number (L_e) (Katta et al., 1994; Cuenot and Poinsot, 1996; Labor, 2003), a dimensionless ratio that compares the phenomena of thermal diffusivity to mass diffusivity, defined in equation 6.8.

$$Le = \frac{\text{thermal diffusion rate}}{\text{mass diffusion rate}} = \frac{\alpha}{D} \tag{6.8}$$

where α is thermal diffusivity in $[m^2/s]$ and D is the mass diffusivity in $[m^2/s]$. A Lewis number of unity indicates that thermal boundary layer and mass transfer by diffusion are comparable, and temperature and concentration boundary layers almost coincide with each other. Mass diffusivity or diffusion coefficient is a proportionality constant between the molar flux due to molecular diffusion and the gradient in the concentration of the species (or the driving force for diffusion). The interest in this study is that its variation highlights evidence of very different predominant diffusion phenomena depending on the area observed, then influencing the temperature field.

Figure 6.41 illustrates the Lewis numbers for oxygen and hydrogen as function of the temperature and for different values of the mass mixture coefficient n_s in an oxygen-

Cette thèse est accessible à l'adresse : http://theses.insa-lyon.fr/publication/2022LYSEI044/these.pdf
© [K. Utria Salas], [2022], INSA Lyon, tous droits réservés

hydrogen mixture (Sacadura, 1997). As observed, for rich injection conditions of hydrogen is majority, the value of the Lewis number is located in the around 0.2. In contrast, the Lewis number of oxygen is greater than 1 with a value between three and four. It also appears that the temperature does not influence the values of the Lewis number. Therefore, the presence of hydrogen is the main responsible for its evolution. Indeed, the heat transfer in the flow is linked to gases present in the combustion, affecting the temperature distribution.

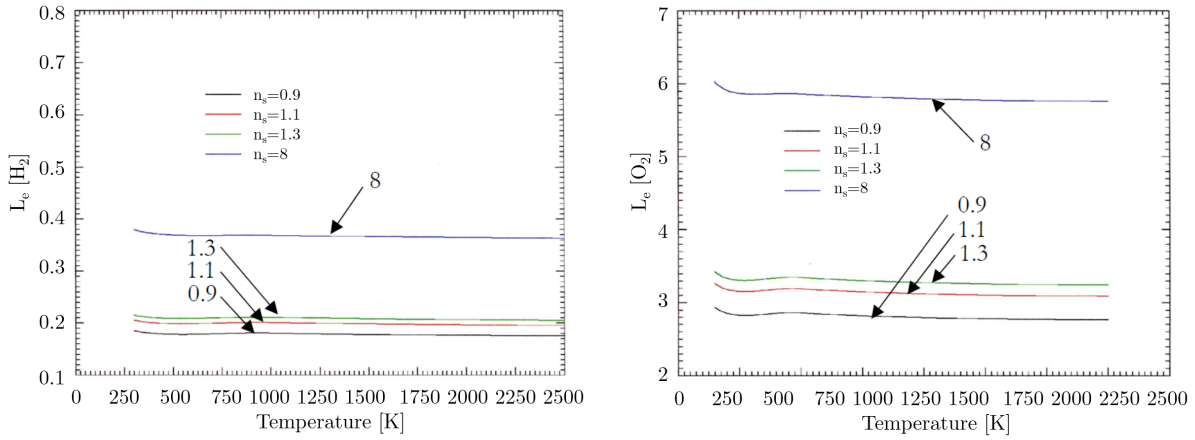

(a) H_2 (b) O_2

Figure 6.41: Evolution of Lewis number in function of the temperature for different mass mixture coefficient n_s (Sacadura, 1997)

Katta et al. (1994) proposed for a classic H_2/air diffusion flame that the maximum temperature is located not at the end of the flame but close to the nozzle outlet for a hypothetical non proved case of $Le = 1$. Accordingly to this study, this effect appears due to two different behaviours depending on the area observed. Close to the injection area, the main direction flow is parallel to the reaction zone, where the lowest heat diffusion compared to molecular diffusion is found; thus, the temperature increases. Contrarily, further downstream, the reaction zone becomes concave concerning the direction of fuel flow (configuration with fuel in the centre), initiating two competing effects. At first, the curvature causes a "Convergence" of heat inside the flame, which results in a temperature increase. Differently, owing to the diffusion of fuel, this same curvature will swell a decrease in temperature. When the Lewis unity hypothesis is obtained, these two effects cancel out, and the temperature approaches to the adiabatic temperature. In contrast, when $Le < 1$, the effect of curvature on mass diffusion is predominant, causing cooling. Thus, the maximum temperature decreases to the end of the flame.

Furthermore, Cuenot and Poinsot (1996) found that for $Le_o = 0.6$, the adiabatic flame temperature is not impacted by Le_F, whereas it is the case for higher values of Le_o. For small Le_F, the amount of fuel is insufficient at the flame, decreasing with Le_F–however, the diffusion speed increases, leading to smaller flame temperatures and shifting its dis-

Cette thèse est accessible à l'adresse : http://theses.insa-lyon.fr/publication/2022LYSEI044/these.pdf
© [K. Utria Salas], [2022], INSA Lyon, tous droits réservés

tribution close to the nozzle.

6.4.2 Temperature distribution prediction in a Verneuil furnace

In the following the heat release distribution is described through temperature distribution in order to better understand the mechanism developing in the flow and the reaction zone. The notable difference between the gases characteristics influence the thermal interactions within the reaction zone significantly. The heat produced in this region heats the two flow zones located at the proximity, leading to different behaviour depending on the side of the reaction zone observed (O_2 or H_2).

For the current study, the Lewis numbers of each species present in the H_2-O_2 combustion reaction show that only oxygen and water vapour have values close to or greater than 1. Thereby, mass diffusion is predominant over the heat diffusion on the fuel side of the reaction and inside the flame.

As discussed in section 4.2.2, a linear regression can be used to predict the temperature distribution from the OH^* chemiluminescence. In order to predict the temperature distribution of this unique flame, linear regressions were used based on the experimental results.

Figure 6.42 shows the measured temperatures (T_m) and the predicted temperatures (T_{OH^*}) along with the OH^* emission intensities. The maximum temperature was assumed to be 3000°C (3300K) according to Gaydon and Wolfhard. (1953) and Takagi et al. (1996).

The predicted results concord with Patel and Shah (2019) for the flames with 80% hydrogen. This study obtained temperatures of inverse diffusion flames with non-swirl and swirl with addition of H_2. They observed that the high combustibility of the hydrogen shifts the centreline maximum temperature upstream. As observed, with the current results the increase in hydrogen (ϕ) shows the shift in the maximum temperature. These findings indicate a good prediction of the temperature distribution, and it could be used as an indicator of heat release distribution in the flow.

Regarding the increase in O_2 injection, it can be observed in figure 6.43 that the reaction zone shifts downstream due to the excess of O_2. The mixing is fast on the side, and all the fuel is burnt within this zone. The increase in ϕ decreasing O_2 improves the mixing, and the temperature at the centreline increases downstream. As noticed, since the inner potential core decreases, the mixing is enhanced as the combustion rates. With the increase in ϕ, the central reaction zone appears and moves closer to the O_2 nozzle with the increase in H_2. The impact of the O_2 injection is more significant because the

Cette thèse est accessible à l'adresse : http://theses.insa-lyon.fr/publication/2022LYSEI044/these.pdf
© [K. Utria Salas], [2022], INSA Lyon, tous droits réservés

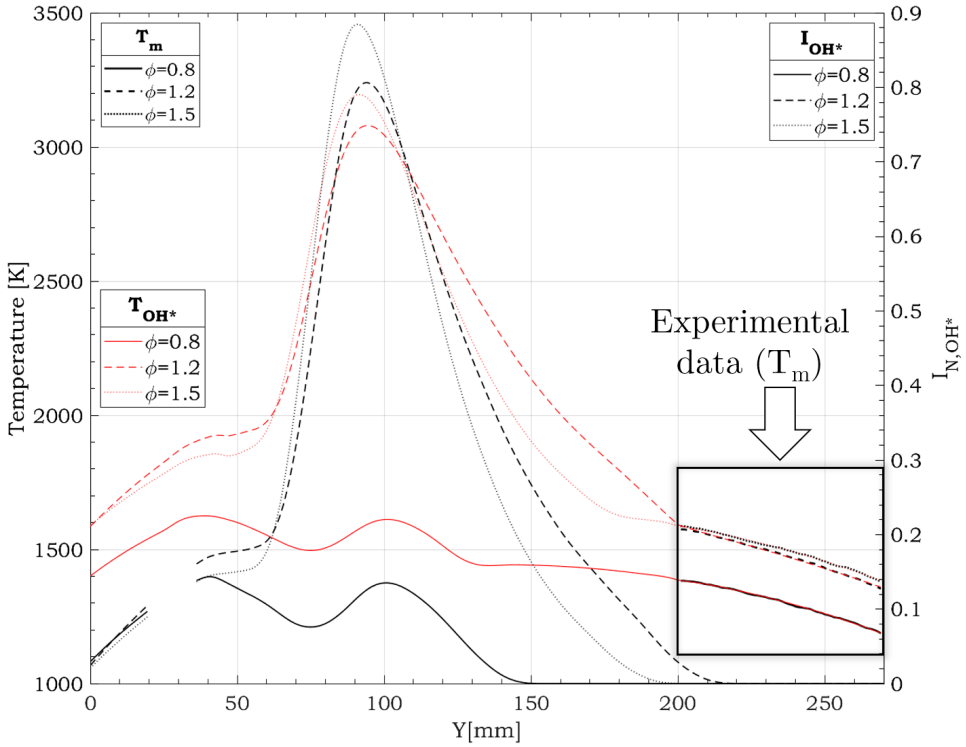

Figure 6.42: Temperature distribution at the centreline U_{0,H_2}

flow is a central jet dominant ($r_u < 1$, see appendix B.1.3, 278). Besides, for lower ϕ, the temperature decay rate is slower since some fuel is not burnt at the central reaction zone.

Furthermore, the flame temperature distributions as compared to those obtained by Sze et al. (2006) are also in concordance. Accordingly, the current results show to behave as an inverse diffusion flame with a coflow fuel jet whose principal mode of combustion is non-premixed, as the temperature distributions indicate in figures 6.44 and 6.45. These findings also highlights the laminar nature of the flow owing to the buoyancy effects. Because the mixing at the O_2 nozzle exit is not fast, the fuel is burning on the side in non-premixed mode. The central reaction zone is formed with sufficient excess of H_2, and the maximum temperature is found within this zone, which at some regions presents premixed mode characteristics. Another important observation is that the increase in ϕ moves upstream the maximum temperature due to the high combustibility of the hydrogen.

Cette thèse est accessible à l'adresse : http://theses.insa-lyon.fr/publication/2022LYSEI044/these.pdf
© [K. Utria Salas], [2022], INSA Lyon, tous droits réservés

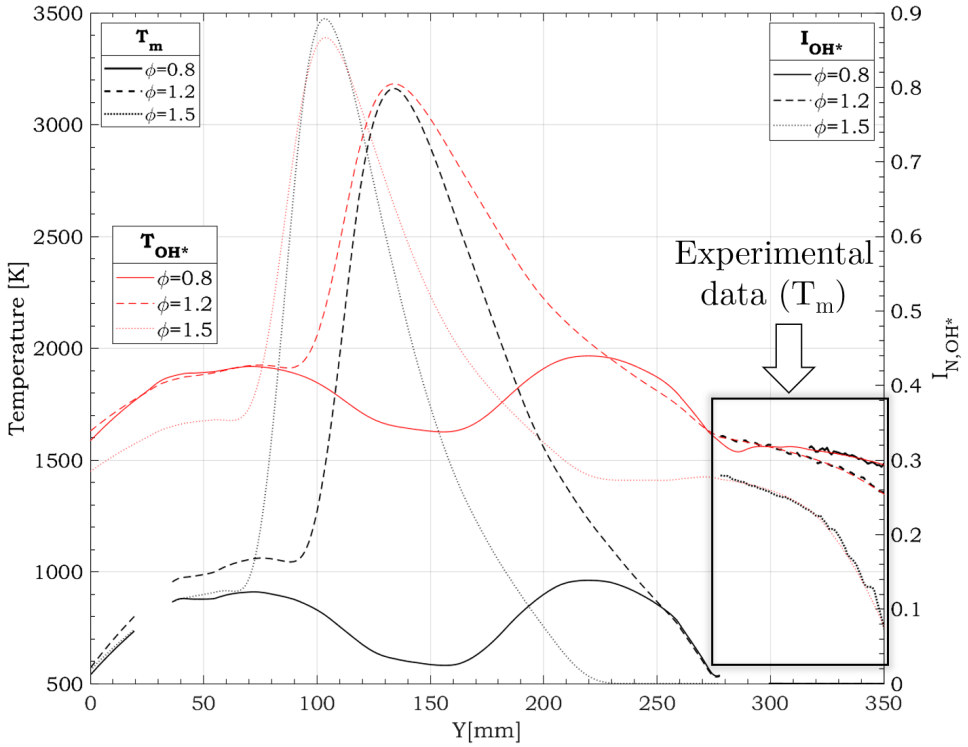

Figure 6.43: Temperature distribution at the centreline with constant U_{0,O_2}

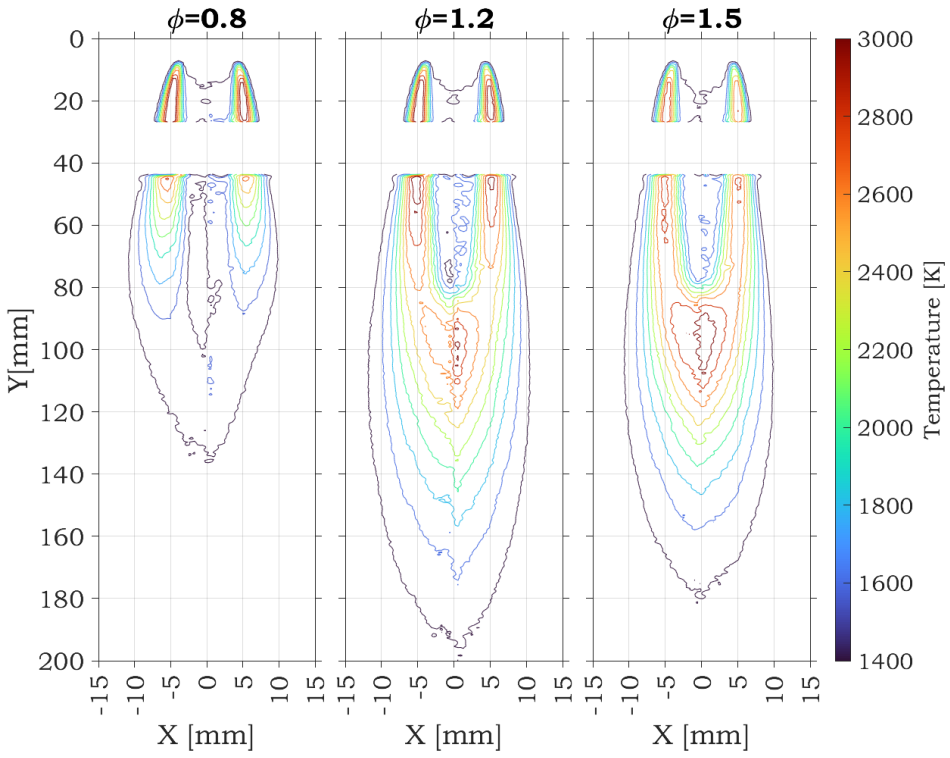

Figure 6.44: Temperature distribution with constant U_{0,H_2}

Moreover, these results also reveal the recirculation that can occur behind the O_2 nozzle lip. It can be inferred due to the flame temperature distribution, since the recirculation at

Cette thèse est accessible à l'adresse : http://theses.insa-lyon.fr/publication/2022LYSEI044/these.pdf
© [K. Utria Salas], [2022], INSA Lyon, tous droits réservés

the entrainment induces faster and more complete combustion at the central reaction zone of the flame. As a consequence, there is less fuel left to burn in the post-combustion region. Therefore, the combustion products in the post-combustion region are more influenced by dilution and cooling of the entrained cold ambient air, leading the centreline temperature to drop at a faster rate (Sze et al., 2006; Zhen et al., 2011, 2013).

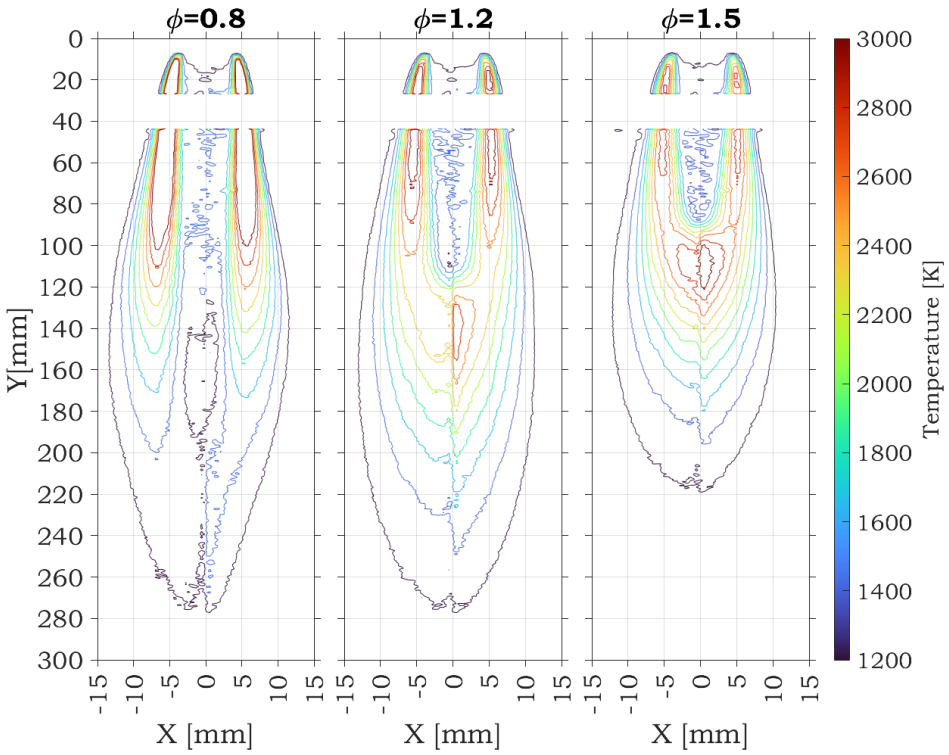

Figure 6.45: Temperature distribution with constant U_{0,O_2}

A combination between the hydrogen and swirl properties causes the temperature distribution of this flame which is also influenced by the buoyancy effects that enlarges the inner potential core and move streamwise the zone of centreline maximum temperature, explaining the differences between the literature and the current results.

Cette thèse est accessible à l'adresse : http://theses.insa-lyon.fr/publication/2022LYSEI044/these.pdf
© [K. Utria Salas], [2022], INSA Lyon, tous droits réservés

6.5 Conclusions

The aerothermodynamic behaviour of the flow was analysed under different flow rates conditions for three different flame topologies in a Verneuil burner. This study outlines the aerodynamic mechanisms involved in this very particular configuration. The flow development was analysed, and the mechanism that impacted this kind of flames were also exposed. The influence of the buoyancy and the coaxial flow effects were revealed, explaining the laminar characteristics of the flames.

The flow structure development was characterised and allows to understand how the flame performs under certain initial conditions—for instance, the turbulent behaviour for $\phi = 0.8$ at the O_2 nozzle, and the increase in the turbulence intensities at the flame closure.

Furthermore, the importance of the reaction zone was also revealed. The combustion increases the buoyancy effects with self-similarities obtained at $1D_{O_2}$. The laminar behaviour is always observed at the reaction zones, especially for $\phi > 1.2$.

Moreover, the influence of the peripheral jets was accentuated at the highest U_{0,O_2}. Indeed, the temperatures are lower when the flow behaves as a coaxial flow. On the other hand, laminar behaviour is achieved especially with the diminution of O_2 inlet velocity, higher ϕ; thus, higher temperature. The changes in U_{0,H_2} affects the coaxial jet behaviour and the flow development. The increase in U_{0,H_2} spreads the secondary flow width ($X_{0.5}$).

The heat release distribution was described through temperature predictions. It was observed that the inverse diffusion flames report four zones at the centreline. The first zone corresponds to the entrainment zone, and the temperature are low. At zone 2, the region of mixing is found, and the temperature at the centreline conserves low values. At the end of the mixing appears the central reaction zone where the highest temperatures are found, when $\phi > 1$. The increase in H_2 injection approaches the maximum temperature location to the outlet nozzle. With the decrease in U_{0,O_2} , the reaction zone moves upstream as the zone of maximum temperature. It was also observed the influence of $r_u < 1$ due to the significant impact in the flow development when varying O_2 injection.

Cette thèse est accessible à l'adresse : http://theses.insa-lyon.fr/publication/2022LYSEI044/these.pdf
© [K. Utria Salas], [2022], INSA Lyon, tous droits réservés

Finally, these results and analysis allow to better understand the flow development and the mechanisms involve in the reactive flow. Those, they contribute to develop realistic solutions to optimise the efficiency of the *Verneuil method* as criteria validation the crystal quality. To conclude, the flow development is impacted by different aspects:

- the flame structure,
- the properties of the gases that evolve significantly due to the strong heat release present in the flame, which could lead to significant buoyancy effects,
- and finally the influence of the laminar or turbulent nature of the flow, and the heat transfer that varies depending on the considered region.

Cette thèse est accessible à l'adresse : http://theses.insa-lyon.fr/publication/2022LYSEI044/these.pdf
© [K. Utria Salas], [2022], INSA Lyon, tous droits réservés

Cette thèse est accessible à l'adresse : http://theses.insa-lyon.fr/publication/2022LYSEI044/these.pdf
© [K. Utria Salas], [2022], INSA Lyon, tous droits réservés

Part III

Overall thermal behaviour of the Verneuil device

After analysing and evaluating the most relevant parameters of the sapphire crystallisation process and the characteristics of flame structure and flow development, this part examines the overall thermal behaviour of the flame under the **crystal presence** and through a new ceramic insulation geometry. Experimental and numerical tools were deployed to carry out the analysis.

Cette thèse est accessible à l'adresse : http://theses.insa-lyon.fr/publication/2022LYSEI044/these.pdf
© [K. Utria Salas], [2022], INSA Lyon, tous droits réservés

Cette thèse est accessible à l'adresse : http://theses.insa-lyon.fr/publication/2022LYSEI044/these.pdf
© [K. Utria Salas], [2022], INSA Lyon, tous droits réservés

Contents

Cette thèse est accessible à l'adresse : http://theses.insa-lyon.fr/publication/2022LYSEI044/these.pdf
© [K. Utria Salas], [2022], INSA Lyon, tous droits réservés

Cette thèse est accessible à l'adresse : http://theses.insa-lyon.fr/publication/2022LYSEI044/these.pdf
© [K. Utria Salas], [2022], INSA Lyon, tous droits réservés

Chapter 7 | Influence of stagnation point on H_2/O_2 inverse diffusion flames

The crystal growth environment constitutes a complex system. It consists of different thermal, chemical and aerodynamic interactions that posteriorly define the sapphire crystalline structure. Due to its complexity, implementing traditional optics techniques has become a challenge. Therefore, this chapter analyses the influence of the crystal on the flame structure and flow development through OH^* chemiluminescence and Computational Fluid Dynamics (CFC) modelling. The experimental setup is described in the first sections. Posteriorly, the experimental and numerical results are shown.

7.1 Experimental setup

Two different arrangements were used to study the conditions of the crystal growth environment with the crystal presence. This consists in a classic Verneuil burner configuration (industrial burner), which consists of one central jet of O_2 and nine peripheral jets of H_2, see figure 7.1.

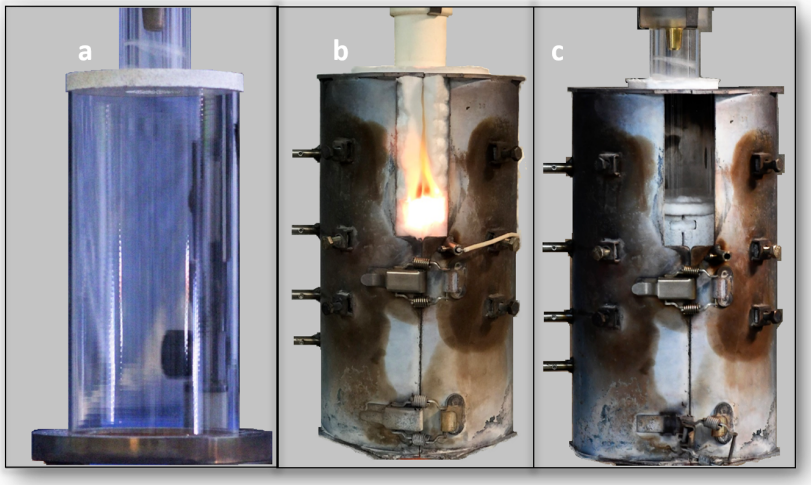

Figure 7.1: Verneuil Burners O_2/H_2: a. Academical approach. Industrial approach: b. Configuration 1. c. Configuration 2

1. Configuration 1 : This arrangement was used to validate the laboratory setup in appendix C.1. The furnace confinement is constituted by an external stainless steel layer, followed by SiO_2 fibre, a polycrystalline alumina fibre and a ceramic confinement.

Cette thèse est accessible à l'adresse : http://theses.insa-lyon.fr/publication/2022LYSEI044/these.pdf
© [K. Utria Salas], [2022], INSA Lyon, tous droits réservés

2. Configuration 2: A modification was executed in the upper part of the confinement. The ceramic layer was cut off at 120 mm from the top of the confinement and replaced by a transparent quartz tube with the same internal diameter (see figure 7.2) of the upper section of the ceramic insulation. This modification was performed to analyse the influence of the crystal on the flame structure.

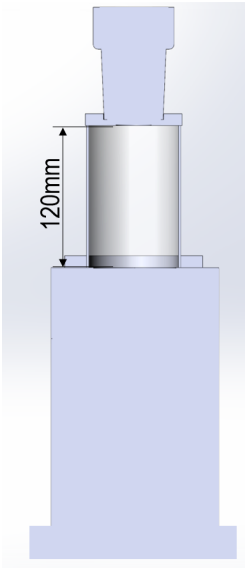

Figure 7.2: Industrial approach Configuration 2

In figure 7.3 the experimental setup is illustrated. The furnace configuration is shown in (a), two insulations hermetic gasket were used to limit gas leak from the confinement and to insulate the confinement of the external air. The ignition of the flame was performed at the top of the furnace (b). The crystal is placed at the bottom of the confinement at the beginning of the experiment to avoid the crystal's break. The *Verneuil boule* moved up slowly until their typical location of 130 mm from the top of the furnace (c). It is possible to observe 110 mm of the flame (d). During the experiment with the crystal presence, high levels of radiation were observed (e).

7.1.1 Analysis method

A *Verneuil boule* was placed inside the confinement at a distance of 130 mm from the burner nozzle in order to analyse the crystal influence. This Y-position corresponds to industrial parameter in order to produce a *Verneuil boule*. The boule diameter was 32 mm with 20 mm of length. Higher lengths could not be used because they broke down at the moment of contact with the flame during the tests. Different actual operation conditions were chosen regarding the insulation life cycle explained in chapter 6. In this chapter, three operation points were identified as essential conditions present during the insulation's life cycle. They were crystallisation No.1, No.15 and No.27, corresponding to

Cette thèse est accessible à l'adresse : http://theses.insa-lyon.fr/publication/2022LYSEI044/these.pdf
© [K. Utria Salas], [2022], INSA Lyon, tous droits réservés

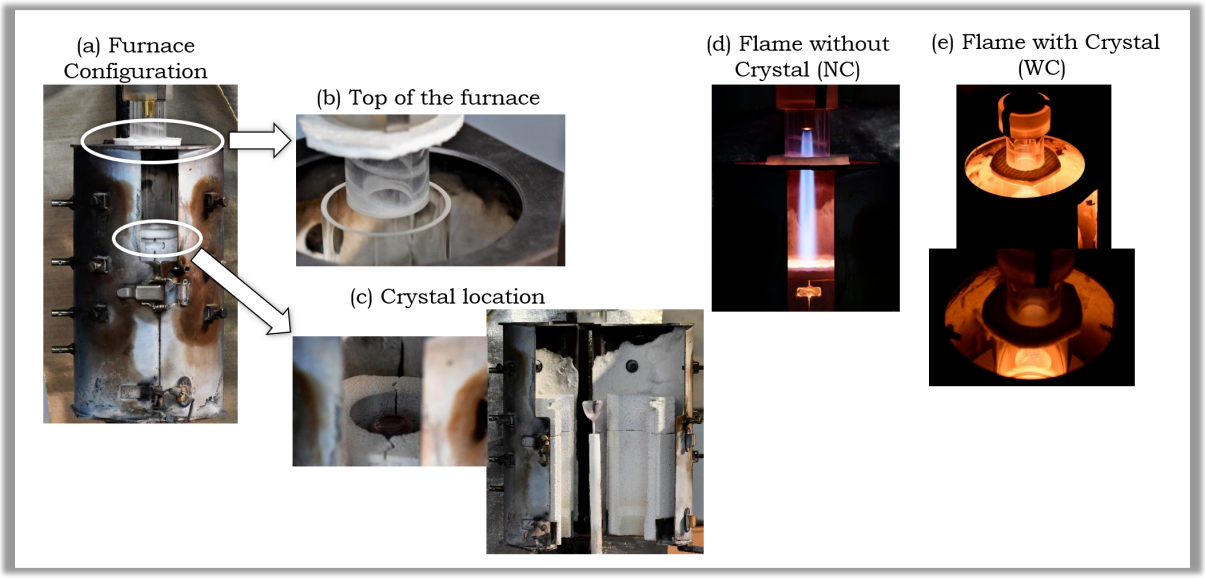

Figure 7.3: Chemiluminescence setup

the beginning, middle and end of the insulation cycle. They also correspond to the most significant changes in flow rates. These points are shown in figure 7.4 and table 7.1.

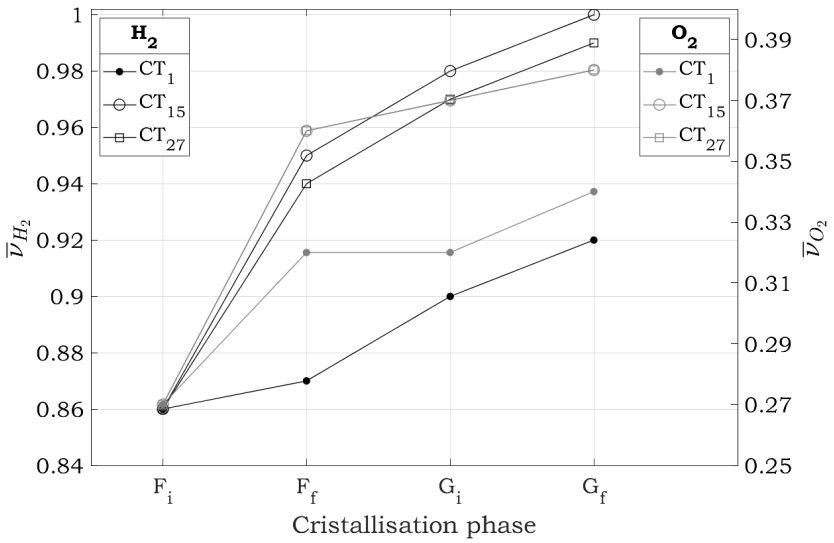

Figure 7.4: Evolution of flow rates for an insulation life cycle

The OH* chemiluminescence was the adequate experimental technique due to the configuration's extremely high temperatures and radiation. Figure 7.5 shows the setup used to acquire the images. The OH* chemiluminescence images were obtained by using a Photon SA4 Fast Camera and an OH* FWHM filter of 310 nm ± 50 nm (curve figure 4.4). A single image of OH* chemiluminescence is obtained by averaging 60 images with an exposure time of 10 ms and a frame rate of 50 images/second, the uncertainties of the measurements were $< 1\%$ due to very stable flames. The OH* chemiluminescence images directly obtained are converted into the planar chemiluminescence images using

Cette thèse est accessible à l'adresse : http://theses.insa-lyon.fr/publication/2022LYSEI044/these.pdf
© [K. Utria Salas], [2022], INSA Lyon, tous droits réservés

Abel inversion transform (discussed in subsection 4.2.3) to quantify the burning intensity.

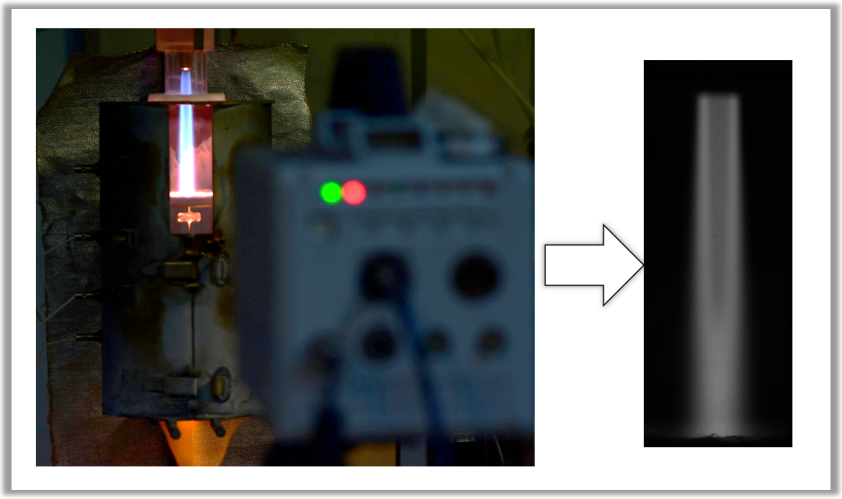

Figure 7.5: Experimental setup with the stagnation point

Phase	CT_1			CT_{15}			CT_{27}		
	H_2	O_2	ϕ	H_2	O_2	ϕ	H_2	O_2	ϕ
$\boldsymbol{F_i}$	0.86	0.27	1.60	0.86	0.27	1.60	0.86	0.27	1.60
$\boldsymbol{F_f}$	0.87	0.32	1.35	0.95	0.36	1.33	0.94	0.36	1.30
$\boldsymbol{G_i}$	0.90	0.32	1.39	0.98	0.37	1.33	0.97	0.37	1.30
$\boldsymbol{G_f}$	0.92	0.34	1.35	1.00	0.38	1.33	0.99	0.38	1.31

Table 7.1: Operation points. The flow rates for H_2 and O_2 are normalised by the highest flow rate

Cette thèse est accessible à l'adresse : http://theses.insa-lyon.fr/publication/2022LYSEI044/these.pdf
© [K. Utria Salas], [2022], INSA Lyon, tous droits réservés

7.2 Flame structure characteristics

Different operating points were used to analyse the influence of the crystal on the flame structure characteristics. Figure 7.6 shows the instant OH^* chemiluminescence image with and without the crystal presence a crystallisation cycle. It was found in chapter 7 that the characteristics of the H_2/O_2 IDF are mainly dependent of the global equivalence ratio, ϕ and velocity of the central O_2 jet and Re_{O_2}. According to the these results, the injection conditions for the different crystallisation cycles produce mainly two types of flame structure, which are type II and type III, already described in chapter 5.

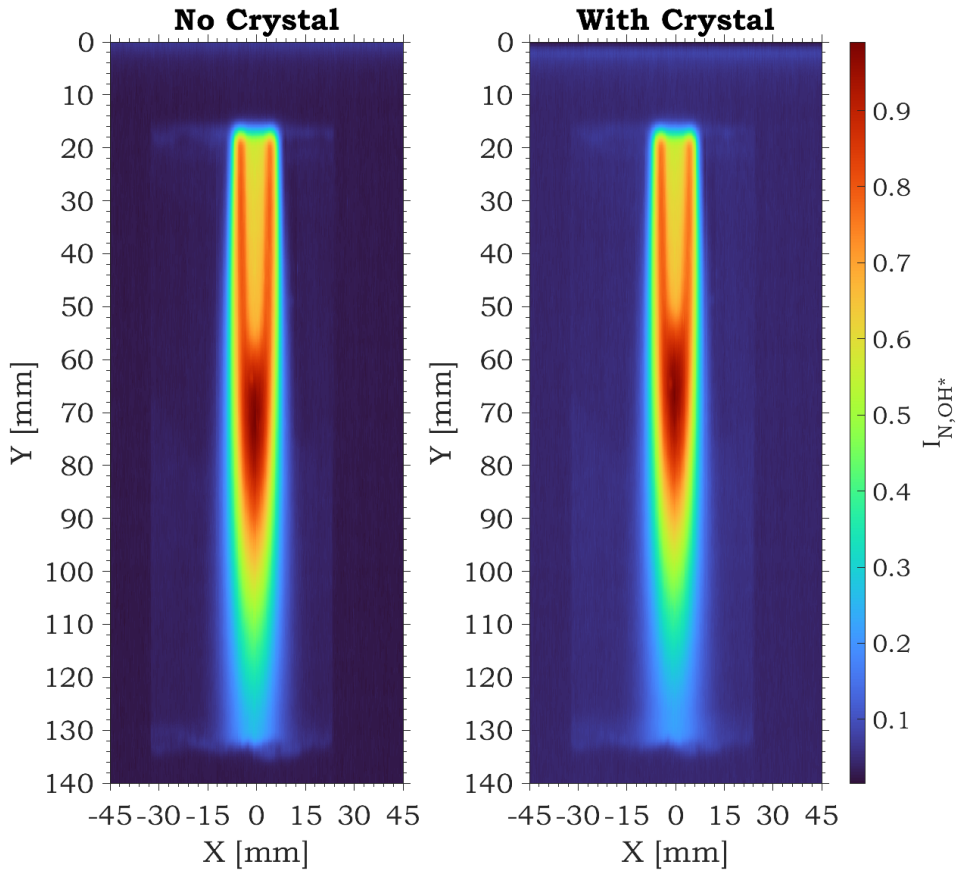

Figure 7.6: Instant image OH* Chemiluminescence CT_1 cycle F_i $\phi = 1.6$

The flame structure characteristics of the chosen operating points are shown through the contours of an instant OH^* chemiluminescence image. These contours were chosen considering the thresholds mentioned in section 1.3(page 31). These describe the external flame layer 0.1 $I_{OH,max}$ (it was augmented because the crystal presence increases the image noise for the isolevel of 0.023), the apparition of the central layer (0.4 and 0.6 $I_{OH,max}$), and the maximum emission zone (0.8 $I_{OH,max}$).

Nevertheless, these images are integrated on the light-of-sight; thus, the Abel deconvo-

Cette thèse est accessible à l'adresse : http://theses.insa-lyon.fr/publication/2022LYSEI044/these.pdf
© [K. Utria Salas], [2022], INSA Lyon, tous droits réservés

lution was used to obtain the OH* intensity distribution on a 2D plane to analyse the reaction zones. Although they are integrated images, it can be used as an useful approach to examine the flame structure.

Figure 7.7 depicts the different flames obtained for the first crystallisation. The initial flow rates of a crystallisation cycle are always the same and correspond to the initial formation cycle. As observed, the presence of the crystal causes different effects. At first instance, the external flame layer is highly perturbed, and this OH* level spreads out at the bottom of the image and close to the highest levels Y-position, some OH* emissions can be detected externally. The central "combustion front" is shifted closer to the O_2 nozzle. This can be explained through the classic impinging diffusion flames.

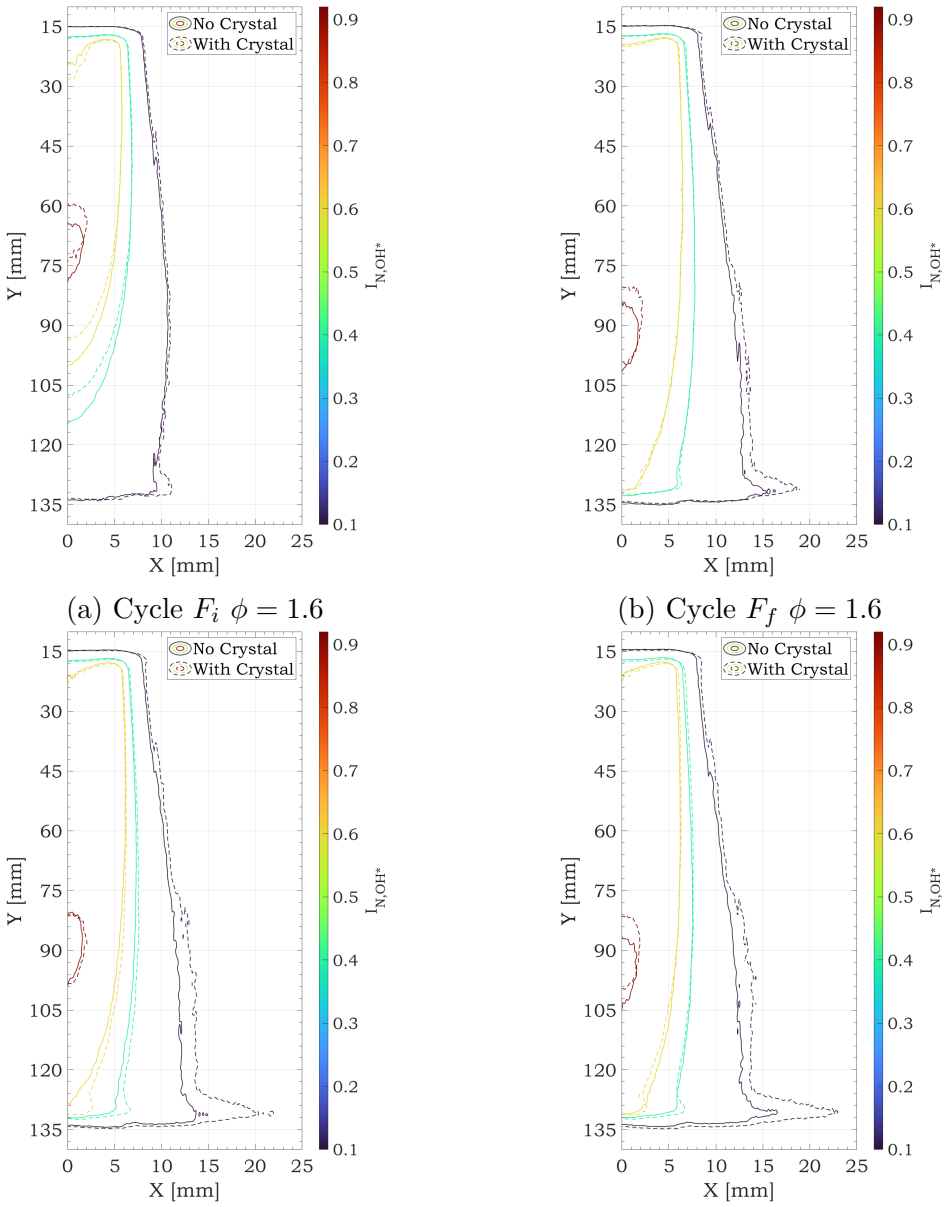

(a) Cycle F_i $\phi = 1.6$

(b) Cycle F_f $\phi = 1.6$

(c) Cycle G_i $\phi = 1.39$

(d) Cycle G_f $\phi = 1.35$

Figure 7.7: Instant image OH* Chemiluminescence CT_1 (I_{N,OH^*} thresholds of 0.1 0.4 0.6 0.8)

Cette thèse est accessible à l'adresse : http://theses.insa-lyon.fr/publication/2022LYSEI044/these.pdf
© [K. Utria Salas], [2022], INSA Lyon, tous droits réservés

Although the system is not a complete impinging IDF, the available literature on this kind of flame can be used to explain some of the flow and flame features. Figure 7.8 shows the flow structure of a typical impinging flame for the central jet.

In a typical impinging jet configuration, three different flow areas are identified: the free jet, the impact zone and the wall jet. The free jet is the area where the jet is not affected by the wall. Its flow is very similar to that of a free jet. In this area, a potential cone is formed, defined as the distance between the injection point and the point where the velocity gradient in the direction of the jet is not zero. The impact area starts when the presence of the wall influences the jet. Lateral velocity increases rapidly when the jet approaches the wall. The flow field contains the stagnation point where the longitudinal velocity becomes zero. The last zone is that of the wall jet where the flow runs parallel to the wall and a boundary layer develops (Poitras et al., 2017).

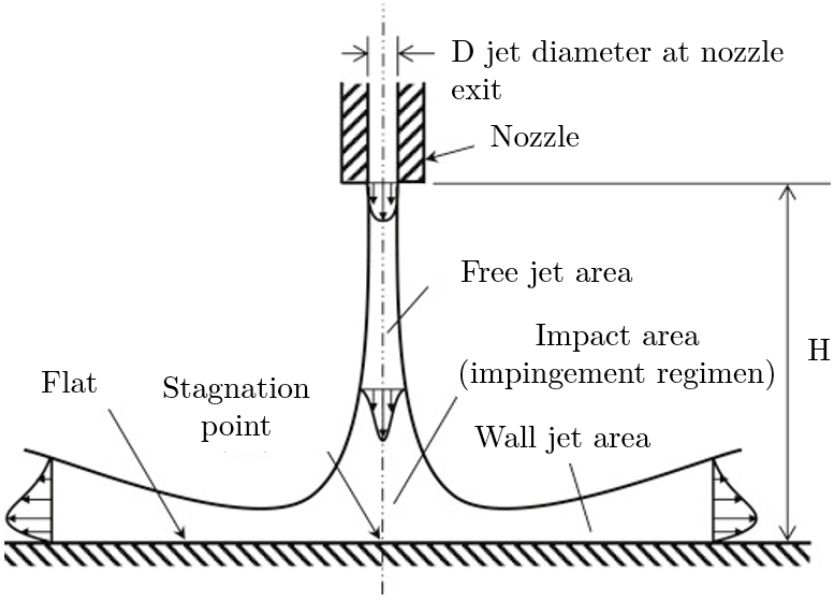

Figure 7.8: Typical impinging jet flow areas. (Poitras et al., 2017)

Fuel jet impingement greatly enhances the mixing of oxidiser and fuel. After the mixing, the gas mixture develops further as a single flame jet. When the mixing level is high enough, a premixed flame could be formed and propagates downstream. For this jet impingement configuration, the intense mixing process could also increase the chemical reaction rate and combustion efficiency, as discussed by Bain et al. (2012).

The reaction rate was found to be proportional to the flow intensities by Witze (1974) and Holve and Sawyer (1975). The characteristics of the system is mainly dependent of the global equivalence ratio, ϕ, the non-dimensional nozzle-to-plate distance, H/D_{O_2}, and the discharging velocity of the oxidiser jet. When $H/D_{O_2} > 11$ (present configuration), it is the outer diffusion flame that impinges on the plate, forming a circular flame adjacent

Cette thèse est accessible à l'adresse : http://theses.insa-lyon.fr/publication/2022LYSEI044/these.pdf
© [K. Utria Salas], [2022], INSA Lyon, tous droits réservés

to the plate, which is the case for the initial formation cycle.

For typical methane/air impinging flames there are two types of flame buoyancy controlled flames and momentum controlled flames ($Re_{air} < 300$ and $Re_{air} > 300$, respectively) (Dong et al., 2007). When the flames are buoyancy controlled, two diffusion flames are produced on the sides by the IDF configuration as for the case of flame type I in chapter 5. Momentum controlled flames exposed a neck structure at the base of the flame, as shown in figure 7.9. This illustration represents the structure of a dual-structure triple-layer IDF, and buoyancy controlled flame on the top and momentum controlled downstream.

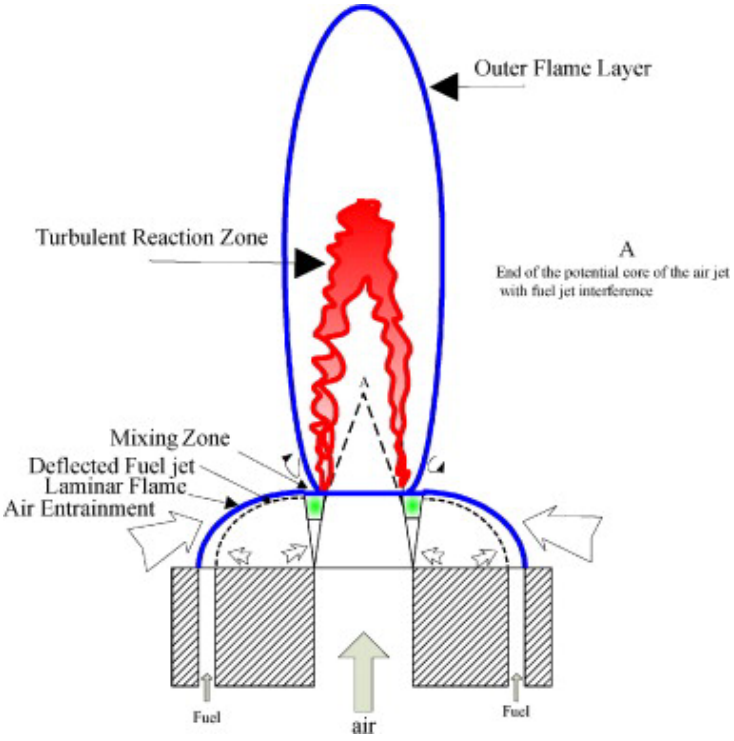

Figure 7.9: Structure of blue dual-structure triple-layer IDF. Printed from Dong et al. (2007)

The configuration of the current study differs from the classic impinging flames at the fuel and oxidiser injection. The nozzle outlets are located in different Y-position, this configuration produces a different flow development as shown in the previous chapter. After a certain Y-position the flow behaves as a single jet. In addition, as observed in chapter 5 the Verneuil flames present two regimes, a buoyancy controlled flow and a momentum controlled flow in the case of flame structure type II and type III flames.

Moreover, the current configuration does not report the neck base flame due to the high diffusivity of the hydrogen. Thus, the momentum controlled flames are found downstream where the flame closure (y_j) occurs.

For the present study conditions $\phi = 1.6$, the system presents a type III flame structure.

Cette thèse est accessible à l'adresse : http://theses.insa-lyon.fr/publication/2022LYSEI044/these.pdf
© [K. Utria Salas], [2022], INSA Lyon, tous droits réservés

This kind of flame structure is characterised by a strong central reaction zone downstream. The crystal or stagnation point produces a recirculation of the O_2 and the peripheral jets above the stagnation point. This zone is the impact area or the impingement regime where the gases mix and burn.

The results obtained suggest that the H_2 excess decreases at the flame tip with the crystal inside the reaction zone-and the mixing within this reaction is improved. This result will be analysed ensuing with the OH^* intensity levels at the centreline.

Returning to figure 7.7, for this crystallisation cycle the final formation and the initial growth phases do not seem to be significantly affected by the presence of the crystal. However, an increase in the central reaction zone is observed for the final formation cycle; the injection conditions for these operating points are $\phi = 1.35$ and $\phi = 1.39$, respectively, which also reported a type III flame structure. For these conditions, the O_2 inlet velocity was constant, so the increase in H_2 inlet velocity was responsible for the difference between the free flame and the " impinging flame".

In addition, it can be observed that an increase of the U_{0,O_2} for the final growth cycle propagates the shift upstream in the central reaction zone, and the external layer of the flame is more impacted than for the lower U_{0,O_2}.

For crystallisation No.15, the flow rates are higher compared to that of crystallisation No.1, and the equivalence ratio decreases ($\phi = 1.33$). These changes seem to impact the flame structure as observed in figure 7.10 except for F_f, this phase does not report significance changes with the crystal presence.

For F_i and G_i a shift upstream of the maximum level of the central reaction zone is observed, the other intensity levels around the centreline also report this shift. Furthermore, G_i shows some perturbation due to the radiation emitted for the crystal, they are observed at a range of [Y=75 - Y=105] and [Y=15 - Y=20].

Cette thèse est accessible à l'adresse : http://theses.insa-lyon.fr/publication/2022LYSEI044/these.pdf
© [K. Utria Salas], [2022], INSA Lyon, tous droits réservés

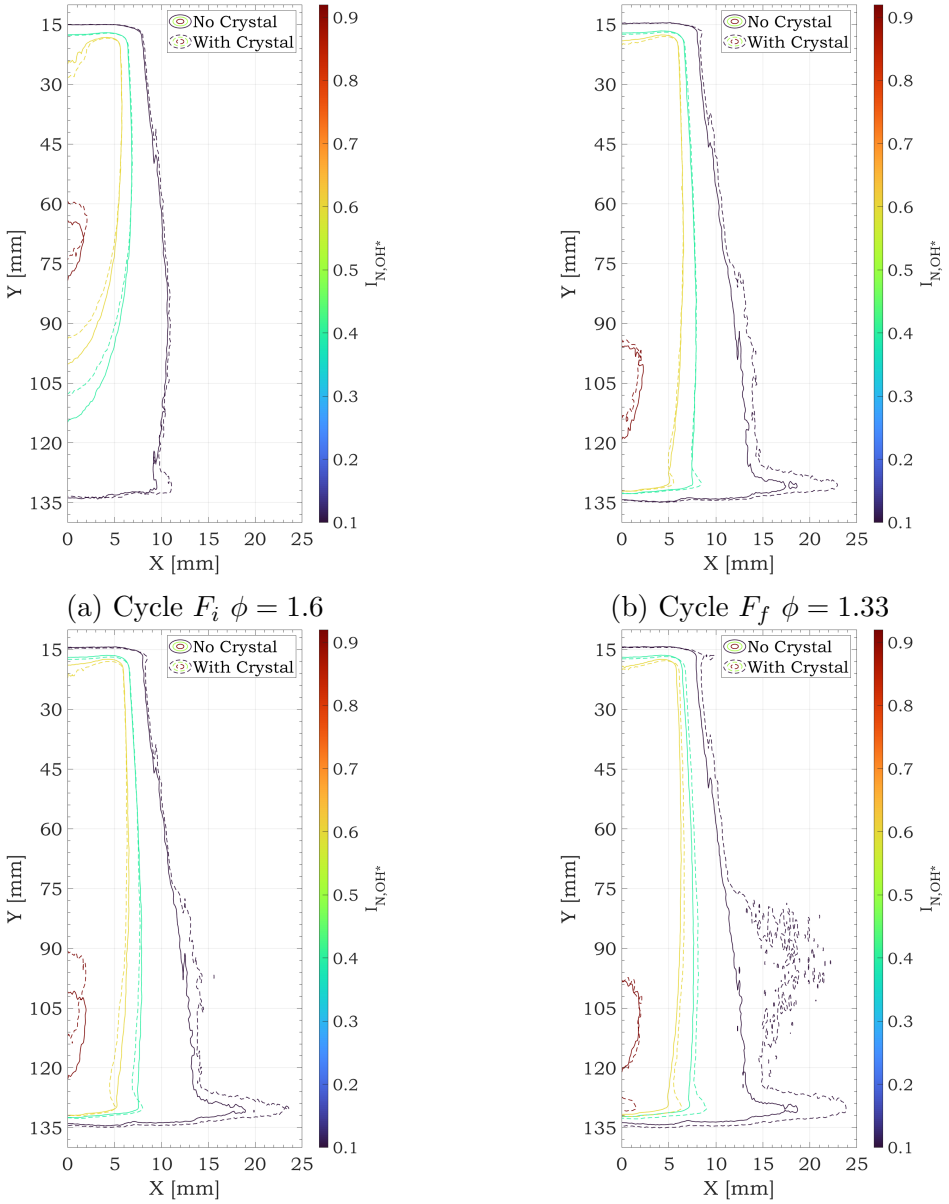

(a) Cycle F_i $\phi = 1.6$

(b) Cycle F_f $\phi = 1.33$

(c) Cycle G_i $\phi = 1.33$

(d) Cycle G_f $\phi = 1.33$

Figure 7.10: Instant image OH* Chemiluminescence CT_{15} (I_{N,OH^*} thresholds of 0.1 0.4 0.6 0.8)

On the other hand, the influence of the crystal radiation can be observed in crystallisation No.27 (figure 7.11) around the same ranges of CT No.15, especially for G_f which corresponds to the highest flow rates. Furthermore, the shift of the reaction zone can also be detected specially for the maximum intensity level. The effect on the flame structure for the final formation and the initial growth cycles is similar, because the O_2 inlet velocities and equivalence rations are similar.

At the border of the flame (threshold 1, $I_{N,OH^*} = 0.1$), a widening is found for almost all the phases except F_i. Nevertheless, it can not be confirmed at this point whether this widening corresponds to the deviation of the reactive flow or it is the noise produced by

Cette thèse est accessible à l'adresse : http://theses.insa-lyon.fr/publication/2022LYSEI044/these.pdf
© [K. Utria Salas], [2022], INSA Lyon, tous droits réservés

the crystal radiation.

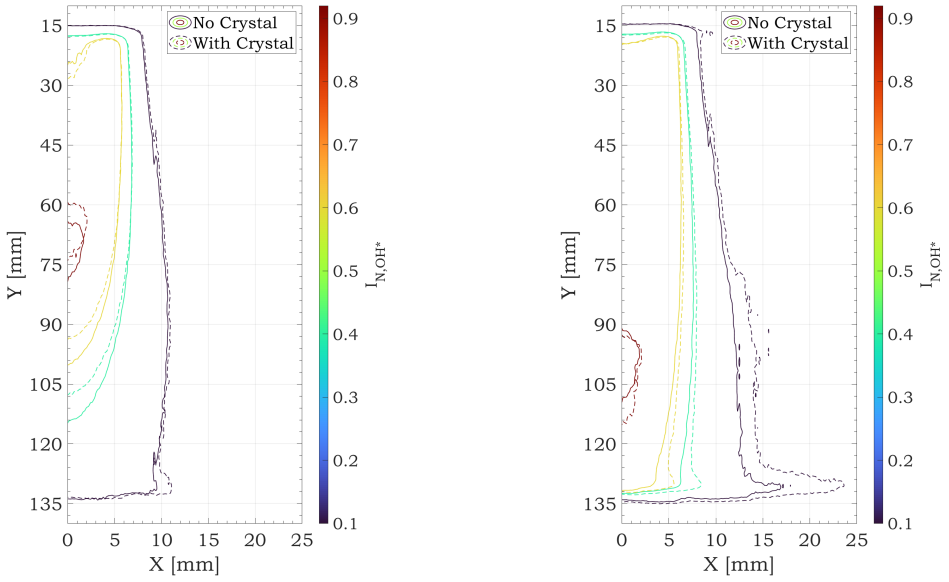

(a) Cycle F_i $\phi = 1.6$ (b) Cycle F_f $\phi = 1.30$

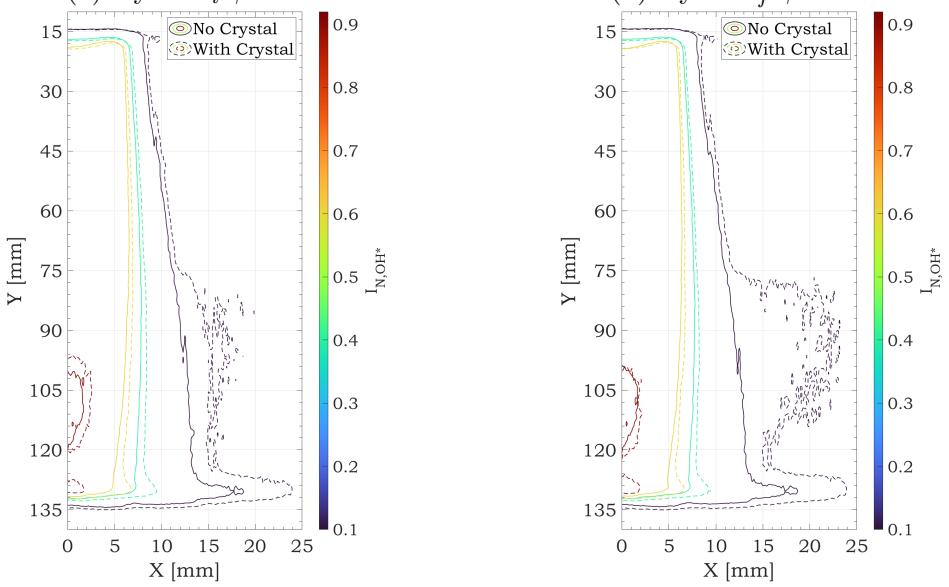

(c) Cycle G_i $\phi = 1.30$ (d) Cycle G_f $\phi = 1.31$

Figure 7.11: Instant image OH* Chemiluminescence CT_{27} (I_{N,OH^*} thresholds of 0.1 0.4 0.6 0.8)

In the following, the OH* intensities along the centreline for the formations phases are analysed in figure 7.12a. These data represents the post-image processing with the Abel deconvolution (section 4.2.3). As observed, the intensity distribution changes with and without crystal. With the crystal presence, the mixing is improved, and the combustion seems to be faster, especially for the highest flow rates, as shown in figure 7.12b. There is a shift upstream in the distribution of the OH* intensities of 4 mm with the crystal, and the flame is located closer to the burner, as observed in figure 7.12a.

Cette thèse est accessible à l'adresse : http://theses.insa-lyon.fr/publication/2022LYSEI044/these.pdf
© [K. Utria Salas], [2022], INSA Lyon, tous droits réservés

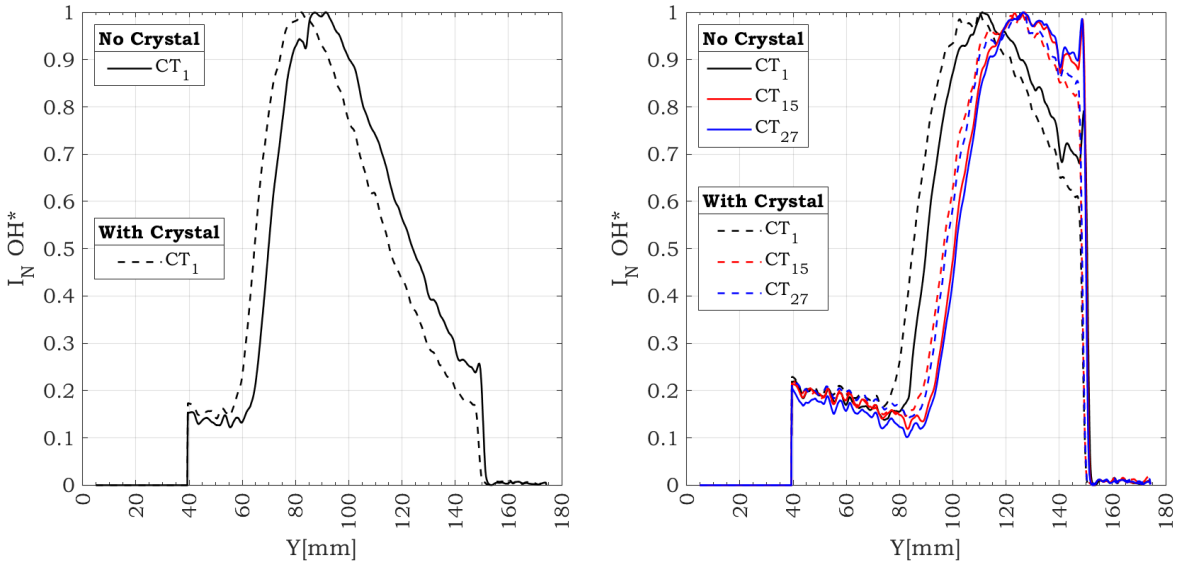

(a) Cycle F_i (b) Cycle F_f

Figure 7.12: OH* intensities along Y-axis at the centreline for the crystal formation phases

In figure 7.13a, it can be observed that the maximum OH* emission intensities at the centreline are not significantly affected by the crystal presence for crystallisation No.15 and No.27. Nevertheless, an increase in the intensity levels is observed upstream before the flame closure. For instance (at value close to the flame closure position), at $Y \cong 80$mm the increase in I_{N,OH^*} for CT No.1 was 0.24 and for CT No.15 and CT No.27 at $Y \cong 96$mm were 0.2 and 0.07, respectively. This increase indicates the enhancement of the mixing and combustion, especially for CT No.1 and CT No.15.

For the final growth cycle, the most affected by the crystal presence is crystallisation No.15, where the intensities increase at the central reaction zone ($\cong 0.1$) as illustrated in figure 7.13b.

Furthermore, it is important to mention that the increase in the OH* intensities is also linked to the increase in the temperature due to the presence of a liquid crystal surface, that also produces high radiation.

Cette thèse est accessible à l'adresse : http://theses.insa-lyon.fr/publication/2022LYSEI044/these.pdf
© [K. Utria Salas], [2022], INSA Lyon, tous droits réservés

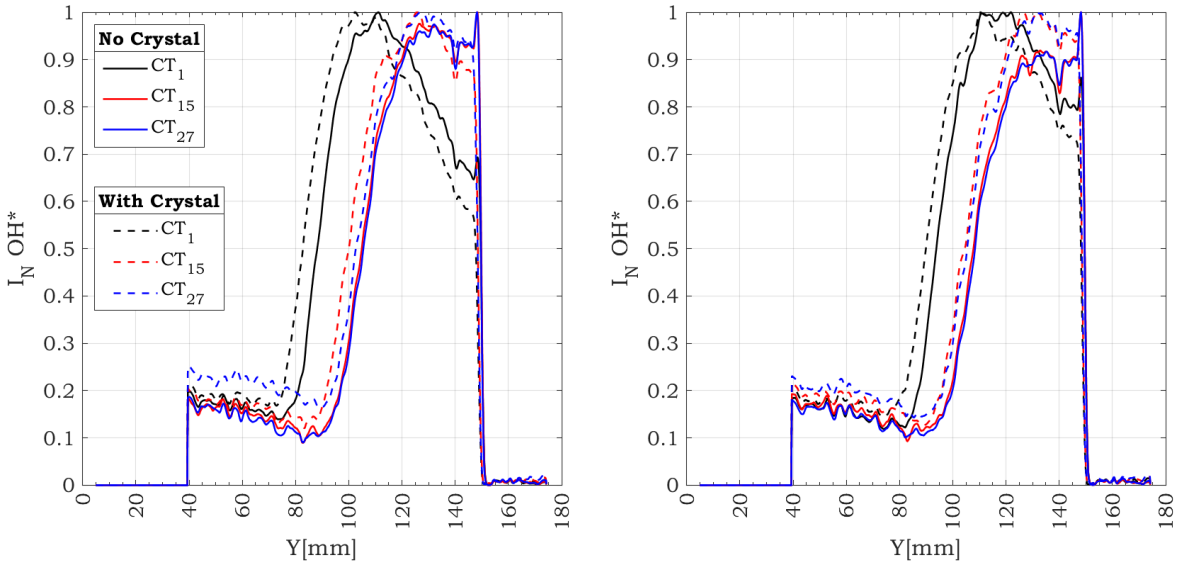

(a) Cycle G_i (b) Cycle G_f

Figure 7.13: OH* intensities along Y-axis at the centreline for the crystal growth phases

The impact in the flame structure characteristics is analysed in figures 7.14, 7.15 and 7.16. The different flame heights are examined to determine the influence of the crystal presence on the reaction zones (see figure 7.14).

The diffusion length, y_d, which indicates the maximum emission intensity on the sides, does not seem highly affected by the stagnation point. The decrease in y_d under the crystal presence is of 2 mm for the initial formation, the other crystallisation cycles reported negligible changes.

The flame closure length, y_j, is a bit more impacted specially for the crystallisation No.1 for the phases different to F_i, the O_2 inlet velocities for the others phases are higher.

The flame lengths, y_f, also decreases with the crystal inside the confinement. However, for the growth cycles in crystallisation No.27 the flame length, y_f, does not change significantly. This could be explained because $\phi = 1.3$ is type II. For these flames at higher U_{0,O_2} the flame closes farther from the nozzle exit, but the central reaction zone is not as strong as the side diffusion mode.

Cette thèse est accessible à l'adresse : http://theses.insa-lyon.fr/publication/2022LYSEI044/these.pdf
© [K. Utria Salas], [2022], INSA Lyon, tous droits réservés

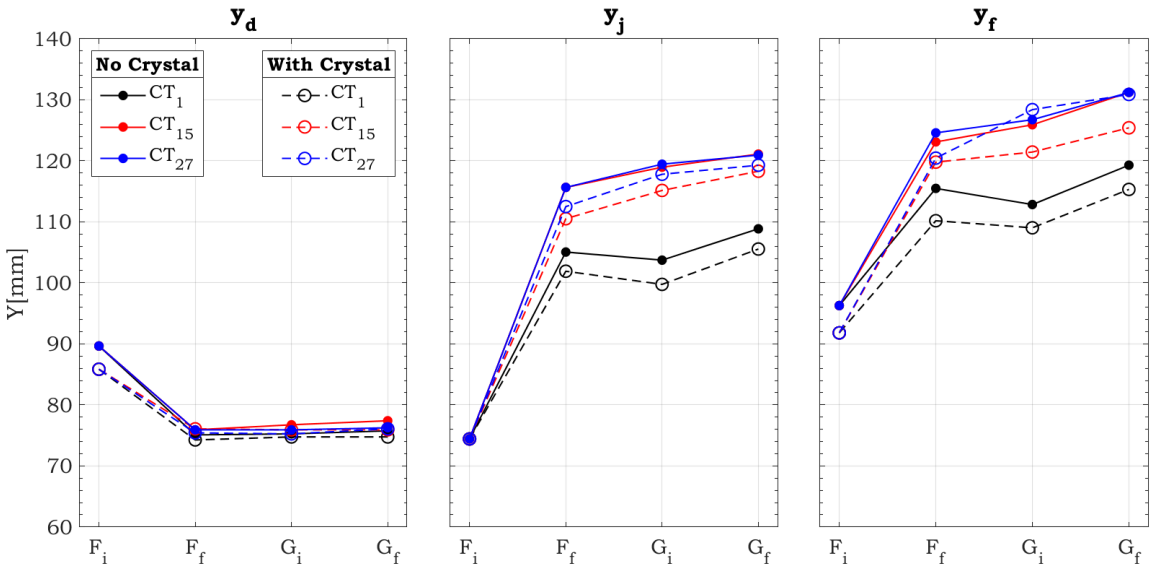

Figure 7.14: Flame Heights

The crystal presence shift the central reaction upstream and increases the maximum intensity within this zone, hence the new maximum intensity is found at the same position of the older one. The results confirm that the mixing and combustion within this zone are enhanced with the presence of the crystal.

The flame thickness, δ_{OH^*}, denotes the thickness of the reaction zone and is analysed in figure 7.15. This parameter does not seem to change upstream for all the cycles of crystallisation No.1.

In contrast, the central reaction zone reported thinner values. It is important to mention that this crystallisation cycle reported the lowest flow rates. These results indicate that the burning is principally effectuated at the central reaction zone, and the burning rate is higher for the case of the "impinging flame", δ_{cer} seems principally affected upstream, wider flames are found. The inlet flow rates are higher for these operating points, so the impact zone is wider for these flames, explaining the spreading out of the flame upstream.

Cette thèse est accessible à l'adresse : http://theses.insa-lyon.fr/publication/2022LYSEI044/these.pdf
© [K. Utria Salas], [2022], INSA Lyon, tous droits réservés

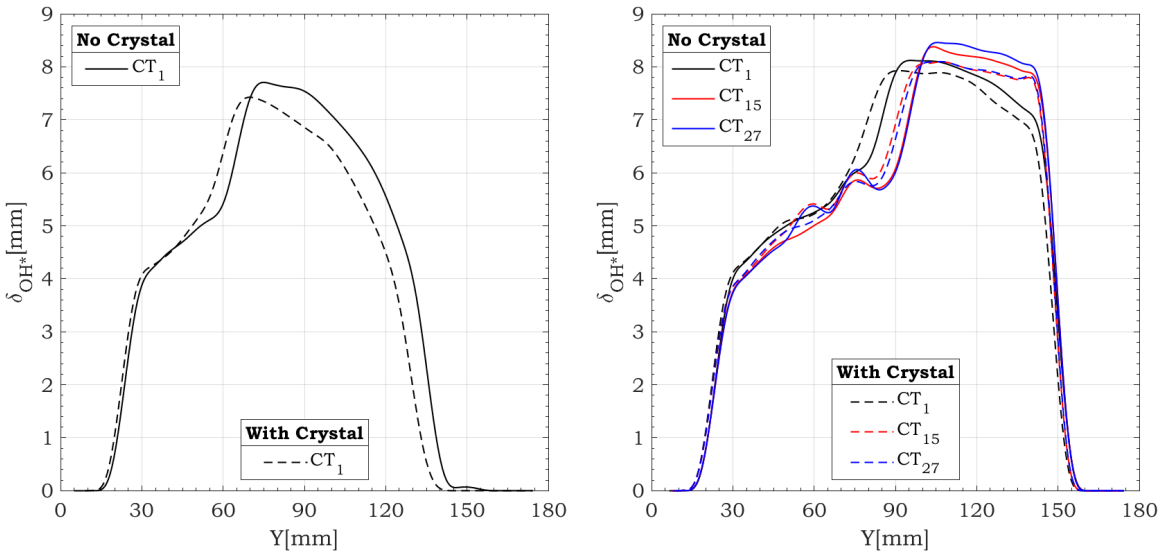

(a) Cycle F_i

(b) Cycle F_f

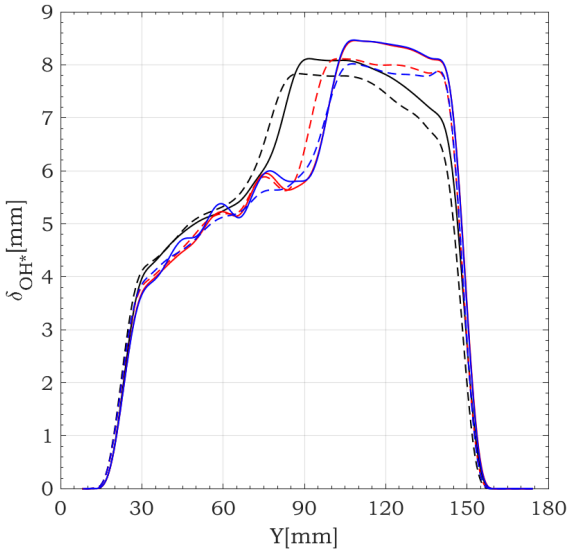

(c) Cycle G_i

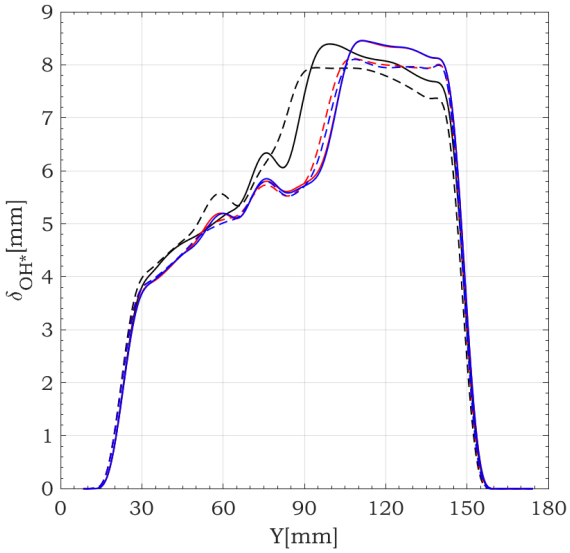

(d) Cycle G_f

Figure 7.15: Thermal thickness δ_{OH^*}

Another particular result is found for the total flame thickness which is related to the threshold of 80% of the maximum intensity level. This region increases downstream with the crystal presence as illustrated in figure 7.16 for the three crystallisation cycles, indicating the enhancement of the combustion.

Even more, in crystallisation No.1 where this zone also increases upstream. The results indicate that the crystal presence enhances the lower flow rates, which also have the highest global equivalence ratio.

Cette thèse est accessible à l'adresse : http://theses.insa-lyon.fr/publication/2022LYSEI044/these.pdf
© [K. Utria Salas], [2022], INSA Lyon, tous droits réservés

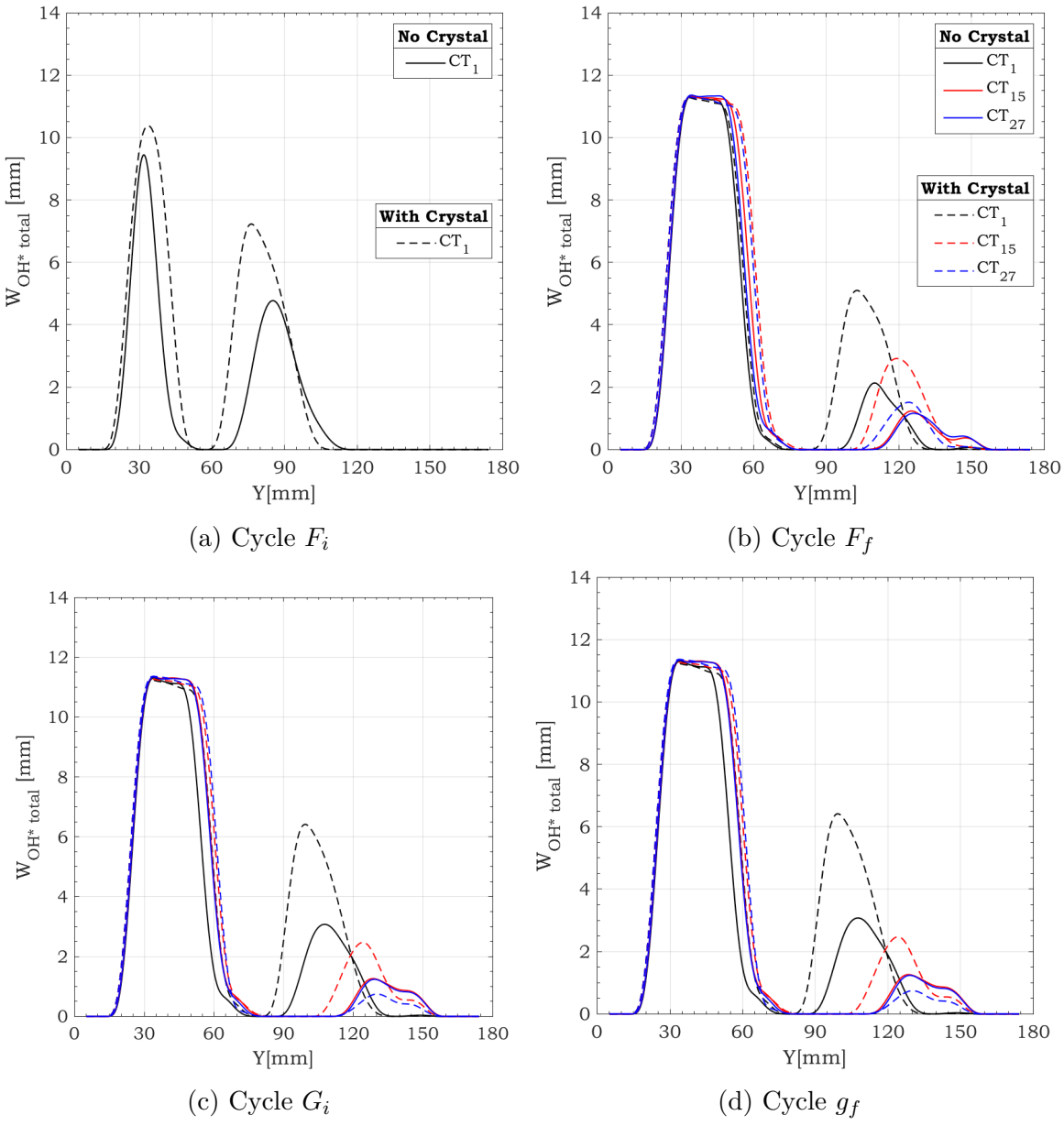

(a) Cycle F_i

(b) Cycle F_f

(c) Cycle G_i

(d) Cycle g_f

Figure 7.16: Total Thermal thickness $W_{OH^*,total}$

Cette thèse est accessible à l'adresse : http://theses.insa-lyon.fr/publication/2022LYSEI044/these.pdf
© [K. Utria Salas], [2022], INSA Lyon, tous droits réservés

As observed, the presence of the crystal in the reaction zone causes various effects on the flame. The increase in the radiation due to the liquid crystal surface increments the OH^* intensities.

Furthermore, the apparition of a contact area and a wall jet area enhances the mixing and the combustion on the reaction zones. This enhancement depending on the flow rates, especially the O_2 discharging velocity, causes an upstream shift of the central combustion zone and a widening of the reaction zone in diffusion mode.

The combustion becomes faster due to the high diffusivity of the hydrogen reacting with the oxygen. It is observed owing to the shorter flames obtained with the crystal presence. These results suggest that the aerodynamics of the flow has an essential role in the flame structure and thermal characteristics. Therefore the next chapter analyses the aerothermodynamic behaviour through numeric simulations.

Cette thèse est accessible à l'adresse : http://theses.insa-lyon.fr/publication/2022LYSEI044/these.pdf
© [K. Utria Salas], [2022], INSA Lyon, tous droits réservés

7.3 Aerothermodynamic behaviour of inverse diffusion flames with crystal presence

The radiation is elevated during the crystallisation of a sapphire crystal, causing significant constraints to implement optical techniques to describe the velocity field. Therefore, the aerothermodynamic behaviour of the **reactive flow** with the crystal presence was analysed by numerical tools, explained in the appendix C.2.

Indeed, this section describes the flow structure and development for three operating points, the crystallisation cycle No.15 was chosen to be examined due to the results obtained experimentally in the previous section. In addition, in chapter 1 this crystallisation cycle shown to have the best external and internal quality features to produce the crystals, the injection conditions are shown in table 7.2.

The difficult thermal conditions of the system results to be complex. The temperature distributions on the wall boundary conditions are unknown. Therefore, the present study explored the possibility to describe the system under adiabatic conditions for all the wall boundaries (e.g. crystal, injector, internal surface of the ceramic insulation).

With the purpose to validate the results, the OH^* emissions found experimentally in the previous section are compared with the OH^* molar concentrations calculated by the numerical simulation. In equation 4.4 can be seen that the OH^* emission intensity is proportional to OH^* concentration, so the intensity distribution of OH^* chemiluminescence can be described **qualitatively** by the OH^* concentration distribution.

Cycle	$\boldsymbol{U_{0,H_2}}$ **[m/s]**	$\boldsymbol{U_{0,O_2}}$ **[m/s]**	$\boldsymbol{\phi}$	$\boldsymbol{U_{0,O_2} - U_{0,H_2}}$ **[m/s]**	$\boldsymbol{U_{0,H_2}/U_{0,O_2}}$ **[m/s]**
F_i	3.00	4.31	1.31	0.30	0.70
F_f	3.30	5.70	2.40	0.42	0.58
G_f	3.48	6.00	2.53	0.42	0.58

Table 7.2: Operating points used to study the aerothermodynamics of the crystal growth environment

In figure 7.17 can be observed the results obtained for the molar concentration of OH^* with and without the presence of the crystal. The reaction zone with the crystal presence seems to be shorter that the free flame. These results indicate an increase in the chemical reaction rate that is a feature of the impinging flames. This can be confirmed with the increase on the maximum concentration of OH^*. The emission intensities are analysed in the following to understand the flame's characteristics with the crystal presence.

Cette thèse est accessible à l'adresse : http://theses.insa-lyon.fr/publication/2022LYSEI044/these.pdf
© [K. Utria Salas], [2022], INSA Lyon, tous droits réservés

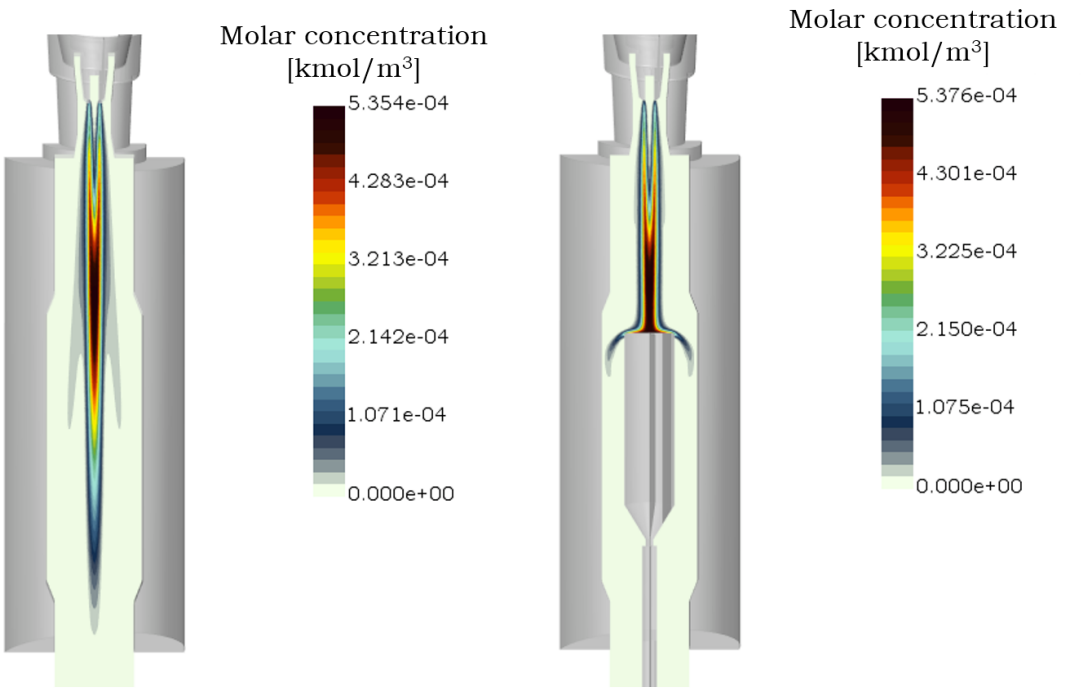

Figure 7.17: OH* molar concentration at Z=0 for crystallisation No.15 Final Growth Cycle

In figure 7.18 the experimental and numerical results of the final growth phase are depicted. It can be seen that the distribution obtained by both approaches seem to be overall concordant. Nevertheless, the experimental results are the emission intensities integrated along with the light-of sight. Therefore, the Abel deconvolution is used to validate the numerical calculations.

The emission intensities obtained after the image post-processing and numerical molar concentrations at Y-axis are depicted in figure 7.19a for the final growth phase which showed to have the highest different in distribution in the previous section.

As observed, the results are globally concordant regarding the positions of the maximum production of OH* radicals. However, the distribution does not seem to be accurate. The differences in the distribution of OH* production between the two results at the Y-axis are probably related to the post-processing effectuated to the OH* chemiluminescence, which uses as revolution axe this position, Y=0. It is important to mention, that the acquisition system must be installed under axisymmetric configuration (at Y=0) to guarantee accurate results.

Cette thèse est accessible à l'adresse : http://theses.insa-lyon.fr/publication/2022LYSEI044/these.pdf
© [K. Utria Salas], [2022], INSA Lyon, tous droits réservés

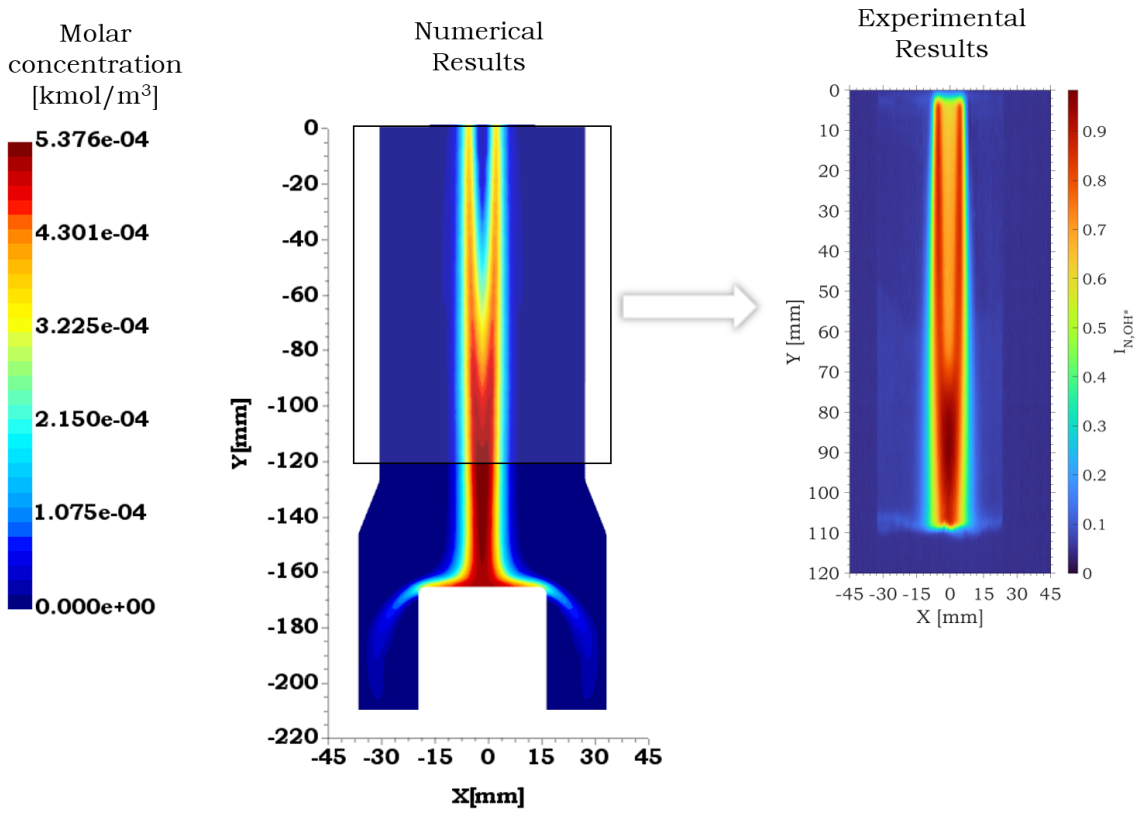

Figure 7.18: OH* molar concentration at Z=0 for crystallisation No.15 Final Growth Cycle

Another important effect could be related to the temperature of the crystal. The wall boundaries (ceramic insulation, injectors, crystal) were defined as adiabatic in the simulation. In real conditions, a small area of the crystal is in the liquid state ($T \cong 2050°$) to achieve crystallisation. The correct temperature distribution on the crystal external surface is unknown due to the extremely high temperatures and radiation. Determining these conditions results challenging for the present study, nevertheless their impact on the thermal behaviour of the crystal growth environment can explain the difference between the experimental and numerical approach on the OH* distribution within this zone.

In addition, the inlets velocities were calculated directly from the flow rate values for the simulation. This could also contribute to the differences between the numerical and experimental results. Nevertheless, these results indicate that the simulation can be used as a reference to examine the flame and flow structure and development.

Hence, the distribution in the crossed section at the maximum emission and concentration are depicted in figure 7.19b to validate the results obtained experimentally and numerically. As shown, the trends of the results are similar, the differences are <10 %.

Cette thèse est accessible à l'adresse : http://theses.insa-lyon.fr/publication/2022LYSEI044/these.pdf
© [K. Utria Salas], [2022], INSA Lyon, tous droits réservés

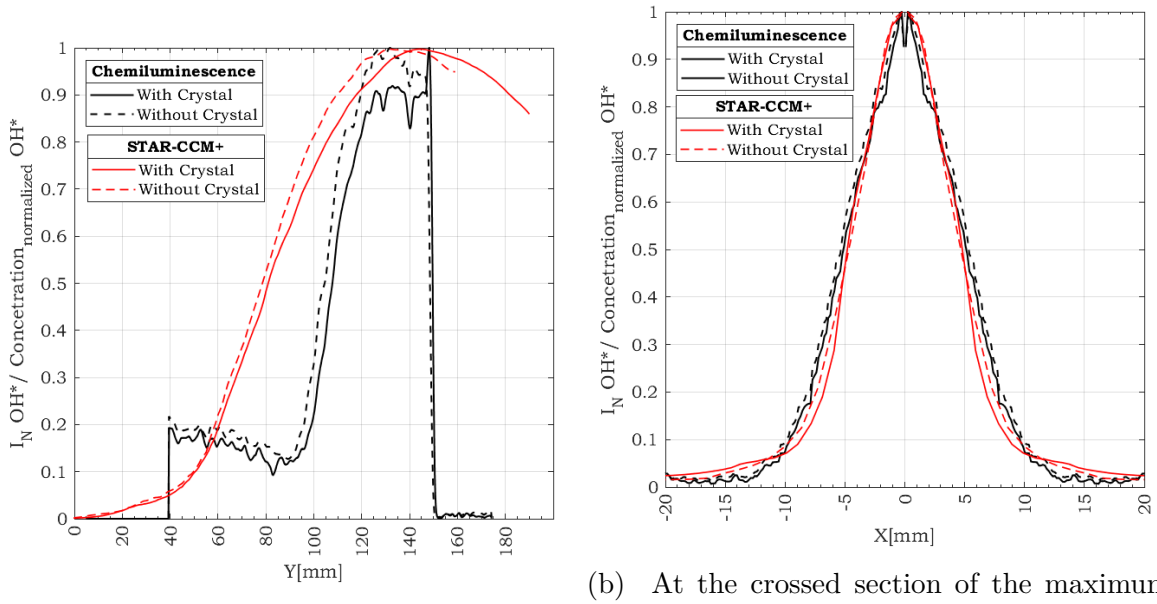

(a) At the centreline (X=0)

(b) At the crossed section of the maximum emission and concentration of OH*

Figure 7.19: OH* normal concentration at centreline for crystallisation No.15 Initial Formation Cycle (Z=0)

Once the numerical results are validated, the reaction flows' initial conditions are analysed in order to determine the flow conditions at the O_2 nozzle exit.

Figure 7.20 illustrates for the initial formation cycle the velocity vectors. It can be observed a small recirculation next to the O_2 nozzle lip. The H_2 jets cover the nozzle lip and some velocity vectors within this zone tend to go up towards the nozzle lip. However, they mostly stay in this region, since the velocity are close to zero, the Y-distance between the O_2 exit and the moment that the transversal component of the velocity is zero, is 10mm. This effect could be responsible for the stabilisation mechanism of the flame.

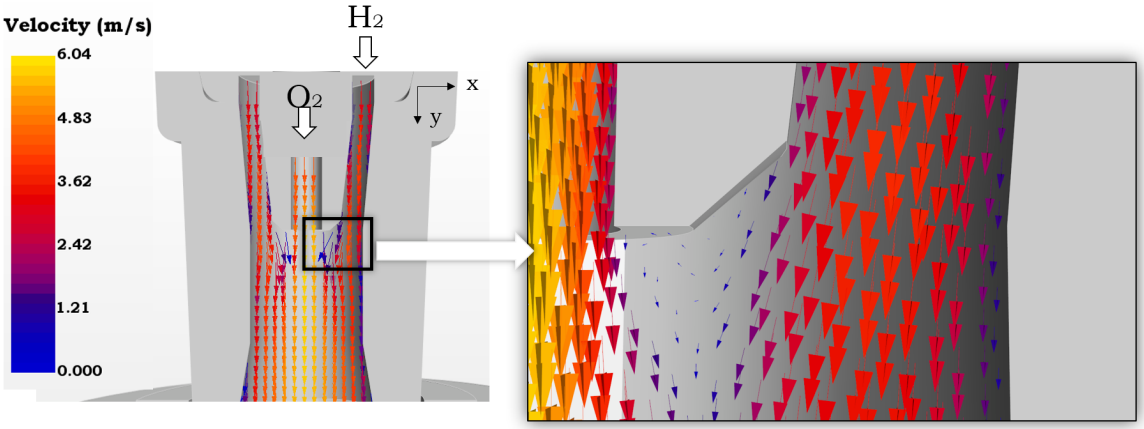

Figure 7.20: Inlet burner injection conditions of crystallisation No.15 for the initial formation cycle - Reacting Flow

Cette thèse est accessible à l'adresse : http://theses.insa-lyon.fr/publication/2022LYSEI044/these.pdf
© [K. Utria Salas], [2022], INSA Lyon, tous droits réservés

The initial conditions for the three operating points with and without the crystal presence are depicted in figure 7.21. The negative values of the axial velocity confirmed the small recirculation next to the O_2 nozzle lip. The increase in $\cong 1.4m/s$ of the velocity with the presence of the reaction zone is also observed in the numerical simulation compared to the cold inlet velocity. The highest transversal velocities are located at the shear layer. This effect is related to two aspects: the velocities difference and the reaction zone located at this zone. The mixing between the two layers occurs in this region.

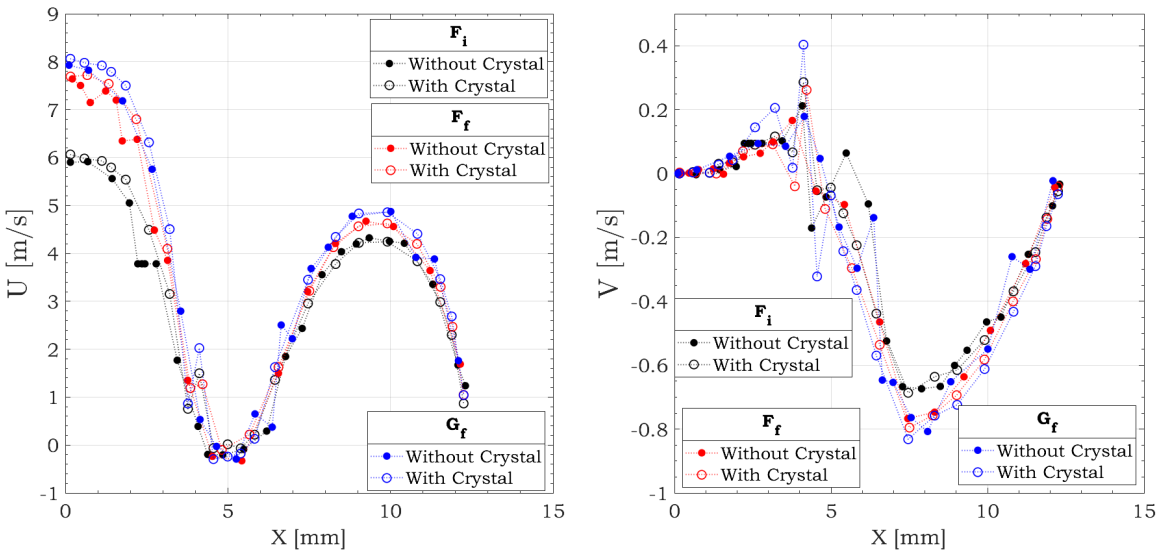

(a) Axial component U (b) Transversal component V

Figure 7.21: Initial conditions for crystallisation No.15 Initial Formation Cycle (at O_2 nozzle exit Y=0)

In addition, the development of the flow was examined in figure 7.22, as observed experimentally the decay rate is low due to the laminar characteristics of the flow that are the results of the coupling of the buoyancy and the coflow effects. The presence of the crystal deviates the flow at $Y \cong 149$mm for the three operating points.

The axial component decreases while the transversal component increases. The most significant changes for the transversal component were found with the final growth cycle velocities. These findings indicate that the flame structure is affected significantly by the velocities difference and their order of magnitude.

For the initial formation cycle the difference of the velocities between the H_2 and O_2 jets is higher than for the other two cycles but the inlet velocities are lower and the central reaction zone is located upstream as observed in figure 7.14 with y_f, which is the Y-position at X=0 where occurs the flame closure.

In the case of the final formation and growth cycles, the difference between the velocities is the same. However, the final formation velocities are lower. Thus, the reaction zone

Cette thèse est accessible à l'adresse : http://theses.insa-lyon.fr/publication/2022LYSEI044/these.pdf
© [K. Utria Salas], [2022], INSA Lyon, tous droits réservés

is closer to the O_2 nozzle exit, which can be one of the reasons for the crystal's higher impact on the flow aerodynamic behaviour for the final growth cycle.

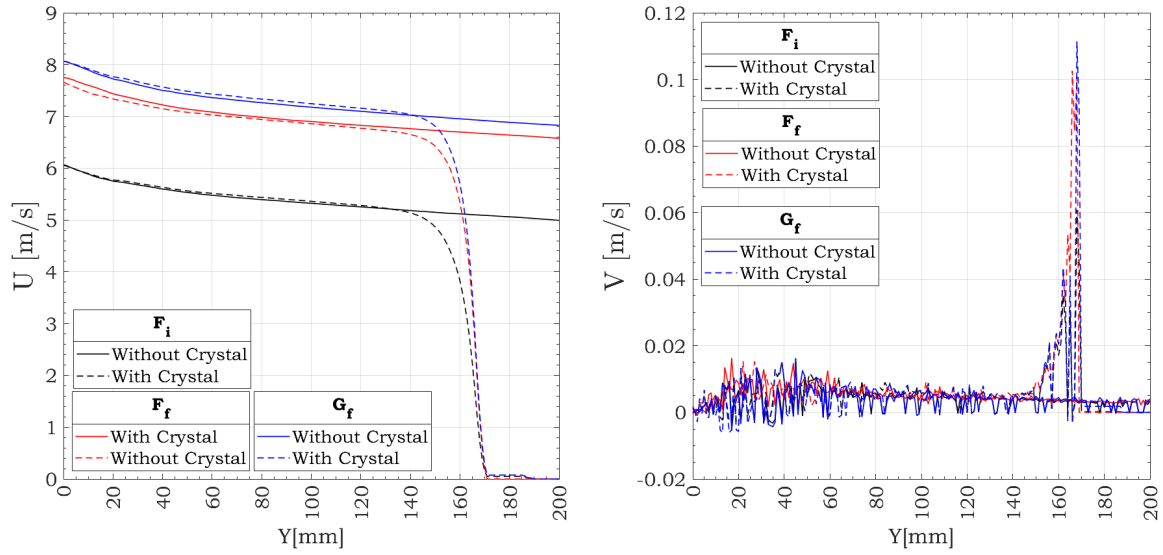

(a) Axial component U (b) Transversal component V

Figure 7.22: Flow development from the O_2 nozzle exit at centreline for crystallisation No.15 (X=0)

In order to understand better the flow behaviour at the contact zone between the flame and the crystal in figure 7.23 the velocity vectors are examined. As shown, the flow surrounds the crystal and a recirculation is observed at the contact point between the flame and the crystal. This recirculation depends on the velocity injection order of magnitude.

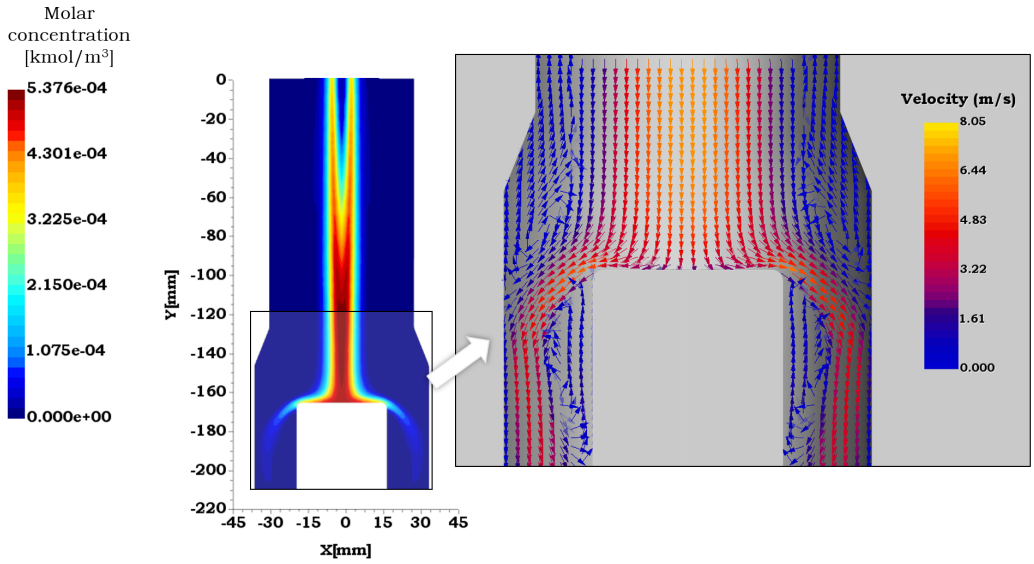

Figure 7.23: Influence of the stagnation point in the velocity vectors for crystallisation No.15 Final Growth Cycle - Reacting Flow

Cette thèse est accessible à l'adresse : http://theses.insa-lyon.fr/publication/2022LYSEI044/these.pdf
© [K. Utria Salas], [2022], INSA Lyon, tous droits réservés

Another important aspect of this zone is the molar concentration of H_2 found upstream and illustrated in figure 7.24. This concentration increases within this zone with the H_2 injection velocity due to higher momentum of H_2. These two effects seem to affect the flow behaviour so they are analysed ensuing.

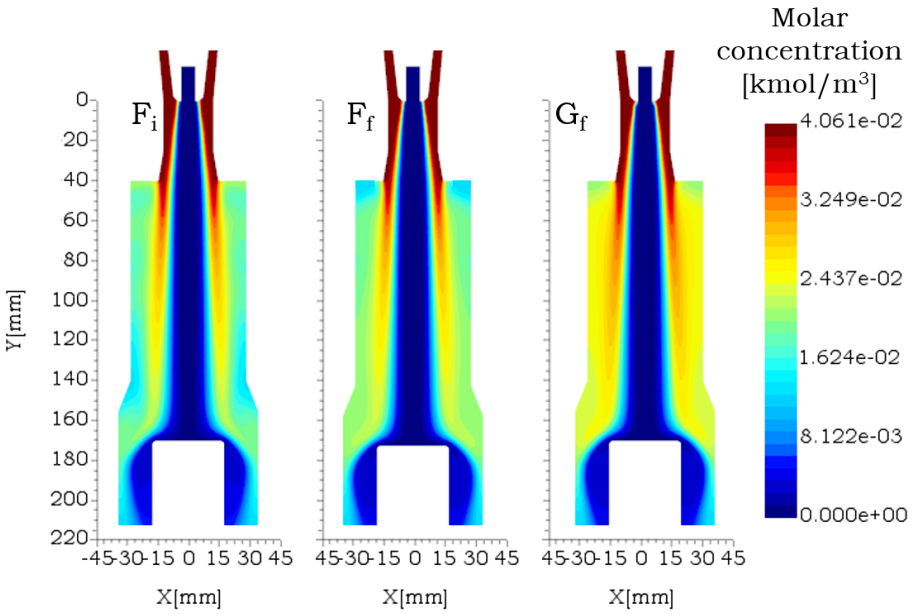

Figure 7.24: H_2 Molar Concentration for crystallisation No.15 Final growth Cycle - Reacting Flow

The velocities within the contact zone are analysed more in detail in figure 7.25. As observed, the higher the inlet velocity, the higher the impact on the flow structure. The final formation and growth cycles represent these conditions. They both have the same velocities difference, and the impact in the flow structure is similar. At the crystal contact, the axial velocities are zero, the transversal velocity increases to achieve their maximum at the end of the top face of the crystal to then decrease. At this point, the axial velocities begin to increment, and at the border close to the ceramic wall negative components are observed. Afterwards, the flow behaviour affects the mixing, the flame structure, and more globally the reaction zone.

Cette thèse est accessible à l'adresse : http://theses.insa-lyon.fr/publication/2022LYSEI044/these.pdf
© [K. Utria Salas], [2022], INSA Lyon, tous droits réservés

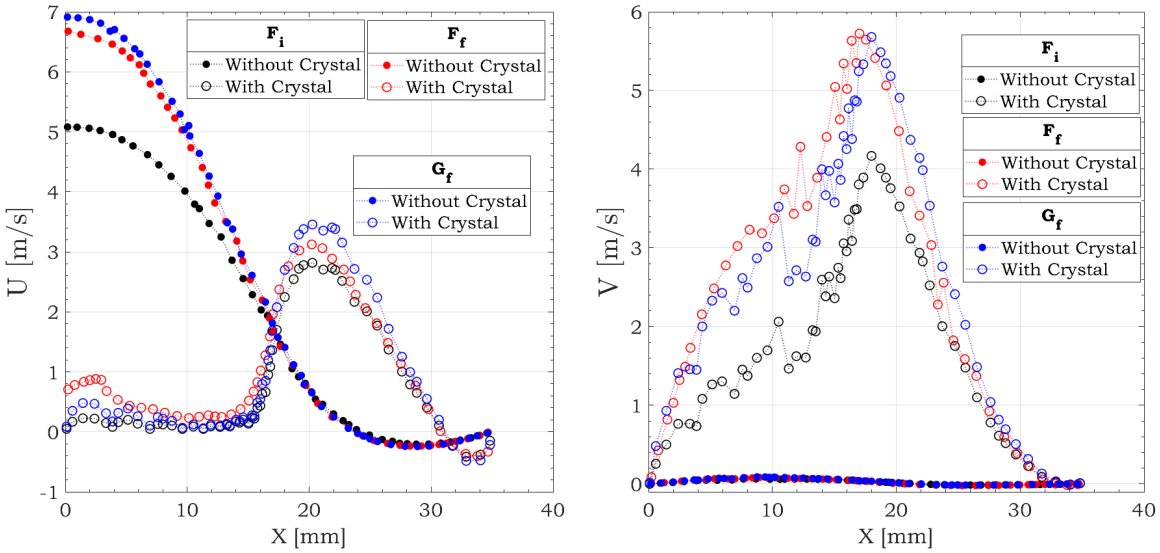

(a) Axial component U (b) Transversal component V

Figure 7.25: Velocities at the stagnation for crystallisation No.15 - Reacting Flow Y=169 mm from the O_2 Nozzle

The link between the aerodynamic and chemical reaction effects explain the shift of the central reaction zone upstream observed experimentally in section 7.2. The highest shift is obtained for the initial formation; this presents the shortest flame due to the lowest injection velocities. Thus, the reaction zone is further from the contact point, the excess of H_2 within this zones recirculates to mix and react with the central O_2 jet, enhancing the reaction. The excess of H_2 decreases with the crystal presence, and it is consumed faster, as observed in the previous section for this operating point.

The central reaction zone is located at the contact point between the reactive flow and the crystal for the two other cycles. The peripheral H_2 jets recirculate and react with the central O_2 also enhancing the reaction observed in the increase of the OH^* emission intensities in the case of the experimental results and on the molar concentration in the numerical results shown in figures 7.26. These results are confirmed in figure 7.27, as observed the highest effective mass diffusivity is found for the initial formation, which has an equivalence ratio of 1.6, hence the mixing is better, and the burning is faster for these injection conditions.

Cette thèse est accessible à l'adresse : http://theses.insa-lyon.fr/publication/2022LYSEI044/these.pdf
© [K. Utria Salas], [2022], INSA Lyon, tous droits réservés

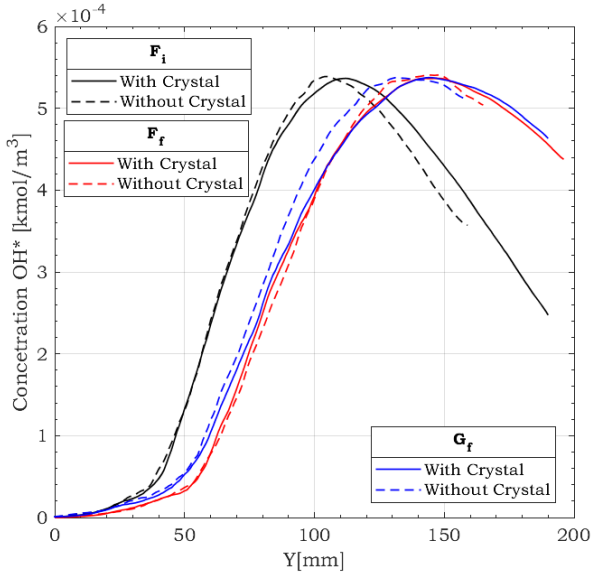

Figure 7.26: OH* Molar Concentration for crystallisation No.15 Final growth Cycle - Reacting Flow

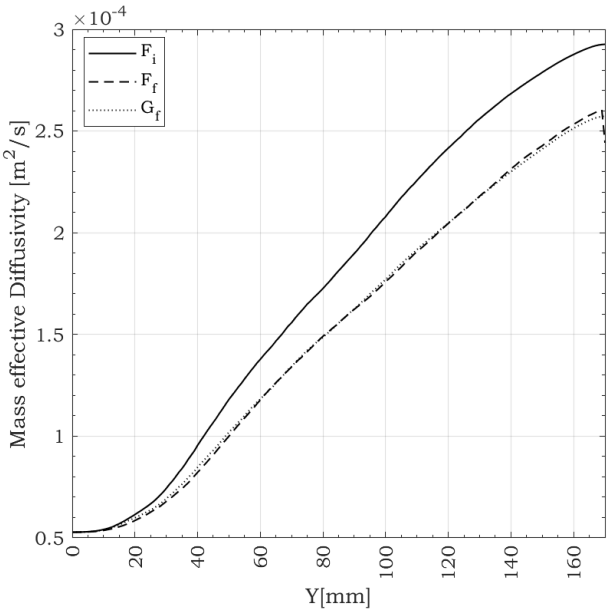

Figure 7.27: Mass effective diffusivity for crystallisation No.15 - Reacting Flow

Furthermore, the stagnation point's influence on the flame's thermal behaviour is analysed by the temperature distribution in the confinement. Figure 7.28 shows the temperature contour for the three crystallisation cycles analysed. In the case of the "free flame", four typical thermal zones are identified. At the O_2 nozzle exit, the temperatures are relatively low. The base flame comprises a cold central core which is located in the potential core region of the O_2 jet. The two reaction zones located on the sides present a gradually increase in the temperature, these zones correspond to the mixing zone beyond the O_2 exit. The cold core still exists, which is due to the existence of the excess O_2 in the

Cette thèse est accessible à l'adresse : http://theses.insa-lyon.fr/publication/2022LYSEI044/these.pdf
© [K. Utria Salas], [2022], INSA Lyon, tous droits réservés

centre. The mixing of fuel and oxidiser is finally completed in this region before it reaches the central reaction zone, which starts at y_j. At this point, the temperature is 40% of the maximum temperature. This result is in good agreement with the results of the concentration of OH^*. The zone of maximum temperature extends with the increase of U_{0,O_2}. The post-flame zone is characterised by an extended high-temperature region, where complete combustion is achieved. This long high-temperature post-flame zone together with the high-temperature reaction zone, is a feature that makes the IDF highly desirable for heating application. The highest maximum temperature is obtained with the initial formation cycle due to the injection condition of $\phi = 1.6$. As observed, this point also represents the flame with the highest effective mass diffusivity. Since the burning is faster for this operation point, the temperatures are lower in the post-flame zone.

Regarding the flames with the crystal present, the temperature distribution is dependent on the injection conditions. As observed, the post-flame temperatures are lower for F_i cycle, the distribution of the temperature beyond the stagnation point making less uniform. The final growth phase represents the distribution temperature most homogeneous of all the operation conditions, as seen, the temperatures are distributed uniformly along the crystal surface which means the temperatures gradients are the lowest. These findings are in good agreement with the operators' process regarding the crystallisation of the sapphire. They explain the necessity of increasing the flow rates during crystallisation. At the beginning of the crystallisation, the melting area is the smallest. Over time, the "boule" diameter increases, which make necessary to increase the liquid zone to maintain the circular shape of the crystal. This is performed through the control of the flame structure, which is executed through the flow rate injections. The crystal needs to touch a wider zone of high temperature at the end of the cycle to keep an adequate temperature gradient that contributes to a good crystalline structure.

The aerodynamic study revealed that the flow structure is impacted principally when the inlets velocities are the highest. The momentums increase; hence the static pressure at the contact zone increases, then more gas recirculates, changing the flow structure.

Cette thèse est accessible à l'adresse : http://theses.insa-lyon.fr/publication/2022LYSEI044/these.pdf
© [K. Utria Salas], [2022], INSA Lyon, tous droits réservés

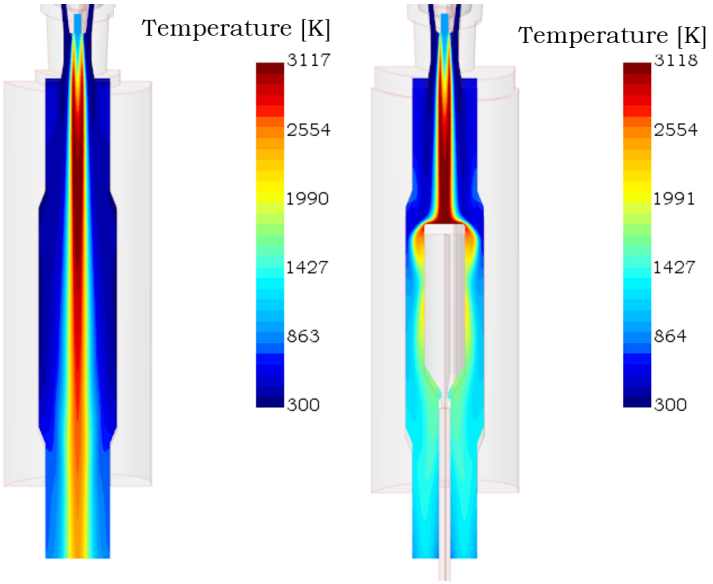

(a) Initial Formation Cycle

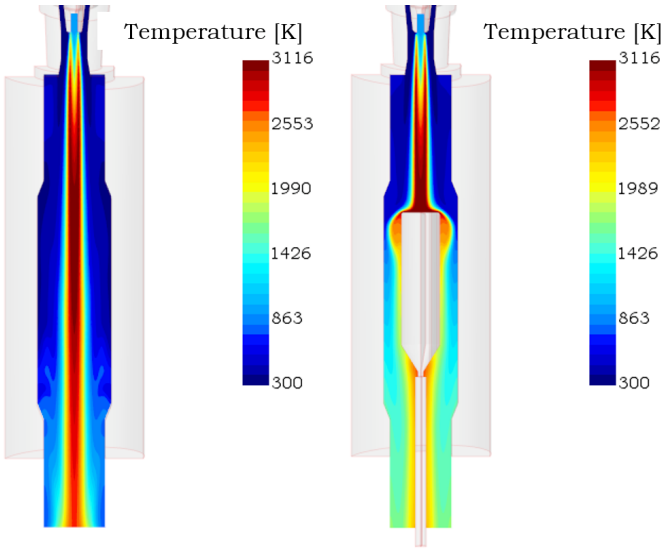

(b) Final Formation Cycle

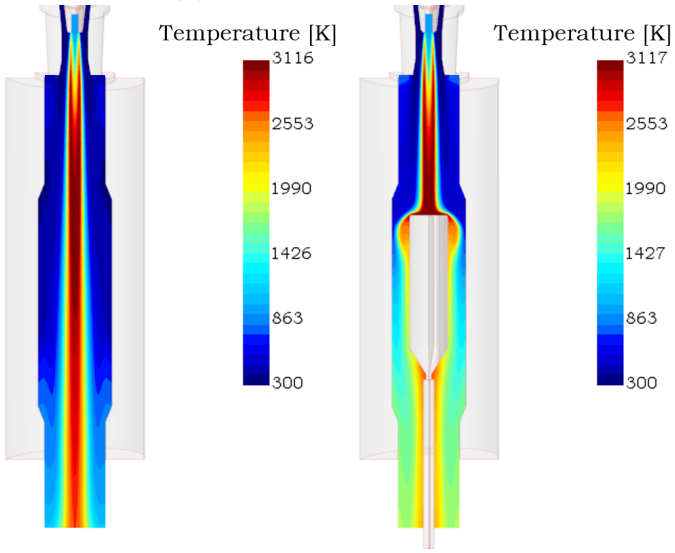

(c) Final Growth Cycle

Figure 7.28: Temperature Distribution of Crystallisation No.15 Final Growth Cycle (Z=0)

Cette thèse est accessible à l'adresse : http://theses.insa-lyon.fr/publication/2022LYSEI044/these.pdf
© [K. Utria Salas], [2022], INSA Lyon, tous droits réservés

7.4 Conclusions

The influence of the crystal presence on the flame structure characteristics and OH^* emission intensities were analysed along with their effect on the flow structure and development. The OH^* chemiluminescence visualisation was used to analyse the flame structure behaviour experimentally. The aerothermodynamics of the system was examined through the implementation of numerical tools. A numerical approach has been adapted to describe this unique burner configuration.

The crystal presence in the reaction zone causes various effects on the flame due to the apparition of a contact area and a wall jet area that enhance the mixing and the combustion on the reaction zones. This enhancement depending on the flow rates, especially the O_2 injection velocity causes an upstream shift of the central combustion zone and a widening of the reaction zone in diffusion mode. The combustion becomes faster, and it is observed owing to the shorter flames obtained with the crystal presence. The crystal also contributes to increase the temperatures in the confinement due to the increase of the heat release produced by the contact of the flame with the crystal liquid phase.

Furthermore, regarding the flow structure, the principal impacts are found when the inlets velocities are the highest. The momentums increase; hence the static pressure at the contact zone increases, then more gas recirculates, changing the flow structure.

However, the reaction zone location is more affected for the lowest inlet velocities. The excess of the H_2 is lower due to the combustion enhancement resulting from the recirculation of the H_2. Because the effective mass diffusivity is higher, the burning of the fuel is faster, resulting in shorter flames.

Finally, the flame obtained with a Verneuil burner in the crystal's presence could be partially compared to a typical impinging flame. Due to the elevated distance between the O_2 nozzle, the effect of the stagnation point is less observed ($H/D_{O_2} > 13$) upstream on the reaction zone. However, the enhancement in the combustion (from the point of view of the industrial constraints) could be observed with this arrangement.

Cette thèse est accessible à l'adresse : http://theses.insa-lyon.fr/publication/2022LYSEI044/these.pdf
© [K. Utria Salas], [2022], INSA Lyon, tous droits réservés

Cette thèse est accessible à l'adresse : http://theses.insa-lyon.fr/publication/2022LYSEI044/these.pdf
© [K. Utria Salas], [2022], INSA Lyon, tous droits réservés

Chapter 8 | Influence of ceramic insulation in crystal features

This chapter has as principal objective to study realistic solutions that can optimise the *Verneuil method*. A new geometry of the internal ceramic insulation surface has been proposed. This is a first approach to increase the efficiency of the process, the impact of this new configuration on the reactive flow is continuously examined in order to develop an adequate solution to optimised this complex system.

The new geometry was conceived from the results observed in chapter 1. These results revealed that the highest crystal quality were obtained between crystallisations No.7 and No.19. The ceramic insulation dimensions of these crystallisations were used considering also the feasible dimensions by the supplier. The classic and new geometry profiles are shown in figure 8.1. In order to analyse the impact of this parameter, all the classic qualities indicators and conditions were examined, two different tests were carried out for the two furnaces already used in chapter 1 (see figure 1.3):

- *Furnace 1*: The change of the geometry is implemented at crystallisation No.11. At this point, the classic ceramic insulation achieved the geometry close to the new geometry
- *Furnace 2*: The new geometry is used during all the insulation life cycle.

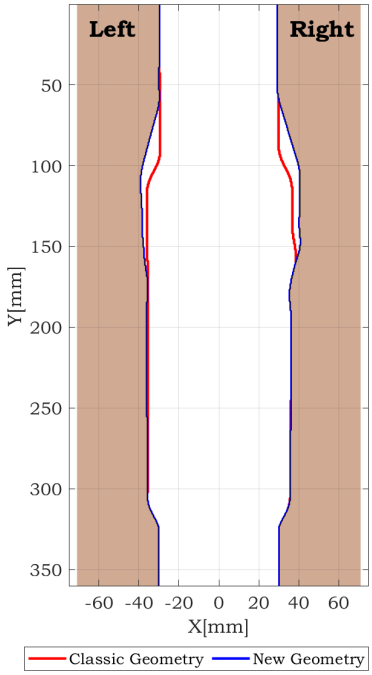

Figure 8.1: New Geometry

Cette thèse est accessible à l'adresse : http://theses.insa-lyon.fr/publication/2022LYSEI044/these.pdf
© [K. Utria Salas], [2022], INSA Lyon, tous droits réservés

8.1 Evolution of operating conditions

In this section, the flame controlled variables as flow rates injections and dependent variables as temperature and ceramic thickness were analysed in order to determine the initial conditions of the combustion.

The flow rates used for this study are shown in figure 8.2, which corresponds to the initial insulation conditions in the case of crystallisation No.1 and crystallisations No.11 (change of the geometry). As observed before, the injection flow rates determine the flame structure and flow development, which likewise define the conditions of the crystal growth environment. Therefore, it is important to corroborate that the initial conditions for each test are similar during the study to compare the different quality indicators and crystal features.

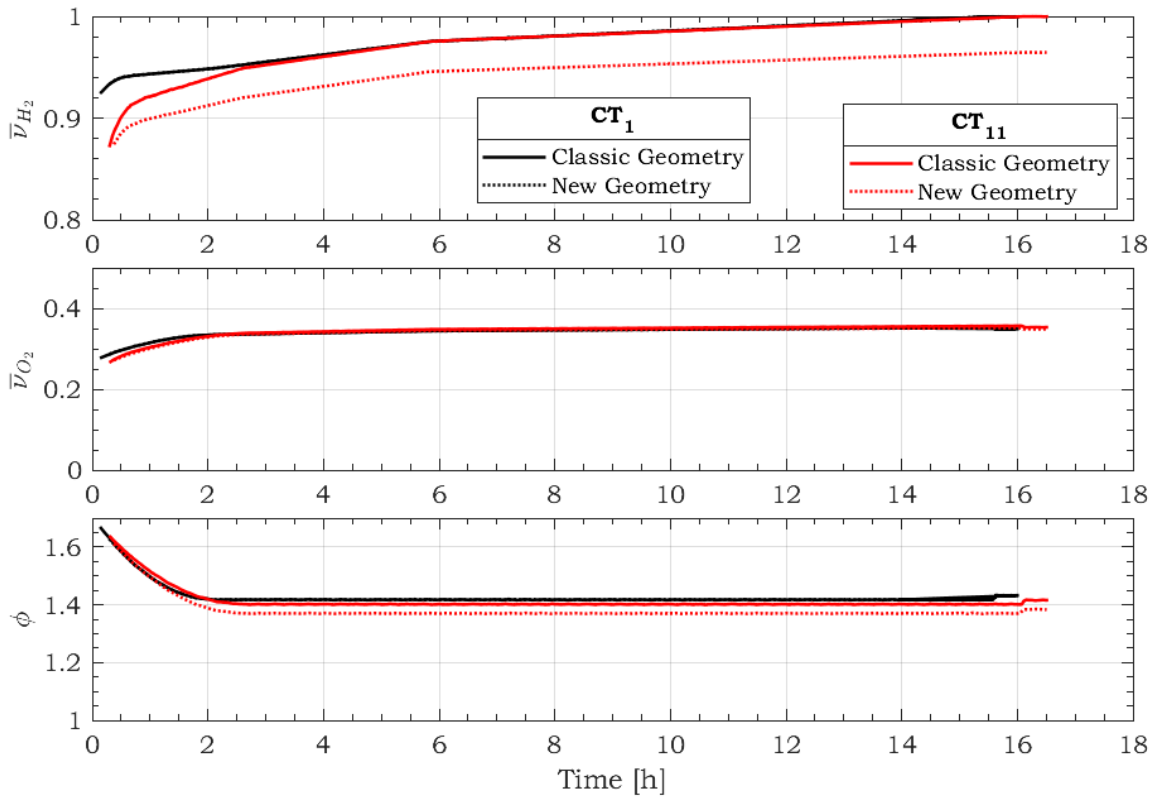

Figure 8.2: Flow rates evolution

Some differences were detected during the development of the tests, for instance a decrease of 5% on the oxygen flow rates was observed for the three crystallisations. Nevertheless, hydrogen flow rates stayed constant, as the injection equivalence ratios, confirming that the flame structure is the same for the three tests performed.

Cette thèse est accessible à l'adresse : http://theses.insa-lyon.fr/publication/2022LYSEI044/these.pdf
© [K. Utria Salas], [2022], INSA Lyon, tous droits réservés

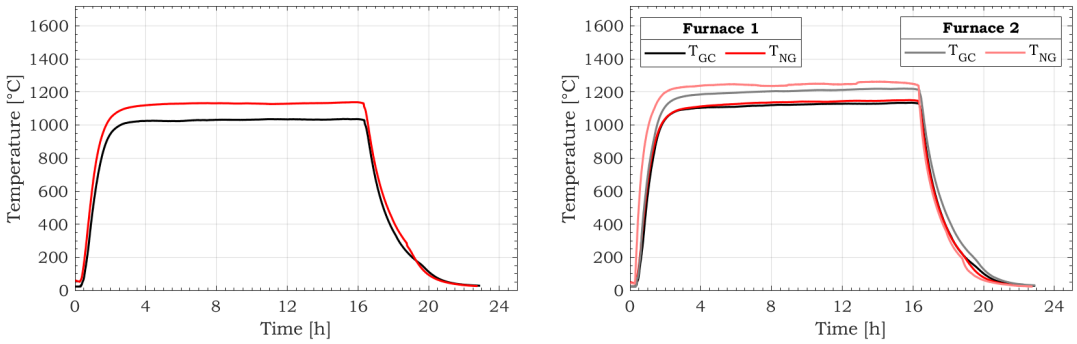

(a) T_1 $Y = 80mm$ side

(b) T_2 $Y = 160mm$ side

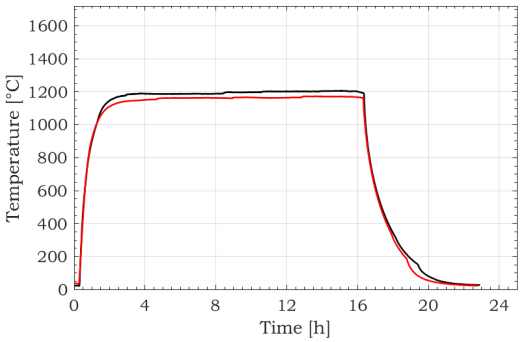

(c) T_5 $Y = 160mm$ front

Figure 8.3: Temperature evolution CT_1

The thermal conditions of the crystalline growth environment are analysed through the temperatures for the two geometries at the positions previously mentioned in section 1.2.2.1. These temperatures were also analysed from two different approaches. In the first instance, the temperatures obtained in crystallisations No.1 and No.11 for the classic and new geometry are compared at the upper part of the confinement to acknowledge each test's thermal conditions at the beginning of the insulation life cycle.

Secondly, the temperatures between two consecutive crystallisations are examined. These crystallisations correspond to the moments before and after the change of geometry, and this is performed with the purpose to compare the thermal conditions before and after the geometry change in *Furnace 1*.

In figure 8.3 temperatures for the first crystallisation cycle are illustrated. As observed, at Y= 80 mm (T_1) in *Furnace 2*, the temperatures varied in $\cong 150°C$ between the classic geometry (NC) and the new geometry (NG). The increase is probably related to the change in the ceramic thickness at this Y-position. In *Furnace 1*, although the two tests have the same classic geometry. The materials used to perform the tests were different. This is because, during the development of the study, it could be observed that the upper part of the ceramic insulation and the bottom part do not share the same conductivity because two different suppliers fabricate them. At first, it was assumed that the materials

Cette thèse est accessible à l'adresse : http://theses.insa-lyon.fr/publication/2022LYSEI044/these.pdf
© [K. Utria Salas], [2022], INSA Lyon, tous droits réservés

were the same as the thermal properties. Nevertheless, a first test with the new geometry revealed the differences between the two materials. The new geometry was fabricated with the bottom part material of the ceramic insulation, which, as observed in the temperature results, presents a higher conductivity. Therefore, in order to have an accurate comparison of the two geometries, a second test was used to develop the analysis. The same material was used for all the crystallisations.

Another important observation of the two temperatures is at the highest values. It could be observed that the temperatures are almost the same for the front temperatures (T_5), analysing the results closely. This could be explained owing to the heat release rate at this point. The thermocouples are positioned close to the flame and the crystal; then, the two materials behave similarly. In contrast, for the temperature of the side, the difference is more remarkable. The diminution of the temperature is also related to the decrease of 5% on the flow rates.

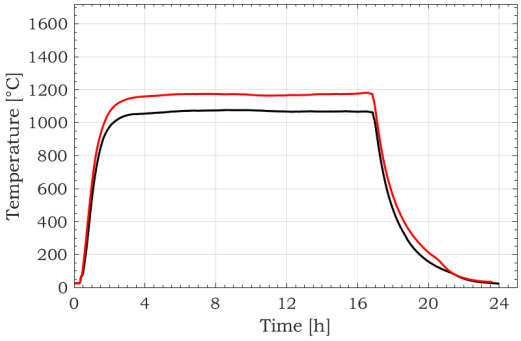

(a) T_1 $Y = 80mm$ side

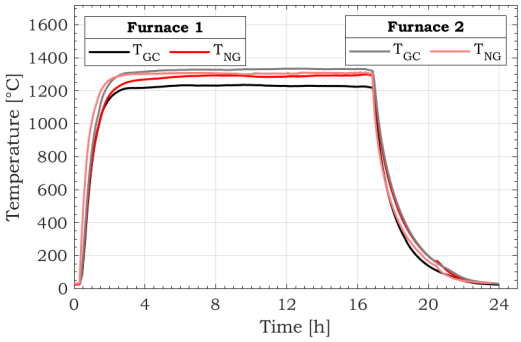

(b) T_2 $Y = 160mm$ side

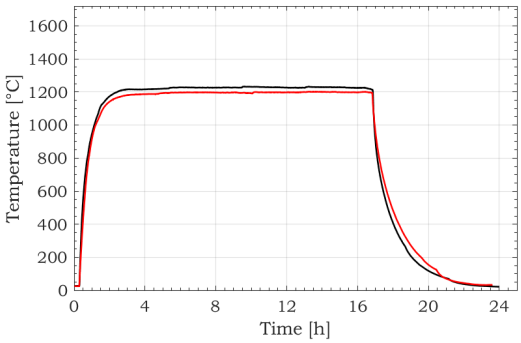

(c) T_5 $Y = 160mm$ front

Figure 8.4: Temperature evolution CT_{11}

As mentioned, the thermal conditions of the crystalline growth environment with the two geometries are examined through the temperatures. In the case of *Furnace 1*, the temperatures of the classic and new geometry correspond to crystallisation No.11. The respective temperatures are compared in figure 8.4. It can be observed an augmentation of the temperature for the second test on the sides due to the diminution of the ceramic insulation for this crystallisation, as observed in figure 8.7. The front shows similar temperatures because the geometries on the front did not change. This denotes that the influence on the front side is less observed because the thermocouple is also closer to the flame, since the ceramic thickness in the front is lower.

Cette thèse est accessible à l'adresse : http://theses.insa-lyon.fr/publication/2022LYSEI044/these.pdf
© [K. Utria Salas], [2022], INSA Lyon, tous droits réservés

The thermal conditions between the two geometries were also examined through the temperatures before and after the change in the geometry, for *Furnace* 1. In figure 8.5, temperatures are illustrated for the three *Y-positions* at the upper part of the confinement in order to understand the growth environment conditions. With the same purpose, the ceramic thickness is depicted in figure 8.7.

For T_1 (Y=80 mm), the temperatures are almost the same, which indicates that the thermal conditions were similar. The δ_{cer} diminished, which should also decrease the temperature. However, the material is a new one in which thermal conductivity is higher because it has been less used. Besides, it has not been exposed to high temperatures yet, changing the thermal insulation properties. This is confirmed by examining the values of δ_{cer} and T_2 (Y=160 mm) in figures 8.5 and 8.7, respectively. These two parameters decrease, indicating that the thermal conductivity has increased due to the younger material. On the other hand, it can be observed the augmentation in T_5 (front of the confinement) $\cong 100°C$ for the new geometry due to the decrease in the ceramic thickness (see figure 8.7).

These results are essential to better understand the crystalline growth environment and their influence on the crystal features, which is analysed in the next section. Higher temperatures for the new geometries indicate lower temperature gradients which affect the ovalisation index and the internal quality of the crystal (see sections 1.3.1.2 and 1.3.2.2).

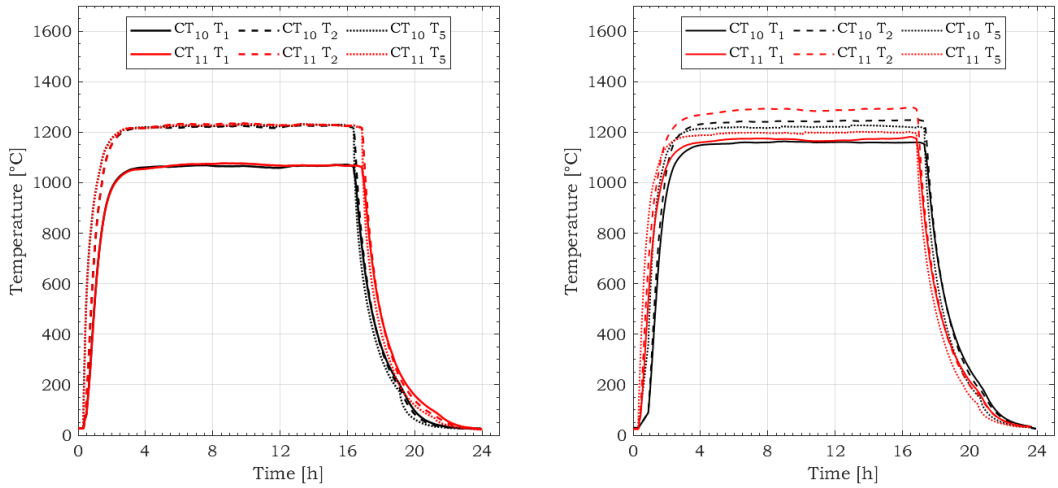

(a) Classic Geometry (b) New Geometry

Figure 8.5: Comparison between Temperatures CT_{10} and CT_{11} Furnace 1

The temperatures along Y-axis were also analysed in figure 8.6. As observed, the temperature gradient in *Furnace 1* increases with the new geometry between the top temperature and the bottom temperature. This effect could affect the number of foils in the crystalline

Cette thèse est accessible à l'adresse : http://theses.insa-lyon.fr/publication/2022LYSEI044/these.pdf
© [K. Utria Salas], [2022], INSA Lyon, tous droits réservés

structure, which is analysed in 8.2.4.

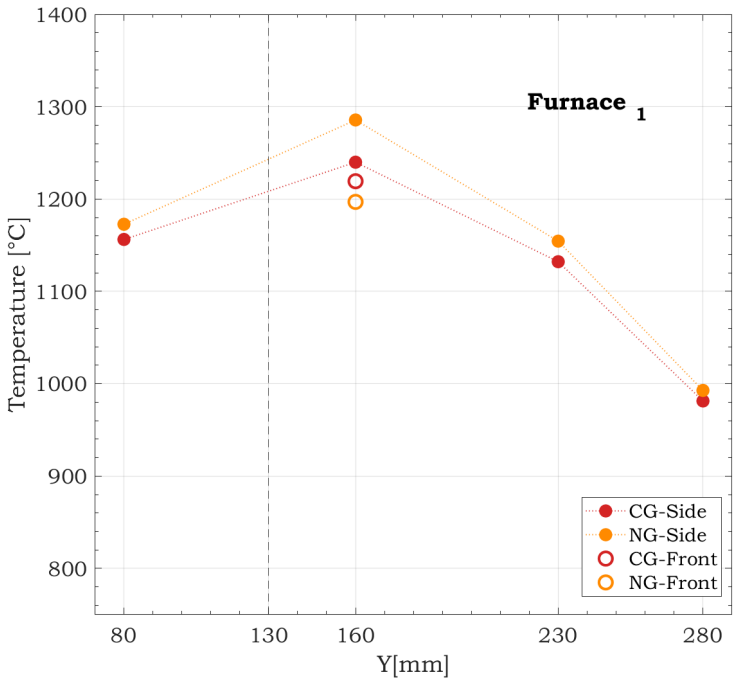

Figure 8.6: Temperature distribution along Y-axis, Furnace 1 CT No.10 (CG) and CT No.11 (NG)

It is important to mention that the ceramic geometry also affects the aerodynamics of the flame. Since the space of the flow development is increased, then the recirculation upstream of the jets decreases which can increase the temperature on the growth environment due to the increase in the combustion rate at the contact zone between the reactive flow and the crystal in growth.

Hence, the decrease of the temperature T_2 between the two crystallisations can only be explained by the used of a more recent material in crystallisation No.11, since this is located above the contact area. At the same time, the increase in the temperature for crystallisations No.1 and No.10 between the two materials can only be explained by the difference of the thermal properties.

Cette thèse est accessible à l'adresse : http://theses.insa-lyon.fr/publication/2022LYSEI044/these.pdf
© [K. Utria Salas], [2022], INSA Lyon, tous droits réservés

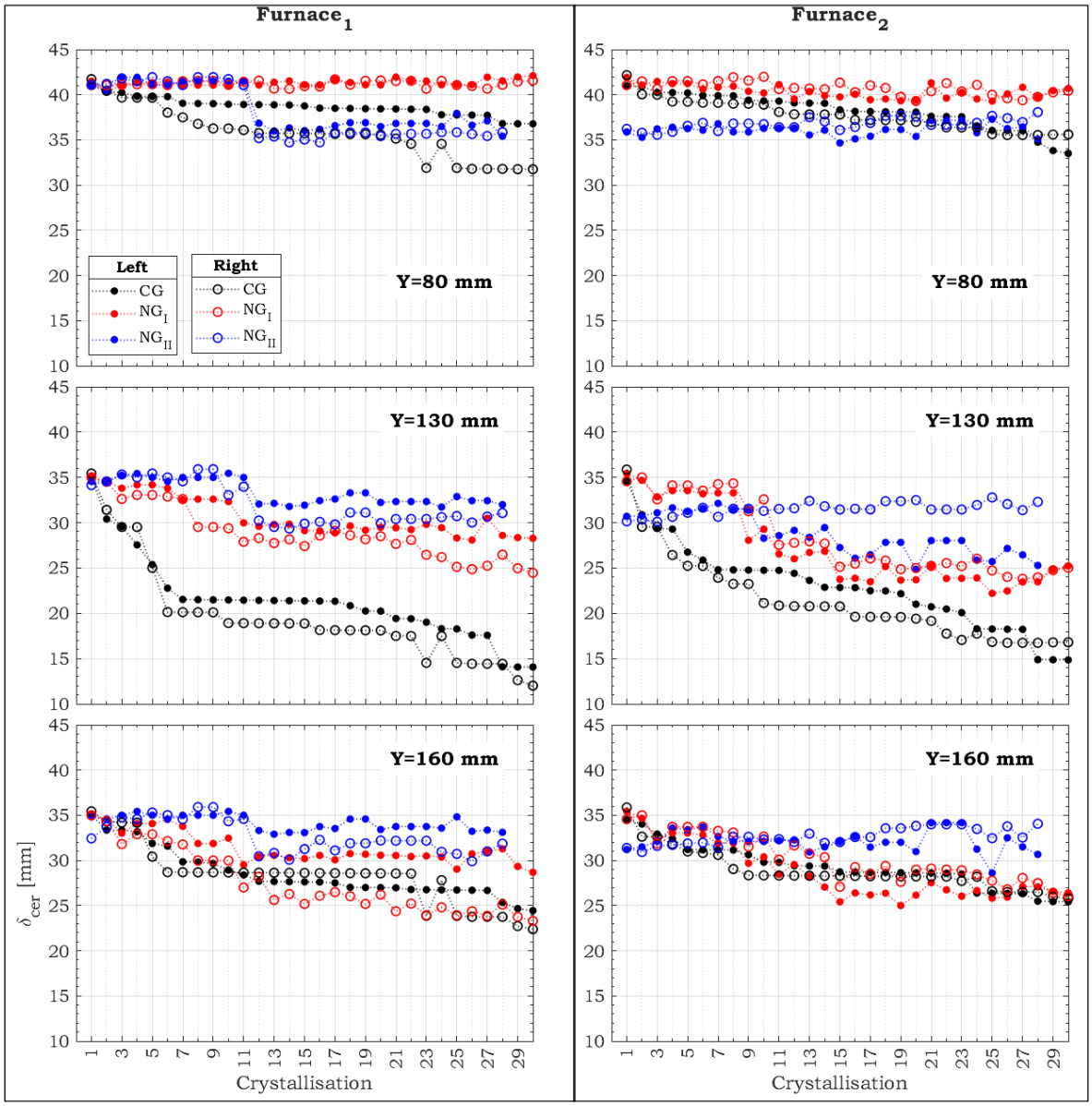

Figure 8.7: Ceramic thickness δ_{cer}

The new geometry reported higher temperatures compared to that of the classic geometry, these results indicate a lower heat loss and a lower thermal gradient between the internal and external surface of the ceramic insulation

Cette thèse est accessible à l'adresse : http://theses.insa-lyon.fr/publication/2022LYSEI044/these.pdf
© [K. Utria Salas], [2022], INSA Lyon, tous droits réservés

8.2 Crystal geometrical features

After exploring the thermal conditions of the crystal growth environment, the crystal's geometrical features were analysed to define the type of crystal obtained with each operating and geometrical conditions. The first analysis performed was to the diameter crystal and ensuing the ovalisation index.

8.2.1 Diameter evolution

Figure 8.8 depicts the crystal diameters ($\oslash_{boule}$) for the three tests during their insulation life cycles. At first sight, the diameter of the new geometry are lower for furnace 1 except in crystallisations No.8 and 9, where $\oslash_{boule}$ reported higher values. In contrast, in *Furnace 2* it is higher after crystallisation No.14. In chapter 1, it was found that the diameter dependency is essentially on the flow rates. These are similar for both geometries. As observed, the trends are not evident; thus, an one-Way ANOVA was performed to examine the influence of the geometry for this parameter.

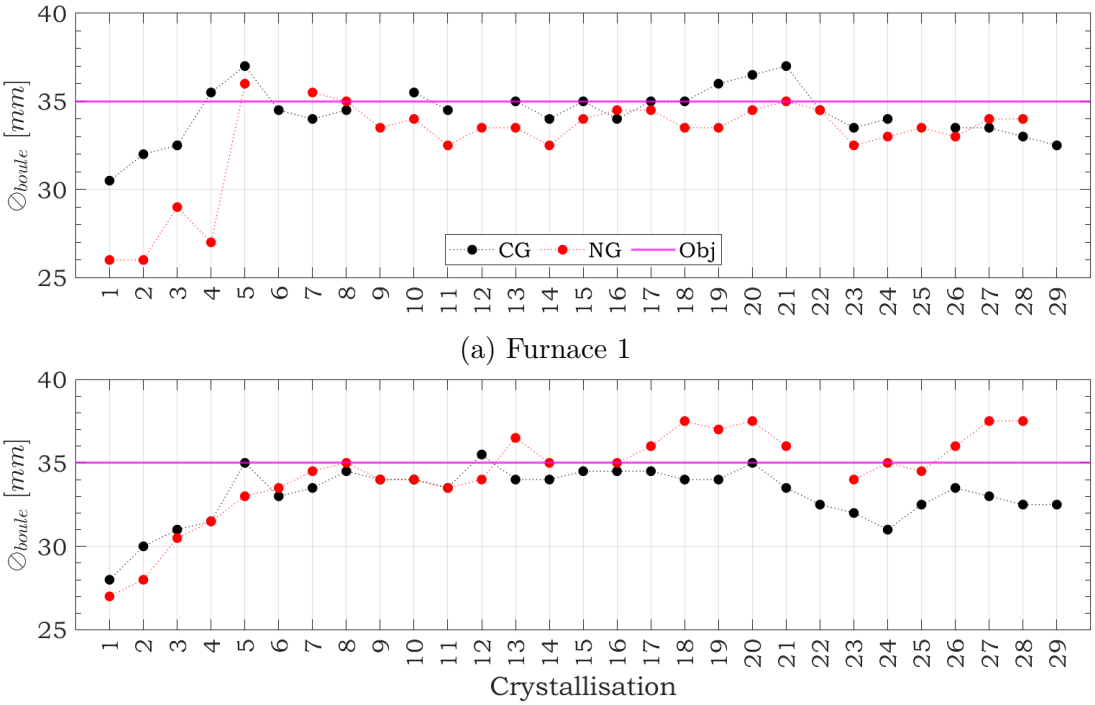

(a) Furnace 1

(b) Furnace 2

Figure 8.8: Diameter Evolution

In table 8.1 the $p-value > 0.05$ indicates that the boule diameter is not influence by the ceramic insulation geometry. The new geometry shows the same median value as classic geometry see figure 8.9.

Cette thèse est accessible à l'adresse : http://theses.insa-lyon.fr/publication/2022LYSEI044/these.pdf
© [K. Utria Salas], [2022], INSA Lyon, tous droits réservés

Source	SS	df	MS	F	Prob>F
Groups	4.3	1	4.3	1.2	0.3
Error	316.8	88	3.6		
Total	321.1	89			

Table 8.1: Results one-Way ANOVA $\oslash_{boule}$

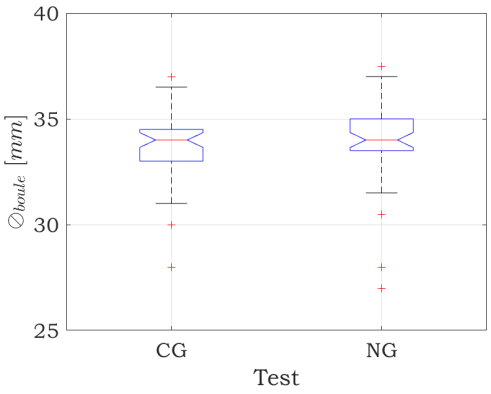

Figure 8.9: Anova Analysis Diameter

8.2.2 Ovalisation index evolution

In the case of the ovalisation index the analysis was performed independently for each furnace position since this index showed dependency on the furnace location. As observed in figure 8.10, for *Furnace 1* the ovalisation index seems to decrease with the new geometry, contrarily in *Furnace 2*. In order to analyse the influence of the new geometry on the ovalisation an one-Way ANOVA was performed.

Cette thèse est accessible à l'adresse : http://theses.insa-lyon.fr/publication/2022LYSEI044/these.pdf
© [K. Utria Salas], [2022], INSA Lyon, tous droits réservés

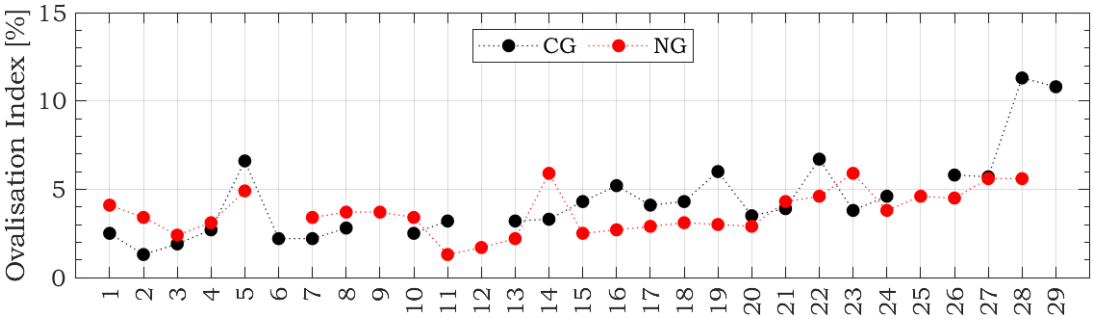

(a) Furnace 1

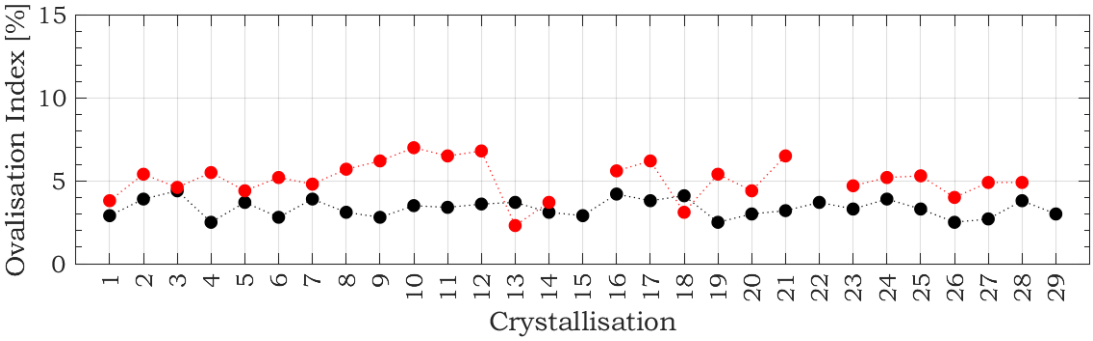

(b) Furnace 2

Figure 8.10: Ovalisation Index Evolution

Tables 8.2 and 8.3 confirm the influence of the internal insulation geometry on the ovalisation index. In both cases the $p - value < 0.05$, indicating that the means are statistically significant.

Source	SS	df	MS	F	Prob>F
Groups	27.3	1	27.3	6.52	0.01
Error	142.6	34	4.2		
Total	169.9	35			

Table 8.2: Results one-Way ANOVA Ovalisation Index *Furnace 1*

Source	SS	df	MS	F	Prob>F
Groups	33.2	1	33.2	27.5	2.6E-06
Error	65.1	54	1.2		
Total	98.3	55			

Table 8.3: Results one-Way ANOVA Ovalisation Index *Furnace 2*

Furthermore, the median values are calculated for each furnace in figure 8.11. It can be seen that *Furnace 1* reported a lower median for the new geometry, in contrast for *Furnace*

Cette thèse est accessible à l'adresse : http://theses.insa-lyon.fr/publication/2022LYSEI044/these.pdf
© [K. Utria Salas], [2022], INSA Lyon, tous droits réservés

2 this parameter increased.

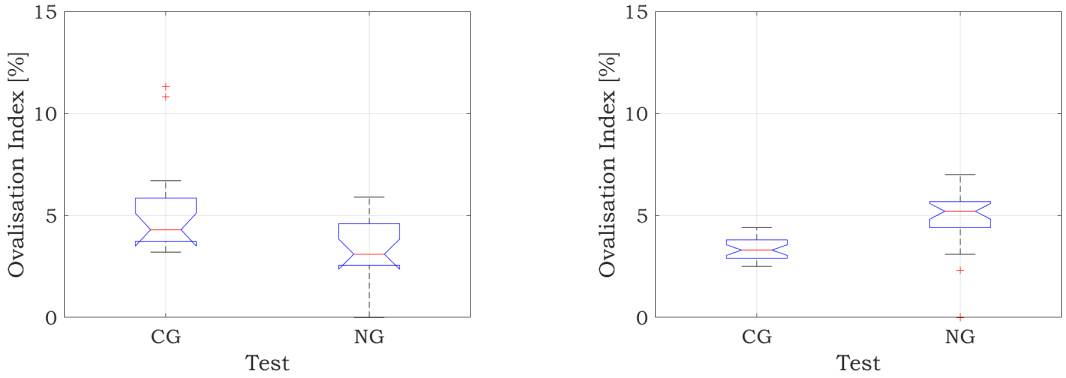

(a) Furnace 1 (b) Furnace 2

Figure 8.11: ANOVA Analysis Ovalisation Index

The new geometry did not report to influence the boule diameter. Nevertheless, the ovalisation index shows to be dependent of this parameter. In the case of ***Furnace 1****, "O_{in}" is lower with the new geometry, in contrast Furnace 2 showed higher values with the change, this can be explained by the fact that the change in* ***Furnace 2*** *was performed from the beginning of the cycle.*

8.2.3 Geometrical quality parameters

The influence of the insulation geometry was also analysed on the geometrical quality parameters. In figure 8.12 the quantity of geometrical defects are illustrated for the two furnaces and are also classified according their type. As observed the new geometry for *Furnace 1* reported less geometrical defects as compared to the classic geometry, in the figure the results are compared from the change in geometry (CT_{11}). In the case of *Furnace 2* , the comparison is done from the beginning since the geometry was place at this moment. The new geometry shows more geometrical defects, increasing specially the ovalisation.

The results confirm the correlation between the geometry of the insulation and the injection flow rates. The correct choice of the two parameters produce the crystals with the less geometrical defects. As observed, for *Furnace 1* the change was performed at the crystallisation No.11, and for the *Furnace 2* it was effectuated at the beginning of the insulation cycle, explaining the increase in the geometrical defects.

It is important to mention that the thermal conditions for the two furnaces are not the same due to their location in the production line. *Furnace 1* is located at one extreme of

Cette thèse est accessible à l'adresse : http://theses.insa-lyon.fr/publication/2022LYSEI044/these.pdf
© [K. Utria Salas], [2022], INSA Lyon, tous droits réservés

the production line and *Furnace 2* is in the centre of the line. The former present higher heat loss than the latter. Therefore, the different performance of each furnace regarding the geometrical defects.

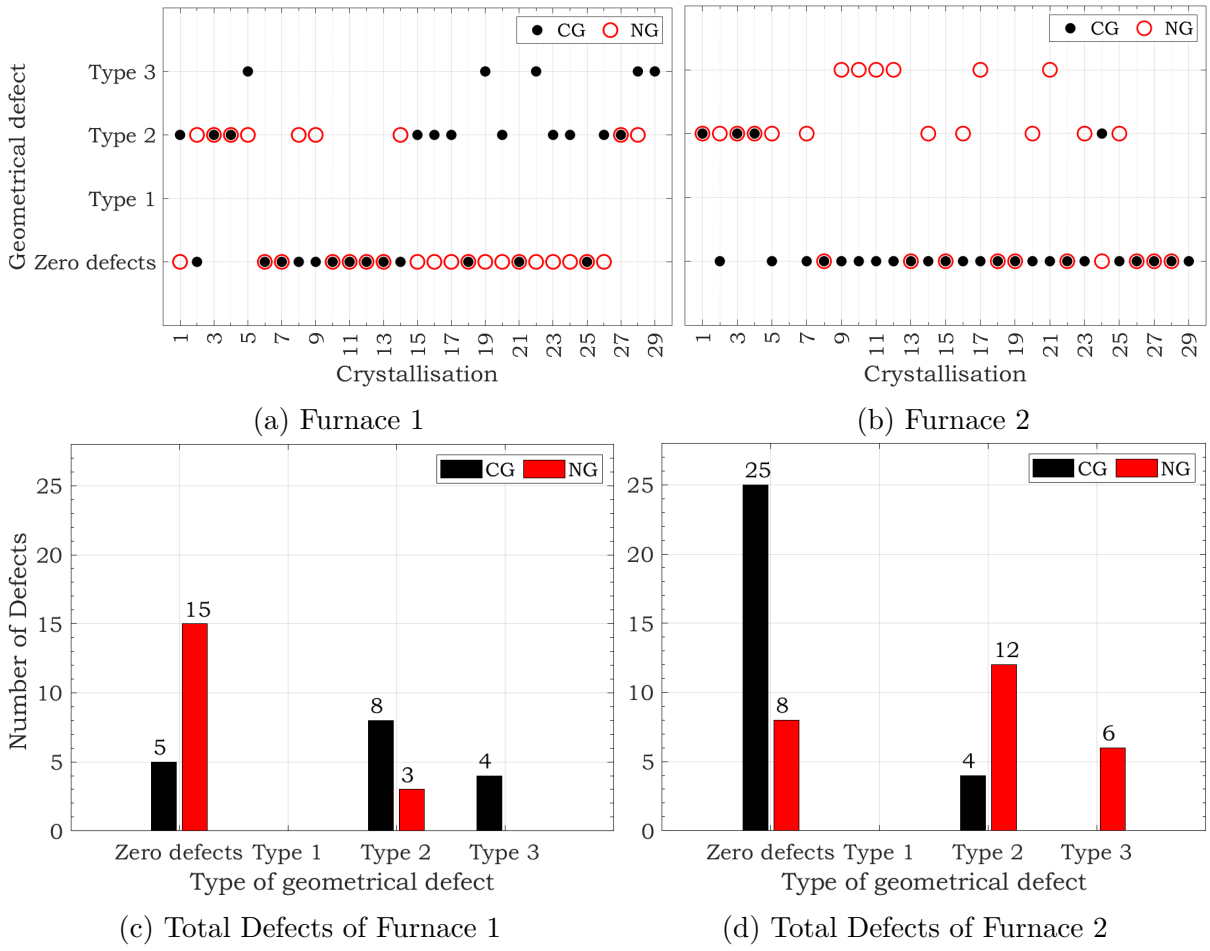

(a) Furnace 1

(b) Furnace 2

(c) Total Defects of Furnace 1

(d) Total Defects of Furnace 2

Figure 8.12: Geometrical defects

8.2.4 Internal quality parameters

The internal quality of the crystal highly depends on the thermal conditions of the crystalline growth environment (explained in subsection 1.3.2.2). The effect of the insulation geometry is analysed in order to determine their impact on the crystal internal quality. Figure 8.13 shows the number of bubbles and foils found for the two geometries along with the difference crystallisation. As before, the trends are not easy to identify; thus, an one-way ANOVA was performed.

Cette thèse est accessible à l'adresse : http://theses.insa-lyon.fr/publication/2022LYSEI044/these.pdf
© [K. Utria Salas], [2022], INSA Lyon, tous droits réservés

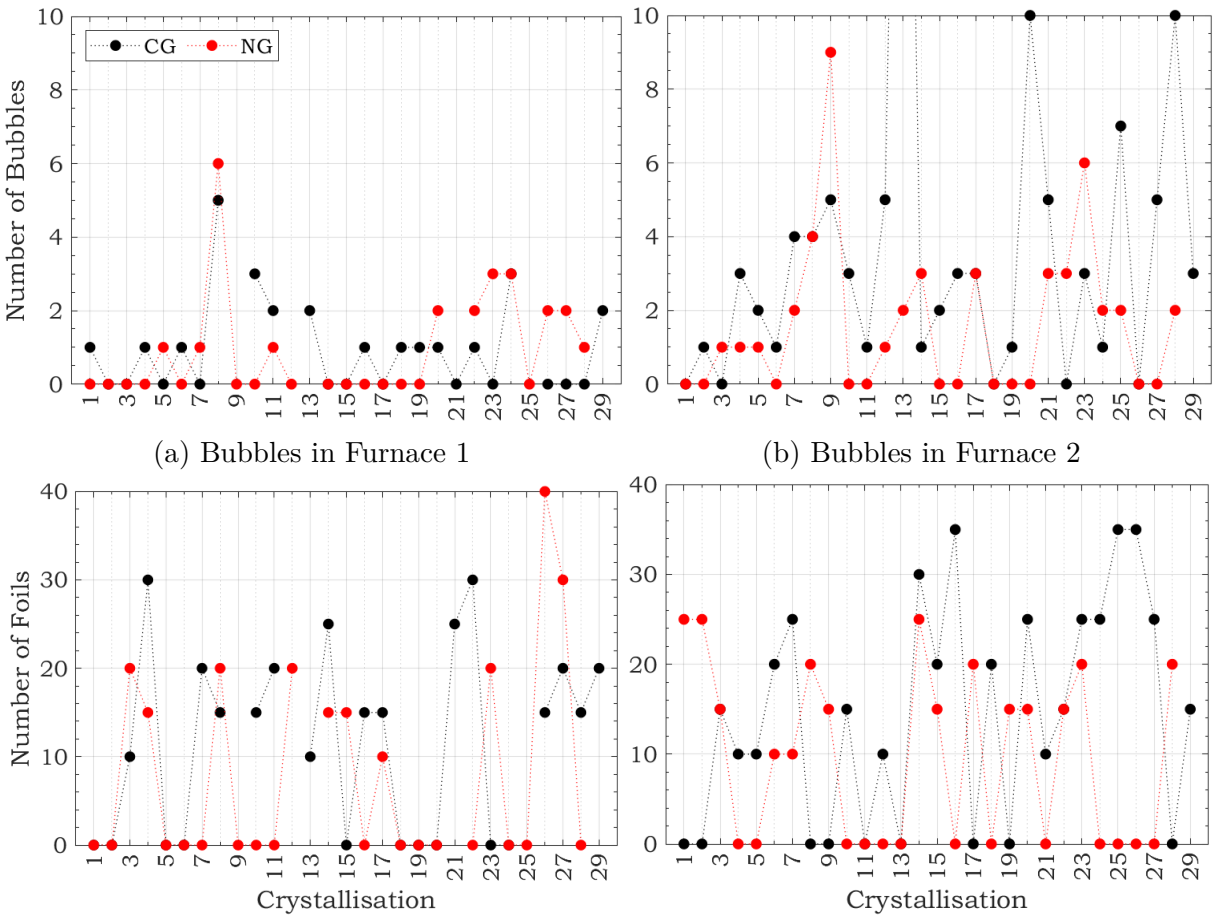

(a) Bubbles in Furnace 1

(b) Bubbles in Furnace 2

(c) Foils in Furnace 1

(d) Foils in Furnace 2

Figure 8.13: Internal defects

The analysis was performed independently for each furnace and type of defect. Table 8.4 shows a $p - value$ higher than 0.05, which indicates that there is not a statistically significant difference between the means of each geometry. The results denote that the new geometry does not impact the number of bubbles in *Furnace 1*. Contrarily, in table 8.5 the $p - value < 0.05$ which means that the new geometry influence the quantity of bubbles for the thermal conditions in *Furnace 2*, figure 8.14 a decrease in the median is observed.

Source	**SS**	**df**	**MS**	**F**	**Prob>F**
Groups	2.2	1	2.2	1.8	0.2
Error	24.8	21	1.2		
Total	26.9	22			

Table 8.4: Results one-way ANOVA Bubbles Furnace 1

Cette thèse est accessible à l'adresse : http://theses.insa-lyon.fr/publication/2022LYSEI044/these.pdf
© [K. Utria Salas], [2022], INSA Lyon, tous droits réservés

Source	SS	df	MS	F	Prob>F
Groups	81.2	1	81.2	15.8	3E-04
Error	211.1	41	5.1		
Total	292.3	42			

Table 8.5: Results one-way ANOVA Bubbles Furnace 2

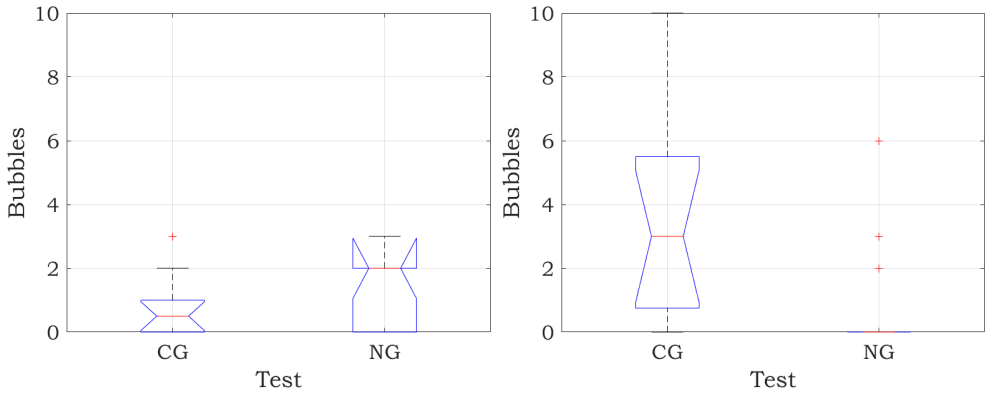

(a) Furnace 1 (b) Furnace 2

Figure 8.14: Anova Analysis for internal defects, Bubbles

For the foils defects the insulation geometry was found statistically significant for the *Furnace 2* with a $p-value < 0.05$ (see table 8.7) with a lower median than for the classic geometry (figure 8.15). Although in the case of *Furnace 1* the value was not statistically significant (table 8.6), the median was lower for the new geometry as observed in figure 8.15.

Source	SS	df	MS	F	Prob>F
Groups	73.0	1	73.1	0.5	0.5
Error	4.2E+03	31	135.5		
Total	4.3E+03	32			

Table 8.6: Results one-way ANOVA Foils, Furnace 1

Source	SS	df	MS	F	Prob>F
Groups	470.6	1	470.6	3.9	0.05
Error	6.8E+03	57	119.3		
Total	7.3E+03	58			

Table 8.7: Results one-way ANOVA Foils, Furnace 2

Cette thèse est accessible à l'adresse : http://theses.insa-lyon.fr/publication/2022LYSEI044/these.pdf
© [K. Utria Salas], [2022], INSA Lyon, tous droits réservés

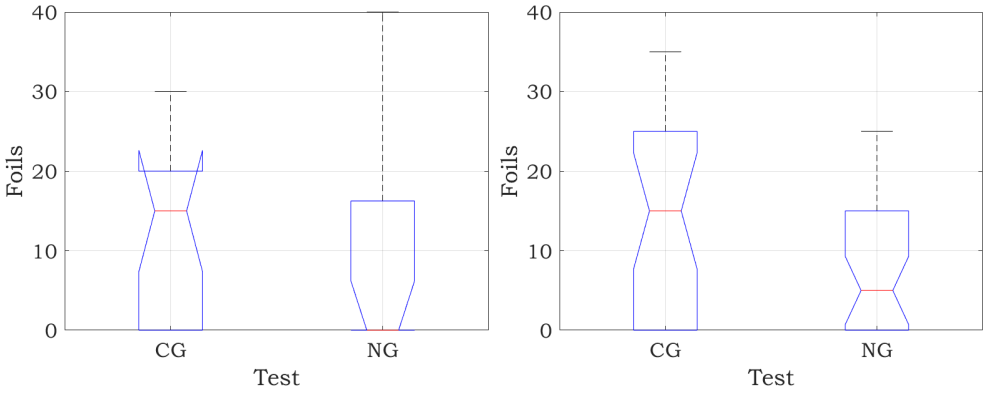

(a) Furnace 1 (b) Furnace 2

Figure 8.15: Anova Analysis for internal defects, Foils

The one-way ANOVA revealed that the influence of the new geometry depends on the furnace position. For the thermal conditions in ***Furnace 1****, the new geometry decreases the geometrical defects. Nevertheless, for* ***Furnace 2*** *these defects are more usually found. For the internal defects,* ***Furnace 1*** *did not seem to be affected by the insulation geometry, contrarily to* ***Furnace 2*** *where these kind of defects were diminished due to the decrease in the thermal gradient.*

Cette thèse est accessible à l'adresse : http://theses.insa-lyon.fr/publication/2022LYSEI044/these.pdf
© [K. Utria Salas], [2022], INSA Lyon, tous droits réservés

8.3 Influence of the insulation geometry on the aerothermodynamic behaviour

The influence of the ceramic insulation geometry on the flame structure and thermal interactions are analysed through numerical tools. The models are described in C.2 and the final growth cycle of crystallisation No.15 was chosen to be analysed because it presented the highest flow rates that seem to affect the most the flow development and structure. The results obtained by this simulations are dependent of the contraints imposed by the defined boundary conditions previously exposed in section 7.3.

The flame structure is examined with the distribution of OH* molar concentration. In figure 8.16 the contours are depicted. It can be observed a spreading out of the external zone of the flame with the new geometry. The central reaction zone is shifted downstream, and it is located closer to the *crystal boule*. The flame below the stagnation point is more opened, and it directs faster towards the ceramic boundary. This is observed owing to the Y-position of the contact point between the flame and the ceramic boundary. With the classical geometry, the flame does not touch this wall boundary. In addition, the value of the maximum concentration increases by 1%.

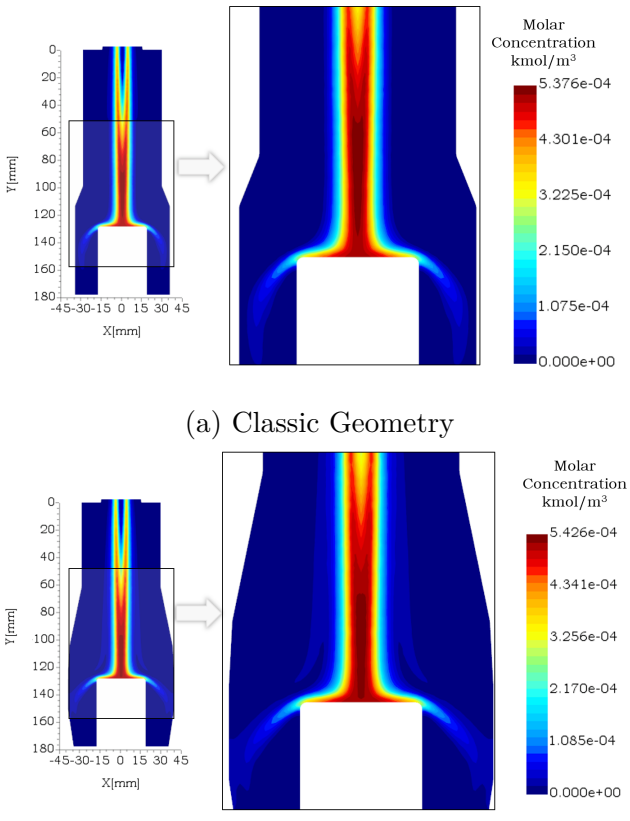

(a) Classic Geometry

(b) New Geometry

Figure 8.16: Molar Concentration of OH* $[kmol/m^3]$

The production of the concentration of OH* at the centreline is analysed in figure 8.17. It reveals the combustion enhancement in the zone close to the stagnation point from Y≅130 mm. Above the crystal, the concentrations of OH* are lower from Y≅55 mm for the new geometry. The flame closure y_j that occurs at 40% of the maximum production of OH*

Cette thèse est accessible à l'adresse : http://theses.insa-lyon.fr/publication/2022LYSEI044/these.pdf
© [K. Utria Salas], [2022], INSA Lyon, tous droits réservés

radicals is slightly shifted downstream. The reasons for these behaviours are analysed through the aerodynamics of the flow in the following.

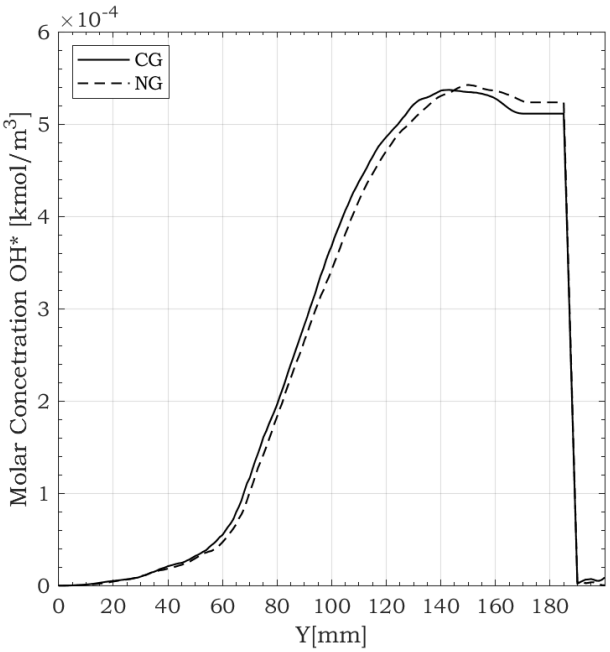

Figure 8.17: OH* Molar Concentration at Z=0 of crystallisation No.15-Final Growth Cycle (Z=0)

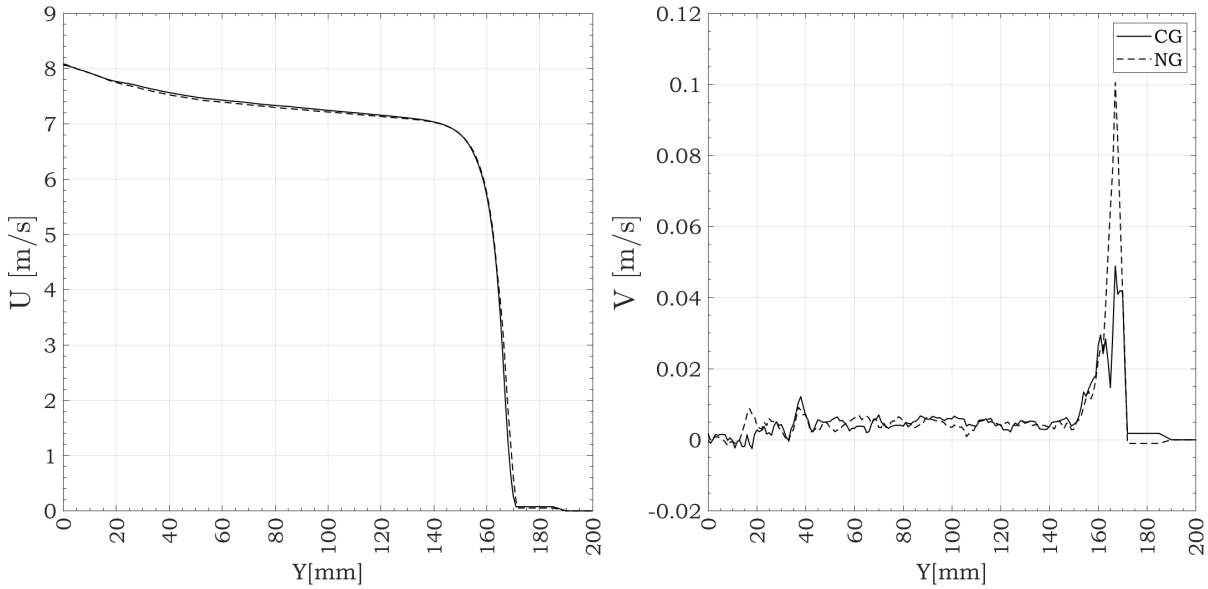

(a) Axial component (b) Transversal component

Figure 8.18: Flow developement at the centreline

The aerodynamic behaviour is analysed through the flow development. Figure 8.18 shows the axial and transversal velocities at the centreline for the two type of geometries. As observed, the change of the internal insulation geometry does not seem to affect the axial

Cette thèse est accessible à l'adresse : http://theses.insa-lyon.fr/publication/2022LYSEI044/these.pdf
© [K. Utria Salas], [2022], INSA Lyon, tous droits réservés

component; no major changes are seen. Contrarily, the transversal component reports an increase of 2.5 times for the new geometry. Besides, the contact area appears to have the same size for the two configurations.

The velocity field for the two geometries is analysed at the contact area in figure 8.19, in order to examine the impact of the new geometry on the aerodynamics of the system. As observed, the flow spreads out with the new insulation geometry. An increase of $\cong 0.02$ m/s is obtained for the maximum velocity magnitude.

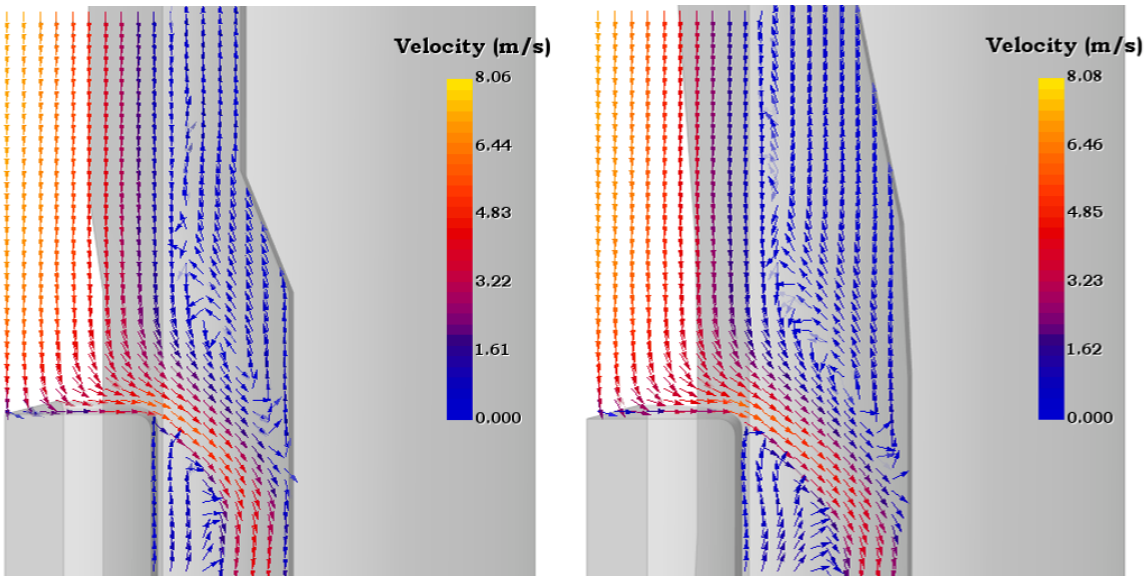

(a) Classic Geometry (b) New Geometry

Figure 8.19: Field Velocity at the contact point between the flow and the crystal

The transversal components are higher within the contact zone as can be seen in figure 8.20, an increment of $\cong 1.1$ m/s is observed, which explains the increase of the velocity magnitude. The axial component does not seem to be affected by the change in the geometry. Small increases are observed at the crystal borders. They are $\cong 0.01$ m/s and close to the ceramic boundary $\cong 0.4$ m/s. This means that the new confinement geometry enhances the recirculation of the peripheral jets towards the ceramic boundaries, spreading out the flame.

Cette thèse est accessible à l'adresse : http://theses.insa-lyon.fr/publication/2022LYSEI044/these.pdf
© [K. Utria Salas], [2022], INSA Lyon, tous droits réservés

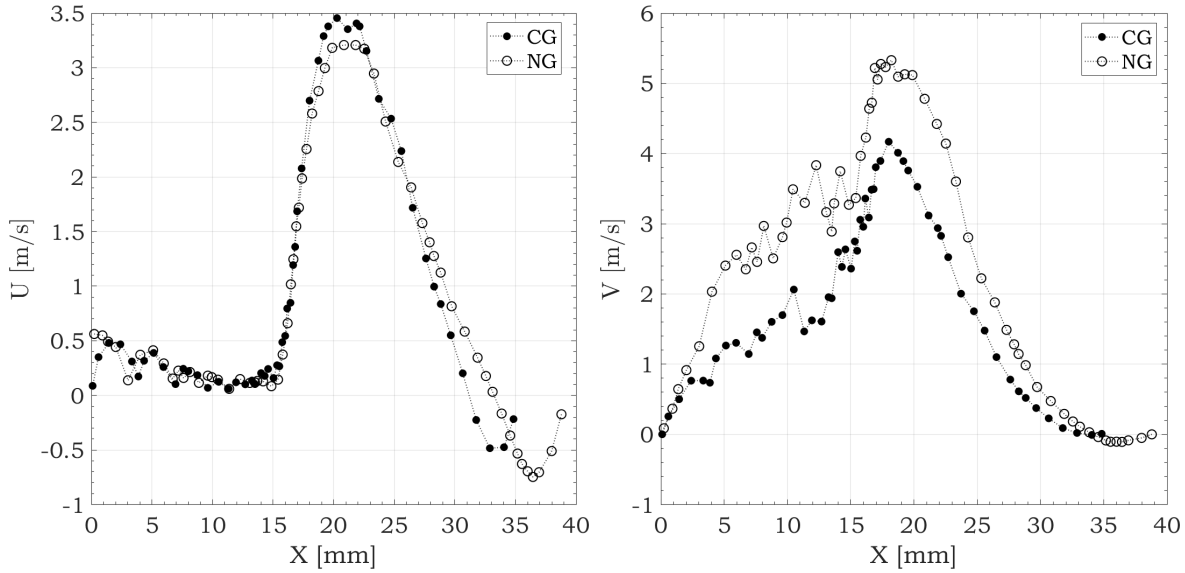

(a) Axial component (b) Trasversal component

Figure 8.20: Field Velocity at the contact point between the flow and the crystal

The thermal behaviour of the flames with the two configurations is examined by flame temperatures distribution. Figure 8.21 shows the temperature contours. It is important to mention that this is an approach of the thermal conditions of the crystal growth environment, due to the limitations of the simulation regarding the boundary conditions on the wall (e.g. the distribution of the crystal external surface temperature). Nevertheless, this study can be use as an indicator of the thermal behaviour of the *Verneuil method*.

In figure 8.21, it can be observed that the distribution is more homogeneous due to the increase in the recirculation of the jets. The "cold zone" that surrounds the flame (above the stagnation point) caused by the peripheral jet of H_2 decreased the temperatures close to the ceramic boundary show an increase in the cold jet diminishes.

Below the crystal, the high temperature zone extends as observed in figure 8.22. This indicates a diminution of the temperature gradient upon the crystalline growth environment. The numerical results are in good agreement with those obtain experimentally in figure 8.5 where an increase in the temperature of the external ceramic surface was observed.

Cette thèse est accessible à l'adresse : http://theses.insa-lyon.fr/publication/2022LYSEI044/these.pdf
© [K. Utria Salas], [2022], INSA Lyon, tous droits réservés

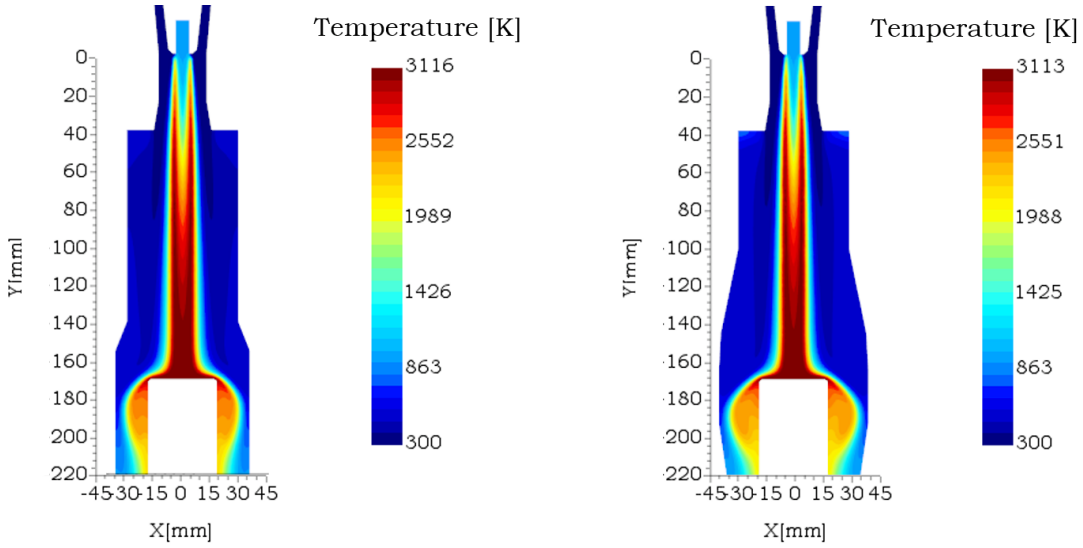

(a) Classic Geometry (b) New Geometry

Figure 8.21: Temperature Distribution

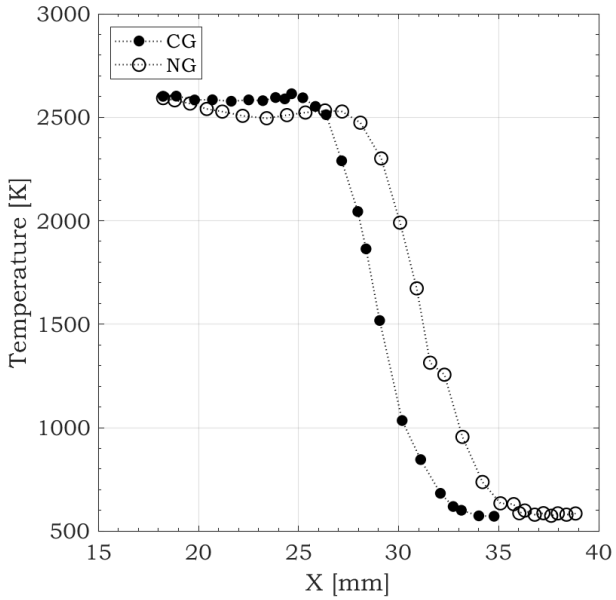

Figure 8.22: Temperatures at Y=171 mm

The new geometry enhances the recirculation of the peripheral jets towards the internal insulation surface. In addition, with the new geometry a more homogeneous temperature distribution is observed in the crystal growth environment

Cette thèse est accessible à l'adresse : http://theses.insa-lyon.fr/publication/2022LYSEI044/these.pdf
© [K. Utria Salas], [2022], INSA Lyon, tous droits réservés

8.4 Conclusions

A new geometry of the ceramic insulation was placed in order to obtain a better quality of crystals. The geometry was based on the results and analysis of the study described in chapter 1.

It was observed that thermal conditions of the crystalline growth are significantly affected by this change, and higher temperatures of the ceramic external surface were found for the new insulation configuration.

On the other hand, the new geometry did not affect the dimensions of the crystals. However, the ovalisation is lowered in *Furnace 1* and increased in *Furnace 2*, revealing the strong correlation between the ceramic geometry and the injection flow rates. An adequate choice of flow rates is necessary to obtain the best qualities of the crystal under the correct thermal crystalline growth conditions.

The geometrical defects confirmed the crucial importance of an accurate choice of ceramic geometry and flow rates. For the internal defects, the new geometry decreases the number of defects, which confirms the importance of lower temperature gradients to have a better internal quality of the crystals.

Finally, the numerical study revealed the importance of aerodynamics behaviour on the flame structure, and it also confirms the essential role of the correct choice of the flow rates.

The new ceramic insulation geometry spreads out the central reaction zone, decreasing the temperature gradient in the crystalline growth environment. At the same time, this widening of the reaction zone also increases the zone of contact between the crystal and the high temperature zone. The temperature gradients are diminished and the foils inside the crystalline structure decrease. Nevertheless, these gradients must maintain an adequate value in order not to increase the ovalisation index. At low temperature gradients, the crystal grows in an uncontrolled direction, thus losing its cylindrical shape. Therefore, the correct injection flow rates will produce the crystal boule with the desired quality features.

Cette thèse est accessible à l'adresse : http://theses.insa-lyon.fr/publication/2022LYSEI044/these.pdf
© [K. Utria Salas], [2022], INSA Lyon, tous droits réservés

Cette thèse est accessible à l'adresse : http://theses.insa-lyon.fr/publication/2022LYSEI044/these.pdf
© [K. Utria Salas], [2022], INSA Lyon, tous droits réservés

Conclusions and Perspectives

Cette thèse est accessible à l'adresse : http://theses.insa-lyon.fr/publication/2022LYSEI044/these.pdf
© [K. Utria Salas], [2022], INSA Lyon, tous droits réservés

Cette thèse est accessible à l'adresse : http://theses.insa-lyon.fr/publication/2022LYSEI044/these.pdf
© [K. Utria Salas], [2022], INSA Lyon, tous droits réservés

Conclusions

The production of artificial sapphire crystal by bulk through H_2/O_2 inverse diffusion flames is a complex technique that involves many physics mechanisms. The downward configuration and the stagnation point constituted a great challenge. The literature and the experience acquired by Le Rubis SA have shown that the internal and external quality of the crystal are highly dependent of the thermal conditions of the crystalline growth environment. In order to achieve a detailed understanding of this particular environment, a study of aerothermodynamic interactions present in this reacting system was performed.

Indeed, this research aimed to understand the overall thermal behaviour of the device and to specify the role of heat transfers between the different elements constituting the crystal growth environment. With the current study a better understanding of the overall thermal operation of the Verneuil Furnace was achieved, as well as the identification of the parameters that can modify the thermal behaviour of the crystal growth environment. Furthermore, the influence of the thermal field in the crystal growth environment was also analysed. The role of temperature levels and gradients on crystal growth was studied taking as validation criteria the quality of the crystal. These results were found through experimental and numerical tools.

It was necessary to divide the research into two experimental approaches and a numerical approach. The experimental approaches were divided in turn in three studies to understand the different physical mechanisms involved. Following, the conclusions achieved by these studies are expose:

The crystalline growth environment

The different parameters that are involved in a crystallisation cycle were analysed in real production conditions in order to find their correlations and their influence on the crystal quality, drawing the following conclusions:

The injection conditions of H_2 and O_2 define the boule diameter and length, the temperature distribution and the external and internal quality of the crystal. Furthermore, it was found that the geometry of the ceramic insulation is an essential parameter that defines the thermal conditions of the crystalline growth environment which later on determines the external and internal quality of the crystal. Therefore, a new geometry was defined according to ceramic geometry obtained with which the best geometric features and crystalline structure were found.

Cette thèse est accessible à l'adresse : http://theses.insa-lyon.fr/publication/2022LYSEI044/these.pdf
© [K. Utria Salas], [2022], INSA Lyon, tous droits réservés

H_2/O_2 inverse diffusion flames

The adequate control of flame appearance, structure characteristics, and heat release distribution of this kind of flame are essential to define the crystal quality. Therefore, the aerodynamics and chemistry interactions that affect them were examined for different fuel and oxidiser Reynolds numbers. In addition, the influence of the equivalence ratio, momentum oxidiser to fuel ratio were also analysed.

To describe this complex flow, the techniques applied were mainly experimental. Direct visualisations and OH^* chemiluminescence were used to obtain a rather qualitative aspect of the flame behaviour, then the velocity field was explored by Laser Doppler Anemometry to complete the analysis by quantitative data. The following conclusions were found:

According to their morphology and appearance, H_2/O_2 inverse diffusion flames were classified into three types, which were defined principally by the fuel/oxidiser momentum ratio. Two reaction zones characterised the flames: an upstream reaction zone and a central reaction zone. The upstream zone was always found and behaved as a classical diffusion flame and presented two separated flames. The central reaction zone appeared for momentum ratios smaller than 9.

The results found indicated that the oxidiser momentum affects the flame structure characteristics such as flame heights and the extension of the diffusion mode upstream, hence the location of the central reaction zone. Furthermore, oxidiser momentum also defined the extension of the stoichiometric zone downstream.

Regarding the production of OH^*, the fuel momentum and the ratio G_O/G_f impacted the OH^* emission intensities, hence the OH^* concentration. For flames with injection conditions between $\phi = 1$ and $\phi = 1.4$, the higher the fuel momentum, the higher the production of OH^*. This result suggests that the mixing fuel/oxidiser is strong. Consequently, brighter reaction zones are observed. This behaviour can be interpreted as a higher heat release rate. For higher ϕ the decrease in G_O/G_f diminishes the production of OH^* due to the decrease in the enhancement of the H_2 jets.

In addition, the velocity field study outlined the aerodynamic mechanisms involved in this very particular configuration. The flow development was analysed, and the mechanism that impacted this kind of flames were also exposed. The results showed the link between the chemistry and the aerodynamic interactions that affect the flow development. The influence of the buoyancy and the coaxial flow effects were revealed, explaining the laminar characteristics of the flames. Besides, the importance of the reaction zone was also revealed and showed to increases the buoyancy effects.

Moreover, the influence of the peripheral jets was accentuated at the highest U_{0,O_2}. Indeed,

Cette thèse est accessible à l'adresse : http://theses.insa-lyon.fr/publication/2022LYSEI044/these.pdf
© [K. Utria Salas], [2022], INSA Lyon, tous droits réservés

the temperatures are lower, the flow behaves as a coaxial flow. On the other hand, laminar behaviour is achieved especially with the diminution of O_2 inlet velocity, higher ϕ; thus, higher temperature and lower viscosities. The changes in U_{0,H_2} affects the coaxial jet behaviour and the flow development.

Additionally, the heat release was analysed through the temperature distribution in the flame. It was observed that the inverse diffusion flames report four zones. The first zone corresponds to the entrainment zone, and the temperature are low. At zone 2 the region of mixing is found, and the temperature at the centreline conserves low values. At the end of the mixing appears the central reaction zone where the highest temperatures are found, when $\phi > 1$. The increase in H_2 injection approaches the maximum temperature location to the outlet nozzle. With the decrease in U_{0,O_2} , the reaction zone moves upstream as the zone of maximum temperature. It was also observed the influence of $r_u < 1$ due to the significant impact in the flow development when varying O_2 injection.

To conclude, the flow development is impacted by different aspects:

- the flame structure,
- the properties of the gases that evolve significantly due to the strong heat release present in the flame, which could lead to significant buoyancy effects,
- and finally the influence of the laminar or turbulent nature of the flow, and the heat transfer that varies depending on the considered region.

Overall thermal behaviour of a Verneuil device

The study of the crystal presence influence on the flame structure characteristics and OH^* emission intensities along with their effect on the flow structure and development. The OH^* chemiluminescence technique was used to analyse experimentally the flame structure behaviour, and numerical tools were implemented to examine the aerothermodynamics of the system.

The presence of the crystal in the reaction zone revealed the effects of the contact and the wall jet area on the flame structure and heat release distribution. The mixing and the combustion are enhanced with the crystal inside the confinement. This enhancement depending on the flow rates specially the O_2 discharging velocity, causes a upstream shift of the central combustion zone and a widening of the reaction zone in diffusion mode. The combustion becomes faster and it is observed owing the shorter flames obtained with the crystal presence. The crystal also contributes to increase the temperatures in the confinement due to the increase of the heat release produced by the contact of the flame with the crystal liquid phase.

Cette thèse est accessible à l'adresse : http://theses.insa-lyon.fr/publication/2022LYSEI044/these.pdf
© [K. Utria Salas], [2022], INSA Lyon, tous droits réservés

Furthermore, the flow structure was mainly impacted when the inlets velocities are the highest. The momentums increase hence there is more gas to recirculate, changing significantly the flow structure.

Moreover, the flame obtained with a Verneuil burner in the presence of the crystal could be compare to a typical impinging flame. Due to the elevated distance between the O_2 nozzle the effect of the stagnation point is less observed ($H/D_{O_2} > 13$) upstream on the reaction zone. However, the enhancement in the combustion could be observed with this arrangement.

A new geometry of the ceramic insulation was placed in order to obtain a better quality of crystals. It was observed that thermal conditions of the crystalline growth is significantly affected by this change. Higher temperatures were found for the new configuration.

The new geometry did not affect the dimensions of the crystals. However, the ovalisation is lowered in *Furnace 1* and increased in *Furnace 2*, revealing the strong correlation between the ceramic geometry and the injection flow rates. An adequate choice of flow rates according to the ceramic geometry is necessary to obtain the best qualities of the crystal under the correct thermal conditions. Additionally, the diminution of the geometrical defects confirmed the crucial importance of this choice.

Finally, the numerical study revealed the importance of the aerodynamics behaviours on the flame structure. The central reaction zone spreads out with the new geometry decreasing the temperature gradients.

This aerothermodynamic study of a classic Verneuil burner configuration with the crystal presence, allowed us to highlight the various constraints acting during a crystallisation cycle. The correlations and dependencies of the crystallisation parameters were examined and evaluated to obtained crystal with better internal and external quality. The study of the flame structure and aerodynamics interactions defined different flame structures that can be used to improve the overall efficiency of the system.

Cette thèse est accessible à l'adresse : http://theses.insa-lyon.fr/publication/2022LYSEI044/these.pdf
© [K. Utria Salas], [2022], INSA Lyon, tous droits réservés

Perspectives

The study of the Verneuil crystal growth environment constitutes a significant problem that the current work only outlines. In order to deepen the analysis of the behaviours encountered in this process, many aspects can be addressed, some of them are:

- From a thermal point of view, the optimisation of the conduction heat model numerical simulation would help to improve the understanding of the role of the heat transfer involved in the crystalline growth environment. In addition, the adequate calculation of the heat transfer coefficients would contribute to the appropriate modelisation of the system. These calculations could be performed through numerical tools.
- Furthermore, it would be interesting to carry out a quantitative study of OH^* production and the distribution of heat release, with and without the crystal boule presence. Besides, it is of great interest to develop an experimental study of the velocity field with the presence of the crystal. This study would be of utmost importance to determine the influence of the latter on the temperature gradients.
- A numerical study that includes the temperature distributions of the crystal and the internal surface of the insulation ceramic will contribute to better understand the thermal interactions between the crystal and the flame.
- A design of experiments is necessary to be implemented to better study statistically the influences and correlations of the Verneuil production parameters (e.g. used constant flow rates and varying boule diameters and ceramic thickness). Such a study would contribute to develop optimisations of the system in order to improve the current *Verneuil method* efficiency in terms of crystal quality.

Cette thèse est accessible à l'adresse : http://theses.insa-lyon.fr/publication/2022LYSEI044/these.pdf
© [K. Utria Salas], [2022], INSA Lyon, tous droits réservés

Cette thèse est accessible à l'adresse : http://theses.insa-lyon.fr/publication/2022LYSEI044/these.pdf
© [K. Utria Salas], [2022], INSA Lyon, tous droits réservés

Bibliography

Abdel-Rahman, A. (2010). A review of effects of initial and boundary conditions on turbulent jets. *WSEAS Transactions on Fluid Mechanics*, 5:257–275.

Antonia, R. A. and Bilger, R. W. (1973). An experimental investigation of an axisymmetric jet in a co-flowing air stream. *Journal of Fluid Mechanics*, 61(4):805–822.

Antonia, R. A. and Zhao, Q. (2001). Effect of initial conditions on a circular jet. *Experiments in Fluids*, 31(3):319–233.

Auctions, G. R. (2019). What is Gemstone Birefringence? | Gem Rock Auctions.

Ayoola, B. O., Balachandran, R., Frank, J. H., Mastorakos, E., and Kaminski, C. F. (2006). Spatially resolved heat release rate measurements in turbulent premixed flames. *Combustion and Flame*, 144(1-2):1–16.

Badiger, S., Anil, T. R., Hindasageri, V., and Katti, V. V. (2020). Heat transfer characteristics of an inverse diffusion flame with induced swirl. *Journal of the Brazilian Society of Mechanical Sciences and Engineering*, 42(5):252.

Bain, D. B., Smith, C. E., and Holdeman, J. D. (2012). Mixing analysis of axially opposed rows of jets injected into confined crossflow. *https://doi.org/10.2514/3.23913*, 11(5):885–893.

Barbir, F. (2009). Transition to renewable energy systems with hydrogen as an energy carrier. *Energy*, 34(3):308–312.

Barr, J. (1953). Diffusion flames. *Symposium International on Combustion*, 4(1):765–771.

Barreto, L., Makihira, A., and Riahi, K. (2003). The hydrogen economy in the 21st century: A sustainable development scenario. *International Journal of Hydrogen Energy*, 28(3):267–284.

Bates, C. J. (2008). ANEMOMETERS (LASER DOPPLER).

Benduneau, J.-L. (2001). *Caracterisation experimentale des flammes non-premelangees H_2/O_2 : application aux cas des injecteurs coaxiaux de moteurs fusees.* PhD thesis, Institut National de Sciences Apliquées de Rouen.

Bhat, H. L. (2014). Growth from the solide phase. In *Introduction to Crystal Growth: Principles and Practice*, pages 111–122. CRC Press.

Cette thèse est accessible à l'adresse : http://theses.insa-lyon.fr/publication/2022LYSEI044/these.pdf
© [K. Utria Salas], [2022], INSA Lyon, tous droits réservés

Bindar, Y. and Irawan, A. (2012). Characteristics of flame shapes and map for LPG and hydrogen inverse confined diffusion flames at high level of fuel excess. *ASEAN Journal of Chemical Engineering*, 12(1):1–10.

Blevins, R. D. (1984). *Applied fluid dynamics handbook.* Van Nostrand Reinhold Co. Ltd.

Borghi, R. and Champion, M. (2000). *Modélisation et théorie des flammes.* Technip.

Borghi, R. and Destriau, M. (1995). *La combustion et les flammes.* Editions Technip.

Boyat, A. K. and Joshi, B. K. (2015). A Review Paper: Noise Models in Digital Image Processing. *Signal and Image Processing : An International Journal*, 6(2):63–75.

Cengel, Y. (1997). *Heat and Mass Transfer.* McGraw-Hill Professional, 2nd editon edition.

Champagne, F. H. and Wygnanski, I. J. (1971). An experimental investigation of coaxial turbulent jets. *International Journal of Heat and Mass Transfer*, 14:1445–1464.

Chaudhuri, S., Kostka, S., Renfro, M. W., and Cetegen, B. M. (2010). Blowoff dynamics of bluff body stabilized turbulent premixed flames. *Combustion and Flame*, 157:790–802.

Chen, C. J., Rodi, W., Chen, C. J., and Rodi, W. (1980). Vertical turbulent buoyant jets: A review of experimental data. *STIA*, 80:23073.

Cheng, T. S., Wehrmeyer, J. A., and Pitz, R. W. (1992). Simultaneous temperature and multispecies measurement in a lifted hydrogen diffusion flame. *Combustion and Flame*, 91:323–345.

Choi, S., Kim, T. Y., Kim, H. K., Jeung, I. S., Koo, J., and Kwon, O. C. (2017). Combustion stability of gaseous CH4/O2 and H2/O2 coaxial jet flames in a single-element combustor. *Energy*, 132:57–64.

Chung, S. H. (2007). Stabilization, propagation and instability of tribrachial triple flames. *Proceedings of the Combustion Institute*, 31:877–892.

Clark, T. P. and Bittker, D. A. (1954). A study of the radiation from laminar and turbulent open propane-air flames as a function of flame area, equivalence ratio, and fuel flow rate. *NACA - Research Memorandum*, E54F29.

Council, H. (2017). How hydrogen empowers the energy transition. Technical report, Hydrogen Council.

Council, H. (2021). Hydrogen for net-zero. Technical report, Hydrogen Council.

Cremers, M., Remie, M., Schreel, K., and Goey, P. (2005). Heat transfer of laminar flames of hydrogen+oxygen and methane+oxygen. *Brain Research - BRAIN RES.*

Cette thèse est accessible à l'adresse : http://theses.insa-lyon.fr/publication/2022LYSEI044/these.pdf
© [K. Utria Salas], [2022], INSA Lyon, tous droits réservés

Cuenot, B. and Poinsot, T. (1996). Asymptotic and numerical study of diffusion flames with variable lewis number and finite rate chemistry. *Combustion and Flame*, 104:111–137.

Dahm, W. J. A., Frieler, C. E., and Tryggvason, G. (1992). Vortex structure and dynamics in the near field of a coaxial jet. *Journal of Fluid Mechanics*, 241:371–402.

De Leo, M., Saveliev, A., Kennedy, L. A., and Zelepouga, S. A. (2007). OH and CH luminescence in opposed flow methane oxy-flames. *Combustion and Flame*, 149(4):435–447.

Departement, U. E. (1992). Doe fundamentals handbook thermodynamics , heat transfer , and fluid flow. Technical report, U.S. Energy Departement.

Dienes, G. J., Welch, D. O., Fischer, C. R., Hatcher, R. D., Lazareth, O., and Samberg, M. (1975). Shell-model calculation of some point-defect properties in $\alpha - Al_2O_3$. *Phys. Rev. B*, 11:3060–3070.

Dobrovinskaya, E. R., Lytvynov, L. A., and Pishchik, V. (2009). Properties of Sapphire. In *Sapphire*, pages 55–176. Springer, Boston, MA.

Dong, L. L., Cheung, C. S., and Leung, C. W. (2007). Heat transfer characteristics of an impinging inverse diffusion flame jet - Part I: Free flame structure. *International Journal of Heat and Mass Transfer*, 50(25-26):5108–5123.

Dowling, D. R. and Dimotakis, P. E. (1990). Similarity of the concentration field of gas-phase turbulent jets. *Journal of Fluid Mechanics*, 218:109–141.

Drake, M. C., Pitz, R. W., and Shyy, W. (1986). Conserved scalar probability density functions in a turbulent jet diffusion flame. *Journal of Fluid Mechanics*, 171:27–51.

du Toit, S. H. C., Steyn, A. G. W., and Stumpf, R. H. (1986). Graphics for univariate and bivariate data. In *Graphical Exploratory Data Analysis*, pages 13–35. Springer, New York, NY.

Duncan, D. B. (1955). Multiple range and multiple f tests. *Biometrics*, 11(1):1–42.

Dunn, J. (1961). Multiple comparisons among means. *Journal of the American Statistical Association*, 56(293):52–64.

Elbaz, A. M. and Roberts, W. L. (2014). Flame structure of methane inverse diffusion flame. *Experimental Thermal and Fluid Science*, 56:23–32.

Fiedler, H. E. and Hilberg, D. (1991). Control of Turbulent Shear Flows via Stationary Boundary Conditions. In *The Global Geometry of Turbulence*, pages 57–65. Springer, Boston, MA.

Cette thèse est accessible à l'adresse : http://theses.insa-lyon.fr/publication/2022LYSEI044/these.pdf
© [K. Utria Salas], [2022], INSA Lyon, tous droits réservés

Fisher, R. A. (1919). Xv.—the correlation between relatives on the supposition of mendelian inheritance. *Transactions of the Royal Society of Edinburgh*, 52(2):399–433.

Fisher, R. A. (1992). Statistical Methods for Research Workers. pages 66–70.

Gaydon, A. G. (1942). Flame spectra in the photographic infra-red. *Rev. Sci. Instrum*, 11(1936):260.

Gaydon, A. G. (1974). Hydrogen Flames. In *The Spectroscopy of Flames*, pages 99–126. Springer, Dordrecht.

Gaydon, A. G. and Egerton, A. C. (1948). Spectroscopy and combustion theory. Chapman and Hall.

Gaydon, A. G. and Wolfhard., H. G. (1953). *Flames. Their Structure, Radiation and Temperature.* Chapman and Hall.

George, W. and Gibson, M. (1992). The self-preservation of homogeneous shear flow turbulence. *Experiments in Fluids*, 13:229–238.

Glassman, Irvin Yetter, R. A. and Glumac, N. G. (2015). Chapter 6 - Diffusion Flames. In *Combustion*, chapter Diffusion, pages 301–361. Academic Press, 5th edition.

Gollahalli, S. R., Savaş, ., Huang, R. F., and Azara, J. L. R. (1988). Structure of attached and lifted gas jet flames in hysteresis region. *Symposium (International) on Combustion*, 21:1463–1471.

Hardalupas, Y. and Orain, M. (2004). Local measurements of the time-dependent heat release rate and equivalence ratio using chemiluminescent emission from a flame. *Combustion and Flame*, 139(3):188–207.

Harran, G., Chassaing, P., Joly, L., and Chibat, M. (1996). Numerical study of density effects on a turbulent mixing jet in microgravity. *Revue Generale de Thermique*, 35:151–176.

He, L., Guo, Q., Gong, Y., Wang, F., and Yu, G. (2019). Investigation of OH* chemiluminescence and heat release in laminar methane–oxygen co-flow diffusion flames. *Combustion and Flame*.

Hennessy, W. (2005). Chapter 10 - flow and level sensors. In Wilson, J. S., editor, *Sensor Technology Handbook*, pages 237–254. Newnes, Burlington.

Hinze, J. (1975). *Turbulence*. McGraw-Hill Series in Mechanical Engineering. McGraw-Hill, New York., 2nd edition edition.

Cette thèse est accessible à l'adresse : http://theses.insa-lyon.fr/publication/2022LYSEI044/these.pdf
© [K. Utria Salas], [2022], INSA Lyon, tous droits réservés

Holm, S. (1979). A simple sequentially rejective multiple test procedure. *Scandinavian Journal of Statistics*, 6(2):65–70.

Holve, D. J. and Sawyer, R. F. (1975). Diffusion controlled combustion of polymers. *Symposium (International) on Combustion*, 15:351–361.

Hout, R. V., Murugan, S., and Mitra, A. (2021). Coaxial Circular Jets—A Review. *Fluids*, 6(147):1–22.

Incropera, F., Dewitt, D., Bergman, T., and Lavine, A. (2015). *Fundamental of Heat and Mass Transfer*. John Wiley and sons, sixth edit edition.

Jeon, M. K. and Kim, N. I. (2017). Direct estimation of edge flame speeds of lifted laminar jet flames and a modified stabilization mechanism. *Combustion and Flame*, 186:140–149.

Kapusta, Ł. J., Shuang, C., Aldén, M., and Li, Z. (2020). Structures of inverse jet flames stabilized on a coaxial burner. *Energy*, 193.

Kasim, M. F., Holloway, J., Ceurvorst, L., Levy, M. C., Ratan, N., Sadler, J., Bingham, R., Burrows, P. N., Trines, R., Wing, M., and Norreys, P. (2015). Quantitative single shot and spatially resolved plasma wakefield diagnostics. *Phys. Rev. ST Accel. Beams*, 18:081302.

Katta, V. R., Goss, L. P., and Roquemore, W. M. (1994). Effect of nonunity lewis number and finite-rate chemistry on the dynamics of a hydrogen-air jet diffusion flame. *Combustion and Flame*, 96:60–74.

Kim, H. K., Kim, Y., Lee, S. M., and Ahn, K. Y. (2007). Studies on combustion characteristics and flame length of turbulent oxy-fuel flames. *Energy and Fuels*, 21(3):1459–1467.

Kim, T. Y., Choi, S., Kim, Y. H., Ahn, Y. J., Kim, H. K., and Kwon, O. C. (2018). Combustion characteristics of gaseous inverse O2/H2 coaxial jet flames in a single-element model combustor. *Energy*, 155:262–271.

Kim, T. Y., Kim, Y. H., Ahn, Y. J., Choi, S., and Kwon, O. C. (2019). Combustion stability of inverse oxygen/hydrogen coaxial jet flames at high pressure. *Energy*, 180:121–132.

Kioni, P. N., Rogg, B., Bray, K. N. C., and Linan, A. (1993). Flame Spread in Laminar Mixing Layers: The Triple Flame. *Combustion and Flame*, (95):276–290.

Ko, N. W. M. and Kwan, A. S. H. (1976). The initial region of subsonic coaxial jets. *Journal of Fluid Mechanics*, 73(02):305.

Cette thèse est accessible à l'adresse : http://theses.insa-lyon.fr/publication/2022LYSEI044/these.pdf
© [K. Utria Salas], [2022], INSA Lyon, tous droits réservés

Kutner, M. H., Nachtsteim, C. J., Neter, J., and Li, W. (1975). Analysis of Factor Level Means. In *Applied Linear Statistical Models*, pages 746–750. McGraw-Hill Irwin, fith edition edition.

Labor, S. (2003). *Etude expérimentale d'une flamme de diffusion Oxygène-Hydrogène ensemencée en particules solides d'alumine*. PhD thesis, L'Ecole Centrale Lyon.

Lam, W.H., Robinson D.J., Hamill, G.A., J. H. (2012). An effective method for comparing the turbulence intensity from LDA measurements and CFD predictions within a ship propeller jet | Elsevier Enhanced Reader. *Ocean Engineering*, 52:105–104.

Lamige, S. (2014). *Analyse de l ' Influence des Conditions aux Limites Thermiques sur la Stabilisation des Flammes Non-Prémélangées*. PhD thesis, L'Institut National des Sciences Appliquées de Lyon.

Lamige, S., Lyons, K. M., Galizzi, C., André, F., Kühni, M., and Escudié, D. (2014). Burner lip temperature and stabilization of a non-premixed jet flame. *Experimental Thermal and Fluid Science*, 56:45–52.

Lamige, S., Lyons, K. M., Galizzi, C., Kühni, M., Mathieu, É., and Escudié, D. (2015). Lifting and splitting of nonpremixed methane/air flames due to reactant preheating. *Combustion Science and Technology*, 187(12):1937–1958.

Lamige, S., Min, J., Galizzi, C., André, F., Baillot, F., Escudié, D., and Lyons, K. M. (2013). On preheating and dilution effects in non-premixed jet flame stabilization. *Combustion and Flame*, 160(6):1102–1111.

Lauer, M. (2011). *Determination of the Heat Release Distribution in Turbulent Flames by Chemiluminescence Imaging*. PhD thesis, Technische Universität München.

Lawn, C. J. (2009). Lifted flames on fuel jets in co-flowing air. *Progress in Energy and Combustion Science*, 35:1–30.

Leung, T. and Wierzba, I. (2009). The effect of co-flow stream velocity on turbulent non-premixed jet flame stability. *Proceedings of the Combustion Institute*, 32(2):1671–1678.

Liao, Y. (2007). *Alpha (α)-Alumina (Sapphire)*. GlobalSino.

Lyons, K. M. (2007). Toward an understanding of the stabilization mechanisms of lifted turbulent jet flames: Experiments. *Progress in Energy and Combustion Science*, 33:211–231.

Mahesh, S. and Mishra, D. P. (2010). Flame structure of LPG-air Inverse Diffusion Flame in a backstep burner. *Fuel*, 89(8):2145–2148.

Cette thèse est accessible à l'adresse : http://theses.insa-lyon.fr/publication/2022LYSEI044/these.pdf
© [K. Utria Salas], [2022], INSA Lyon, tous droits réservés

Marchese, A. J., Dryer, F. L., Nayagam, V., and Colantonio, R. O. (1996). Hydroxyl radical chemiluminescence imaging and the structure of microgravity droplet flames. *Symposium (International) on Combustion*, 26:1219–1226.

MATLAB (2021). *version 9.10.0 (R2021a)*. The MathWorks Inc., Natick, Massachusetts.

McNaughton, K. J. and Sinclair, C. G. (1966). Submerged jets in short cylindrical flow vessels. *Journal of Fluid Mechanics*, 25(2):367–375.

Menon, E. S. (2015). Fluid flow in pipes. In *Transmission Pipeline Calculations and Simulations Manual*, pages 149–234. Gulf Professional Publishing.

Miao, J., Leung, C. W., Cheung, C. S., Huang, Z., and Jin, W. (2016). Effect of H2 addition on OH distribution of LPG/Air circumferential inverse diffusion flame. *International Journal of Hydrogen Energy*, 41(22):9653–9663.

Miao, J., Leung, C. W., Cheung, C. S., and Leung, R. C. K. (2013). Flame Stability and Structure of Liquefied Petroleum Gas-Fired Inverse Diffusion Flame with Hydrogen Enrichment. *International Journal of Mechanical and Mechatronics Engineering*, 7(1):70–75.

Miller, R. J. (1997). *Beyond ANOVA: Basics of Applied Statistics*. Science, Chapman and Hall/CRC Texts in Statistical.

Muñiz, L. and Mungal, M. G. (2001). Effects of heat release and buoyancy on flow structure and entrainment in turbulent nonpremixed flames. *Combustion and Flame*, 126:1402–1420.

Muzy, J. (2021). *Caractérisation mécanique du saphir en fonction de son élaboration et de sa qualité cristalline*. PhD thesis, Université Grenoble Alpes.

Newman, D. (1939). The distribution of range in samples from a normal population, expressed in terms of an independent estimate of standard deviation. *Biometrika*, 31(1-2):20–30.

Ng, T. K., Leung, C. W., and Cheung, C. S. (2007). Experimental investigation on the heat transfer of an impinging inverse diffusion flame. *International Journal of Heat and Mass Transfer*, 50(17-18):3366–3375.

Nowotny, J., Sorrell, C. C., Sheppard, L. R., and Bak, T. (2005). Solar-hydrogen: Environmentally safe fuel for the future. *International Journal of Hydrogen Energy*, 30(5):521–544.

Ogden, J. M. (1999). Prospects for building a hydrogen energy infrastructure. *Annual Review of Energy and the Environment*, 24:227–279.

Cette thèse est accessible à l'adresse : http://theses.insa-lyon.fr/publication/2022LYSEI044/these.pdf
© [K. Utria Salas], [2022], INSA Lyon, tous droits réservés

Ott, R. L. and Longnecker, M. (2016). Multiple Comparisons . In *An Introduction to Statistical Methods & Data Analysis*, page 445. Cengage Learning, 7th edition.

Padley, P. J. (1960). The origin of the blue continuum in the hydrogen flame. *Transactions of the Faraday Society*, 56(0):449–454.

Pagé, J., Blanchard, J., Sarh, B., and Gökalp, I. (1999). Etude par visualisations des caractéristiques géométriques du champ proche de jets axisymétriques a masse volumique variable. In *8ème Colloque de Visualisation et Traitement d'Images en Mécaniques des Fluides (FLUVISU99)*, Toulouse.

Pagé, J., Sarh, B., and Gökalp, I. (1998). Experimental determination of the turbulent kinetic energy and the dissipation rate in variable density turbulent jets. In *Ninth International Symposium on Applications of Laser Techniques to Fluid Mechanics*, pages 17.2.1–17.2.7, Lisbon.

Panton, R. (2013). *Incompressible Flow.* John Wiley and sons Inc.

Papadopoulos, G. and Pitts, W. M. (1999). A generic centerline velocity decay curve for initially turbulent axisymmetric jets. *Journal of Fluids Engineering, Transactions of the ASME*, 121:80–85.

Patel, V. and Shah, R. (2019). ScienceDirect Effect of hydrogen enrichment on combustion characteristics of methane swirling and non- swirling inverse diffusion flame. *International Journal of Hydrogen Energy*, page 28317.

Patzelt, W. J. (1974). *Polarized-light microscopy: Principles, instruments, applications.* Leitz, 2nd edition.

Phillips, H. (1965). Flame in a buoyant methane layer. *Symposium (International) on Combustion*, 10:1277–1283.

Pitts, W. (1991). Reynolds number effects on the mixing behavior of axisymmetric turbulent jets. *Experiments in Fluids*, 11:135–141.

Poitras, G. J., Babineau, A., Roy, G., and Brizzi, L. E. (2017). Aerodynamic and heat transfer analysis of a impinging jet on a concave surface. *International Journal of Thermal Sciences*, 114:184–195.

Raghib Shakeel, M., Sanusi, Y. S., and Mokheimer, E. M. (2017). Numerical Modeling of Oxy-Fuel Combustion in a Model Gas Turbine Combustor: Effect of Combustion Chemistry and Radiation Model. *Energy Procedia*, 142:1647–1652.

Rajaratnam, N. (1976). Chapter 1 the plane turbulent free jet. In *Turbulent Jets*, volume 5 of *Developments in Water Science*, pages 1–26. Elsevier.

Cette thèse est accessible à l'adresse : http://theses.insa-lyon.fr/publication/2022LYSEI044/these.pdf
© [K. Utria Salas], [2022], INSA Lyon, tous droits réservés

Rice, J. A. (1995). Covariance and Correlation. In *Mathematical Statistics and Data Analysis*, chapter Expected V, pages 129–130. Duxbury Press, Belmont, California.

Richards, C. D. and Pitts, W. M. (1993). Global density effects on the self-preservation behaviour of turbulent free jets. *Journal of Fluid Mechanics*, 254:417–435.

Roberts, M. (2011). Simple, Powerful Statistics: An Instantiation of a Better 'Mousetrap'. *Journal of Methods and Measurement in the Social Sciences*, 2(2):63–79.

Russo, G. P. (2011). Laser anemometry. In Russo, G. P., editor, *Aerodynamic Measurements*, pages 99–142. Woodhead Publishing.

Sacadura, J.-C. (1997). *Etude expérimentale des flammes non-prémélangées hydrogène-oxygène. Caractérisation des champs dynamiques et scalaires.* PhD thesis, Université de Rouen.

Sautet, J.-C. (1992). *Effets des différences de densités sur le développement scalaire et dynamique des jets turbulents.* PhD thesis, Université de Rouen.

Schefer, R. W., Kulatilaka, W. D., Patterson, B. D., and Settersten, T. B. (2009). Visible emission of hydrogen flames. *Combustion and Flame*, 156(6):1234–1241.

Schlichting, H. and Gersten, K. (2016). *Boundary-Layer Theory.* Springer Berlin Heidelberg.

Shackelford, J. F., Han, Y.-H., Kim, S., and Kwon, S.-H. (2015). *Materials Scienece and Engineering Handbook (4th ed.).* CRC Press.

Shu, Z., Aggarwal, S. K., Katta, V. R., and Puri, I. K. (1997). Flame-vortex dynamics in an inverse partially premixed combustor: The Froude number effects. *Combustion and Flame*, 111(4):276–295.

Sobiesiak, A., Rahbar, S., and Becker, H. A. (1998). Performance Characteristics of the Novel Low-NOx CGRI Burner For Use with High Air Preheat. *Combustion and Flame*, 115(1-2):93–125.

Sobiesiak, A. and Wenzell, J. C. (2005). Characteristics and structure of inverse flames of natural gas. *Proceedings of the Combustion Institute*, 30(1):743–749.

Stansel, D. M., Laurendeau, N. M., and Senser, D. W. (1995). CO and NOx Emissions from a Controlled-Air Burner: Experimental Measurements and Exhaust Correlations. *Combustion Science and Technology*, 104(4-6):207–234.

Sutton, J. A. and Driscoll, J. F. (2007). Imaging of local flame extinction due to the interaction of scalar dissipation layers and the stoichiometric contour in turbulent non-premixed flames. *Proceedings of the Combustion Institute*, 31:1487–1495.

Cette thèse est accessible à l'adresse : http://theses.insa-lyon.fr/publication/2022LYSEI044/these.pdf
© [K. Utria Salas], [2022], INSA Lyon, tous droits réservés

Sze, L. K., Cheung, C. S., and Leung, C. W. (2004). Temperature distribution and heat transfer characteristics of an inverse diffusion flame with circumferentially arranged fuel ports. *International Journal of Heat and Mass Transfer*, 47(14-16):3119–3129.

Sze, L. K., Cheung, C. S., and Leung, C. W. (2006). Appearance, temperature, and NOx emission of two inverse diffusion flames with different port design. *Combustion and Flame*, 144(1-2):237–248.

Takagi, T., Shin, H. D., and Ishio, A. (1981). Properties of turbulence in turbulent diffusion flames. *Combustion and Flame*, 40:121–140.

Takagi, T., Xu, Z., and Komiyama, M. (1996). Preferential diffusion effects on the temperature in usual and inverse diffusion flames. *Combustion and Flame*, 106:252–260.

Takahashi, F. and Schmoll, W. J. (1991). Lifting criteria of jet diffusion flames. *Symposium (International) on Combustion*, 23:677–683.

U.S. Energy Departement (1999). Industrial Combustion Technology Roadmap A Technology Roadmap by and for the Industrial Combustion Community. Technical report, U.S. Energy Departement.

Utria, K., Labor, S., Kühni, M., Escudié, D., and Galizzi, C. (2022). Experimental study of H_2/O_2 downward multi-fuel-jet inverse diffusion flames. *Experimental Thermal and Fluid Science*, 134:110583.

Vanpee, M. and Mainiero, R. J. (1979). The spectral distribution of the blue hydrogen flame continuum and its origin in hydrogennitric oxide flames. *Combustion and Flame*, 34:219–230.

Villermaux, E. and Rehab, H. (2000). Mixing in coaxial jets. *Journal of Fluid Mechanics*, 425:161–185.

Vranos, A., Taback, E. D., and Shipman, C. W. (1968). An experimental study of the stability of hydrogen-air diffusion flames. *Combustion and Flame*, 12(3):253–260.

Warda, H. A., Kassab, S. Z., Elshorbagy, K. A., and Elsaadawy, E. A. (1999). An experimental investigation of the near-field region of free turbulent round central and annular jets. *Flow Measurement and Instrumentation*, 10:1–14.

White, F. (2010). Fluid Mechanics. *McGraw-Hill,New York*, page 862.

Witze, P. (1974). *A study of impinging axisymmetric turbulent flows: the wall jet, the radial jet, and opposing free jets.* PhD thesis, University of California, Davis.

Wu, C. Y., Chao, Y. C., Cheng, T. S., Li, Y. H., Lee, K. Y., and Yuan, T. (2006). The blowout mechanism of turbulent jet diffusion flames. *Combustion and Flame*, 145:481–494.

Cette thèse est accessible à l'adresse : http://theses.insa-lyon.fr/publication/2022LYSEI044/these.pdf
© [K. Utria Salas], [2022], INSA Lyon, tous droits réservés

Wu, K.-T. and Essenhigh, R. H. (1984). Mapping and structure of a inverse diffusion flames of Methane. *Proceedings of the Combustion Institute*, 20:1925–1932.

Wygnanski, I. and Fiedler, H. (1969). Some measurements in the self-preserving jet. *Journal of Fluid Mechanics*, 38:577–612.

Wyzgolik, A. and Baillot, F. (2007). Response of the non-premixed lifted flameto coaxial jet mixing layers. *Proceedings of the Combustion Institute*, pages 1593–1590.

Yuan, Z.-G. (2003). The Filtered Abel Transform and Its Application in Combustion Diagnostics. Technical Report March, NASA-National Center for Microgravity Research, Cleveland, Ohio.

Zhang, X. R., Yamaguchi, H., and Cao, Y. (2010). Hydrogen production from solar energy powered supercritical cycle using carbon dioxide. *International Journal of Hydrogen Energy*, 35(10):4925–4932.

Zhen, H. S., Cheung, C. S., Leung, C. W., and Choy, Y. S. (2012). Effects of hydrogen concentration on the emission and heat transfer of a premixed LPG-hydrogen flame. *International Journal of Hydrogen Energy*, 37(7):6097–6105.

Zhen, H. S., Cheung, C. S., Leung, C. W., and Li, H. B. (2013). Thermal and heat transfer behaviors of an inverse diffusion flame with induced swirl. *Fuel*, 103:212–219.

Zhen, H. S., Choy, Y. S., Leung, C. W., and Cheung, C. S. (2011). Effects of nozzle length on flame and emission behaviors of multi-fuel-jet inverse diffusion flame burner. *Applied Energy*, 88(9):2917–2924.

Cette thèse est accessible à l'adresse : http://theses.insa-lyon.fr/publication/2022LYSEI044/these.pdf
© [K. Utria Salas], [2022], INSA Lyon, tous droits réservés

Cette thèse est accessible à l'adresse : http://theses.insa-lyon.fr/publication/2022LYSEI044/these.pdf
© [K. Utria Salas], [2022], INSA Lyon, tous droits réservés

Appendices

Cette thèse est accessible à l'adresse : http://theses.insa-lyon.fr/publication/2022LYSEI044/these.pdf
© [K. Utria Salas], [2022], INSA Lyon, tous droits réservés

Cette thèse est accessible à l'adresse : http://theses.insa-lyon.fr/publication/2022LYSEI044/these.pdf
© [K. Utria Salas], [2022], INSA Lyon, tous droits réservés

Appendix A | Analyse of crystalline growth environment

A.1 Solution of the heat conduction equation with finite-difference

The general conduction heat transfer equation in cylindrical coordinates for our study is according to figure 1.15 and can be express as:

$$\frac{1}{r}\frac{\partial}{\partial r}\left(kr\frac{\partial T}{\partial r}\right)+\frac{1}{r^2}\frac{\partial}{\partial \varphi}\left(k\frac{\partial T}{\partial \varphi}\right)+\frac{\partial}{\partial y}\left(k\frac{\partial T}{\partial y}\right)+\dot{q}=\rho C_p\frac{\partial T}{\partial t} \tag{A.1}$$

Considering the furnace as axisymmetric along Y-axis the equation A.1 is:

$$\frac{1}{r}\frac{\partial}{\partial r}\left(kr\frac{\partial T}{\partial r}\right)+\frac{\partial}{\partial y}\left(k\frac{\partial T}{\partial y}\right)+\dot{q}=\rho C_p\frac{\partial T}{\partial t} \tag{A.2}$$

Considering that after three hours of operation the changes in the temperatures are almost negligent, the heat transfer can be consider as constant. Hence the equation for the conduction heat transfer along r and y is:

$$\frac{1}{r}\frac{\partial}{\partial r}\left(kr\frac{\partial T}{\partial r}\right)+\frac{\partial}{\partial y}\left(k\frac{\partial T}{\partial y}\right)+\dot{q}=0 \tag{A.3}$$

$r_i \leq r \leq r_0;\ 0 \leq y \leq L_{cer}$
where
r_i is the internal radius of the ceramic insulation
r_0 is the external radius of the ceramic insulation
L_{cer} is the total length of the ceramic insulation

Simplifying:

$$\frac{\partial^2 T}{\partial r^2}+\frac{1}{r}\frac{\partial T}{\partial r}+\frac{\partial^2 T}{\partial y^2}+\frac{\dot{q}}{k}=0 \tag{A.4}$$

Cette thèse est accessible à l'adresse : http://theses.insa-lyon.fr/publication/2022LYSEI044/these.pdf
© [K. Utria Salas], [2022], INSA Lyon, tous droits réservés

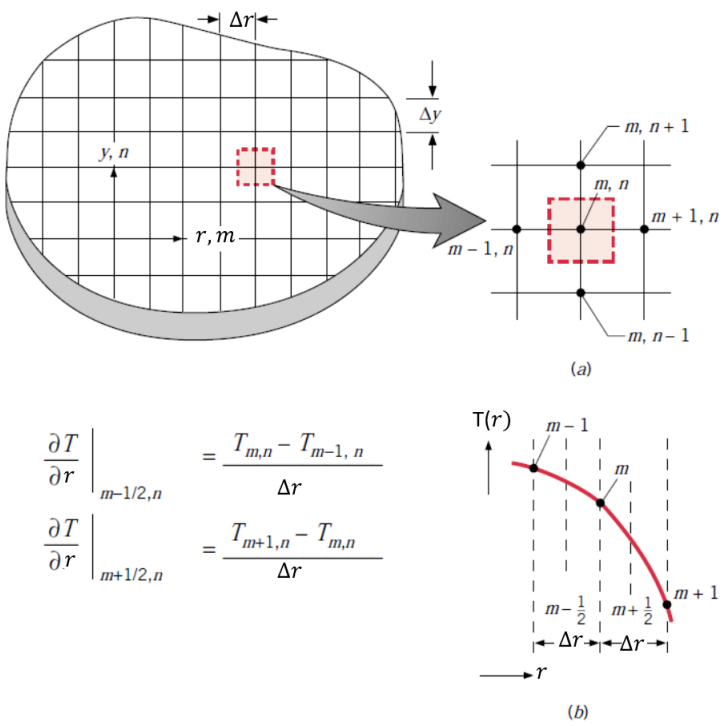

$$\left.\frac{\partial T}{\partial r}\right|_{m-1/2,n} = \frac{T_{m,n} - T_{m-1,n}}{\Delta r}$$

$$\left.\frac{\partial T}{\partial r}\right|_{m+1/2,n} = \frac{T_{m+1,n} - T_{m,n}}{\Delta r}$$

Figure A.1: Two-dimensional conduction. (a) Nodal network (b) Finite-difference approximation (Incropera et al., 2015)

$$\frac{\partial^2 T}{\partial r^2} \approx \frac{T_{m+1,n} - 2T_{m,n} + T_{m-1,n}}{\Delta r^2} \tag{A.5}$$

$$\frac{\partial T}{\partial r} \approx \frac{T_{m+1,n} - T_{m-1,n}}{2\Delta r} \tag{A.6}$$

$$\frac{\partial^2 T}{\partial y^2} \approx \frac{T_{m,n+1} - 2T_{m,n} + T_{m,n-1}}{\Delta y^2} \tag{A.7}$$

Substituting equations A.5, A.6 and A.7 in 1.8, and according to figure A.2, the heat conduction equation for the internal nodes is:

$$\frac{T_{m+1,n} - 2T_{m,n} + T_{m-1,n}}{\Delta r^2} + \frac{T_{m+1,n} - T_{m-1,n}}{2r\Delta r} + \frac{T_{m,n+1} - 2T_{m,n} + T_{m,n-1}}{\Delta y^2} + \frac{\dot{q}}{k} = 0 \tag{A.8}$$

Cette thèse est accessible à l'adresse : http://theses.insa-lyon.fr/publication/2022LYSEI044/these.pdf
© [K. Utria Salas], [2022], INSA Lyon, tous droits réservés

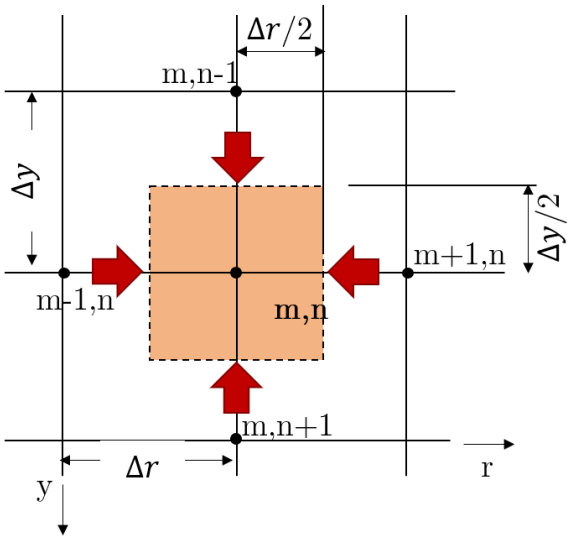

Figure A.2: Internal Node

Reorganising:

$$\frac{1}{\Delta r^2}\left(1+\frac{\Delta r}{2r}\right)T_{m+1,n}+\frac{1}{\Delta r^2}\left(1-\frac{\Delta r}{2r}\right)T_{m-1,n}+\frac{1}{\Delta y^2}T_{m,n+1}+\frac{1}{\Delta y^2}T_{m,n-1} -2\left(\frac{1}{\Delta r^2}+\frac{1}{\Delta y^2}\right)T_{m,n}=-\frac{\dot{q}\Delta r^2}{k} \tag{A.9}$$

where $r = r_0 - \delta_{cer}$, $r_0 = 71\ mm$ on the sides and $r_0 = 65\ mm$ front and back.

From equation A.16:

$$C_1 = \frac{1}{\Delta r^2}\left(1+\frac{\Delta r}{2r}\right) \tag{A.10}$$

$$C_2 = \frac{1}{\Delta r^2}\left(1-\frac{\Delta r}{2r}\right) \tag{A.11}$$

$$C_3 = \frac{1}{\Delta y^2} \tag{A.12}$$

$$C_4 = \frac{1}{\Delta r^2}+\frac{1}{\Delta y^2} \tag{A.13}$$

$$C_5 = \frac{q}{k} \tag{A.14}$$

$$C_6 = \frac{h}{k\Delta r} \tag{A.15}$$

Cette thèse est accessible à l'adresse : http://theses.insa-lyon.fr/publication/2022LYSEI044/these.pdf
© [K. Utria Salas], [2022], INSA Lyon, tous droits réservés

Replacing equations from A.10 to A.14 in equation A.9:

$$C_1 T_{m+1,n} + C_2 T_{m-1,n} + C_3 T_{m,n+1} + C_3 T_{m,n-1} - 2C_4 T_{m,n} = -C_5 \tag{A.16}$$

with boundary conditions (BC) on the sides as follows, the temperature on the lateral side can be determined:

1. $T(r_0, y = 80) = T_1$
2. $T(r_0, y = 160) = T_2$
3. $T(r_0, y = 230) = T_3$
4. $T(r_0, y = 280) = T_4$

Furthermore the temperatures on the top and bottom $T(r_0, y_1 = 0)$ and $T(r_0, y = l)$ of the ceramic insulation can be measured as well. Nevertheless, the current study estimated these temperatures with a curve calculated from the measured points.

The heat conductions equations for the external nodes are according to figure A.3:

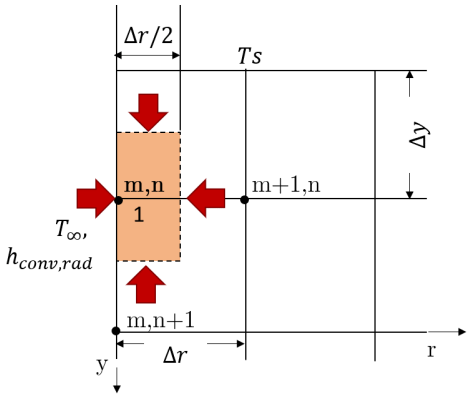

(a) Lateral superior node (internal ceramic surface, node 1):
$2C_1 T_{m+1,n} + C_3 T_{m,n+1} - 2\left(C_1 + C_3 + C_6\right) T_{m,n} = -2\left(C_5 + C_6 T_\infty\right) - C_3 T(r, y = 0)$

Figure A.3: Boundary conditions

Cette thèse est accessible à l'adresse : http://theses.insa-lyon.fr/publication/2022LYSEI044/these.pdf
© [K. Utria Salas], [2022], INSA Lyon, tous droits réservés

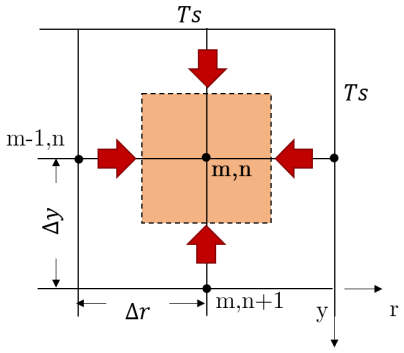

(b) Superior external node:
$C_3T_{m,n+1} - 2C_4T_{m,n} = -C_5 - (C_1 + C_3)T(r, y = 0)$

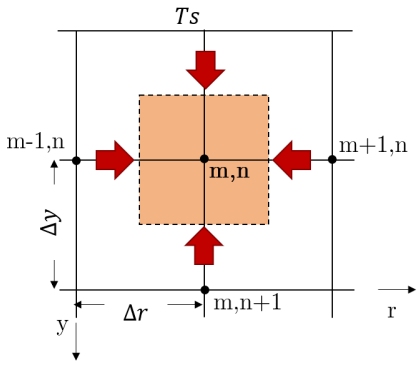

(c) Superior external nodes first row:
$C_1T_{m+1,n} + C_3T_{m,n+1} - 2C_4T_{m,n} = -C_5 - C_3T(r, y = 0)$

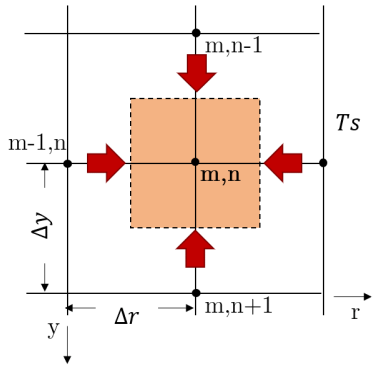

(d) External nodes last column:
$C_2T_{m-1,n} + C_3T_{m,n+1} + C_3T_{m,n-1} - 2\,(C_1 + C_3)\,T_{m,n} = -C_5 - C_1T(r, y = 0)$

Figure A.3: Boundary conditions

Cette thèse est accessible à l'adresse : http://theses.insa-lyon.fr/publication/2022LYSEI044/these.pdf
© [K. Utria Salas], [2022], INSA Lyon, tous droits réservés

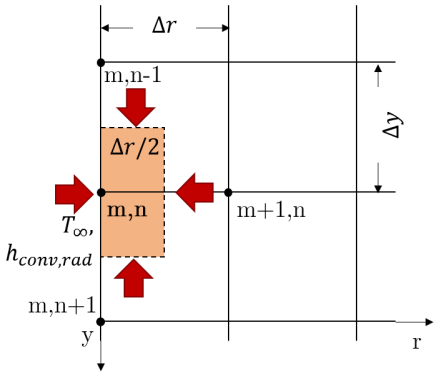

(e) Lateral external nodes (internal ceramic surface):

$$2C_1T_{m+1,n} + C_3T_{m,n+1} + C_3T_{m,n-1} - 2\left(C_1 + C_3 + C_6\right)T_{m,n} = -2\left(C_5 + C_6T_\infty\right)$$

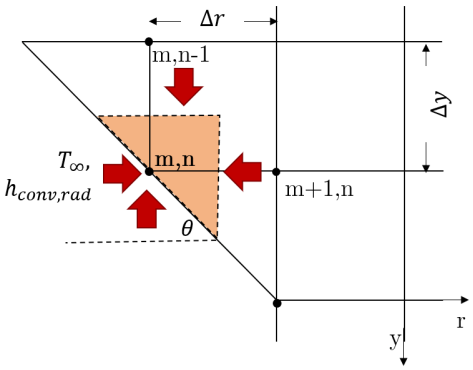

(f) Lateral external nodes (internal ceramic surface):

$$C_1T_{m+1,n}+C_3T_{m,n-1}-\left[C_1 + C_3 + C_6 * \left(sin\theta + \frac{\Delta r}{\Delta y}\right)\right]T_{m,n} = -C_5 sin\theta - C_6 * \left(sin\theta + \frac{\Delta r}{\Delta y}\right)T_\infty$$

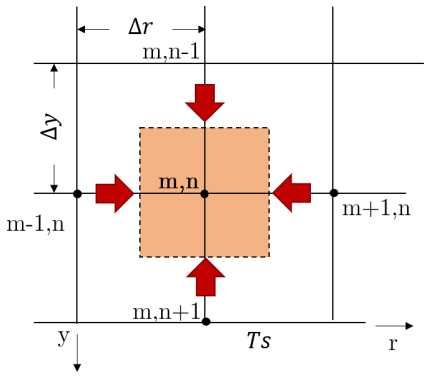

(g) Bottom external nodes:

$$C_1T_{m+1,n} + C_2T_{m-1,n} + C_3T_{m-1,n-1} - 2C_4T_{m,n} = -C_5 - C_3T(r, y = l)$$

Figure A.3: Boundary conditions

Cette thèse est accessible à l'adresse : http://theses.insa-lyon.fr/publication/2022LYSEI044/these.pdf
© [K. Utria Salas], [2022], INSA Lyon, tous droits réservés

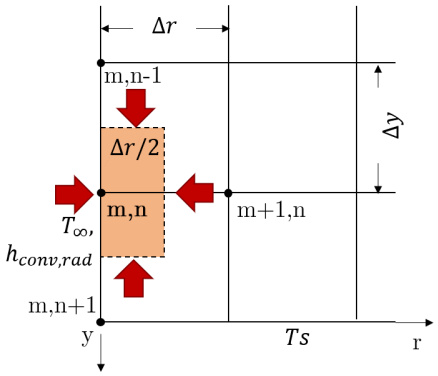

(h) Last node, first column:
$$2C_1T_{m+1,n} + C_3T_{m,n-1} - 2\left(C_1 + C_3 + C_6\right)T_{m,n} = -2\left(C_5 + C_6T_\infty\right) - C_3T(r, y = l)$$

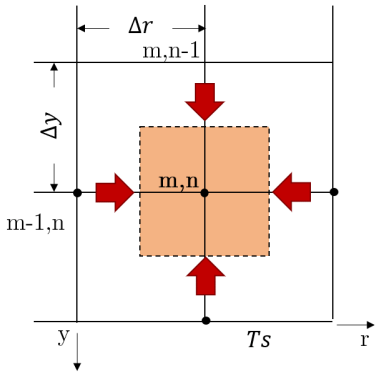

(i) Last node:
$$C_2T_{m-1,n} + C_3T_{m-1,n-1} - 2C_4T_{m,n} = -C_5 - (C_1 + C_3)T(r, y = l)$$

Figure A.3: Boundary conditions

The domain was divided into 20 449 nodes that corresponds to a grid of 96 × 144 (in r and y, respectively). The properties of the system were: $k = 6.27\ W/m \cdot K$ at 1200°C (Shackelford et al., 2015), the heat transfer coefficient, $h = 0.16\ W/cm^2 \cdot K$ and heat generation, $\dot{q} = 190\ W/cm^2$ at 2000 K (Cremers et al., 2005). The domain was considered as semi-transparent and the heat source is due to the flame and the particles of alumina within it. These values were approximated and they do not represent the real conditions.

Cette thèse est accessible à l'adresse : http://theses.insa-lyon.fr/publication/2022LYSEI044/these.pdf
© [K. Utria Salas], [2022], INSA Lyon, tous droits réservés

A.2 Evolution of the ceramic insulation geometry

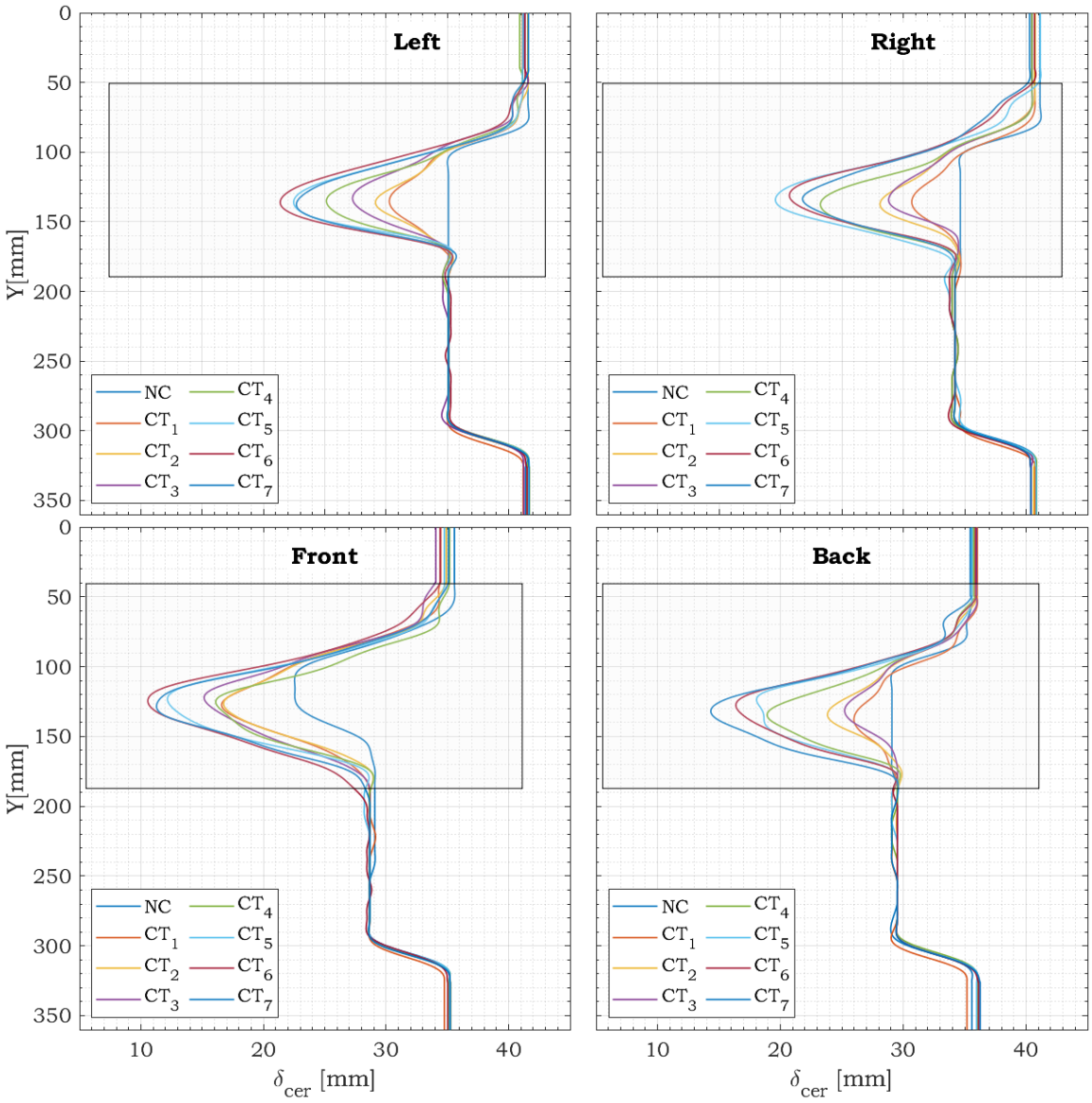

Figure A.4: Ceramic Thickness (δ_{cer}) Evolution for crystallisation cycles 1-9 in *Furnace 1*

Cette thèse est accessible à l'adresse : http://theses.insa-lyon.fr/publication/2022LYSEI044/these.pdf
© [K. Utria Salas], [2022], INSA Lyon, tous droits réservés

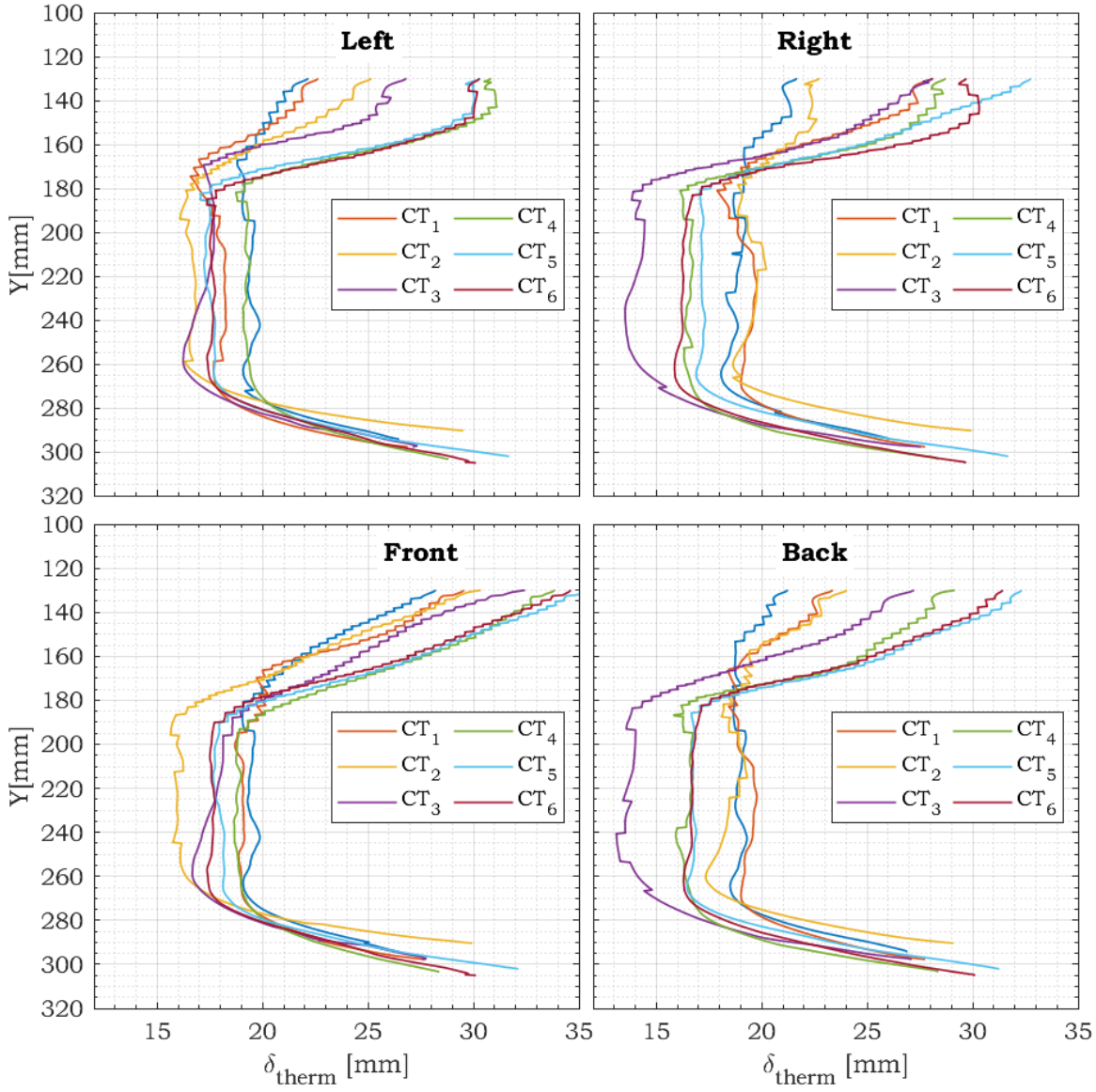

Figure A.5: Thermal Thickness Evolution Furnace 1 for cycle crystallisations 1-6

Cette thèse est accessible à l'adresse : http://theses.insa-lyon.fr/publication/2022LYSEI044/these.pdf
© [K. Utria Salas], [2022], INSA Lyon, tous droits réservés

A.3 Tukey's test tables

Table A.1: Multiple Comparisons Tukey's test Temperatures vs δ_{cer} (1-11, correspond to the δ_{cer} between 25-35, respectively)

I (technique)	J (technique)	Mean Difference (I-J)	95% Confidence Interval		p-value
			Lower Bound	Upper Bound	
1	2	-253.19	-2.90	247.39	1.00
1	3	-216.72	-18.85	179.02	1.00
1	4	-198.91	-14.06	170.79	1.00
1	5	-218.86	-33.24	152.38	1.00
1	6	-248.64	-64.43	119.77	0.98
1	7	-201.77	-3.90	193.97	1.00
1	8	-219.77	-21.90	175.97	1.00
1	9	-144.02	53.85	251.72	1.00
1	10	-133.26	83.50	300.26	0.96
1	11	-113.11	103.65	320.41	0.86
2	3	-213.82	-15.95	181.92	1.00
2	4	-196.01	-11.16	173.69	1.00
2	5	-215.96	-30.34	155.28	1.00
2	6	-245.74	-61.53	122.67	0.99
2	7	-198.87	-1.00	196.87	1.00
2	8	-216.87	-19.00	178.87	1.00
2	9	-141.12	56.75	254.62	1.00
2	10	-130.36	86.40	303.16	0.95
2	11	-110.21	106.55	323.31	0.84
3	4	-98.55	4.79	108.12	1.00
3	5	-119.09	-14.39	90.31	1.00
3	6	-147.76	-45.58	56.60	0.91
3	7	-110.19	14.95	140.09	1.00
3	8	-128.19	-3.05	122.09	1.00
3	9	-52.44	72.70	197.84	0.67
3	10	-50.92	102.35	255.62	0.47
3	11	-30.77	122.50	275.77	0.23
4	5	-96.50	-19.18	58.15	1.00
4	6	-124.25	-50.37	23.51	0.44
4	7	-93.17	10.16	113.50	1.00
4	8	-111.17	-7.84	95.50	1.00
4	9	-35.42	67.91	171.25	0.50
4	10	-38.48	97.56	233.61	0.37
4	11	-18.33	117.71	253.76	0.14
5	6	-106.97	-31.19	44.59	0.94
5	7	-75.36	29.34	134.04	1.00

Cette thèse est accessible à l'adresse : http://theses.insa-lyon.fr/publication/2022LYSEI044/these.pdf
© [K. Utria Salas], [2022], INSA Lyon, tous droits réservés

Table A.1: Multiple Comparisons Tukey's test Temperatures vs δ_{cer} (1-11, correspond to the δ_{cer} between 25-35, respectively)

I (technique)	**J (technique)**	**Mean Difference (I-J)**	**95% Confidence Interval**		**p-value**
			Lower Bound	**Upper Bound**	
5	8	-93.36	11.34	116.04	1.00
5	9	-17.61	87.09	191.79	0.18
5	10	-20.35	116.74	253.83	0.16
5	11	-0.20	136.89	273.98	0.05
6	7	-41.65	60.53	162.71	0.64
6	8	-59.65	42.53	144.71	0.94
6	9	16.10	118.28	220.46	0.01
6	10	12.76	147.93	283.10	0.02
6	11	32.91	168.08	303.25	0.01
7	8	-143.14	-18.00	107.14	1.00
7	9	-67.39	57.75	182.89	0.89
7	10	-65.87	87.40	240.67	0.69
7	11	-45.72	107.55	260.82	0.40
8	9	-49.39	75.75	200.89	0.61
8	10	-47.87	105.40	258.67	0.43
8	11	-27.72	125.55	278.82	0.20
9	10	-123.62	29.65	182.92	1.00
9	11	-103.47	49.80	203.07	0.99
10	11	-156.83	20.15	197.13	1.00

Cette thèse est accessible à l'adresse : http://theses.insa-lyon.fr/publication/2022LYSEI044/these.pdf
© [K. Utria Salas], [2022], INSA Lyon, tous droits réservés

Table A.2: Multiple Comparisons Tukey's test Temperatures vs $\oslash_{boule}$ (1-9, correspond to the $\oslash_{boule}$ between 31-37, respectively)

I (technique)	J (technique)	Mean Difference (I-J)	95% Confidence Interval		p-value
			Lower Bound	Upper Bound	
1	2	-151.08	-19.30	112.48	1.00
1	3	-216.73	-109.13	-1.54	0.05
1	4	-225.79	-126.17	-26.56	0.01
1	5	-219.53	-120.70	-21.87	0.01
1	6	-202.63	-95.03	12.56	0.11
1	7	-231.00	-123.40	-15.80	0.02
2	3	-197.43	-89.83	17.76	0.14
2	4	-206.49	-106.87	-7.26	0.03
2	5	-200.23	-101.40	-2.57	0.04
2	6	-183.33	-75.73	31.86	0.29
2	7	-211.70	-104.10	3.50	0.06
3	4	-81.34	-17.04	47.26	0.97
3	5	-74.65	-11.57	51.52	1.00
3	6	-61.98	14.10	90.18	1.00
3	7	-90.35	-14.27	61.82	1.00
4	5	-42.75	5.47	53.70	1.00
4	6	-33.16	31.14	95.44	0.69
4	7	-61.53	2.77	67.07	1.00
5	6	-37.42	25.67	88.75	0.83
5	7	-65.78	-2.70	60.38	1.00
6	7	-104.45	-28.37	47.72	0.88

Table A.3: Multiple Comparisons Tukey's test $\oslash_{boule}$ vs $\overline{\nu_{H2}}$

I (technique)	J (technique)	Mean Difference (I-J)	95% Confidence Interval		p-value
			Lower Bound	Upper Bound	
1	2	-3.13	-2.50	-1.87	0.00
1	3	-4.63	-4.00	-3.37	0.00
2	3	-2.13	-1.50	-0.87	0.00

Cette thèse est accessible à l'adresse : http://theses.insa-lyon.fr/publication/2022LYSEI044/these.pdf
© [K. Utria Salas], [2022], INSA Lyon, tous droits réservés

Table A.4: Multiple Comparisons Tukey's test ovalisation index vs temperature category

I (technique)	J (technique)	Mean Difference (I-J)	95% Confidence Interval		p-value
			Lower Bound	Upper Bound	
1	2	-0.06	-0.01	0.04	0.97
1	3	-0.05	-0.02	0.01	0.14
1	4	-0.11	-0.07	-0.04	0.00
2	3	-0.06	-0.01	0.03	0.82
2	4	-0.12	-0.07	-0.01	0.01
3	4	-0.08	-0.05	-0.02	0.00

Cette thèse est accessible à l'adresse : http://theses.insa-lyon.fr/publication/2022LYSEI044/these.pdf
© [K. Utria Salas], [2022], INSA Lyon, tous droits réservés

Table A.5: Multiple Comparisons Tukey's test Ovalisation Index vs δ_{cer} (1-11, correspond to the δ_{cer} between 25-35, respectively)

I (technique)	J (technique)	Mean Difference (I-J)	95% Confidence Interval		p-value
			Lower Bound	Upper Bound	
1	2	-0.05	-0.01	0.04	1.00
1	3	0.02	0.06	0.10	0.00
1	4	0.02	0.06	0.10	0.00
1	5	0.04	0.08	0.11	0.00
1	6	0.03	0.08	0.13	0.00
1	7	0.04	0.09	0.13	0.00
1	8	-0.01	0.04	0.09	0.14
1	9	0.04	0.09	0.13	0.00
1	10	0.05	0.10	0.14	0.00
1	11	0.03	0.08	0.13	0.00
2	3	0.02	0.06	0.10	0.00
2	4	0.03	0.06	0.10	0.00
2	5	0.04	0.08	0.12	0.00
2	6	0.04	0.09	0.13	0.00
2	7	0.05	0.09	0.13	0.00
2	8	0.00	0.05	0.10	0.07
2	9	0.05	0.09	0.13	0.00
2	10	0.05	0.10	0.15	0.00
2	11	0.04	0.09	0.14	0.00
3	4	-0.02	0.00	0.03	1.00
3	5	-0.01	0.02	0.04	0.38
3	6	-0.02	0.02	0.06	0.63
3	7	0.00	0.03	0.06	0.11
3	8	-0.06	-0.02	0.02	0.91
3	9	-0.01	0.03	0.06	0.14
3	10	0.00	0.04	0.08	0.09
3	11	-0.02	0.03	0.07	0.47
4	5	0.00	0.02	0.04	0.22
4	6	-0.02	0.02	0.06	0.63
4	7	0.00	0.03	0.05	0.07
4	8	-0.06	-0.02	0.02	0.77
4	9	0.00	0.03	0.05	0.09
4	10	0.00	0.04	0.07	0.07
4	11	-0.01	0.02	0.06	0.46
5	6	-0.03	0.01	0.04	1.00
5	7	-0.02	0.01	0.04	0.93
5	8	-0.07	-0.03	0.01	0.13
5	9	-0.02	0.01	0.04	0.96
5	10	-0.02	0.02	0.06	0.68
5	11	-0.03	0.01	0.05	1.00
6	7	-0.04	0.01	0.05	1.00

Cette thèse est accessible à l'adresse : http://theses.insa-lyon.fr/publication/2022LYSEI044/these.pdf
© [K. Utria Salas], [2022], INSA Lyon, tous droits réservés

Table A.5: Multiple Comparisons Tukey's test ovalisation index vs δ_{cer} (1-11, correspond to the δ_{cer} between 25-35, respectively)

I (technique)	**J (technique)**	**Mean Difference (I-J)**	**95% Confidence Interval**		**p-value**
			Lower Bound	**Upper Bound**	
6	8	-0.09	-0.04	0.01	0.22
6	9	-0.04	0.01	0.05	1.00
6	10	-0.03	0.02	0.06	0.98
6	11	-0.05	0.00	0.05	1.00
7	8	-0.09	-0.04	0.00	0.04
7	9	-0.04	0.00	0.03	1.00
7	10	-0.03	0.01	0.05	1.00
7	11	-0.05	0.00	0.04	1.00
8	9	0.00	0.04	0.09	0.05
8	10	0.00	0.05	0.10	0.03
8	11	-0.01	0.04	0.09	0.15
9	10	-0.03	0.01	0.05	1.00
9	11	-0.05	0.00	0.04	1.00
10	11	-0.06	-0.01	0.04	1.00

Cette thèse est accessible à l'adresse : http://theses.insa-lyon.fr/publication/2022LYSEI044/these.pdf
© [K. Utria Salas], [2022], INSA Lyon, tous droits réservés

Table A.6: Multiple Comparisons Tukey's test geometrical defects vs δ_{cer} (1-11, correspond to the δ_{cer} between 25-35, respectively)

I (technique)	J (technique)	Mean Difference (I-J)	95% Confidence Interval		p-value
			Lower Bound	Upper Bound	
1	2	-4.11	0.00	4.11	0.00
1	3	-1.75	1.50	4.75	0.89
1	4	-1.31	1.73	4.77	0.70
1	5	-0.45	2.60	5.65	0.16
1	6	-0.03	3.00	6.03	0.05
1	7	-0.25	3.00	6.25	0.09
1	8	-1.00	2.25	5.50	0.42
1	9	-2.25	1.00	4.25	0.99
1	10	-0.56	3.00	6.56	0.17
1	11	-2.56	1.00	4.56	1.00
2	3	-1.75	1.50	4.75	0.89
2	4	-1.31	1.73	4.77	0.70
2	5	-0.45	2.60	5.65	0.16
2	6	-0.03	3.00	6.03	0.05
2	7	-0.25	3.00	6.25	0.09
2	8	-1.00	2.25	5.50	0.42
2	9	-2.25	1.00	4.25	0.99
2	10	-0.56	3.00	6.56	0.17
2	11	-2.56	1.00	4.56	1.00
3	4	-1.47	0.23	1.93	1.00
3	5	-0.62	1.10	2.82	0.54
3	6	-0.18	1.50	3.18	0.12
3	7	-0.56	1.50	3.56	0.35
3	8	-1.31	0.75	2.81	0.97
3	9	-2.56	-0.50	1.56	1.00
3	10	-1.02	1.50	4.02	0.64
3	11	-3.02	-0.50	2.02	1.00
4	5	-0.40	0.87	2.14	0.43
4	6	0.06	1.27	2.49	0.03
4	7	-0.43	1.27	2.97	0.31
4	8	-1.18	0.52	2.22	0.99
4	9	-2.43	-0.73	0.97	0.93
4	10	-0.96	1.27	3.51	0.69
4	11	-2.96	-0.73	1.51	0.99
5	6	-0.85	0.40	1.65	0.99
5	7	-1.32	0.40	2.12	1.00
5	8	-2.07	-0.35	1.37	1.00
5	9	-3.32	-1.60	0.12	0.09
5	10	-1.85	0.40	2.65	1.00
5	11	-3.85	-1.60	0.65	0.38
6	7	-1.68	0.00	1.68	0.00

Cette thèse est accessible à l'adresse : http://theses.insa-lyon.fr/publication/2022LYSEI044/these.pdf
© [K. Utria Salas], [2022], INSA Lyon, tous droits réservés

Table A.6: Multiple Comparisons Tukey's test geometrical defects vs δ_{cer} (1-11, correspond to the δ_{cer} between 25-35, respectively)

I (technique)	J (technique)	Mean Difference (I-J)	95% Confidence Interval		p-value
			Lower Bound	Upper Bound	
6	8	-2.43	-0.75	0.93	0.91
6	9	-3.68	-2.00	-0.32	0.01
6	10	-2.22	0.00	2.22	0.00
6	11	-4.22	-2.00	0.22	0.11
7	8	-2.81	-0.75	1.31	0.97
7	9	-4.06	-2.00	0.06	0.06
7	10	-2.52	0.00	2.52	0.00
7	11	-4.52	-2.00	0.52	0.24
8	9	-3.31	-1.25	0.81	0.61
8	10	-1.77	0.75	3.27	0.99
8	11	-3.77	-1.25	1.27	0.84
9	10	-0.52	2.00	4.52	0.24
9	11	-2.52	0.00	2.52	0.00
10	11	-4.91	-2.00	0.91	0.43

Table A.7: Multiple Comparisons Tukey's test foils vs temperature category

I (technique)	J (technique)	Mean Difference (I-J)	95% Confidence Interval		p-value
			Lower Bound	Upper Bound	
1	2	-11.65	-4.13	3.39	0.39
1	3	-24.40	-12.50	-0.60	0.04
2	3	-20.42	-8.37	3.68	0.22

Table A.8: Multiple Comparisons Tukey's test bubbles vs temperature category

I (technique)	J (technique)	Mean Difference (I-J)	95% Confidence Interval		p-value
			Lower Bound	Upper Bound	
1	2	-5.21	-0.17	4.88	1.00
1	3	-4.12	-0.74	2.63	0.94
1	4	-6.45	-3.06	0.34	0.09
2	3	-4.63	-0.58	3.48	0.98
2	4	-6.97	-2.89	1.19	0.25
3	4	-3.90	-2.31	-0.73	0.00

Cette thèse est accessible à l'adresse : http://theses.insa-lyon.fr/publication/2022LYSEI044/these.pdf
© [K. Utria Salas], [2022], INSA Lyon, tous droits réservés

Cette thèse est accessible à l'adresse : http://theses.insa-lyon.fr/publication/2022LYSEI044/these.pdf
© [K. Utria Salas], [2022], INSA Lyon, tous droits réservés

Appendix B | H_2/O_2 inverse diffusion flames

B.1 Jets regimes

The current section discusses three jet structures in order to understand the flow development and characteristics. In the first part, the laminar jet characteristics are described, secondly the turbulent jets and finally the coaxial jets that are the burner configuration of this study.

B.1.1 Laminar jets

The jet development depends on the initial laminar of turbulent characteristics. The laminar jets are usually defined for low Reynolds numbers, Re, (< 5000) jets. McNaughton and Sinclair (1966) performed a study that constitutes a solid basis for studying laminar jets. They proposed a classification for jet flows as a function of the Reynolds number, which considers both the jet structure and its possible laminar-turbulent transition. Thus, a jet initially laminar, characterised by stable boundaries and undeveloped flow, can move towards a downstream region where the flow is thoroughly turbulent. A transition region is found between the two positions-value of the Reynolds number conditions the laminar length after which the jet becomes turbulent and the existence of this zone. McNaughton and Sinclair (1966) also establishes that the cylindrical geometry in which the flow develops (geometry characterised by its diameter and length) plays a significant role. Therefore, the following relation is established for the laminar hydrodynamics length, $Y_{laminar}$:

$$\frac{Y_{laminar}}{D_i} = 9.97E7 \; Re^{-2.46} \left(\frac{D}{D_i}\right)^{-0.48} \left(\frac{L}{D_i}\right)^{0.74} \tag{B.1}$$

with D and L represent the diameter and length of the cylindrical enclosure in which the flow develops, D_i is the jet outlet diameter and Re is the Reynolds number calculated from the injection velocity at the nozzle. According to McNaughton and Sinclair (1966) results the jets have the ensuing classification according to the Reynolds number:

- $Re < 300$ Dissipative laminar jet
- $300 < Re < 1000$ Full laminar jet
- $1000 < Re < 3000$ Semi-turbulent jet

Cette thèse est accessible à l'adresse : http://theses.insa-lyon.fr/publication/2022LYSEI044/these.pdf
© [K. Utria Salas], [2022], INSA Lyon, tous droits réservés

- $Re > 3000$ Completely turbulent jet

Traditionally the injection regimen is determine by (Menon, 2015):

- Laminar flow – $Re < 2000$
- Critical flow – $Re > 2000 and Re < 4000$
- Turbulent flow – $Re > 4000$

B.1.2 Turbulent jets

Practical applications in hydraulic engineering have demonstrated that velocity profiles measured in wide open channels can be well represented by the Power-Law (Departement, 1992) which gives the simplest velocity turbulent profile. Regarding this law, the velocity profile in turbulent flow is flatter in the central part of the pipe (i.e. in the turbulent core) than in laminar flow, as shown in figure B.1. The flow velocity drops rapidly extremely close to the walls owing to the diffusivity of the turbulent flow.

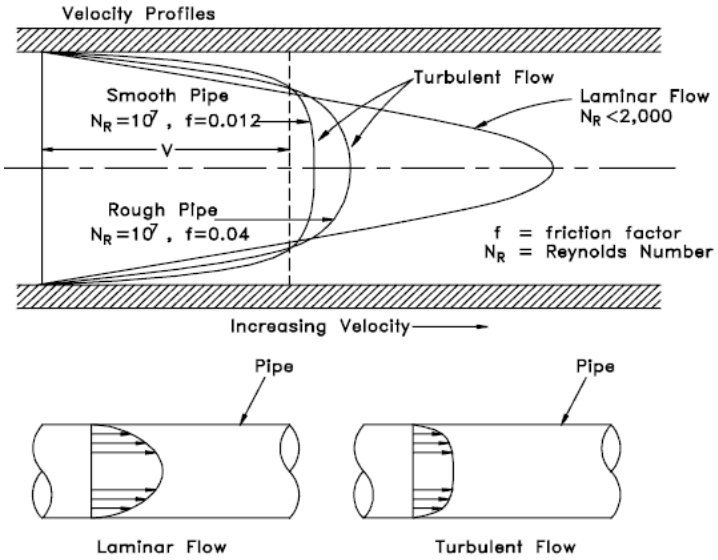

Figure B.1: Flow development in a pipe. (Departement, 1992)

The Power-law is defined as :

$$\frac{\overline{u}}{U_{max}} = \left(\frac{y}{R}\right)^{1/n}, \ or \ \frac{\overline{u}}{U_{max}} = \left(1 - \frac{r}{R}\right)^{1/n} \tag{B.2}$$

where $\overline{u}$ is the streamwise, time-mean flow velocity, U_{max} is the maximum velocity, R is the radius of the pipe, y or r is the position radial or axial, and the exponent n is a

Cette thèse est accessible à l'adresse : http://theses.insa-lyon.fr/publication/2022LYSEI044/these.pdf
© [K. Utria Salas], [2022], INSA Lyon, tous droits réservés

constant whose value increases with Reynolds number (figure B.2b). $1/n$ values varies from 1/4 down to 1/12 depending upon the boundary friction and cross-sectional shape. Many industrial flows follow the one-seventh power-law velocity profile closely.

In figure B.2 different turbulent flow profiles are shown for different n.

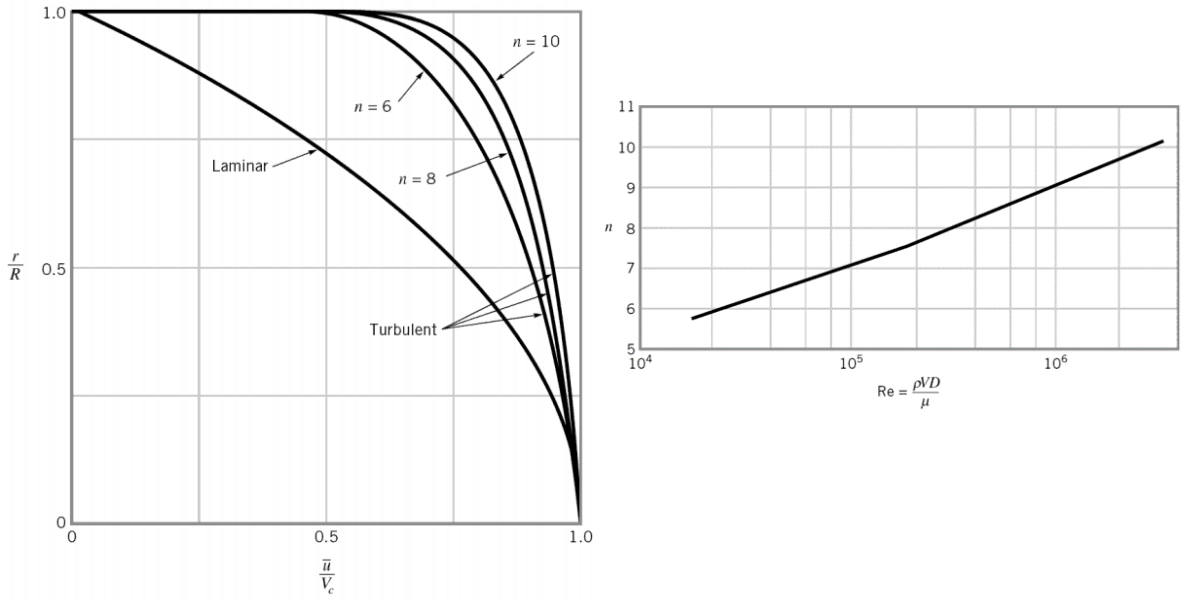

(a) (b)

Figure B.2: (a) Typical laminar flow and turbulent flow velocity profiles, (b) n coefficient for power-law velocity profile (Departement, 1992)

On the other hand, the structure of a turbulent jet is composed of three regions: the near-field, the intermediate-field and the far-field, as shown in figure B.3. The near-field or initial region contains the potential core. This is characterised by a constant axial velocity equal to the injector velocity output (in the case of a uniform output profile). This conical region is limited on its edges by a layer of mixture with the external fluid at rest, and is usually found within $0 < y/d < 6$, where d is the nozzle diameter (Fiedler and Hilberg, 1991). The far-field region is located at $y/d > 30$ (Fiedler and Hilberg, 1991), within this region the mixing layer becomes very turbulent near the exit of the jet (Rajaratnam, 1976). This region is characterised by a fully-developed flow, and is also called self-similar region. The intermediate-field region lies between the near- and far-fields of the jet. The end of the potential core is characterised by the mixture layer that occupies the entire section of the flow. This is highlighted when exploring relative turbulence's intensity along the axis, defined as:

$$\frac{I}{I_0} = \frac{\left(\sqrt{\overline{u'^2}}/\overline{U}\right)}{\left(\sqrt{\overline{u'^2}}/\overline{U}_{C,0}\right)} \tag{B.3}$$

Cette thèse est accessible à l'adresse : http://theses.insa-lyon.fr/publication/2022LYSEI044/these.pdf
© [K. Utria Salas], [2022], INSA Lyon, tous droits réservés

With $\overline{U}$ the longitudinal velocity on the jet axis and $\overline{U}_{C,0}$, the centreline value of $\overline{U}$ at the nozzle exit.

The near- and intermediate-fields compose the development portion of the jet. They are usually found in practical applications of jets for which upstream conditions can significantly influence heat, mass, and momentum transfer. Therefore, the ability to control the flow development in this region would have a vital impact on many of those engineering applications.

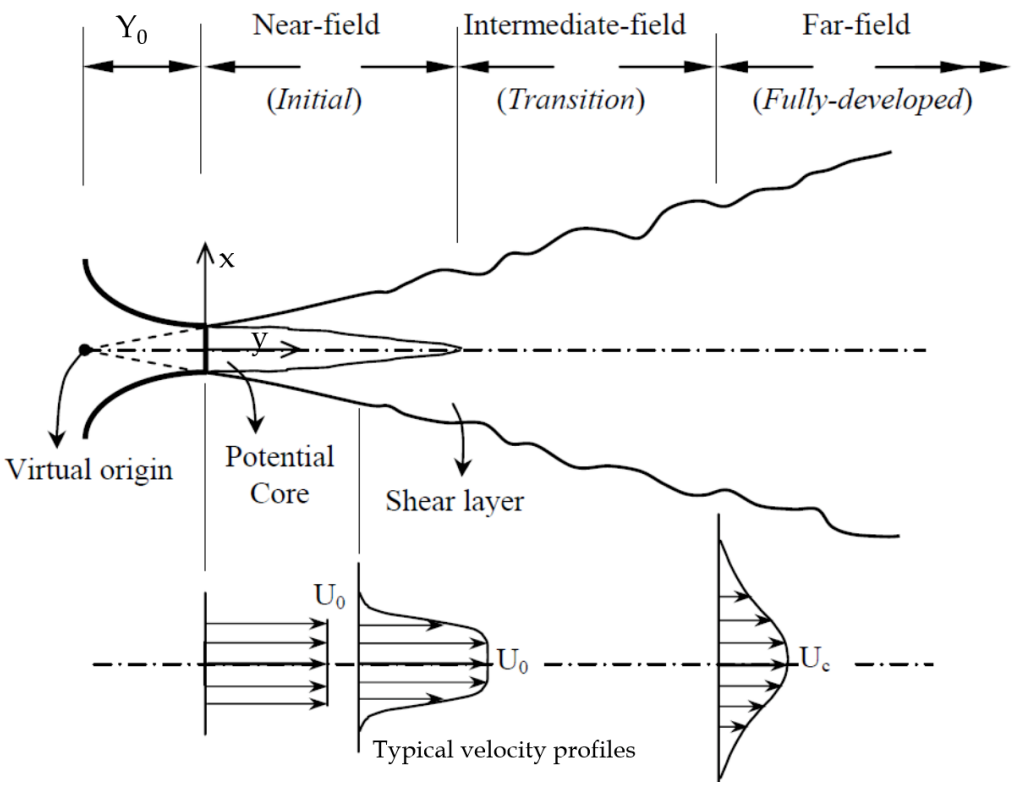

Figure B.3: Schematic of the free turbulent jet and coordinate system (Abdel-Rahman, 2010)

According to Panton (2013), the overall turbulence intensity can be defined for each velocity component as the root mean square (RMS) referenced to a mean flow velocity (V_{ref}), as (Lam, W.H., Robinson D.J., Hamill, G.A., 2012)

$$I_{turb} = \frac{\sqrt{2/3k}}{V_{ref}} \tag{B.4}$$

$$k = \frac{1}{2}\left(u'^2 + v'^2 + w'^2\right)$$

where k is the turbulence kinetic energy, V_{ref} is the reference velocity, specified as the maximum of the mean velocities, and u', v', w' are the turbulent fluctuation in x, y and z directions. For this case, the Dantec BSA Manual does not provide the turbulence

Cette thèse est accessible à l'adresse : http://theses.insa-lyon.fr/publication/2022LYSEI044/these.pdf
© [K. Utria Salas], [2022], INSA Lyon, tous droits réservés

intensity as a direct calculated output, but provides turbulent fluctuations, $\sqrt{\overline{u'^2}}$ for x and y components velocity as a direct output. From now on, u' referrers to the component of the turbulent fluctuation in Y-axis (longitudinal velocity) and v' is the transversal component of the turbulent fluctuation (transversal velocity $\overline{V}$). V_{ref} is the measured mean velocity at the centreline of the oxygen outlet, $\overline{U}_{C,0}$. The norm of the velocity vector, U is calculated as :

$$U = \sqrt{\overline{U}^2 + \overline{V}^2} \tag{B.5}$$

The far-field of the jet has been extensively studied (Abdel-Rahman, 2010). In the fully developed region, the longitudinal velocity decreases continuously from a maximum U_C value on the axis to zero for a considerable value of y. At this point comes the notion of self-similarity for which Hinze (1975) gives the following definition. Self-similarity appears in unsteady flows in decrease when for a fixed Reynolds number, the structure reaches similarity. That is to say that a velocity scale and a length scale are sufficient (full similarity or perfect) to make the decay velocity distributions identical as a function of the coordinates. Thus, Rajaratnam (1976) presents velocity results in the far-field for which the profiles overlap perfectly. The axial velocities were rendered dimensionless by $\overline{U_C}$ and the transversal coordinate by the half-width of the jet $X_{0.5}$ (X-position of the velocity profile at which the velocity is equal to half of that observed on the axis). Despite a large number of studies on the far-field, there are conflicting results regarding universal self-similarity. Several pieces of research support the hypothesis of universal self-similarity (Dowling and Dimotakis, 1990; Pitts, 1991; Richards and Pitts, 1993; Antonia and Zhao, 2001). Antonia and Zhao (2001) showed that the self similar-region is independent of the initial conditions. In other words, the spread rates of all jets are universal, and the asymptotic normalized scalar and velocity fields of all jets are identical, regardless of jet initial conditions. Other studies claim that the self-similar region is not universal, but it depends on the initial conditions, especially (George and Gibson, 1992). In contrast to the classical treatment of Hinze (1975), in a theoretical analysis (George and Gibson, 1992) suggested that turbulent flows can become asymptotic to a variety of self-similar states that are determined by initial conditions.

B.1.3 Coaxial jets

Regarding coaxial jets, a large body of research has been accumulated since the 1940s and perfectly summarised by Hout et al. (2021). Figure B.4 illustrates schematically the model proposed by Ko and Kwan (1976). A coaxial jet is composed of two inlet jets which interaction defines its complex structure. As observed, the circular inner jet interacts with

Cette thèse est accessible à l'adresse : http://theses.insa-lyon.fr/publication/2022LYSEI044/these.pdf
© [K. Utria Salas], [2022], INSA Lyon, tous droits réservés

an annular outer jet—the flow field of the coaxial jet breaks down into three zones. The initial merging zone spreads from the jet exit plane to the outer potential tip core. Ko and Kwan (1976) also proposed a simple model that described this zone as two separate arrays of non-interacting vortex rings generated in the inner and outer mixing layers. They assumed that the outer mixing layer results from a single jet of diameter D_o and jet exit velocity U_o shearing with the ambient fluid. The inner mixing layer outcomes from a single jet of diameter D_i and jet exit velocity U_i submerged in a uniform velocity stream U_o. In addition, they considered that the fully merged zone is similar to that of an equivalent single jet of equal thrust. Based on this simple model, the average separation distance of consecutive inner and outer mixing layer vortices was estimated as $1.25D_o$ and $1.25D_i$, respectively, while inner mixing layer vortex convection velocities were estimated to be $0.6(U_i + 2U_o/3)$.

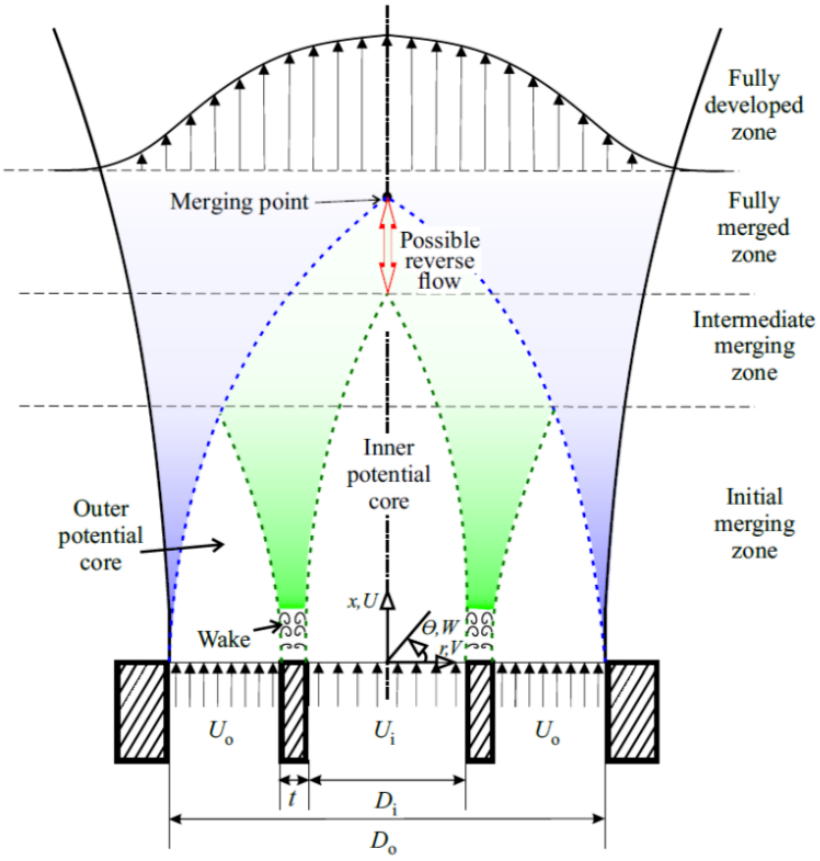

Figure B.4: Coaxial jet nozzle configuration and different identified near-field flow regions and zones. Green and blue shaded areas represent the inner and the outer mixing layers, respectively (Hout et al., 2021)

The fully merged zone starts when the inner and outer jets have fully merged and start to behave as a single jet. Available results show that at a certain distance, the velocity profile in the fully merged zone becomes fully developed and self-similar. Accordingly Antonia and Bilger (1973), self-similarity is reached for the crossed profiles of mean axial

Cette thèse est accessible à l'adresse : http://theses.insa-lyon.fr/publication/2022LYSEI044/these.pdf
© [K. Utria Salas], [2022], INSA Lyon, tous droits réservés

velocity in $Y/D_i = 38$, for velocity ratio $r_u < 1$ (dominant central jet), given by :

$$r_u = \frac{U_o}{U_i} \tag{B.6}$$

where U_o and U_i denote the mean jet exit velocities of the outer and inner jet, respectively.

Champagne and Wygnanski (1971) suggests a self-similarity on the turbulence intensity profiles in $y/Di \cong 60$. He shows for high Reynolds number(24 000), that an asymptotic evolution is reached, whatever the case considered, in $(y-Y_0)/D_o > 11$ for the longitudinal velocity and $(y - Y_0)/D_o > 8$ for the half-width (Y_0: virtual origin).

The intermediate zone is more complicated and has properties intermediate to those of the previously described. Note that due to the velocity 'jumps' between the inner and outer jet velocities, (U_o and U_i), inner and outer mixing layers (green and blue shaded areas) exist that give rise to Kelvin–Helmholtz instabilities that result in the generation of toroidal vortices close to the nozzle exit. Furthermore, even when $(U_o - U_i) = 0$ (i.e., when $r_u = 1$), wake-like instabilities will form as a result of the finite lip thickness (Ko and Kwan, 1976).

On the other hand,Villermaux and Rehab (2000) showed that the length of the inner potential core region depends strongly on the velocity ratio, r_u. However, the length of the outer potential core only weakly depends on r_u and is essentially fixed by the diameter ratio given by:

$$b = \frac{D_o}{D_i}. \tag{B.7}$$

Increasing b leads to an increase in the outer potential core length and vice versa. Note that when U_i is much lower than U_o, the outer jet deflects towards the central axis and reverse flow may occur. Villermaux and Rehab (2000) shows that reverse flow forms when r_u exceeds 5 to 8 (the actual value depends on the jet exit velocity profiles). The resulting recirculation region is located between the merging point and the end of the inner potential core region (Figure 1, note that the inner potential core region is shorter than the outer one for $r_u > 5$ (Villermaux and Rehab, 2000). Additional parameters pertinent to the coaxial jet are the inner and outer jet's nozzle exit area given by:

$$A_i = \frac{\pi D_i^2}{4},\ and\ A_0 = \frac{\pi(D_0^2 - (D_i + 2t)^2)}{4} \tag{B.8}$$

respectively, where t is the lip thickness, i.e., the thickness of the inner nozzle at the exit plane (see figure B.4). The area ratio is defined as:

$$A_r = \frac{A_0}{A_i} \tag{B.9}$$

Cette thèse est accessible à l'adresse : http://theses.insa-lyon.fr/publication/2022LYSEI044/these.pdf
© [K. Utria Salas], [2022], INSA Lyon, tous droits réservés

while inner and outer jet Reynolds numbers are defined by:

$$Re_i = \frac{u_i D_i}{v} \; and \; Re_o = \frac{u_o(D_o - (D_i + 2t))}{v} \tag{B.10}$$

respectively, where v denotes the fluid kinematic viscosity.

Furthermore, apropos the initial configuration velocities, the ratio r_u is not the only parameter that influences the development of the flow. Warda et al. (1999) showed that the absolute values of the mean axial output velocities play an essential role in setting the jet. In their study, they used the same value of $r_u = 0.5$ and changed the values of $U_{i,0}$ (from 20 *to* 10 m/s and $U_{e,0}$ (10 *to* 5 m/s). Their results show that when the absolute value of the average velocity decreases, the decrease on the velocity axis $\overline{U}$ as well as the flow development are more significant. According to Warda et al. (1999), this behaviour is due to the development of the mixing layer whose turbulence generation process varies according to the velocity difference between the two flows.

Cette thèse est accessible à l'adresse : http://theses.insa-lyon.fr/publication/2022LYSEI044/these.pdf
© [K. Utria Salas], [2022], INSA Lyon, tous droits réservés

Appendix C | Overall thermal behaviour of the Verneuil device

C.1 Validation of the laboratory text bench

The experimental test bench developed by the CETHIL was validated through a test with the same production injection conditions without the crystallisation, in other words the confinement had a free flame. Figure C.1 represents the experimental set up of both conditions. Temperatures were obtained through thermocouples type R and a LabVIEW^{TM} code was develop to acquire the experimental data at laboratory conditions, the acquisition frequency was 1 sample/sec. At production conditions, the temperatures were recollected through a TC Direct paperless data recorder which posses an indication accuracy of $\pm 0.1\%$. The results are the average temperatures captured with a frequency of 30 samples/min.

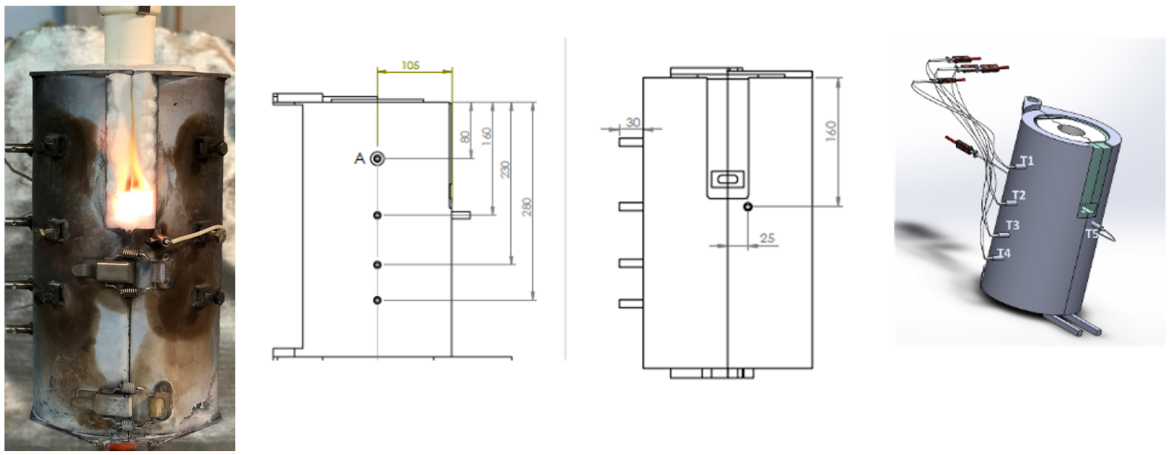

Figure C.1: Industrial Furnace under laboratory conditions

The flow rate increase for the laboratory was faster due to the high flow rates required by the production conditions. At the first hour of experiment the increment was the same for both tests, during the second hour the maximum flow rates were achieved faster at the laboratory, as shown in figure C.2.

The results of the temperatures are shown in figure C.3. As observed, the differences between the laboratory setup and the industrial setup are related to the thermal conditions of the Verneuil furnaces. At real production conditions the furnaces are surrounded by

Cette thèse est accessible à l'adresse : http://theses.insa-lyon.fr/publication/2022LYSEI044/these.pdf
© [K. Utria Salas], [2022], INSA Lyon, tous droits réservés

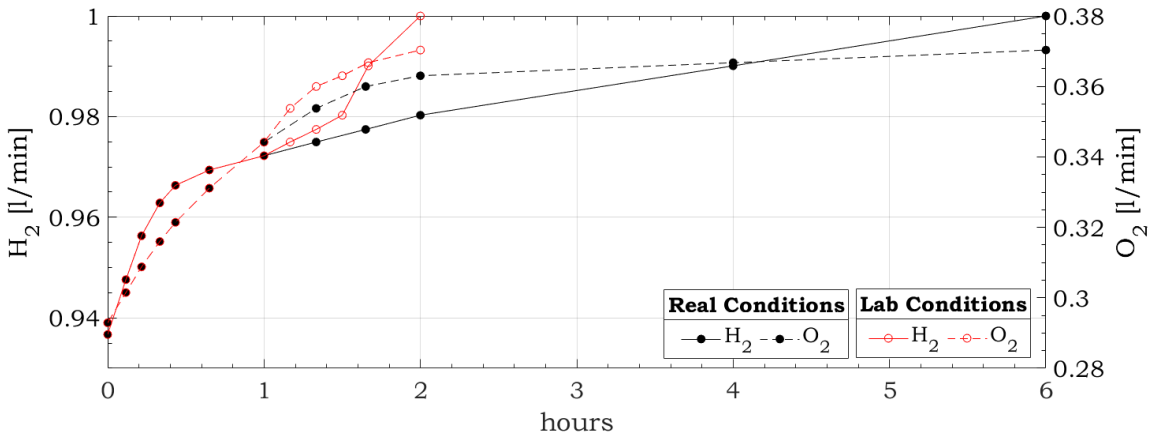

Figure C.2: Flow rates

others, contrarily in the laboratory there is only one furnace and this is opened. Therefore, the heat loss rate at laboratory conditions are higher due to the non-confinement conditions of the furnace. Nevertheless, the temperatures reported are higher, this is probably due to pressure lost across the pipeline at production conditions.

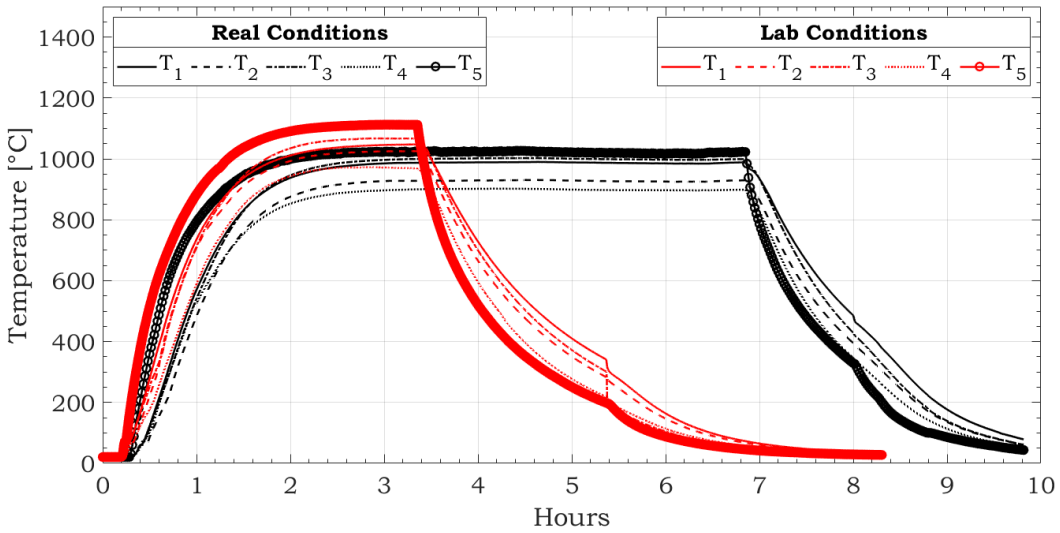

Figure C.3: Temperatures

On the other hand, at the beginning of the cycle, it can be observed that the trends and temperature differences between the positions are similar. The laboratory furnace showed a higher rate of temperature increase as a result of the faster increase in flow rates, as already mentioned. At the end of the cycle, when the flame is turn off it can be observed the beginning of the temperature decrease for both tests, particularly the temperature position 5. This is the temperature located the closest to the flame. Furthermore, the furnace are usually opened at industrial conditions after eight hours of the cycle beginning. At the laboratory, this was performed at five hours and an-half. The consequence of this

Cette thèse est accessible à l'adresse : http://theses.insa-lyon.fr/publication/2022LYSEI044/these.pdf
© [K. Utria Salas], [2022], INSA Lyon, tous droits réservés

event can be observed as a faster decrease in the temperature for the two conditions especially temperatures in positions 2 and 5.

Even though the thermal conditions are not the same, the differences obtained between the industrial and laboratory results are lower than 10% *for the maximum temperatures. These results showed that they are similar enough to validate the experimental bench.*

Cette thèse est accessible à l'adresse : http://theses.insa-lyon.fr/publication/2022LYSEI044/these.pdf
© [K. Utria Salas], [2022], INSA Lyon, tous droits réservés

C.2 Numerical tools

In order to complete the analysis associated with the experimental results, a numerical study was carried out using Computation Fluid Dynamics (CFD). The software chosen to develop the study was the commercial sofware STAR-CCM+. This section briefly describes the models and solver used to examine the aerodynamics of the crystal growth environment (this section is base on the documentation given by the software).

C.2.1 STARCCM+

Simcenter STAR-CCM+ is a multiphysics computational fluid dynamics (CFD) commercial software for the products operating simulation under real conditions. The single integrated environment includes CAD, automated meshing, multiphysics CFD, sophisticated post-processing, and design exploration to explore the entire design space. This tool allows multidisciplinary problems in fluid and solid continuum mechanics within a single integrated user interface. The system was simulated in non-reactive and reactive flow for three different operating points of crystallisation No.15, which were highlighted in previous sections and corresponded to the initial formation, initial growth and final growth (see table 7.1).

C.2.2 Governing equations for the non-reactive flow

Numeric simulations were performed in order to examine the interaction between the O_2 jet and H_2 jets. Their principal objective is to determine the flow development without the reaction zones. The complete study of the non-reacting flow is described in appendix C.3.

The models used are described above:

- Steady state
- Non-reactive
- Laminar flow
- Multi-segregated flow (Isothermal)
- Three-dimensional
- Gravity

Cette thèse est accessible à l'adresse : http://theses.insa-lyon.fr/publication/2022LYSEI044/these.pdf
© [K. Utria Salas], [2022], INSA Lyon, tous droits réservés

STAR-CCM+ simulates internal and external fluid flow for a wide range of flow regimes and various fluid types. It solves the conservation for mass, momentum, and energy for general incompressible and compressible fluid flows.

The software considered a reference frame that rotates with constant angular velocity, w, around an axis and translates with a translation velocity v_t relative to a stationary reference frame.

Equation C.1 defines the velocity relative to the moving reference frame (relative velocity) v_r from the velocity in the stationary reference frame (absolute velocity) v:

$$v_r = v - v_g = v - (v_t + w \times r) \tag{C.1}$$

where : v_g : the reference frame velocity relative to the inertial laboratory frame.

r: position vector from the origin of the moving reference frame to a point in the computational domain.

with equation C.1, and integrating over a finite control volume, the governing equations of fluid flow are define as:

Continuity equation through conservation of mass

$$\frac{\partial}{\partial t}\int_V (\rho dV) + \oint_A \rho v_r \cdot da = \int_V S_u dV \tag{C.2}$$

Conservation of Linear Momentum

$$\frac{\partial}{\partial t}\int_V (\rho dV) + \oint_A \rho v_r \otimes v \cdot da = \oint_A pI \cdot da + \oint_A T \cdot da - \int_V \rho \left[w \times (v - v_t)\right] dV + \int_V f_b dV \tag{C.3}$$

Where $\otimes$ denotes the Kronecker product, f_b is the resultant of body forces (such as gravity and centrifugal forces per unit volume acting on the continuum). The stress tensor is often written as a sum of normal stresses and shear stresses, $-pI + T$ where p is the pressure and T is the viscous stress tensor.

Energy conservation

$$\frac{\partial}{\partial t}\int_V (\rho E dV) + \oint_A \left[\rho H v_r p\right] \cdot da = \oint_A \dot{q}" \cdot da + \oint_A T \cdot v da + \int_V f_b \cdot v dV + \int_V S_E dV \tag{C.4}$$

Where E is the total energy per unit mas, $\cdot q$" is the heat flux, and S_E is an energy source per unit volume.

Cette thèse est accessible à l'adresse : http://theses.insa-lyon.fr/publication/2022LYSEI044/these.pdf
© [K. Utria Salas], [2022], INSA Lyon, tous droits réservés

Gravity

As observed in chapter 6, the forces due to the buoyancy play an important role in the momentum balance for this kind of configuration. The body forces due to gravity are added to the momentum equation as a source term:

$$f_g = \rho g \tag{C.5}$$

where g is the gravity vector.

For variable density flows, the buoyancy source term is

$$f_g = (\rho - \rho_{ref})g \tag{C.6}$$

where ρ_{ref} is the reference density.

C.2.2.1 Discretisation and Solution

Discretisation methods are used by STAR-CCM+ to convert the continuous system of equations to a set of discrete algebraic equations, which can be solved using numerical techniques. The procedure is as follows:

- the continuous domain is divided into a finite number of subdomains (cells/elements)
- the unknowns are stored at specific locations of the mesh (vertices, cell centroids, face centroids, or edges)
- an integral or weak form of the differential equations is employed for spatial discretisation.

After discretising the time derivative, the result is a coupled system of algebraic equations (non-linear, in general) that are solved at each time-step.

Depending on the mathematical model, STAR-CCM+ discretises the continuous equations using either the Finite Volume or the Finite Element Method.

The Finite Element is similar to other numerical techniques that approximate continuous partial differential equations with discrete algebraic equations.

Discretisation of the Continuous Domain

Cette thèse est accessible à l'adresse : http://theses.insa-lyon.fr/publication/2022LYSEI044/these.pdf
© [K. Utria Salas], [2022], INSA Lyon, tous droits réservés

The mathematical models of STAR-CCM+ that describe the physics phenomena is a closed set of equations, consisting of a set of partial differential equations (PDE) and constitutive equations. The software's first step is discretising the continuous space domain into a finite number of subdomains, called elements. In order to reduce the continuous set to a discrete set of algebraic equations. For the current simulation, two continuum models were used in order to discretise the continuous domain:

- Polyhedral Mesher
- Surface Remesher

The fluid domain is shown in figure C.4, which consists of 317935 cells. A mesh diagnostic was run to guarantee the correct choice of the mesh size.

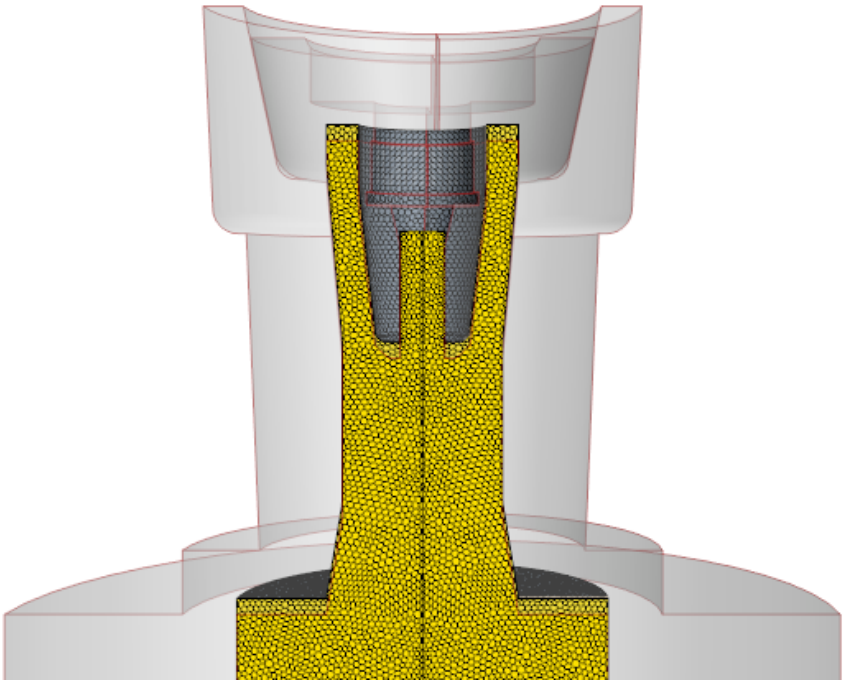

Figure C.4: Discretisation of the fluid domain

The partial differential equations (PDE) are converted to an integral or weak form satisfied over each element domain. The weak form of a PDE is usually constructed as follows:

- The PDE is multiplied by an arbitrary test function and integrated over the element domain.
- The order of the derivatives is reduced using integration by parts.
- Appropriate Dirichlet and Neumann boundary conditions are applied.

Cette thèse est accessible à l'adresse : http://theses.insa-lyon.fr/publication/2022LYSEI044/these.pdf
© [K. Utria Salas], [2022], INSA Lyon, tous droits réservés

On the other hand, the software performs the **discretisation of the unknowns**. For each element, the distribution of the dependent variables is constructed from the discrete values that the variables assume at specific locations. Shape functions interpolate the discrete values to any other point in the element, providing the dependent variables' local (per-element) distribution. Continuous variables across adjacent elements are ensured by mapping operations between the local element domain and the global physical domain .

The final result is a set of discrete algebraic equations obtained by approximating all the integrals with numerical techniques. The system of algebraic equations is solved using a sparse direct solver.

Segregated Flow

The segregated flow and energy is an alternative flow model of incompressible or mildly compressible flows, mainly when computational resources are an issue. The segregated flow model invokes the segregated solver, which solves each of the momentum equations, one for each dimension.

Numerical Flow Solution

The solution domain, for the finite volume method, is subdivided into a finite number of small control volumes corresponding to the cells of a computational grid. To each control volume discrete versions of the integral form of the conservation equations are applied. In order to obtain a set of linear algebraic equations, with the total number of unknowns in each equation system. These are related to the number of cells in the grid. The dependent variable values are stored at the cell centre.

The segregated flow solver solves the integral conservation equations of mass and momentum sequentially. The non-linear governing equations are solved iterating one after the other. This solver uses a pressure-velocity coupling algorithm. A pressure-correction equation is used to achieve the mass conservation constraint on the velocity field. STAR-CCM+ implements two pressure-velocity coupling algorithms:

- SIMPLE
- PISO

The general transport equation is given by:

$$\underbrace{\frac{d}{dt}\int_V \rho\phi dV}_{\text{Transient Term}} + \underbrace{\int_A \rho v\phi \cdot da}_{\text{Convective Flux}} = \underbrace{\int \Gamma\nabla\phi da}_{\text{Diffusive Flux}} + \underbrace{\int_V S_\phi dV}_{\text{Convective Flux}} \tag{C.7}$$

Cette thèse est accessible à l'adresse : http://theses.insa-lyon.fr/publication/2022LYSEI044/these.pdf
© [K. Utria Salas], [2022], INSA Lyon, tous droits réservés

The semi-discrete transport equation is defined as:

$$\frac{d}{dt}(\rho\phi V)_0 + \sum_f [\rho\phi(v \cdot a)]_f = \sum_f (\Gamma \nabla\phi \cdot a)_f + (S_\phi V)_0 \tag{C.8}$$

where ϕ represents the transport of a scalar property, A is the surface area of the control volume and $a$denotes the surface vector. Γ the diffusion coefficient.

Convective Flux

The discretised convective term at a face is define as:

$$(\phi v \cdot a)_f = \dot{m}\phi)_f = \dot{m}_f \phi_f \tag{C.9}$$

where f: indicates fluid and $\dot{m}_f$ is the mass flow rate at the face.

Diffusive Flux

The diffusive flux in C.7 is discretised for a cell as:

$$D_f = (\Gamma \nabla\phi \cdot a)_f \tag{C.10}$$

where $\nabla\phi$ is the gradient of fluid property ϕ and $\boldsymbol{a}$ is the surface area vector.

Discretisation of the Momentum Equation

The momentum equations are discretised in a similar way to the scalar transport equation as described in Generic Transport Equation by setting :

$$\frac{\partial}{\partial t}(\rho v V)_0 + \sum_f [\rho v v \cdot a]_f = -\sum_f (pI \cdot a)_f + \sum_f T \cdot a \tag{C.11}$$

C.2.3 Governing Equations for the reacting flow

The models used in the reacting flow are described above:

- Implicit Unsteady
- Reactive
- Laminar flow
- Multi-segregated flow (Segregated fluid enthalpy)

Cette thèse est accessible à l'adresse : http://theses.insa-lyon.fr/publication/2022LYSEI044/these.pdf
© [K. Utria Salas], [2022], INSA Lyon, tous droits réservés

- Three-dimensional
- Reacting Species Transport
- Complex Chemistry

In reacting flow simulations, the continuity equation and the conservation equation for flow are solved according to equations C.2 and C.3, respectively. The conservation equation for energy is solved, with the addition of the source term that accounts for the heat that is released in the reaction: Differential form:

$$\frac{\partial(\rho E)}{\partial t} + \nabla \cdot (\rho E v) = f_b \cdot v + \nabla \cdot (v \cdot \sigma) - \nabla \cdot q + S_E \tag{C.12}$$

Integral form is the equation C.4

where S_E is the source term (which includes the source term from the reactions).

Additionally, conservation equations for species mass fractions (Y_i) are solved:

Differential form:

$$\frac{\partial(Yi)}{\partial t} + \nabla \cdot (\rho U Y_i) = \nabla \cdot \left(J_i + \frac{\mu_t}{\sigma_t} \nabla Y_i \right) + S_{Y_i} \tag{C.13}$$

Integral form:

$$\frac{\partial}{\partial t} \int_{\widetilde{V}} \left(\rho Y_i d\widetilde{V} \right) + \oint_A \rho Y_i (v - vg) \cdot d\widetilde{a} = \oint_A \left[J_i + \frac{\mu_t}{\sigma_t} \nabla Y_i \right] \cdot d\widetilde{a} + \int_{\widetilde{V}} S_{Y_i} d\widetilde{V} \tag{C.14}$$

where S_{Y_i} is the mass fraction source term from reactions.

Chemical Kinetics

The chemical species mechanisms and rates of reaction at the molecular level concern the chemical kinetics. Their analysis requires modelling the reacting species transport to provide the source term to the transport equations for all reactions in the chemical mechanism.

The reaction rate for elementary reactions is calculated for a general one-step reaction, as follows:

$$\frac{d[A]}{dt} = v_A \left[k_f \cdot [A]^{v'_A} [B]^{v'_B} ... - k_b [C]^{v'_C} [D]^{v'_D} ... \right] \tag{C.15}$$

where $v_A = v''_a - v'_A$

Cette thèse est accessible à l'adresse : http://theses.insa-lyon.fr/publication/2022LYSEI044/these.pdf
© [K. Utria Salas], [2022], INSA Lyon, tous droits réservés

Each reaction proceeds at its own rate; hence, at a given location, it has a unique time scale that depends on the concentrations of different species at that location, the temperature, and pressure.

The production (or consumption) rate (r_i) of $\boldsymbol{i}$ species; , depends on the reaction rates of the reactions which produce and consume the species, and on the concentration of all species which participate in those reactions. The total net rate is therefore a sum of C.15 over all reactions in which species participates. In the equation below, $\boldsymbol{j}$(=1, 2, … ,) denotes reactions and $\boldsymbol{i}$ denotes species.

$$r_i = \frac{d[A]}{dt} = \sum_{j=1}^{N_j} v_{ij} r_j \tag{C.16}$$

$$r_j = k_{f,j} \Pi [A]^{v'_{j,i}} - k_{b,j} \Pi [A]^{v'_{j,i}} \tag{C.17}$$

where the rate coefficients, k_f for the forwards reaction and k_b for the backwards reaction, are determined by rate constant:

Rate Constant

The rate constant is most often determined using the Arrhenius equation, in which the rate has a non-linear dependence on temperature:

$$k = AT^{\beta} exp\left(-\frac{E_a}{R_u T}\right) \tag{C.18}$$

where R_u is the universal gas constant and the following values are empirical factors that are supplied by the chemical mechanism:

- the temperature exponent, β
- the activation energy, $text(E_a)$
- the frequency factor, or pre-exponential factor $\boldsymbol{A}$

The simulation uses the reaction-species transport model and complex chemistry to solve the chemical reaction between the hydrogen and oxygen jets.

Reactions—Species Transport

Using reacting species transport, all species in the mechanism are convected and diffused through the computational domain and react using the prescribed chemical mechanism.

Cette thèse est accessible à l'adresse : http://theses.insa-lyon.fr/publication/2022LYSEI044/these.pdf
© [K. Utria Salas], [2022], INSA Lyon, tous droits réservés

The used reacting species transport model available in STAR-CCM+ was *Complex Chemistry*. An ODE solver is used to integrate the chemical source terms for all species over the CFD time-step through adaptive time-step subcycling in each cell.

Complex Chemistry

Complex Chemistry is solved by STAR-CCM+ in detail using a stiff ODE (Ordinary Differential Equation) solver— DARS-CFD—to integrate the chemical source terms. This model can solve thousands of reactions among hundreds of species. Since an ODE solver is used to integrate the chemical source terms, the Complex Chemistry model can handle stiff reaction systems (reaction systems with a wide range of reaction time scales). This model also requires detailed reaction mechanism information about species, reactions, thermodynamics, and transport properties. These details are provided by complex chemistry definition files that are imported in the Chemkin format.

The general species transport equation is formulated as follows:

$$\frac{\partial}{\partial t}\rho Y_i + \frac{\partial}{\partial t}\left(\rho u_j Y_i + F_{k,j}\right) = w_i \tag{C.19}$$

where $F_{k,j}$ is the diffusion flux and source term w_i is the rate of production of species $\boldsymbol{i}$.

The Laminar Flame Concept consider the turbulence effects on combustion implicitly through the increased turbulent diffusivity that is provided by the turbulence model.

The model uses DARS-CFD solver to integrate the stiff chemistry over a time-step. The evolution of mean species mass fractions and temperature in a given CFD cell is calculated by integrating at the cell conditions using Jacobian matrices to solve the ordinary differential equation:

$$Y_i = Y_i(t_0) + \int_0^{\tau_{rest}} \dot{w}_t dt \tag{C.20}$$

The transport equations that are solved for a reacting flow contain the chemical source term, w .

$$\frac{d(Y_i)}{dt} = \dot{w}_n\left(Y_i, T, p\right) \tag{C.21}$$

Where Y_i is the mass fraction of species. The Jacobian J_w is defined as:

$$J_w = \frac{\partial w}{\partial Y} \tag{C.22}$$

Cette thèse est accessible à l'adresse : http://theses.insa-lyon.fr/publication/2022LYSEI044/these.pdf
© [K. Utria Salas], [2022], INSA Lyon, tous droits réservés

C.3 Numerical simulation of the stagnation point in non-reacting conditions

Numeric simulations were performed in order to examine the interaction between the O_2 jet and H_2 jets. Their principal objective is to determine the flow development without the reaction zones. The initial conditions at the O_2 nozzle outlet are analysed in figure C.5 for the three injection conditions previous mentioned in table 7.2. Besides, the numerical models are described in subsection C.2.2.

As observed, for the oxygen jet the three flow rates reported the same trend. As reported previously, the profiles describe a behaviour between the laminar profile and the power law *1/7*. These differences with the laminar profiles are related with the geometry of the nozzle and the influence and the influence of the coaxial jets.

The most significant differences between the operating conditions are observed at the region of the H_2 jets, the F_i cycle has an equivalence ratio equal to 1.6 which is highest between the injection flow rates.

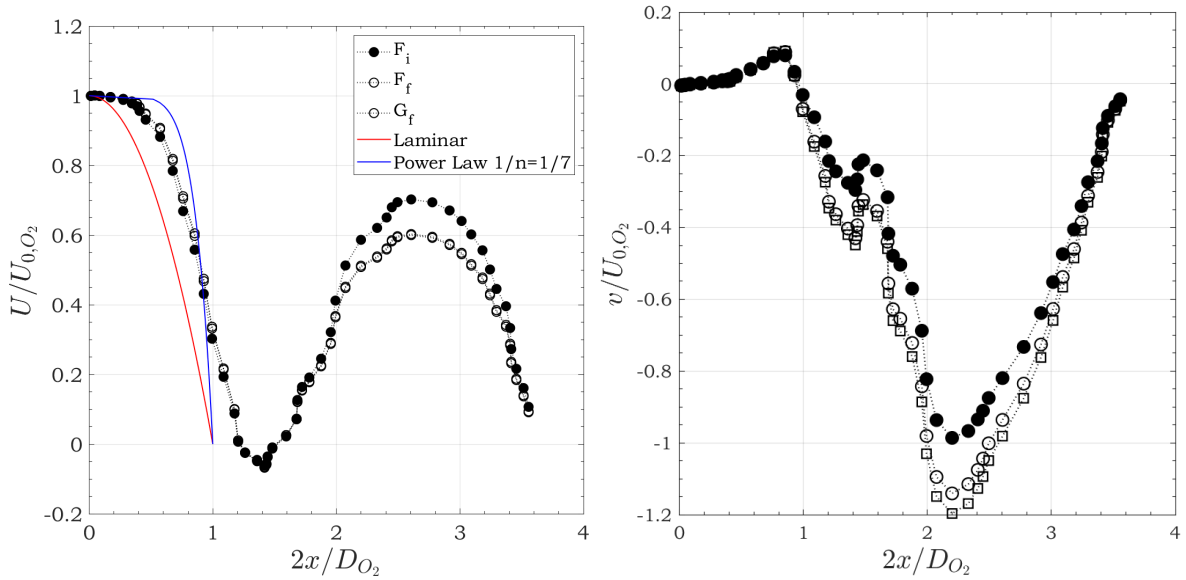

(a) Profiles of Axial Velocities (b) Profiles of Transversal Velocities

Figure C.5: Initial Conditions

In order to analyse the mixing zone, the velocity gradient is examined at the O_2 nozzle outlet along the crossed-section and depicted in figure C.6. It can be observed that the injection conditions have similar velocity gradients being the highest for the initial formation at the share layer. The F_i cycle has the lowest O_2 injection velocity and the lowest velocity difference, however the velocity ratio was the highest (see table 7.2). Moreover, close to the shear layer between the H_2 jets and the static air around, the

Cette thèse est accessible à l'adresse : http://theses.insa-lyon.fr/publication/2022LYSEI044/these.pdf
© [K. Utria Salas], [2022], INSA Lyon, tous droits réservés

velocity gradients are significant.

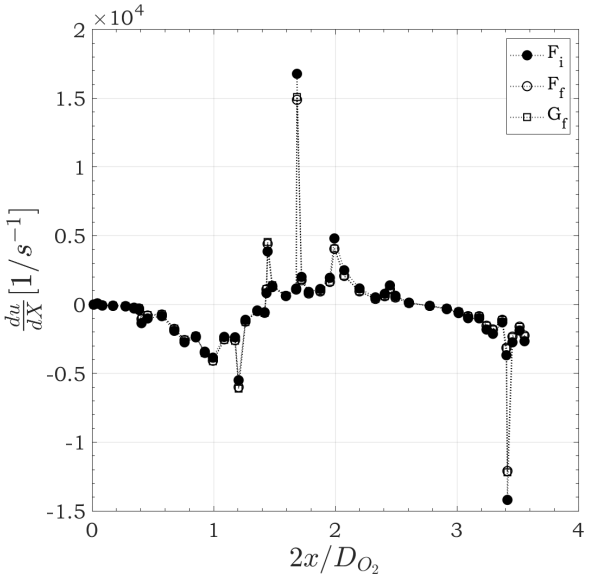

Figure C.6: Velocity gradient $\frac{du}{dX}$ $[1/s^{-1}]$

Furthermore, flow development is examined in figure C.7. As observed, final formation and growth cycles have the same central flow development. The curves intersect and behave equally. They show a low decay rate and velocity are maintained along the centreline until Y=$22D_{O_2}$ where the influence of the stagnation point can be perceived. A sudden decrease in the velocity is found at this moment.

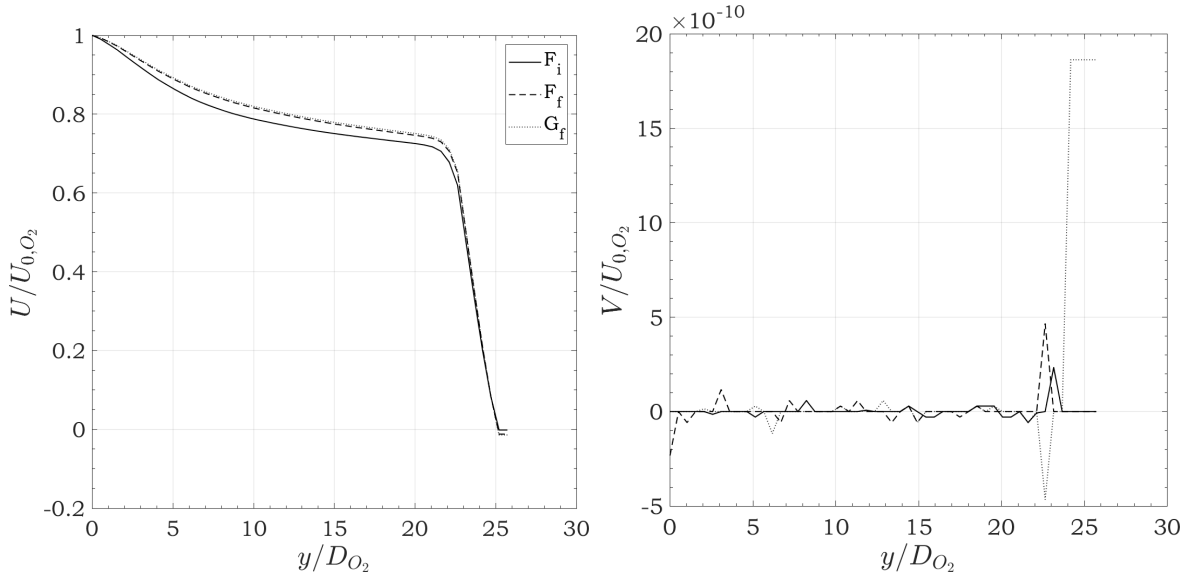

(a) Profiles of Axial Velocities (b) Profiles of Transversal Velocities

Figure C.7: Flow development at the centreline

From these results, the decay rate can be divided into three moments, the first decay

Cette thèse est accessible à l'adresse : http://theses.insa-lyon.fr/publication/2022LYSEI044/these.pdf
© [K. Utria Salas], [2022], INSA Lyon, tous droits réservés

rate is located between the O_2 outlet and Y=$5D_{O_2}$, and corresponds to the highest decay rate. From this point the decay rate seems to decrease and is kept until Y=$10D_{O_2}$. At this position the decay rate seems to be less significant and continues downstream until Y=$22D_{O_2}$. These events are related to the buoyancy effects and the influence of the coaxial jets. As observed in the experimental results, the buoyancy effect seems to affect this burner configuration until Y≅ $21D_{O_2}$. It means all the zone above the stagnation point that is located at Y≅ $25D_{O_2}$.

The influence of the coaxial flow is examined in figure C.8 with the axial velocities at different crossed sections along the Y-axis. The influence of the coaxial jets is observed until Y$6D_{O_2}$ for the three operating points. Downstream, the flow seems to behave as one single jet.

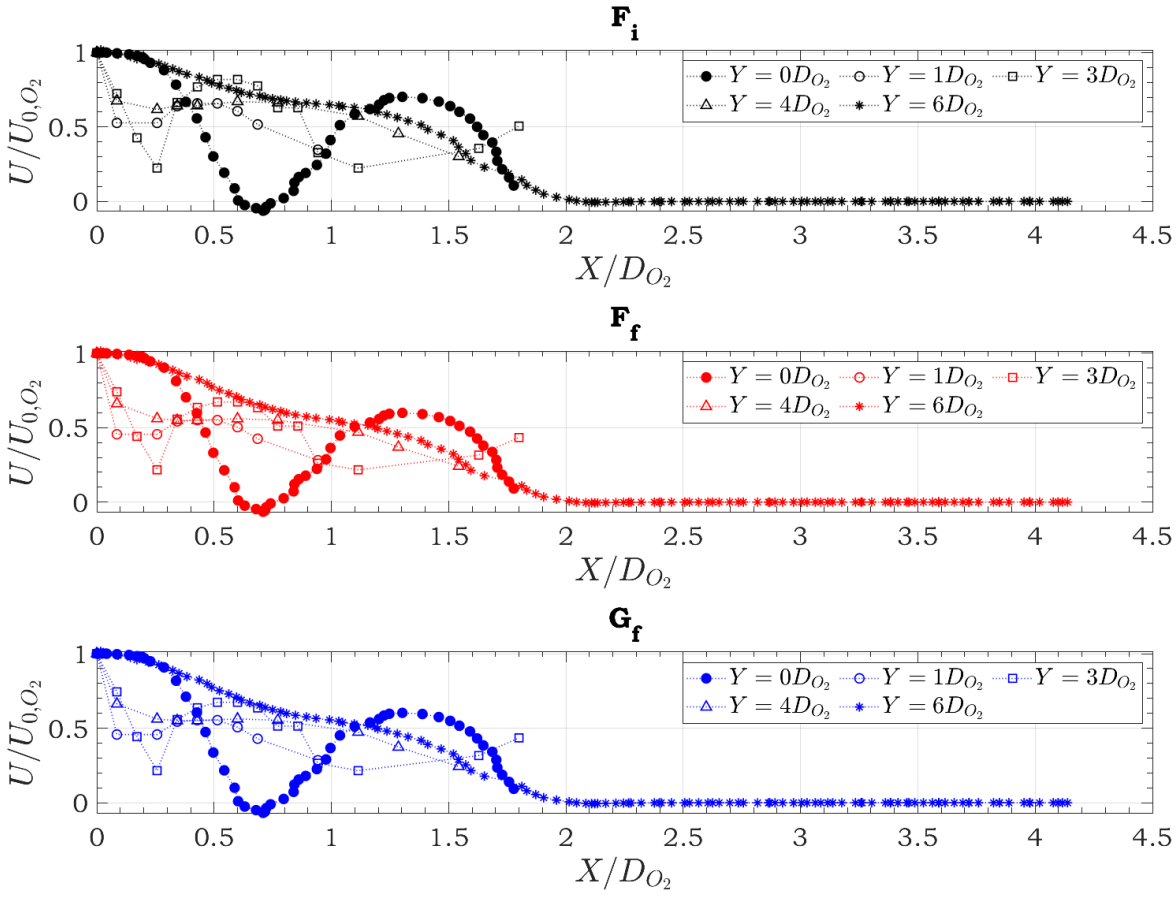

Figure C.8: Axial velocity profiles for different crossed sections

The secondary flow development is examined in figure C.9 with the half-width ($X_{0.5}$). As mentioned before, F_f and G_f behave the same, with these results it can be confirmed that this operating points show the same aerodynamic behaviour. The development is divided into four zones and shown in table C.1

- the upper part of the furnace which crossed section is smaller than the bottom part,

Cette thèse est accessible à l'adresse : http://theses.insa-lyon.fr/publication/2022LYSEI044/these.pdf
© [K. Utria Salas], [2022], INSA Lyon, tous droits réservés

- between the burner nozzle outlet and Y≅ $8D_{O_2}$, where the effects of the coaxial jets are no longer present.
- between Y≅ $8D_{O_2}$ and close to the stagnation point Y≅ $14D_{O_2}$
- the contact area, from Y≅ $16D_{O_2}$ until the stagnation point

Table C.1: Linear Equation of $X_{0.5}$ ($2X_{0.5}/D_{O_2} = ay/D_{O_2} + b$)

	Zone 1		**Zone 2**	
	Flow Establishment		Self-similarity zone	
	a	b	a	b
F_i	0.6	0.92	0.18	1.57
F_f	0.47	0.79	0.11	1.65
G_f	0.47	0.79	0.11	1.65

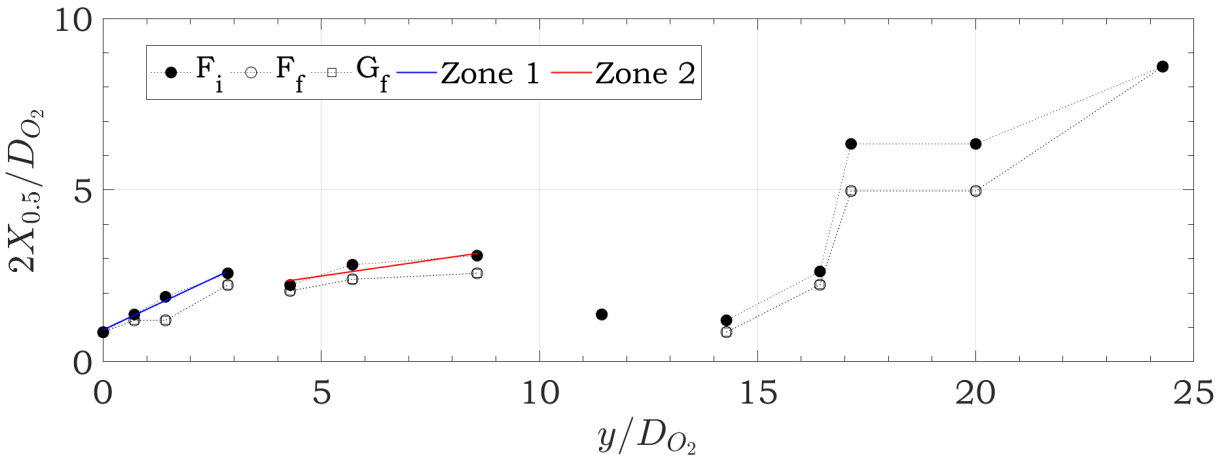

Figure C.9: Evolution of the secondary flow

The calculated values of $X_{0.5}$ are used to determine whether the self-similarity is achieved by this kind of configuration o not. The dimensionless axial velocity profiles are depicted in function of the dimensionless value $x/X_{0.5}$ across different crossed sections in figure C.10. This is found for three operating conditions at $17D_{O_2}$

Cette thèse est accessible à l'adresse : http://theses.insa-lyon.fr/publication/2022LYSEI044/these.pdf
© [K. Utria Salas], [2022], INSA Lyon, tous droits réservés

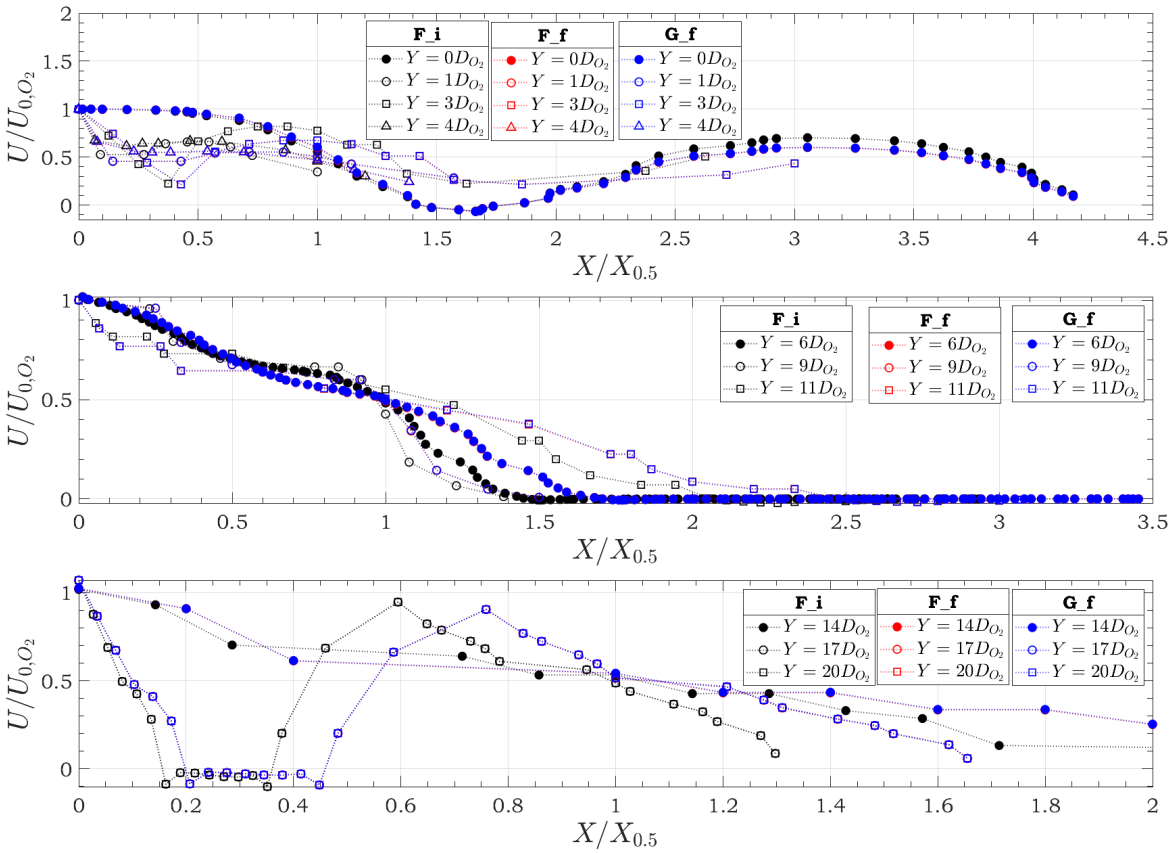

Figure C.10: Self-similarity

C.3.1 Influence of the reaction zone

Following the influence of the reaction zone is analysed for the final growth cycle. The velocity at the O_2 outlet reported an increase of 1.5 m/s for the reacting flow. In figure C.11 is depicted the axial and transversal velocity for the non-reacting flow and the reacting flow. The axial velocity profiles are almost the same except for small difference at the shear layer, the reacting flow showed higher axial velocities. In contrast at this zone the transversal velocity decreased for the reacting flow, highlighting the laminar features of the reacting flow.

Cette thèse est accessible à l'adresse : http://theses.insa-lyon.fr/publication/2022LYSEI044/these.pdf
© [K. Utria Salas], [2022], INSA Lyon, tous droits réservés

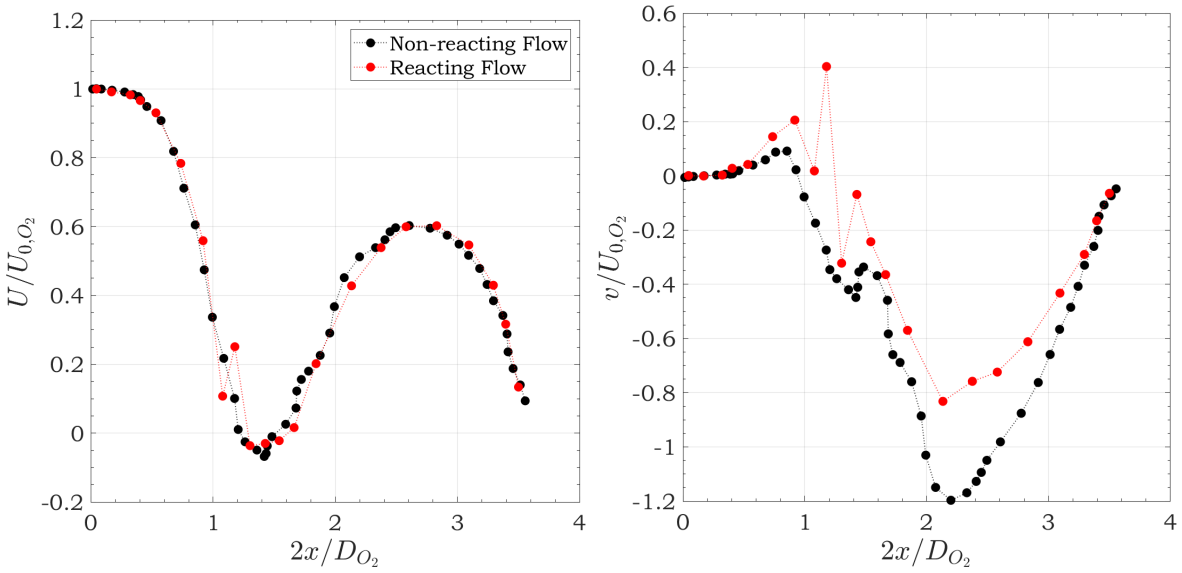

(a) Profiles of axial velocities (b) Profiles of transversal velocities

Figure C.11: Initial Conditions

The velocity gradients were also compared for the two conditions. As observed in figure C.12, the velocities gradients show close values in the O_2 jet zone. This behaviour was also obtained close to the shear layer being higher for the non-reacting flow. At the shear layer the non-reacting flow showed the highest velocity gradient. Moreover,the most significant differences are found at the H_2 jets zone close to the share layer where the velocity gradients are higher for the non-reacting flow, the presence of the reaction zone laminarised the flow as already mentioned in 6 decreasing the velocity gradient.

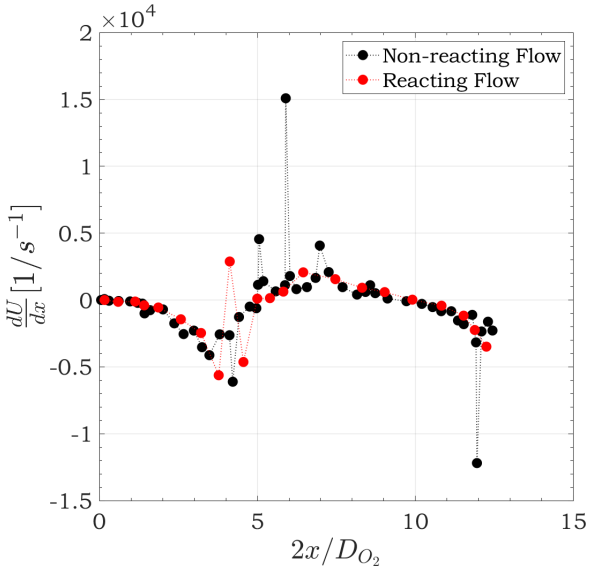

Figure C.12: Velocity gradient $\frac{du}{dX}$ $[1/s^{-1}]$

The flow development at the centreline was also examined in figure C.13. The presence

Cette thèse est accessible à l'adresse : http://theses.insa-lyon.fr/publication/2022LYSEI044/these.pdf
© [K. Utria Salas], [2022], INSA Lyon, tous droits réservés

of the reaction zone influence the flow development significantly. The decay rate for the reacting flow is lower for this condition. In contrast, the transversal component increase with the reaction zone presence, this confirms the findings of Labor (2003). The indicated that the transversal component is related to the intensity of the mixing and burning in the stoichiometric line.

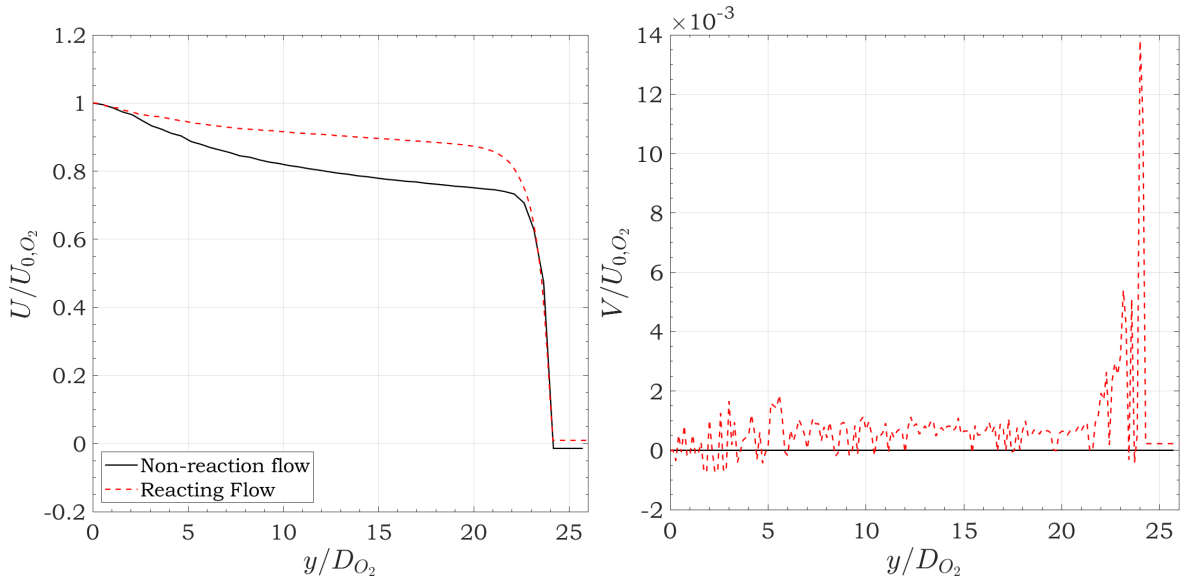

(a) Profiles of axial velocities

(b) Profiles of transversal velocities

Figure C.13: Flow development at the centreline

The evolution of the secondary flow is analysed through $X_{0.5}$ values, see figure C.14. As observed, the reacting flow shows a laminar behaviour as compared to that of the literature. The upper zone of the furnace corresponds to the establishment zone, and shows an greater slope than the bottom part of it that constitutes the self-similarity zone. In table C.2 the linear equation that defined the secondary flow field for these two zones are shown. The stagnation flow influence is observed from Y$\cong 20D_{O_2}$ with a higher slope.

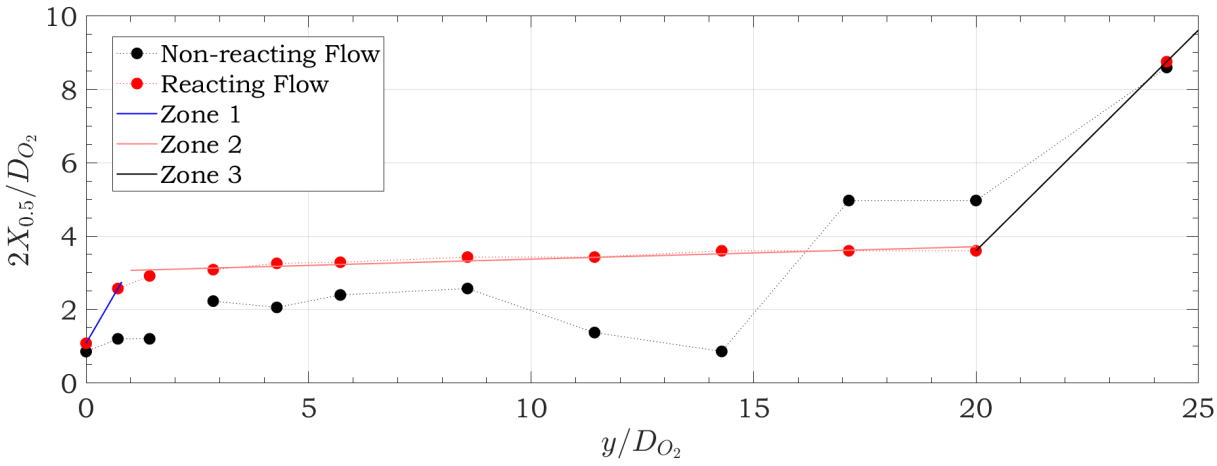

Figure C.14: Evolution of the secondary flow

Cette thèse est accessible à l'adresse : http://theses.insa-lyon.fr/publication/2022LYSEI044/these.pdf
© [K. Utria Salas], [2022], INSA Lyon, tous droits réservés

Table C.2: Linear Equation of $X_{0.5}$ ($2X_{0.5}/D_{O_2} = ay/D_{O_2} + b$)

	Zone 1 Flow Establishment		**Zone 2** Self-similarity zone		**Zone 3** Contact zone	
	a	b	a	b	a	b
Non-reacting flow	0.47	0.79	0.11	1.65		
Reacting flow	2.09	1.08	0.03	3.03	1.2	-20.46

The self-similarities are also compared in figure C.15. This is obtained downstream at Y≅ $14D_{O_2}$ for the reacting flow. It is also observed that for the reacting flow the profiles are similar to the gauss obtained experimentally in chapter 6. The gauss equation is defined as :

$$u/U_{0,O_2} = a_1 * exp(-((x/X_{0.5} - b_1)/c_1)^2) + a_2 * exp(-((x/X_{0.5} - b_2)/c_2)^2) \qquad \text{(C.23)}$$

where the coefficients are (with 95% confidence bounds):
a_1 = 0.9901 (0.8497, 1.13) b_1= 0.1029 (-0.1107, 0.3165) c_1 = 0.6844 (-0.1215, 1.49)
a_2 = 0.3571 (-0.6805, 1.395) b_2 = 0.8848 (0.5414, 1.228) c_2 = 0.4401 (0.1294, 0.7509)

Figure C.15: Self-similarity

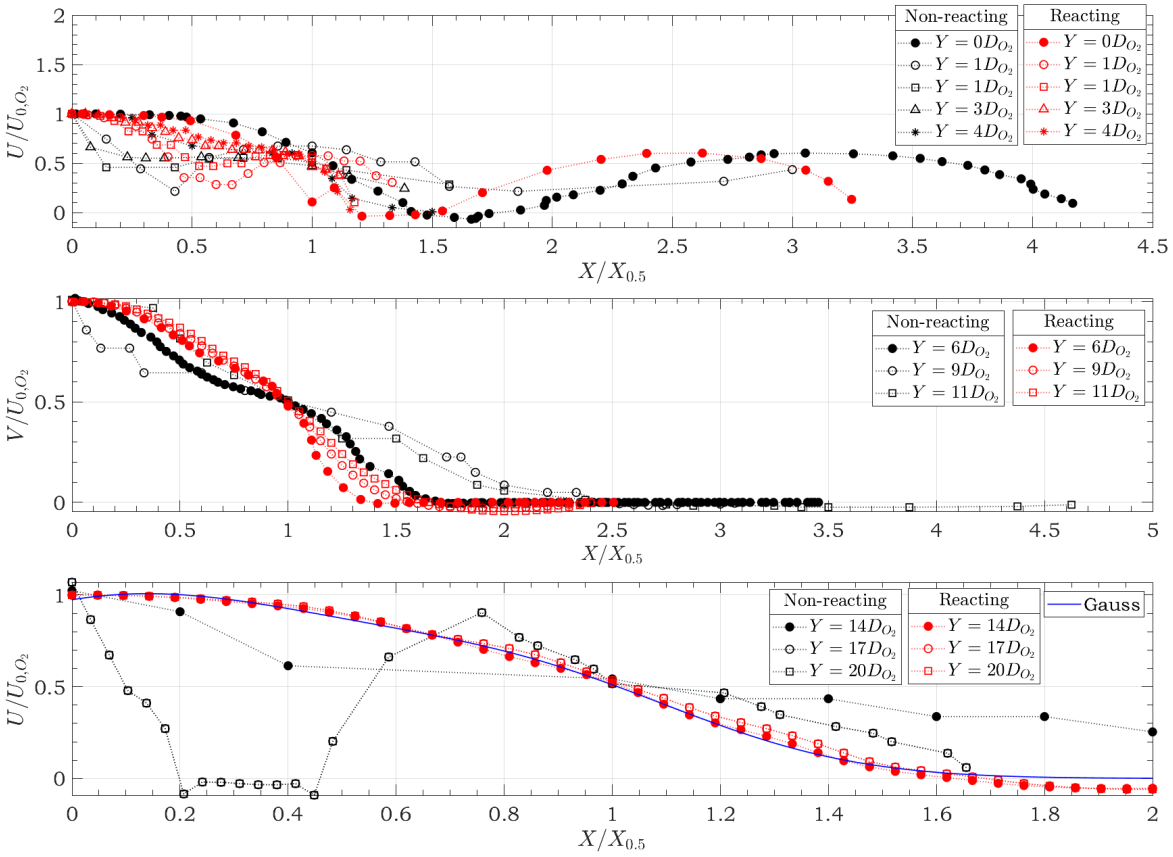

Cette thèse est accessible à l'adresse : http://theses.insa-lyon.fr/publication/2022LYSEI044/these.pdf
© [K. Utria Salas], [2022], INSA Lyon, tous droits réservés

C.3.2 Conclusions

The aerodynamics of the non-reacting flow was analysed with the crystal presence by numerical tools. A numerical model was solved using Computation Fluid Dynamics methods. The interaction of the oxidiser and fuel jets are examined finding that the three injection conditions showed a similar aerodynamics behaviour characterised by laminar features.

The influence of the coaxial flow was observed until Y$\cong 6D_{O_2}$. The self-similarities were found for the non-reacting flows at Y$\cong 16D_{O_2}$.

The reaction zone presence decreased the decay rate at the centreline and laminarised the flow at the initial conditions. Furthermore, the self-similarity is achieved before with the reacting flow. This indicates the influence of the buoyancy effects on the flow development.

Cette thèse est accessible à l'adresse : http://theses.insa-lyon.fr/publication/2022LYSEI044/these.pdf
© [K. Utria Salas], [2022], INSA Lyon, tous droits réservés

FOLIO ADMINISTRATIF

THESE DE L'UNIVERSITE DE LYON OPEREE AU SEIN DE L'INSA LYON

NOM : UTRIA SALAS
(avec précision du nom de jeune fille, le cas échéant)

DATE de SOUTENANCE : 29 avril 2022

Prénoms : Khriscia Sirelg Cecilia

TITRE : Study of stabilisation and development of a downward inverse diffusion flame for an industrial optimisation

NATURE : Doctorat

Numéro d'ordre : 2022LYSEI044

Ecole doctorale : MEGA de Lyon

Spécialité : Thermique et énergétique

RESUME :

La combustion est la pierre angulaire du développement industriel depuis près de deux siècles, fournissant de la chaleur pour de nombreux procédés industriels et représentant plus de 80% de la puissance utilisée par les turbines pour produire de l'électricité. Au fil des ans, de nombreux progrès ont été réalisés dans la compréhension de la science fondamentale de la combustion. Néanmoins, les forces réglementaires et concurrentielles engendrent le besoin d'équipements de combustion plus performants, avec un impact environnemental moindre et une plus grande flexibilité, le tout à un coût raisonnable (par exemple, accord de Paris 2015, Conférence des Nations Unies sur le changement climatique (COP26) 2021). Dans l'esprit que le système énergétique existant est principalement non renouvelable, utilisant des sources d'énergie à base de carbone. Les nouveaux enjeux de la transition énergétique nécessitent d'installer et d'intégrer un nouveau système d'énergie renouvelable tout en sécurisant l'approvisionnement et la résilience de la demande réelle. L'hydrogène, considéré par beaucoup comme le carburant alternatif propre, semble être l'une des réponses. Malgré les problèmes de sécurité associés, le développement de cette technologie contribue à ce que les pays atteignent leurs objectifs climatiques, stimulent la croissance verte et créent des emplois durables.

Cette thèse s'inscrit dans le cadre des actions menées au sein du laboratoire collaboratif RAInBOV qui associe le Cethil et la société RSA. Ils sont spécialisés dans la fabrication de verres saphir, principalement utilisés dans le domaine de l'horlogerie et du verre. Leur production nécessite de fondre la matière première et de la cristalliser. Pour cela, ils utilisent la méthode Verneuil qui consiste en un brûleur vertical descendant qui génère une flamme à diffusion inverse H_2/O_2 située dans une enceinte confinée et chargée de particules d'alumine déposées sur une germe cristalline. Dans ce cadre, l'objectif principal de cette thèse est de comprendre les mécanismes aérothermochimiques présents dans cette configuration. Concrètement, la stabilisation, la structure et le développement des flammes produites par cette configuration particulière sont analysés, ainsi que le comportement thermique du milieu de croissance cristalline.

MOTS-CLÉS : Hydrogène, flamme de diffusion inversée, oxycombustion, écoulement active, émissions radicales OH*, structure de flamme, point d'arrêt, zone de réaction

Laboratoire (s) de recherche : Centre d'Énergétique et de thermique de Lyon (CETHIL, UMR 5008)

Directeur de thèse : GALIZZI, Cédric

Président de jury : MORIN, Céline

Composition du jury :

HONORE, David	Professeur des Universités	Université de Rouen	Rapporteur
SCHULLER, Thierry	Professeur des Universités	Université Paul Sabatier	Rapporteur
MORIN, Céline	Professeur des Universités	Université Polytechnique Hauts-De-France	Examinatrice
KÜHNI, Manuel	Maître de Conférences	INSA-Lyon	Examinateur
LABOR, Serge	Docteur	RSA Le Rubis	Examinateur
GALIZZI, Cédric	Maître Conférences HDR	INSA-Lyon	Directeur de thèse

Cette thèse est accessible à l'adresse : http://theses.insa-lyon.fr/publication/2022LYSEI044/these.pdf
© [K. Utria Salas], [2022], INSA Lyon, tous droits réservés